

Nanocomposite Tribological Corrosion Resistant Coating for Robust Bearings and Gears

Vladimir I. Gorokhovsky (PhD) and Chris Bowman
Arcomac Surface Engineering, LLC.

FEBRUARY 2009 Phase II SBIR Final Report (Data Item A001)

Distribution authorized to Department of Defense only; proprietary technology; February 2009. Refer other requests for this document to AFRL/VAAL, WPAFB, OH 45433-7542.

WARNING – This document contains technical data whose export is restricted by the Arms Export Control Act (Title 22, U.S.C, Sec 2751, et seq.) or the Export Administration Act of 1979, as amended, Title 50, U.S.C., App. 2401, et seq. Violations of these export laws are subject to severe criminal penalties.
Disseminate in accordance with the provisions of DoD Directive 5230.25. (*Include this statement with all reproduced portions.*)

DESTRUCTION NOTICE – Destroy by any method that will prevent disclosure of the contents or reconstruction of the document.

© 2009 Arcomac Surface Engineering, LLC.

This work was funded in whole or in part by the Department of the Air Force contract FA8650-05-C-5007. The U.S. Government has for itself and others acting on its behalf a paid-up, nonexclusive, irrevocable worldwide license to use, modify, reproduce, release, perform, display, or disclose the work by or on behalf of the U.S. Government.

AIR FORCE RESEARCH LABORATORY
MATERIALS DIRECTORATE
WRIGHT-PATTERSON AIR FORCE BASE, OH 45433-7542
AIR FORCE MATERIAL COMMAND
UNITED STATES AIR FORCE

REPORT DOCUMENTATION PAGE

*Form Approved
OMB No. 0704-0188*

Public reporting burden for this collection of information is estimated to average 1 hour per response, including the time for reviewing instructions, searching existing data sources, gathering and maintaining the data needed, and completing and reviewing this collection of information. Send comments regarding this burden estimate or any other aspect of this collection of information, including suggestions for reducing this burden to Department of Defense, Washington Headquarters Services, Directorate for Information Operations and Reports (0704-0188), 1215 Jefferson Davis Highway, Suite 1204, Arlington, VA 22202-4302. Respondents should be aware that notwithstanding any other provision of law, no person shall be subject to any penalty for failing to comply with a collection of information if it does not display a currently valid OMB control number. PLEASE DO NOT RETURN YOUR FORM TO THE ABOVE ADDRESS.

1. REPORT DATE (DD-MM-YYYY)	2. REPORT TYPE		3. DATES COVERED (From - To)	
February 2009	SBIR Phase II Final Report A001		Jan 2005 to Feb 2009	
4. TITLE AND SUBTITLE		5a. CONTRACT NUMBER		
Nanocomposite Tribological Corrosion Resistant Coatings for Robust Bearings and Gears		FA8650-05-C-5007		
6. AUTHOR(S)		5b. GRANT NUMBER		
Vladimir I. Gorokhovsky, Chris Bowman				
7. PERFORMING ORGANIZATION NAME(S) AND ADDRESS(ES)		5c. PROGRAM ELEMENT NUMBER		
Arcomac Surface Engineering 6575 Butler Creek Rd Missoula MT 59808		5d. PROJECT NUMBER		
9. SPONSORING / MONITORING AGENCY NAME(S) AND ADDRESS(ES)		5e. TASK NUMBER		
Materials Directorate Air Force Research Laboratory Air Force Material Command Wright-Patterson AFB OH 45433		5f. WORK UNIT NUMBER		
8. PERFORMING ORGANIZATION REPORT NUMBER				
12. DISTRIBUTION / AVAILABILITY STATEMENT				
13. SUPPLEMENTARY NOTES This report contains color				
14. ABSTRACT The objective of this Phase II SBIR contract was to conduct research and develop a commercially viable coating solution to protect heavily loaded high speed gears used in aircraft power transmission. Specifically this research addresses a multi-functional coating solution needed to secure corrosion, wear, and fatigue performance on gear teeth. The program focuses exclusively on advanced metallic/ceramic coatings deposited by large area filtered cathodic arc (LAFAD) deposition technology patented by Arcomac Surface Engineering. Coatings developed during the program were thoroughly characterized in terms of physical and mechanical properties and in terms of commercial production interests such as repeatability and uniformity. Extensive performance testing in corrosion, wear and fatigue was conducted on the developed coatings and compared with the performance of the baseline gear material. The results indicate the coatings require further development to meet the program performance improvement goals. Future recommendations are provided for continued development and commercialization success.				
15. SUBJECT TERMS Coating, gears, tribology, wear, corrosion, fatigue, aerospace				
16. SECURITY CLASSIFICATION OF:		17. LIMITATION OF ABSTRACT	18. NUMBER OF PAGES	19a. NAME OF RESPONSIBLE PERSON
a. REPORT	b. ABSTRACT Unclassified	c. THIS PAGE Unclassified	62 (Report) (278 page Appendix)	Vladimir Gorokhovsky
				19b. TELEPHONE NUMBER (include area code) 406-522-7620

Standard Form 298 (Rev. 8-98)
Prescribed by ANSI Std. Z39.18

Table of Contents

<u>Section</u>	<u>Page</u>
Table of Contents.....	iii
List of Figures	iv
List of Tables	iv
Preface.....	v
Summary	1
1. Introduction.....	2
1.1 Background and Research Purpose.....	2
1.2 Arcomac Surface Engineering Coating Technology	4
1.3 Report Overview	7
2. Experimental Methods	8
2.1 Coating Deposition	8
2.2 Material Characterization.....	10
2.2.1 Substrate Identification	10
2.2.2 Coating Characterization Methods	11
2.3 Performance Testing Methodology.....	16
2.3.1 Corrosion Evaluation – Modified Navy Corrosion Test.....	17
2.3.2 Corrosion Evaluation – ASTM B117 Salt-Fog Corrosion Test.....	17
2.3.3 Wear Resistance – Unidirectional Dry Sliding Wear (Ball-on-Disc).....	18
2.3.4 Gear Simulation, Scuffing – Wedeven Load Capacity Protocol	19
2.3.5 Gear Simulation, Scuffing – Wedeven Performance Mapping Protocol.....	20
2.3.6 Contact Fatigue – Rolling Contact Fatigue Test.....	21
3. Results and Discussion	22
3.1 Coating Properties.....	22
3.1.1 Coating Thickness and Architecture	22
3.1.2 Coating Composition, Structure and Phase	23
3.1.3 Coating Morphology	26
3.1.4 Coating Roughness	26
3.1.5 Coating Hardness and Elastic Modulus	28
3.1.6 Coating Residual Stress	29
3.1.7 Coating Adhesion.....	31
3.1.8 Coating Surface Energy	33
3.2 Performance Testing Results	34
3.2.1 Corrosion Evaluation – Modified Navy Corrosion Test.....	34
3.2.2 Corrosion Evaluation – ASTM B117 Salt-Fog Corrosion Test.....	35
3.2.3 Wear Resistance – Unidirectional Dry Sliding Wear (Ball-on-Disc).....	37
3.2.4 Gear Simulation, Scuffing – Wedeven Load Capacity Protocol	41
3.2.5 Gear Simulation, Scuffing – Wedeven Performance Mapping Protocol.....	43
3.2.6 Contact Fatigue – Rolling Contact Fatigue Test.....	45
3.3 Coating Uniformity Study.....	48
4. Conclusions.....	53
5. Recommendations.....	55
References.....	56
Appendices.....	57

List of Figures

<u>Figure</u>	<u>Page</u>
Figure 1. Plan view schematic of FAPSID-700 coating system.....	5

List of Tables

<u>Table</u>	<u>Page</u>
Table 1. Material Types and Properties (Coating Substrates)	11
Table 2. Coating Thickness.....	23
Table 3. XPS Results - Coating Composition (Atomic %).....	24
Table 4. XRD Results - Coating Structure, Phase, Crystal Size.....	24
Table 5. RMS Surface Roughness	27
Table 6. Coating Hardness and Elastic Modulus	28
Table 7. Coating Residual Stress	30
Table 8. Coating Rockwell (HF) Adhesion Results (Polished P675).....	31
Table 9. Coating Scratch (Lc) Adhesion Results (Polished P675)	32
Table 10. Coating Contact Angle (Oil Wet-ability) Results.....	33
Table 11. % Area Coverage of Red Corrosion	36
Table 13. Uni-directional Sliding Wear Results, 1N Load	38
Table 14. Uni-directional Sliding Wear Results, 5N Load	39
Table 15. Load Capacity (LC) Test Results.....	42
Table 16. Performance Mapping (PM) Test Results	44
Table 17. RCF Results	46
Table 18. Coating Uniformity - Vertical Thickness Distribution	49
Table 19. Coating Uniformity – Composition	50
Table 20. Coating Uniformity - Adhesion (Rockwell HF)	51
Table 21. Coating Uniformity - Hardness and Modulus.....	51
Table 22. Coating Thickness Uniformity – Spur Gear	52

Preface

This effort was wholly funded by the Department of Defense and issued by USAF/AFMC under SBIR Phase II contract number FA8650-05-C-5007. Arcomac Surface Engineering would like to thank the SBIR program manager Dr. Andrey A. Voevodin (AFRL/MLBT) for his help and support in this effort. We would also like to thank the Steve Hammond, Subhash Naik, Sushil Jain, and Robert Stusrud of Rolls-Royce for there guidance and support throughout the research effort. Lastly we would like to thank David Van Vorous, Erik Rassi, Ben Kaluza, and Paul Gannon all of Arcomac Surface Engineering for the invaluable parts they played in the Phase II research effort.

Summary

This report details the culmination of the extensive research and characterization effort conducted by Arcomac Surface Engineering under Phase II contract funding, topic AF04-142 titled Robust Bearings and Gears (DoD contract FA8650-05-C-5007). The contract effort dates were January 2005 to November 2008. The objective of this Phase II SBIR contract was to conduct research and develop a commercially viable coating solution to protect heavily loaded high speed gears used in aircraft power transmission. Specifically this research is aimed at improving the performance of Lift Fan gears which are critical components of the F-35B (Joint Strike Fighter) short take-off and vertical landing airframe variant. The current gear material is Pyrowear 675 a carburizing steel with 13% chromium content which shows good scuffing and fatigue properties but is under specification in regards to corrosion resistance. The Lift Fan component system is under JSF contract production by Rolls-Royce Corporation and Arcomac has worked in parallel with AFRL and Rolls-Royce throughout the Phase II effort to define research and commercialization goals.

Successful surface engineering of Pyrowear 675 Lift Fan gears requires a multi-functional coating solution in order to secure corrosion, wear, and fatigue performance on gear teeth. All coatings included in this effort were deposited using Arcomac Surface Engineering's LAFAD technology. Research and development during the Phase I and Phase II efforts was directed at optimization of coating design through iteration and parallel improvement of LAFAD technology to improve coating repeatability and reliability. The culmination of the research optimization effort was the down selection of three coating formulations; a TiCr-TiCrN, a Cr-CrN and a CrC coating.

Coatings developed during the program were thoroughly characterized in terms of physical and mechanical properties and in terms of commercial production interests such as repeatability and uniformity. The resulted showed that LAFAD technology can deposit coatings with excellent repeatability and due to well characterized uniformity results on complex shapes provides a high level of confidence towards coating scale up and commercial production of coated Lift Fan gears. Extensive performance testing in corrosion, wear and fatigue was conducted on the developed coatings and compared with the performance of the baseline gear material. Cr-CrN and CrC coatings performed well in fatigue and corrosion while the TiCr-TiCrN performed poorly. Significant improvement in wear performance for dry sliding conditions was realized for TiCr-TiCrN coatings in contact with Cr-CrN and CrC coatings. Scuffing resistance of TiCr-TiCrN coatings in contact with Cr-CrN and CrC coatings was not as good as the baseline P675 case although TiCr-TiCrN/CrC contact passed the industry standard for gear scuffing performance. In summary the TiCr-TiCrN, Cr-CrN, and CrC coatings demonstrated some marked improvements in certain performance areas but a unified solution to corrosion, wear, and fatigue was not reached.

The overall conclusion of the program is that the LAFAD process demonstrated significant potentials, although the current research and design state of the coatings achieved in this effort requires additional development to meet the Lift Fan design goals. Future recommendations are provided for continued development and commercialization success.

1. Introduction

1.1 Background and Research Purpose

Air Force Small Business Innovation Research (SBIR) topic AF04-142 was posted in the first quarter of 2004. The stated objective of the topic is to “*Develop and produce surface treatments and materials for bearings and/or gears capable of exceeding the current physical limitations of material systems and design architectures of jet engines*”. Arcomac Surface Engineering’s patented surface engineering technologies provide a unique means to deposit advanced coatings on bearing and gears which provide performance improvements in demanding wear, corrosion and fatigue applications. Arcomac Surface Engineering was awarded a Phase I SBIR contract in 2004 which was successfully completed and followed with a Phase II research contract, FA8650-05-C-5007, in May of 2005. The AF04-142 topic is specifically aimed at performance improvements for the F-35B (Joint Strike Fighter) vertical take-off and landing airframe variant. Forward airframe vertical thrust is provided by a Lift Fan system while rear airframe vertical thrust is provided by a vectored thrust system denoted as the 3-Bearing Swivel Duct (3BSD). Both the Lift Fan and 3BSD component systems are under JSF contract production by Rolls-Royce Corporation. Arcomac has worked in parallel with AFRL and Rolls-Royce since Phase I research to define research and commercialization goals. Technically the AF04-142 topic encompassed improvements to both the Lift Fan and 3BSD systems but early in the Phase II effort a combined decision was made to focus research on the Lift Fan gears as the scale of the research effort was deemed to broad for a single Phase II funded program. The duration of the Phase II research technical effort spanned May 2005 to December 2008 with the culmination of the program results being presented in this report.

The Lift Fan system provides a serious challenge for gear design and protective coating design. A two-stage low-pressure turbine on the engine provides the horsepower necessary to power the Rolls-Royce designed Lift Fan. The Lift Fan generates a column of cool air that provides nearly 20,000 pounds of lifting power using variable inlet guide vanes to modulate the airflow, along with an equivalent amount of thrust from the downward vectored rear exhaust to lift the aircraft. The Lift Fan system is comprised of three helical bevel gears approximately 30-40cm (12”-16”) in diameter, the driver gear is directly powered from the main turbine engine while the two driven gears power the counter rotating intake and outtake thrust fans. To produce the required thrust the gears are heavily loaded and rotate at very high meshing speeds of ~7.7m/sec (1520ft/min). Lubrication is provided by Royco 555 synthetic oil (or similar DOD-L-85734) at temperatures up to 150°C. Two gear materials have been pursued by Rolls-Royce both with unique design challenges. Pyrowear 53 is a carburizing steel with significantly higher case temper resistance than conventional gear materials such as AISI 9310, 3310, or 8620, although the low chromium content in all of these steels makes them particularly susceptible to corrosion. Pyrowear 675 is a carburizing steel with 13% chromium content that possesses better hot hardness and fracture toughness but lower yield strength than Pyrowear 53. During the Phase II effort a combined decision was made for Arcomac to focus coating research efforts on Pyrowear 675 largely due to the incompatibility of the low tempering temperature of Pyrowear 53 and coating processing temperatures. Early in the Phase II effort it also became clear that the corrosion resistance of Pyrowear 675 did not meet Rolls-Royce specifications. Rolls-Royce

conducted extensive trials from 2005-2008 to optimize the carburization process for Pyrowear 675 while at the same time Arcomac conducted coating research under Phase II funding.

Successful surface engineering of Pyrowear 675 Lift Fan gears must be viewed as a multi-functional task. Lift Fan gears require a solution which can provide and maintain corrosion protection on gear teeth which are heavily loaded and subject to high sliding speeds. Traditional corrosion coatings applied to Lift Fan gear teeth fail very early in wear and fatigue exposing the gear teeth to corrosion, even though non-contact surfaces of the gear are protected. Corrosion protection can not be separated from wear and fatigue performance as any failure of a coating which exposes the Pyrowear 675 substrate compromises corrosion performance. Therefore corrosion, wear, and fatigue were defined as the three coating design issues of primary importance.

- Corrosion Performance – Develop coatings(s) which demonstrate 100% corrosion protection under Rolls-Royce modified Navy corrosion test protocol. It is desirable to show 100% corrosion protection for the ASTM B117 salt-fog corrosion test protocol after 336hrs of exposure.
- Wear Performance – Wear failure of the coating(s) which results in Pyrowear 675 exposure constitutes corrosion failure and failure of the coating design goals. All three Lift Fan gears require corrosion protection therefore a coating solution must provide favorable friction and wear properties in coating versus coating sliding contact. Develop coating(s) which demonstrate low friction sliding response as compared to Pyrowear 675 and wear at a rate which meets or exceeds the design lifetime of the Lift Fan gear. Specifically the coating(s) must show equivalent or better scuffing performance under simulated Lift Fan gear operation and improved performance under emergency oil-off (dry sliding) conditions.
- Fatigue Performance – Develop coating(s) which meet or exceed the contact fatigue and bending fatigue performance of Pyrowear 675. Fatigue failure of the coating(s) which results in Pyrowear 675 exposure constitutes corrosion failure and failure of the coating design goals.

In addition to the three primary design performance goals the following commercial production concerns were also considered of primary importance; process repeatability, process scale-up to actual Lift Fan gears, and process cost. A design specification of $7\mu\text{m}$ maximum coating thickness was imposed by Rolls-Royce as the maximum thickness which would not require redesign of the gear tolerances.

During the Phase I and Phase II research efforts Arcomac conducted iterative research and design methodologies to continually optimize coating design and performance as well as to demonstrate process repeatability and scale-up. This report focuses almost entirely on the final outcome of the research effort, which is the characterization and performance testing on the final coatings selected to have the best chance to meet the design goals for the Lift Fan gear system. As appropriate to understanding the current results, discussion is included regarding early research, proto-type coatings, early coating performance, etc, but for the sake of keeping the report to a manageable length this type of discussion is kept to a minimum.

1.2 Arcomac Surface Engineering Coating Technology

In many applications PVD and low pressure CVD sources are used for deposition of coatings and surface treatment. Conventional metal vapor sources can provide high deposition rates but low energy of the metal vapor atoms results in low density, poor adhesion, poor structure and morphology of the coatings. It is well established that assistance of the coating deposition process with bombardment by energetic particles can dramatically improve coatings by densification of the depositing materials, reducing the grain size and improving coating adhesion. In these processes, the surface layer is affected by a high rate of bombardment by energetic ions, which affects the mobility of depositing metal vapor atoms and in many cases creates metastable structures with unique functional properties. This approach is especially productive in deposition of nano-structured and/or nanocomposite coatings with ultra-fine or glass-like amorphous structure. The ratio of high energetic particles to the total oncoming mass flow represents one of the most important characteristics of such processes. It is essential that this ratio is calculated at the deposition spot. If ion bombardment is provided in a different part of the coating chamber where the substrates are transferred *after* coating deposition by conventional magnetron or thermal evaporator, this cannot be considered as ion assisted deposition but rather as a post deposition ion treatment. In the context of a popular structure-zone model, the energetic ions produced by the cathodic arc process lead to denser coatings at lower deposition temperatures. Ion bombardment of the coating surface influences gas adsorption behavior by increasing the sticking coefficient of gases such as nitrogen and changing the nature of adsorption sites from lower energy physi-sorption sites to higher energy chemi-sorption sites. These concepts explain why the vacuum arc process which is able to generate strongly ionized plasma in large areas is so effective in forming oxides, nitrides and carbides during reactive deposition of compound coatings.

During the past thirty years, from the time when it was first introduced by the Kharkov Physical-Technical Institute research group, filtered cathodic arc deposition (FCAD) technology has slowly but surely made inroads into the world of physical vapor deposition (PVD) [1,2]. The main advantage of the FCAD process is that it can generate fully ionized metal vapor plasma consisting of atomic ions with a substantial concentration of multi-charged ions, but without contamination from multi-atomic clusters and macro particles. The filtered arc vapor plasma beam consists of dense plasma with a relatively high electron temperature on the order of 3 to 5eV; this contributes to an increased ionization rate of the gaseous atmosphere via electron collisions with gas atoms and molecules.

The kinetic energy of the FCAD metal ion flow exceeds the thermal energy of the FCAD plasma by an order of magnitude, ranging from 40 to 200 eV [1-5]. In sharp contrast to sputtering processes, the cathodic arc evaporation process (both direct arc and filtered arc) does not require a minimum background pressure of inert gas, and can generate metal vapor plasma in any reactive gas atmosphere or even in deep vacuum [1]. These properties of the FCAD process make it advantageous compared to conventional -- and even ionized -- magnetron sputtering processes in many applications requiring high ionization rate of the depositing metal-gaseous vapor to increase coating density and other functional properties and eliminate or substantially reduce the defects in the coatings.

The main obstacle to using conventional FCAD technology is the low productivity of this process, which restricts its usage to semiconductors, optical coatings and some ultra-thin hard coatings used in bio-medical and tribological applications. On the other hand, Large Area Filtered Arc Deposition (LAFAD) technology, developed by Arcmac overcomes these limitations by providing a highly productive, robust, industry-friendly process which combines the high productivity rate of conventional direct cathodic arc deposition (DCAD) and magnetron technologies, with the capability of generating a nearly 100% ionized metal-gaseous vapor plasma with large kinetic energy and with no macro particles, droplets, multi-atom clusters and other contaminants [2,3,6-9]. The unidirectional dual arc LAFAD vapor plasma sources can be used as an alternative to conventional DCAD and magnetron based processes when the high productivity and uniformity needed for most industrial applications must be accompanied by the high ionization and high kinetic energy of atomically clean vapor plasma. Since the LAFAD plasma source operating pressure regimes are overlapping with most of the conventional vacuum vapor deposition technologies (magnetron sputtering, EBPVD, thermal evaporation, PACVD etc.) it can be used in hybrid processes combining its high deposition and high ionization rates in conjunction with conventional PVD and low pressure PACVD processes as was demonstrated in [1,3,6,7,9-12].

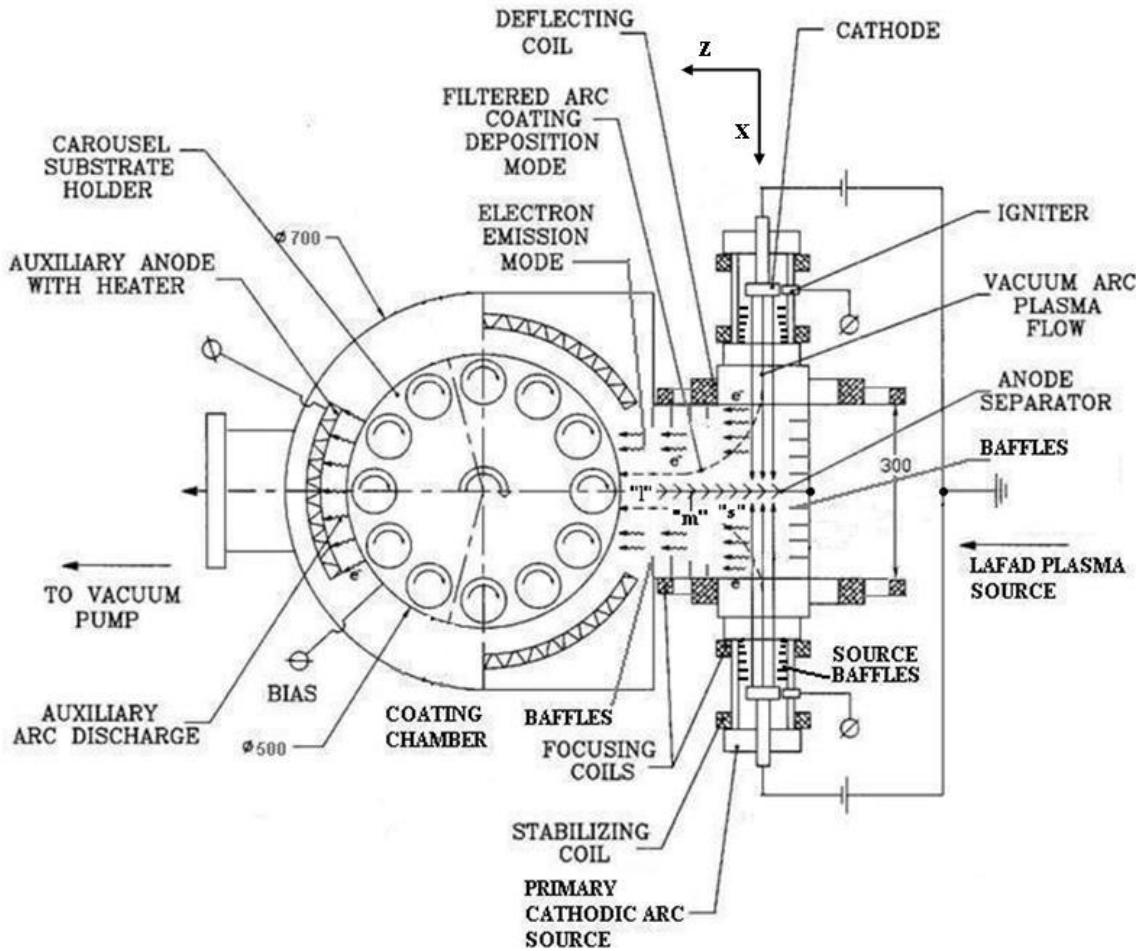


Figure 1. Plan view schematic of FAPSID-700 coating system

The hybrid Filtered Arc Plasma Source Ion Deposition (FAPSID) system developed and built at Arcomac R&D center in Bozeman MT provides a hybrid filtered arc-magnetron vapor plasma environment for depositing multi-elemental multiphase nanocomposite coatings with complex architectures [8,10,11]. This design layout, combining LAFAD sources with conventional UBM and EB-PVD metal vapor sources integrated in one vacuum chamber, as illustrated in **Figure 1**, enables the evaporation of different ceramics and metals in highly ionized vapor plasma. This process technically immerses the substrates in a highly ionized environment. Plasma immersion technology deposits nano-structured coatings having functionally graded or multiple-layer architecture. Coatings deposited from highly ionized metal vapor plasma by vacuum arc based coating deposition processes are characterized by their thermodynamically metastable nature. Understanding the phase transformations, morphological and structural evolution in nanostructured coatings deposited under conditions of intense ion bombardment will allow optimizing their functional properties for wide range of applications.

Figure 1 shows the Arcomac's hybrid FAPSID-700 surface engineering system utilizing a vacuum chamber 0.7 meters in diameter by one meter tall, equipped with a unidirectional dual arc LAFAD plasma sources. The rotatable substrate turntable, 0.5 meters in diameter, is installed in the center of the coating chamber and allows for single or double rotation of the substrates that are being coated. The coating chamber is equipped with an array of radiant heaters and with diagnostic equipment including optical pyrometers and thermocouples to measure substrate temperature. The LAFAD plasma source consists of the plasma guide chamber with baffles installed along its walls and the exit tunnel window which is 300 mm wide by 400 mm tall. Two pairs of deflection coils are located along the opposite walls of the plasma duct chamber. The primary direct cathodic arc deposition (DCAD) sources, consisting of the cathode target, surrounded by tubular anodes with steering and focusing coils, are attached to opposite walls of the plasma guide chamber adjacent to the exit tunnel portion. In addition, two vertical rastering coils are positioned on the top and bottom flanges of the plasma guide chamber for rastering the filtered arc flow [9,11]. This provides high uniformity of the coating thickness distribution over large deposition areas. An anode separator or dividing baffle can optionally be installed into the plasma duct to separate the two vapor plasma flows generated by the two primary cathodic arc sources [9,11]. A separation of the opposite vapor plasma flows generated by the two primary DCAD sources of the LAFAD plasma source allows the production of nanolaminated coatings by exposing the rotating substrates in turn to the plasma flows generated by the opposing primary DCAD sources equipped with different targets (e.g. Ti and Cr, Ti and Al etc.) [11,13]. When the dividing baffle is removed, the two opposite plasma flows generated by the primary DCAD sources with cathode targets of the same or different composition are mixed in the exit tunnel area, forming a uniform unidirectional plasma stream for deposition of a wide variety of single component or multi-elemental nanocomposite coatings [8,9,11].

When the deflection/focusing coils of the filter chamber are turned on, the vapor plasma generated by the primary DCAD sources flows into the plasma guide chamber from opposite directions and turns around the corner of the plasma guide exit tunnel toward the coating chamber. The ability of fast opening and closing the LAFAD source by turning on and off the deflecting magnetic field operating as a magnetic shutter provide a capability of interrupting and/or modulating deposition which is especially suitable for forming a nanostructured coating architectures. When the deflection/focusing coils of the filter chamber are turned off, an

auxiliary arc discharge can be established between the primary arc cathodes of the LAFAD source and the auxiliary arc anode located in a coating chamber behind the turntable (see **Figure 1**). This discharge provides ionization and activation of the gaseous atmosphere in the main chamber, producing a highly ionized gaseous plasma during such technological stages as ion cleaning/etching, gaseous ion implantation and ionitriding/oxynitriding/carburizing [3,6,7,8,11]. The auxiliary arc plasma immersion environment provide thermal-chemical treatment of substrates (ionitriding, carbonitriding, carburizing). A combination of ionitriding followed by coating deposition (duplex process) can be accomplished in a single vacuum cycle [3,6,7,8,11]. This process is in use coating various kinds of steel for applications such as medical instruments, cutting and forming tools, and engine components. This duplex filtered arc plasma immersion surface engineering process can be used to provide the entire multiphase multiple-layer treatment of bearings and gears, including ionitriding or plasma carburizing followed by tribological coating, in one vacuum cycle.

In LAFAD process the stream of 100% ionized metal vapor plasma is propagating along magnetic field lines from primary cathodic arc targets throughout the plasma guide chamber toward substrates to be coated installed in a processing chamber. The topology of the plasma confining curvilinear magnetic field of the LAFAD plasma filtering arrangement suppressing the transversal diffusion of the vapor plasma across magnetic field lines which effectively suppressing the metal vapor plasma losses on walls of plasma guide chamber, resulting in high deposition and target utilization rates which approaches and even exceeds the outcome of the conventional non-filtered direct cathodic arc deposition sources [3,9,11]. The deposition rate of the TiN based coatings deposited by one unidirectional LAFAD vapor plasma source on substrates installed on rotating turntable 0.5 in diameter of the batch coating system reaches 2.5 $\mu\text{m}/\text{hr}$ for 140 amperes of the primary cathodic arc source current and 5 amperes for 200 amperes of the primary cathodic arc source currents. The LAFAD process also allows vertical rastering of the metal vapor plasma, which is not possible in a conventional direct cathodic arc deposition consisting of large amount of neutral atoms, clusters and macroparticles. Using vertical magnetic rastering the coating thickness uniformity of LAFAD process is better than +/- 15% for 6" deposition area in a vertical direction and +/- 25% in 11" vertical deposition area [9]. Magnetic field of LAFAD source extends into the coating chamber or, when two or more LAFAD sources are integrated in one processing chamber, their magnetic force streamlines are coupled forming a magnetically confined vapor plasma corridors inside of the processing chamber which results in high conformity of LAFAD coating process when it is used for coating of 3D complex shape components [1,2,6,7,9,11].

1.3 Report Overview

This report details the culmination of the extensive research and characterization effort conducted by Arcomac Surface Engineering under Phase II contract funding, topic AF04-142 titled Robust Bearings and Gears (DoD contract FA8650-05-C-5007). The contract effort dates were January 2005 to November 2008. The structure of the report follows the standard format for technical papers; introduction followed by description of experimental methods, presentation and discussion of results, conclusions and future recommendations. Appendices in this report have a weighted importance, please see special note below.

SPECIAL NOTE - The report contains a large amount of data relating to coating characterization and performance testing. Much of the data presented is in image, plot, or table format which benefits from large scale and high resolution presentation. Often the clarity of data of this type is compromised by having to fit/shrink it within the formatting requirements of a formal technical report. As such the decision was made to create an extensive set of appendices (17 appendices in all) where each appendix is used to present data from a specific type of test in detail with full size images and plots. This allowed for the report to be written as succinctly as possible with minimal use of figures and tables in the body of the report for the reader who wants a good overview, while still providing the option to review data in detail by referencing the appendices. All appendices have a title which logically relates to the type of testing covered, e.g. the Salt Fog corrosion testing appendices is titled Appendix SF. The appendices are referenced in this report by title and page in the following format (**page #SF_3**), which indicates the reader should refer to Appendix SF page 3. It is strongly recommended that the reader print out only the report and not the appendices. While reading the report the reader is encouraged to refer to the full color appendices in digital format, which is more convenient for quickly finding the referenced appendix page.

2. Experimental Methods

2.1 Coating Deposition

All coatings included in this effort were deposited using Arcomac Surface Engineering's LAFAD technology which is described in detail in section 1.2 of this report. Research and development during the Phase I and Phase II efforts was directed at optimization of coating design through iteration and parallel improvement of LAFAD technology to improve coating repeatability and reliability. The primary coating design parameters iterated on were coating architecture, coating deposition bias, coating deposition pressure, and coating deposition temperature. The primary markers used for down selection of coatings were coating adhesion, coating residual stress, coating corrosion performance, coating wear performance, coating fatigue performance, and coating production cost. The culmination of the research optimization effort was the down selection of three coating formulations; a TiCr-TiCrN, a Cr-CrN and a CrC coating. The experimental description for production of these coatings follows.

All substrates were initially wiped clean with acetone and lint free wipes and then sequentially subjected to; ultrasonic cleaning in HPLC grade acetone for 5min, removal and brief air drying, a second ultrasonic cleaning in fresh HPLC grade acetone for 5min, removal and brief air drying, a final ultrasonic cleaning in HPLC grade isopropyl alcohol, and then air dried. Cleaned samples were loaded into fixtures which had been sand blasted to bare metal and ultrasonically cleaned in acetone for 10min. The fixture-sample assemblies were then de-magnetized, the samples faces to be coated were force air blown with dry air to remove any dust and then the samples were immediately loaded into the coating chamber. The substrate table rotation was set to 9rpm and all samples except ball geometries were fixed in single rotation about the table axis. Plasma distribution at the duct exit can be considered uniform in the horizontal direction due to sample rotation. In the vertical direction the plasma has a Gaussian distribution which logically results in a Gaussian thickness distribution. For this reason all samples were positioned in the chamber

to be equally spaced vertically about the maximum deposition zone of the plasma. The concept of coating uniformity is further addressed in section 3.3.

In integral part of the coating plan was to demonstrate basic coating process repeatability as evaluated by the consistency of testing results for coating properties and performance. To achieve this two separate coating depositions were performed for each TiCr-TiCrN, Cr-CrN and CrC coating. The notation used is Dep1 to indicate coatings produced in the first process and Dep2 to indicate coatings produced in the second process.

All coating deposition processes began with a 12hr (overnight) pump down to reach ultimate vacuum (~0.001mTorr); this was performed at 250°C which also served to bake out any moisture present on the samples, fixtures, chamber walls, etc. Upon reaching ultimate vacuum a 1hr step at 250°C at 0.8mTorr in argon (Ar) was performed. The deposition processes started with a 20min Ar+ ion sputtering cleaning step with the following set points; 0.8mTorr pressure in Ar, 250°C chamber temperature, -250V bias, 100A target current, 60A auxiliary anode current, magnetic filter off. Ionization of argon for sputtering is facilitated by the auxiliary arc discharge established between the primary arc cathodes and the auxiliary arc anode located in the coating chamber, for this step the metal ion deflection filter is turned off and only electrons enter the chamber. Following sputtering a 120sec high voltage metal ion implantation step was conducted to secure good adhesion of the coating to the substrate, set points were as follows; 0.8mTorr pressure in Ar, 250°C chamber temperature, -1000V bias, 100A target current and 20A auxiliary anode current, magnetic filter on. The aforementioned steps are common to all deposition processes; the unique deposition steps for the TiCr-TiCrN, Cr-CrN and CrC coatings follow.

The TiCr-TiCrN coating was produced by using one 99.99% Ti target and one 99.99% Cr target mounted in the LAFAD source. This approach allowed for control of the ratio of Ti/Cr plasma flow by changing the ratio of current applied to the Ti and Cr targets. It was established during this research effort that the ratio of volumetric erosion rates for the Ti and Cr targets was directly related to the Ti/Cr atomic% composition of the coating, which allowed for predictable process control of the Ti/Cr ratio and optimization studies of coating properties. Immediately following the 120sec Ti ion implantation step metallic TiCr was deposited for 600sec with the following set points; 1mTorr pressure in Ar, ~300°C chamber temperature (includes plasma heating effect), -40V bias, Cr target 200A total arc current and Ti target 140A total arc current. A brief 60sec step was programmed to transition the chamber gas concentration from Ar to N for deposition of the TiCrN layer. The TiCrN layer was deposited for 1200sec (1140sec + 60sec gradient transition) with the following set points; 1mTorr pressure in 97% N/3% Ar, ~300°C chamber temperature (includes plasma heating effect), -40V bias, Cr target 200A total arc current and Ti target 140A total arc current. The TiCr(600sec) followed by TiCrN(1200sec) is referred to as a single bi-layer. The bi-layer architecture was repeated 11 times for a total deposition time of 19800sec to meet the goal thickness of ~6 μ m. The TiCr-TiCrN coating is thus referred to as a multi-layer coating comprised of alternating TiCr(metallic) and TiCrN(ceramic) layers.

The Cr-CrN coating was produced by using two 99.99% Cr targets mounted in the LAFAD source. Immediately following the 120sec Cr ion implantation step metallic Cr was deposited for 300sec with the following set points; 0.4mTorr pressure in Ar, ~300°C chamber temperature (includes plasma heating effect), -40V bias, each Cr target 200A total arc current. A brief 60sec

step was programmed to transition the chamber gas concentration from Ar to N and gas pressure from 0.4mTorr to 1mTorr for deposition of the CrN layer. The CrN layer was deposited for 1500sec (1440sec + 60sec gradient transition) with the following set points; 1mTorr pressure in 97%N/3%Ar, ~300°C chamber temperature (includes plasma heating effect), -40V bias, each Cr target 200A total arc current. The Cr(300sec) deposition followed by CrN(1500sec) deposition is referred to as a single bi-layer. The bi-layer architecture was repeated 16 times for a total deposition time of 28800sec to meet the goal thickness of ~6 μ m. The Cr-CrN coating is thus referred to as a multi-layer coating comprised of alternating Cr(metallic) and CrN(ceramic) layers.

The CrC coating was produced by using two 99.99% Cr targets mounted in the LAFAD source. Immediately following the 120sec Cr ion implantation step metallic Cr was deposited for 300sec with the following set points; 0.4mTorr pressure in Ar, ~300°C chamber temperature (includes plasma heating effect), -40V bias, each Cr target 200A total arc current. A brief 60sec step was programmed to transition the chamber gas concentration from Ar to N for deposition of a CrN layer. A CrN layer was deposited for 1200sec (1140sec + 60sec gradient transition) with the following set points; 0.4mTorr pressure in 97%N/3%Ar, ~300°C chamber temperature (includes plasma heating effect), -40V bias, each Cr target 200A total arc current. This single bi-layer of Cr and CrN was followed by a Cr-N-C gradient coating deposited over 180sec with incremental decreases in N gas concentration and incremental increases in CH₄ gas concentration every 60sec. The CrC coating was then deposited for 10200sec at the following set points; 0.8mTorr pressure in 90%CH₄/10%Ar, ~300°C chamber temperature (includes plasma heating effect), -40V bias, each Cr target 200A total arc current. The CrC coating is described as a monolithic CrC coating with a thin (300nm) Cr-CrN + CrCN (gradient) adhesion bond layer.

2.2 Material Characterization

The term material characterization refers to the determination of the inherent physical and mechanical properties of the substrates and coatings used in this research effort. Detailed characterization of the Pyrowear 675 (P675) Lift Fan gear material is presented in this section which pertains directly to baseline uncoated P675 performance testing results and to coating properties when the P675 functions as a substrate. The section also details the various methods used to characterize coating properties and references are made to the appendices to supplement the information provided.

2.2.1 Substrate Identification

Pyrowear 675 (P675) is a carburizing, corrosion resistant steel with a ~13% chromium content (similar to 440 stainless steels) is known for good wear resistance and a tough ductile core similar to that of AISI 9310 steel. Rolls-Royce had selected P675 as a primary candidate for the Lift Fan gears for the fatigue and wear properties with the anticipation that the corrosion performance would be much improved over standard low chromium containing carburizing gear steels. Testing has shown that the P675 steel once carburized does not provide the desired level of corrosion protection needed on the Lift Fan gears. It is this result which precipitated the creation of this SBIR research program and has driven coating development to meet the three multifunctional goals of corrosion, wear, and fatigue performance. Over the duration of the SBIR Phase II research program extensive efforts were made to work with Rolls-Royce to obtain

Pyrowear 675 material which would exactly match what would be used for the Lift Fan gears in terms of material source, manufacturing, carburization profile, and surface roughness. Logistically this was very involved work due to the fact that Rolls-Royce was developing the heat treatment and carburization protocols for P675 in parallel with Arcomac's development of coatings. As such, a number of delays totaling almost 1.5 years were endured in the program plan and fortunately ended with nearly identical P675 material being available to both Arcomac and Rolls-Royce for use in corrosion, wear, and fatigue performance tests.

Table 1. Material Types and Properties (Coating Substrates)

Material	Condition	Rockwell C HRC	Surface Roughness RMS	Notes
P675, Disc	Super-finished	64	56nm 1.4 μ inch	Primary sample type used for all performance testing and coating characterization
P675, Ball	Super-finished	64	113nm 4.4 μ inch	Substrate for TiCr-TiCrN coating, used in Wedeven Load Capacity and Performance Map
P675, Disc	Hard grind	64	190nm 7.5 μ inch	Rolls-Royce sample for Wedeven Load Capacity and Performance Map testing evaluation of effect of surface roughness (super-finished vs. ground)
P675, Ball	Hard grind	64	279nm 11 μ inch	Rolls-Royce sample for Wedeven Load Capacity and Performance Map testing evaluation of effect of surface roughness (super-finished vs. ground)
P675, Disc	Polished	64	5nm 0.2 μ inch	Samples used for coating characterization techniques which require low surface roughness
M50, Ball	Grade 5, SKF	65	<1 μ inch	¼"dia balls used as substrates for TiCr-TiCrN coating, uncoated and coated balls used in ball-on-disc unidirectional sliding wear tests
440A	Polished	58	25nm 1 μ inch	Standard reference substrates used to evaluate coating uniformity and to provide additional data on coating thickness, hardness, modulus, etc.

P675 material in rod form was obtained directly from the manufacturer, Car-Tech (division of Carpenter Steel) and machined into test geometries. This P675 material was sent to Rolls-Royce's heat treatment and carburization vendor and processed in the same batch as Rolls-Royce's testing samples for gear simulation testing. After heat treatment and carburization all samples were ground so that case carbon content was identical between all samples and surface finished to a roughness of Ra = 10 μ inch. Arcomac and Rolls-Royce samples were then sent to REM Chemical for isotropic surface finishing, also known as super-finishing. After all steps were completed both Arcomac and Rolls-Royce P675 samples had the same heat treatment, case carbon profile, and surface finish, the only difference was the material production batches which was deemed to be a minor concern by both parties. Unless otherwise noted this material was used exclusively in all coating characterization and performance testing results presented in this report. **Table 1** provides a summary of the various materials used in this research effort.

2.2.2 Coating Characterization Methods

The TiCr-TiCrN, Cr-CrN and CrC coatings developed in this effort were thoroughly characterized by the following methods which are described below. Detailed information can be referenced in the individual appendices.

Reference Appendix Th

Coating thickness was measured using the CALOTest™ method. This test is also referred to more generally as a spherical abrasion technique. Accuracy of thickness measurement is +/- 0.1µm when the substrate has a low roughness, i.e. RMS <25nm. Greater substrate roughness introduces measurement inaccuracies due to roughness at the coating/substrate interface. For each coating deposition thickness was measured on qty(6) 440A samples and qty(3) P675 samples to ensure statistically accurate data. Coating architecture as determined by the coating process formulation (e.g. multilayer thickness and bi-layer period) was confirmed by scanning electron microscope (SEM) imaging of polished cross-sections of the substrate coating stack.

Reference Appendix XPS and XRD

Coating composition, crystalline structure, and phase was analyzed using x-ray photoelectron spectroscopy (XPS) and x-ray diffraction (XRD) techniques.

The composition and bonding structure of the coatings were investigated using an X-ray photoelectron spectroscopy (XPS) instrument (PHI Model 5600ci, Casa XPS Analytical Software). A monochromatic Al K α x-ray source was used for all samples. The conditions used for the survey scans were as follows: energy range, 1100-0 eV; pass energy, 160 eV; step size, 0.7 eV; sweep time, 180 s; and x-ray spot size, 700×400 µm. For the high-resolution spectra, an energy range of 40-20 eV was used, depending on the peak being examined, with a pass energy of 10 eV and a step size of 0.05 eV. All samples were sputter cleaned in Ar for 5min prior to data collection to remove near surface impurities such as oxides. Data presented for multilayered TiCr-TiCrN and Cr-CrN coatings represents the composition of the topmost TiCrN and CrN layers only. The analysis volume (i.e. depth) for XPS does not encompass the metallic TiCr or Cr layers. The ~6µm thick CrC coating is monolithic (with the exception of the bond Cr-CrN single bi-layer) and hence the analysis interaction volume concerns mentioned for multilayer coatings do not apply; the data presented represents the composition of the CrC coating only. In order to characterize the composition and bonding structure of the TiCr-TiCrN, Cr-CrN, and CrC coatings, high-resolution spectra of Ti 2p, N 1s, Cr 2p, and C 1s, were collected and fitted using the Gaussian function. All spectra were calibrated using the adventitious C 1s peak with a fixed value of 284.6 eV. The background from each spectrum was subtracted and the area of under each peak was used to calculate the coating composition using relative sensitivity factors from the manufacturer's handbook: Ti (1.798), N (0.477), Cr (2.201), and C (0.296). One sample for each coating type, i.e. TiCr-TiCrN, Cr-CrN, and CrC as deposited on super-finished P675 was analyzed. After the first analysis where oxygen was found to be present in the coating a second set of data was collected on different Cr-CrN and CrC samples. Sputter time was increased to 20min (~30nm of coating removed) and atomic percent quantification was re-calculated with oxygen included.

Coating structure, phase and grain size identification analysis was subcontracted to Evans Analytical Group Labs (EAG), Job Number: T08V9336, performed by Delrose Winter Senior Scientist. Data was collected on the Rigaku Ultima III in standard 0:20 coupled focusing mode, with CuKa radiation with a standard wavelength of 1.54051nm, with variable slits and no diffracted beam monochrometer. Data was also collected on the Panalytical X'pert system in GI (Grazing Incidence) mode with parallel beam, with a GI incident angle of 0.9°. The most

representative data is included in the report. Phase identification is accomplished by searching the ICDD/ICSD data base to obtain the best matches on the standard materials from the ICDD/ICSD data base. All compounds (phases) are not present in the data base, so in some cases a good match can not be obtained. Since XRD is not used to determine the chemistry, it is likely that the exact formulas of the phase(s) present are somewhat different, this is particularly true for the Cr/N or Cr/Ti ratios of the tested coatings. The broadening of an observed diffraction peak can be characterized in a simplistic way by its FWHM (Full Width at Half Maximum) value at a particular 2θ angle. Because the apparent FWHM of a peak is a mathematical combination (convolution) of the specimen broadening FW(S) and the instrumental broadening FW(I), instrumental broadening is subtracted from that of the observed diffraction peak. If the crystallites (i.e., crystalline domains) in the specimen are free of lattice strain, their average size can be estimated from the specimen broadening FW(S) of any single peak in the observed pattern according to the Scherrer formula: Crystallite Size = $K^{-1} / (FW(S) \cdot \cos(\theta))$, where θ is the peak position, and K is the shape factor of the average crystallite. One sample for each coating type, i.e. TiCr-TiCrN, Cr-CrN, and CrC as deposited in super-finished P675 was analyzed.

Reference Appendix MOR

A Ziess Supra 55VP field emission scanning electron microscope (FE-SEM) was used to characterize coating morphology. Standard settings were; secondary electron mode, 5keV accelerator voltage, 15mm working distance, and 30 μm aperture. SEM images at 500x magnification were collected for both depositions (Dep1 and Dep2) of each coating type to demonstrate basic repeatability. It was standard practice to collect three morphology images at 500x from random locations on each sample in order to asses particle defect density in the coating. A SEM image at 5000x was also collected for each coating type; characteristic particle defects are intentionally included in each 5000x image as well. Images of the most commonly observed particle defect types were also collected to compliment discussion on defect related failures in coating performance tests such as corrosion and rolling contact fatigue.

Reference Appendix RMS

Surface roughness was measured per ASME standard B46.1-2002. This standard is concerned with the geometric irregularities of surfaces. It defines surface texture and its constituents: roughness, waviness, and lay. It also defines parameters for specifying surface texture. Roughness is defined as the finer irregularities of the surface texture that usually result from the inherent action of the production process or material condition. Lay is the predominant direction of the surface pattern ordinarily determined by the production method used. Waviness is the more widely spaced component of the surface texture. Roughness may be considered as superimposed on a wavy surface. Root Mean Square (RMS, also referred to as Rq) roughness is reported as the roughness parameter. RMS roughness is the root mean square average of the profile height deviations taken within the evaluation length and measured from the mean line. This is in contrast to Average Roughness (Ra) which is also commonly reported and is calculated as the arithmetic average of the absolute values of the profile height deviations. Accurate RMS measurements were made per B46.1 guidelines for selection of profile length and cutoff filter length. In the practical range of surface RMS values profile length is 1250 μm for surfaces in the RMS range of 20-100nm and profile length is set to 4000 μm for surface in the RMS range of 100nm-2000nm. The profile cutoff filter is the filter which separates the roughness from

waviness and form error components of the primary profile. This filter consists of a digital implementation of a 2RC filter. The filter cutoff length is set to 1/5 of the profile length for a given scan. Measurements were made using a Veeco Dektak8 advanced skidless contact profilometer. A 5 μ m radius tip diamond stylus tip was used. Scan resolution is normally set to 0.5 μ m/scan. A statistical dataset was generated in the following way: RMS data from 5 profiles was averaged for each sample, in all cases 3-6 samples were measured per substrate/coating type resulting in a final reported RMS value. One sigma covariance (CoV) was calculated for each RMS profile measured then averaged over the total number of profiles collected and reported to allow indication of the deviation of the RMS dataset for a given substrate type.

Reference Appendix H-E

Instrumented Indentation Testing (IIT) was conducted per ISO/DIS 14577-4 for determination of coating hardness and elastic modulus. A MTS Nanoindenter XP was used with a Continuous Stiffness Measurement (CSM) module and a standard Berkovich tip. The CSM option allows for the continuous measurement of contact stiffness during loading, not just at the point of initial unload. This is accomplished by superimposing a small oscillation on the primary loading signal and analyzing the resulting response of the system by means of a frequency-specific amplifier. With a continuous measure of contact stiffness one obtains the hardness and elastic modulus as a continuous function of depth from a single indentation experiment. Elastic modulus was calculated for all coatings with the assumption that Poisson's ratio $\nu=0.25$ since this value is unknown. To improve the statistical viability of collected data for each coated sample, qty(10) indent locations were visually located using a 250x microscope to avoid coating defects and spaced at least 50 μ m apart to avoid indent interaction. To minimize any substrate effects hardness and modulus data for each indent are reported as an average which was calculated over the range of %5-10% of the total coating thickness (coating thickness was directly measured on each sample using the CALOTest method). The final coating hardness and modulus reported for a given sample represent the average of the qty(10) indents performed with percent covariance reported to indicate the statistical scatter in the data. For each coating deposition qty(2) P675 polished samples were measured. Super-finished P675 samples were not measured as the increased coating roughness resulted in greater data scatter.

Reference Appendix RS

Coating residual stress was calculated by measuring the coating stress induced curvature on coated silicon beams. Si <111> beams of dimensions 5mm x 50mm x 0.300mm were laser cut from 100mm diameter wafers. Curvature of each beam was "pre" measured using a Dektak8 contact profilometer and then "post" measured after a coating had been applied. A 5th order polynomial was used to fit the pre and post beam profiles and the curvature was calculated as a function of position. Coating residual stress as a function of beam position was then directly calculated using the modified Stony equation [Jaccodine, Schlegel, 1965]. The effective modulus $E'=E/(1-\nu)$ for Si <111> of 229GPa was referenced from [14]. One Si beam was coated and used as a residual stress reference for each of the TiCr-TiCrN, Cr-CrN, and CrC coating depositions. Curvature of beams was only measured if the coating was intact, i.e. without any signs of delamination or cracking. Coating thickness was directly measured on the Si beam by CALOTest after curvature measurements were made. It is important to note that residual stress calculations on Si are best compared relatively to other coatings deposited on Si.

The stress state on Si can only be considered a general reference to the stress state for identical coatings deposited on the P675 substrates.

Reference Appendix HF

Coating adhesion and cohesion was evaluated qualitatively using the Rockwell adhesion indent test. This test consists of indenting a coated specimen under the standard Rockwell C testing protocol and qualitatively assessing and rating coating damage induced by plastic deformation of the substrate. A 120° angle diamond Rockwell C indenter with a 200 μm tip radius is indented with a force of 1470N per ASTM E18-08a standard which causes a repeatable deformation strain in the coating that can result in adhesive and/or cohesive coating failure modes. It should be noted that Rockwell indent adhesion results can only be correctly compared between coatings on substrates of equivalent hardness, comparison between substrates of different hardness is not advised as coating strain is inversely related to substrate hardness. Damage assessment is performed using an optical microscope at 75x and 150x magnifications, where the variable “a” is defined as the radius of the indent. For example, if coating cracking is reported to extend to a distance of “1.5a” this implies that the crack extends from the indent edge to a distance of 1.5a as measured from the center of the indent. Damage assessment is performed only for regions directly outside of the indent edge; damage inside the indent is usually severe, does not provide for repeatable comparisons, and cannot be imaged by optical microscopes due to a lack of reflected light. The resulting damage is rated on a HF1 to HF 6 scale with HF1 being the best and HF6 being the worst. The detailed description of the HF scale categorization can be referenced ([page #HF_1](#)). For each coating deposition Rockwell adhesion testing was conducted on qty(6) 440A samples and qty(3) P675 samples to ensure statistically accurate data.

Reference Appendix SA

Quantitative coating adhesion and cohesion was assessed by scratch testing methods per ASTM C1624 testing protocol. This test consists of producing and assessing controlled damage in a hard ceramic coating by single point scratch action (see schematic on [page #SA_2](#)). The scratch is developed on a coated test specimen by drawing a diamond stylus of defined geometry and tip size (Rockwell C, 200 μm radius) across the flat surface of the specimen for a distance of 10mm at a constant speed of 10mm/min and a controlled and measured normal force of 0-100N (progressively increasing at a rate of 10N/mm). With increasing applied normal force, the stylus produces progressive mechanical damage in the coating and the substrate through the complex combination of elastic/plastic indentation stresses, frictional forces, and residual internal stresses in the coating/substrate system. The specific levels and types of progressive damage in the scratch track were assessed and associated with the applied normal stylus forces. The normal force which produced a specific, defined, reproducible type/level of damage was defined as a critical scratch load (Lc). Five unique critical scratch loads (Lc1, Lc2...Lc5) were used to identify various modes of cohesive and adhesive failures in the coatings (as defined on [page #SA_2](#)). Coating damage was assessed by optical microscopy or scanning electron microscopy, or both, after the scratch test was completed. Tangential force (CoF) and acoustic emission (AE) signals were measured and recorded during the scratch test process and used as supplementary test data to identify different coating damage levels. To provide statistical relevance to the identified critical loads two unique scratch tests were performed on each sample for each coating deposited. Polished P675 substrates were used in this evaluation rather than super-finished P675 substrates in order to facilitate visualization of fine cracks using optical microscopy. Lc data is

presented in table form, representative CoF and AE plots are included for each coating type as deposited on P675 polished and super-finished substrates. Representative microscope images of Lc2, Lc3 and Lc5 failure modes are included for each coating type as deposited on P675 polished and super-finished substrates. Failure mode identification follows the criteria set forth in ASTM C 1624 Appendix X1 primarily established by Bull, Blau, et al.

Reference Appendix CA

Contact angle measurement is a convenient and useful parameter to determine the surface free energy and wet-ability of any given solid surface due to the non-deformability of the solid. According to definition, the contact angle is read from the angle formed between substrate surface where a liquid droplet is placed and the tangent to the drop surface from the 3-phase point. The contact angle measurement is a useful and precise empirical technique to determine the interaction between a liquid and a substrate. It must be stated that contact angle is not a property of the liquid or the substrate but the interaction between the two. Contact angle measurements were conducted for coatings in contact with Aeroshell 555 turbine oil (DOD-L-85734A) to determine any possible oil interaction differences from baseline uncoated Pyrowear 675. No specific performance inferences were made as to small differences in the absolute values of measured contact angles; the aim of the testing was to demonstrate that coatings exist which show similar oil wet-ability characteristics to uncoated Pyrowear 675.

A video-based optical contact angle measuring system OCA 20 with software SCA21 manufactured by DataPhysics GmbH was used for contact angle measurement. Future Digital Scientific Corporation (www.FDSC.com) was subcontracted to perform the testing. Coated specimens were placed into a temperature controlled environment chamber at 80 ± 0.5 degree C. The chamber was placed on a sample stage of the OCA 20 device, a 500 μ l micro syringe filled with Aeroshell 555 turbine oil and 0.18 mm diameter dosing needle was used. A droplet of 3 μ l volume of oil was dispensed at the dosing rate 0.2 μ l per second and deposited on the sample surface. The entire placement procedure of the drop onto the sample surface was recorded using an automated video recording function. A total of 30 seconds of images were captured using a recording rate of 12.5 images/sec. The contact angles were automatically calculated for each image using the ellipse fitting. Average of at least two tests is reported for contact angle of oil on the samples versus drop age. Contact angle testing was conducted as a screening test for aid in down selection of coatings under evaluation for the Lift Fan gear application; TiCr-TiCrN, TiCrC, Ti(Si)Cr-Ti(Si)CrN, Ti(Si)CrC, Cr-CrN, and CrC coatings were tested and compared with a baseline uncoated P675 sample.

2.3 Performance Testing Methodology

Performance testing is logically defined as testing which is meant to provide indication of the actual full scale performance of a Lift Fan gear. Following the identified research performance goals, testing is categorized into the same three conceptual areas; corrosion, wear, and fatigue. The following performance testing methodologies were used to evaluate the baseline P675 gear material and the TiCr-TiCrN, Cr-CrN, and CrC coatings.

2.3.1 Corrosion Evaluation – Modified Navy Corrosion Test

Reference Appendix NCT

The Modified Navy Corrosion Test (NCT) method sets forth the conditions for testing corrosion resistance of a material by exposing specimens to a humid, sea-water environment. Samples are suspended above sea-water in a sealed container and subjected to alternate temperature cycles which result in alternating condensing and drying cycles on the test samples. It is important to note that the samples are never actually submerged in the salt water solution so this test can also be thought of as a cyclic humidity test. The test protocol was obtained from Rolls-Royce as a less aggressive corrosion test to supplement ASTM B117 salt-fog corrosion testing. In addition Rolls-Royce has a historical database of NCT test results which allows for comparison with Arcomac coatings. A schematic of the test setup is provided ([page #NCT_2](#)). Super-finished P675 samples were tested uncoated to provide baseline comparison data and with TiCr-TiCrN, Cr-CrN and CrC coatings. No corrosion masking was applied to the samples. Qty (6) samples were suspended by zip ties and spaced so they did not contact each other in a sealed plastic corrosion cell containing approximately 100ml of seawater (ASTM D1141). Note that the samples were suspended about the seawater and at no point made physical contact with the seawater during the test. The sealed corrosion cells were temperature cycled; one cycle consisted of 24 hours, beginning with 8 hours in an oven at 150°F (65°C), and ending with 16 hours in a refrigerator at 37°F (3°C). The corrosion test was conducted for 14 cycles (336 hours total). Upon test completion the samples were air dried and photographed. Samples were then ultrasonically cleaned in acetone to remove loosely adhered corrosion products and then photographed. Additional analysis including optical microscopy, profilometry, and SEM imaging was conducted as appropriate. Corrosion performance was gauged qualitatively from comparison on the percent surface area of corrosion formation on the sample face.

2.3.2 Corrosion Evaluation – ASTM B117 Salt-Fog Corrosion Test

Reference Appendix SF

The ASTM B117 protocol can be used to test the relative resistance to corrosion of coated and uncoated metallic specimens, when exposed to a salt spray climate at an elevated temperature. The terms salt spray, salt fog and salt mist are all in widespread use for this type of testing and are generally interchangeable terms, as is the term cabinet or chamber, which is used to describe the equipment in which the test is conducted. ASTM B117 testing was subcontracted to Assured Testing Services (www.assuredtestingservices.com) and results were analyzed by Arcomac. Super-finished P675 samples were tested uncoated to provide baseline comparison data and with TiCr-TiCrN, Cr-CrN and CrC coatings. All samples were masked with epoxy paint (see schematic on [page #SF_2](#)) on the circumference and bottom face to ensure that all corrosion would occur on the sample face of interest. A 5% salt solution, prepared by dissolving sodium chloride into water that meets the requirements of ASTM D1193 Specification for Reagent Water, Type IV was supplied to the chamber. At the time the samples were placed into test, the cabinet was pre-conditioned to the operating temperature of 35°C and fogging a 5% salt solution at a rate of 1-2ml/hr over 80cm² surface area. The fog collection rate was determined by placing a minimum of two 80 sq. cm. funnels inserted into measuring cylinders graduated in ml. inside the chamber. One collection device was located nearest the nozzle and one in the farthest corner. The test sample(s) face of interest was oriented at a 15° angle to allow condensation to run down the sample. Test duration was set to 336hrs with interruption at 96hrs to allow for digital

photographs of the sample condition. At the end of testing corrosion performance was evaluated by qualitative visual assessment of corrosion formation and semi-quantitatively by measurement of percent red corrosion surface area coverage. Additional analysis including optical microscopy, profilometry, and SEM imaging was conducted as appropriate.

2.3.3 Wear Resistance – Unidirectional Dry Sliding Wear (Ball-on-Disc)

Reference Appendix BoD

Unidirectional sliding wear performance was evaluated using a ball-on-disc (BoD) testing configuration per ASTM G99 as shown schematically ([page #BoD_1](#)). The term ball-on-disc refers to a fixed ball in sliding contact with the flat face of a rotating disc, which results in a point on flat contact geometry. The primary experimental parameters for BoD testing are material contact pairing, load (contact stress), sliding speed, sliding distance, temperature, atmosphere and lubrication. Wear performance is normally evaluated on the volume of material worn from the disc and/or the ball. For the current program all three meshing Lift Fan gears need to be coated for corrosion protection which forces the tribological contact material pairing to the coating-coating case. As such it was important to evaluate the sliding performance of various coated contact pairs.

TiCr-TiCrN coated M50 balls (6.35mm diameter, grade 5, SKF) were used in contact with Cr-CrN and CrC coated super-finished P675 discs to represent Lift Fan gears. The same M50 balls (uncoated) were used in contact with uncoated super-finished P675 discs to represent the baseline Lift Fan gear case. Although P675/P675 contact would have been more ideal, P675 balls are not normally manufactured so M50 was used as a close substitute. Each contact pair was evaluated at 100m, 500m, and 1000m sliding distances for normal loads of 1N and 5N. Three tests were conducted on each disc; 100m distance at 9mm radius, 500m distance at 10.5mm radius and 1000m distance at 13mm radius. Sliding speed was held constant at 300mm/sec for different test radii by adjusting the rotational speed. Test temperature (ambient, ~24°C) and atmosphere (RH = 20% +/-5%) were monitored but not controlled. To improve the statistical viability of the wear results and to demonstrate repeatability of coating wear properties each load and sliding distance test was performed two times. To provide an example, a 1N load 100m distance test was conducted on a CrC (Dep1) sample and another duplicate test at 1N load 100m distance was conducted on a CrC (Dep2) sample. This test duplication was performed on the Cr-CrN and CrC discs for all load and distance combinations. Similarly, duplicate tests were performed on two different P675 samples for each load and sliding distance. The test matrix resulted in a total of 36 tests (18 unique tests + 18 duplicate tests), or 12 tests per each contact pair; M50/P675, TiCr-TiCrN/Cr-CrN and TiCr-TiCrN/CrC.

Testing was conducted using a CETR UMT-3 tribo-tester (www.cetr.com). Normal load, test radius and disc rotational speed were closed-loop feedback controlled by the UMT-3 tester. Normal load, tangential load, and sliding speed data was acquired at a rate of 20Hz. Sliding coefficient of friction (CoF, μ) was calculated as the measured tangential load divided by the applied normal load. Sliding speed was calculated as the disc rotational speed multiplied by the test radius. Prior to testing both disc and ball were cleaned with acetone, and post testing the disc and ball were physically scrubbed in acetone followed by 5min ultrasonic cleaning in acetone to remove any loosely adhered wear debris that would interfere with wear volume

calculations. Ball wear was observed by optical microscopy; wear features were noted, wear scar diameter was measured and an image at 75x magnification of the wear scar was recorded for each test. In addition a ball wear profile scan 1500 μ m in length was measured across the ball meridian and wear scar center. Disc wear was observed by optical microscopy and SEM techniques; wear features were noted, optical microscope images were recorded at 50x and SEM images of the wear track center and edge were recorded at 500x. Three profiles 1500 μ m in length were recorded for each disc wear track at random positions approximately 120° opposed around the track. Disc wear depth, cross-sectional wear area, and wear track width were measured from each profile and reported as an average for each test. EDX compositional analysis was performed on the wear track for each test to assess the presence of wear debris formation in the wear track. To review the methods used for calculation of wear volumes on discs and balls reference ([page #BoD_1](#)). Wear of materials in sliding contact was assumed to be the result of dissipated energy due to friction between the contacting bodies, which was defined as the average tangential force multiplied by the total sliding distance, in other words the total work of sliding ([page #BoD_2](#)).

2.3.4 Gear Simulation, Scuffing – Wedeven Load Capacity Protocol

Reference [Appendix WLC](#)

The Load Capacity (LC) testing method was designed and conducted by Wedeven Associates (www.wedeven.com) and is sophisticated means to simulate gear contact kinematics. Wedeven Associates was subcontracted for this effort to perform all testing and data collection. Analysis was conducted by Wedeven Associates and Arcomac Surface Engineering. Some of the included text for testing description has been provided courtesy of Wedeven Associates. The original purpose of this test method was to evaluate oils according to the Ryder Gear Test Method, with enhanced sensitivity for lower than average lubricating performance. Additionally the method has been used to evaluate material/oil compatibility and as a means to evaluate performance improvements based on surface morphology (roughness) for specific material/oil combinations. In the present evaluation Royco 555 oil is used exclusively and the scuffing performance of Pyrowear 675 and TiCr-TiCrN, Cr-CrN, and CrC coatings were evaluated with contact pair material and surface finish as the primary variables.

The LC test protocol was conducted with a WAM test facility. The test machine controls specimen position, contact load and motions of a single contact in space ([page #WLC_2](#)). A computerized run file controls load and contact kinematics between the specimens. Specimen temperatures were recorded with trailing thermocouples. Load was exponentially increased from 1.8 kg (4 lbs) to 63.6 kg (140 lbs) in 30 stages (0.7Gpa to 2.4GPa). The entraining velocity (U_e) and sliding velocity (U_s) are key parameters that control the degree of surface separation and the rate of surface tangential shear that the oil must accommodate. The sliding velocity was set at 8.8m/sec (345in/sec) which exceeds the worst case Lift Fan gear mesh sliding velocity of 7.7m/sec (304in/sec). With the parameters selected, the initiation of a load capacity test is similar to the Ryder Gear Test in that there is generally little or no evidence of surface damage during the first load stage. Test duration was until a macro-scuff event occurred, or test suspension (30 stages = 30 minutes). Failure criteria; macro-scuff (test stop) is defined by loss of surface integrity and sudden increase in traction; micro-scuff is defined by rapid decline in traction coefficient. Performance is judged by the load at which macro-scuff failure occurs.

Specimen temperature was dictated by frictional heating and surface temperatures increase with load stage from ambient to ~200 °C. Oil supply was computer controlled by a peristaltic pump at approximately 1 drop/sec and oil flow rate was selected for adequate lubrication without significant cooling. Arcomac conducted qty(8) load capacity tests using TiCr-TiCrN coated super-finished P675 balls in contact with Cr-CrN and CrC coated super-finished P675 discs. Four tests were conducted for each coating contact pair; two duplicate tests on a given coating to establish repeatable results and two duplicate tests on identical coatings deposited in different processes to establish repeatability of results between coating depositions. Rolls-Royce conducted identical LC testing on super-finished and as-ground P675 to establish baseline performance and to compare the effect of surface roughness of uncoated P675. The detailed test matrix and test parameters can be referenced ([page #WLC_3](#)).

2.3.5 Gear Simulation, Scuffing – Wedeven Performance Mapping Protocol

Reference [Appendix WPM](#)

The Performance Mapping (PM) testing method was designed and conducted by Wedeven Associates (www.wedeven.com) and is sophisticated means to simulate gear contact kinematics. Wedeven Associates was subcontracted for this effort to perform all testing and data collection. Analysis was conducted by Wedeven Associates and Arcomac Surface Engineering. Some of the included text for testing description has been provided courtesy of Wedeven Associates. The PM test method is primarily used to evaluate oils over a range of lubrication regimes; full EHD lubrication (no asperity contact), boundary lubrication (asperity contact), and oil film breakdown (full contact between pairs). Additionally the method has been used to evaluate material/oil compatibility and as a means to evaluate performance improvements based on surface morphology (roughness) for specific material/oil combinations. In the present evaluation Royco 555 oil was used exclusively and the scuffing performance of Pyrowear 675 and TiCr-TiCrN, Cr-CrN, and CrC coatings were evaluated with contact pair material and surface finish as the primary variables.

The PM test protocol was conducted with a WAM test facility. The test machine controls specimen position, contact load and motions of a single contact in space ([page #WPM_2](#)). A computerized run file controls load and contact kinematics between the specimens. Specimen temperatures were recorded with trailing thermocouples. Two test series were run; a “cold scuffing” series in which the sliding/entraining velocities ranged from ~0.5m/sec to ~9m/sec and ~1.3m/sec to 0m/sec respectively and a “hot scuffing” series in which the sliding/entraining velocities ranged from ~2.5m/sec to ~25m/sec and ~5m/sec to 0m/sec respectively. A test stage is defined as a sliding/entraining velocity combination which falls within a specific lubrication regime; 14 test stages are performed for the cold-scuffing series and 13 test stages for the hot-scuffing series. Each test stage was run for 10min and test duration was until a macro-scuff event occurred, or test suspension. Successive test stages were conducted at the same track location of the previous stage, in other words wear and damage accumulated until failure. Load was held constant at 344N which imparted a 1.95GPa max contact stress. Failure criteria; macro-scuff (test stop) defined by loss of surface integrity and sudden increase in traction, micro-scuff defined by rapid decline in traction coefficient. Performance was judged by sliding/entraining velocity stage at which failure occurs. Specimen temperature was dictated by frictional heating. Oil supply was computer controlled by a peristaltic pump at approximately 1 drop/sec and oil flow rate is selected for adequate lubrication without significant cooling.

Arcomac conducted performance mapping tests for TiCr-CrN coated super-finished P675 ball versus Cr-CrN and CrC coated super-finished P675 disc contact pairs. Rolls-Royce conducted performance mapping tests for super-finished and as-ground P675 to establish baseline performance and to compare the effect of surface roughness of uncoated P675. The detailed test matrix and test parameters can be referenced ([page #WPM_3,4,5,6](#)).

2.3.6 Contact Fatigue – Rolling Contact Fatigue Test

Reference [Appendix RCF](#)

The purpose of rolling contact fatigue (RCF) testing was to determine the high contact stress cyclic fatigue life of Pyrowear 675 and TiCr-TiCrN, Cr-CrN, and CrC coatings. The RCF test protocol was designed by Arcmac and is classified as a half-thrust bearing arrangement, very similar to rigs used by a number of researchers and companies such as Timken Bearing and also Rolls-Royce in a large study of turbine bearing materials [15]. The contact kinematics of the RCF test are point-on-flat with minimal sliding occurring, i.e. bearing conditions. This is in contrast to the line contact and slip conditions present in gear kinematics, although the RCF test still serves to delineate fatigue performance between coatings and substrates and the data produced is more easily compared with the wealth of bearing fatigue data available in the literature.

The schematic and the detailed test parameters can be reviewed ([page # RCF_2](#)). The basic design of the test can be described as a half-thrust bearing arrangement where an upper grooved thrust washer (SKF part# 51200) is used to drive qty(8) 5.5mm diameter grade 5 chrome steel (AISI 52100) balls against a flat coated or uncoated super-finished P675 test sample. The contact geometry is such that the contact stress generated on the flat test sample is much higher than the conformal contact stress developed on the grooved thrust washer ensuring that fatigue failure occurs on the test sample. Phenolic cages were specially made to radially locate 8 balls and the thrust washer holder was specially designed to allow for auto-leveling of the applied load ensuring even contact stresses all around the rolling track. The test load was applied via a loading arm and monitored with a load cell to create a contact stress of 4.5GPa. The sample surface, balls and cage were submerged in ~20mL 555 jet oil (DOD-L-85734) and intake and outtake peristaltic pumps provided for a constant 1mL/sec circulation of Aeroshell 555 jet oil from a 1000mL reservoir. The test was run at 3450RPM which resulted in 1,656,000 contact fatigue cycles per hour. For RCF testing a contact cycle is defined as a pass of a loaded ball over a finite section of the sample, i.e. one revolution of the thrust bearing (with 8 balls) equals eight contact cycles. A computer with LabView software controls the RCF test apparatus and allows constant monitoring of revolutions of the AC motor, contact cycles, and oil flow. Acoustic signals were monitored using Physical Acoustic Corporation's PCI-2 DAQ Card and a R15-A sensor. A minimum of three RCF tests were conducted for each material type; uncoated P675, TiCr-TiCrN, Cr-CrN, and CrC. The detailed sample matrix can be referenced ([page #RCF_3](#)). All tests were run to failure or to test suspension at 8-10E+06 contact cycles, whichever occurred first.

RCF failure was determined by a combination of acoustic emission (AE) monitoring and post-test analysis by optical microscope and surface profilometry. When fatigue damage initiates, energy is released in the form of elastic waves with high frequency. Acoustic emission sensors

are piezoelectric transducers that convert these elastic waves into a voltage signal and allow for monitoring and determination of material failure in fatigue. Micro-pitting (coating cohesive or adhesive delamination) and/or macro-pitting (sub-surface crack formation and subsequent pull-out of material) are identified as the primary modes of fatigue failure. Material fatigue failure was determined by a rapid drop in AE signal counts at which point the RCF test was stopped. Post RCF test samples were examined using optical microscopy to confirm and characterize fatigue damage and profilometry was used to characterize fatigue damage depth. A precision mass scale was used to assess RCF test ball wear by assessing changes in pre/post test ball mass.

3. Results and Discussion

Results are categorized into three areas; coating properties, performance testing, and coating uniformity. Sub-sections are reported in a summarized format with detailed information referenced in the appendices. Each sub-section contains supplementary discussion concerning the repeatability of the coating results in two areas; the first being repeatability of results as measured on multiple samples from the same coating deposition run, and the second being repeatability of results as measured on multiple samples of the same coating designation deposited in separate runs (Dep1 versus Dep2). As mentioned in section 2.1 two separate coating depositions were performed for each TiCr-TiCrN, Cr-CrN and CrC coating solely for the purpose of repeatability evaluation. In the data that follows the notation used is Dep1 to indicate coatings produced in the first process and Dep2 to indicate coatings produced in the second process.

3.1 Coating Properties

3.1.1 Coating Thickness and Architecture

Reference Appendix Th

Coating thickness is dependent on the deposition rate of a given coating which is in turn dependent on the characteristic mass erosion rate of the targets used to deposit the coating. Target mass erosion rate can be increased or decreased by increasing or decreasing the arc current per target within the limits of arc stability and the LAFAD coating system power supplies. Coating thickness was controlled by adjustment of the total deposition time based on characterization of the deposition rate. Increased coating thickness increases corrosion performance but can negatively affect wear or fatigue performance due to the possibility of increased residual stress with increasing coating thickness. From an economical standpoint coating thickness should be minimized to reduce cost and yet still provide the necessary functional properties. A coating thickness constraint of $<7\mu\text{m}$ was imposed by Rolls-Royce to ensure that the coating would not cause redesign issues with the Lift Fan gear mesh tolerances. With these design balance issues in mind the coating thickness goal was set at $6\mu\text{m}$ to ensure maximum chance of corrosion performance, while possible negative affects such as residual stress were addressed through optimization of coating composition and architecture. The results for coating thickness as measured on P675 (polished, RMS = 5nm [0.2 μinch], HRC-64) are presented in **Table 2**.

Table 2. Coating Thickness

Coating	Coating ID	Sample ID	Thickness [μm]	Appendix Page CALO Image @75x
TiCr-TiCrN	ASE-8-9-1 (Dep1)	C170	5.6	Th_3
TiCr-TiCrN	ASE-8-14-1 (Dep2)	C78	5.8	Th_4
Cr-CrN	ASE-8-29-1 (Dep1)	C33	6.3	Th_5
Cr-CrN	ASE-8-34-1 (Dep2)	C79	6	Th_6
CrC	ASE-8-19-1 (Dep1)	C81	6.3	Th_7
CrC	ASE-8-26-1 (Dep2)	C60	5.4	Th_8

Deposition rates for the TiCr-TiCrN, Cr-CrN, and CrC coatings were 1μm/hr, 0.75μm/hr, and 2μm/hr respectively. Images of the CALOscars used to measure coating thickness can be referenced ([page #Th_3-8](#)), which show the multilayer structure of the TiCr-TiCrN and Cr-CrN coatings and the Cr-CrN +CrCN bond layer of the CrC monolithic coating. Coating thickness was also measured on the super-finished P675 which was well correlated to the data in **Table 2** although this data was not reported due to the added inaccuracy in measurement on rougher substrates. CALOscar SEM images of the coatings as deposited on super-finished P675 ([page #Th_9-11](#)) show the coating thickness and illustrate the lack of sharp layer interface definition required for accurate thickness measurement.

Repeatability of coating thickness among samples measured from the same run was +/-0.2μm which is close to the error in thickness measurement (+/-0.1μm). Coating process repeatability between Dep1 and Dep2 coatings was within +/-0.15μm for the TiCr-TiCrN and Cr-CrN coatings. The variation in coating thickness from Dep1 to Dep2 for the CrC coating was 1μm (or +/-0.5μm). This deviation was caused by the use of different Cr targets and is not a property of the LAFAD process for CrC coatings but rather a modifiable limitation of the current target/source design.

3.1.2 Coating Composition, Structure and Phase

Reference Appendix XPS and Appendix XRD

As a primary experimental parameter, coating composition was varied extensively during coating development with the effects ranked in regards to changes in coating properties and performance testing results. Fatigue performance of the TiCr-TiCrN coating was found to be particularly sensitive to the ratio of Ti/Cr in the TiCr-TiCrN coating, with a decreasing Ti/Cr ratio showing improved fatigue performance. The amount of carbon content in the CrC coating was a primary development parameter with the aim of optimizing carbon content to reduce friction and minimize wear. CrC coatings with too much carbon became sooty and had poor adhesion while CrC coatings with too little carbon demonstrated wear performance similar to metallic Cr, i.e. high friction and adhesive wear. Work was also conducted with increased nitrogen pressures during deposition which resulted in slightly improved adhesion/cohesion properties and improved fatigue performance. Composition of the coatings was measured by XPS while structure, phase, and crystalline grain size were measured by XRD; the results are presented in **Table 3** and **Table 4** respectively.

Table 3. XPS Results - Coating Composition (Atomic %)

Coating	Coating ID	Sample ID	Atomic % Concentration				
			Ti	Cr	N	C	O
TiCr-TiCrN	ASE-8-14-1 (Dep2)		37.8	19.8	42.4	n/a	n/a
Cr-CrN	ASE-8-29-1 (Dep1)	SF2	-	64.5	35.5	n/a	n/a
Cr-CrN	ASE-8-34-1 (Dep2)	P3	-	55.8	34.1	4.1	6.0
CrC	ASE-8-19-1 (Dep1)	P74	-	63.3	-	36.7	n/a
CrC	ASE-8-26-1 (Dep2)	P57	-	62.8	-	34.9	2.3

Table 4. XRD Results - Coating Structure, Phase, Crystal Size

Coating	Coating ID	Sample ID	Crystalline Structure	Best Match ICDD/ICSD Phase ID	Second Best Match ICDD/ICSD Phase ID	Crystal Size <111> [nm]	Crystal Size <200> [nm]
TiCr-TiCrN	ASE-8-14-1 (Dep2)	P47	FCC	Ti _{0.5} Cr _{0.5} N	TiN _{0.9}	23.5	14.0
Cr-CrN	ASE-8-29-1 (Dep1)	P74	FCC	CrN	n/a	11.7	16.7
CrC	ASE-8-19-1 (Dep1)	P43	amorphous	n/a	n/a	n/a	n/a

The interaction volume of the XPS technique is a few nanometers deep so the XPS data for the TiCr-TiCrN and Cr-CrN coatings is actually the composition of the TiCrN and CrN layers (metallic layers are not part of the analysis interaction volume). High resolution XPS spectrum plots of all three coatings showing the peak deconvolutions used to determine bonding states are provided ([page #XPS_4-6](#)) with detailed discussion. To summarize, the primary bonding states for the TiCrN layer were TiN, CrN, and TiCrN, and secondary bonding states were indicative of Ti-O bonds and Cr₂O₃. No evidence of Ti-Ti, Cr-Cr bonding or Cr₂N was indicated in the TiCrN XPS spectrum. The primary bonding state of the CrN layer was CrN, with secondary bonding states for Cr₂O₃. No evidence of Cr-Cr bonding or Cr₂N was indicated in the CrN XPS spectrum. The primary bonding state of the CrC coating was Cr-C bonding, with secondary bonding indicative of Cr₂O₃. Analysis of the carbon 1s spectrum peak showed evidence of amorphous carbon bonds but the ratio of peak intensities suggested that most of the carbon in the coating exists as Cr-C bonds.

Standard XRD 2-theta intensity plots for all three coatings and detailed discussion are provided ([page #XRD_2-7](#)). The crystalline structure of the TiCr-TiCrN coating was determined to be FCC with no apparent preferred orientation. The TiCr-TiCrN coating is nanocrystalline; crystal size calculations for the (111) and (200) planes were measured to be 23.5nm and 14.0nm respectively. The Cr-CrN coating structure is also FCC and the Cr-CrN coatings showed a strong preferred orientation on the (200) plane ([page #XRD_5](#)). The Cr-CrN coating is nanocrystalline; crystal size calculations for the (111) and (200) planes were measured to be 11.7nm and 16.7nm respectively. The CrC coating is primarily amorphous. No clear crystalline peaks were observed ([page #XRD_7](#)), and the one broad peak that was observed was too broad to be considered crystalline. It may be that the coating has too small a crystallite size to observe distinct lattice spacing. It is also possible that crystallites started to form, but did not form three

dimensional crystallites with reasonable unit cell stacking order in three dimensions. Percent crystallinity measurements were not performed.

When taking in to account the composition and bonding information from XPS and combining it with XRD phase identification data clear answers are not easily obtained for the coatings which all appear to have complicated stoichiometries.

XRD phase identification for the TiCr-TiCrN coating showed a formula similar to (although not exactly) $Ti_{0.5}Cr_{0.5}N$. A significant line shift from the standard ICDD/ICSD card for $Ti_{0.5}Cr_{0.5}N$ suggests a different Ti/Cr ratio (page #XRD_4), which was correlated by the XPS data which shows a 2:1 Ti/Cr ratio rather than 1:1. A FCC TiN_x match is almost as good (almost equal Figure of Merit) to that of the $Ti_{0.5}Cr_{0.5}N$ phase. Therefore, TiN_x osbornite is listed under the “Second best match” column in Table 4. XRD phase identification for CrN was negative while XPS data suggested CrN bonds. Phase identification for hexagonal and/or BCC pure Ti or Cr were negative, indicating no crystalline metallic phases are present in the coating (page #XRD_4), this data was also correlated by XPS which showed no Cr-Cr or Ti-Ti bonding. This was somewhat surprising given that the XRD interaction volume samples the metallic layers of the TiCr-TiCrN coating which infers either that the metallic TiCr layers are amorphous, or that the thin ~100nm TiCr layers are diffusion nitrided during subsequent deposition of a TiCrN layer. From a purely compositional point of view the TiCrN coating appears to be of the formula $TiCr_{0.5}N$ which is not surprising as the coating deposition parameters were setup to produce a 2:1 Ti/Cr ratio. There is no ICDD/ICSD card for $TiCr_{0.5}N$ but the XRD peaks closely match $Ti_{0.5}Cr_{0.5}N$ and TiN_x which makes logical sense given that the $TiCr_{0.5}N$ coating could be referred to as a TiN rich pseudo $Ti_{0.5}Cr_{0.5}N$ phase.

For the Cr-CrN coating the best ICDD/ICSD phase match was CrN, although this match shows significant line shift from the card which is indicative of a Cr/N ratio other than 1:1. Due to strong (200) orientation, a 2D detector and x-ray point source was also used to generate a higher resolution scan which allowed for better certainty in the CrN FCC structure and phase identification (page #XRD_6). Phase identification for BCC pure Cr was negative, indicating no crystalline metallic phases are present in the coating (page #XRD_6). As with the TiCr-TiCrN coating the lack of crystalline metallic phases infers either that the metallic Cr layers are amorphous, or that the thin ~40nm TiCr layers are diffusion nitrided during subsequent deposition of a CrN layer. The composition of the CrN coating complicated the identification of the phase as CrN since the ratio is not 1:1 but rather ~1.8:1. A second XPS assessment of a Dep2 Cr-CrN coating was conducted to included quantification of 6at% O and 4at% C contaminants in the coating; the Cr/N ratio for this assessment only changed slightly to 1.6:1. While this ratio suggests Cr_3N_2 the XRD phase identification and XPS bonding data don’t support this phase; rather it seems more likely that the CrN coating is primarily composed of a CrN FCC phase with the balance of elemental Cr existing as possible amorphous Cr at grain boundaries and/or Cr interstitials in the CrN lattice.

XRD phase identification of the CrC coating was not possible due to the lack of diffraction peaks. XPS data suggests that the bulk of the coating exists as Cr-C bonds with evidence of some amorphous C. The compositional Cr/C ratio is ~1.75:1. Considering both XRD and XPS data it seems most logical that the CrC coating is primarily composed of a Cr_3C_2 phase with

crystallite size below the detection limit of XRD with some form of an amorphous C matrix at grain boundaries.

Due to the expense involved with XPS and XRD measurement limited repeatability assessment was conducted. One sample from Dep1 and Dep2 for both the Cr-CrN and CrC coatings were measured in XPS and the composition repeatability was excellent (**see Table 4**). Detailed discussion on composition repeatability and uniformity as measured by EDX is provided in section 3.3.

3.1.3 Coating Morphology

Reference Appendix MOR

Images at 500x magnification were collected using SEM for super-finished P675 and the TiCr-TiCrN, Cr-CrN, and CrC coatings as deposited on super-finished P675 (**page #MOR_2-9**).

SEM images at 500x magnification were collected for both depositions (Dep1 and Dep2) of each coating type to demonstrate basic repeatability. It was standard practice to collect three morphology images at 500x from random locations on each sample in order to asses particle defect density in the coating; the presented images are the most representative morphology for a given coating. A SEM image at 5000x was also collected for each coating type; characteristic particle defects are intentionally included in each 5000x image as well. The results for all of the coatings were as expected; dense fine grained structure with low particle density. Particles embedded in coatings can be poorly adhered, give rise to stress concentrations in the coating, and are likely to have different thermal expansion coefficients than that surrounding coating. All of these factors combined can result in delamination of a small percent of particles from the coating a phenomenon termed as “particle fall-out”. A small percentage of the total particle fall-outs that occur expose the underlying P675 substrate and become likely corrosion initiation spots.

Examples of particle fall-out are provided (**page #MOR_10-12**) and further discussion of the implications on corrosion is provided in sections 3.2.1 and 3.2.2.

3.1.4 Coating Roughness

Reference Appendix MOR

Surface roughness is a particularly important property in relation to all types of wear, with the general rule being that lower surface roughness equates to better wear performance. For dry contacts in sliding wear a higher surface roughness implies that the contact between surface asperities is less conformal resulting in higher contact stress, increased run-in wear, and more initial wear debris formation. For lubricated contacts the same considerations apply as in dry contact. Oil film thickness is inversely proportional to load and directly proportional to relative sliding speed between contacts and wear only occurs when the average roughness of the contacting bodies exceeds the oil film thickness. Therefore lubricated surfaces such as gear teeth can run without wear at higher loads and slower speeds if the mating surfaces both have low surface roughness. The results for RMS roughness of super-finished P675 and TiCr-TiCrN, Cr-CrN and CrC coated super-finished P675 are shown in **Table 5**. Surface profile plots are provided (**page #RMS_3-9**) to allow for visual comparison of each surface on an equal scale.

Table 5. RMS Surface Roughness

Substrate Type	Coating	Coating Thickness [μm]	RMS [nm] / [μinch]		CoV [%]
P675, disc, super-finished	n/a	n/a	56 / 1.4	+/-	5.5%
P675, ball, super-finished	n/a	n/a	113 / 4.4	+/-	16.0%
P675, disc, super-finished	TiCr-TiCrN (Dep1)	5.6	247 / 9.7	+/-	26.4%
P675, disc, super-finished	TiCr-TiCrN (Dep2)	5.8	223 / 8.7	+/-	21.4%
P675, ball, super-finished	TiCr-TiCrN	~4	166 / 6.5	+/-	6.4%
P675, disc, super-finished	Cr-CrN (Dep1)	6.3	153 / 6.0	+/-	10.0%
P675, disc, super-finished	Cr-CrN (Dep2)	6.0	160 / 6.3	+/-	16.2%
P675, disc, super-finished	CrC (Dep1)	6.3	153 / 6.0	+/-	12.0%
P675, disc, super-finished	CrC (Dep2)	5.4	132 / 5.2	+/-	12.2%

The results show a 3x to 5x increase in surface roughness over the P675 baseline 56nm roughness once the coatings are applied. The TiCr-TiCrN coating has the highest RMS roughness at ~230nm, while the Cr-CrN and CrC though very different in architecture demonstrate similar RMS roughness of ~150nm. For all coated samples the increase in surface roughness is in part due to roughening of the P675 substrate that occurs during the 20min Ar+ sputter cleaning step prior to deposition of the coating. Preliminary work to characterize the affect of sputtering showed that 440A samples with an initial RMS = 12nm were roughened by 2x to RMS = 23nm after 30min of sputter cleaning at -250V bias. Surface roughening during Ar+ sputtering is caused by preferential sputtering at grain boundaries but given that sputtering is necessary to secure adhesion of the coating it is an unavoidable step. TiN and CrN monolithic coatings often form a columnar structure whose roughness is dependent on the thickness of the coating. Multi-layer coatings with metallic inter-layers can interrupt the columnar growth of the ceramic layers and effectively produce a saturated roughness which is dependent on the ceramic (columnar) layer thickness and not the total thickness of the coating. With this in mind it is interesting to compare the roughness of the TiCr-TiCrN coating on the P675 disc (5x roughness increase) and the P675 ball (1.5x increases in roughness). The difference in the coatings which were deposited at the same time is that the P675 ball was mounted in double rotation which results in a bi-layer thickness ~60% of the TiCr-TiCrN coating on disc samples; possibly limiting columnar growth of the TiCrN layers and resulting in a lower RMS roughness. One sigma covariance (%CoV in **Table 5**) is related to the uniformity of the coating morphology and the density of particles on the surface. Values for %CoV of less than 10% indicate a uniform morphology and a relatively defect free surface, for coatings values in the range of 10%-20% generally indicate a uniform morphology and low defect density, and values greater than 25% percent can be indicative of a uniform morphology and low defect density but larger particle sizes.

The data in **Table 5** represents over 30 averaged measurements per coating deposition; therefore the repeatability of coating surface roughness is excellent. Repeatability between Dep1 and Dep2 for each coating was also better than +/-7% in all cases.

3.1.5 Coating Hardness and Elastic Modulus

Reference Appendix H-E

Hardness (H) refers to the ability of a material to resist plastic deformation when subjected to high compressive stresses by a contacting body. High hardness can very often be related to wear resistance, which often comes at the expense of excessive wear to the lower hardness counter body. While this type of wear is ideal for certain applications such as cutting tools it is not for tribological applications such as gears where protection of one gear and excessive wear of the mating gear would be unacceptable. In the case of gears, solutions are required were mating gears wear at a similar rate suggesting that coatings designed with similar hardness provide a better chance of meeting this goal. Elastic Modulus (E) refers to the stress developed in a coating for a given amount of induced strain. It is a common misconception that thin (<10 μm) hard PVD coatings can effectively stiffen the contact zone to reduce total deformation in a beneficial way. For example, finite element analysis of a 5.5mm diameter M50 steel ball in contact with a P675 substrate with a 5 μm thick coating (E = 400GPa) results in a surface displacement of ~375nm at 5N loading. If the coating is removed and the same analysis is conducted again, the surface displacement only increases by 2% to 383nm. The relative stiffening effect of a coating is even less when scaled contact geometries and loads are considered for actual large gears or bearings. Considered this way it is clear that coatings on bearing and gears must act as flexible membranes which provide wear and corrosion protection. Since the coating must follow the substrate deformation, a low elastic modulus is desirable which results in a low deformation induced stress in the coating. It is for this reason that the ratio of hardness to elastic modulus (H/E ratio) has become of interest in coating design; i.e. a relatively high H/E implies that the coating will have good wear and fatigue (elastic) properties. The results for coating hardness and elastic modulus are presented in **Table 6**.

Table 6. Coating Hardness and Elastic Modulus

Coating	Thickness [μm]	RMS Roughness [μm]	Hardness [GPa]	Elastic Modulus [GPa]	H/E
TiCr-TiCrN (Dep1)	5.6	0.097	34.5 +/-5.6	401 +/-44	0.086
TiCr-TiCrN (Dep1)	5.6	0.112	36.3 +/-5.3	430 +/-42	0.084
TiCr-TiCrN (Dep2)	5.8	0.124	34.1 +/-4.5	404 +/-36	0.084
TiCr-TiCrN (Dep2)	5.8	0.086	35.5 +/-2.7	429 +/-31	0.083
TiCr-TiCrN (average)	5.7	0.105	35.1 +/-4.5	416 +/-38	0.084
Cr-CrN (Dep1)	6.3	0.084	27.3 +/-2.7	329 +/-25	0.083
Cr-CrN (Dep1)	6.3	0.046	27.6 +/-3.7	328 +/-33	0.084
Cr-CrN (Dep2)	6	0.076	26.2 +/-2.4	321 +/-24	0.082
Cr-CrN (Dep2)	6	0.051	26.8 +/-2.7	322 +/-28	0.083
Cr-CrN (average)	6.2	0.064	27.0 +/-2.9	325 +/-28	0.083
CrC (Dep1)	6.3	0.164	33.5 +/-5.3	446 +/-57	0.075
CrC (Dep1)	6.3	0.067	31.2 +/-3.7	423 +/-41	0.074
CrC (Dep1)	5.4	0.102	32.8 +/-3.7	434 +/-43	0.076
CrC (Dep1)	5.4	0.038	31.1 +/-3.5	411 +/-35	0.076
CrC (average)	5.9	0.093	32.2 +/-4.1	429 +/-44	0.075

The results presented in **Table 6** are for coatings as deposited on super-finished P675; values are presented for each coating on two samples from each deposition (Dep1 and Dep2), and as average values for the three coating types. Coating thickness and RMS values are presented in accordance with ISO 14577-4 standard recommendations. Hardness = 10GPa and E = 225GPa was measured for super-finished P675 (case hardness). It is important to note that the reported H-E values for the TiCr-TiCrN and Cr-CrN coatings are composite hardness or modulus values. Roughly, the rule of superposition applies for multilayer coatings where the hardness and modulus are weighted compositional averages between the ceramic layer properties and metallic layer properties. Although the hardness of the TiCr-TiCrN coating is higher than the Cr-CrN coating, 35GPa versus 27GPa, the H/E ratio for each coating is nearly identical. It is possible that the reported hardness for the TiCr-TiCrN is higher due to the high compressive stress in this coating; in contrast the Cr-CrN and CrC coatings have negligible compressive residual stresses. The hardness of the CrC coating is quite high at 32GPa. This strongly indicates that the coating is primarily comprised of nanocrystalline Cr_3C_2 grains (crystalline size below XRD detection limit) with a small % volume of amorphous carbon (as proposed in section 3.1.2). Coatings with a large % volume amorphous carbon matrix have hardness = 15-20GPa. The H/E ratio for the CrC coating is 0.075 which is lower than the other coatings, but as shown in section 3.2.6 this did not correlate to low fatigue performance.

In regard to repeatability of the LAFAD coating process, review of **Table 6** shows ample evidence that hardness and elastic modulus are consistent within +/-3% from sample to sample and between Dep1 and Dep2.

3.1.6 Coating Residual Stress

Reference Appendix RS

Residual stress in coatings is often unavoidable and can be controlled to some extent through coating design and processing parameters. Residual stress can be broken into two components; thermal residual stress and intrinsic residual stress. Thermal residual stress refers to the stress generated as a result of thermal expansion mismatch between the coating and the substrate. Thermal residual stress can be controlled by intentional matching of the coating/substrate thermal expansion coefficients, coating at lower temperatures, and experimenting with post deposition thermal annealing and or reheat treatment, although the latter is often not an option with precision components (e.g. gears) due to warping of part tolerances. Intrinsic stress refers to the stress developed by the unique atomic state of the coating. Intrinsic stresses are generated by the coating growth characteristics which include crystalline structure, lattice mismatch at layer interfaces, grain growth competition and lattice strain (interstitials). In some cases residual stress can be considered beneficial, e.g. compressive residual stress in a coating can increase the energy needed to propagate cracks improving surface initiated fatigue and impact performance. In most cases though it is desirable to minimize coating residual stress as high stresses result in poor coating adhesion/cohesion and reduce the contact load capacity of the coating (earlier onset of plastic deformation). Residual stress results for the TiCr-TiCrN, Cr-CrN, and CrC coatings as deposited on prime grade polished silicon <111> beams are shown in **Table 7**.

Table 7. Coating Residual Stress

Coating	Coating ID	Coating Thickness on Si [μm]	Coating Residual Stress (average) [GPa]
TiCr-TiCrN	ASE-8-9-1 (Dep1)	n/a	See Discussion
TiCr-TiCrN	ASE-8-14-1 (Dep2)	n/a	See Discussion
Cr-CrN	ASE-8-29-1 (Dep1)	5.7	-0.12, 0.15
Cr-CrN	ASE-8-34-1 (Dep2)	n/a	n/a
CrC	ASE-8-19-1 (Dep1)	6.0	-0.7
CrC	ASE-8-26-1 (Dep2)	5.4	-0.66

Residual stress data for the TiCr-TiCrN coating was not obtained due to in-situ deposition delamination or in-situ breaking of the silicon beams used for stress measurement. The observed in-situ delamination failure mode was quite remarkable in that the TiCr-TiCrN generated enough residual stress to delaminate sections of silicon from the silicon beam surface, implying that the adhesion between the coating/silicon was stronger than the internal cohesive strength of the silicon beams. In-situ beam breakage was also common, where the 5mm x 50mm beam would simply shatter under the coating stress induced curvature. In either case intact beams for post deposition curvature measurement and stress calculation were not available, therefore it was estimated that the TiCr-TiCrN coating has a residual compressive stress greater than 6GPa. For multi-layer coatings the principle of superposition can be applied just as already discussed in terms of coating roughness and coating hardness. In the case of multilayer coatings many researcher have shown a decrease in coating residual stress by increasing the volume fraction (layer thickness) of low stress metallic layers versus high stress ceramic layers. The stress evolution characteristics of the ceramic layer must also be taken into account, for example some ceramic coatings such as TiN initiate growth with a high compressive stress which begins to relax as the coating thickness increases and grain growth competition begins to relax. During the Phase II program extensive experimentation was conducted including multilayer optimization, thermal annealing, deposition bias, and deposition pressure, with the aim of bringing the compressive stress below 2GPa. All efforts were without success, although in the process improvements were made in the adhesive/cohesive performance of the TiCr-TiCrN coating. The residual stress for the Cr-CrN coating can be considered to be zero, as part of the beam shows very low compressive stress and the other part very low tensile stress (**page #RS_2-3**). The residual stress for the CrC coating is also a low compressive stress at ~0.7GPa. While it is not entirely correct, the results presented for residual stress of coatings on silicon are intended to generally represent the coating stress states on steel samples; since this assumption is commonly made in the literature it has been applied for the current work as well. Given the aforementioned difficulties it was difficult to prove repeatability of the LAFAD coating technology in this area of results. The CrC coating was the only coating to produce two good beams from separate Dep1 and Dep2 runs and in this case the repeatability was within +/-3%.

3.1.7 Coating Adhesion

Reference Appendix HF and SA

Coating adhesion assessment is a blanket term which encompasses all types of coating load/deformation failure modes. These types include adhesive delamination, cohesive cracking, and cohesive delamination. Adhesion refers to the bond strength between two different materials; for coatings adhesive failure refers to delaminations that occur at the coating/substrate interface. Cohesion refers to the bond strength within a material; for coatings it refers to the bond strength within a given monolithic coating, multilayer coating, or coating stack. Cohesive cracking refers to any cracking that occurs in a coating that propagates perpendicular to the coating surface (i.e. towards to substrate). Cohesive delamination refers to interlayer delamination at layer transitions within a coating, for example the transition from a metallic to ceramic layer in a multilayer coating. Coating adhesive/cohesive strength is a property of fundamental importance to all areas of coating performance. In the current effort coating adhesion/cohesion assessment was used extensively as a “gated” parameter, in other words coatings which did not produce good adhesion/cohesion results were immediately removed from consideration and were not subjected to further performance testing. As described in detail in section 2.2.2 (experimental description) of this report two types of adhesion/cohesion testing were conducted; Rockwell (HF) testing and instrumented scratch adhesion (SA) testing. Rockwell (HF) adhesion results are presented in **Table 8** for coatings deposited on polished P675.

Table 8. Coating Rockwell (HF) Adhesion Results (Polished P675)

Coating	Coating ID	Thickness [μm]	HF1-HF6 Rating	Appendix Page SEM Image @75x	Appendix Page SEM Image @250x
TiCr-TiCrN	ASE-8-9-1 (Dep1)	5.6	HF1	Page #HF_3	Page #HF_4
TiCr-TiCrN	ASE-8-14-1 (Dep2)	5.8	HF1	Page #HF_5	Page #HF_6
Cr-CrN	ASE-8-29-1 (Dep1)	6.3	HF1	Page #HF_9	Page #HF_10
Cr-CrN	ASE-8-34-1 (Dep2)	6	HF3	Page #HF_13	Page #HF_14
CrC	ASE-8-19-1 (Dep1)	6.3	HF1	Page #HF_17	Page #HF_18
CrC	ASE-8-26-1 (Dep2)	5.4	HF1	Page #HF_21	Page #HF_22

Rockwell (HF) results were nearly identical for all of the coatings deposited on super-finished P675 ([page #HF_2](#)). SEM images were collected for each indent and can be referenced ([page #HF3-24](#)). Note that HF ratings were assessed normally through observation by optical microscope; SEM images of indents are provided in order to show representative failure modes for each coating type in better quality and resolution than possible with an optical microscope. This is an important distinction because the HF rating is made only considering the damaged outside of the indent edge, which is convenient for optical microscopy since the center of the indent is not resolved and appears black, but can be confusing when viewing SEM images which resolve the damage features within the indent. Overall all coatings can be considered to have HF1 (best) ratings on P675. Minor exceptions were observed for the Cr-CrN coating ([page #HF_14](#)) on polished P675 and the TiCr-TiCrN coating ([page #HF_7-8](#)) on super-finished P675 where very small cohesive delaminations at the indent edge resulted in an HF3 rating. A HF1 rating implies that no cohesive or adhesive delamination exists and that only cohesive cracking can be observed with crack lengths extending no further than half the radius of the indent (as

measured from the indent edge). For all three coating types cohesive radial cracks were the primary damage mode. This result implies a cohesive brittle tensile fracture failure mode dominates and that the coatings are stronger in cohesive brittle compressive fracture, cohesive interlayer shear, and adhesive shear modes.

Table 9. Coating Scratch (Lc) Adhesion Results (Polished P675)

Coating	Lc1 (AE) [N]	Lc1 (visual) [N]	Lc2 (AE) [N]	Lc2 (visual) [N]	Lc3 (AE) [N]	Lc3 (visual) [N]	Lc4 (visual) [N]	Lc5 (CoF) [N]	Lc5 (visual) [N]
TiCr-TiCrN (average)	29.8		50.9	37.2	54.4	55.3	n/a	74.8	76.1
TiCr-TiCrN (%CoV)	4%		9%	5%	5%	8%	n/a	8%	7%
Cr-CrN (average)	11.6	11.7	20.5	27.6	36.9	35.2	n/a	78.0	78.7
Cr-CrN (%CoV)	9%	14%	41%	14%	12%	12%	n/a	3%	3%
CrC (average)	12.9	11.1	13.6	23.2	27.6	28.5	n/a		
CrC (%CoV)	6%	n/a	6%	7%	9%	6%	n/a		

Critical loads (Lc) are presented in **Table 9** for each coating type as deposited on polished P675. The reader is highly encouraged to review the Lc definitions on ([page #SA_2](#)). Detailed Lc data in table form for each coating and deposition can be referenced ([page #SA_3,10,17](#)) while the data in **Table 9** represents the average of all measurements for each coating. Recall from section 2.2.2 that the Lc loads are identified by acoustic emission (AE) data, coefficient of friction (CoF) data and visually confirmed when possible by optical microscopy. For each coating type representative AE plots, CoF plots, and optical microscope images of the Lc2, Lc3, and Lc5 damage modes can be referenced ([page #SA_4-23](#)). Consistent cohesive cracking in the scratch track (Lc2) was visually observed at 37N (TiCr-TiCrN), 28N (Cr-CrN), and 23N (CrC) loads. For all three coatings the Lc2 cohesive cracking mode was tensile which correlates with the Rockwell HF results ([page #SA_7,14,21](#)). This implies that as plastic deformation is generated in the substrate the coatings generate cohesive cracks in regions of tensile stress to accommodate strain deformation. At higher loads and deformations, areas of delaminations are observed (Lc3). For the TiCr-TiCrN and Cr-CrN coatings this occurs at 55N and 35N respectively, and is characterized by compressive buckling cohesive interlayer failures. For the CrC coating delaminations initiate at 29N load with material pull-out occurring between tightly nested arc tensile and compressive buckling cohesive cracks ([page #SA_22](#)). Complete adhesive failure (Lc5) of all three coatings occurred at approximately 75-80N loads (data for CrC was not included in Table 9 as visual confirmation of the Lc5 load was difficult using optical microscopy but later roughly confirmed using SEM back-scatter imaging). The consistency of the Lc5 failure loads suggests that coating adhesion strength is dependant on the ion-implantation deposition step, which is essentially the same for each coating, rather than unique coating properties such as architecture and residual stress.

While scratch adhesion and Rockwell adhesion testing provide a means to differentiate coatings from a design and optimization standpoint, from a practical standpoint it is difficult to correlate to wear and fatigue performance. This is primarily due to the fact that the coating failure modes are only identified through extensive plastic deformation of the substrate material. Equivalent plastic damage in operation to an actual gear or bearing would represent a major component failure. Historically many researchers have presented Lc5 data as the critical load of importance for coatings. In the current effort Lc1 and Lc2 data was focused on as these values represent the

load at which a coating first fails (cohesive cracking) and were thought to better represent optimization parameters for fatigue performance. Rolling contact fatigue results in section 3.2.6 show otherwise as the CrC and Cr-CrN coatings performed much better in fatigue than the TiCr-TiCrN coating.

Repeatability of the LAFAD deposition process for coating adhesion/cohesion results was excellent. As shown in Table 9, one sigma covariance was less than 15% between coating depositions (Dep1 and Dep2).

3.1.8 Coating Surface Energy

Reference Appendix CA

Contact angle measurements, i.e. oil wet-ability measurements, were conducted for coatings in contact with Aeroshell 555 turbine oil (DOD-L-85734A) to determine any possible differences with the baseline uncoated Pyrowear 675 case. No specific performance inferences were made as to small differences in the absolute values of measured contact angles; the aim of the testing was to demonstrate that coatings exist which show similar oil wet-ability characteristics to uncoated Pyrowear 675. Aeroshell 555 oil was used and tested at 80°C to model the Lift Fan gear operating conditions per Rolls-Royce information. The results, which include some of the preliminary development coatings, are presented in **Table 10**.

Table 10. Coating Contact Angle (Oil Wet-ability) Results

Coating	Coating ID	Sample ID	RMS Roughness [μm]	Average Contact Angle @ 4sec Drop Age [degree]
n/a	P675 Baseline	C133	0.005	13.8±0.2
CrC	ASE-7-92-1	C34	0.069	13.1±0.6
Ti(Si)CrC	ASE-7-142-1	C88	0.088	11.9±0.0
Ti(Si)Cr-Ti(Si)CrN	ASE-7-133-1	C36	0.102	11.0±0.5
Cr-CrN	ASE-8-5-1	C75	0.062	8.5±0.9
TiCr-TiCrN	ASE-7-136-1	C108	0.070	7.3±1.8
TiCrC	ASE-7-140-1	C40	0.114	6.1±0.7

Oil drop contact angle measurements are for coatings as deposited on polished P675, lower contact angle infers better surface wet-ability. It can be seen in **Table 10** that Aeroshell 555 turbine oil spreads and can be considered to have excellent wet-ability on all samples tested at 80°C. Oil wet-ability increases from baseline P675 (highest contact angle, worst wet-ability in sample set) to a TiCrC coating (lowest contact angle, best wet-ability in sample set). In general a value <20° is considered as acceptable wet-ability. The results show that there is not cause for concern for any of the coatings tested in regards to oil wet-ability when compared with the baseline uncoated Pyrowear 675 oil wet-ability. Since all coatings performed well, the outcome was that oil wet-ability could be removed as a down-selection parameter for potential coatings for the Lift Fan gear application. The other coatings listed in **Table 10** were eventually ruled out in other performance tests in favor of the TiCr-TiCrN, Cr-CrN and CrC coatings.

3.2 Performance Testing Results

3.2.1 Corrosion Evaluation – Modified Navy Corrosion Test

Reference Appendix NCT

The modified Navy corrosion test (NCT) protocol provided a means to assess P675 and coated P675 corrosion performance in a less aggressive environment than B117 salt fog corrosion testing. The NCT protocol is essentially a cyclic condensing/drying humidity test and does not subject the samples to alkaline salt solutions. Nevertheless early reports on corrosion performance submitted by Arcomac under Phase I and early Phase II research showed that low chromium gear/bearing steels such as M50 were subject to relatively severe pitting corrosion under the NCT protocol and that P675 was subject to isolated pitting. In early NCT tests coatings generally showed complete protection of the P675 substrate with a notable exception for coatings less than $2\mu\text{m}$ thick where accelerated pitting corrosion at coating pin-hole defect sites resulted in overall worse performance than uncoated P675. The NCT results for super-finished P675 and TiCr-TiCrN, Cr-CrN, and CrC coated super-finished P675 can be referenced ([page #NCT_4-15](#)) as pre-test and post-test images of the samples.

Prior to discussion of the results it is important to mention a particular short-coming of the NCT test protocol in that the nylon zip ties which are wrapped around the circumference of the disc samples tend to accelerate corrosion of the P675 where the nylon contacts the metal. Since the sample face is the only area of interest, corrosion of the sample circumference is not a direct concern, but indirectly there is a detrimental effect in that the run-off flow of corrosion products (iron oxides, etc) tends to cover the sample face. Since it is important to discern the origination of corrosion as the sample face, the samples are thoroughly cleaned after testing to remove any loosely adhered corrosion films that have migrated from the sample circumference. Additionally there is the valid concern that corrosion which initiates on the circumference of the sample can grow over the sample edges and onto the sample face. This has occurred in the past and occurred in the current test set. When this occurs the corrosion is noted with the caveat that it did not originate on the sample face.

Corrosion results for uncoated super-finished P675 can be referenced ([page #NCT_4,5](#)). The results on super-finished P675 are very good but not perfect; on both samples 1-2 small oxide pit formation sites were observed. Both P675 samples tested experience general pitting and surface corrosion along the bottom edge of the sample but this was thought to be growth from the sample circumference. The current results represent a marked improvement over previous P675 NCT tests. The primary reasons are thought to be related to the optimization of the carburization process and from the super-finishing process which other researchers have shown to improve corrosion performance possibly due to inherent passivation of the metals during the process chemistry. Results for the TiCr-TiCrN coating can be referenced ([page #NCT_6,7](#)). No pitting sites on the coated sample face were observed, but significant corrosion encroachment was observed from the P675 sample circumference (circumference and back of samples are not coated). The observed edge corrosion appeared to be a result of P675 corrosion and the specific placement of the nylon tie close to the coating face, but it can't be entirely ruled out that the

TiCr-TiCrN coating is more susceptible to corrosion than the Cr-CrN and CrC coatings. Results for the Cr-CrN coating can be referenced ([page #NCT_8-11](#)). No pitting sites or edge corrosion was observed on any of the four Cr-CrN samples tested. Additionally all four samples either had RCF tracks or BoD wear tracks on them and no corrosion was observed within the tracks indicating that the Cr-CrN coating can maintain corrosion protection in service. Results for the CrC coating can be referenced ([page #NCT_12-15](#)). No pitting sites or edge corrosion was observed on any of the four CrC samples tested. Additionally all four samples either had RCF tracks or BoD wear tracks on them and no corrosion was observed within the tracks indicating that the CrC coating can maintain corrosion protection in service.

The NCT test results allowed for the following conclusions to be drawn. Rolls-Royce has improved the corrosion performance for P675 over the last two years, although isolating pitting has not been eliminated. Pin-hole defects which expose the P675 substrate are invariably present in the TiCr-TiCrN, Cr-CrN, and CrC coatings (as will be shown in the next section). The unfavorable galvanic coupling that occurs at pin-hole sites between the electrochemically noble coating and less noble P675 substrate did not result in accelerated pitting corrosion under the relatively mild NCT protocol. As a result Cr-CrN and CrC coatings provided complete protection of the P675 substrate under the condensing/drying humid environment of the NCT test. Based on previous NCT results the TiCr-TiCrN also provides complete protection although in the current test group the coating was subject to edge corrosion most likely as a result of corrosion encroachment from the P675 circumference. Repeatability of the LAFAD process in NCT results was excellent for all coatings, no outlying corrosion results were observed.

3.2.2 Corrosion Evaluation – ASTM B117 Salt-Fog Corrosion Test

Reference Appendix SF

The ASTM B117 salt fog protocol is an aggressive corrosion evaluation test that is primarily used to evaluate automobile undercarriage components and body panels which are routinely subjected to wet, dirty and salty environments. The applicability of the test to simulate the corrosion performance of lubricated engine parts which are normally protected from the aforementioned environments has been brought into question on many occasions by the general scientific population and specifically in the current effort by AFRL and Rolls-Royce staff. Therefore observed performance delineations are best considered relative rankings of general corrosion performance rather than simulations of actual Lift Fan gear operating conditions. Defined as such, B117 testing provided very useful delineation of corrosion performance between P675 and the coatings for the current effort. Images of each test sample are provided in pre-test surface condition, surface condition after 96hrs exposure, surface condition after 336hrs exposure and surface condition after mild lapping to remove the red oxide film and expose the pitting morphology ([page #SF_5-18](#)).

Corrosion results were assessed semi-quantitatively by measurement of %Area coverage of red corrosion, the results are presented in **Table 11**. P675 super-finished samples demonstrated 100% red corrosion coverage for both samples tested. This result is well correlated with previous ASTM B117 testing of P675 conducted by Rolls-Royce. Examination of the samples after they were lapped ([page #SF_5-8](#)) showed evidence of severe pitting coupled with general surface corrosion over ~50-60% of the sample surface. Pitting features were common up to 1mm in diameter and 1mm depth.

Table 11. % Area Coverage of Red Corrosion

Coating	Sample ID	%Area Coverage Red Corrosion	Notes
n/a	P61	100%	
n/a	P62	100%	
TiCr-TiCrN (Dep1)	SF9	80%	
TiCr-TiCrN (Dep1)	SF12	99%	
TiCr-TiCrN (Dep2)	SF4	70%	
TiCr-TiCrN (Dep2)	SF6	60%	
Cr-CrN (Dep1)	SF2	0%	
Cr-CrN (Dep1)	P23	4%	Corrosion originates from RCF track
Cr-CrN (Dep2)	P60	2%	
Cr-CrN (Dep2)	P50	7%	Corrosion originates from RCF track
CrC (Dep1)	SF10	~50%	Red oxide did not adhere, see discussion
CrC (Dep1)	SF1	~50%	Red oxide did not adhere, see discussion
CrC (Dep2)	SF8	5%	
CrC (Dep2)	P39	~40%	Red oxide did not adhere, see discussion

TiCr-TiCrN samples demonstrated surprisingly poor corrosion protection with an average of 75% red corrosion coverage for four test samples. This result represents a decrease in corrosion performance as compared with TiCr-TiCrN coatings deposited in 2007 that were evaluated by Rolls-Royce and showed on average ~5-10% red corrosion coverage. Examination of the TiCr-TiCrN samples after lapping ([page #SF_9-12](#)) showed evidence of pitting although the primary failure mode appeared to be sequential delamination of the coating as general surface corrosion worked outwards from pitting sites. Because of the delamination/surface corrosion mode corrosion coverage on TiCr-TiCrN coated samples was ~50% and showed no measurable improvement over the base line P675 case. Coating delamination of this nature was not expected and was not observed around pitting sites on the Cr-CrN or CrC coatings, suggesting that the high residual compressive stress in the TiCr-TiCrN may have played role in propagating coating delaminations once pits had formed. As with uncoated P675 pitting features were common up to 1mm in diameter and 1mm in depth. The Cr-CrN coating demonstrated excellent corrosion protection with an average of ~4% red corrosion coverage for four test samples. Two of the four Cr-CrN samples were rolling contact fatigue tested prior to corrosion testing and in both cases small coating delaminations in the rolling track became corrosion pit initiation sites.

Examination of the samples after lapping ([page #SF_11-14](#)) showed pitting as the only corrosion failure mechanism with ~1% surface coverage. The few pit features that occurred on Cr-CrN samples were up to 1mm in diameter and 1mm deep, i.e. similar in scale to those measured on P675 and TiCr-TiCrN coatings. The CrC coating demonstrated improved corrosion performance over the baseline P675 case with an average of ~40% red corrosion coverage for four samples tested. One CrC sample showed only 5% red corrosion coverage while the red oxide film for the other three samples was poorly adhered to the coating so the presented values are estimates. Examination of the samples after lapping ([page #SF_15-18](#)) showed pitting as the only corrosion failure mechanism with ~10%-15% surface coverage. Pit features were common up to 1mm in diameter and 1mm in depth. For the LAFAD process repeatability of corrosion results for the TiCr-TiCrN, Cr-CrN, and CrC coatings between like coated samples and between Dep1 and Dep2 samples was very good.

Arcomac's LAFAD technology produces extremely dense coatings due to the high energy impedance of nearly 100% ionized plasma flow to the substrate as compared with other PVD techniques such as magnetron sputtering which transfer a high percentage of neutral (low energy) ions to the substrate. LAFAD coatings exhibit excellent low temperature diffusion barrier characteristics and are considered to be primarily inert to alkaline aqueous corrosion conditions. Regardless, particle defects occur in the coatings which expose the P675 substrate. Images of commonly observed particle defect types are included ([page #MOR10-12](#)). During coating deposition particle defects can become embedded in the coating and result in isolated stress risers. During continued deposition and/or post coating cool down stress buildup around embedded particles can result in particle delamination from the coating, also referred to as particle "fall-out". Depending on many factors particle fall-out can result in small area exposure of the P675 substrate. Even though exposure of the substrate is estimated to be in the worst case less than 0.1% of the total surface area being coated any exposure of the substrate can compromise corrosion performance. Particle defects of this type and/or any sliding or fatigue wear that exposes the P675 substrate provide sites for corrosion initiation due to unfavorable galvanic coupling between the coating and the substrate. The excellent performance of the Cr-CrN coating is thought to be the result of the multi-layer structure which serves to deflect cracks generated by particle fall-out and also due to lower defect incorporation into the coating due to increased in-situ particle sputtering by high energy Cr ions. In comparison the decreased performance of the CrC coating is most likely due to the monolithic structure of the CrC layer being more susceptible to cracking around particles.

3.2.3 Wear Resistance – Unidirectional Dry Sliding Wear (Ball-on-Disc)

Reference Appendix BoD

Ball-on-Disc (BoD) testing represented a significant portion of the Phase II coating development program. A particularly challenging aspect of this program was the need to optimize the tribological contact between two coatings. The Lift Fan system is comprised of three gears, all of which need to be protected from corrosion by coatings. This creates a situation of coating versus coating contact and it logically follows that if corrosion protection is to be maintained then the wear resistance of the coatings must be such that the coatings do not wear through within the design lifetime. BoD testing was used extensively during the program to evaluate various coating/coating contacts with the primary optimization parameters being volumetric wear rate, coefficient of friction (CoF), and ratio of wear rates between the contact pairs. Early in development it was confirmed that dissimilar coating contact pairing would be required as like coating contact pairs performed poorly. Based on these results extensive testing of various mixed contact pairs was conducted resulting in the optimized selection of TiCr-TiCrN in contact with Cr-CrN and CrC coatings.

Characterization of volumetric wear rate is important to estimate the operational lifetime of a contact pair leading ultimately to prediction of the gear lifetime. CoF directly relates to the amount of heat generated by the contacting pair; for the Lift Fan system this affects the tolerances of the gear design and load on the component cooling system. Ratio of volumetric wear rate is also considered a primary design parameter as ratios other than 1:1 dictate that one counter body (gear) will wear faster and hence fail earlier. The applicability to actual gear

operation is uncertain as the BoD test does not accurately simulate the complex sliding conditions of gear teeth meshing. BoD testing was run without lubrication to elucidate fundamental wearing properties aimed at simulation of worst case gear operating conditions, e.g. oil-interruption and dry startup. Certain characteristics of the BoD test protocol are also important to consider. The first is the dependence of contact stress on wear. The initial contact stress is dictated by the applied load and the contact area produced by elastic deformation of the ball (hemi-sphere) and disc (flat). As wear occurs for the ball-on-flat contact geometry the contact area increases rapidly while the load remains constant effectively reducing the contact stress. Resultantly, BoD testing contact stress is variable and can only be specified as an initial value and contact pairs which wear less experience more sliding cycles at higher contact stress than contact pairs which wear more. Another consideration is the formation of wear debris in dry sliding BoD testing, which by the nature of the test tends to remain in the contact zone, while for actual lubricated gears this would likely not be the case. With the above limitations taken into account, the BoD test matrix as conducted, served to provide a good means to differentiate the fundamental wear properties of the coatings and P675.

The amount of BoD data produced for TiCr-TiCrN, Cr-CrN, CrC coatings and baseline P675 was extensive and can be generally referenced in the 81 page BoD appendix. M50 balls were run against super-finished P675, and that TiCr-TiCrN coated balls were run against Cr-CrN and CrC coated discs. For 5N and 1N loads, tests were conducted at 100m, 500m, and 1000m sliding distances. The composite wear volume is defined as the sum of ball and disc wear volumes. Composite volume wear rate was calculated as volumetric wear as a function of dissipated energy for 100m, 500m and 1000m sliding distances. In other words the wear rate linear fit is based on sliding distance for a given load, meaning that the reported wear rates can only be compared for testing conducted at the same load and cannot be compared between like contact pairs conducted at different loads. For each BoD test images and surface profiles were collected for the ball wear scar and disc wear track, SEM images were collected for the disc wear track, EDS compositional analysis was conducted in the wear track, and CoF plots were collected, all of which can be referenced in the BoD appendix. Detailed information about the testing protocol can be reviewed in section 2.3.3 or the BoD appendix. The overall wear results for 1N loading and 5N loading are presented in **Table 13** and **Table 14** respectively.

Table 12. Uni-directional Sliding Wear Results, 1N Load

Sliding Distance [m]	Ball	Disc	Ball Wear Volume [um ³]	Disc Wear Volume [um ³]	Composite Wear Volume [um ³]	Average CoF	Composite Volume Wear Rate (linear fit, R ² > 0.99) [um ³ /J]
100	M50	P675	1.21E+05	negligible	1.21E+05	0.82	2356
500	M50	P675	7.49E+05	2.28E+05	9.77E+05	0.88	
1000	M50	P675	1.57E+06	4.79E+05	2.05E+06	0.90	
100	TiCr-TiCrN	Cr-CrN	1.22E+04	negligible	1.22E+04	0.26	550
500	TiCr-TiCrN	Cr-CrN	7.75E+04	negligible	7.75E+04	0.30	
1000	TiCr-TiCrN	Cr-CrN	1.86E+05	negligible	1.86E+05	0.34	
100	TiCr-TiCrN	CrC	1.50E+03	3.02E+05	3.03E+05	0.57	1638
500	TiCr-TiCrN	CrC	1.50E+03	9.24E+05	9.25E+05	0.55	
1000	TiCr-TiCrN	CrC	1.50E+03	1.13E+06	1.13E+06	0.55	

Table 13. Uni-directional Sliding Wear Results, 5N Load

Sliding Distance [m]	Ball	Disc	Ball Wear Volume [um^3]	Disc Wear Volume [um^3]	Composite Wear Volume [um^3]	Average CoF	Composite Volume Wear Rate (linear fit, R^2 > 0.99) [um^3/J]
100	M50	P675	8.91E+05	7.60E+06	8.49E+06	0.70	32000
500	M50	P675	2.85E+07	3.25E+07	6.10E+07	0.87	
1000	M50	P675	6.33E+07	7.86E+07	1.42E+08	0.90	
100	TiCr-TiCrN	Cr-CrN	1.53E+05	negligible	1.53E+05	0.34	50
500	TiCr-TiCrN	Cr-CrN	1.96E+05	negligible	1.96E+05	0.48	
1000	TiCr-TiCrN	Cr-CrN	2.81E+05	negligible	2.81E+05	0.52	
100	TiCr-TiCrN	CrC	2.82E+04	4.81E+06	4.83E+06	0.32	12000
500	TiCr-TiCrN	CrC	4.06E+04	1.27E+07	1.27E+07	0.35	
1000	TiCr-TiCrN	CrC	5.05E+04	2.63E+07	2.63E+07	0.36	

M50/P675 sliding contact wear was consistent with what would be expected for dry sliding metal to metal contact. For 1N and 5N loads, wear volume was evenly distributed between the M50 ball and the P675 disc indicating that both wore at about the same rate. Average friction values over 100m, 500m and 1000m sliding distances for 1N and 5N loads were nearly identical, indicating no CoF dependence on load for M50/P675 contact. For 1N and 5N loads, transient friction behavior was similar with a rapid rise to ~0.7CoF followed by steady state CoF = ~0.95 after ~350m sliding distance. Imaging and profile analysis of the M50 ball wear scar consistently showed (1N and 5N loads and all sliding distances) evidence of a well adhered oxide layer covering 50%-100% of the scar area. In areas where the oxide layer was removed abrasive wear mechanisms were apparent from the polished wear scar morphology with abrasion grooves running parallel to the direction of sliding. Imaging and profile analysis of the P675 wear track consistently showed (1N and 5N loads and all sliding distances) evidence of a well adhered oxide transfer layer which often completely filled the track wear profile. EDX analysis was used to confirm the presence of excess oxygen in the track (**page #BoD_11**) and it was assumed that the transformed layer is primarily iron oxide (post test wear debris has an orange color). Contact pressure greatly decreases as wear occurs, e.g. the starting contact pressure for a 5N load was 2GPa while the ending contact pressure for M50/P675 after 1000m sliding distance was 0.004GPa. The fact that wear rate is relatively constant over 100m-1000m sliding distances, even though the contact pressure decreases greatly suggests that wear for M50/P675 contact is primarily driven by the contact temperature generated and oxidation kinetics. Based on the results, the wear mechanism for M50/P675 contact is presented as primarily oxidative wear and 3-body abrasion. Elevated temperatures in the sliding contact zone cause oxidation of the M50 and P675 contacting bodies; the transformed oxide layer is easily sheared on sliding contact and forms abrasive debris (third body contact).

TiCr-TiCrN versus Cr-CrN sliding contact was characterized by preferential wear of the TiCr-TiCrN coating and no measurable wear of the Cr-CrN coating for all tests conducted at 1N and 5N. Preferential wear of the TiCr-TiCrN ball coating occurred at a very low rate. Increasing the test load from 1N to 5N increased TiCr-TiCrN ball wear volume by approximately 2x for

equivalent sliding distances. TiCr-TiCrN ball wear volume at 1N load was 10x less than M50 ball wear, and 100x less than M50 ball wear at 5N load tests. Transient friction response showed a slow and steady increase from ~0.3CoF at test start to ~0.6CoF steady state friction after ~500-700m sliding distance. This transient response occurred at a faster rate for 5N load testing and a much slower rate for 1N coatings, hence the lower average friction value reported over equivalent sliding distances. Imaging and profile analysis of the TiCr-TiCrN ball wear scar consistently showed (1N and 5N loads and all sliding distances) a well polished scar with no evidence of adhered debris and minor evidence of abrasive directional grooving. For both 5N, 1000m tests the TiCr-TiCrN wore through at some point late in testing, evidence of the exposed M50 substrate was clear in images of the ball wear scar ([page #BoD_76](#)). Imaging and profile analysis of the Cr-CrN disc wear track consistently showed (1N and 5N loads and all sliding distances) no evidence of any wear occurring on the Cr-CrN coating, even the surface morphology appeared undisturbed under high magnification SEM imaging of the track (example on [page #BoD_63](#)). A very thin transfer layer was observed to be adhered in the surface roughness “valleys” of the Cr-CrN disc wear track; EDX analysis showed increased oxygen concentration suggesting the transfer layer is oxide debris from the worn TiCr-TiCrN ball. Oxide transfer layer coverage of the Cr-CrN track increased with increasing sliding distance and load (i.e. increased TiCr-TiCrN ball wear) which suggests that the observed transient friction is a result of maturing TiCr-TiCrN sliding contact with the oxide layer as the Cr-CrN coating is covered over. The proposed wear mechanism in dry sliding for TiCr-TiCrN in contact with Cr-CrN is steady, slow rate, oxidative wear of the TiCr-TiCrN coating and negligible wear of the Cr-CrN coating due to a protective oxide transfer layer.

TiCr-TiCrN versus CrC sliding contact was characterized by preferential wear of the CrC coating and low wear to the TiCr-TiCrN coating for all tests conducted at 1N and 5N. In general wear volume of the CrC disc was 100x greater than the wear volume of the TiCr-TiCrN ball at equivalent sliding distances and loads. Increasing the load from 1N to 5N increased the wear volume by ~20x on TiCr-TiCrN balls and CrC discs at equivalent sliding distances. Compared to baseline M50/P675 results the TiCr-TiCrN ball wear was ~1000x less than M50 ball wear and the CrC disc was ~2x less than P675 disc wear. Imaging and profile analysis of the TiCr-TiCrN ball wear scar consistently showed (1N and 5N loads and all sliding distances) a well polished scar with little to no evidence of directional grooving. For 1N tests the TiCr-TiCrN ball often showed evidence of a well adhered light blue to white color layer, presumably a titanium oxide. Imaging and profile analysis of the CrC disc showed a highly polished track for 1N loads and a highly polished track plus signs of micro-cohesive delaminations at 5N loads ([page #BoD_79](#)). Profiles of CrC wear tracks showed that the wear track depth was essentially the same for 1N and 5N loads when compared at 100m, 500m, and 1000m sliding distances. Even though the wear track depths were the same, the CrC disc wear for volumes for 5N load tests were on average 20x greater than those for 1N load tests. This was due to wear of the TiCr-TiCrN ball in 5N load tests resulting in a wider contact area and hence wider wear track of equivalent depth, i.e. greater volume . A significant amount of loose powdered wear debris was observed on the CrC discs post test. The debris was not adhered to the wear track and was removed in cleaning; this was confirmed by compositional EDX analysis which showed no presence of oxides in the track. A slight green tint to the wear debris was observed which strongly suggests chromium oxide Cr₂O₃ is primarily formed in wear. Almost no transient friction response was observed, steady state friction values were reached within 50m sliding distance at 1N and 5N loads.

Interestingly, steady state friction values for 1N load tests were ~0.55CoF, while 5N load tests were ~0.35CoF. The decrease in friction at 5N test loads may be the result of some small amount of graphitization (lubricious phase formation) of the amorphous carbon phase in the CrC coating. If this is the case then the lubricious phase contribution is small and mixed with the primary chromium oxide phase given the steady state friction of 0.35. Literature reports on coatings with high percentage content of amorphous carbon often report friction values <0.1. Overall it appears that CrC preferentially wears by abrasive and oxidative wear mechanisms in contact with TiCr-TiCrN resulting in almost no wear to the TiCr-TiCrN coating at 1N test loads while at 5N test loads the increase in dissipated energy results in mild oxidative wear of the TiCr-TiCrN coating.

Comparison of the coatings and P675 in terms of the composite volume wear rate provides some practical information. For 1N test loads, M50/P675 contact had the highest wear rate, the TiCr-TiCrN/Cr-CrN contact wear rate was 4x lower than M50/P675, and the TiCr-TiCrN/CrC wear rate was 1.5x lower than M50/P675. For 5N test loads, M50/P675 contact had the highest wear rate, the TiCr-TiCrN/Cr-CrN contact wear rate was 650x lower than M50/P675, and the TiCr-TiCrN/CrC wear rate was 2.5x lower than M50/P675. In all BoD tests the coatings out performed the baseline M50/P675 contact and a general trend was observed that as load increased the margin of improvement provided by the coatings increased. For both coating pairings preferential wear occurred, so the ideal ratio of ~1:1 was not met in either case. Even though the TiCr-TiCrN coating wore preferentially against Cr-CrN the rate was very low which provides an advantage over the TiCr-TiCrN/CrC pairing for which the CrC coating wore at a higher rate. Repeatability of wear results for the LAFAD deposition process was excellent between Dep1 and Dep2 coatings.

3.2.4 Gear Simulation, Scuffing – Wedeven Load Capacity Protocol

Reference Appendix WLC

The original purpose of this load capacity (LC) test method was to evaluate oils according to the Ryder Gear Test Method, with enhanced sensitivity for lower than average lubricating performance. In the present evaluation Royco 555 oil is used exclusively and the scuffing performance of Pyrowear 675 and TiCr-TiCrN, Cr-CrN, and CrC coatings are evaluated with contact pair material and surface finish as the primary variables. The test simulates gear operation and the LC test parameters were set to produce a 345in/sec sliding velocity, which exceed the worst case gear sliding velocity mesh condition for Lift Fan gears which is 304in/sec. Arcomac conducted tests to characterize coating versus coating contacts and Rolls-Royce conducted tests to characterize P675 versus P675 contact with super-finished and hard-grind surface finishes; the testing parameters were identical for every test (detailed test parameters and test matrix [page #WLC_3](#)). Failure loads for P675 tests were made available by Rolls-Royce but post test disc/ball condition were not, so only the former are included in this report. LC testing results are provided in **Table 15**.

Super-finished P675 and ground-finish P675 test groups performed extremely well in LC testing with Ryco 555 oil. Incremental run-in wear was observed as friction ratcheting, apparent in the test plots for ground-finish P675 ([page #WLC_14](#)). About halfway through testing the run-in wear improved the surface finish to the point where the CoF started to decrease, but run-in friction ratcheting increased as the oil chemistry struggled to provide recovery from boundary to EHD

lubrication modes. Test plots for super-finished P675 ([page #WLC_15](#)) show the dramatic effect that improved average surface roughness between the ball and the disc has on the LC results. For the super-finished P675 tests very slight friction ratcheting occurred indicating that EHD lubrication was maintained up to ~270N (~1.8GPa) after which only minor run-in asperity wear occurred. Both super-finished P675 tests ran to test suspension at 621N load (2.4GPa) without failure. Repeatability of friction behavior was good for both the ground-finish and super-finished P675. LC performance data was provided (**Table 13**) by Wedeven Assoc on M50 and 9310, both common gear materials, for comparison with the current test matrix. According to Wedeven Assoc the desired performance criteria for oil/material combinations for advanced gearing applications is a macro-scuff failure load greater than 288N (1.86GPa).

Table 14. Load Capacity (LC) Test Results

Ball	Disc	Macro-Scuffing Failure @ Load [N]	Macro-Scuffing Failure @ Stress [GPa]
TiCr-TiCrN (Dep1)	Cr-CrN (Dep1)	277	1.84
TiCr-TiCrN (Dep1)	Cr-CrN (Dep2)	168	1.54
TiCr-TiCrN (Dep1)	Cr-CrN (average)	223	1.69
TiCr-TiCrN (Dep2)	CrC (Dep1)	145	1.43
TiCr-TiCrN (Dep2)	CrC (Dep2)	517	2.26
TiCr-TiCrN (Dep2)	CrC (average)	331	1.95
P675 (ground finish)	P675 (ground finish)	468	2.18
P675 (super-finish)	P675 (super-finish)	No failure	No Failure
M50 (ground finish)	M50 (ground finish)	517	2.26
9310 (ground finish)	9310 (ground finish)	315	1.91

TiCr-TiCrN versus Cr-CrN test groups failed at loads 2x-5x lower than baseline P675. Incremental run-in wear was more severe than baseline P675, evidenced by higher oil temperatures and pronounced friction ratcheting behavior at the beginning of each incremental load stage ([page #WLC_6,8](#)). Given the higher average surface roughness for TiCr-CrN and Cr-CrN contact (as compared with super-finished P675) increased run-in wear results were to be expected. EHD friction decrease occurred earlier than baseline P675 tests due to more rapid run-in polishing of the TiCr-TiCrN ball and Cr-CrN disc. Analysis by optical microscope and profilometry suggest that the run-in wear results in minor polishing wear of the TiCr-TiCrN ball and Cr-CrN disc. Two of four tracks on the Cr-CrN coatings showed evidence of mild polishing wear with ~20% of the track area failed by cohesive interlayer delamination to maximum depths of 2/3 of the total coating thickness ([page #WLC_7,9](#)). The other two tracks showed uniform abrasive wear through the Cr-CrN disc coating to depths of ~6-9µm and wear through the TiCr-TiCrN ball coating ([page #WLC_7,9](#)). These results suggest a wear progression timeline, the hypothesis is that the Cr-CrN coating fails first by cohesive breakup which generates abrasive wear debris and results in aggressive wear of the ball and Cr-CrN coating. The fact that the Cr-CrN fails by cohesive delamination at contact stresses of ~1.75GPa cannot be explained, especially when considering that the Cr-CrN coating performed well in RCF testing at 4.5GPa

and extremely well in BoD testing at initial contact stresses of 2.0GPa. Repeatability of results between Dep1 and Dep2 Cr-CrN coatings was marginal given that Dep1 failed at 277N (1.84GPa) and Dep2 failed at 168N (1.54GPa). The TiCr-TiCrN versus Cr-CrN (Dep1) contact pair essentially passes the industry desired performance criteria and while this is promising the marginal repeatability and significantly lower performance than baseline P675 suggests further development would be beneficial.

TiCr-TiCrN versus CrC test groups performed better than the TiCr-TiCrN versus Cr-CrN contact pairing. Incremental run-in wear was indicated by friction ratcheting, the friction response was somewhat erratic as compared with other contact pairs but less pronounced than the TiCr-TiCrN Cr-CrN contact pair ([page #WLC_10,12](#)). Again, given the higher average surface roughness for TiCr-CrN and CrC contact (as compared with super-finished P675) increased run-in wear results were to be expected. During testing of this contact pair a large difference in the failure load between Dep1 and Dep2 CrC occurred. The CrC (Dep2) disc failed at 517N (2.26GPa); the CrC disc track was highly polished and evenly worn to a depth of ~1.2 μ m and the TiCr-TiCrN ball showed mild polishing wear with isolated cohesive delamination sites ([page #WLC_11](#)). The CrC (Dep1) disc failed at 145N (1.43GPa); the CrC disc track was mildly polished to a depth of ~0.2-0.3 μ m and the TiCr-TiCrN ball showed very mild polishing wear with isolated cohesive delamination sites ([page #WLC_13](#)). The small cohesive delaminations from the TiCr-TiCrN ball coating apparently caused a friction spike high enough to meet the LC test protocol for failure, even though the damage to the CrC disc and TiCr-TiCrN ball were negligible. This suggests that the TiCr-TiCrN and CrC contact pair performs on a similar level to baseline ground-finish and possibly to super-finished P675, but that the testing protocol would need to be modified in the future to account for higher friction spikes that for most materials would normally indicate macro-scuff failure but are recoverable for the TiCr-TiCrN and CrC contact pair.

3.2.5 Gear Simulation, Scuffing – Wedeven Performance Mapping Protocol

Reference Appendix WPM

The performance mapping (PM) protocol is very similar to the load capacity protocol in that both methods simulate severe gear operating conditions by incrementally reducing oil film thickness and forcing boundary lubrication (wear) conditions. The PM method achieves this by increasing sliding velocity and decreasing oil entraining velocity while load is held constant, whereas the LC method achieves this by increasing load while the velocities are constant. Arcomac conducted tests to characterize coating versus coating contacts and Rolls-Royce conducted tests to characterize P675 versus P675 contact with super-finished and hard-grind surface finishes; the testing parameters were identical for every test (detailed test parameters and test matrix [page #WPM_1-6](#)). Failure stages for P675 tests were made available by Rolls-Royce but post test disc/ball condition were not, so only the former are included in this report. PM testing results are provided in **Table 16**.

Table 15. Performance Mapping (PM) Test Results

Test Series	Ball	Disc	Sliding Velocity [m/sec]	Entrainig Velocity [m/sec]	Lubrication Regime	Stage @ Failure
Cold-Scuffing	TiCr-TiCrN (Dep1)	CrC (Dep2)	5.71	0.46	Boundary	4
Hot-Scuffing	TiCr-TiCrN (Dep1)	CrC (Dep2)	25.4	1.27	Wear	11
Cold-Scuffing	TiCr-TiCrN (Dep2)	Cr-CrN (Dep1)	2.5	0.91	Boundary	4
Hot-Scuffing	TiCr-TiCrN (Dep2)	Cr-CrN (Dep1)	7.6	3.9	Boundary	4
Cold-Scuffing	P675 (ground finish)	P675 (ground finish)	1.3	1.1	EHD/Boundary	2
Hot-Scuffing	P675 (ground finish)	P675 (ground finish)	25.4	1.27	Wear	11
Cold-Scuffing	P675 (super-finish)	P675 (super-finish)	8.3	0.1	Wear	13
Hot-Scuffing	P675 (super-finish)	P675 (super-finish)	n/a	n/a	Wear	>13, No Failure

Performance mapping results are presented in **Table 14** based on the test stage when failure occurred; failure greater than stage 6 for cold-scuffing and greater than stage 8 for hot-scuffing are considered excellent results. Overall the ranking of materials for PM were very similar to what was found for the LC method. The CrC coating in contact with the TiCr-TiCrN coating posted better results over the P675 ground-finish contact pair but did not perform as well as super-finished P675. The importance of low average surface roughness between contacting pairs was illustrated by super-finished P675 results as compared to ground-finish P675 results. In particular the ground-finish P675 performed very poorly in the cold scuffing series, failing just as the transition to boundary wear is made (a duplicate test was run to confirm this result). In correlation with the LC results the PM failure mechanisms for the TiCr-TiCrN and CrC contact pair were mild polishing with isolated cohesive delamination of the TiCr-TiCrN ball coating and steady abrasive wear of the CrC disc coating. The PM test results provided additional evidence that steady wear of the CrC coating occurred until the coating was worn through and the underlying P675 substrate was exposed. The Cr-CrN coating in contact with the TiCr-TiCrN coating performed marginally; both the hot and cold scuffing series failed relatively early into the boundary lubrication regime. As in LC tests, isolated cohesive delamination areas were observed in the Cr-CrN disc track while most of the track was polished and evenly worn to ~0.5µm depth. The correlation between PM and LC failure modes for the Cr-CrN coating strongly suggest that the Cr-CrN fails structurally by cohesive interlayer failure and the resulting wear debris causes accelerated damage to both the Cr-CrN disc and the TiCr-TiCrN ball. Due to the high cost of PM testing only one contact pair was tested for each material type so no repeatability assessment could be made.

3.2.6 Contact Fatigue – Rolling Contact Fatigue Test

Reference Appendix RCF

Contact fatigue performance is the third primary coating design goal identified for the Lift Fan gear application. Contact fatigue failure of the P675 substrate refers to the classic definition of macro-pit (spallation) formation due to subsurface crack formation and propagation. Knowledge of the contact stress field is helpful. The ductile yield stress of a material can be compared with failure criteria stresses, such as the Von Mises stress, to determine if plastic deformation occurs in a material. The maximum Von Mises stress for contacting pairs (ball-on-flat in this case) occurs below the contact surface at a depth which is dependent on the load and radius of the contacting ball. For the RCF test setup using 2.75mm radius balls and a 4.5GPa maximum Hertz contact stress (principal compressive stress component at the surface) results in a maximum Von Mises stress of ~3.0GPa at ~80 μm below the contact surface. For scale Lift Fan gear contacts at equivalent stress the maximum stress depth is much greater. Shear stresses of opposite sign also occur below the contact surface ahead and behind the center of contact. For the RCF test the maximum shear stress depth is ~25 μm below the surface. In rolling fatigue a stress cycle occurs each time a ball passes over the contact zone at a frequency equal to the RPM of the test multiplied by the number of balls; for the RCF test the contact cycle frequency is 460cycles/sec. For the maximum Von Mises stress location the stress cycle range is zero to the Von Mises stress. At the location of the maximum alternating shear stress the stress range is usually greater because of the opposite sign of these stresses even though the magnitude of the shear stresses is smaller than the Von Mises stress. Therefore it is the alternating shear stresses which are thought to be responsible for macro-pitting fatigue failure of bearing/gear materials. Contact fatigue failure of a coating refers to delamination of the coating within the contact rolling track. Since the maximum stresses related to ductile failure are not located in the coating it is possible that the coating fails due cohesive brittle crack formation onset by cyclic tensile stresses at the contact edge. For multilayer coatings it is also possible that the relatively soft metallic layers fail in ductile fatigue generated by albeit lower magnitude stress field present in the coating versus the substrate. In the case that coating adhesive delamination occurs, the P675 substrate becomes exposed and corrosion and wear protection are compromised. In the case that cohesive delamination occurs the contact rolling track becomes roughened which leads to insufficient oil film thickness and excessive wear. It is in this manner that coating rolling contact fatigue performance can be viewed as the necessary foundation for corrosion and wear performance of a coating. From a performance standpoint the coating must meet or exceed the baseline fatigue performance of the P675 substrate. If the P675 substrate fails first in fatigue and material delaminates from the substrate (in the RCF test this would likely occur at a depth of ~17-25 μm) the coating will be removed with the substrate and corrosion protection compromised, so in this sense the coating fatigue performance cannot truly exceed the substrate performance. It is not anticipated that a coating can improve the fatigue performance of the P675 substrate in regards to subsurface crack formation. There is a possibility that the coating could improve the P675 fatigue response by improving surface initiated fatigue failure modes. Surface initiated fatigue refers to crack generation at the material surface as a result of surface stress concentrations due to manufacturing defects, wear particle embedment, etc. RCF test results are presented in **Table 17** for the super-finished P675 baseline and the TiCr-TiCrN, Cr-CrN, and CrC coatings as deposited on super-finished P675. All results presented in **Table 17** were conducted at 4.5GPa contact stress, detailed testing parameters can be referenced either in section 2.3.6 or ([page #RCF_1-2](#)). Ball wear results in table format can be referenced as well ([page #RCF_4](#)).

Table 16. RCF Results

	# of Cycles @ FAILURE	# of Cycles @ STOP	Notes
P675, super-finished	n/a	8.0E+06	No failure, test suspended
P675, super-finished	n/a	9.0E+06	No failure, test suspended
P675, super-finished	n/a	18.0E+06	No failure, test suspended
TiCr-TiCrN (Dep2)	0.09E+06	0.25E+06	Failure, coating delamination (100% of track)
TiCr-TiCrN (Dep2)	0.25E+06	1.0E+06	Failure, coating delamination (100% of track)
TiCr-TiCrN (Dep2)	0.33E+06	0.7E+06	Failure, coating delamination (100% of track)
Cr-CrN (Dep1)	3.0E+06	3.0E+06	Failure, coating delamination (~30% of track)
Cr-CrN (Dep1)	n/a	8.0E+06	No failure, test suspended
Cr-CrN (Dep1)	n/a	4.0E+06	No failure, test stopped due to EHD Breakdown
Cr-CrN (Dep2)	n/a	10.0E+06	No failure, test suspended
Cr-CrN (Dep2)	n/a	6.3E+06	No failure, test stopped due to mechanical problem
Cr-CrN (Dep2)	n/a	8.0E+06	No failure, test stopped due to EHD Breakdown
CrC (Dep1)	n/a	10.0E+06	No failure, test suspended
CrC (Dep1)	n/a	10.0E+06	No failure, test suspended
CrC (Dep2)	n/a	9.5E+06*	No failure, test stopped due to EHD Breakdown
CrC (Dep2)			test not completed by time of reporting
CrC (Dep2)			test not completed by time of reporting
CrC (Dep2)			test not completed by time of reporting

RCF testing of baseline super-finished P675 was performed on three samples; all tests were run to suspension over a range of 8E+06 to 18E+06 contact cycles and no failures were observed. Optical microscope analysis of the rolling tracks on P675 ([page #RCF_11](#)) showed a mild reduction in track roughness indicated by the higher reflectivity of the track surface as compared to the non-contact surface. Plastic deformation is the hypothesized mechanism for morphology differences between the track and surrounding non-contact areas. Track profiles ([page #RCF_13](#)) collected by contact profilometry showed a consistent conformal (to ball) deformation of the track to depths of ~0.3µm to 0.5µm. The shape of the profile and the surface characteristics suggest plastic deformation rather than wear. Ball wear (% mass loss) was less than 0.01% for all P675 samples tested which further suggests full EHD lubrication was achieved in testing and little to no wear occurred. The ~350µm track width measured on all samples correlates well with the theoretical Hertz elastic contact width of 350µm at 4.5GPa contact stress. The initial goal for baseline P675 testing was to test at least six samples to failure and it was thought that this might be accomplished within 10E+06cycles for the given RCF testing conditions. After testing had begun an exceptional reference [15] was found, which was a detailed study conducted by the Rolls-Royce turbine bearing group in the 1980's. The findings after years of fatigue testing conducted at nearly identical parameters to the present RCF testing was that advanced bearing materials were failing between 50-120E+06 cycles. To evaluate P675 to this extent would have required ~3months which was beyond the scope of the remaining testing timeline and budget, but it seems reasonable to assume that P675 performance would fall into the range identified for other advanced bearing materials. As such the current dataset is best considered a screening assessment for the coated P675 samples.

RCF testing of the TiCr-TiCrN coating as deposited on super-finished P675 was only performed on three samples primarily because of consistently poor fatigue performance. All TiCr-TiCrN coatings failed catastrophically in less than 0.4E+06 contact cycles. The failure mode for all three TiCr-TiCrN samples tested was complete removal of the coating over 100% of the track contact surface area. Exposed P675 substrate and coating cohesive interlayer failures along the edges of the rolling track are shown in optical microscope images (**page #RCF_5**). Profile scans of a TiCr-TiCrN coating RCF tracks confirmed coating delamination failure and the possibility of some wear occurring to the P675 substrate (**page #RCF_6**). Track profiles averaged ~6 μ m in depth (TiCr-TiCrN coating thickness 5.8 μ m +/-0.2 μ m). At the track edges profile steps showed evidence of cohesive interlayer delaminations at various bi-layers within the coating. Ball wear (% mass loss) was averaged at ~0.3% which is relatively high considering the short run-time and indicates that wear occurred in addition to delamination. Scratch adhesion showed a susceptibility to tensile cracking for the TiCr-TiCrN coating but the load at which cracking occurred was higher than the load for the Cr-CrN and CrC coatings both of which performed well in fatigue. The most likely property of the TiCr-TiCrN coating to explain the poor fatigue performance is the very high compressive residual stress. Considering all of the data, a reasonable hypothesis for the failure of the TiCr-TiCrN coating is as follows; fatigue related crack generation followed by cohesive interlayer delamination encouraged by the sum of the residual and contact stresses leading to debris formation, oil film breakdown, and rapid wear and breakup of the coating until the P675 substrate is reached. During Phase II development of the TiCr-TiCrN coating fatigue performance was poor for many experimental design iterations on coating architecture, coating Ti/Cr ratio and coating deposition temperature. The current TiCr-TiCrN formulation was shown to reach 8E+06 cycles without failure as deposited on polished P675, but as the final results show, this performance did not transfer to super-finished P675.

RCF testing of the Cr-CrN coating as deposited on super-finished P675 was performed on six samples and results were generally good. Five of six of the Cr-CrN samples evaluated reached test suspension without failure; although two of the five were stopped earlier due to mechanical problems with the RCF test rig (see Table 11 notes). One of the Cr-CrN samples failed in RCF testing over 30% of the track area (**page #RCF_7**). Similar to the TiCr-TiCrN coatings the Cr-CrN failed completely to the substrate with evidence of multiple cohesive interlayer delaminations along the track edge. The result suggests that coatings are subject to the same type of statistical defects which affect metallic substrates and produce early failures in a low percentage of samples. In this case it is hypothesized that a large particle defect in the track provided a stress riser large enough to initiate delamination failure in the coating. In general Cr-CrN coating RCF tracks showed only light discoloration and no wear or change in surface morphology was visually apparent when compared with the non-contact surfaces outside of the track (**page #RCF_7**). Conformal profiles were observed with depths of ~0.5-0.75 μ m (**page #RCF_8**) which were hypothesized to be primarily the result of plastic deformation of the P675 substrate and secondarily the result of polishing run-in wear of the coating. Ball wear (% mass loss) was averaged at ~0.1% for tests that ran to completion under full EHD lubrication. The increase in ball wear over the baseline P675 case is due to the higher surface roughness of the Cr-CrN coating resulting in a run-in wear period where the Cr-CrN coating preferentially wears the balls as the Cr-CrN asperities are removed. This effect may not be detrimental as the ball surface RMS is likely polished in the process creating better EHD conditions. RCF test rig oil contamination occurred for some of the tests conducted on Cr-CrN and CrC coatings, these tests

were stopped due to breakdown of the EHD oil film thickness and excessive wearing of the balls and coatings. Ball wear in these tests against Cr-CrN coatings was ~2.3%; 20x the wear for tests which ran normally. Cr-CrN coating wear in these tests was observed and track wear depths were from 1 μ m-3 μ m, although no fatigue related failures were noted.

RCF testing of the CrC coating as deposited on super-finished P675 was performed on three samples while testing of the remaining three samples was not completed by the time of reporting. All three CrC samples tested ran for 10E+06 contact cycles until test suspension without failure. Optical microscope analysis of the rolling tracks ([page #RCF_9](#)) showed a mild reduction in track roughness indicated by the higher reflectivity of the track surface as compared to the non-contact surface. Track profiles ([page #RCF_10](#)) collected by contact profilometry showed a consistent conformal (to ball) deformation of the track to depths of ~0.3 μ m to 0.5 μ m which is consistent with the plastic deformation depth expected from the P675 substrate. Track profiles show a reduction in track roughness suggesting run-in wear occurred for the CrC coating in a similar manner discussed for the Cr-CrN coating. Ball wear (% mass loss) was ~0.2%, about 2x the wear for Cr-CrN coatings which was somewhat unexpected given that the Cr-CrN coating was shown to be more abrasive in dry sliding tests. This result suggests that the CrC coating may be more abrasive in lubricated contacts versus dry contacts where formation of a solid lubricant phase plays a strong role. One of the CrC tests was compromised by EHD breakdown due to oil contamination RCF rig failure; coating ball and coating wear increased but no fatigue related failures were noted.

From a practical standpoint for the Lift Fan gear application the RCF test effort provided some important distinctions. RCF testing conducted on P675 did not produce failure up to 18E+06 cycles and literature reviews indicated that P675 could be expected to perform with the range of 50-120E+06 contact cycles. CrC and Cr-CrN coatings effectively matched P675 results up to 10E+06 contact cycles. When EHD lubrication was maintained (i.e. the RCF test ran properly) P675 demonstrated essentially no disc or ball wear, CrC and Cr-CrN coatings having a higher RMS surface roughness than super-finished P675 demonstrated polishing run-in wear of the disc and balls. For P675, Cr-CrN, and CrC further testing would be required to characterize a true fatigue life. The TiCr-TiCrN coating performed poorly in fatigue clearly indicating that more development is needed in this area.

3.3 Coating Uniformity Study

Reference Appendix UNI

For any coating solution to be ultimately successful it must be transferred from flat substrate geometries commonly used for coating development to the complex geometry of the Lift Fan helical bevel gears. Uniformity is defined as a measure of the capability of the LAFAD coating process to produce coatings with consistent properties over a deposition zone area large enough to coat full scale Lift Fan gears. Early in the Phase II SBIR effort acquisition of a Lift Fan gear section was planned to demonstrate coating uniformity, although the gear acquisition ended up not being possible. Instead two methods were used to characterize coating uniformity; placement of witness samples at different positions and angles to the plasma flow to replicate the angles of Lift Fan gear teeth and coating of 2"dia spur gears with tooth-to-root aspect ratios matching the Lift Fan gear to demonstrate coating thickness uniformity on complex shapes.

A vertical distribution sample fixture was used to assess the dependence of coating thickness, coating composition and coating mechanical properties on position and angle in the plasma flow. Qty(6) 19mm diameter 440A samples (RMS ~25nm, HRC ~58) were loaded into a fixture which distributed the samples vertically over a 15cm (6in) coating zone with 2.5cm (1in) spacing between the centers of the samples ([page #UNI_3](#)). The samples were coated in fixed single rotation mode and were set at specific angles to the plasma flow to encompass the range of plasma exposure angles for Lift Fan gear teeth. The reader is encouraged to reference ([page #UNI_2](#)) to understand the notation for the various sample facing angles. Variations due to position or facing angle in coating thickness, coating adhesion, coating composition, coating hardness were assessed.

Table 17. Coating Uniformity - Vertical Thickness Distribution

Angular Position →	-90deg (normal)	0deg (normal)	+45deg*	-45deg**	0deg*** (normal)	+90deg	0deg (normal)
Coating →	Cr-CrN (Dep1)	Cr-CrN (Dep2)	TiCr-TiCrN (Dep1)	TiCr-TiCrN (Dep2)	TiCr-TiCrN (Dep2)	CrC (Dep1)	CrC (Dep2)
Thickness [μm] Position 1	2.93	4.45	3.57	4.02	n/a	2.13	4.22
Thickness [μm] Position 2	3.38	5.84	4.23	5.13	n/a	2.84	5.47
Thickness [μm] Position 3	3.62	6.65	5.07	5.97	5.65	3.51	5.70
Thickness [μm] Position 4	3.28	6.67	5.44	6.01	5.82	2.54	5.56
Thickness [μm] Position 5	2.68	5.70	4.97	6.07	n/a	2.42	5.33
Thickness [μm] Position 6	2.26	4.14	3.67	4.74	n/a	1.91	4.03
% Change in Thickness Versus 0deg (normal) Orientation	48% decrease	-	8% decrease	4.5% increase	-	46% decrease	-
Nominal Thickness [μm]	2.94	5.4	4.51	5.05	n/a	2.71	4.87
Uniformity Over ~13mm Deposition Zone	+/-23%	+/-23%	+/-21%	+/-20%	n/a	+/-30%	+/-17%

The results presented in [Table 18](#) allowed for insight into the coating thickness distribution to be expected on actual gear teeth. Sample facing angles up to +/-45° from normal to the plasma duct did not result in reduction of coating deposition rate. Sample facing angles of 90° to the plasma duct (parallel to the plasma flow) resulted in ~50% decrease in deposition rate. Coating vertical uniformity (thickness distribution) was not dependent on sample facing angles up to +/-90°. All orientations showed approximately +/-20% uniformity in thickness over a 13mm (5in) vertical coating zone. The maximum thickness was in the center of this vertical 13mm (5in) zone with the coating thickness distribution being roughly Gaussian in the vertical direction. Sample rotation in the horizontal direction across the plasma duct eliminates any concerns for non-uniformity in the horizontal direction, hence it is not addressed. Overall the coating thickness

uniformity results indicate that Lift Fan gear teeth surface with facing angles greater than +/-45° would be expected to be coated to thicknesses up to 50% less.

Table 18. Coating Uniformity – Composition

Coating	Orientation	Atomic % Concentration				
		Ti	Cr	N	C	O
TiCr-TiCrN (Dep1)	+0deg (normal)	51.0	21.6	27.4	-	-
TiCr-TiCrN (Dep2)	+0deg (normal)	50.7	24.8	24.5	-	-
TiCr-TiCrN (Dep1)	+45deg (towards Cr target)	47.6	29.6	22.8	-	-
TiCr-TiCrN (Dep2)	-45deg (towards Ti target)	56.8	20.0	23.2	-	-
Cr-CrN (Dep1)	+0deg (normal)	-	82.5	17.5	-	-
Cr-CrN (Dep2)	+0deg (normal)	-	82.4	17.6	-	-
CrC (Dep1)	+0deg (normal)	-	70.2	-	23.7	6.0
CrC (Dep2)	+0deg (normal)	-	71.9	-	21.5	6.6
CrC (Dep1)	+90deg		68.9		26.0	5.1

Coating composition (atomic %) was measured by energy dispersive x-ray spectroscopy (EDS or EDX), the results are presented in **Table 19**. Accurate quantification with this technique is difficult with light elements such as N, C, and O. For this reason XPS techniques were used for actual coating composition calculation and these results are reported in section 3.1.2 and Appendix XPS. Even though the absolute quantification of coating composition is not accurate for EDX measurements, relative comparisons were confidently made to assess uniformity of composition between samples with different orientation angles. Relative comparisons were also be made to assess the repeatability of identical coating formulations produced in different deposition runs. Coating composition (atomic %) was reported as an average of 2 EDX measurements per samples over ~3-5samples measured per coating deposition. A (-) entry in **Table 19** denotes that the element was not part of the quantification. It is likely ~2-4% of C and O exist in all coatings due to imperfect vacuum conditions; Ti and N were not present if not measured.

The results in **Table 19** show that coating composition repeatability is excellent between separate deposition runs (Dep1 and Dep2) for all coating types; TiCr-TiCrN, Cr-CrN, and CrC. No compositional variation was measured in coating composition over the 13mm (5in) vertical deposition zone as such the results presented are averaged over the vertical range. Coating composition is consistent for CrC coatings deposited at +90deg and +0deg (normal) orientations, indicating that coating composition is not dependent on sample orientation as long as identical target materials are used in the LAFAD source. In the case of the TiCr-TiCrN coating one Ti and one Cr target was installed in the LAFAD source. This non-symmetry in target composition results in sample facing angles towards or away from a given target; positive facing angles were towards the Cr target, while negative facing angles were towards the Ti target. For the TiCr-TiCrN coating, sample orientation angle showed the expected Ti composition increase for -45° facing angle and Cr composition increase for +45° facing angle. In both cases the composition increase was ~5% at +/-45° facing angles. This data is correlated with the increase in coating thickness observed for the -45deg orientation (**Table 18**) since the Ti erosion rate is higher than Cr, and also supports the reduction in adhesion for the -45deg orientation since it is known that a

higher Ti/Cr ratio results in reduction in adhesion. Since the non-uniformity in TiCr-TiCrN coating composition is based on the use of a Ti and a Cr target in the LAFAD source it can be anticipated that uniformity would be achieved independent of sample orientation angle if two composite Ti/Cr targets were used instead.

Table 19. Coating Uniformity - Adhesion (Rockwell HF)

Angular Position →	-90deg (normal)	0deg (normal)	+45deg (facing Cr target)	-45deg (facing Ti target)	0deg (normal)	+90deg	0deg (normal)
Coating →	Cr-CrN (Dep1)	Cr-CrN (Dep2)	TiCr-TiCrN (Dep1)	TiCr-TiCrN (Dep2)	TiCr-TiCrN (Dep2)	CrC (Dep1)	CrC (Dep2)
Position 1	HF1	HF1	HF1	HF1	HF1	HF3	HF3
Position 2	HF1	HF1	HF1	HF1	HF1	HF3	HF3
Position 3	HF1	HF1	HF1	HF3	HF1	HF3	HF3
Position 4	HF1	HF1	HF1	HF3	HF1	HF3	HF3
Position 5	HF1	HF1	HF1	HF3	HF1	HF3	HF3
Position 6	HF1	HF1	HF1	HF1	HF1	HF3	HF3

Uniformity of coating adhesion as assessed by Rockwell adhesion (HF scale) testing is presented in **Table 20**. Coating adhesion was uniform with respect to vertical position and all facing angles within +/-90°. A minor exception was observed for the TiCr-TiCrN coatings deposited at -45deg orientation which showed a small decrease from HF1 to HF3 rating in positions 3, 4, and 5. This was the result of a preferential exposure to the Ti target plasma flow at -45° facing angles. The increased Ti/Cr compositional ratio resulted in cohesive interlayer failure mode which did not occur for +45° facing angles with a higher coating Cr content. As already mentioned this result would be expected to be resolved by using two Ti/Cr composite targets rather than one Ti and one Cr target in the LAFAD source.

Table 20. Coating Uniformity - Hardness and Modulus

Angular Position →	-90deg (normal)	0deg (normal)	+45deg	-45deg	0deg (normal)	+90deg	0deg (normal)
Coating →	Cr-CrN (Dep1)	Cr-CrN (Dep2)	TiCr-TiCrN (Dep1)	TiCr-TiCrN (Dep2)	TiCr-TiCrN	CrC (Dep1)	CrC (Dep2)
Hardness, Modulus [GPa] Position 3	H = 28.5 E = 354	H = 25.5 E = 315	H = 36.3 E = 432	H = 34.3 E = 416	H = 35.4 E = 415	H = 29.6 E = 400	H = 30.0 E = 422
Hardness, Modulus [GPa] Position 4	H = 27.3 E = 334	H = 25.7 E = 325	H = 34.3 E = 410	H = 36.3 E = 436	H = 34.8 E = 417	H = 30.1 E = 404	H = 31.8 E = 435

Uniformity of coating hardness and elastic modulus is presented in **Table 20**. Facing angle for the CrC coating had no effect on the hardness and mechanical properties. The CrC coating is monolithic so no change in architecture and therefore no change in properties occur as a result of decreasing deposition rate at facing angles greater than +/-45°. In contrast the Cr-CrN coating showed a slight increase of ~10% in hardness and modulus for -90° facing angle. In this case the decrease in deposition rate that occurs for facing angles greater than +/-45° also affects the

coating multilayer architecture by reducing the bi-layer thickness. Even though the Cr-CrN coating bi-layer ratio (Cr layer thickness to CrN layer thickness) and number of bi-layers remained constant the change in bi-layer thickness resulted in increased hardness and modulus for the Cr-CrN coating. The TiCr-TiCrN coating showed no change in hardness or elastic modulus for facing angles up to +/-45deg. This is attributed to the fact that no change in coating multi-layer architecture occurred within this facing angle range, i.e. no change in deposition rate. It was interesting to note that although non-uniformity in Ti/Cr composition in the TiCr-TiCrN for +/-45° facing angles affected adhesion, hardness and modulus were unaffected. For the TiCr-TiCrN and Cr-CrN coatings hardness and elastic modulus varied by <10% over the vertical range of 13mm (5in) as a result of coating deposition rate Gaussian distribution in the vertical direction. Overall the following conclusions were made. For monolithic coatings hardness and elastic modulus are independent of vertical position or facing angle. For multilayer coatings hardness and modulus are altered for vertical positions or facing angles which result in changes in deposition rate.

Coating thickness uniformity was assessed on spur gears to simulate coating of scale Lift Fan gears. The important parameter in determining coating uniformity on complex shapes is the ratio of tooth height to tooth spacing. The tooth geometry can be generalized as a trench feature and the height/width ratio is generally referred to as “trench aspect ratio” or just aspect ratio. Even though the helical bevel design of Lift Fan gears is more complex than simple spur gears used in this evaluation, the aspect ratio is the same for both types of gears at ~1.4. Therefore the results obtained on the spur gears should simulate coating uniformity on actual Lift Fan gears with minimal error. A cross-section profile of a spur gear section with a CrC coating (**page #UNI_8**) shows the locations along the tooth profile where coating thickness was measured. The tooth profile facing angles were measured in the same manner as the ¾"dia 440A samples to allow for correlation between thickness data on each substrate type. SEM images at 1000x and 3000x magnification were collected to demonstrate the coating uniformity and to measure exact coating thickness at each location along the tooth profile (**page #UNI_9-13**). Coating thickness and normalized thickness (versus location 1) are presented in **Table 22**.

Table 21. Coating Thickness Uniformity – Spur Gear

Location	Facing Angle	Coating Thickness	Normalized Thickness	Location Notes (ref page #UNI_8)
1	0°	5.0µm	1	Gear tooth top surface, non-contact surface
2	+62°	4.1µm	0.82	Gear tooth face, contact surface
3	+100°	2.5µm	0.5	Gear tooth flank, non-contact surface
4	+25°	3.8µm	0.76	Gear tooth land (root), non-contact surface
5	0°	3.7µm	0.74	Gear tooth land, non-contact surface

Coating thickness results on an actual gear tooth profile show good agreement in locations 1-3 with thickness data for ¾" diameter 440A samples oriented through the +/-90° facing angle range. Both datasets showed an ~50% decrease in coating thickness when comparing surfaces with 0° facing angles to surfaces with >= +/-90° facing angles. The results for locations 4 and 5 illustrate the difference between coating actual geometries and flat samples with representative facing angles. Locations 4 and 5 have facing angles of <+/-45° and based on the data generated on flat ¾"dia samples in the same facing angle range would be expected to have normalized thickness of 1. This is in fact not the case as the thickness in locations 4 and 5 is 25% less than

location 1. The reason is due to the trench geometry of the tooth “trench” profile. As plasma enters the trench profile the bottom surfaces with <+/-45° facing angles receive less coating as some of the plasma flux is distributed to the walls of the trench (tooth flanks). The LAFAD coating process produces highly ionized plasma which results in a distributed thickness along the surface area of the trench profile. For location 3 (tooth flank) the normalized thickness was 0.5 and for locations 4 and 5 (tooth root, land) the normalized thickness is 0.75. The uniformity results provide for design guidelines for coating actual gears. Location 2 (tooth face) is the only contact surface of the 5 locations measured and therefore is the only surface which is required to provide corrosion, wear, and fatigue performance. Locations 1, 3, and 5 are non-contact surfaces where only corrosion protection must be established and wear and fatigue are not a concern. Location 4 is a non-contact surface although this location is subject to tooth bending fatigue; therefore the coating in this location is not required to provide wear resistance but must provide corrosion protection and have good bending fatigue response. The mechanical properties of the coatings in locations 1-5 are expected with good confidence to follow the same results established on 3/4"dia samples at various facing angles. In other words coating properties are uniform along the tooth profile with the already noted exceptions for multilayer coatings where variation in deposition rate affects the bi-layer thickness. From a design perspective coating thickness on the critical contact surfaces (location 2) is constrained to ~1.5x the coating thickness in location 3 deemed sufficient to provide corrosion protection.

4. Conclusions

The AF04-142 topic Phase II program effort ranged from May 2004 to December 2008 and during this time Arcomac Surface Engineering was able to make significant progress towards solving the design challenges present in high load and high speed gearing applications such as the Lift Fan system. The Lift Fan system is comprised of three helical bevel gears made of Pyrowear 675. While Pyrowear 675 performs well in lubricated sliding wear and fatigue, early failure occurs due to susceptibility to pitting and general surface corrosion in marine operating environments. Traditional corrosion coatings can provide effective corrosion protection on the non-load bearing surfaces of the gear but fail rapidly on gear teeth due to poor wear resistance and low yield strength. For a coating approach the primary goal is corrosion protection, although any failure in wear or fatigue of the coating which exposes the Pyrowear 675 substrate results in corrosion initiation. Therefore the primary performance goals for the current effort were defined as corrosion, wear, and fatigue. Using an iterative coating design approach Arcomac Surface Engineering developed TiCr-TiCrN, Cr-CrN, and CrC coatings in an effort to meet the multi-functional design goals for the Lift Fan gears. Working in tandem with AFRL and Rolls-Royce Arcomac conducted the research effort to thoroughly characterize the material properties and performance of the baseline Pyrowear 675 material and TiCr-TiCrN, Cr-CrN, and CrC coatings with the ultimate goal of providing a viable commercial solution using Arcomac LAFAD coating technologies. The conclusions which were arrived at as a result of the Phase II research effort follow.

All coating characterization and performance results indicate that the LAFAD coating process can be performed with excellent repeatability. In all cases coating properties such as thickness, hardness, composition, roughness, and adhesion were repeatable within <10% variation for multiple samples from the same coating deposition run, and between coatings deposited in separate runs (Dep1 versus Dep2). Coating uniformity results on complex shapes indicate that

scale-up to coating actual Lift Fan gears is feasible if uniformity design constraints are followed. Coating mechanical properties were shown to be independent of surface facing angle for monolithic coatings while multilayer mechanical properties were affected by facing angles which produced a decrease in deposition rate resulting in a change in the multilayer architecture bi-layer thickness. Coating deposition rate was shown to be affected by gear tooth profile; compared to the tooth face respective deposition rate decreases of ~25% and ~50% on tooth lands and tooth flanks were measured. Successful coating scale-up can therefore be achieved by optimizing the coating performance properties for the tooth face based on the minimum thickness on the tooth flank necessary to provide corrosion protection. In conclusion the LAFAD process provides a high level of confidence in regards to coating scale up and commercial production of coated Lift Fan gears.

A clear solution to the SBIR Phase II research goals was not accomplished in this effort. While the TiCr-TiCrN, Cr-CrN, and CrC coatings demonstrated some marked improvements in certain performance areas a unified solution to corrosion, wear, and fatigue was not reached. As was to be expected baseline P675 demonstrated poor corrosion performance and poor dry-sliding performance while at the same time demonstrating excellent scuffing performance and fatigue performance. In regards to corrosion research goals, clear evidence was presented that all of the coatings meet the modified Navy corrosion test protocol specifications. None of the coatings passed ASTM B117 salt fog corrosion specifications although it was clear that the Cr-CrN and CrC coatings provided much improved corrosion performance over baseline P675. In the current effort the TiCr-TiCrN coating corrosion performance was similar to baseline P675 although previous testing conducted in 2007 demonstrated that this coating can be deposited to perform on the same level as the Cr-CrN coating. From the perspective of wear performance the TiCr-TiCrN/Cr-CrN contact pair performed exceptionally in dry sliding, wearing at a rate 650x less than the baseline P675 case, but did not perform as well as baseline P675 in scuffing tests and also did not meet the industry standard for gear scuffing performance. The TiCr-TiCrN/CrC contact pair wore at a rate 2.5x less than baseline P675 in dry sliding and also did not perform as well as baseline P675 in scuffing tests but did meet the industry standard for gear scuffing performance. Rolling contact fatigue performance of the TiCr-TiCrN coating was very poor with average failures measured after 0.25E+06 contact cycles. The fatigue performance of baseline P675, CrC and Cr-CrN coatings exceeded the amount of time available to complete a statistical evaluation. Therefore the CrC and Cr-CrN coatings, which in general survived to 10E+06 contact cycles, were considered to have potential to meet or exceed the fatigue performance of baseline P675. In summary, optimized wear was found for TiCr-TiCrN against Cr-CrN or CrC; when considered as a necessary coating pairing the improved corrosion and fatigue performance realized for Cr-CrN and CrC coatings was hindered by the poor fatigue and corrosion performance of the TiCr-TiCrN coating. An ultimate solution for the Lift Fan gear application requires a coating paring which meets all of the specifications defined in section 1.1 for corrosion, wear and fatigue; given the program results this pairing was not achieved. In conclusion the developed coatings do not show the appropriate technical readiness level to move forward to scale testing, although the current results do show significant potential and may warrant further development funding.

5. Recommendations

The cumulative results of the Phase II research represent a limitation in the progression of coating design optimization rather than a limitation of the inherent potential of Arcmac's LAFAD coating process. The performance of the TiCr-TiCrN coating was in particular disappointing primarily in regard to fatigue performance. In contrast the corrosion, wear and fatigue results for the Cr-CrN and CrC coatings were highly encouraging and provide significant confidence that the Lift Fan gear problem could be solved with further development. The following recommendations are provided in regards to future coating development for the Lift Fan gear application.

- Future Research Approach
 - Abandon development of the TiCr-TiCrN coating.
 - Return to evaluation of Ti-C-N coating systems to determine a coating which performs well in corrosion and fatigue and as an optimized tribological pairing with Cr-CrN or CrC coatings.
 - Continue development and optimization of the Cr-CrN and CrC coatings.
- Corrosion Performance
 - Conduct further development of the Cr-CrN and CrC coatings aimed at particle defect reduction; specifically higher bias or pulse bias deposition trials and experimentation with duct filter baffle setup.
 - Conduct experimentation on intentional passivation of coatings either by depositing a thin chromium oxide layer on top to the Cr-CrN and CrC coatings or by post deposition oxidation in a controlled furnace.
 - Collaborate with researchers who are developing high temperature polymers to seal particle defects in coatings.
 - Explore the possibilities for thicker coatings, e.g. 10-15 μm thick, with Rolls-Royce allowing that Lift Fan gear tolerances would need to be modified.
- Wear Performance
 - Conduct further research into affect of initial coating roughness on gear scuffing results. Create run-in conditions which polish the coating surface roughness prior to scuffing testing and/or experiment with polishing of the coatings prior to scuffing testing.
 - Explore the possibility that oil chemistry which is designed to protect and react with Fe alloys may not provide similar protection with Ti or Cr based coatings. Consider possibility that oils that do not perform well in contact with common gear alloys may perform well in coating versus coating contact.
 - Work to demonstrate load capacity and wear performance of thick coatings.
 - Conduct lubricated fretting wear experiments
 - Conduct "oil-off" testing through Wedeven Assoc
- Fatigue Performance
 - Complete a long term statistical analysis of P675 and coatings to determine actual fatigue life. A minimum of nine tests should be run to failure and the data should be statistically treated by Weibull failure analysis.
 - Continue to explore the effects of coating architecture and thickness on fatigue performance. Ideally 10-15 μm thick coatings could be developed which maintain fatigue performance and improve corrosion performance.
 - Complete single tooth bending fatigue testing in collaboration with Rolls-Royce.

References

1. R.L.Boxman, D.M.Sanders, and P.J.Martin, *Handbook of Vacuum Arc Science and Technology*. Park Ridge, N.J.: Noyes Publications, 1995.
2. D.Sanders and A.Anders, *Surface and Coating Technology*, 139 (2000).
3. V.I. Gorokhovsky, V.P. Polistchook and I.M. Yartsev, "Process in Plasma-Arc Installation for Vacuum Depositions, Part I: Plasma Generation; Part II: Plasma Propagation," *Surface and Coatings Technology*, 61, 101 (1993).
4. Vladimir Gorokhovsky, Chris Bowman, John Wallace, Dave VanVorous, John O'Keefe, Victor Champagne, Marc Pepi, Widen Tabakoff, "LAFAD Hard Ceramic and Cermet Coatings for Erosion Protection of Turbomachinery Components", ASME Paper # GT2009-5939, In Press.
5. Y. H. Cheng, T. Browne, B. Heckerman, J. C. Jiang, E. I. Meletis, C. Bowman, and V. Gorokhovsky, "Internal stresses in TiN/Ti multilayer coatings deposited by large area filtered arc deposition", *JOURNAL OF APPLIED PHYSICS* 104, 093502 (2008).
6. N. Novikov, V.I. Gorokhovsky and B. Uryukov, "Superhard i-C Coatings Used in Complex Processes of Surface Strengthening of Tools and Machine Parts," *Surface and Coatings Technology*, 47, (1991) 770.
7. Vladimir I. Gorokhovsky , Rabi Bhattacharya and Deepak G. Bhat, *Surface and Coating Technology*, 140 (2) 2001, pp. 82-92.
8. V. Gorokovsky, C. Bowman, P.E. Gannon, D. VanVorous, J. Hu, C. Muratore, A.A., Voevodin, Y.S. Kang, "Deposition and Characterization of Hybrid Filtered Arc-Magnetron Multilayer Nanocomposite Cermet Coatings for Advanced Tribological Applications," *Wear* 265 (2008) 741-755.
9. V.Gorokhovsky, C.Bowman, D.VanVorous, J.Wallace, "Deposition of Various Metal, Ceramic and Cermet Coatings by an Industrial-Scale LAFAD Process", *JVST-A*, 2009, In Press.
10. V.I.Gorokhovsky, P.E.Gannon, M.C.Deibert, R.J.Smith, A.Kayani, M.Kopczyk, D.VanVorous, Zhenguo Yang, J.W.Stevenson, S.Visco, C.Jacobson, H.Kurokawa and S.Sofie, "Deposition and Evaluation of Protective PVD Coatings on Ferritic Stainless Steel SOFC Interconnects," *Journal of The Electrochemical Society*, v. 153 (10) A1886-A1893 (2006).
11. V.Gorokhovsky, US Pat. No.7,300,559.
12. V. Gorokhovsky, "Characterization of Cascade Arc Assisted CVD Diamond Coating Technology, Part I: Plasma Processing Parameters," *Surface and Coatings Technology*, 194 (2005).
13. R.J. Smith, C. Tripp, A. Knospe, C.V. Ramana, A. Kayani, V. Gorokhovsky, V. Shunthanandan, D.S. Gelles, "Using CrAlN Multilayer Coatings to Improve Oxidation Resistance of Steel Interconnects for Solid Oxide Fuel Cell Stacks," *J. Journal of Materials Engineering and Performance*, Volume 13, Number 3, June 2004.
14. W.A. Brantley, *J. Appl. Phys.*, Vol. 44 (1973) p.534-535
15. Day, K. L., "Un-steel Testing of Aircraft Engine Bearing Steel," *Rolling Contact Fatigue Testing of Bearing Steels. ASTM STP 771*, J. J. C. Hoo, Ed., American Society for Testing and Materials, 1982, pp. 67-84.

Appendices

The following appendices are intended to be included in electronic format to supplement this report. It is the intent of the authors that each appendix is provided in pdf format and included with either electronic or hardcopy distributions of this report. If the report is in hardcopy the appendices should be references in electronic format to preserve color images and graphs.

Appendix List

- Appendix BoD – Ball-on-Disc Sliding Wear Data (81 pages)
- Appendix CA – Coating Contact Angle (Oil Wettability) Data (3 pages)
- Appendix H-E – Coating Hardness and Elastic Modulus Data (8 pages)
- Appendix HF – Rockwell Indent Adhesion Data (24 pages)
- Appendix MOR – Coating Morphology Characterization (12 pages)
- Appendix NCT – Modified Navy Corrosion Test Results (15 pages)
- Appendix RCF – Rolling Contact Fatigue (RCF) Testing Results (13 pages)
- Appendix RMS – Pyrowear 675 and Coating Roughness Data (9 pages)
- Appendix RS – Coating Residual Stress Data (5 pages)
- Appendix SA - Scratch Adhesion Data (23 pages)
- Appendix SF – ASTM B117 Salt Fog Corrosion Results (19 pages)
- Appendix Th – Coating Thickness Data (11 pages)
- Appendix UNI – Coating Uniformity Study Results (12 pages)
- Appendix WLC – Gear Simulation Testing: Wedeven Load Capacity (LC) Results (15 pages)
- Appendix WPM – Gear Simulation Testing: Wedeven Performance Mapping (PM) Results (15 pages)
- Appendix XPS – Coating XPS Data (6 pages)
- Appendix XRD – Coating XRD Data (7 pages)

Appendix BoD – Ball-on-Disc Sliding Wear Data

Ball-on-Disc Sliding Wear Test Procedure and Analysis overview

1. Unidirectional sliding wear performance was evaluated using a ball-on-disc testing configuration per ASTM G99 as shown schematically. Testing was conducted using CETR UMT-3 tribo-tester (www.cetr.com). Normal load (F), test radius (R) and disc rotational speed (W) are closed-loop feedback controlled. Normal load, tangential load, and sliding speed data is acquired at a rate of 20Hz. Sliding coefficient of friction (CoF, μ) is calculated as the measured tangential load divided by the applied normal load. Sliding speed is calculated as the disc rotational speed multiplied by the test radius.
2. Prior to testing both disc and ball were cleaned with acetone, and post testing the disc and ball were physically scrubbed in acetone followed by 5min ultrasonic cleaning in acetone to remove any loosely adhered wear debris that would interfere with wear volume calculations.
3. Ball wear was observed by optical microscopy; wear features were noted, wear scar diameter was measured and an image at 75x magnification of the wear scar was recorded for each test. In addition the ball wear profile 1500 μm in length was measured across the ball meridian and wear scar center.
4. Ball wear volume for each test was calculated in two ways. Traditional wear volume calculations were performed using the wear scar diameter measurement as follows,

$$\text{Ball_Wear_Volume} = (\pi * (\text{wear scar diameter, } \mu\text{m})^4) / (64 * (\text{ball radius, } \mu\text{m}))$$

In addition the profile trace made across the meridian of the wear scar on the ball was compared to a 3rd order polynomial curve fit representing the unworn profile of the ball. Numerical integration between the unworn profile and worn profile allowed for calculation of the cross-sectional wear area moment (A_c) which was used to estimate wear volume by the formula

$$\text{Ball_Wear_Volume} = 2 * \pi * A_c$$

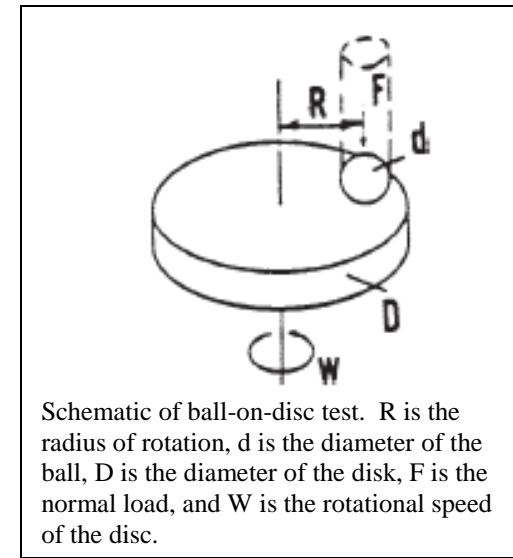
Ball wear volume is reported as an average of the two calculations unless the wear scar diameter was less than 200 μm , in this case the profile volume calculation accuracy was below the reproducible limit of measurement due to inaccuracies in the polynomial fitting the unworn profile.

5. Disc wear was observed by optical microscopy and SEM techniques; wear features were noted, optical microscope images were recorded at 50x and SEM images of the wear track center and edge were recorded at 500x. Three profiles 1500 μm in length were recorded for each disc wear track at random positions approximately 120° opposed around the track. Disc wear depth, cross-sectional wear area (A), and wear track width were measured from each profile and reported as an average for each test. EDX compositional analysis was performed on the wear track for each test to assess the presence of wear debris formation in the wear track.
6. Disc wear volume was calculated for each test using the average disc cross-section wear area (A) as follows,

$$\text{Disc_Wear_Volume} = 2 * \pi * R * A$$

7. In the case where wear occurs to both the ball and the disc a “composite wear” parameter has been defined which represents the total wear volume as

$$\text{Composite_Wear_Volume} = \text{Ball_Wear_Volume} + \text{Disc_Wear_Volume}$$



Schematic of ball-on-disc test. R is the radius of rotation, d is the diameter of the ball, D is the diameter of the disk, F is the normal load, and W is the rotational speed of the disc.

Ball-on-Disc Sliding Wear Test Procedure and Analysis overview (continued)

8. Calculated wear volumes for coatings in this effort current effort represent the wear of the coatings, i.e. no cases were observed where the coating wore through and substrate was exposed creating a mixed contact situation.
9. CoF is plotted as a function of sliding distance for each test and reported as an average over the total sliding distance for a given test.
10. Wear of materials in sliding contacts is assumed to be the result of dissipated energy due to friction between the contacting bodies. The total dissipated energy over the duration of a test in Joules is expressed as follows.
$$\text{Dissipated_Energy(friction)} = \text{average_CoF} * \text{normal_load} * \text{sliding_distance}$$
11. Wear volume dependence on dissipated energy, sliding distance and load under dry sliding conditions was evaluated in this effort. Each contact pair was evaluated at 100m, 500m, and 1000m sliding distances for normal loads of 1N and 5N. Three tests were conducted on each disc; 100m distance at 9mm radius, 500m distance at 10.5mm radius and 1000m distance at 13mm radius, with all duplicate tests conducted at the same radius. Sliding speed was held constant at 300mm/sec for different test radii by adjusting the rotational speed. Test temperature (ambient, ~24°C) and atmosphere (RH = 20% +/-5%) were monitored but not controlled. To improve the statistical viability of the wear results and to demonstrate repeatability of coating wear properties each load and sliding distance test was performed two times. One test on a disc, e.g. CrC (Run1), and another duplicate test on a disc with the same coating deposited in a different coating batch, e.g. CrC (Run2). Similarly, duplicate tests were performed on two different P675 samples for each load and sliding distance. The test matrix resulted in a total of 36 tests (18 unique tests + 18 duplicate tests), or 12 tests per each contact pair; M50/P675, TiCr-TiCrN/Cr-CrN and TiCr-TiCrN/CrC.
12. M50 balls (6.35mm diameter, grade 5, SKF) were used in contact with super-finished P675 discs to represent the baseline LiftFan gear case, although P675/P675 contact would have been more ideal, P675 balls are not normally manufactured so M50 was used as a close substitute.
13. TiCr-TiCrN coated M50 balls (6.35mm diameter, grade 5, SKF) were used in contact with Cr-CrN and CrC coated discs to represent the LiftFan gear case where both contacting gears are coated for corrosion protection.
14. The use of a hemispherical contact (ball or rounded pin) in sliding wear testing has a number of advantages and disadvantages depending on the wear conditions. In the current effort ball on disc geometry was required as a coated pin (flat) cannot be oriented perfectly perpendicular to a disc, resulting in uneven wear through of the thin coating during testing start up. A coated ball on disc geometry has the advantage of always applying a uniform initial contact pressure which ensures the coating will wear evenly. The primary disadvantage to ball on disc geometry is that once wear occurs the contact area is an inverse function of the wear. Since load is constant and contact area is an unknown function of wear, contact pressure also becomes and unknown and can only be specified as an initial value and/or final value. Since progressive wear decreases the initial contact stress, often by a factor of 10-100 times by test end, it is impossible using ball on disc testing to model a wear rate for a gear application operating at a known contact stress. Rather it is best to conceptualize ball-on-disc testing as a screening test to compare wear of materials under a given load, sliding speed, and contact pair geometry, with the consideration that materials that wear the least for an equivalent sliding distance also do so at a higher contact stress as compared to materials that wear more.

BoD_3

Appendix BoD – Ball-on-Disc Sliding Wear Data

Unidirectional Sliding Wear Results

Load – 5N

Sliding Speed – 300mm/sec

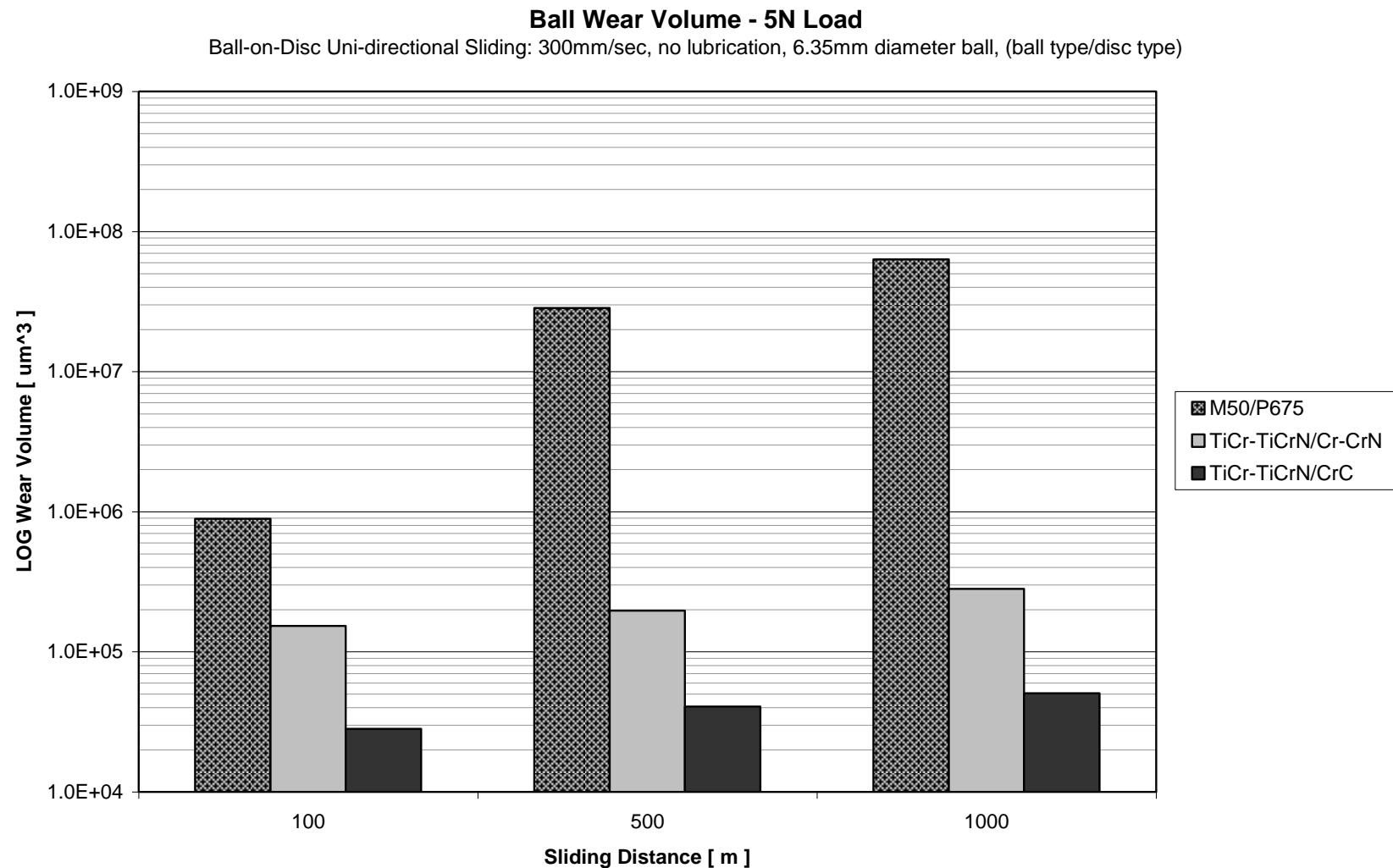
Lubrication – none, dry

Temperature – ~24°C, ambient, not controlled

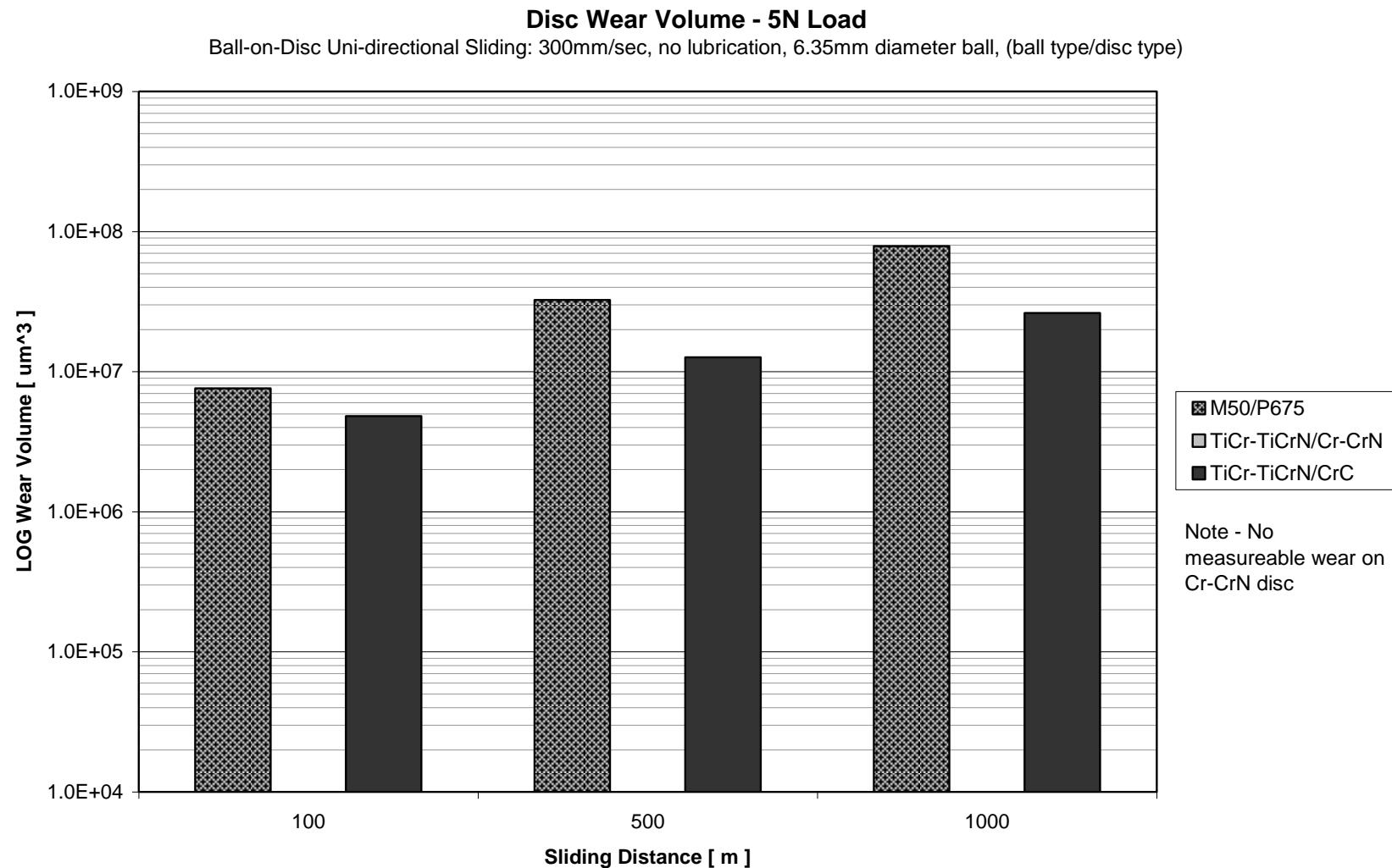
Humidity – RH = 20% +/-5%, ambient, not controlled

Sliding Distance [m]	Ball	Disc	Ball Wear Volume [um^3]	Disc Wear Volume [um^3]	Composite Wear Volume [um^3]	Average CoF	Dissipated Energy [J]	Composite Volume Wear Rate (linear fit, R^2 > 0.99) [um^3/J]
100	M50	P675	8.91E+05	7.60E+06	8.49E+06	0.70	350.0	3.2E+04
500	M50	P675	2.85E+07	3.25E+07	6.10E+07	0.87	2175.0	
1000	M50	P675	6.33E+07	7.86E+07	1.42E+08	0.90	4500.0	
100	TiCr-TiCrN	Cr-CrN	1.53E+05	negligible	1.53E+05	0.34	170.0	0.005E+04
500	TiCr-TiCrN	Cr-CrN	1.96E+05	negligible	1.96E+05	0.48	1187.5	
1000	TiCr-TiCrN	Cr-CrN	2.81E+05	negligible	2.81E+05	0.52	2600.0	
100	TiCr-TiCrN	CrC	2.82E+04	4.81E+06	4.83E+06	0.32	160.0	1.2E+04
500	TiCr-TiCrN	CrC	4.06E+04	1.27E+07	1.27E+07	0.35	875.0	
1000	TiCr-TiCrN	CrC	5.05E+04	2.63E+07	2.63E+07	0.36	1800.0	

Appendix BoD – Ball-on-Disc Sliding Wear Data



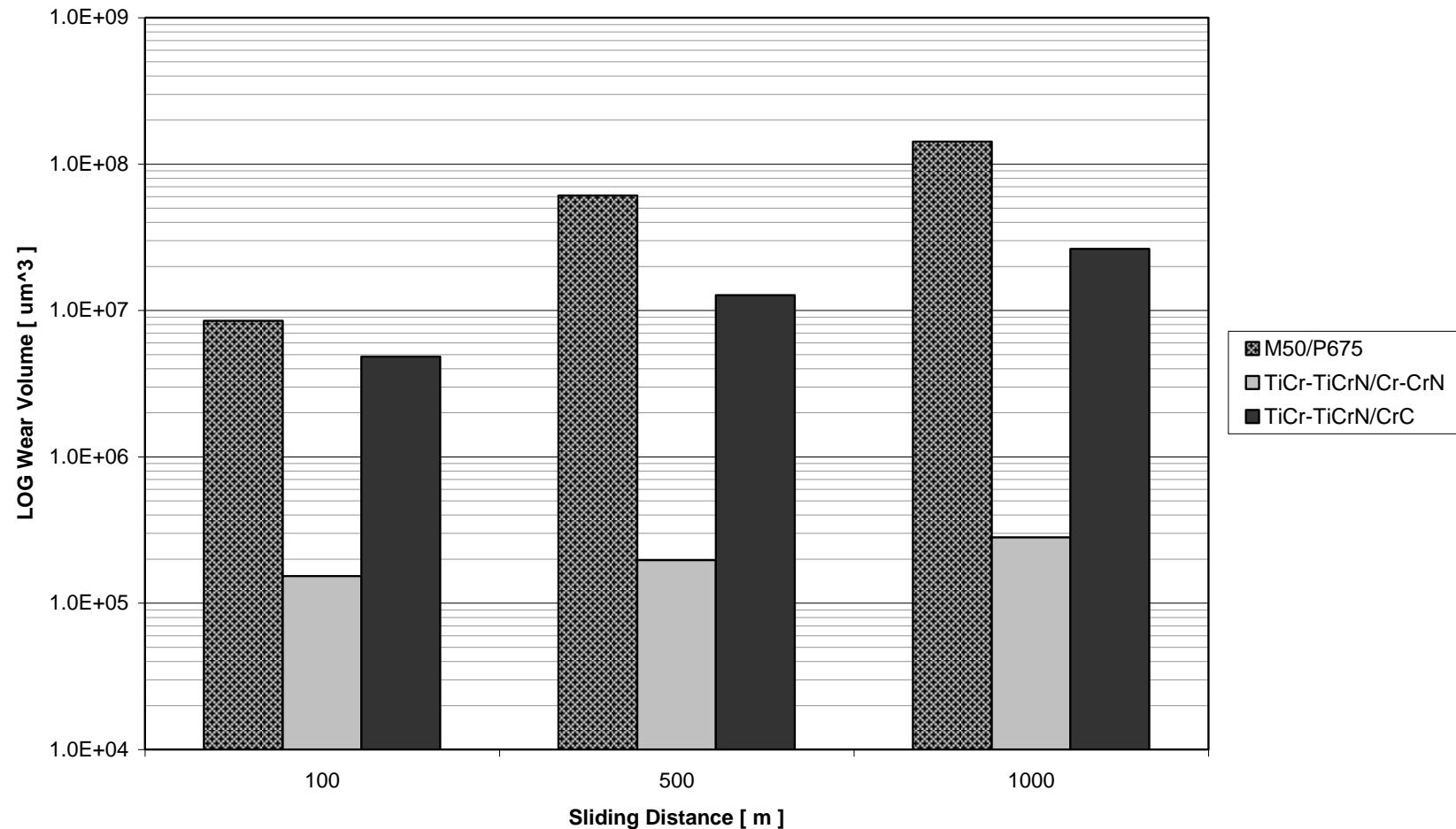
Appendix BoD – Ball-on-Disc Sliding Wear Data



Appendix BoD – Ball-on-Disc Sliding Wear Data

Composite Wear Volume - 5N Load

Ball-on-Disc Uni-directional Sliding: 300mm/sec, no lubrication, 6.35mm diameter ball, (ball type/disc type)



BoD_7

Appendix BoD – Ball-on-Disc Sliding Wear Data

Unidirectional Sliding Wear Results

Load – 1N

Sliding Speed – 300mm/sec

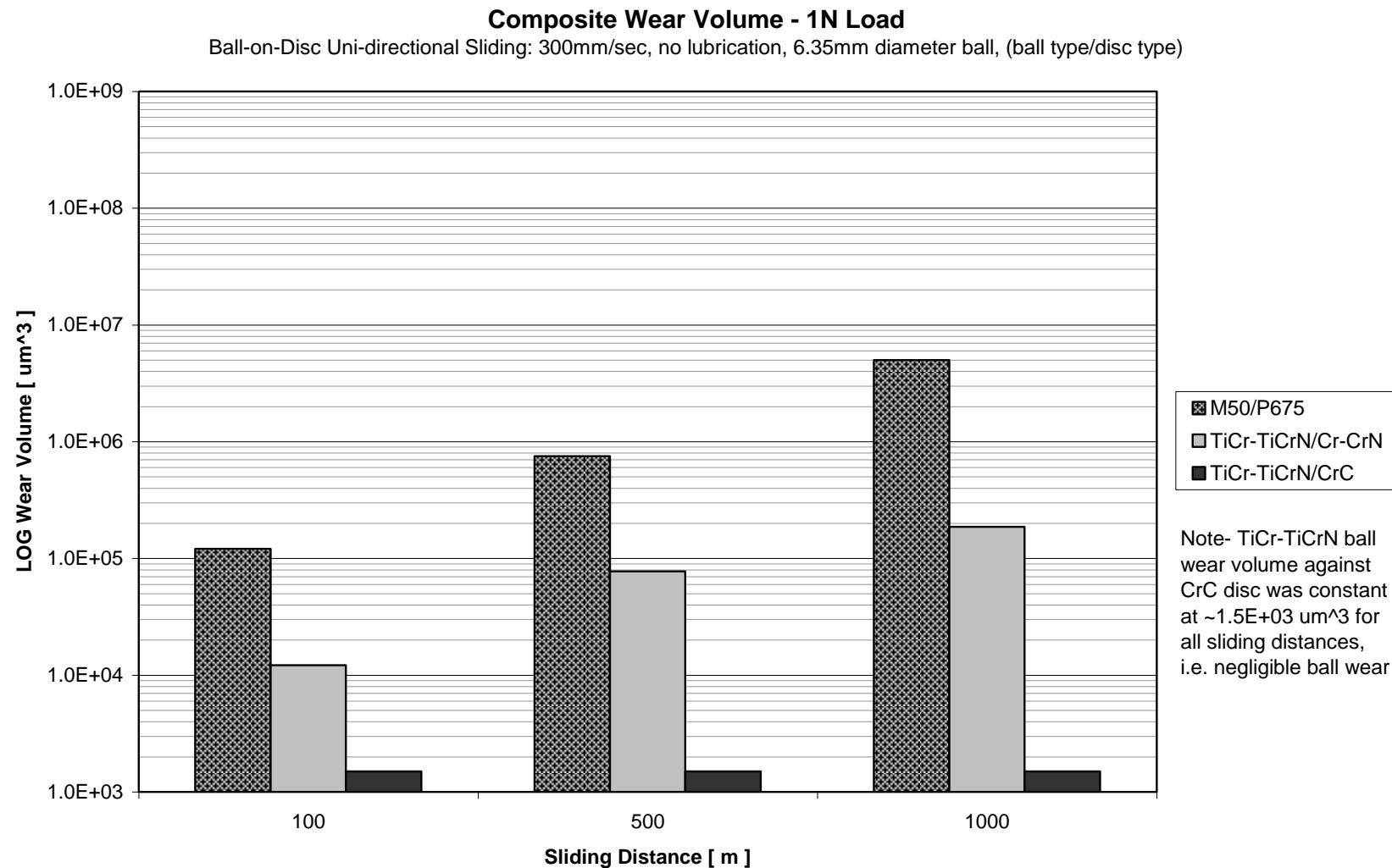
Lubrication – none, dry

Temperature – ~24°C, ambient, not controlled

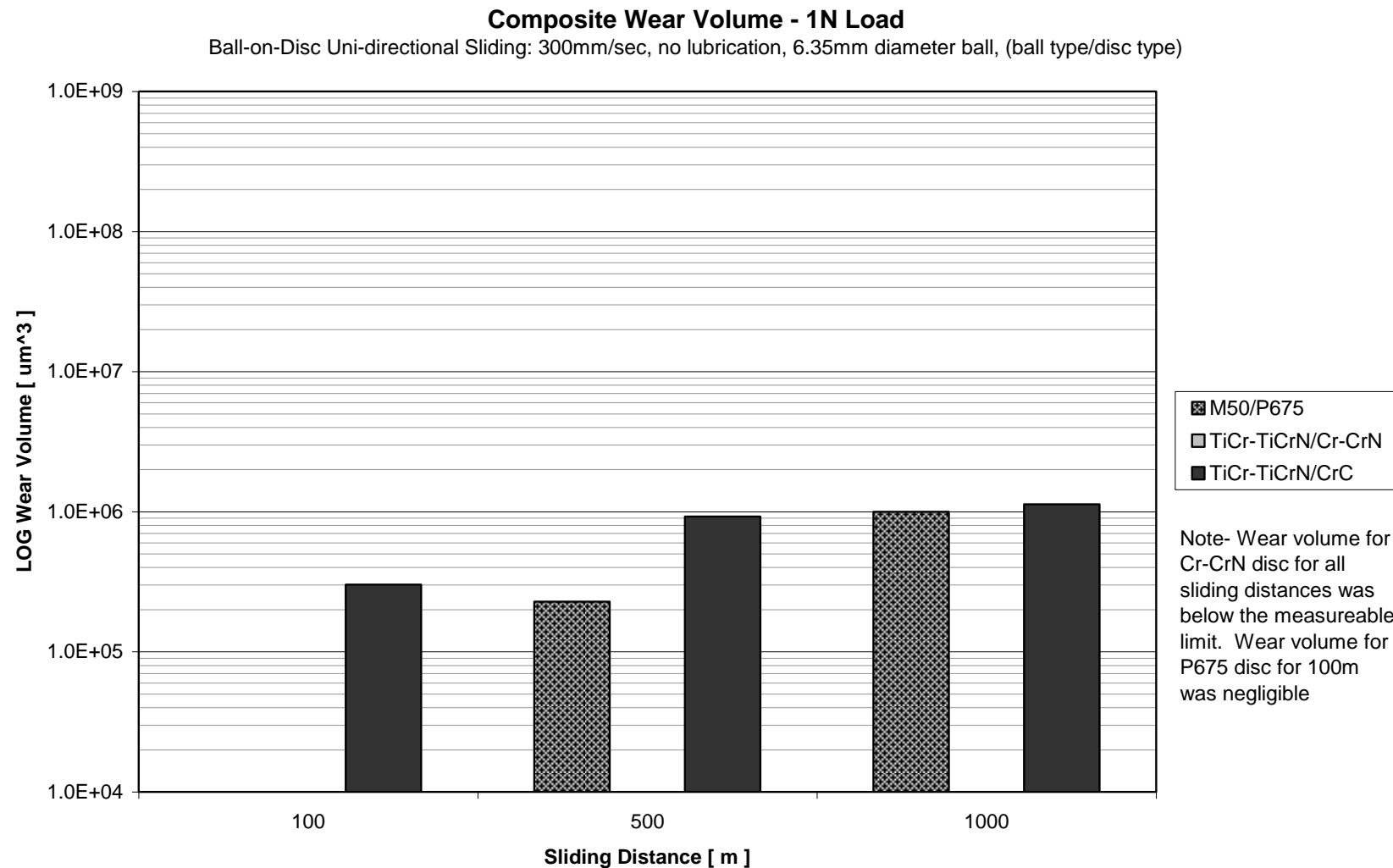
Humidity – RH = 20% +/-5%, ambient, not controlled

Sliding Distance [m]	Ball	Disc	Ball Wear Volume [um^3]	Disc Wear Volume [um^3]	Composite Wear Volume [um^3]	Average CoF	Dissipated Energy [J]	Composite Volume Wear Rate (linear fit, R^2 > 0.99) [um^3/J]
100	M50	P675	1.21E+05	negligible	1.21E+05	0.82	82.0	2356
500	M50	P675	7.49E+05	2.28E+05	9.77E+05	0.88	440.0	
1000	M50	P675	1.57E+06	4.79E+05	2.05E+06	0.90	900.0	
100	TiCr-TiCrN	Cr-CrN	1.22E+04	negligible	1.22E+04	0.26	25.5	550
500	TiCr-TiCrN	Cr-CrN	7.75E+04	negligible	7.75E+04	0.30	150.0	
1000	TiCr-TiCrN	Cr-CrN	1.86E+05	negligible	1.86E+05	0.34	340.0	
100	TiCr-TiCrN	CrC	1.50E+03	3.02E+05	3.03E+05	0.57	57.0	1638
500	TiCr-TiCrN	CrC	1.50E+03	9.24E+05	9.25E+05	0.55	272.5	
1000	TiCr-TiCrN	CrC	1.50E+03	1.13E+06	1.13E+06	0.55	550.0	

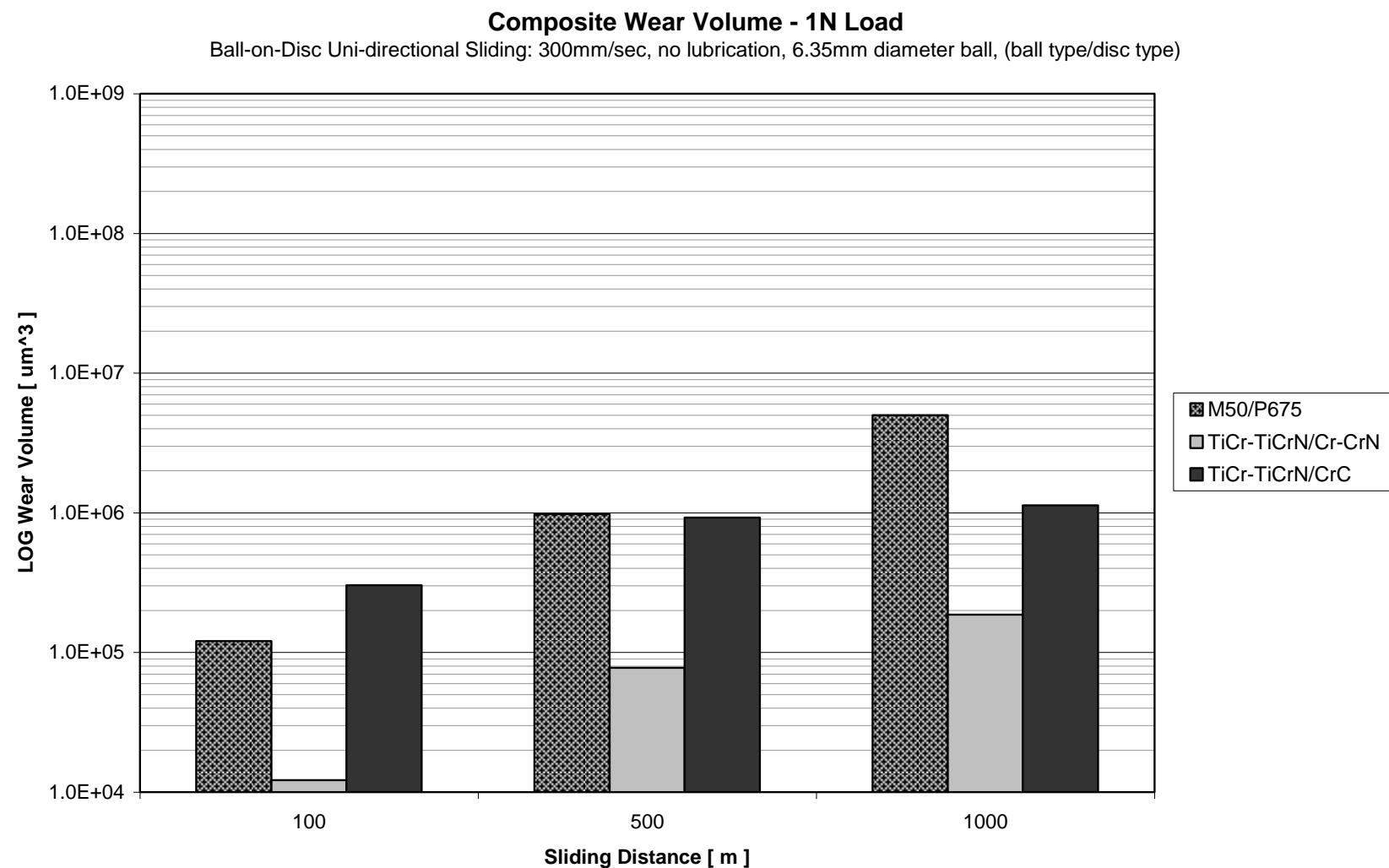
Appendix BoD – Ball-on-Disc Sliding Wear Data



Appendix BoD – Ball-on-Disc Sliding Wear Data



Appendix BoD – Ball-on-Disc Sliding Wear Data



Appendix BoD – Ball-on-Disc Sliding Wear Data

EDS Compositional Analysis of Wear Track and Reference Non-contact Area

- EDS data collection from 600 μm x 1000 μm area (unless noted as spot EDS)
- EDS data is used for determination of relative changes in the sample composition between the track and non-contact reference areas. Atomic concentrations indicated for coatings are not correct due to inaccuracies of the EDS method in quantifying light elements, e.g. C, N, O.

EDS Analysis for M50(ball)/P675(disc)

Analysis Location	Element Atomic Percent Concentration								
	Fe	Cr	Co	Ni	V	Mn	Mo	Si	O
5N, 100m, Track Center	72.0	12.0	3.8	1.7	0.6	0.8	0.6	0.1	17.4
5N, 500m, Track Center	71.8	11.9	3.8	1.5	0.6	0.6	0.8	0.1	18.6
5N, 1000m, Track Center	70.8	12.2	3.4	1.2	0.6	0.5	0.8	0.2	23.7
Non-contact Reference Area	73.5	17.7	4.4	2.1	1.0	0.8	0.6	0.5	0.0

Note—similar EDS results were obtained for all 1N tests as well. Increased oxygen concentration in track for all samples was observed. Wear debris transformed layer is most likely composed primarily of iron oxides, with the possibility of alloying oxide formation, e.g. chromium oxides.

EDS Analysis for TiCr-TiCrN(ball)/Cr-CrN(disc)

Analysis Location	Element Atomic Percent Concentration			
	Cr	N	Ti	O
5N, 100m, Track Center	73.4	22.8	0.4	3.4
5N, 500m, Track Center	74.8	19.8	0.5	4.9
5N, 1000m, Track Center	72.0	24.3	0.4	3.4
Non-contact Reference Area	73.9	23.8	0	2.3
5N, 500m, Spot Analysis of Wear Debris	68.3	9.4	3.0	18.9

Note- micro EDS results of the track do not resolve the composition of wear debris due to the unfavorable beam volume interaction ratio of Cr-CrN coating to sparse volumes of wear debris. High resolution spot EDS data is also inconclusive but does indicate increased concentrations of O and Ti. Assumption is that wear debris is TiO and/or TiO₂ derived from TiCr-TiCrN ball wear.

(continued for CrC coating, next page)

Appendix BoD – Ball-on-Disc Sliding Wear Data

EDS Compositional Analysis of Wear Track and Reference Non-contact Area (cont)**EDS Analysis for TiCr-TiCrN(ball)/CrC(disc)**

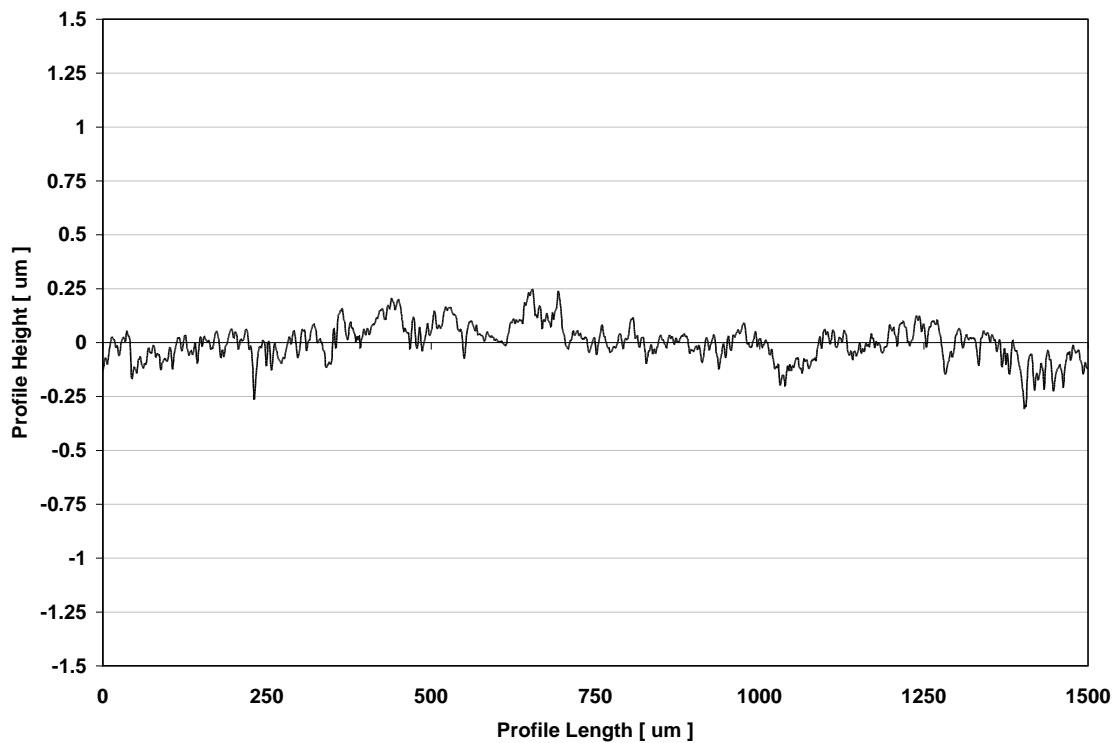
Analysis Location	Element Atomic Percent Concentration				
	Cr	C	Ti	N	O
5N, 100m, Track Center	64.9	31.7	0	0	3.4
5N, 500m, Track Center	61.4	34.2	0	0	4.3
5N, 1000m, Track Center	71.8	25.0	0	0	3.1
Non-contact Reference Area	63.6	33.1	0	0	3.2

Note- EDS results indicate no presence of wear debris/oxides in the CrC coating track. This data conforms to SEM track imaging results which show a highly polished CrC track and no evidence of a transformed layer of adhered debris. Similar EDS results were obtained for 1N tests.

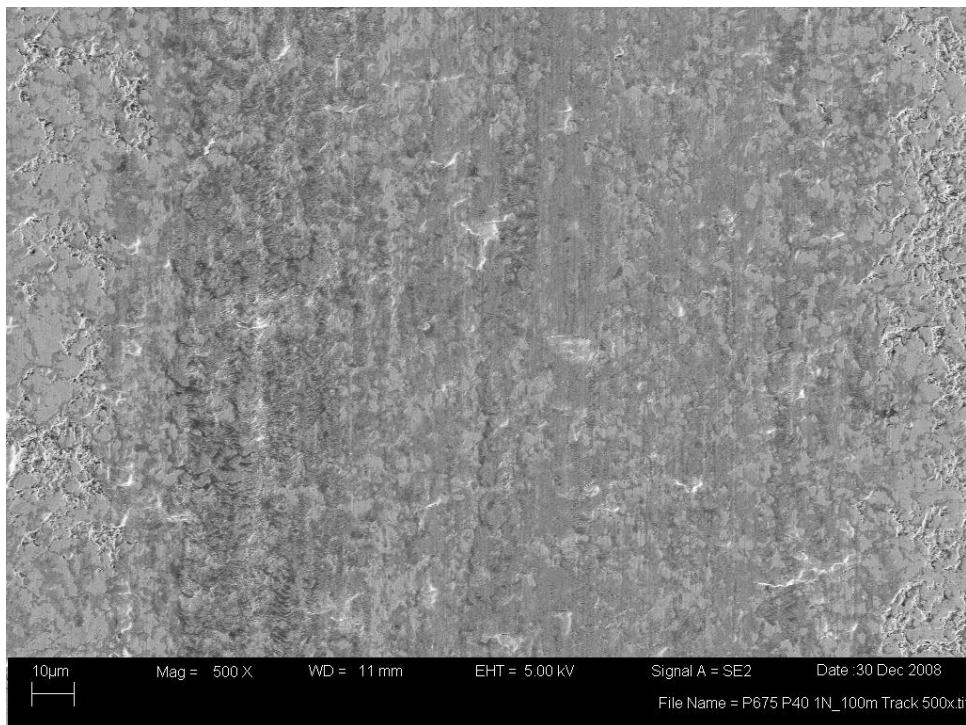
Appendix BoD – Ball-on-Disc Sliding Wear Data



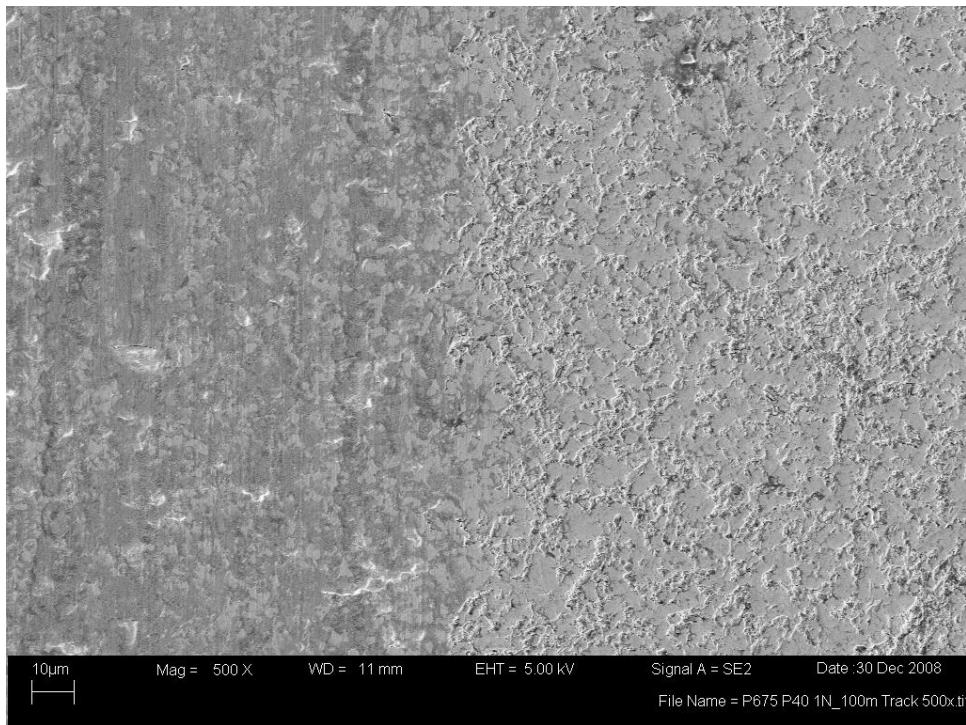
Disc Wear Track Image and Profile
P675 super-finished (Disc) vs. M50 (Ball)
Load = 1N, Distance = 100m, Speed = 300mm/sec, No Lubrication



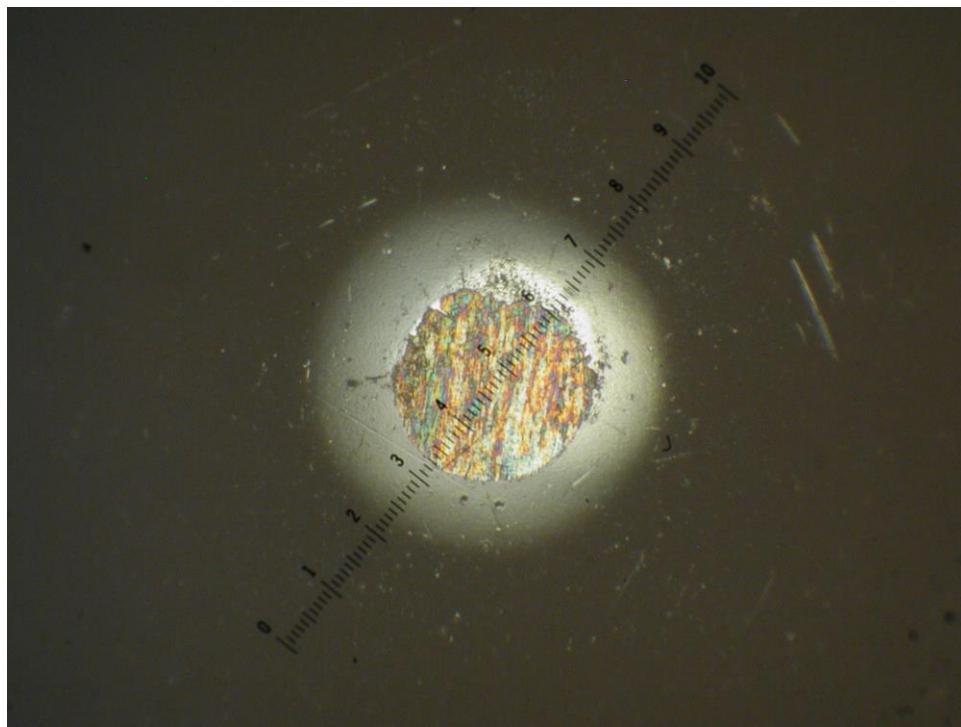
Appendix BoD – Ball-on-Disc Sliding Wear Data



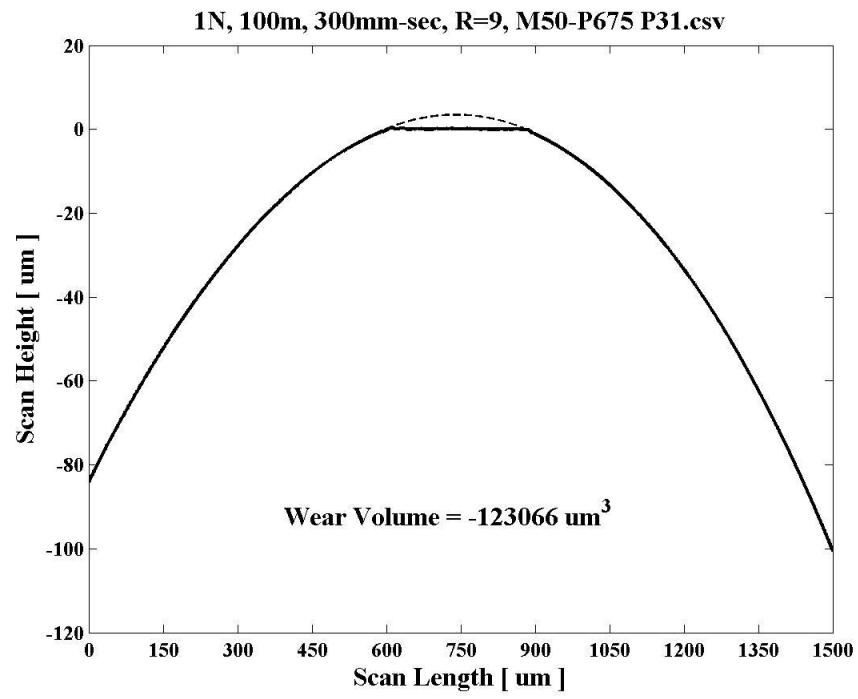
Disc Wear Track Center (above) SEM image @500x
Disc Wear Track Edge (below, non-contact area on right) SEM image @500x
P675 super-finished (Disc) vs. M50 (Ball)
Load = 1N, Distance = 100m, Speed = 300mm/sec, No Lubrication



Appendix BoD – Ball-on-Disc Sliding Wear Data

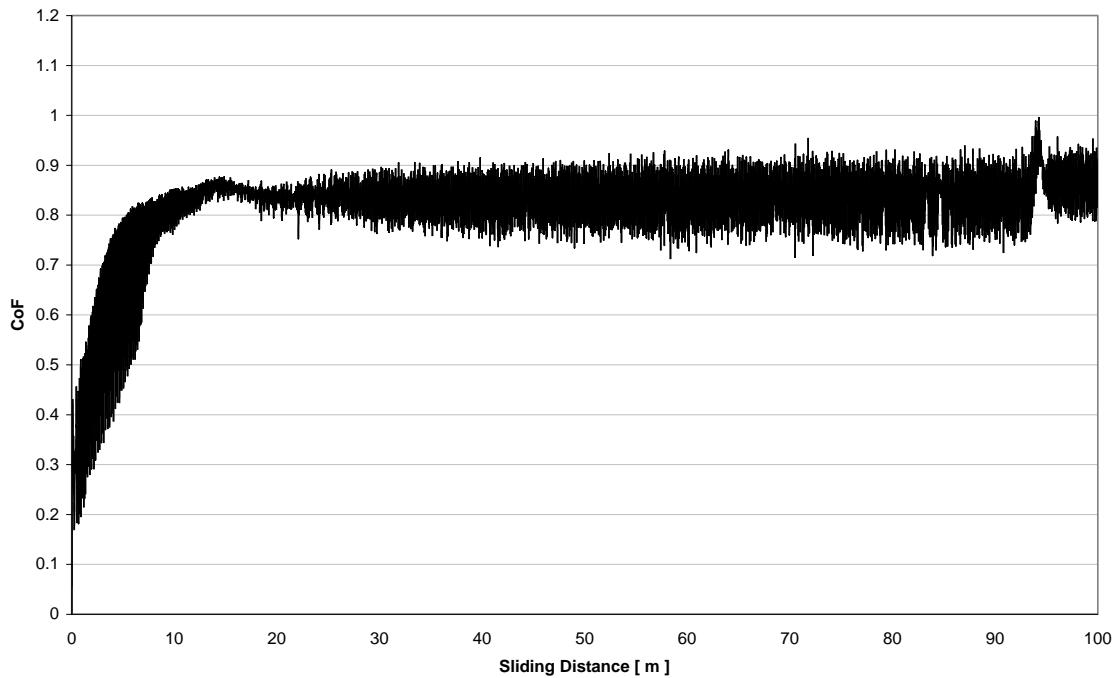


Ball Wear Scar Image and Profile
P675 super-finished (Disc) vs. M50 (Ball)
Load = 1N, Distance = 100m, Speed = 300mm/sec, No Lubrication



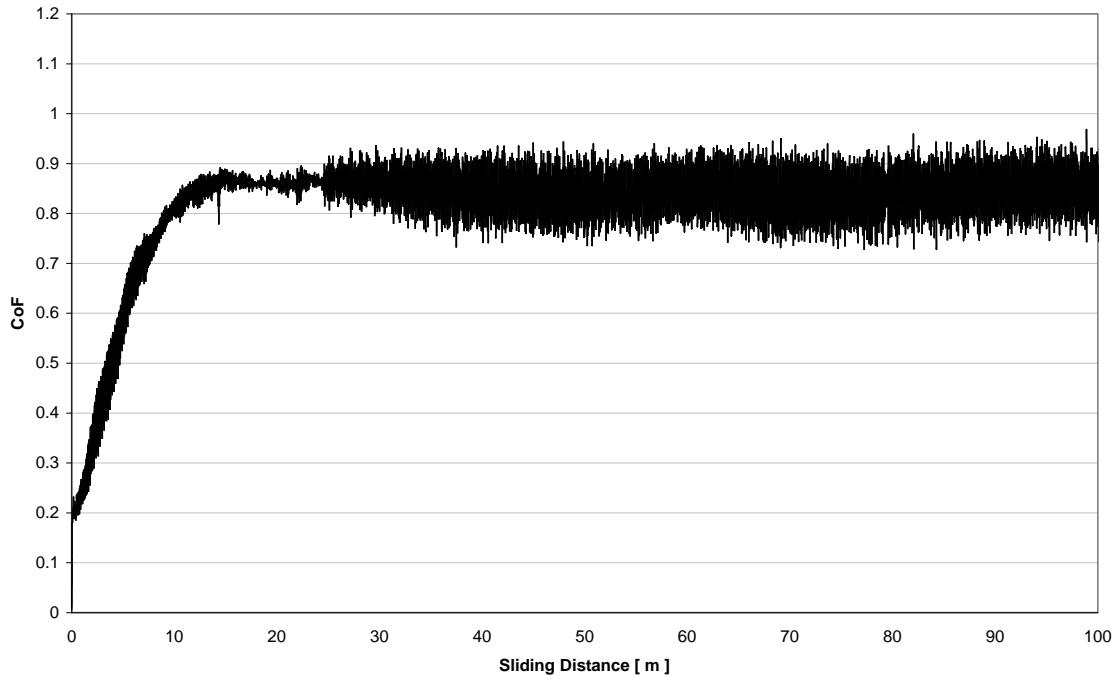
Appendix BoD – Ball-on-Disc Sliding Wear Data

CoF vs. Distance for 1N, 100m, 300mm-sec, R=9, M50-P675 P31.txt

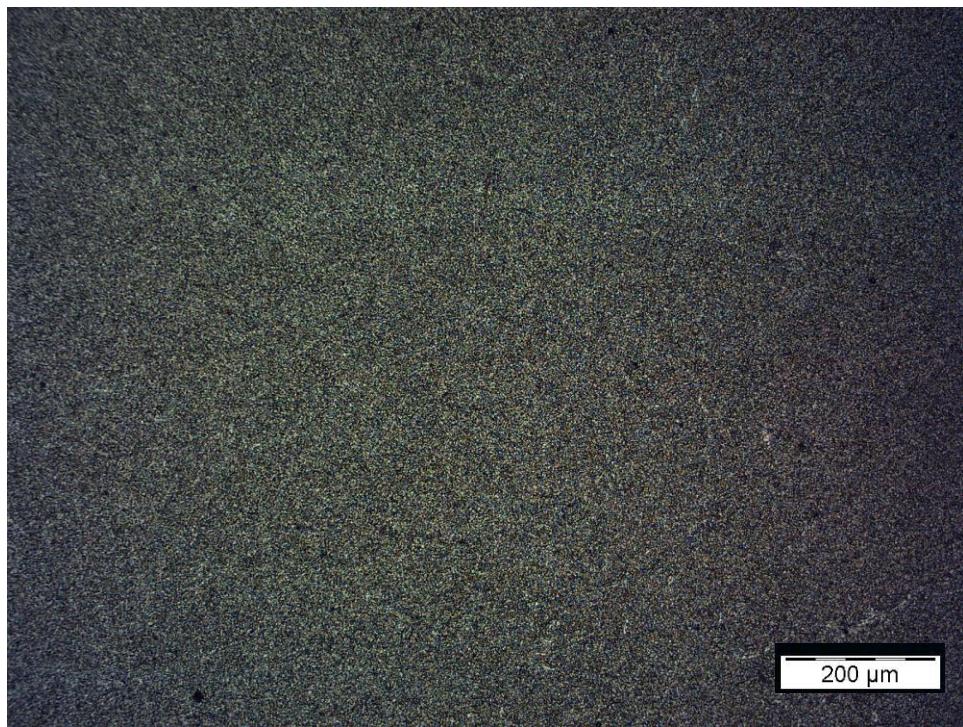


CoF vs. Sliding Distance
P675 super-finished (Disc) vs. M50 (Ball)
Load = 1N, Distance = 100m, Speed = 300mm/sec, No Lubrication

CoF vs. Distance for 1N, 100m, 300mm-sec, R=9, M50-P675 P40.txt

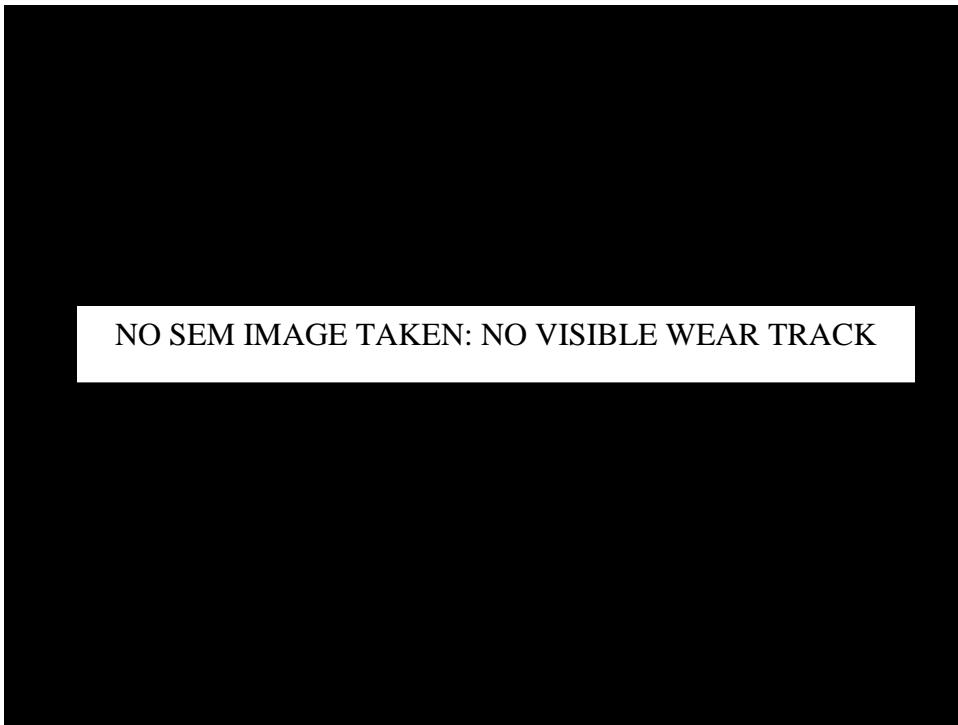


Appendix BoD – Ball-on-Disc Sliding Wear Data

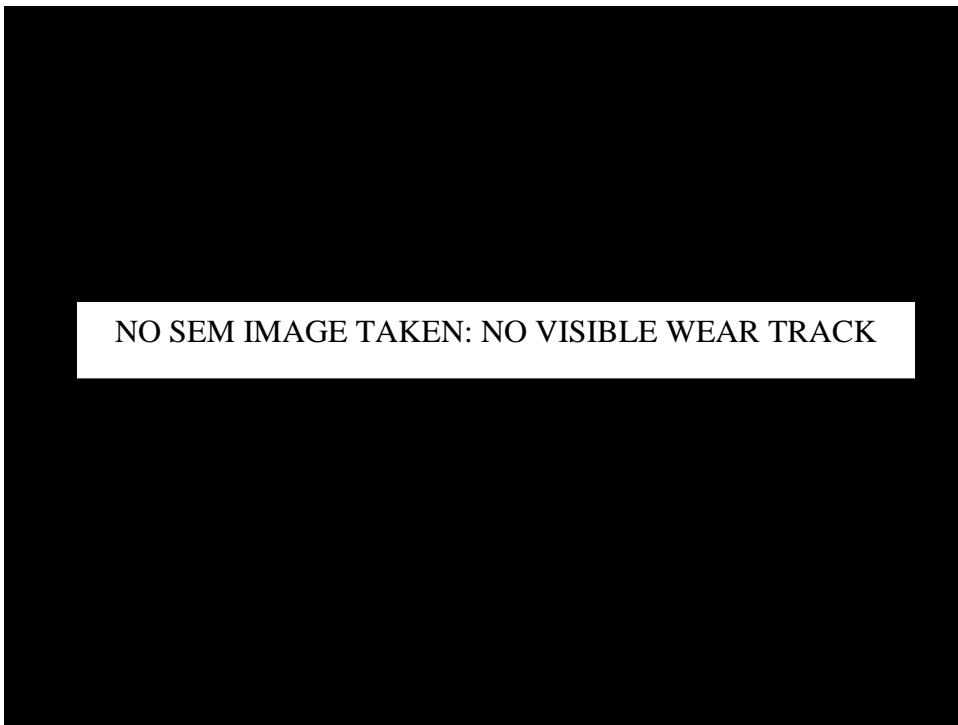


Disc Wear Track Image and Profile
Cr-CrN (Disc) vs. TiCr-TiCrN (Ball)
Load = 1N, Distance = 100m, Speed = 300mm/sec, No Lubrication

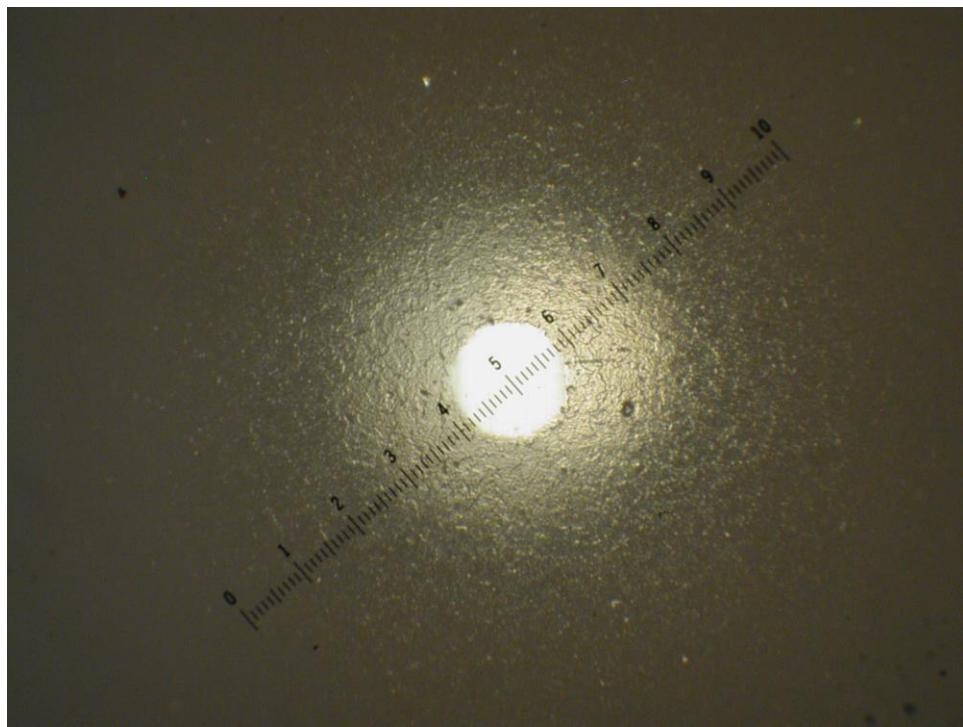
Appendix BoD – Ball-on-Disc Sliding Wear Data



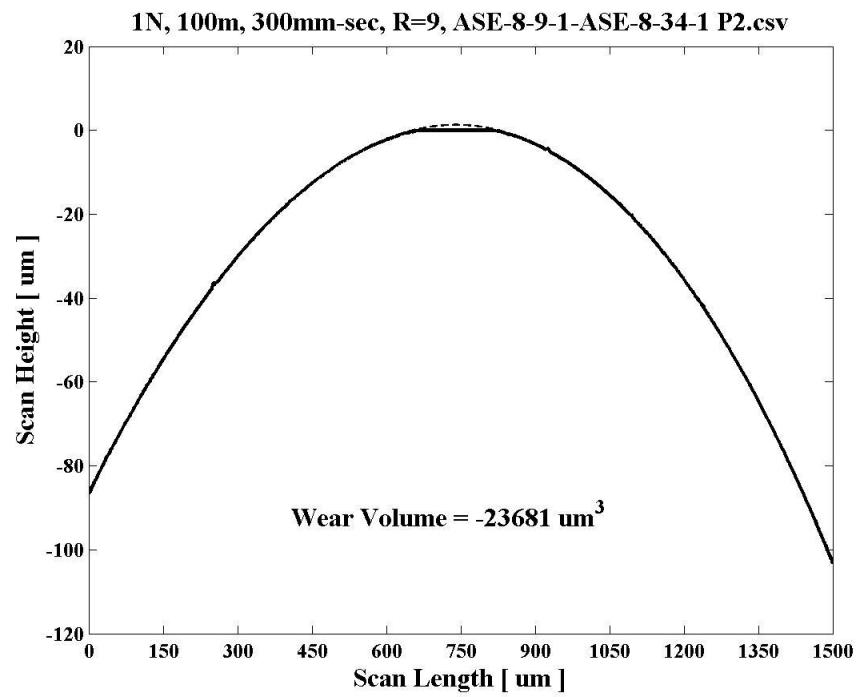
Disc Wear Track Center (above) SEM image @500x
Disc Wear Track Edge (below, non-contact area on right) SEM image @500x
Cr-CrN (Disc) vs. TiCr-TiCrN (Ball)
Load = 1N, Distance = 100m, Speed = 300mm/sec, No Lubrication



Appendix BoD – Ball-on-Disc Sliding Wear Data



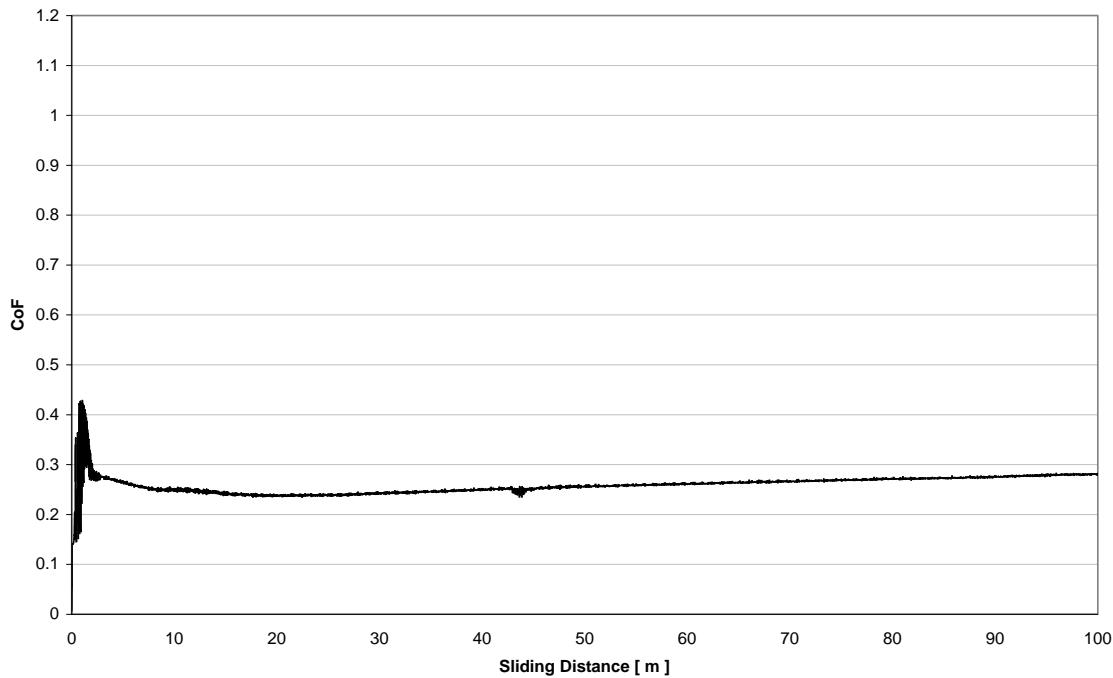
Ball Wear Scar Image and Profile
Cr-CrN (Disc) vs. TiCr-TiCrN (Ball)
Load = 1N, Distance = 100m, Speed = 300mm/sec, No Lubrication



BoD_20

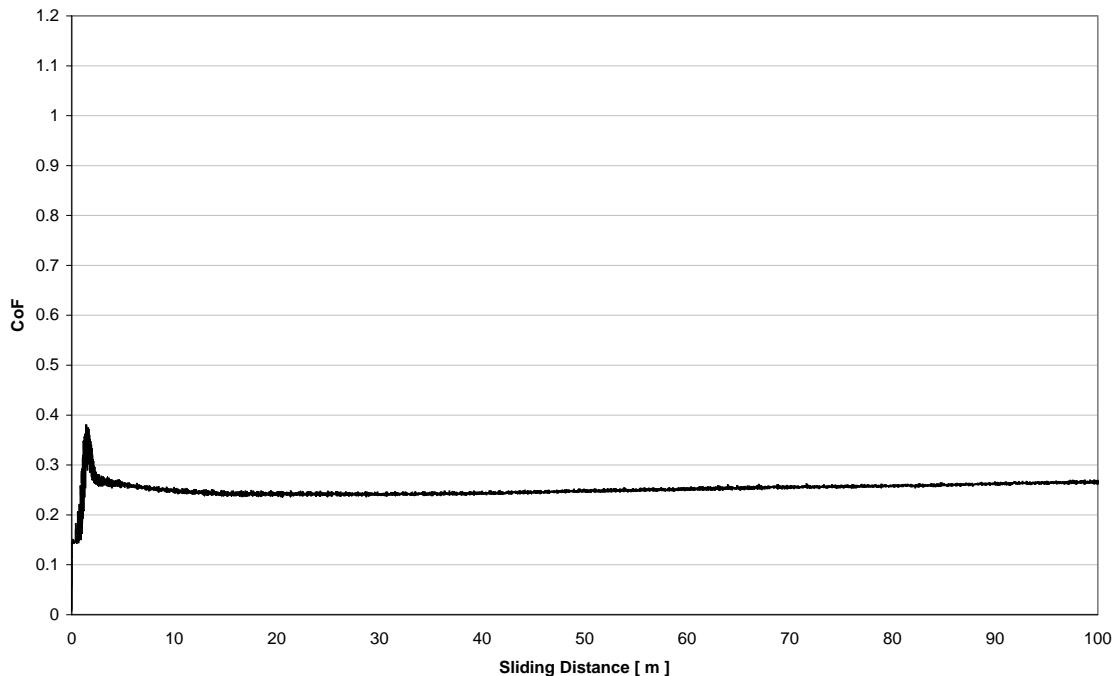
Appendix BoD – Ball-on-Disc Sliding Wear Data

CoF vs. Distance for 1N, 100m, 300mm/sec, R=9, ASE-8-9-1-ASE-8-29-1 P74.txt

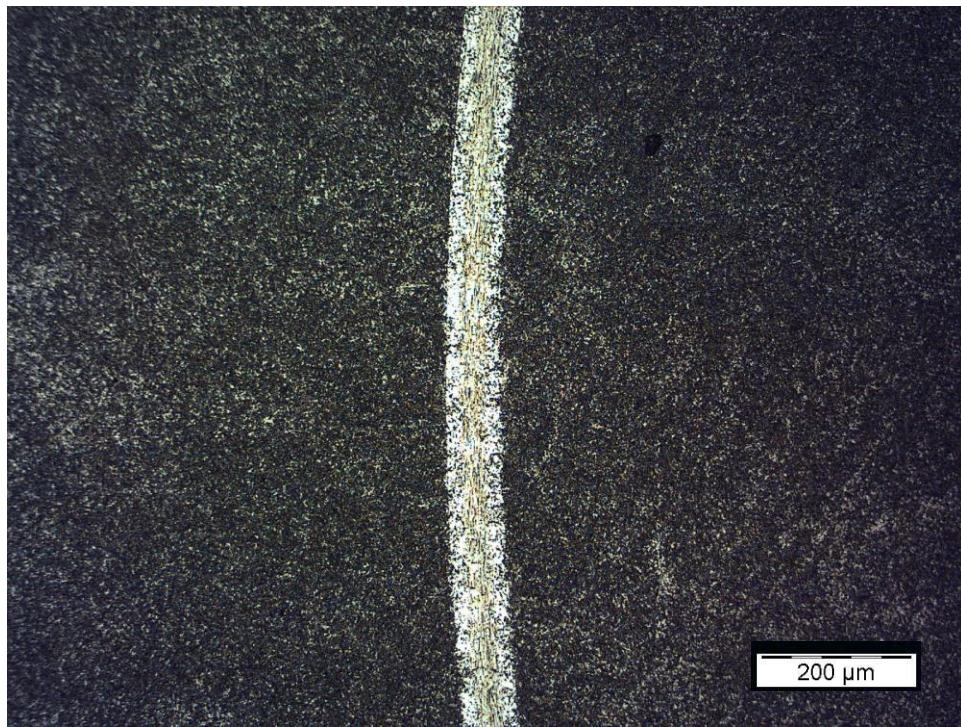


CoF vs. Sliding Distance
Cr-CrN (Disc) vs. TiCr-TiCrN (Ball)
Load = 1N, Distance = 100m, Speed = 300mm/sec, No Lubrication

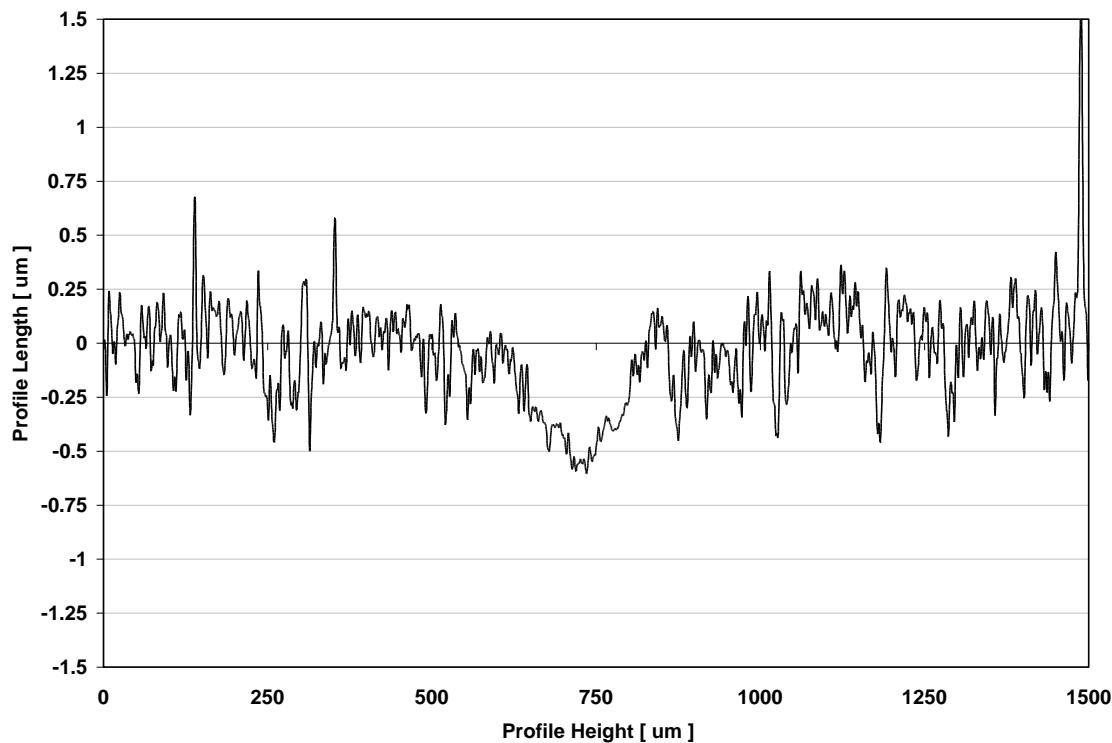
CoF vs. Distance for 1N, 100m, 300mm/sec, R=9, ASE-8-9-1-ASE-8-34-1 P2.txt



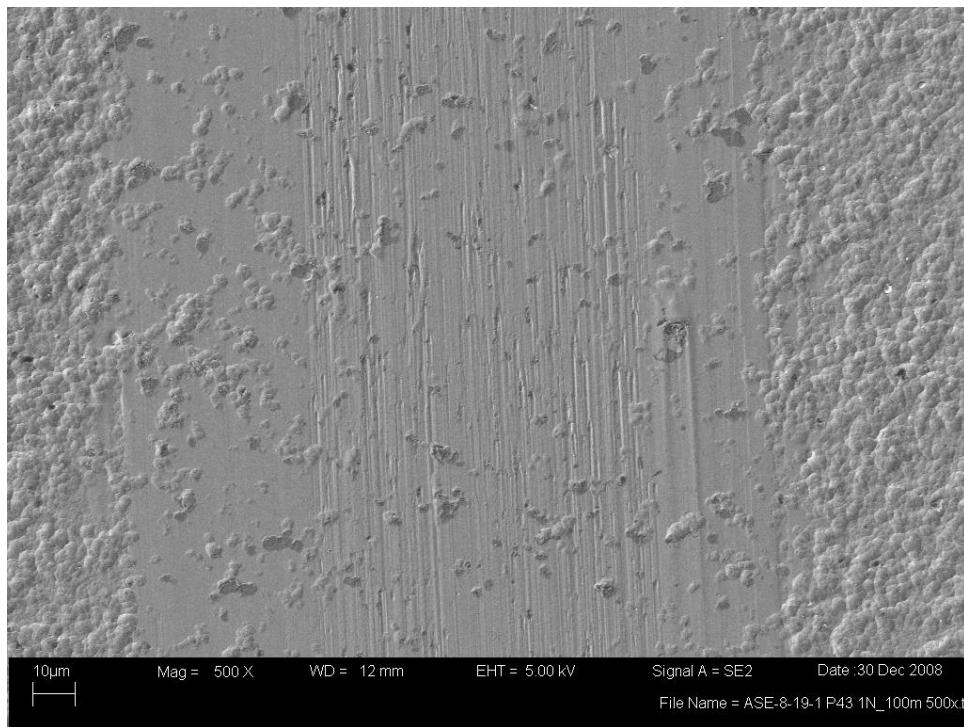
Appendix BoD – Ball-on-Disc Sliding Wear Data



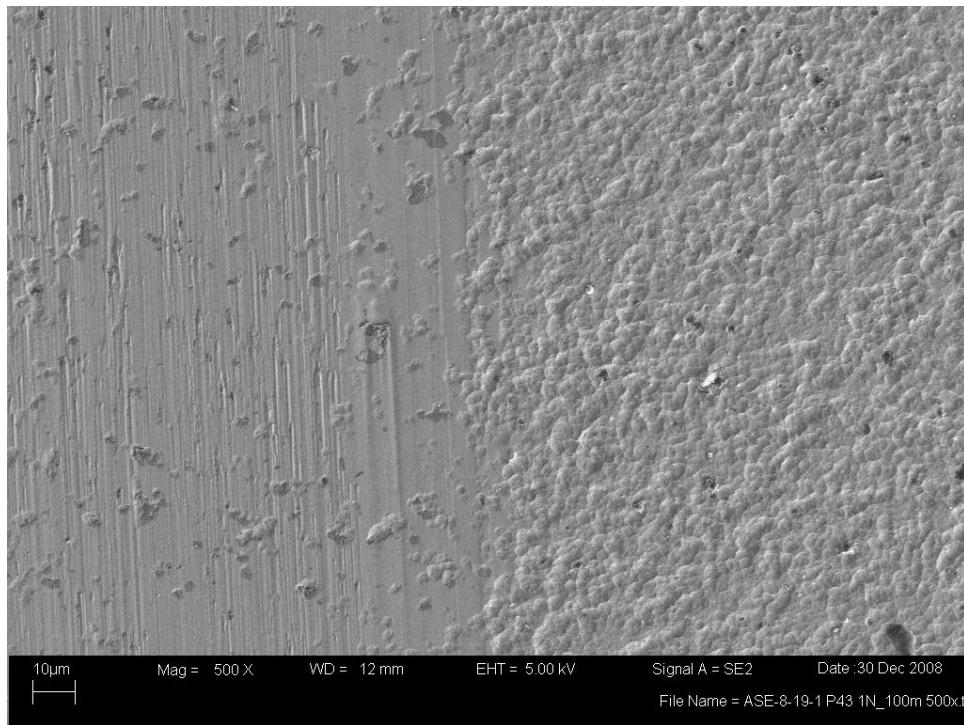
Disc Wear Track Image and Profile
CrC (Disc) vs. TiCr-TiCrN (Ball)
Load = 1N, Distance = 100m, Speed = 300mm/sec, No Lubrication



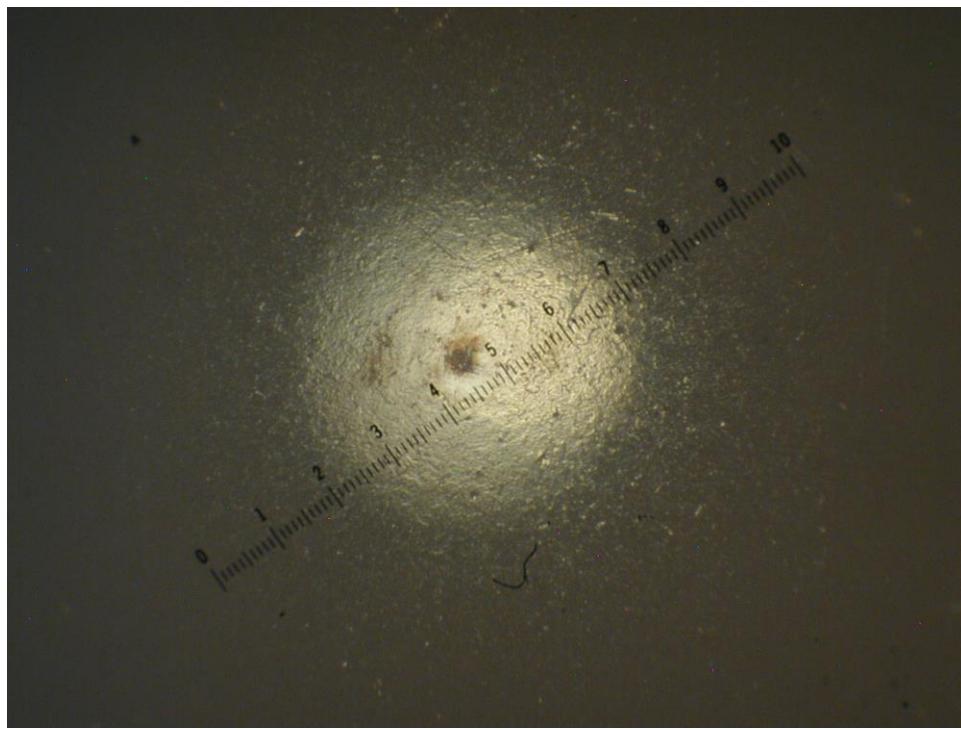
Appendix BoD – Ball-on-Disc Sliding Wear Data



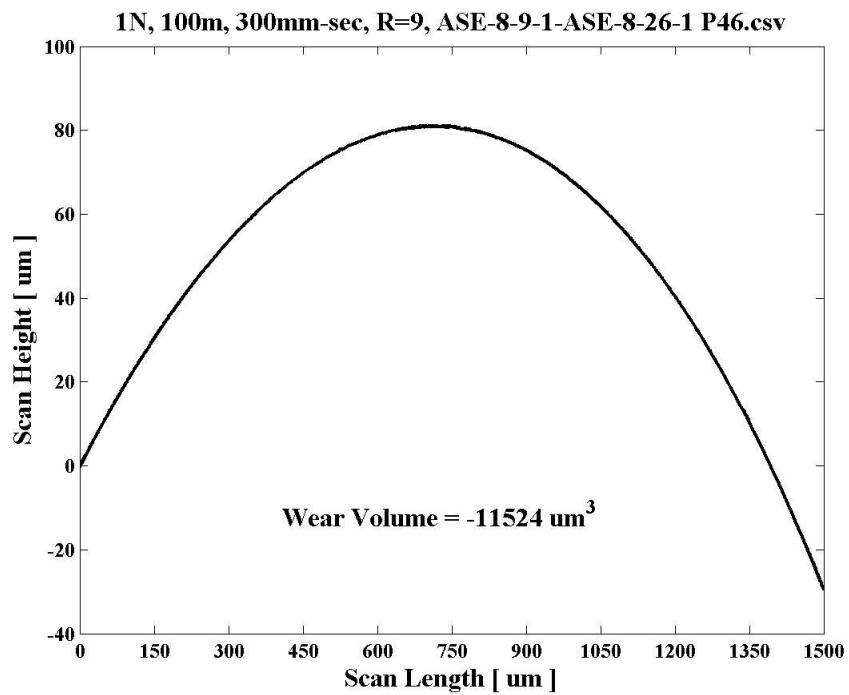
Disc Wear Track Center (above) SEM image @500x
Disc Wear Track Edge (below, non-contact area on right) SEM image @500x
CrC (Disc) vs. TiCr-TiCrN (Ball)
Load = 1N, Distance = 100m, Speed = 300mm/sec, No Lubrication



Appendix BoD – Ball-on-Disc Sliding Wear Data

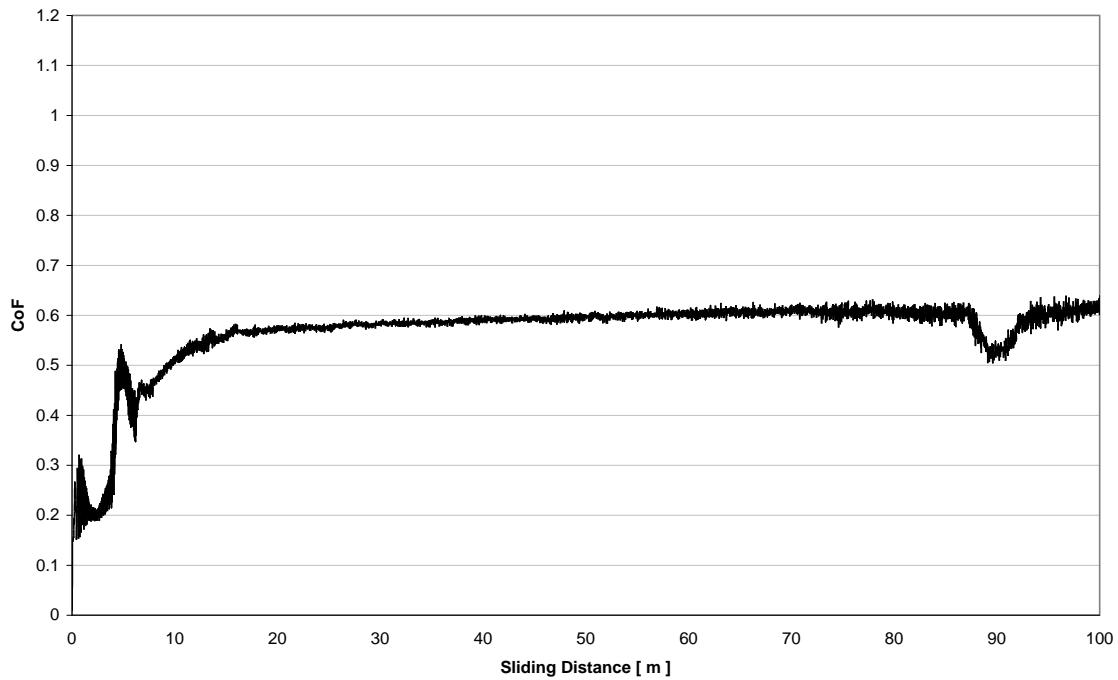


Ball Wear Scar Image and Profile
CrC (Disc) vs. TiCr-TiCrN (Ball)
Load = 1N, Distance = 100m, Speed = 300mm/sec, No Lubrication



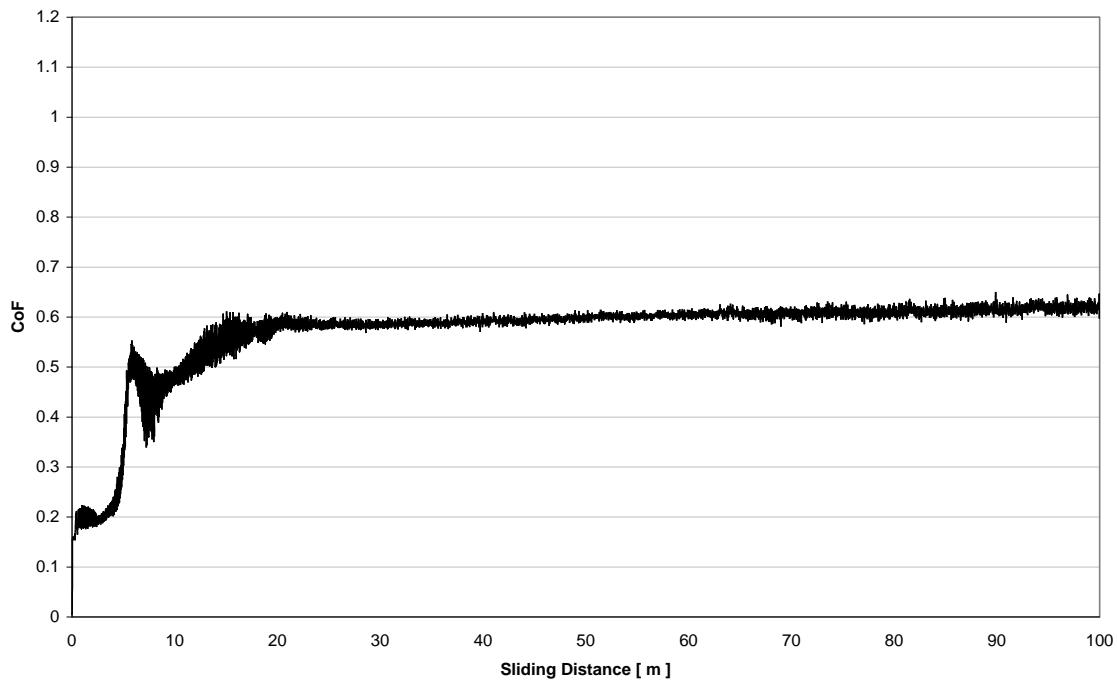
Appendix BoD – Ball-on-Disc Sliding Wear Data

CoF vs. Distance for 1N, 100m, 300mm-sec, R=9, ASE-8-9-1-ASE-8-26-1 P46.txt

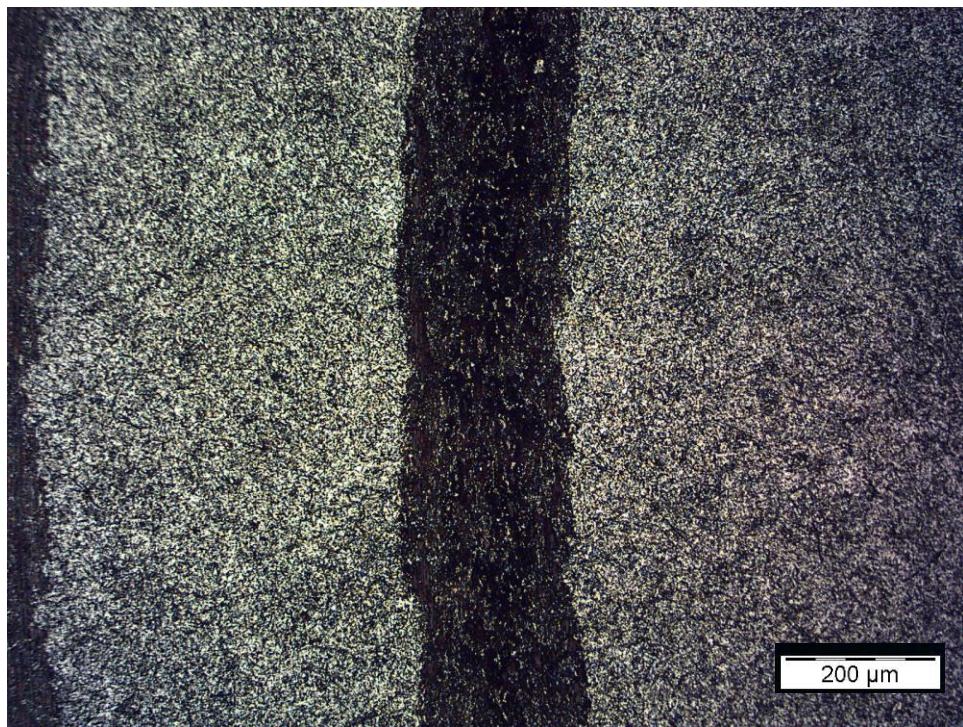


CoF vs. Sliding Distance
CrC (Disc) vs. TiCr-TiCrN (Ball)
Load = 1N, Distance = 100m, Speed = 300mm/sec, No Lubrication

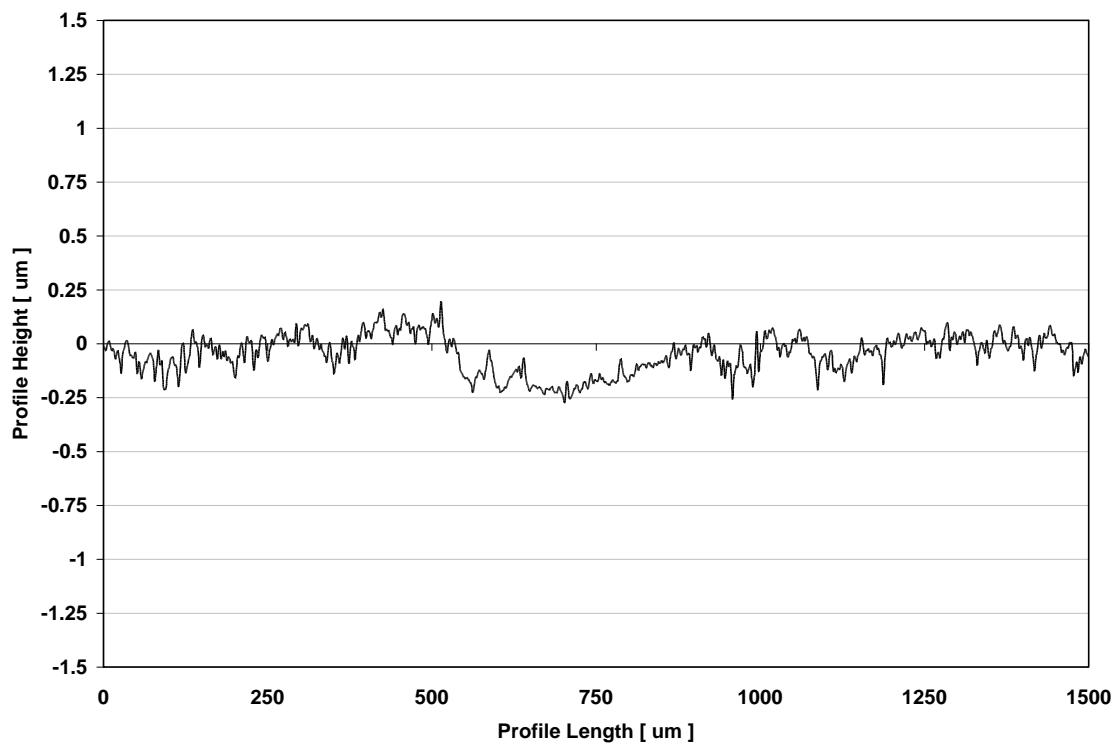
CoF vs. Distance for 1N, 100m, 300mm-sec, R=9, ASE-8-9-1-ASE-8-19-1 P43.txt



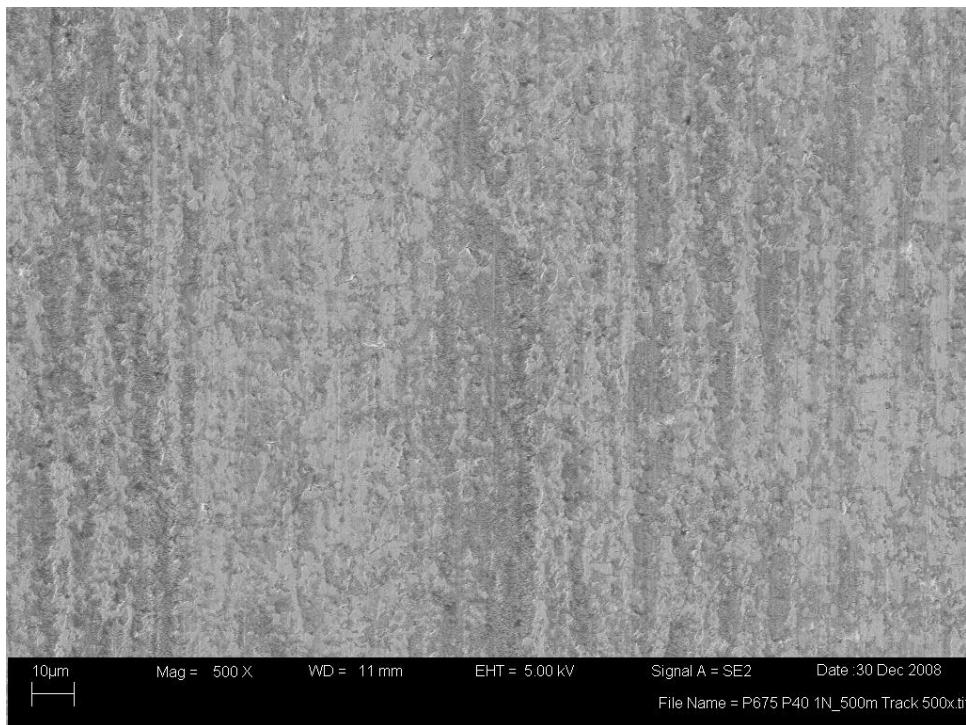
Appendix BoD – Ball-on-Disc Sliding Wear Data



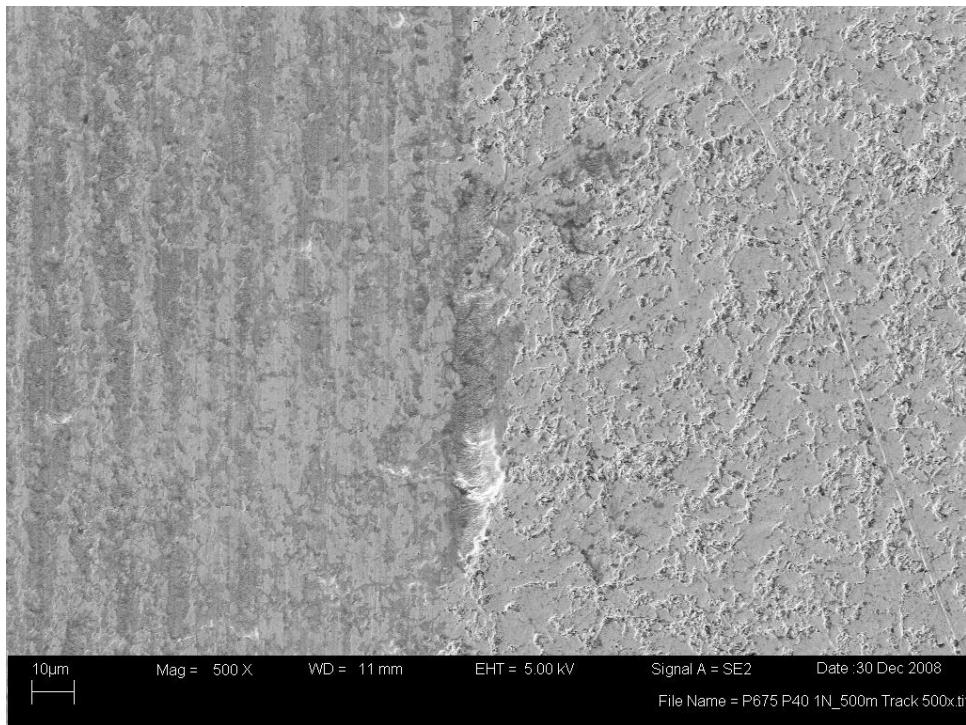
Disc Wear Track Image and Profile
P675 super-finished (Disc) vs. M50 (Ball)
Load = 1N, Distance = 500m, Speed = 300mm/sec, No Lubrication



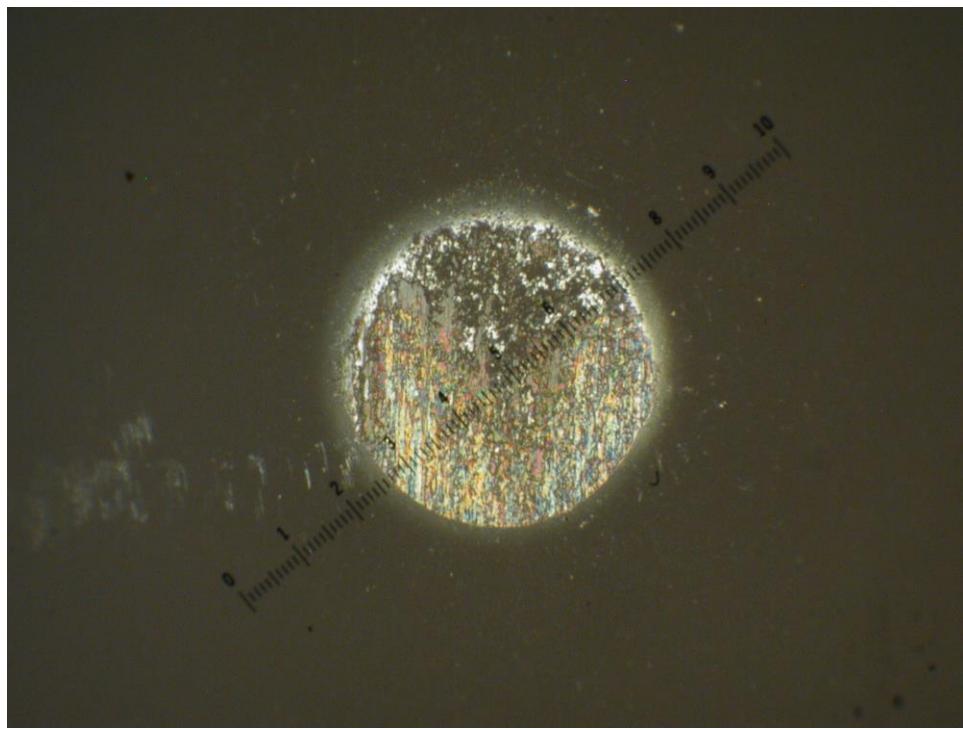
Appendix BoD – Ball-on-Disc Sliding Wear Data



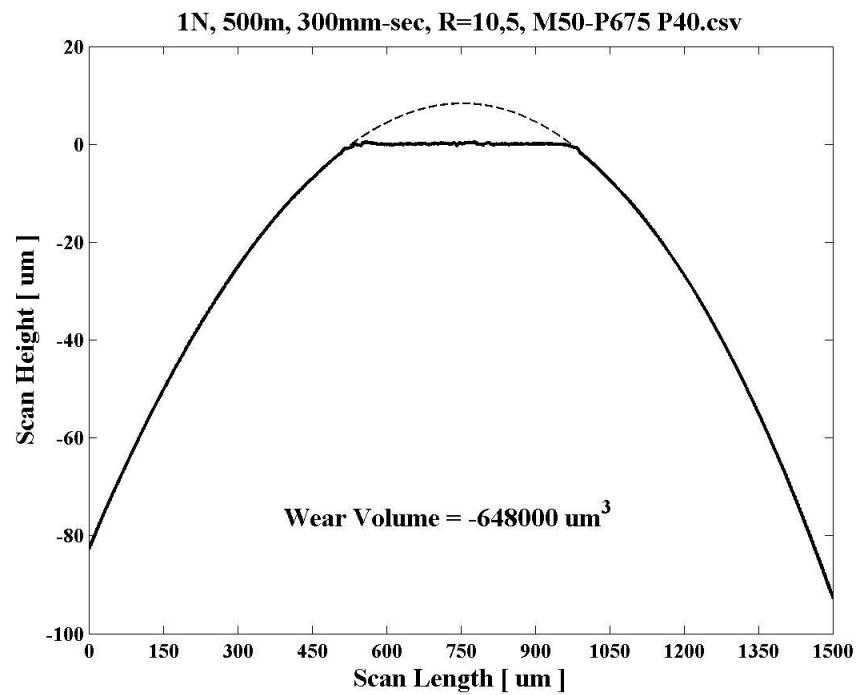
Disc Wear Track Center (above) SEM image @500x
Disc Wear Track Edge (below, non-contact area on right) SEM image @500x
P675 super-finished (Disc) vs. M50 (Ball)
Load = 1N, Distance = 500m, Speed = 300mm/sec, No Lubrication



Appendix BoD – Ball-on-Disc Sliding Wear Data

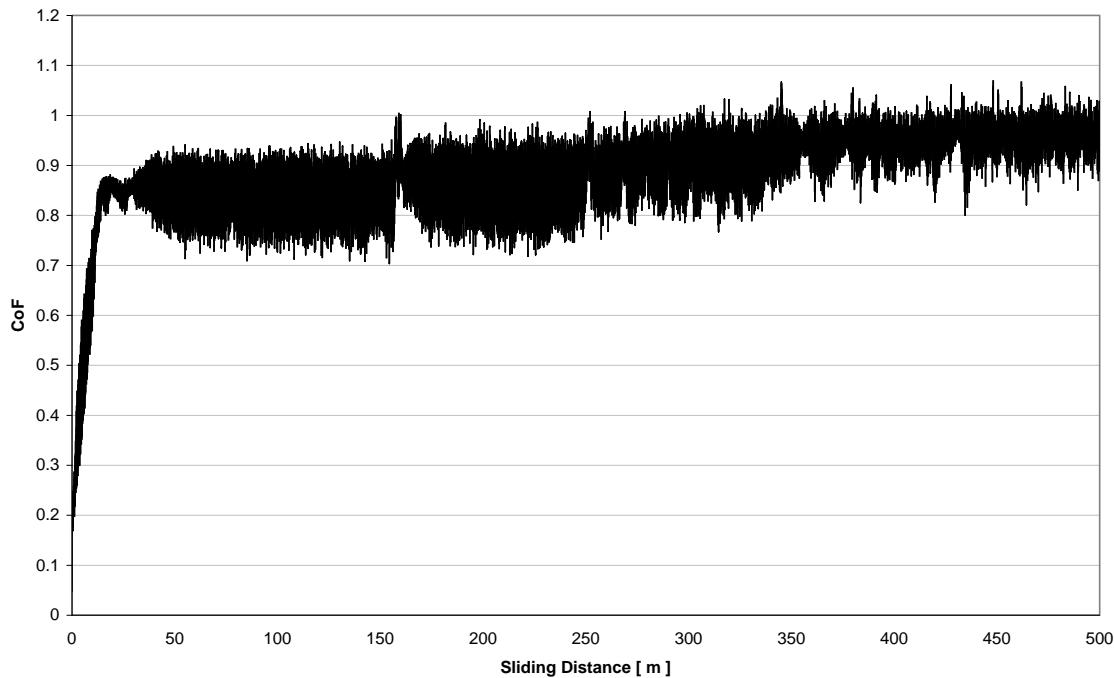


Ball Wear Scar Image and Profile
P675 super-finished (Disc) vs. M50 (Ball)
Load = 1N, Distance = 500m, Speed = 300mm/sec, No Lubrication



Appendix BoD – Ball-on-Disc Sliding Wear Data

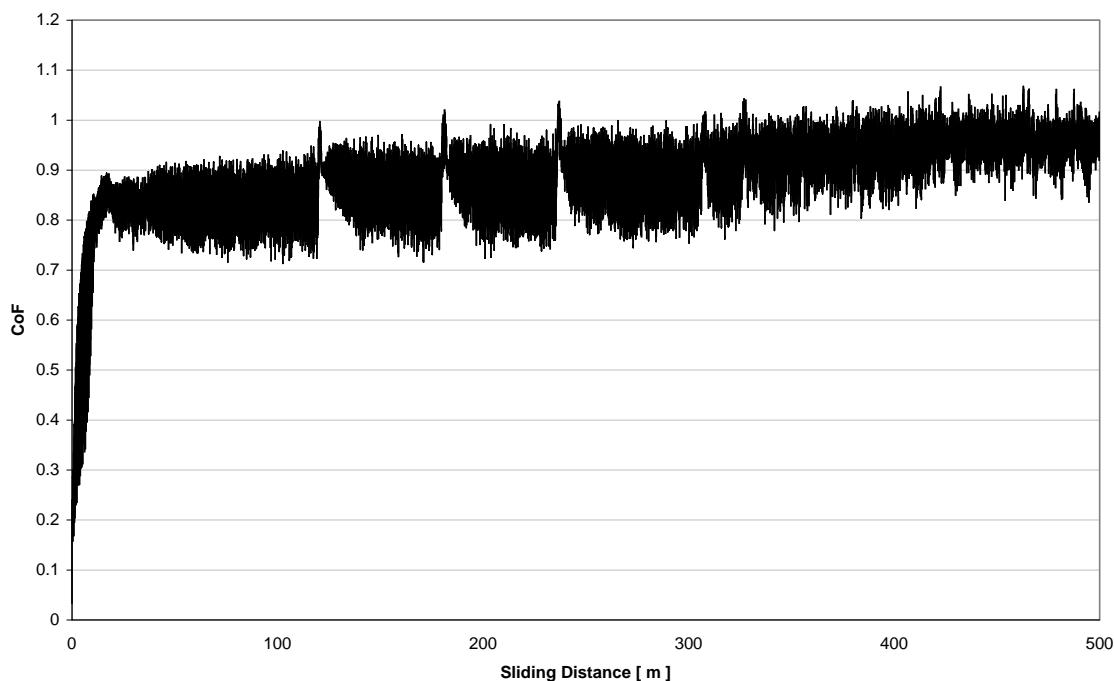
CoF vs. Distance for 1N, 500m, 300mm-sec, R=10.5, M50-P675 P40.txt



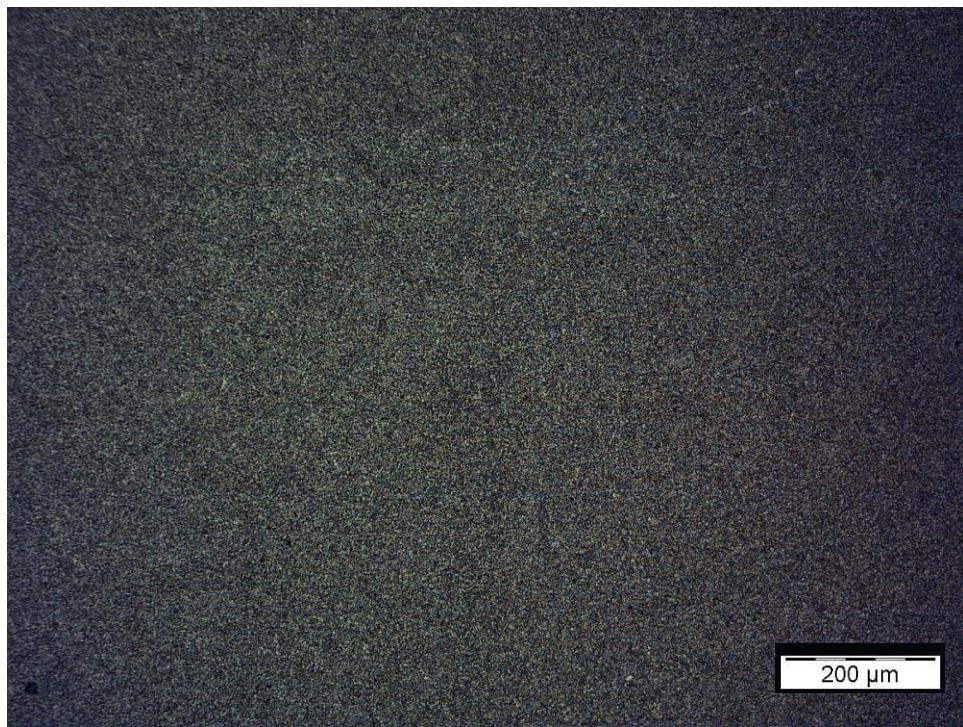
CoF vs. Sliding Distance
P675 (Disc) vs. M50 (Ball)

Load = 1N, Distance = 500m, Speed = 300mm/sec, No Lubrication

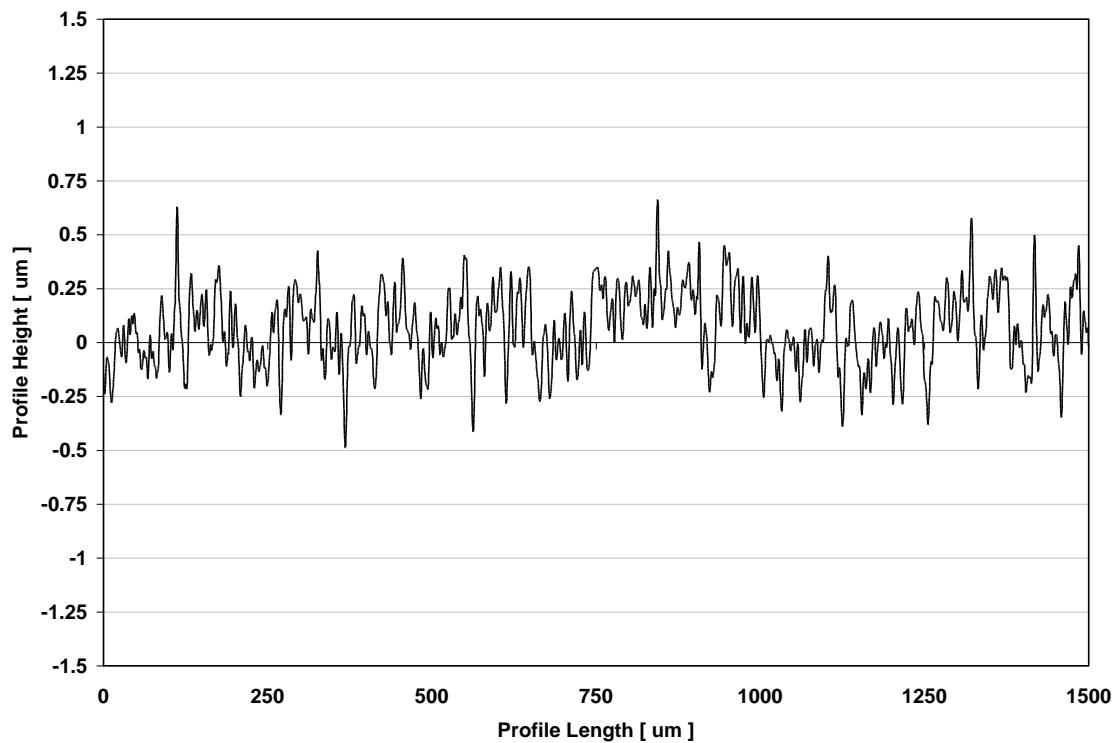
CoF vs. Distance for 1N, 500m, 300mm-sec, R=10.5, M50-P675 P31.txt



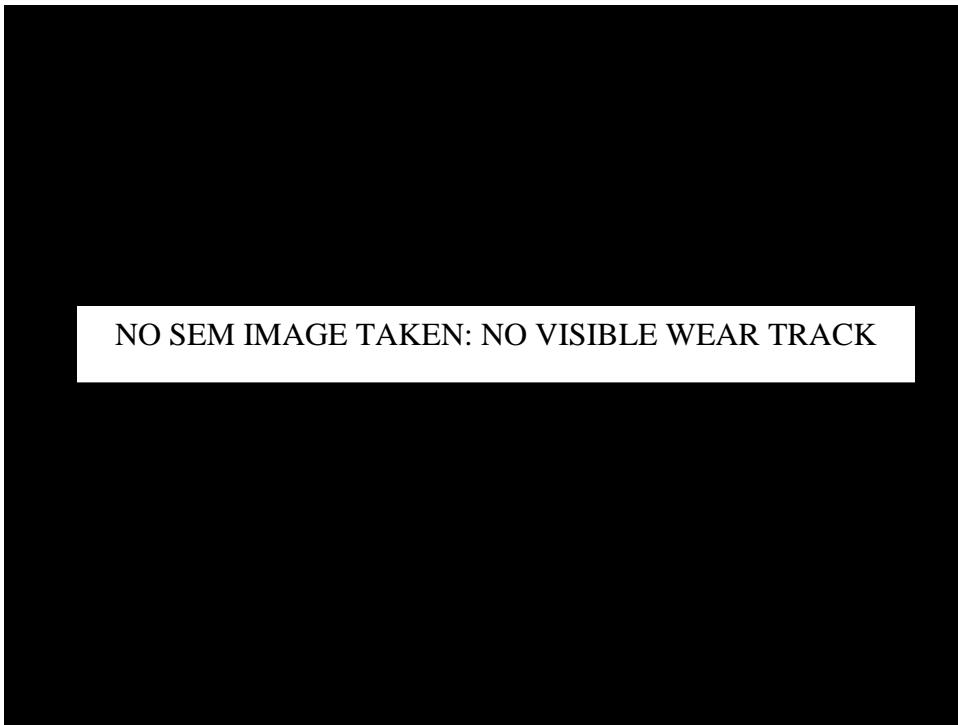
Appendix BoD – Ball-on-Disc Sliding Wear Data



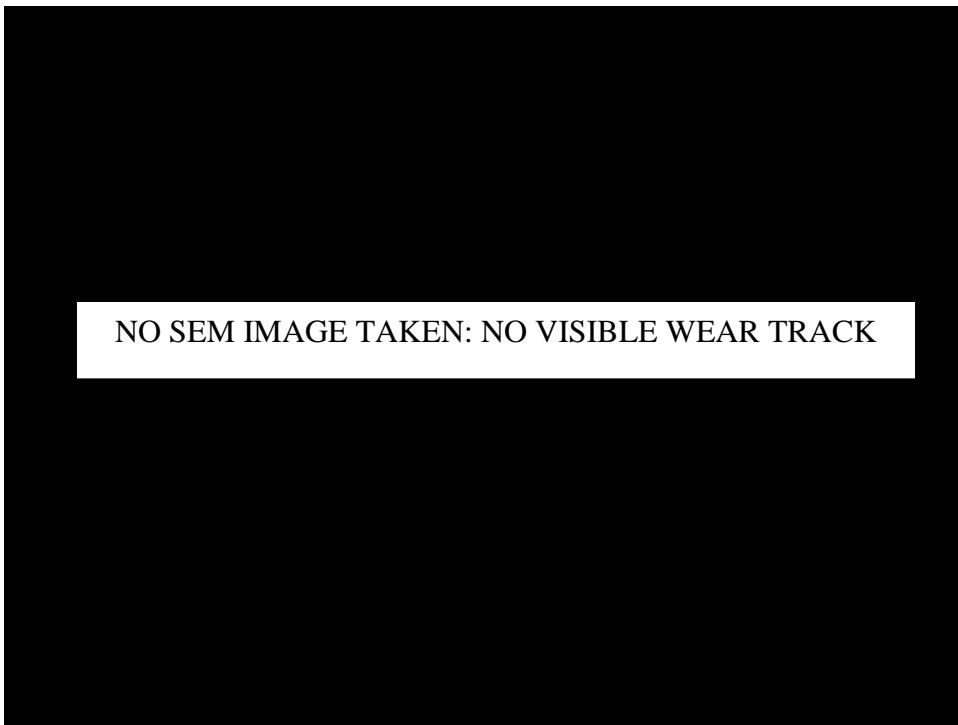
Disc Wear Track Image and Profile
Cr-CrN (Disc) vs. TiCr-TiCrN (Ball)
Load = 1N, Distance = 500m, Speed = 300mm/sec, No Lubrication



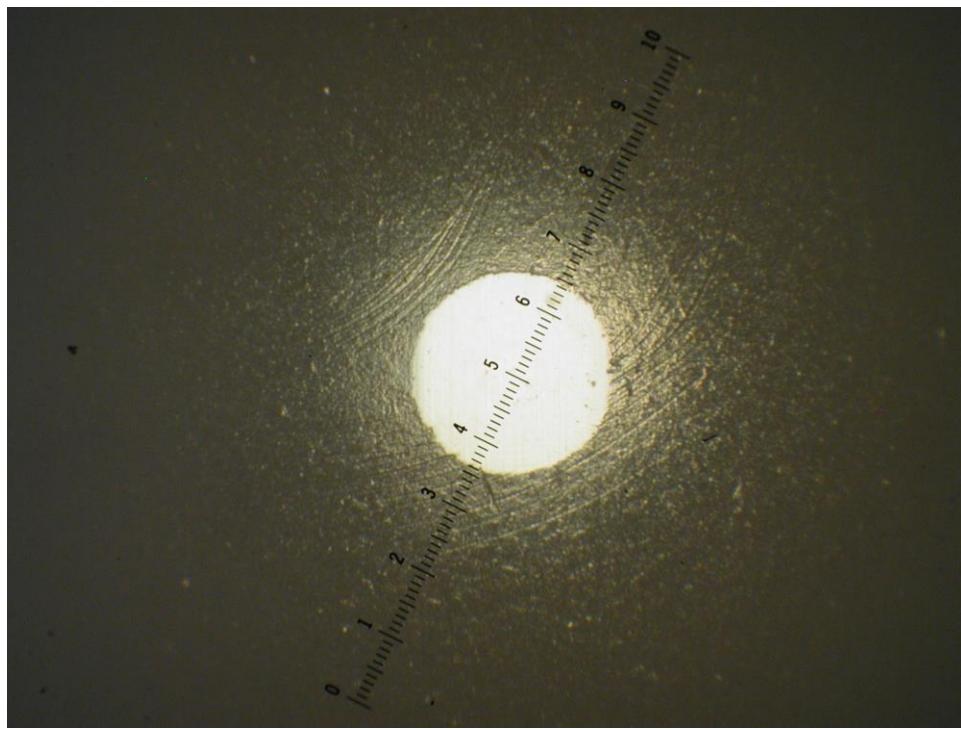
Appendix BoD – Ball-on-Disc Sliding Wear Data



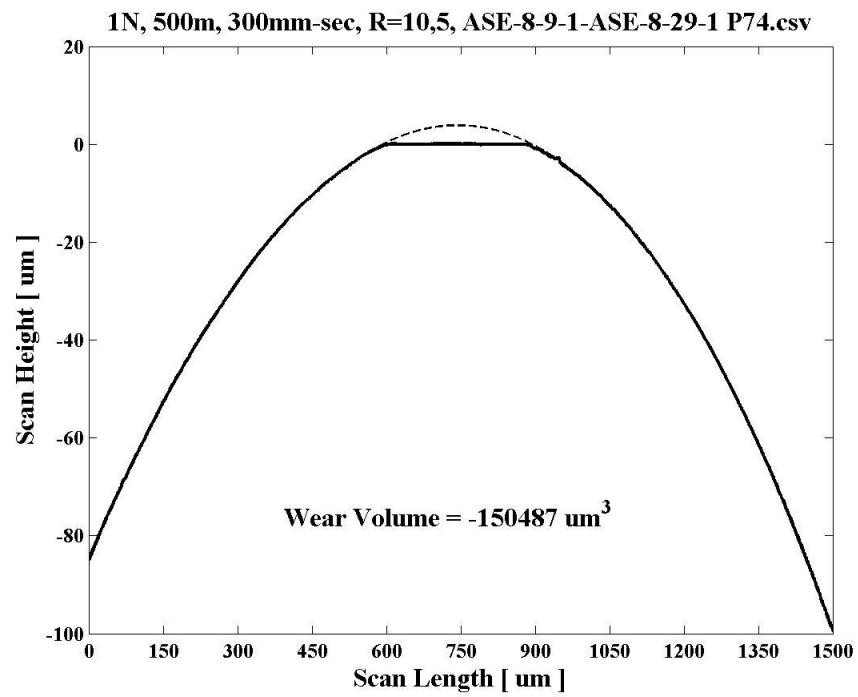
Disc Wear Track Center (above) SEM image @500x
Disc Wear Track Edge (below, non-contact are on right) SEM image @500x
Cr-CrN (Disc) vs. TiCr-TiCrN (Ball)
Load = 1N, Distance = 500m, Speed = 300mm/sec, No Lubrication



Appendix BoD – Ball-on-Disc Sliding Wear Data

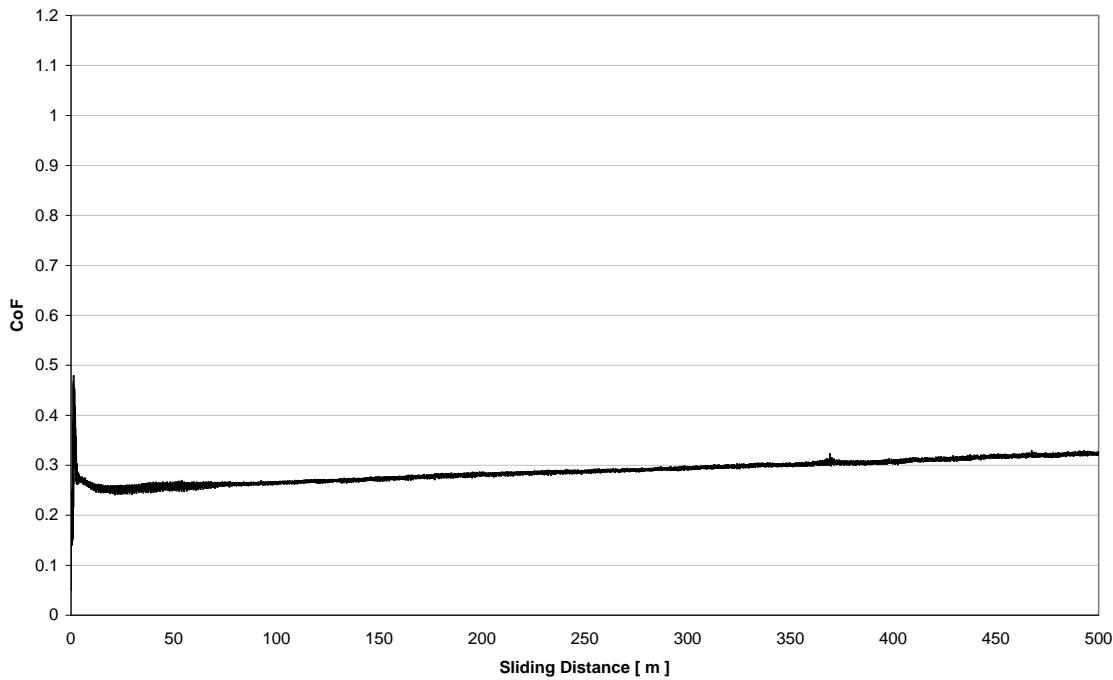


Ball Wear Scar Image and Profile
Cr-CrN (Disc) vs. TiCr-TiCrN (Ball)
Load = 1N, Distance = 500m, Speed = 300mm/sec, No Lubrication



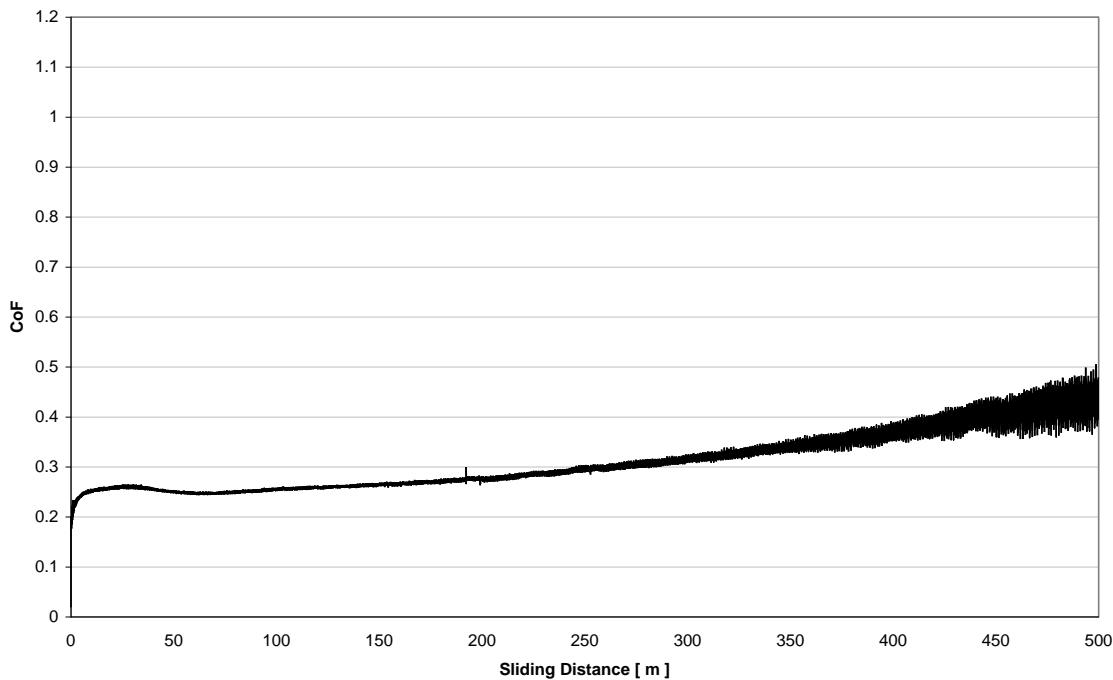
Appendix BoD – Ball-on-Disc Sliding Wear Data

CoF vs. Distance for 1N, 500m, 300mm-sec, R=10.5, ASE-8-9-1-ASE-8-34-1 P2.txt

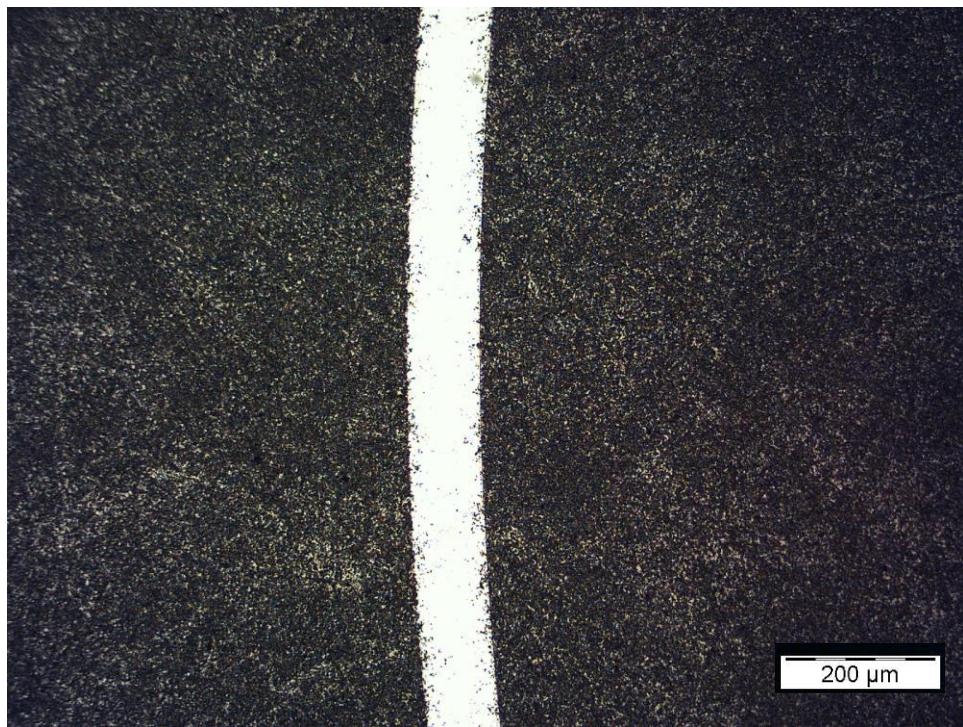


CoF vs. Sliding Distance
Cr-CrN (Disc) vs. TiCr-TiCrN (Ball)
Load = 1N, Distance = 500m, Speed = 300mm/sec, No Lubrication

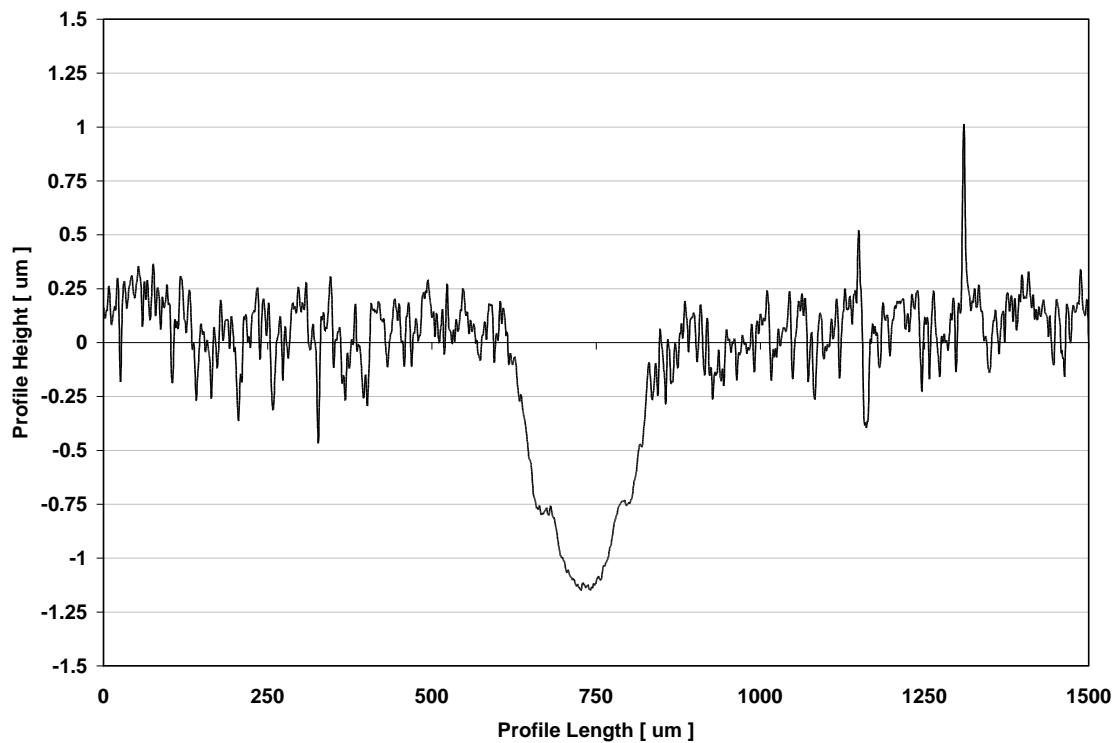
CoF vs. Distance for 1N, 500m, 300mm-sec, R=10.5, ASE-8-9-1-ASE-8-29-1 P74.txt



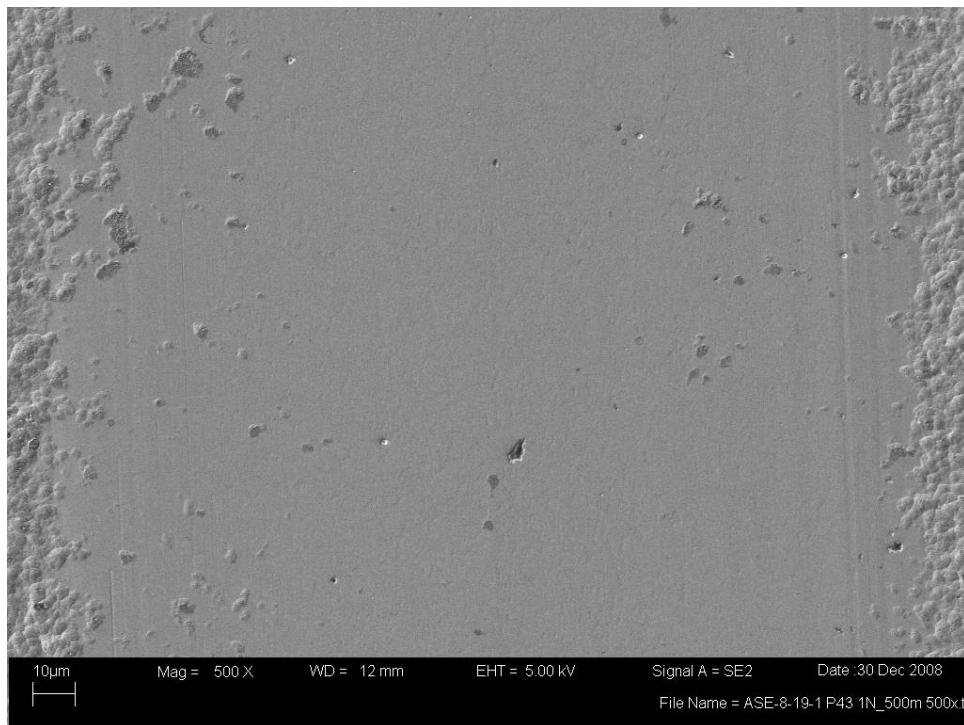
Appendix BoD – Ball-on-Disc Sliding Wear Data



Disc Wear Track Image and Profile
CrC (Disc) vs. TiCr-TiCrN (Ball)
Load = 1N, Distance = 500m, Speed = 300mm/sec, No Lubrication



Appendix BoD – Ball-on-Disc Sliding Wear Data

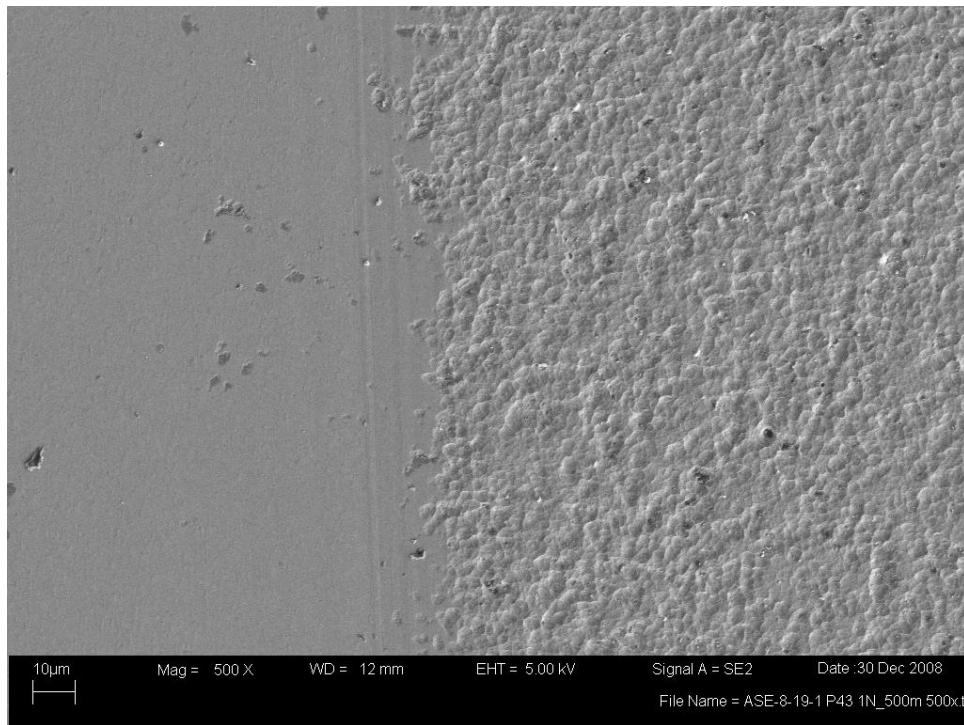


Disc Wear Track Center (above) SEM image @500x

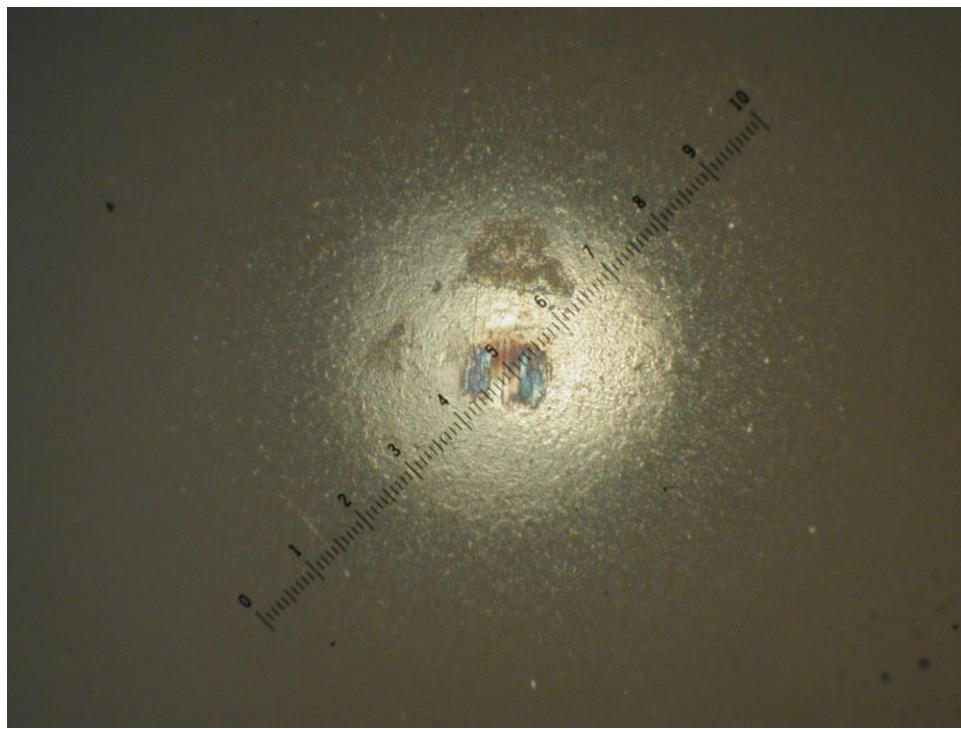
Disc Wear Track Edge (below, non-contact area on right) SEM image @500x

CrC (Disc) vs. TiCr-TiCrN (Ball)

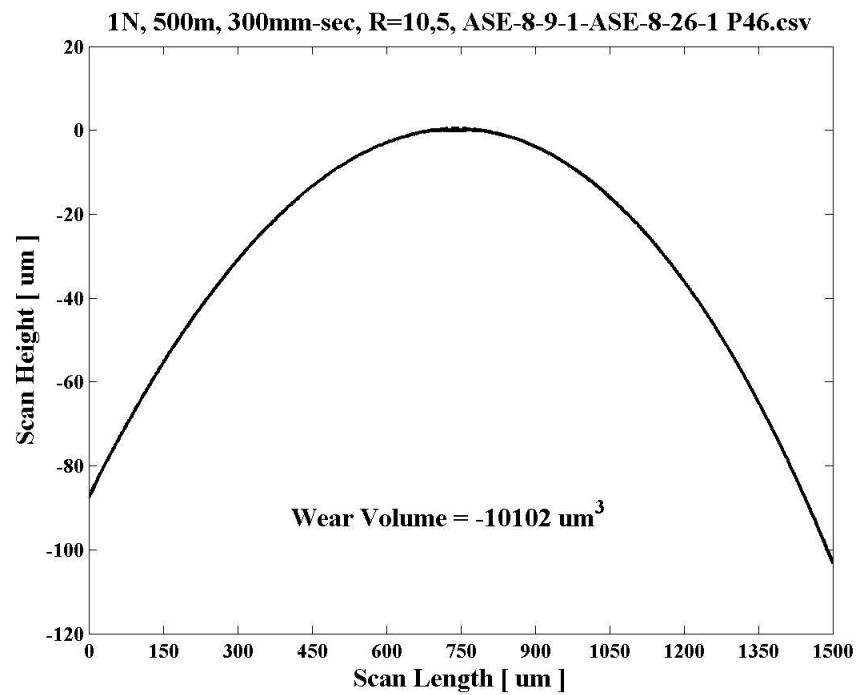
Load = 1N, Distance = 500m, Speed = 300mm/sec, No Lubrication



Appendix BoD – Ball-on-Disc Sliding Wear Data

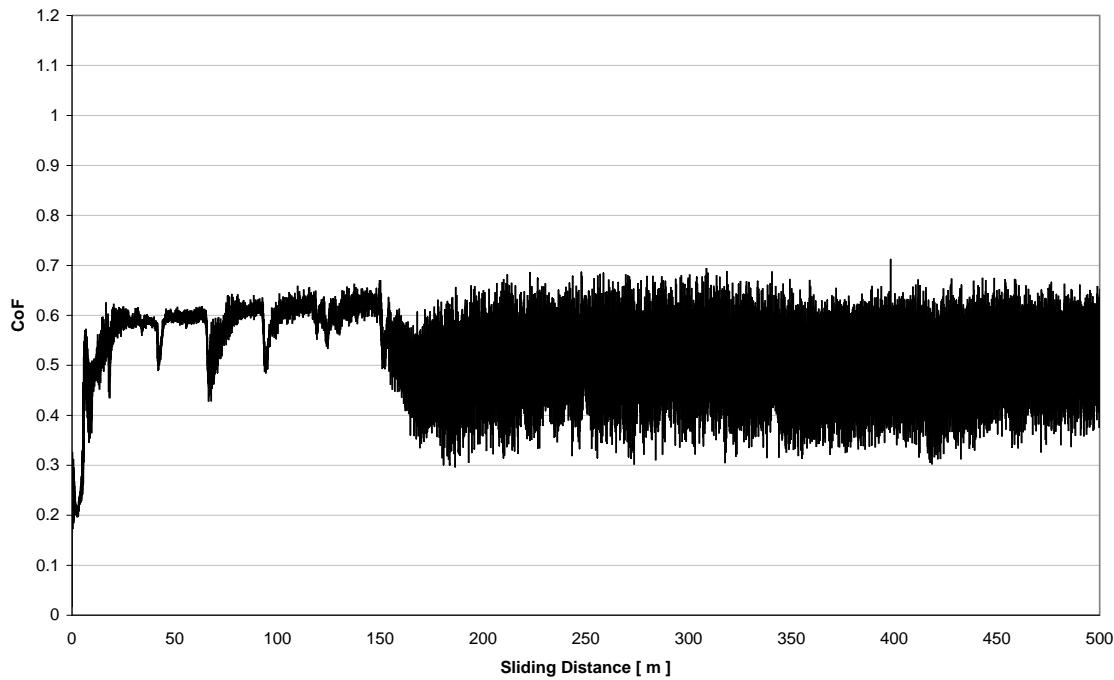


Ball Wear Scar Image and Profile
CrC (Disc) vs. TiCr-TiCrN (Ball)
Load = 1N, Distance = 500m, Speed = 300mm/sec, No Lubrication



Appendix BoD – Ball-on-Disc Sliding Wear Data

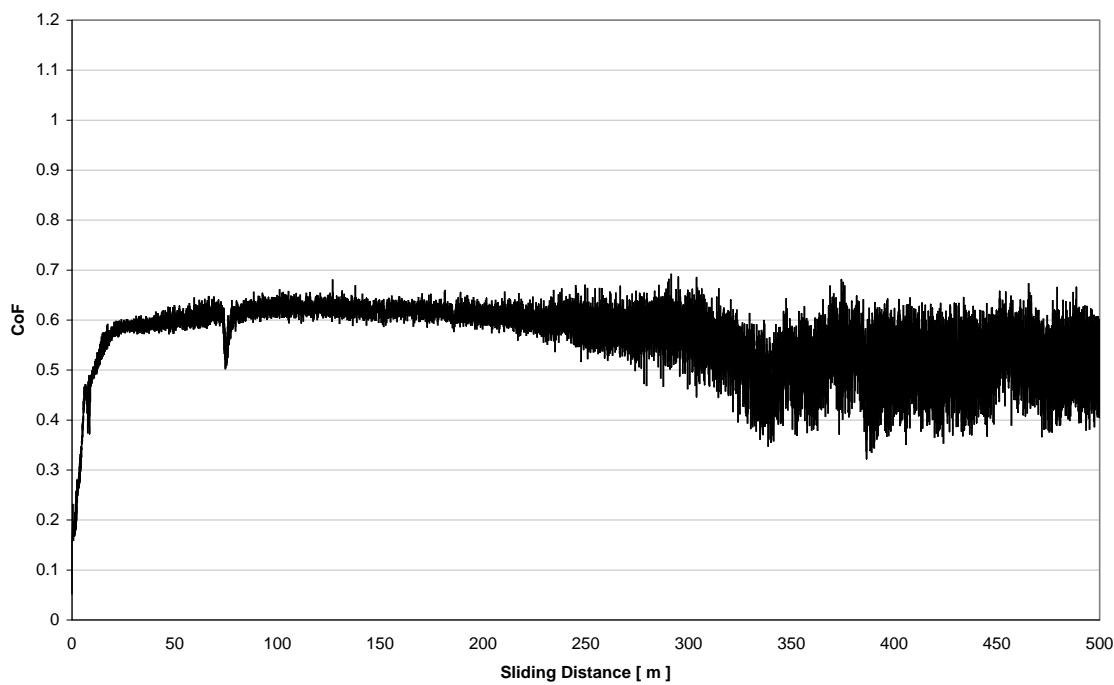
CoF vs. Distance for 1N, 500m, 300mm-sec, R=10.5, ASE-8-9-1-ASE-8-19-1 P43.txt



CoF vs. Sliding Distance
CrC (Disc) vs. TiCr-TiCrN (Ball)

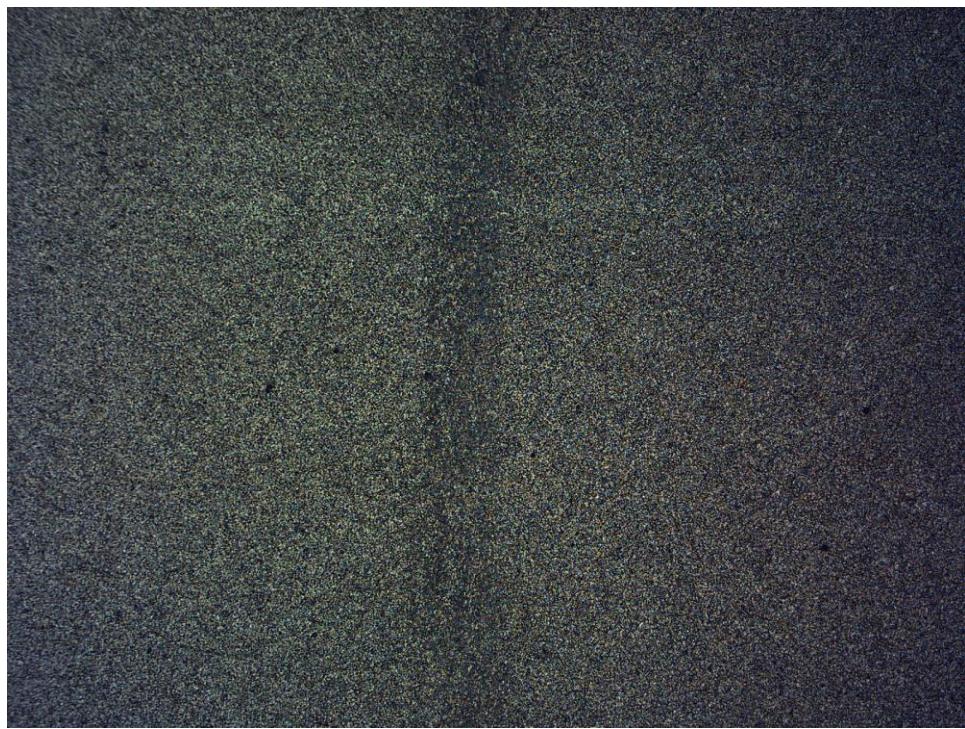
Load = 1N, Distance = 500m, Speed = 300mm/sec, No Lubrication

CoF vs. Distance for 1N, 500m, 300mm-sec, R=10.5, ASE-8-9-1-ASE-8-26-1 P46.txt

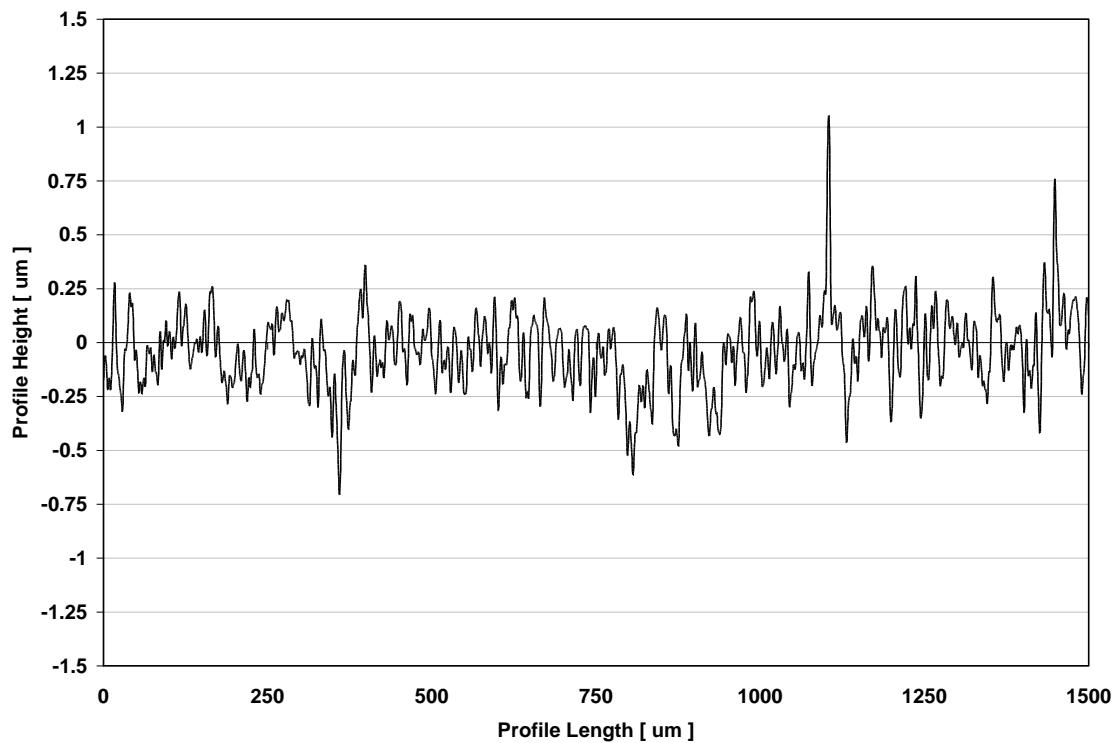


Appendix BoD – Ball-on-Disc Sliding Wear Data

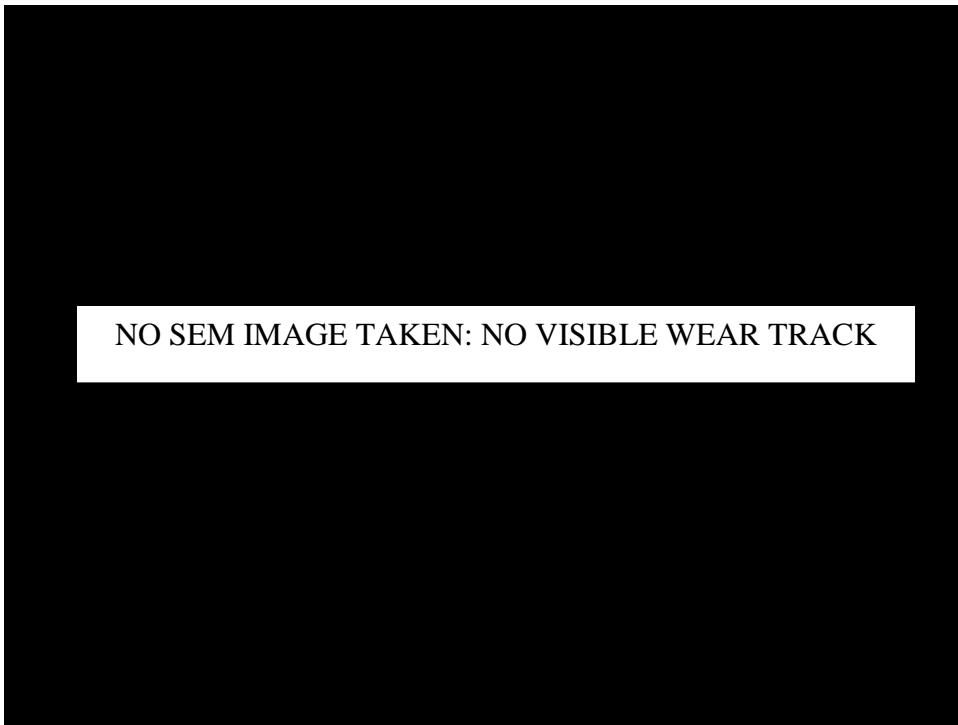
Appendix BoD – Ball-on-Disc Sliding Wear Data



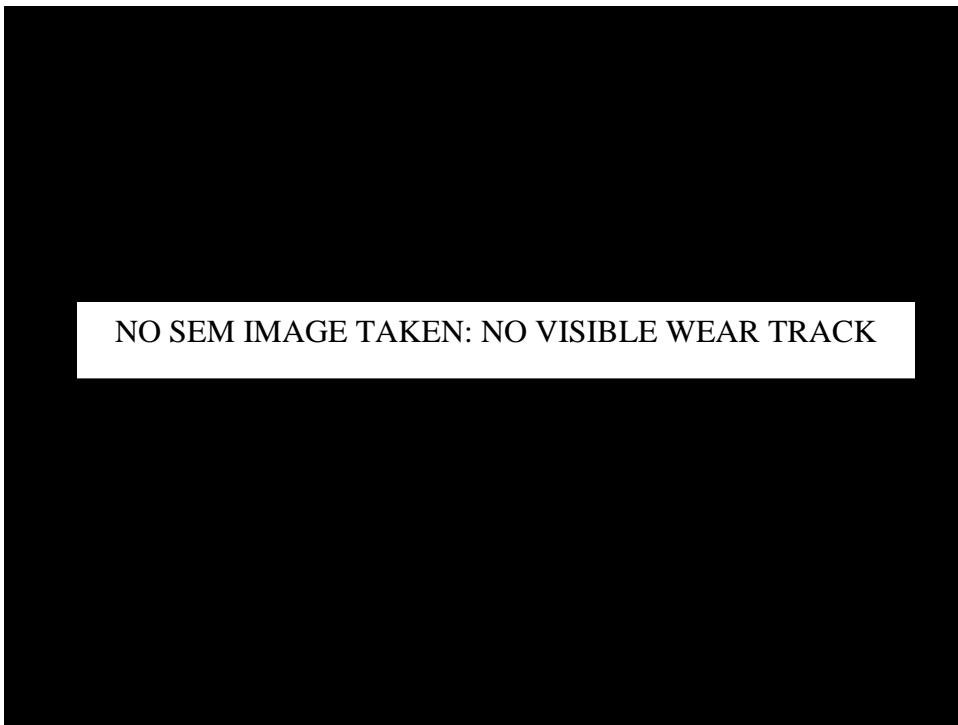
Disc Wear Track Image and Profile
Cr-CrN (Disc) vs. TiCr-TiCrN (Ball)
Load = 1N, Distance = 1000m, Speed = 300mm/sec, No Lubrication



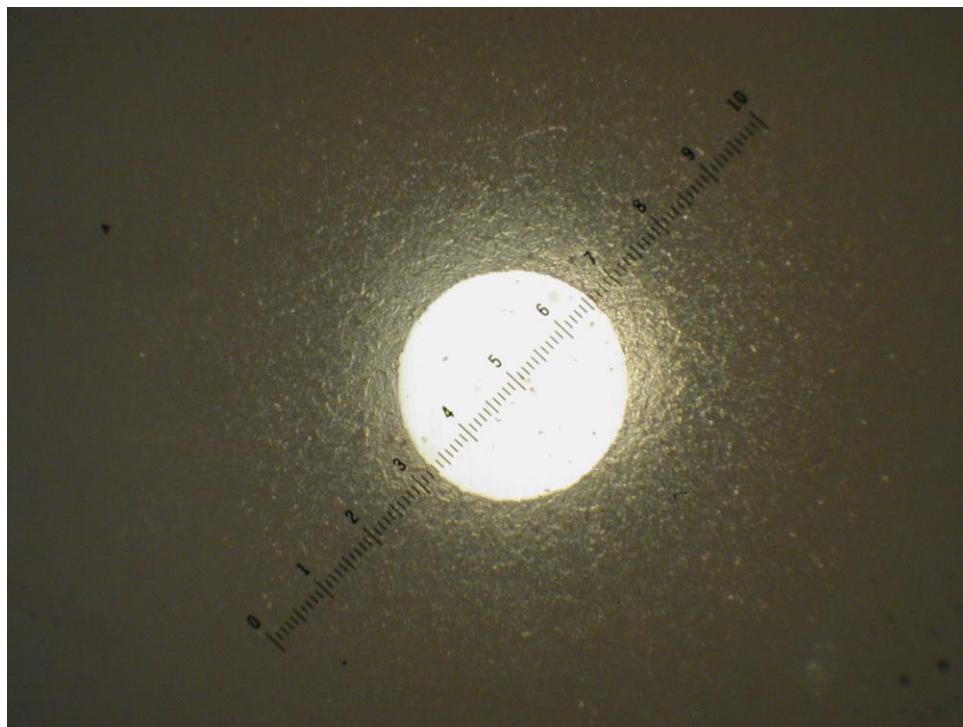
Appendix BoD – Ball-on-Disc Sliding Wear Data



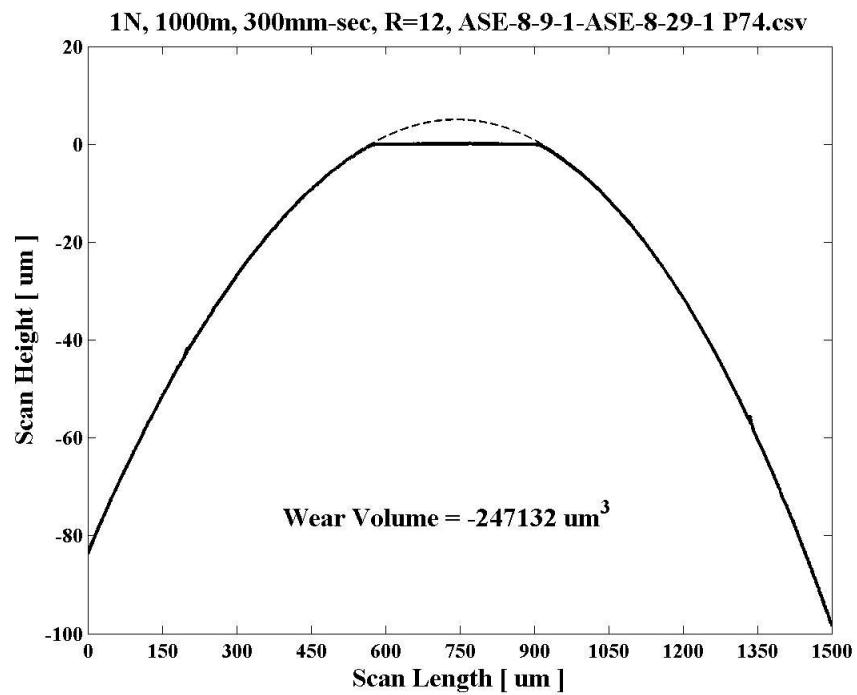
Disc Wear Track Center (above) SEM image @500x
Disc Wear Track Edge (below, non-contact area on right) SEM image @500x
Cr-CrN (Disc) vs. TiCr-TiCrN (Ball)
Load = 1N, Distance = 1000m, Speed = 300mm/sec, No Lubrication



Appendix BoD – Ball-on-Disc Sliding Wear Data

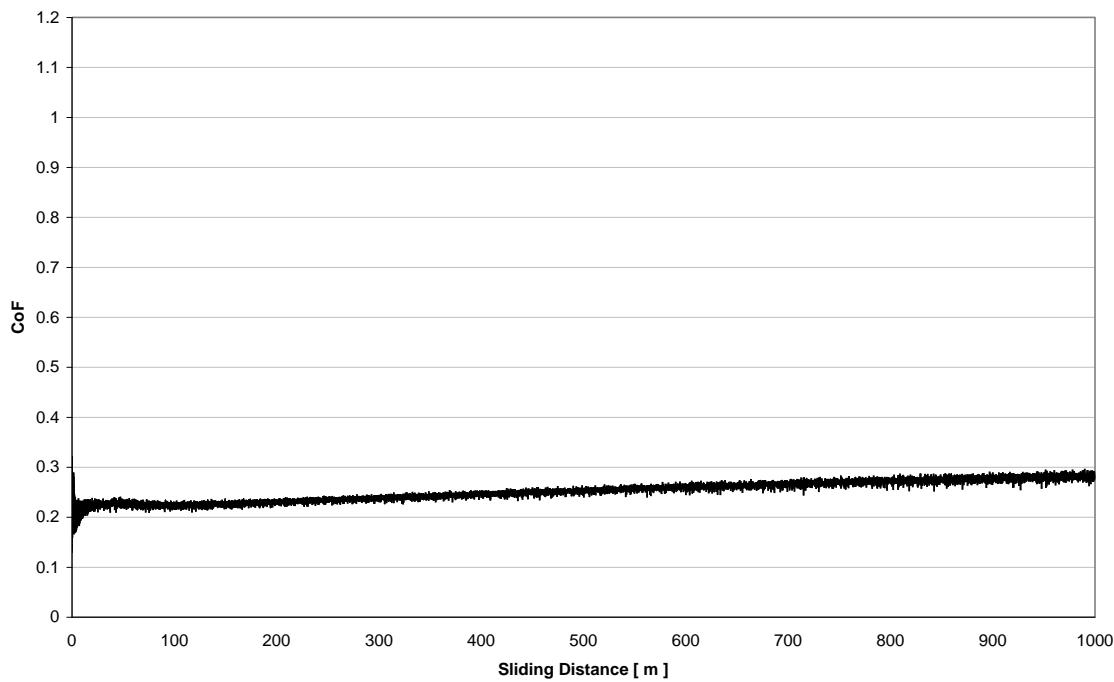


Ball Wear Scar Image and Profile
Cr-CrN (Disc) vs. TiCr-TiCrN (Ball)
Load = 1N, Distance = 1000m, Speed = 300mm/sec, No Lubrication



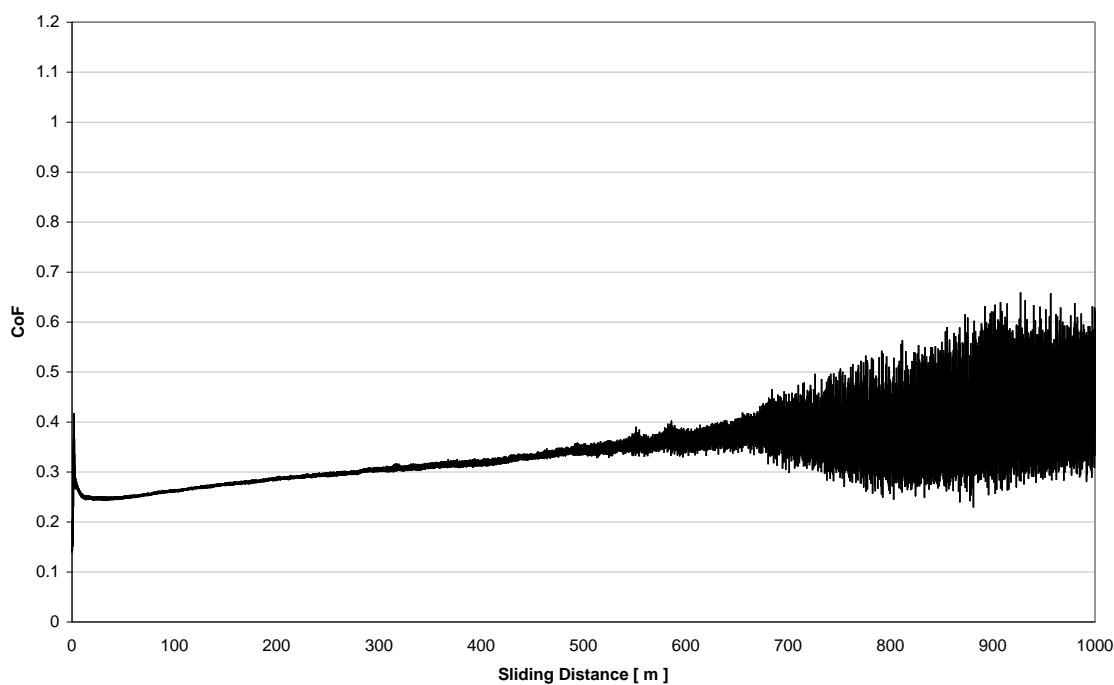
Appendix BoD – Ball-on-Disc Sliding Wear Data

CoF vs. Distance for 1N, 1000m, 300mm-sec, R=13, ASE-8-9-1-ASE-8-29-1 P74.txt



CoF vs. Sliding Distance
Cr-CrN (Disc) vs. TiCr-TiCrN (Ball)
Load = 1N, Distance = 1000m, Speed = 300mm/sec, No Lubrication

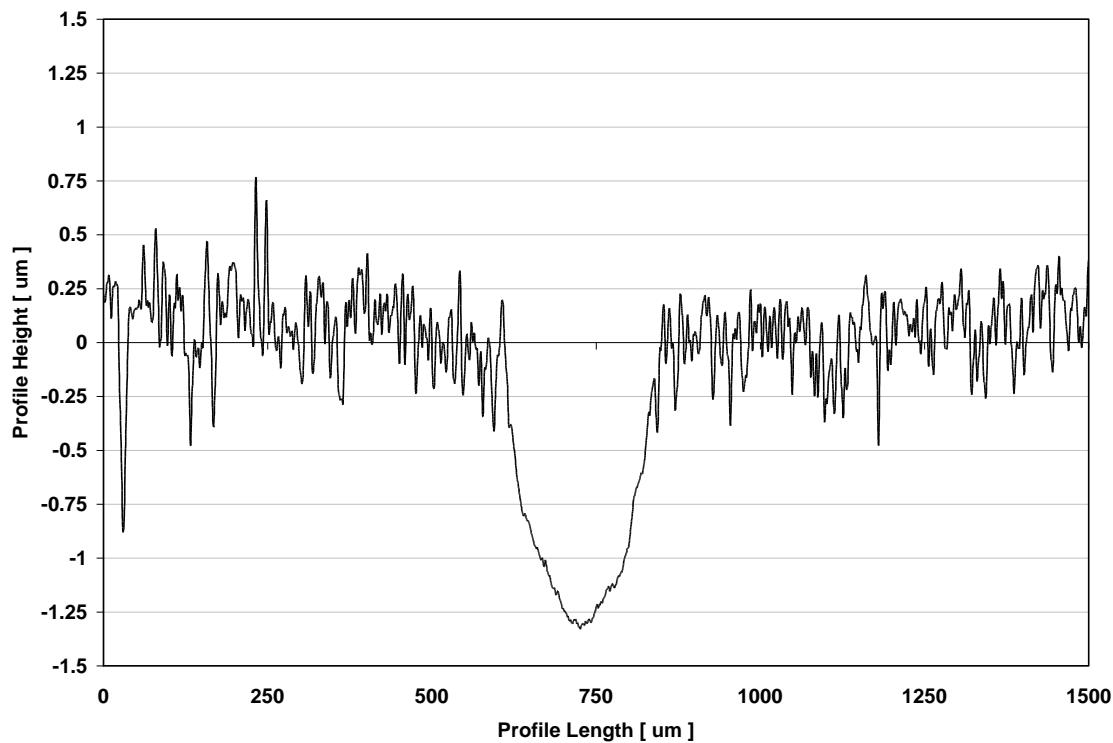
CoF vs. Distance for 1N, 1000m, 300mm-sec, R=13, ASE-8-9-1-ASE-8-34-1 P2.txt



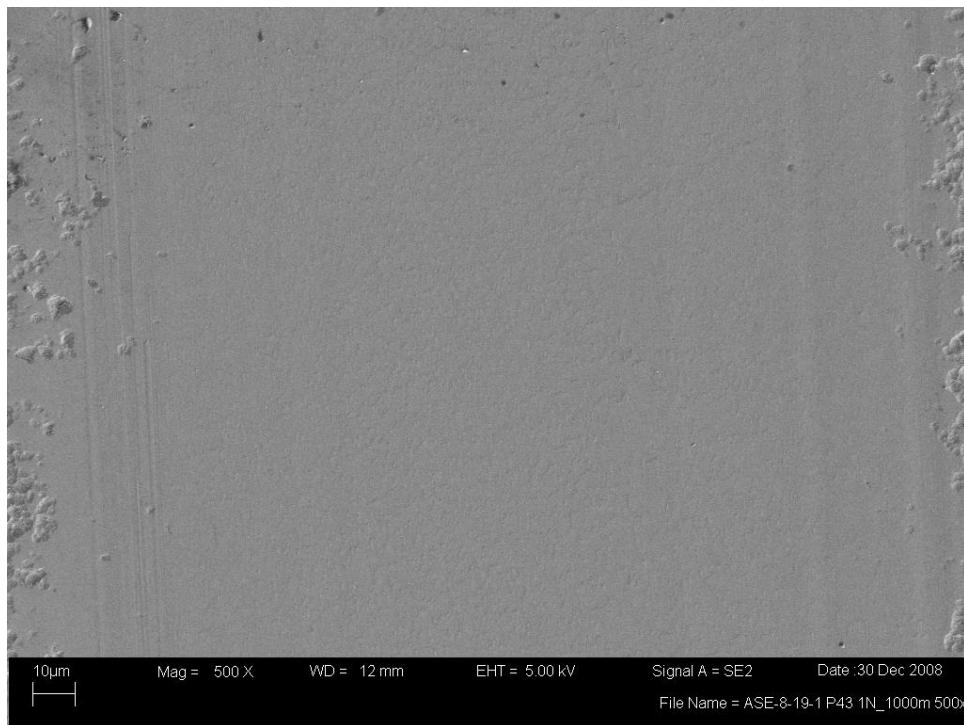
Appendix BoD – Ball-on-Disc Sliding Wear Data



Disc Wear Track Image and Profile
CrC (Disc) vs. TiCr-TiCrN (Ball)
Load = 1N, Distance = 1000m, Speed = 300mm/sec, No Lubrication



Appendix BoD – Ball-on-Disc Sliding Wear Data

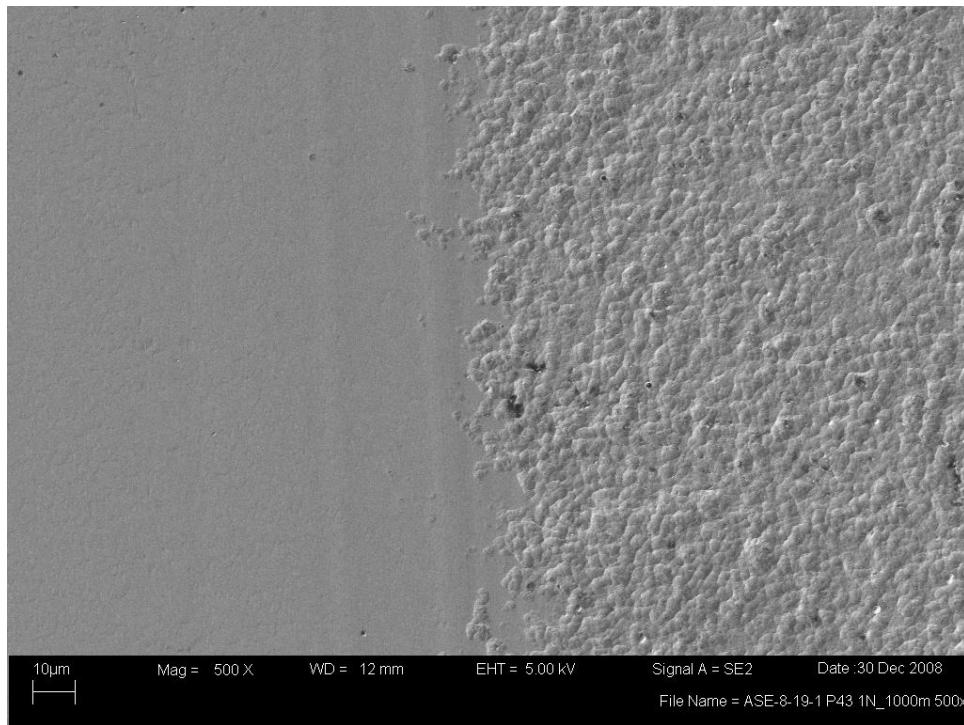


Disc Wear Track Center (above) SEM image @500x

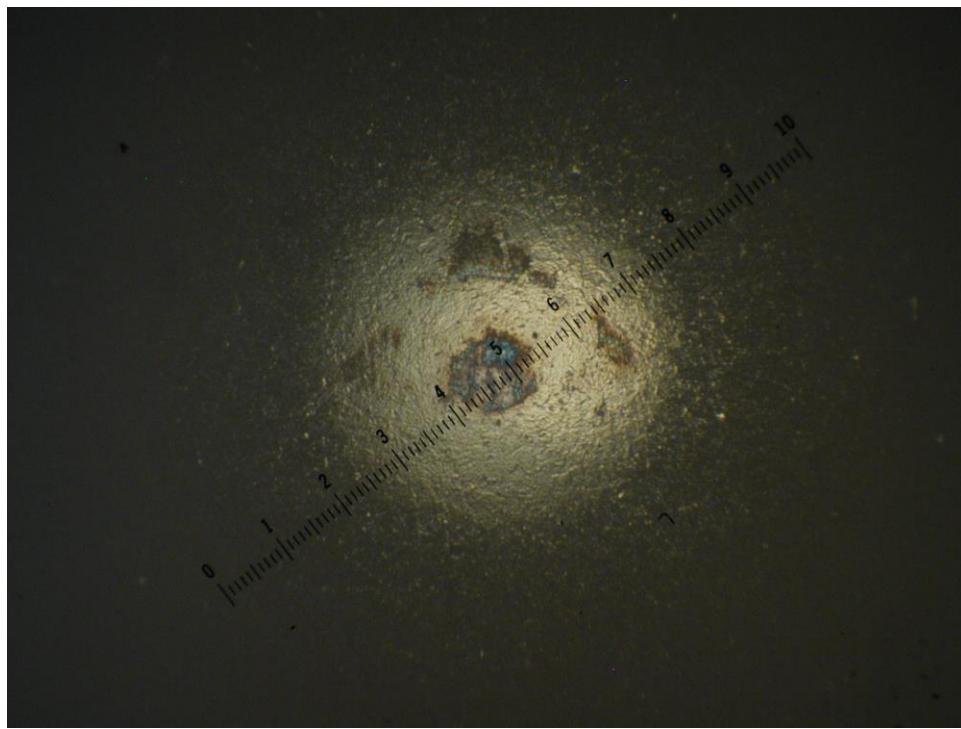
Disc Wear Track Edge (below, non-contact area on right) SEM image @500x

CrC (Disc) vs. TiCr-TiCrN (Ball)

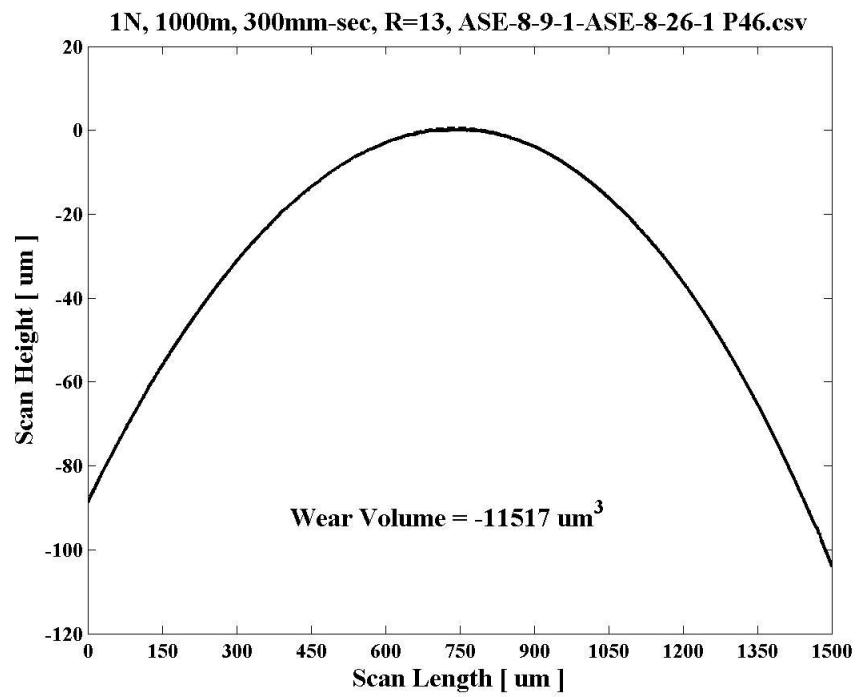
Load = 1N, Distance = 1000m, Speed = 300mm/sec, No Lubrication



Appendix BoD – Ball-on-Disc Sliding Wear Data

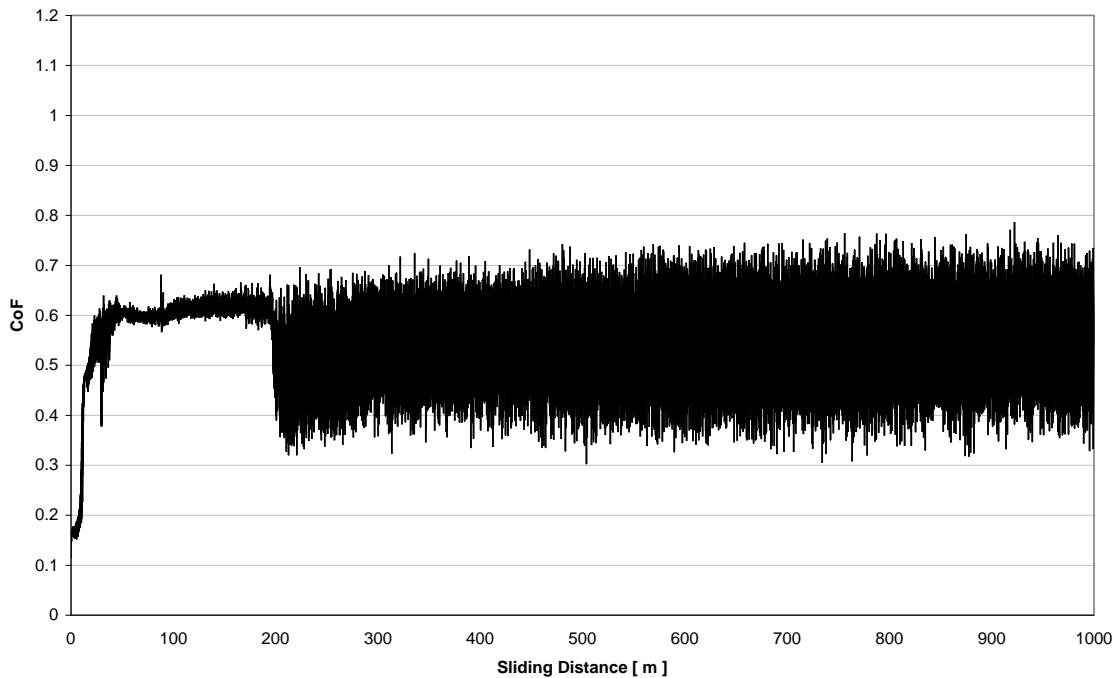


Ball Wear Scar Image and Profile
CrC (Disc) vs. TiCr-TiCrN (Ball)
Load = 1N, Distance = 1000m, Speed = 300mm/sec, No Lubrication



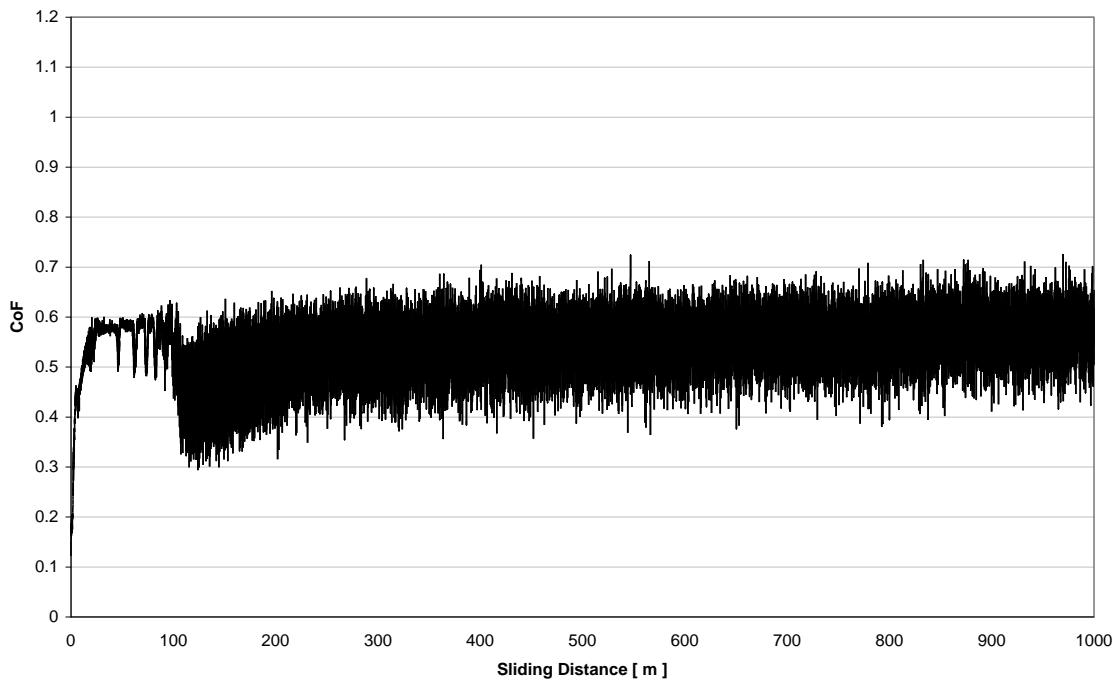
Appendix BoD – Ball-on-Disc Sliding Wear Data

CoF vs. Distance for 1N, 1000m, 300mm-sec, R=13, ASE-8-9-1-ASE-8-19-1 P43.txt

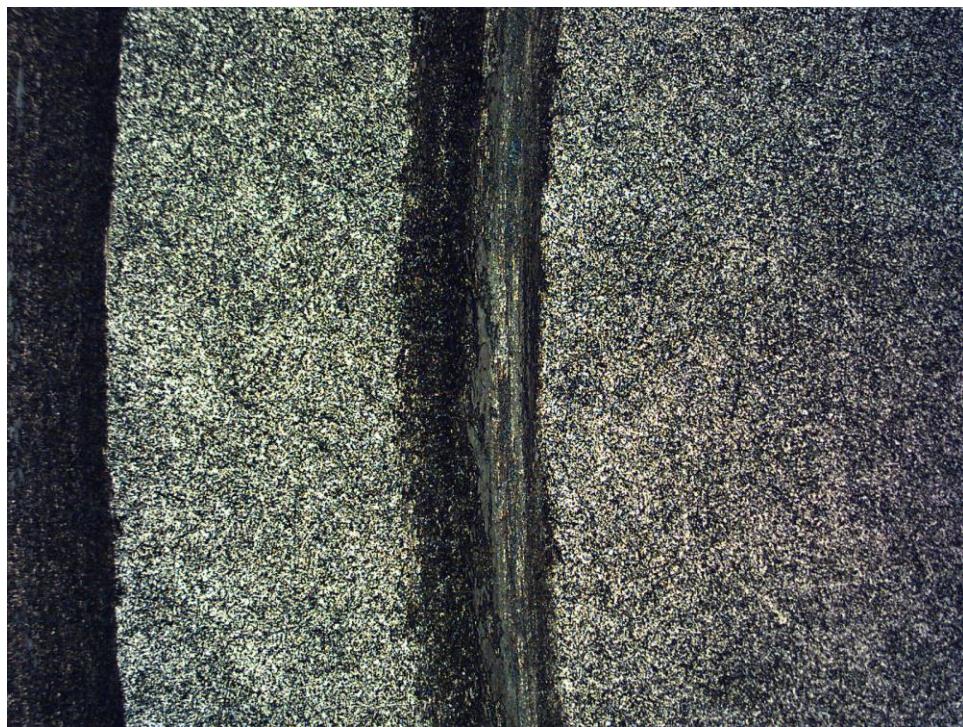


CoF vs. Sliding Distance
CrC (Disc) vs. TiCr-TiCrN (Ball)
Load = 1N, Distance = 1000m, Speed = 300mm/sec, No Lubrication

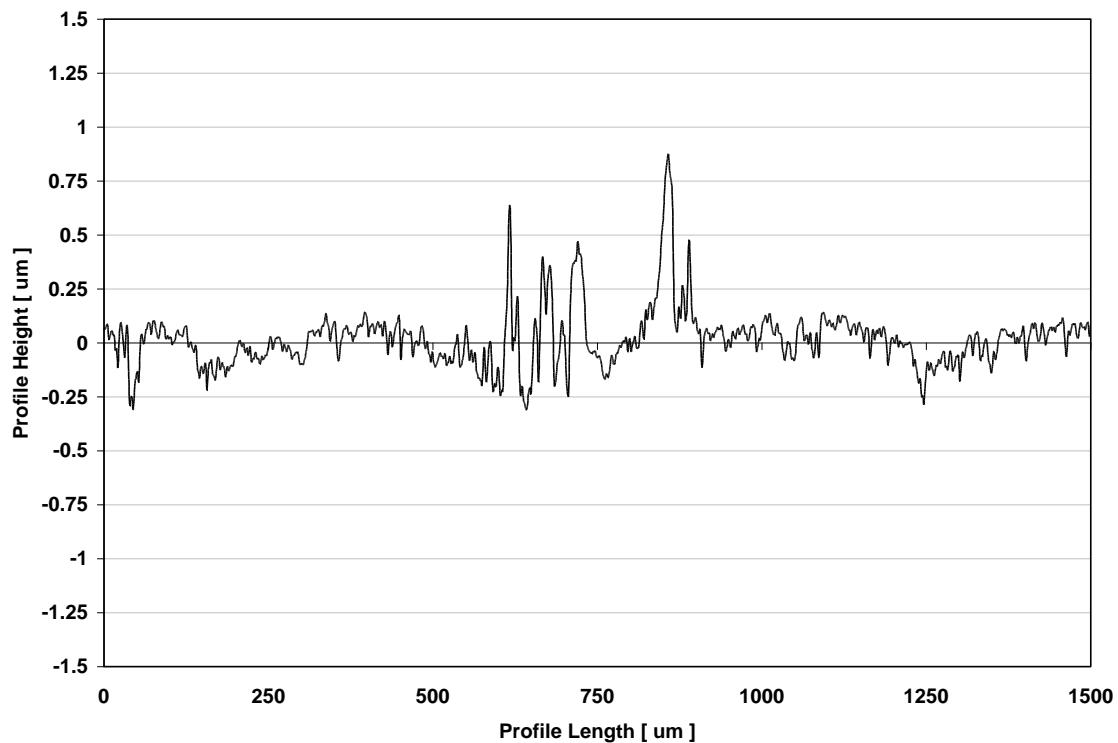
CoF vs. Distance for 1N, 1000m, 300mm-sec, R=13, ASE-8-9-1-ASE-8-26-1 P46.txt



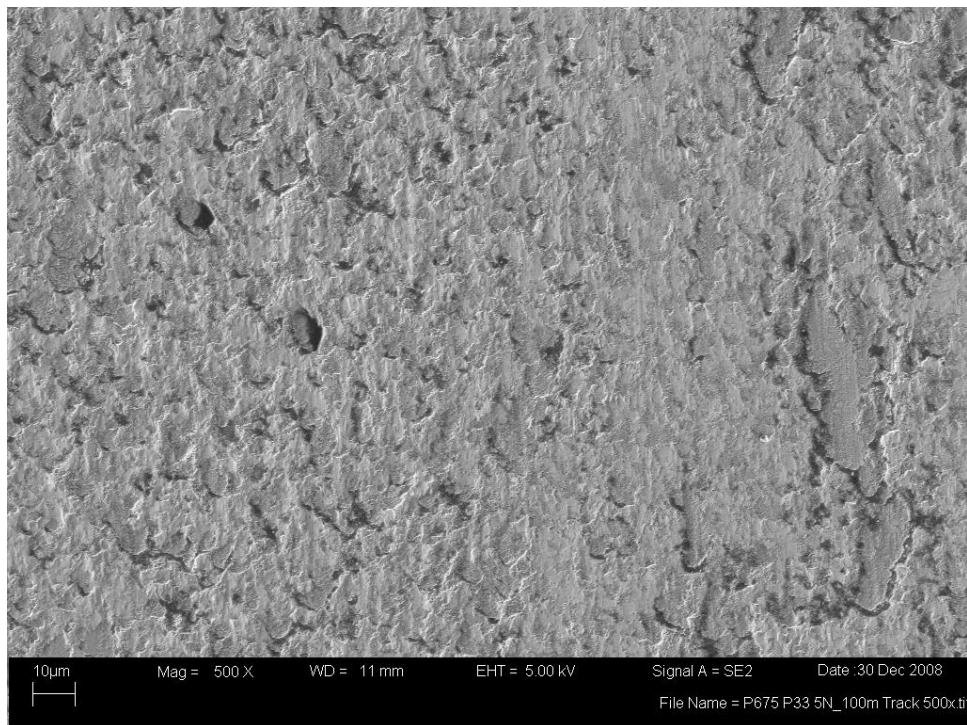
Appendix BoD – Ball-on-Disc Sliding Wear Data



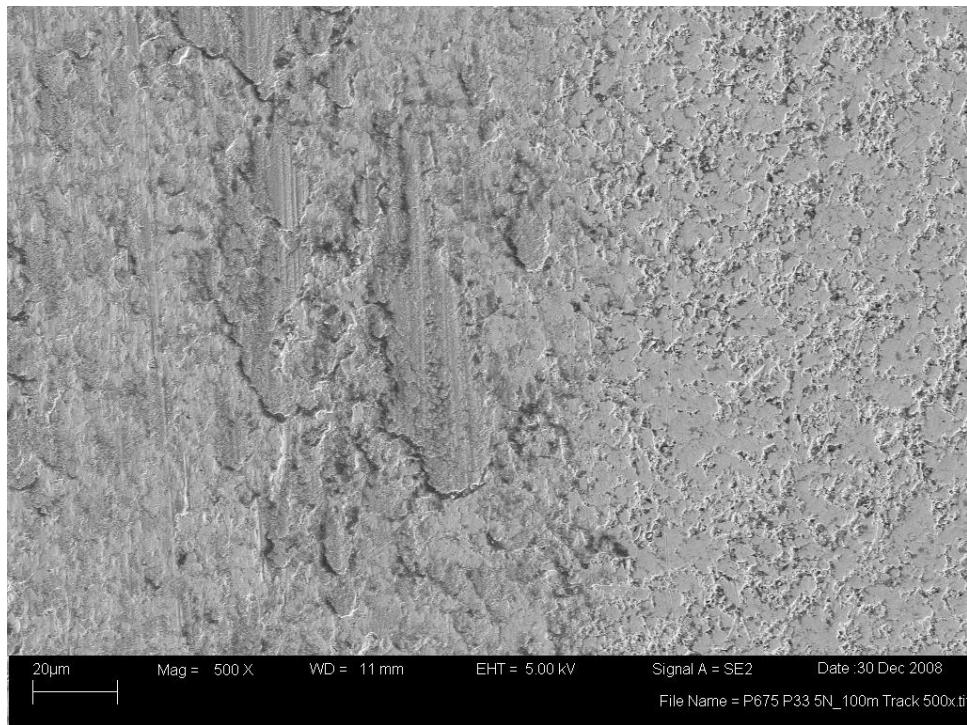
Disc Wear Track Image and Profile
P675 (Disc) vs. M50 (Ball)
Load = 5N, Distance = 100m, Speed = 300mm/sec, No Lubrication



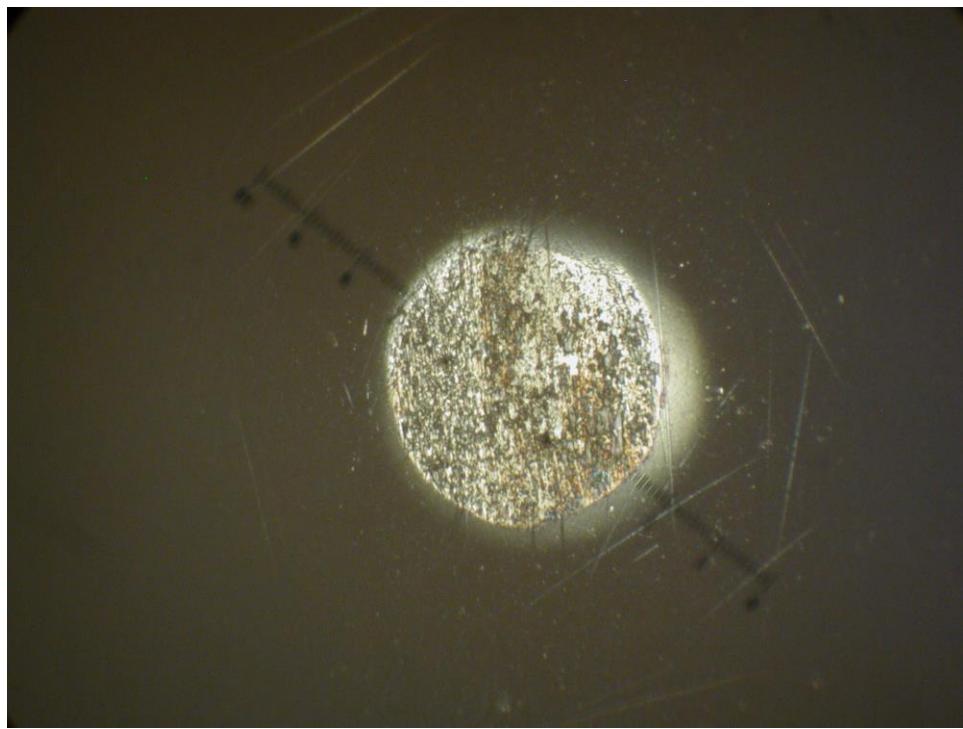
Appendix BoD – Ball-on-Disc Sliding Wear Data



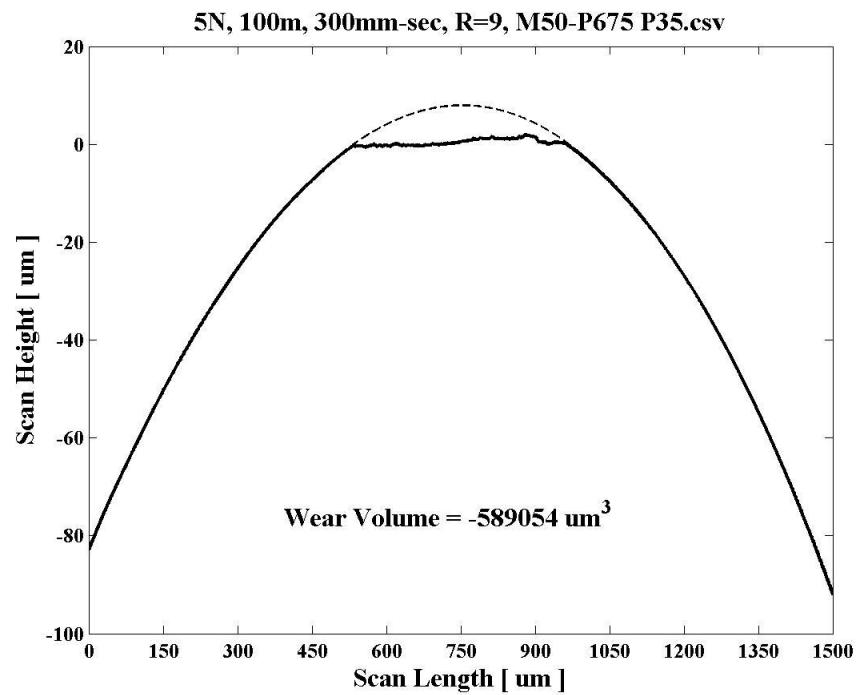
Disc Wear Track Center (above) SEM image @500x
Disc Wear Track Edge (below, non-contact area on right) SEM image @500x
P675 (Disc) vs. M50 (Ball)
Load = 5N, Distance = 100m, Speed = 300mm/sec, No Lubrication



Appendix BoD – Ball-on-Disc Sliding Wear Data

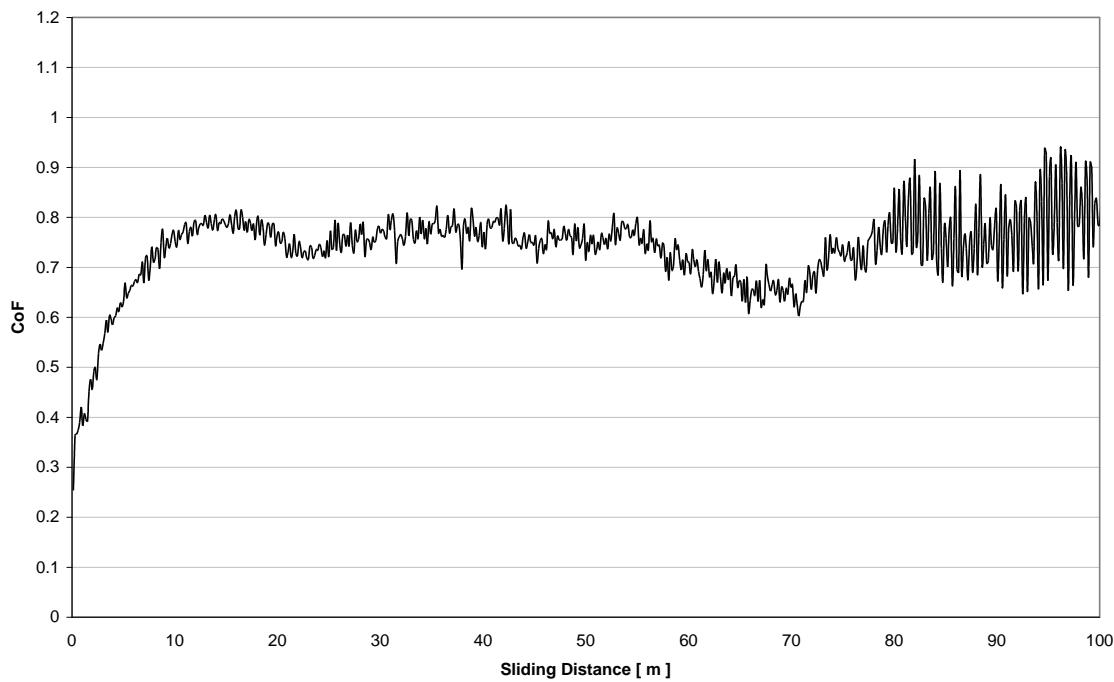


Ball Wear Scar Image and Profile
P675 (Disc) vs. M50 (Ball)
Load = 5N, Distance = 100m, Speed = 300mm/sec, No Lubrication



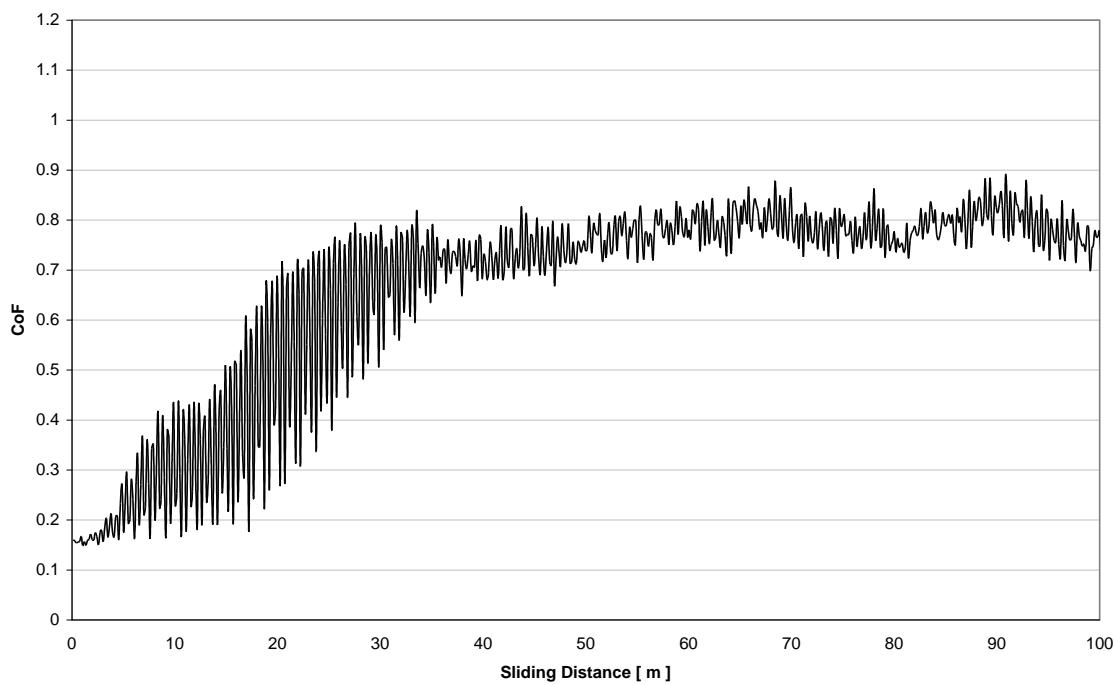
Appendix BoD – Ball-on-Disc Sliding Wear Data

CoF vs. Distance for 5N, 100m, 300mm-sec, R=9, M50-P675 P33.txt

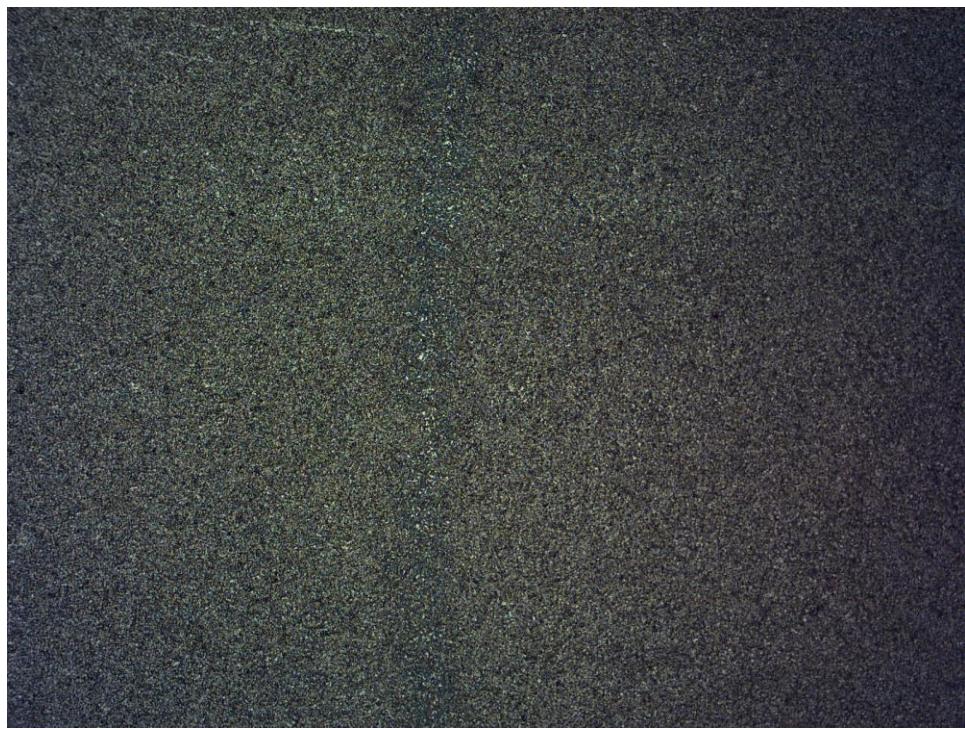
CoF vs. Sliding Distance
P675 (Disc) vs. M50 (Ball)

Load = 5N, Distance = 100m, Speed = 300mm/sec, No Lubrication

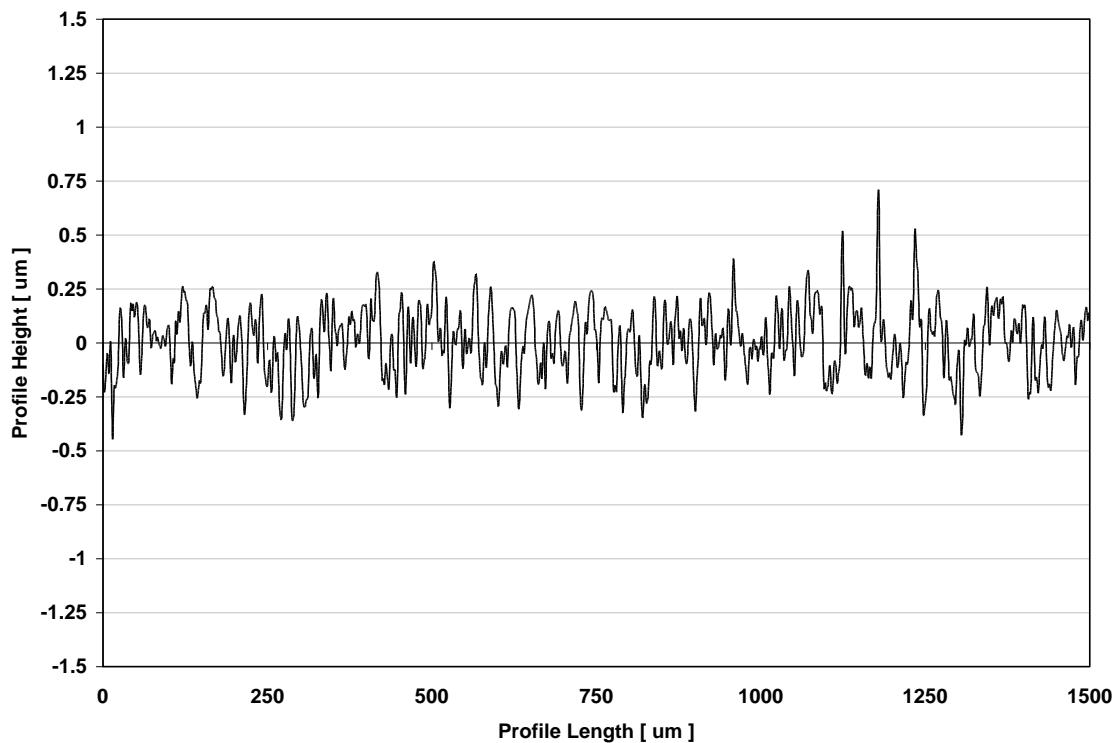
CoF vs. Distance for 5N, 100m, 300mm-sec, R=9, M50-P675 P35.txt



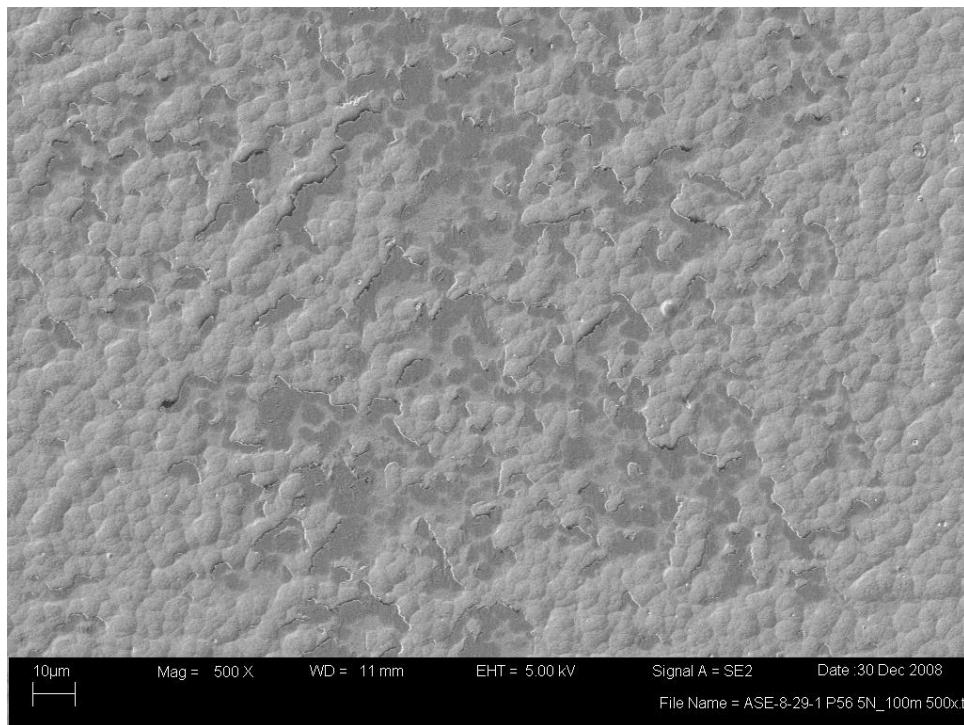
Appendix BoD – Ball-on-Disc Sliding Wear Data



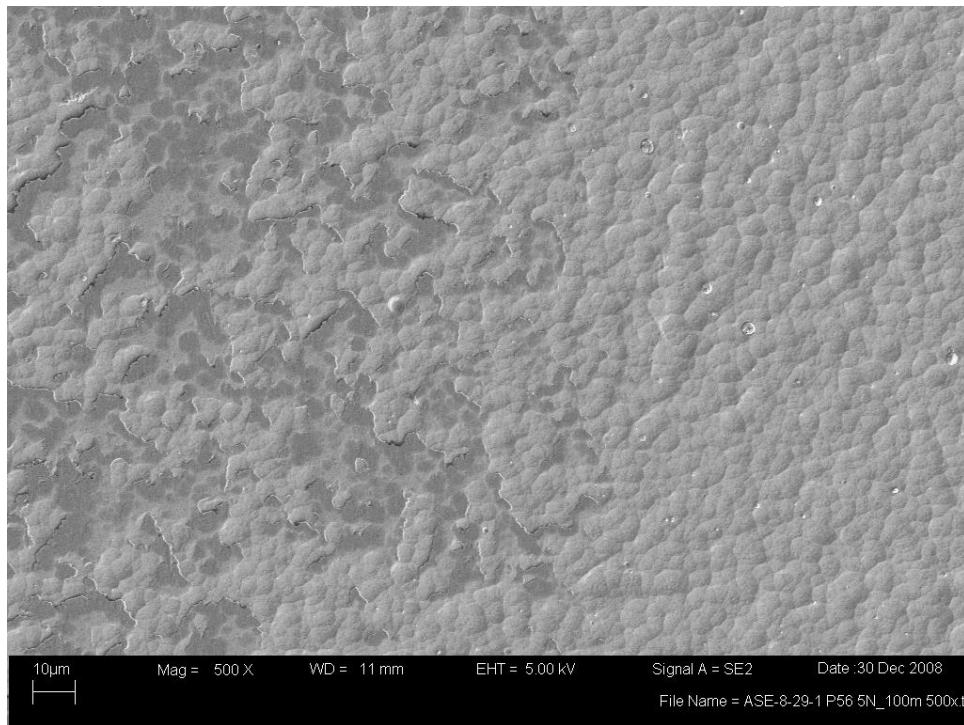
Disc Wear Track Image and Profile
Cr-CrN (Disc) vs. TiCr-TiCrN (Ball)
Load = 5N, Distance = 100m, Speed = 300mm/sec, No Lubrication



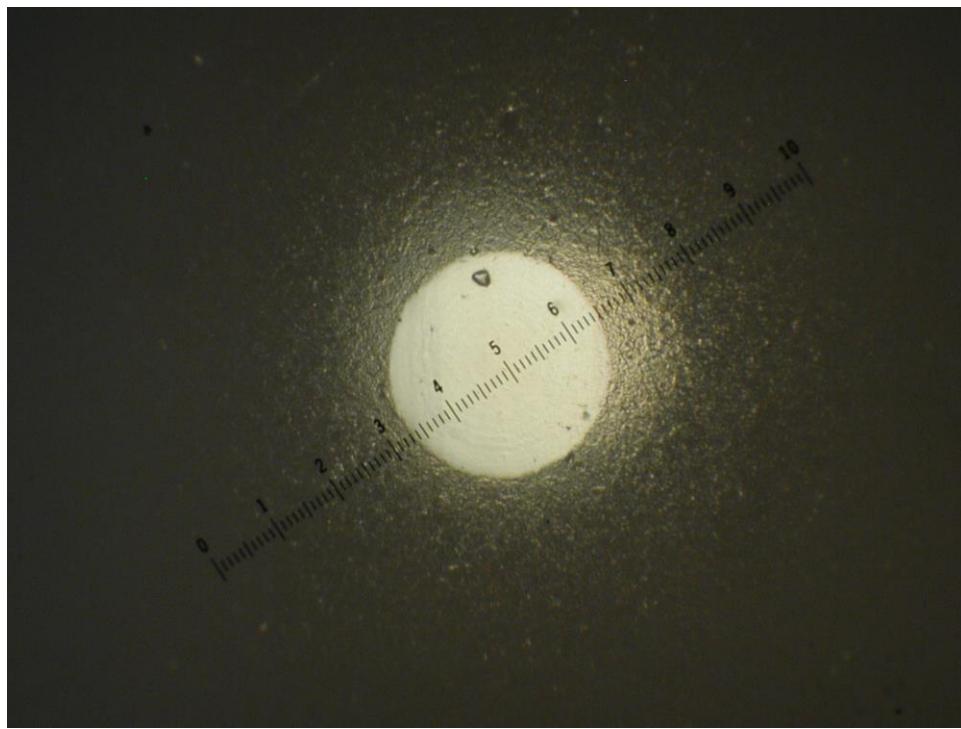
Appendix BoD – Ball-on-Disc Sliding Wear Data



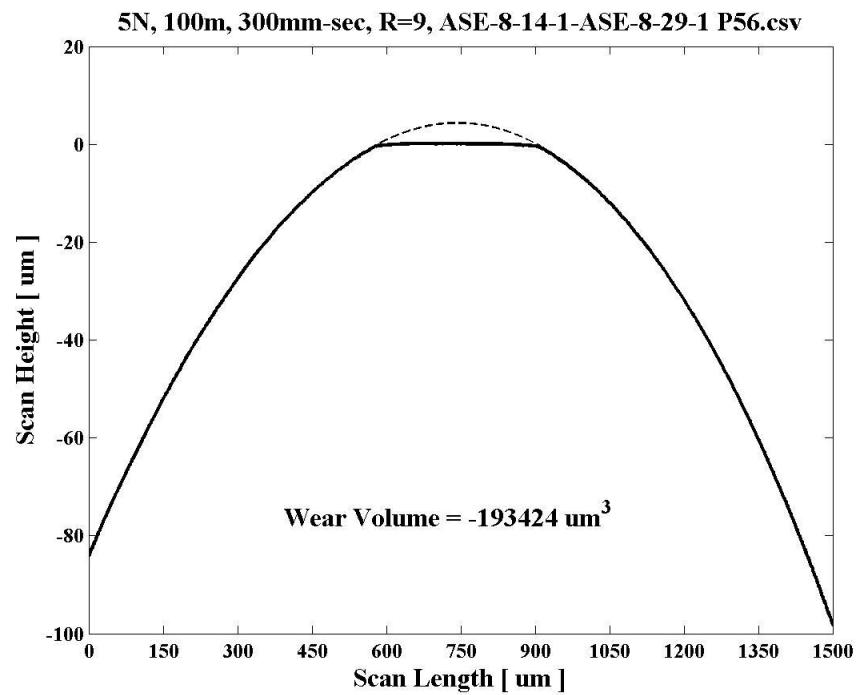
Disc Wear Track Center (above) SEM image @500x
Disc Wear Track Edge (below, non-contact area on right) SEM image @500x
Cr-CrN (Disc) vs. TiCr-TiCrN (Ball)
Load = 5N, Distance = 100m, Speed = 300mm/sec, No Lubrication



Appendix BoD – Ball-on-Disc Sliding Wear Data

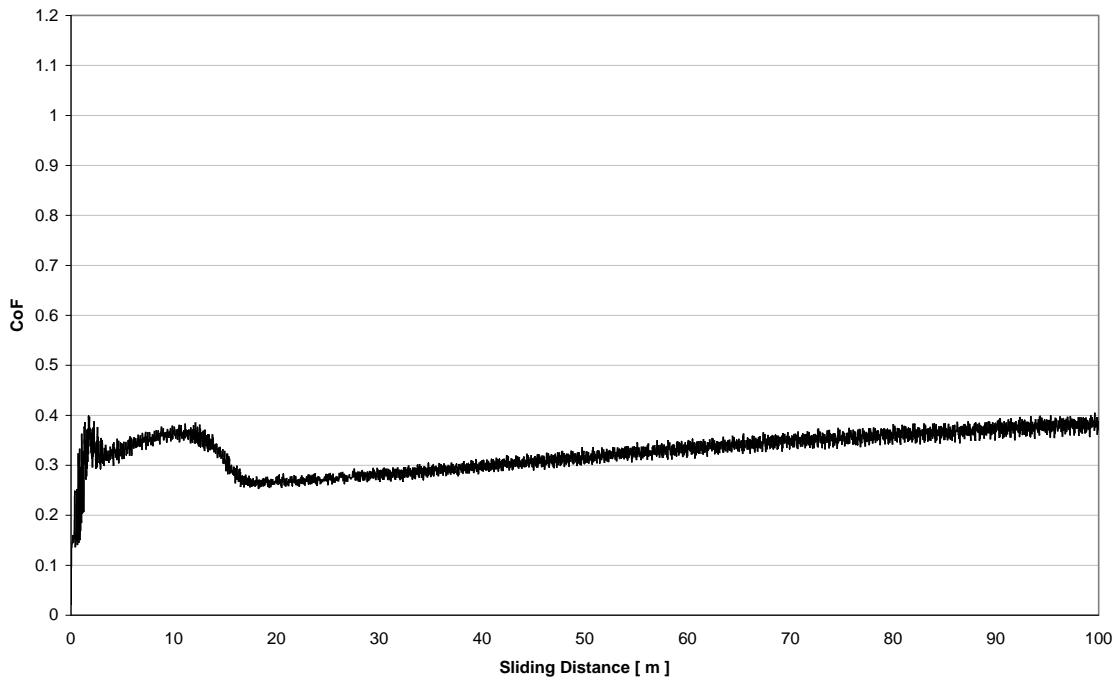


Ball Wear Scar Image and Profile
Cr-CrN (Disc) vs. TiCr-TiCrN (Ball)
Load = 5N, Distance = 100m, Speed = 300mm/sec, No Lubrication



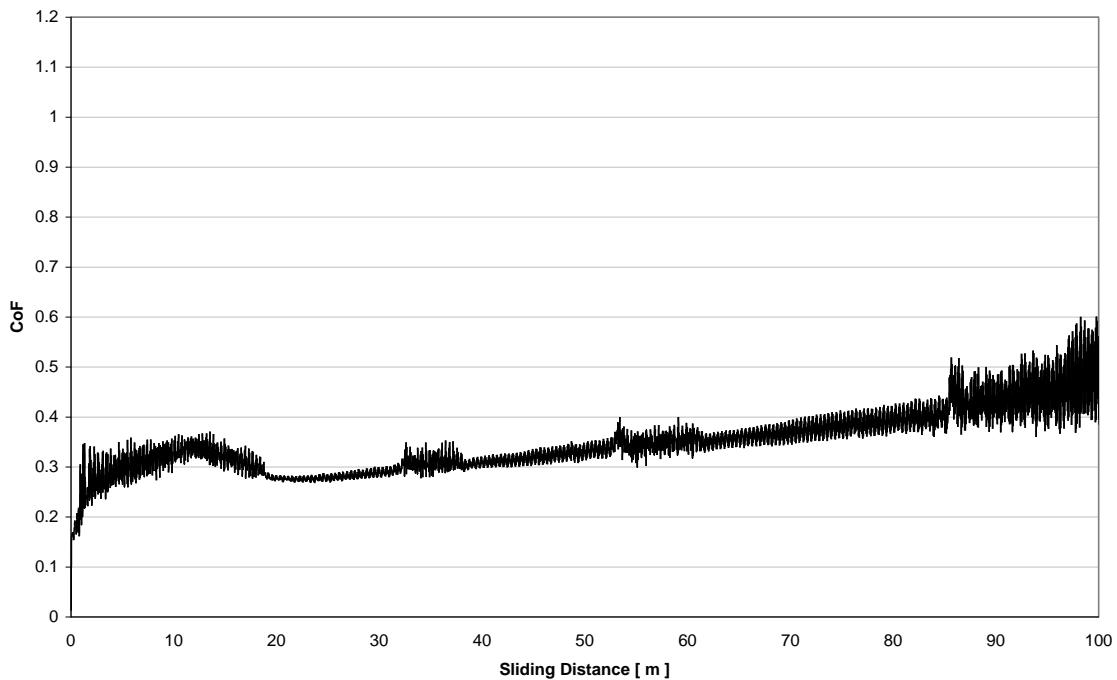
Appendix BoD – Ball-on-Disc Sliding Wear Data

CoF vs. Distance for 5N, 100m, 300mm/sec, R=9, ASE-8-14-1-ASE-8-34-1 P70.txt



CoF vs. Sliding Distance
Cr-CrN (Disc) vs. TiCr-TiCrN (Ball)
Load = 5N, Distance = 100m, Speed = 300mm/sec, No Lubrication

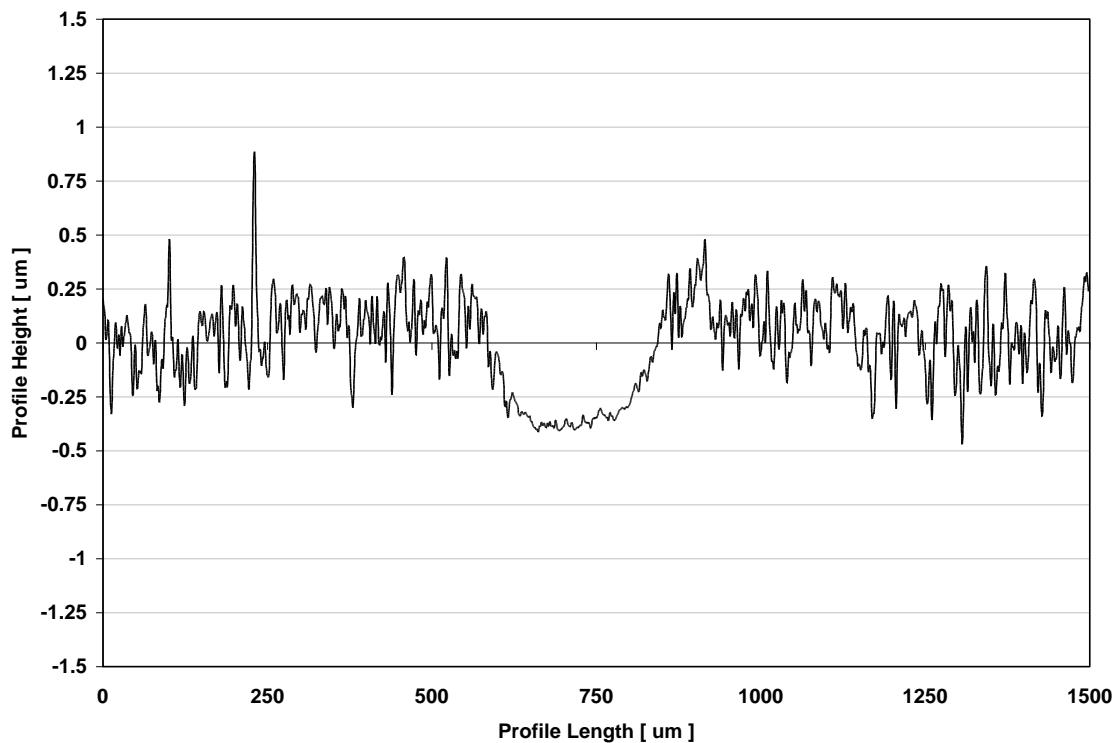
CoF vs. Distance for 5N, 100m, 300mm/sec, R=9, ASE-8-14-1-ASE-8-29-1 P56.txt



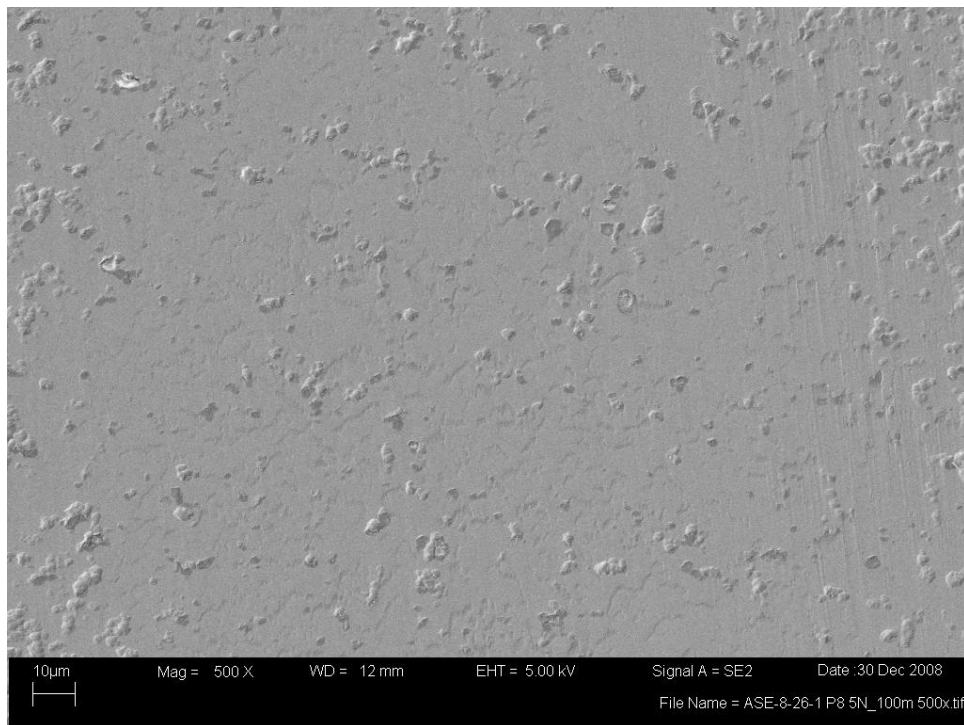
Appendix BoD – Ball-on-Disc Sliding Wear Data



Disc Wear Track Image and Profile
CrC (Disc) vs. TiCr-TiCrN (Ball)
Load = 5N, Distance = 100m, Speed = 300mm/sec, No Lubrication



Appendix BoD – Ball-on-Disc Sliding Wear Data

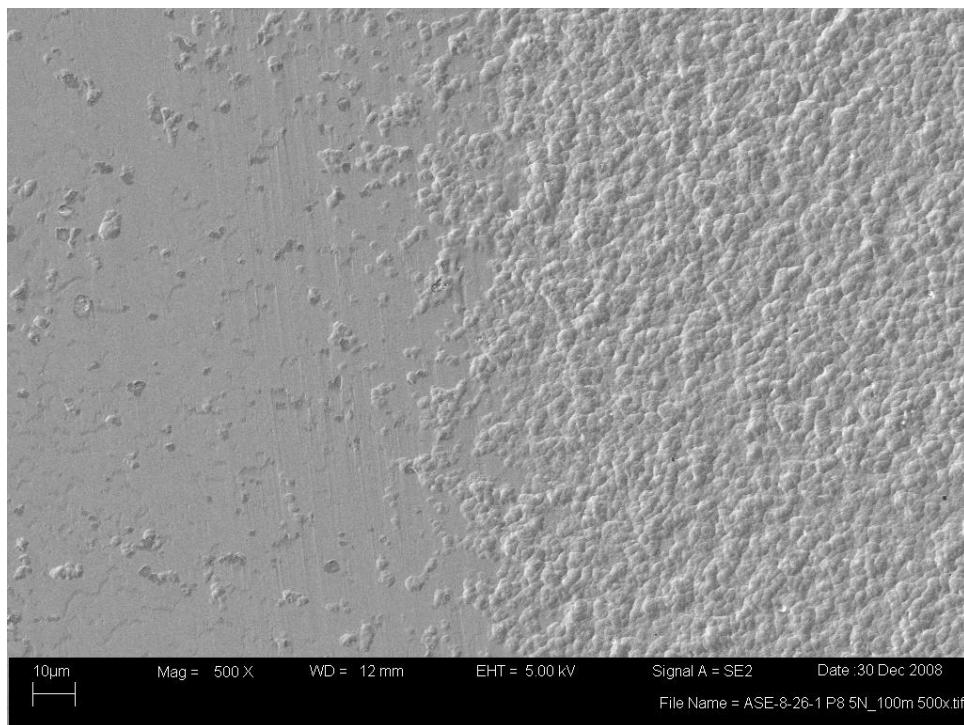


Disc Wear Track Center (above) SEM image @500x

Disc Wear Track Edge (below, non-contact area on right) SEM image @500x

CrC (Disc) vs. TiCr-TiCrN (Ball)

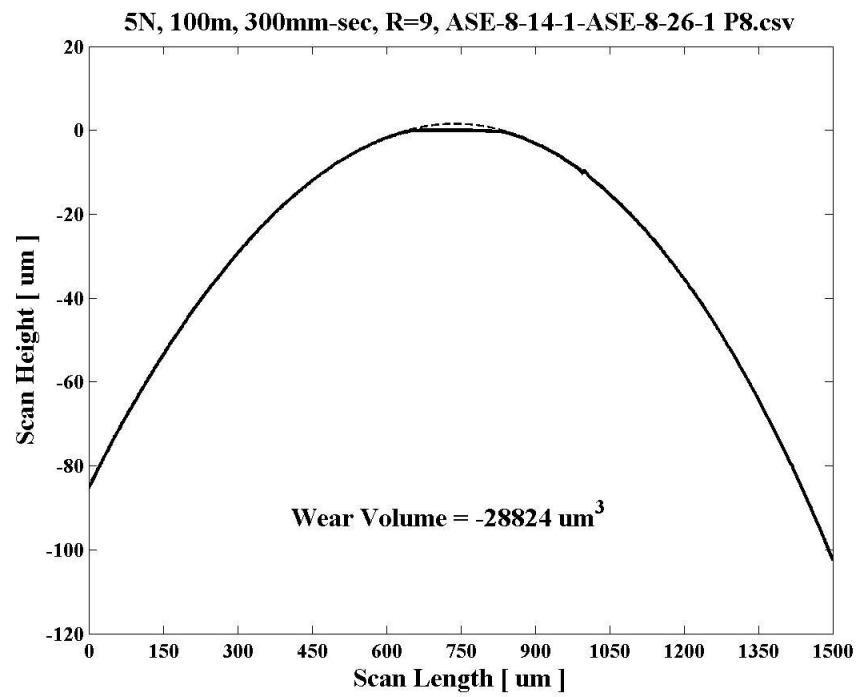
Load = 5N, Distance = 100m, Speed = 300mm/sec, No Lubrication



Appendix BoD – Ball-on-Disc Sliding Wear Data

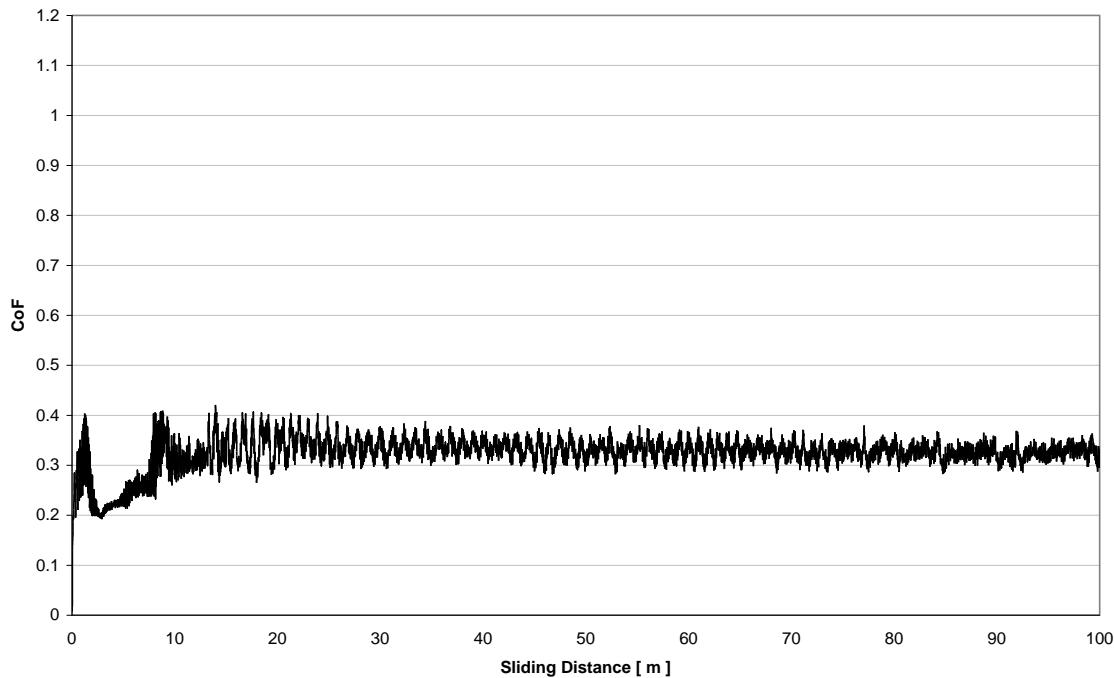


Ball Wear Scar Image and Profile
CrC (Disc) vs. TiCr-TiCrN (Ball)
Load = 5N, Distance = 100m, Speed = 300mm/sec, No Lubrication



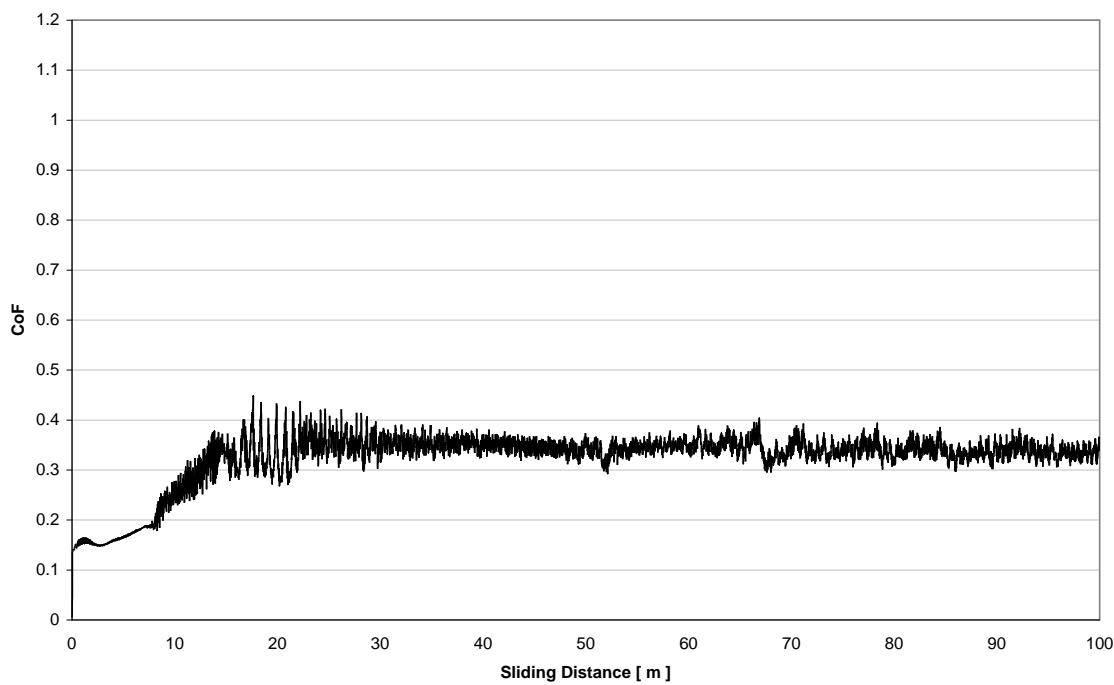
Appendix BoD – Ball-on-Disc Sliding Wear Data

CoF vs. Distance for 5N, 100m, 300mm/sec, R=9, ASE-8-14-1,ASE-8-19-1 P13.txt

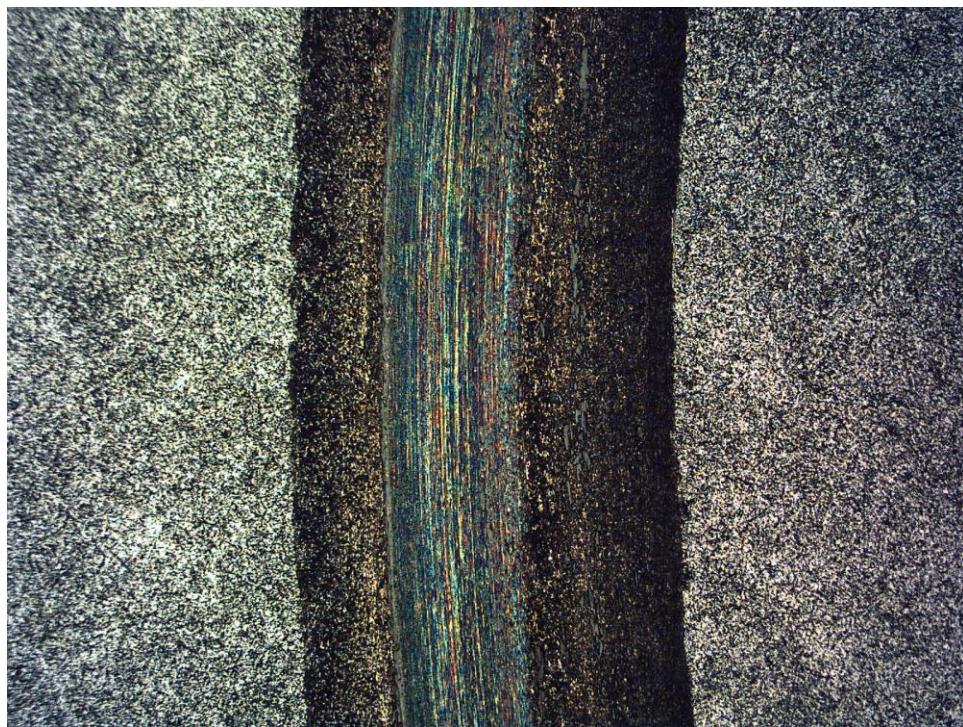


CoF vs. Sliding Distance
CrC (Disc) vs. TiCr-TiCrN (Ball)
Load = 5N, Distance = 100m, Speed = 300mm/sec, No Lubrication

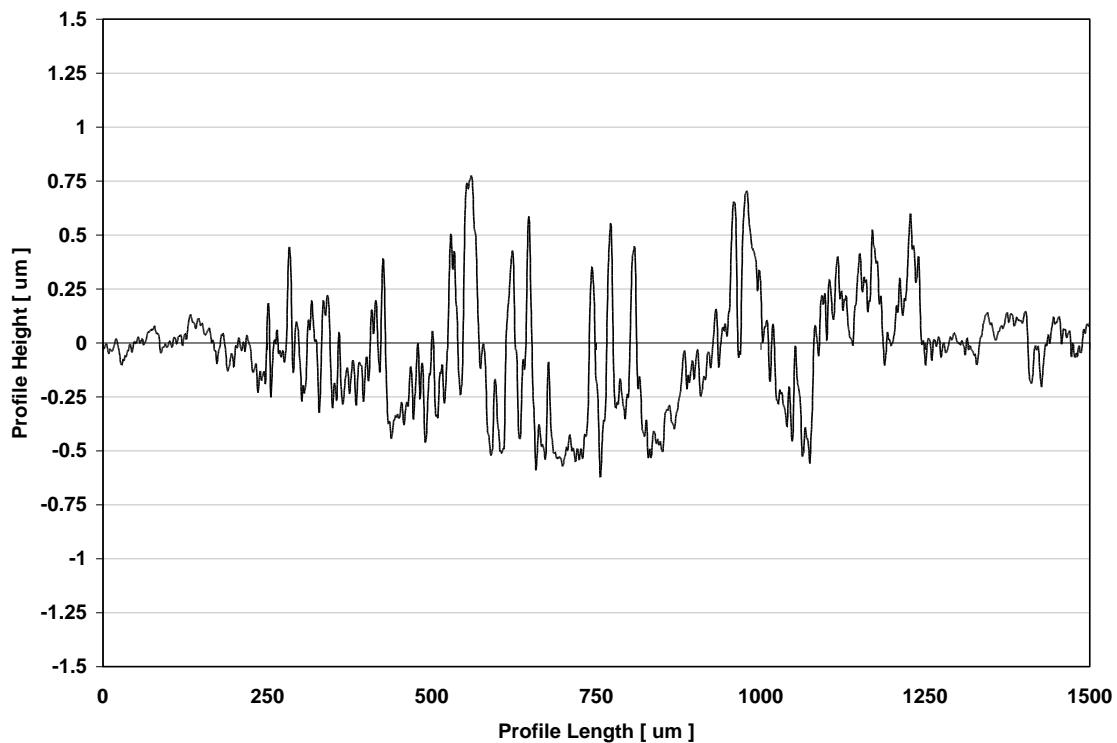
CoF vs. Distance for 5N, 100m, 300mm/sec, R=9, ASE-8-14-1,ASE-8-26-1 P8.txt



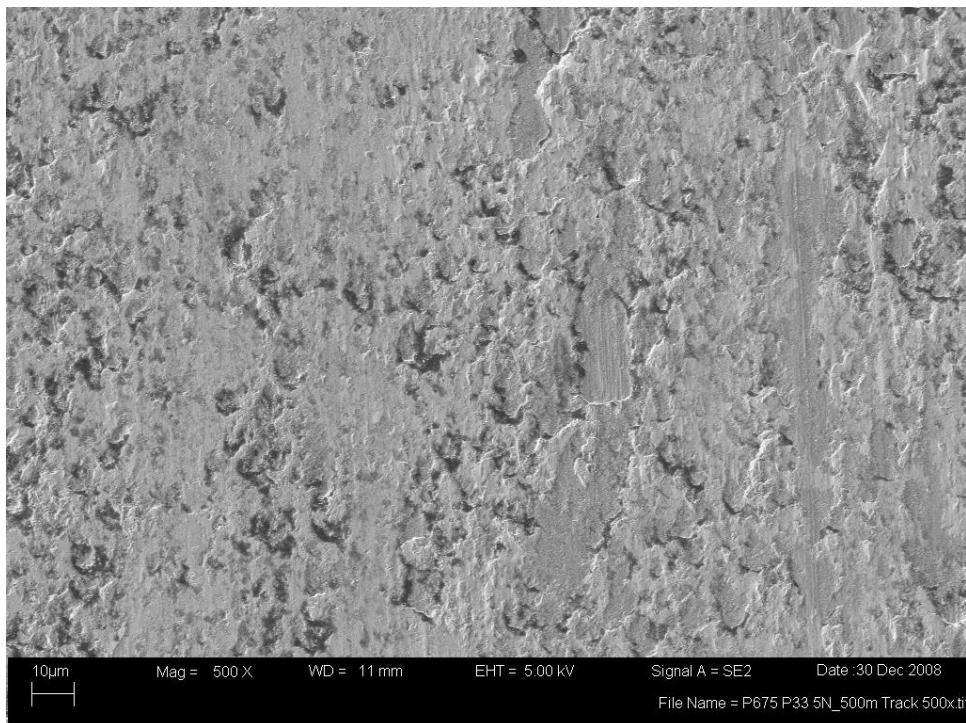
Appendix BoD – Ball-on-Disc Sliding Wear Data



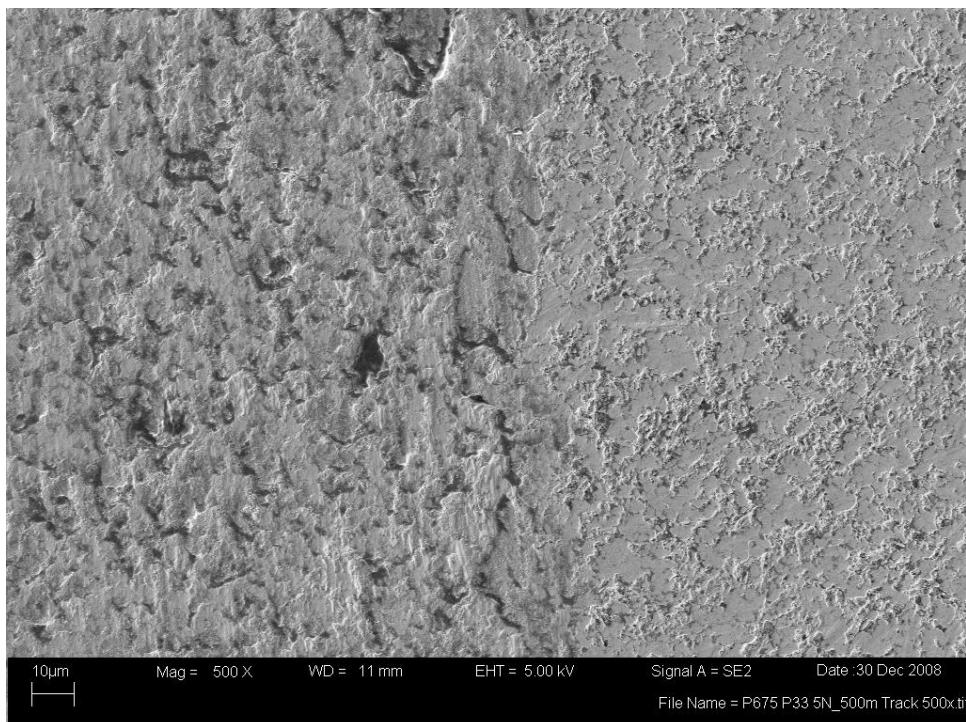
Disc Wear Track Image and Profile
P675 (Disc) vs. M50 (Ball)
Load = 5N, Distance = 500m, Speed = 300mm/sec, No Lubrication



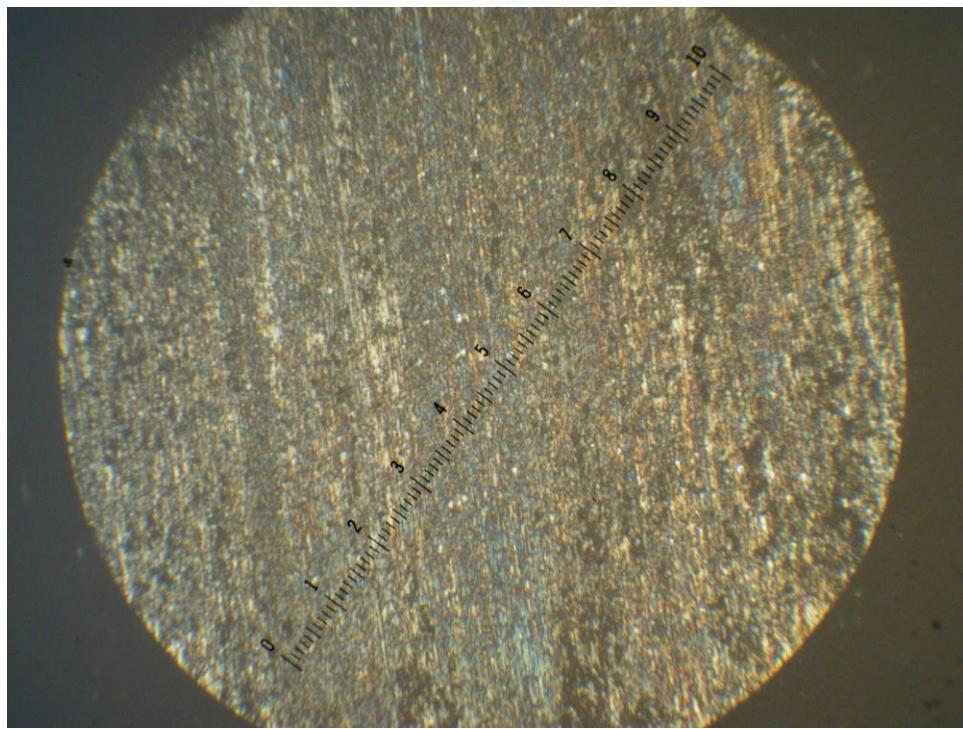
Appendix BoD – Ball-on-Disc Sliding Wear Data



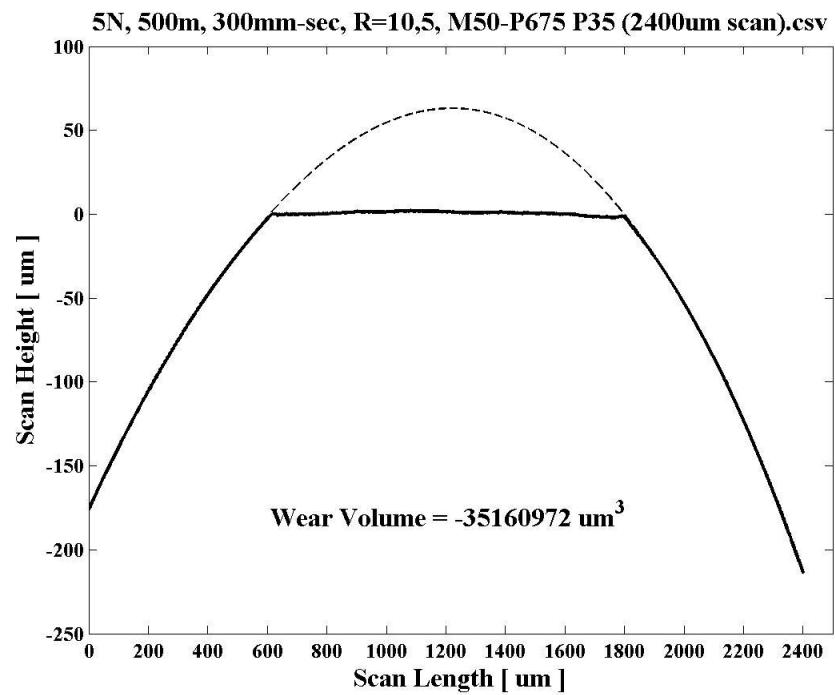
Disc Wear Track Center (above) SEM image @500x
Disc Wear Track Edge (below, non-contact area on right) SEM image @500x
P675 (Disc) vs. M50 (Ball)
Load = 5N, Distance = 500m, Speed = 300mm/sec, No Lubrication



Appendix BoD – Ball-on-Disc Sliding Wear Data

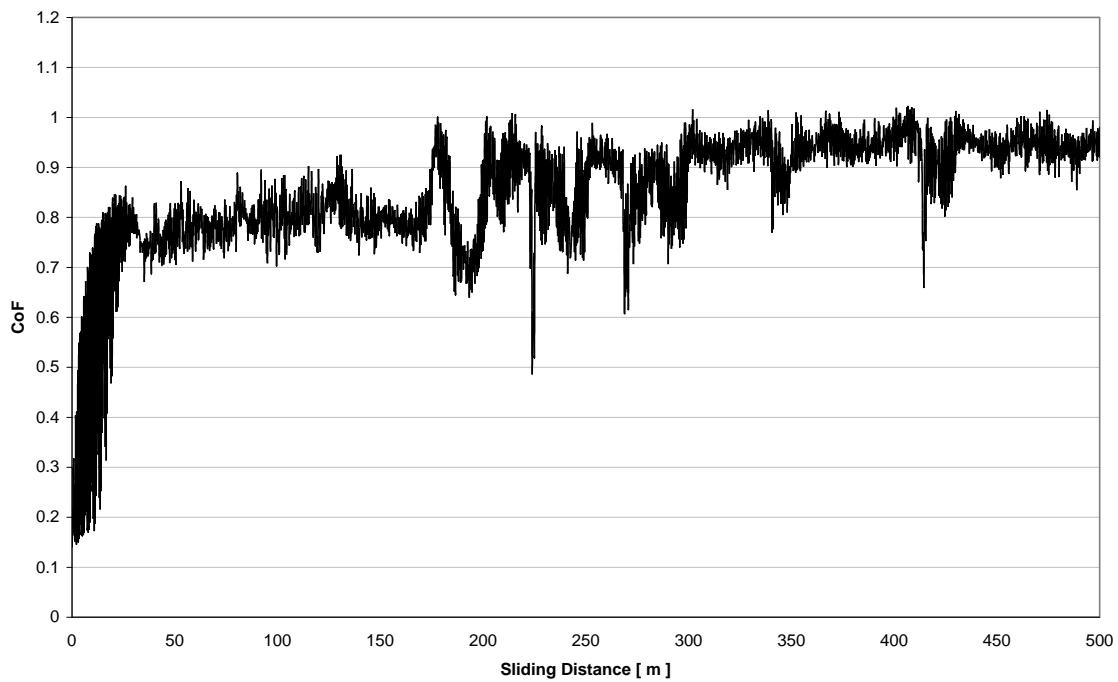


Ball Wear Scar Image and Profile
P675 (Disc) vs. M50 (Ball)
Load = 5N, Distance = 500m, Speed = 300mm/sec, No Lubrication



Appendix BoD – Ball-on-Disc Sliding Wear Data

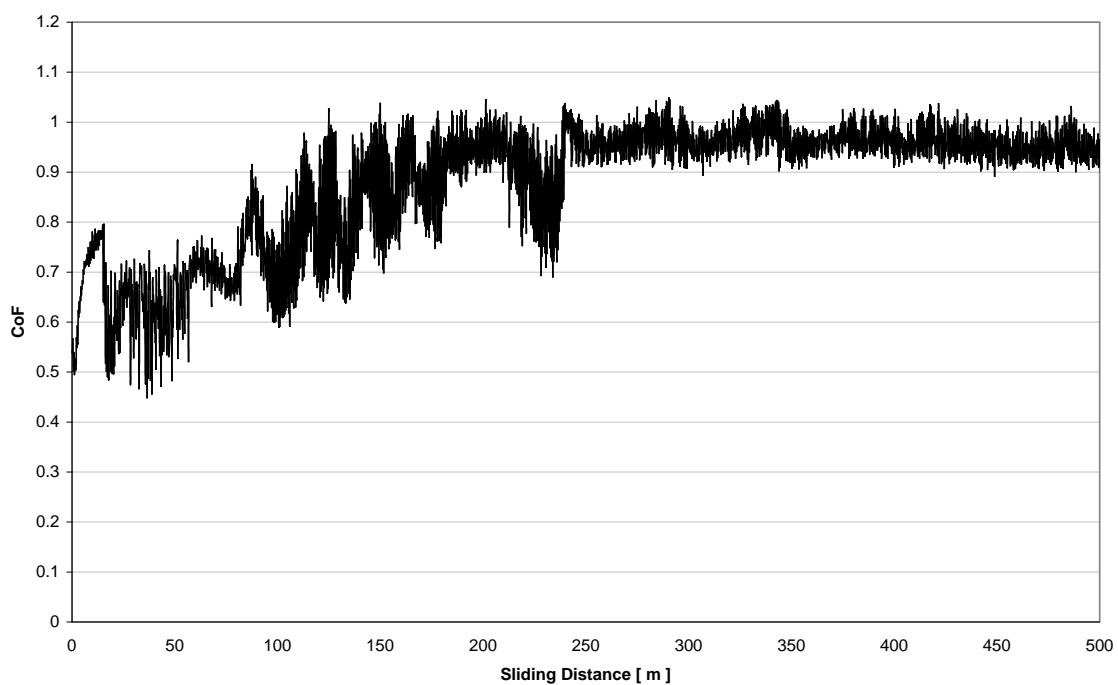
CoF vs. Distance for 5N, 500m, 300mm-sec, R=10.5, M50-P675 P33.txt



CoF vs. Sliding Distance
P675 (Disc) vs. M50 (Ball)

Load = 5N, Distance = 500m, Speed = 300mm/sec, No Lubrication

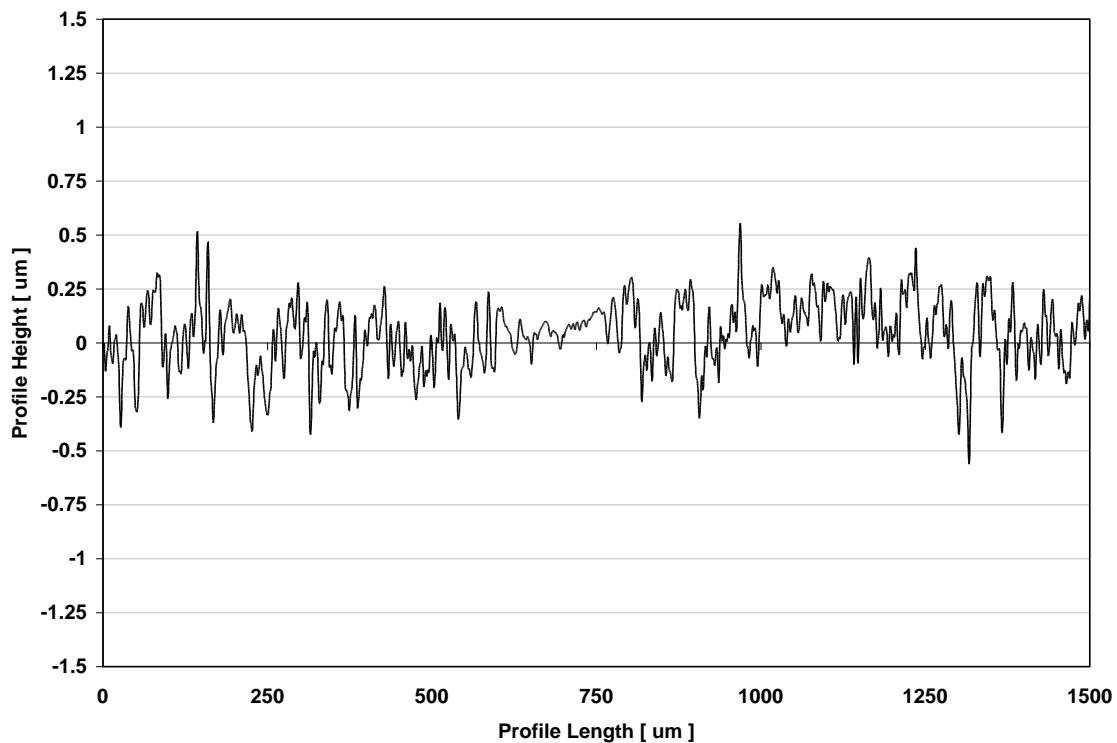
CoF vs. Distance for 5N, 500m, 300mm-sec, R=10.5, M50-P675 P35.txt



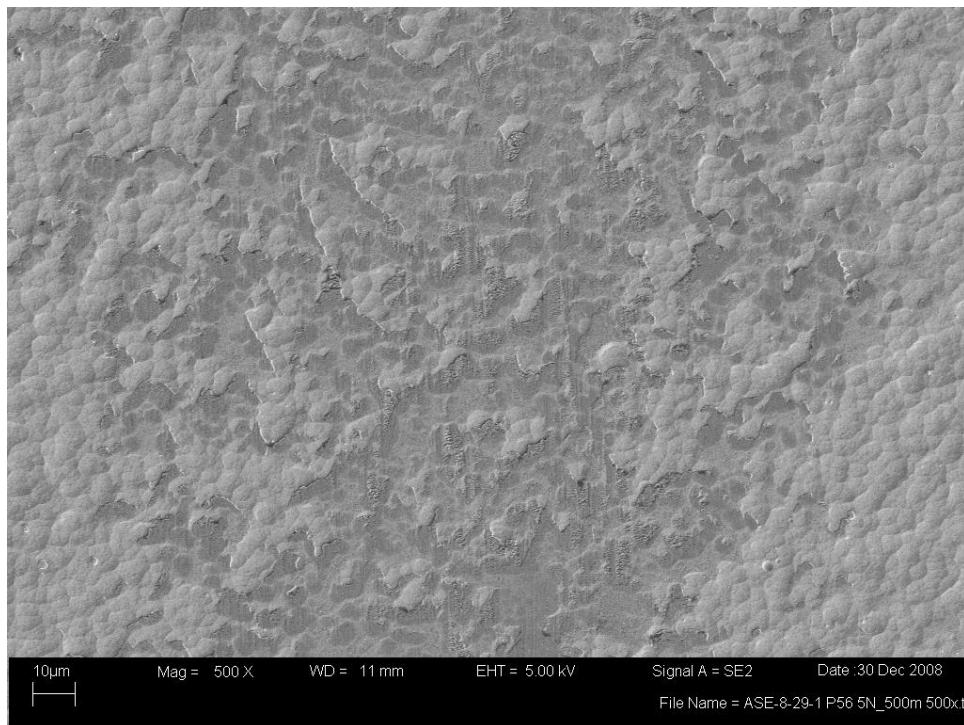
Appendix BoD – Ball-on-Disc Sliding Wear Data



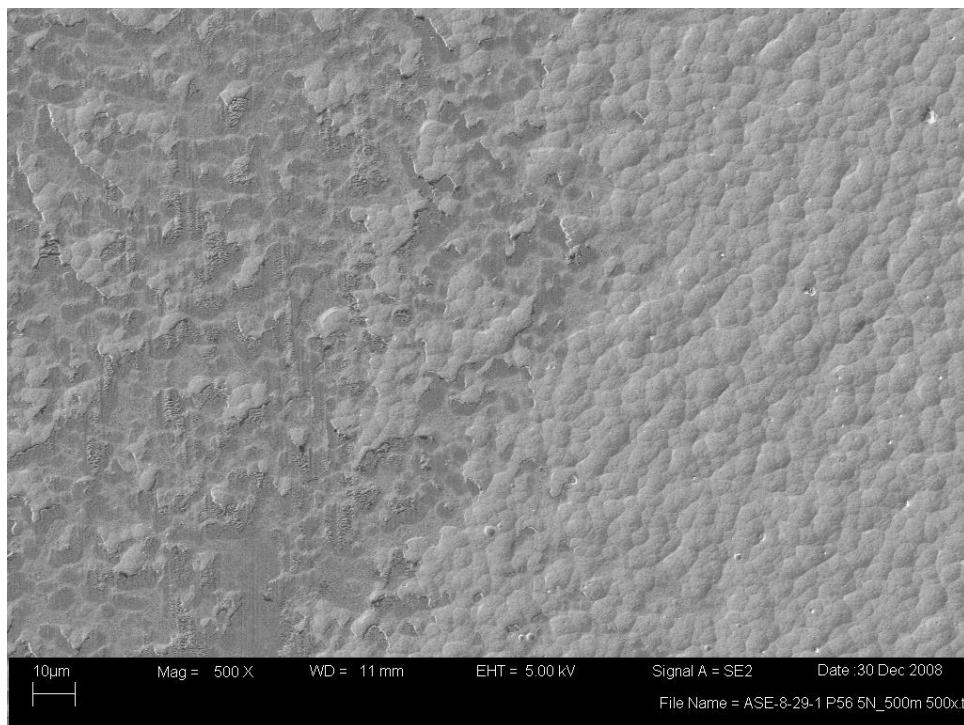
Disc Wear Track Image and Profile
Cr-CrN (Disc) vs. TiCr-TiCrN (Ball)
Load = 5N, Distance = 500m, Speed = 300mm/sec, No Lubrication



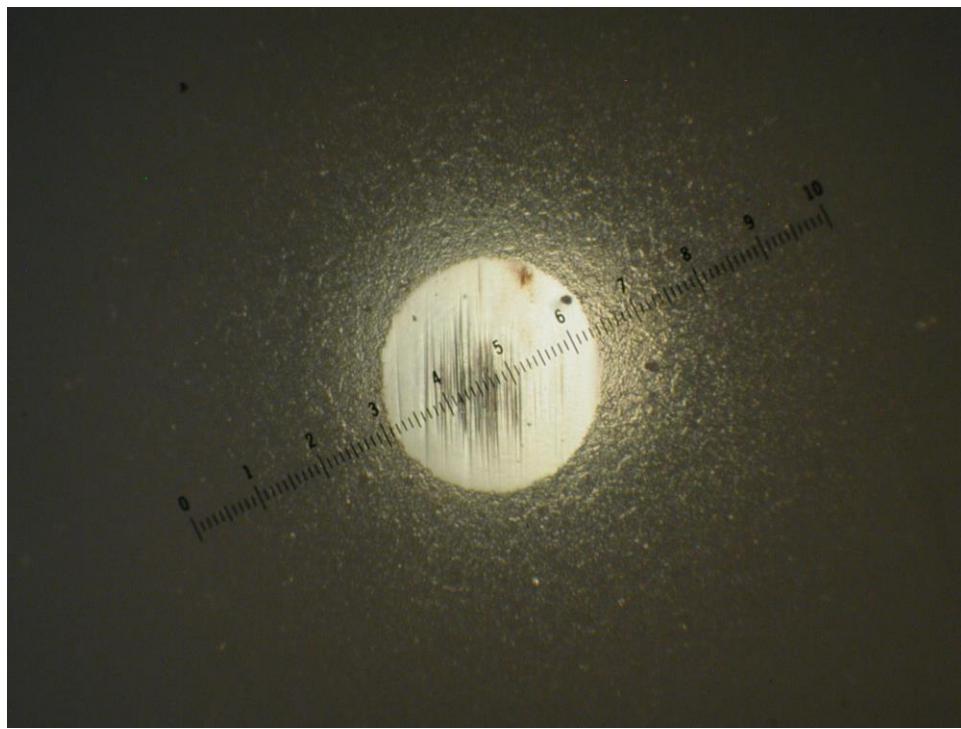
Appendix BoD – Ball-on-Disc Sliding Wear Data



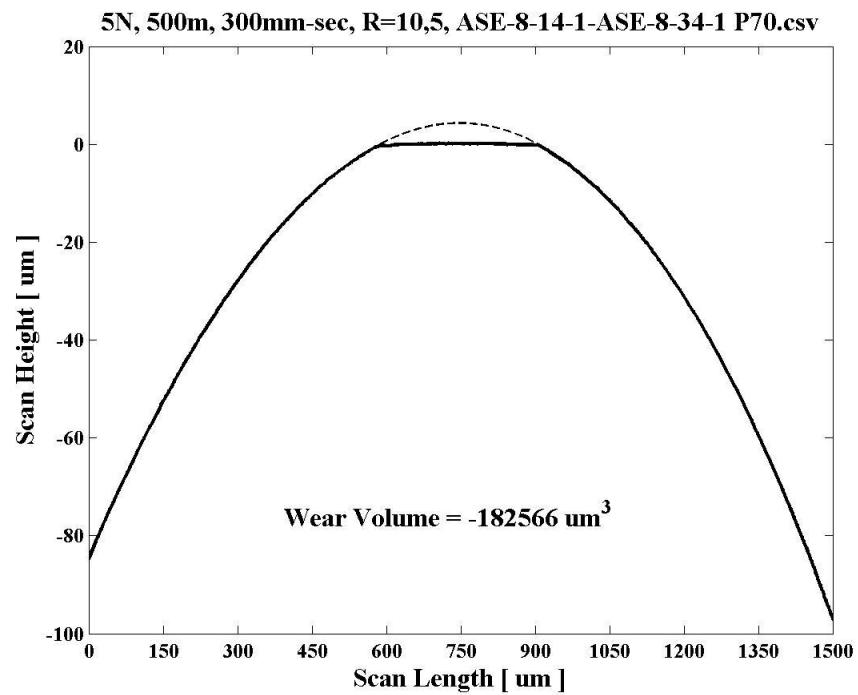
Disc Wear Track Center (above) SEM image @500x
Disc Wear Track Edge (below, non-contact area on right) SEM image @500x
Cr-CrN (Disc) vs. TiCr-TiCrN (Ball)
Load = 5N, Distance = 500m, Speed = 300mm/sec, No Lubrication



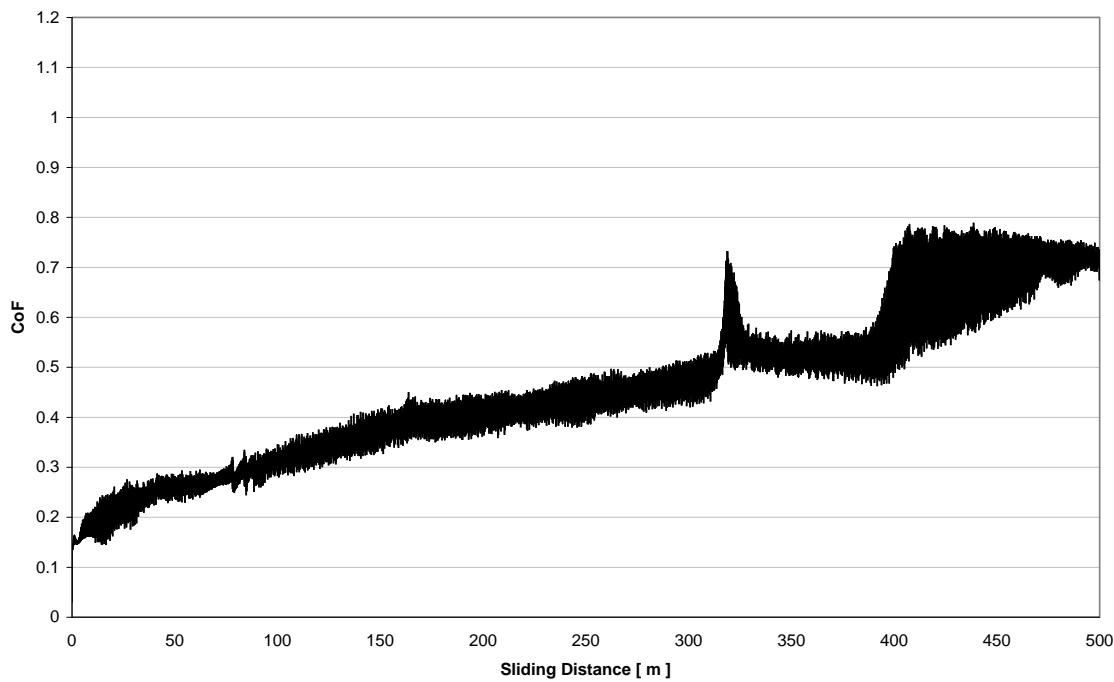
Appendix BoD – Ball-on-Disc Sliding Wear Data



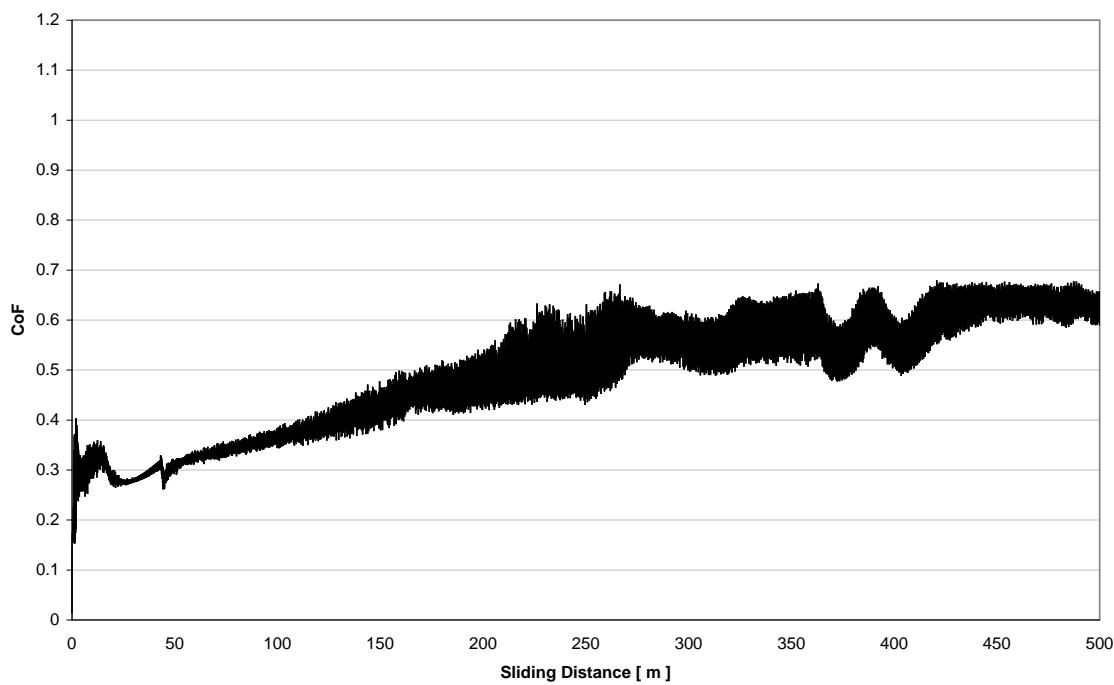
Ball Wear Scar Image and Profile
Cr-CrN (Disc) vs. TiCr-TiCrN (Ball)
Load = 5N, Distance = 500m, Speed = 300mm/sec, No Lubrication



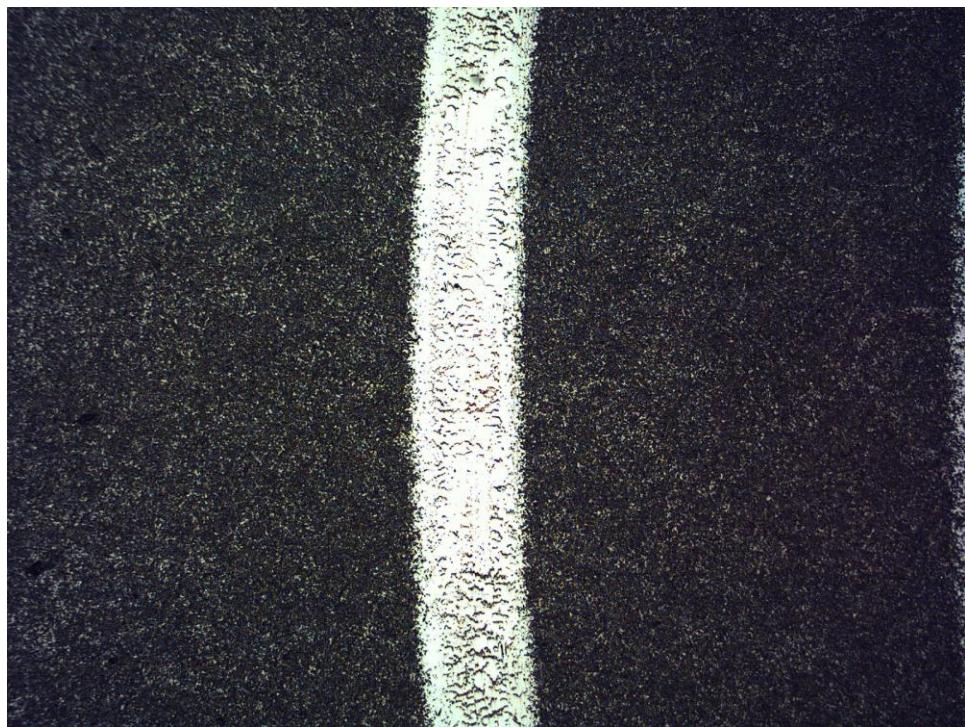
Appendix BoD – Ball-on-Disc Sliding Wear Data

CoF vs. Distance for 5N, 500m, 300mm-sec, R=10,5, ASE-8-14-1-ASE-8-29-1 P56.txt

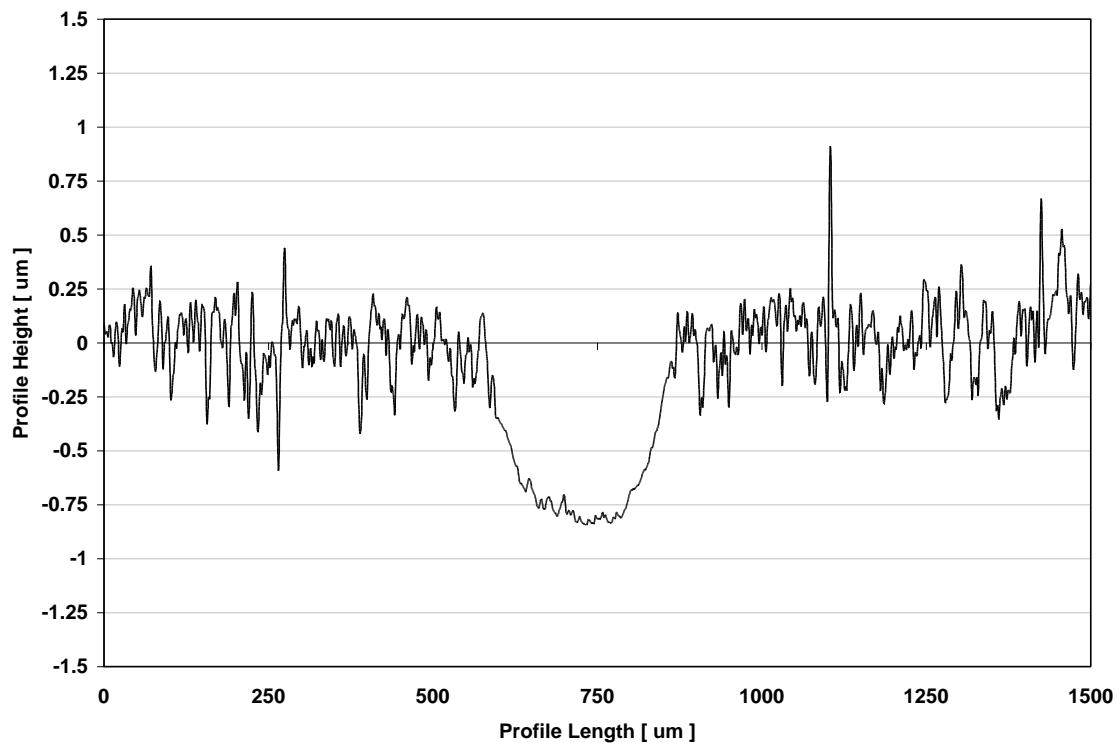
**CoF vs. Sliding Distance
Cr-CrN (Disc) vs. TiCr-TiCrN (Ball)**
Load = 5N, Distance = 500m, Speed = 300mm/sec, No Lubrication

CoF vs. Distance for 5N, 500m, 300mm-sec, R=10,5, ASE-8-14-1-ASE-8-34-1 P70.txt

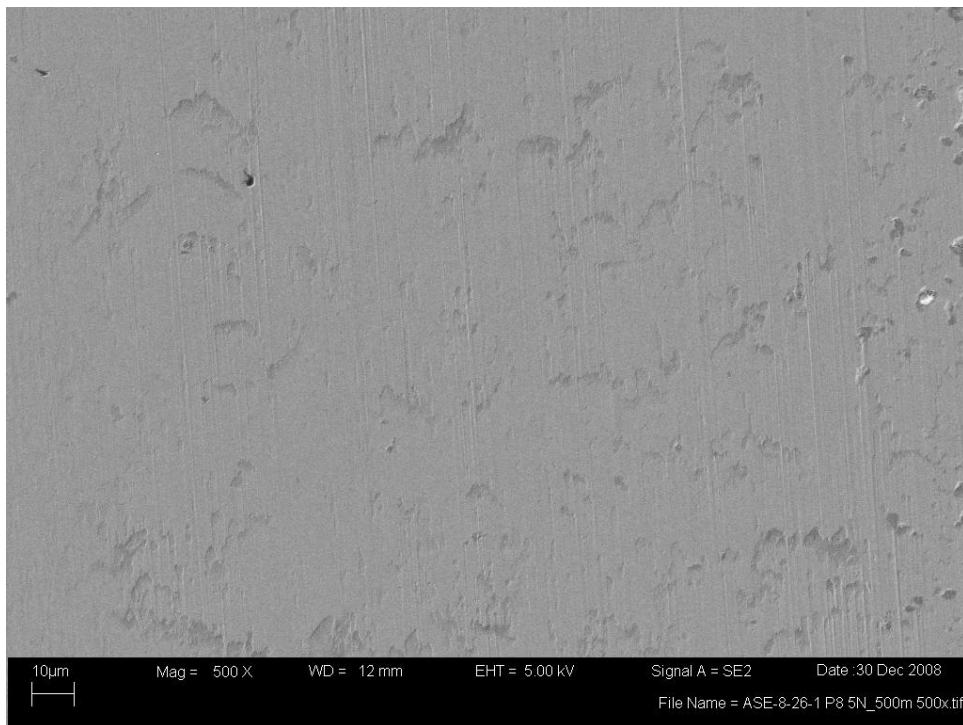
Appendix BoD – Ball-on-Disc Sliding Wear Data



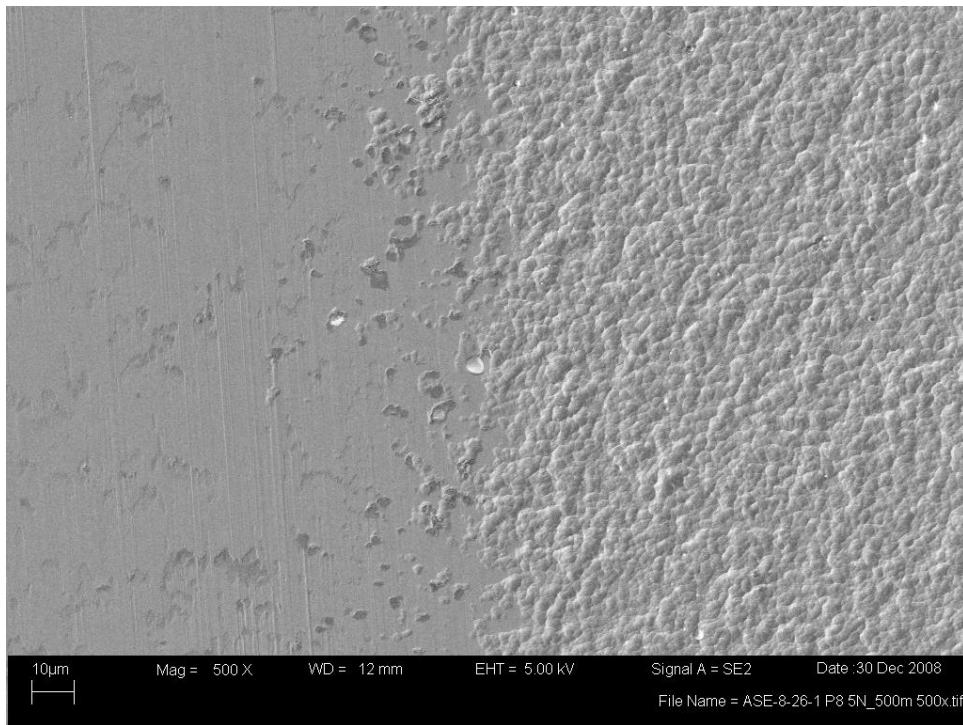
Disc Wear Track Image and Profile
CrC (Disc) vs. TiCr-TiCrN (Ball)
Load = 5N, Distance = 500m, Speed = 300mm/sec, No Lubrication



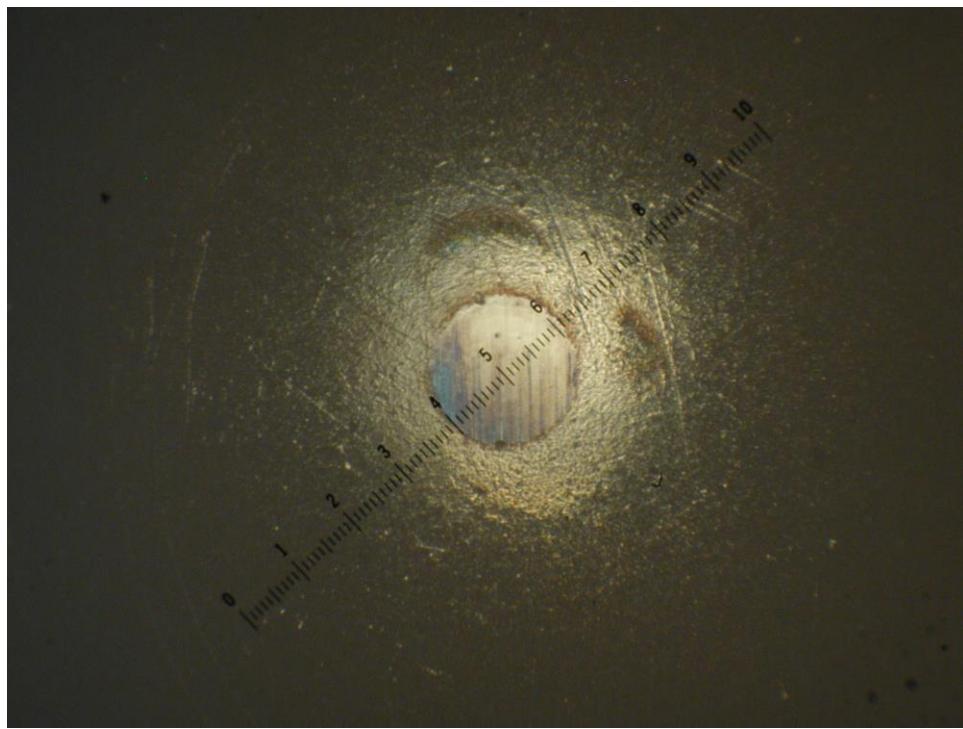
Appendix BoD – Ball-on-Disc Sliding Wear Data



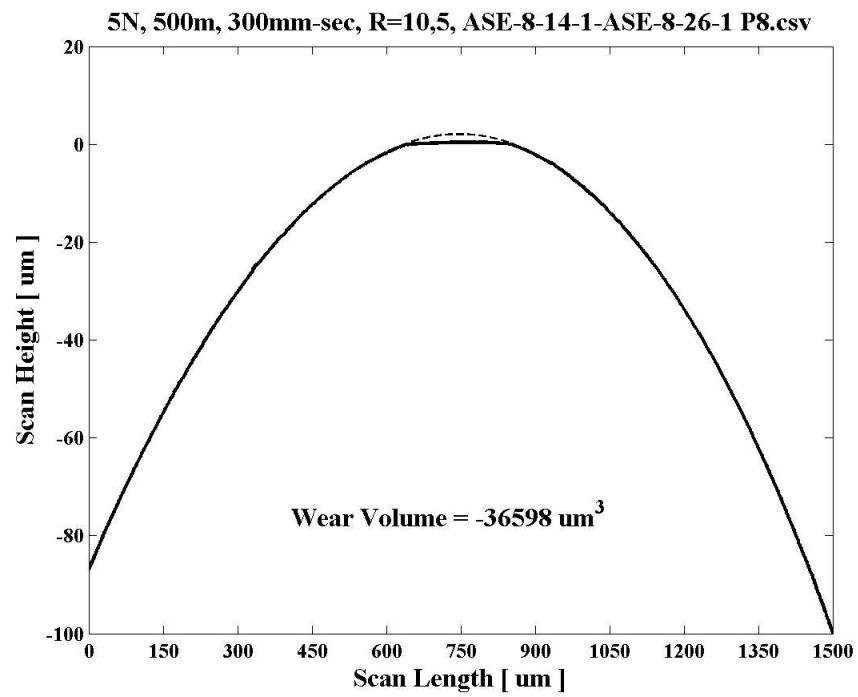
Disc Wear Track Center (above) SEM image @500x
Disc Wear Track Edge (below, non-contact area on right) SEM image @500x
CrC (Disc) vs. TiCr-TiCrN (Ball)
Load = 5N, Distance = 500m, Speed = 300mm/sec, No Lubrication



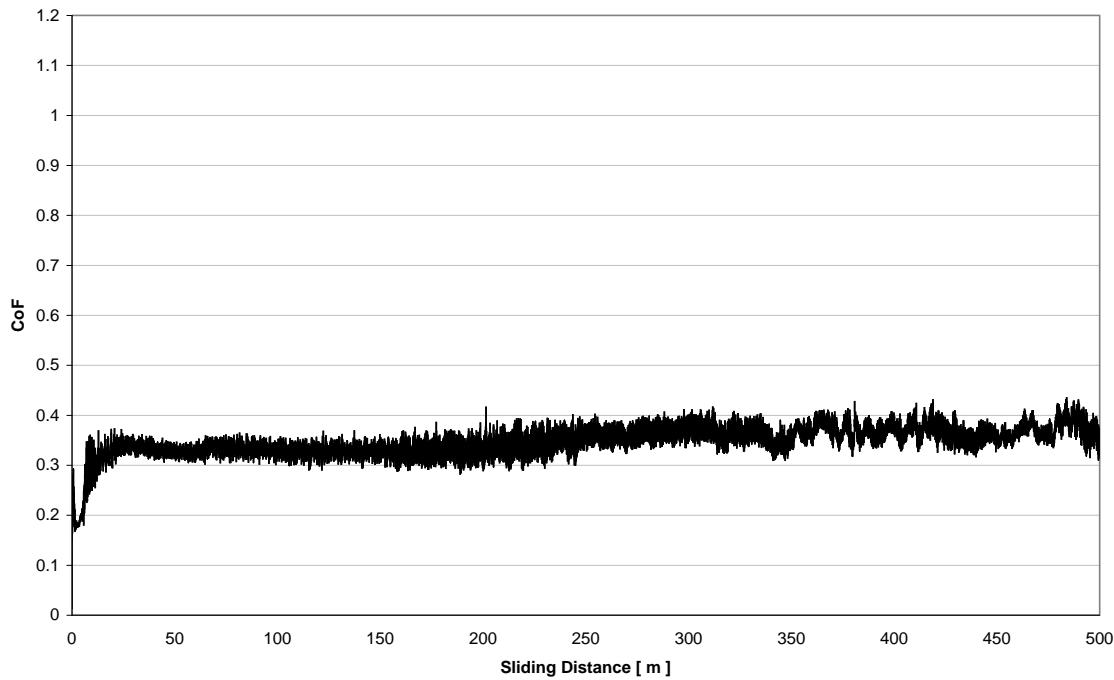
Appendix BoD – Ball-on-Disc Sliding Wear Data



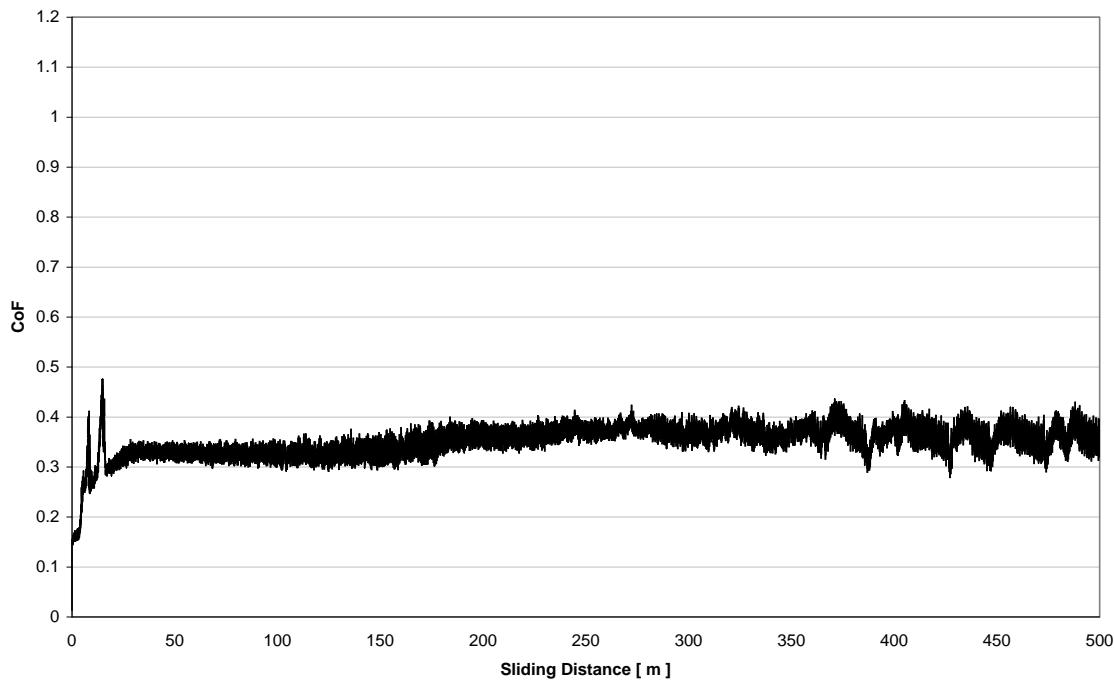
Ball Wear Scar Image and Profile
CrC (Disc) vs. TiCr-TiCrN (Ball)
Load = 5N, Distance = 500m, Speed = 300mm/sec, No Lubrication



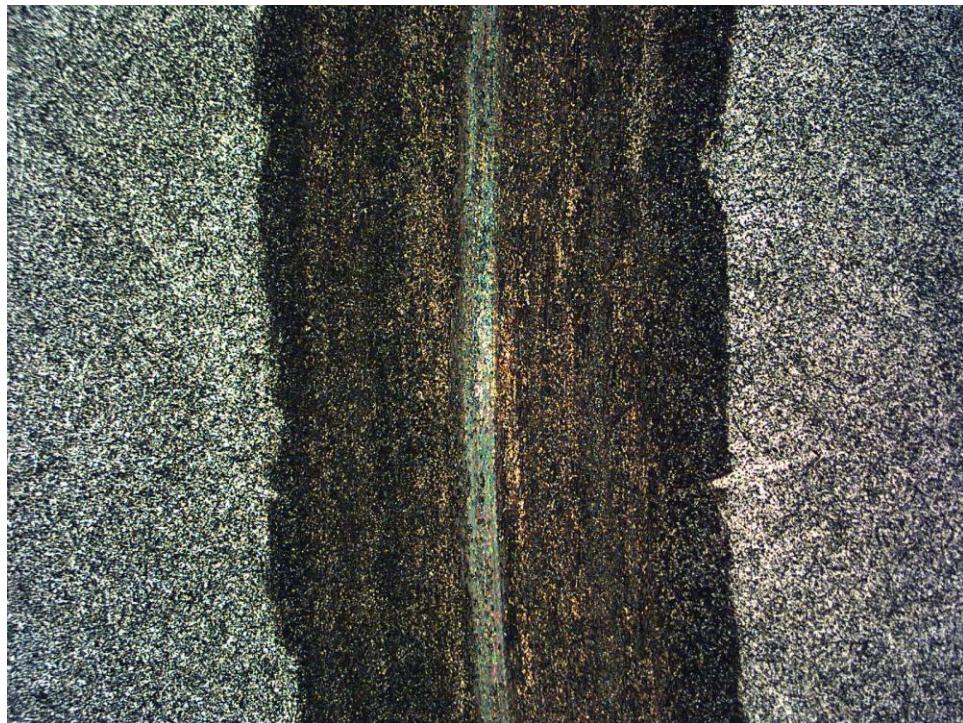
Appendix BoD – Ball-on-Disc Sliding Wear Data

CoF vs. Distance for 5N, 500m, 300mm-sec, R=10,5, ASE-8-14-1, ASE-8-19-1 P13.txt

**CoF vs. Sliding Distance
CrC (Disc) vs. TiCr-TiCrN (Ball)**
Load = 5N, Distance = 500m, Speed = 300mm/sec, No Lubrication

CoF vs. Distance for 5N, 500m, 300mm-sec, R=10,5, ASE-8-14-1, ASE-8-26-1 P8.txt

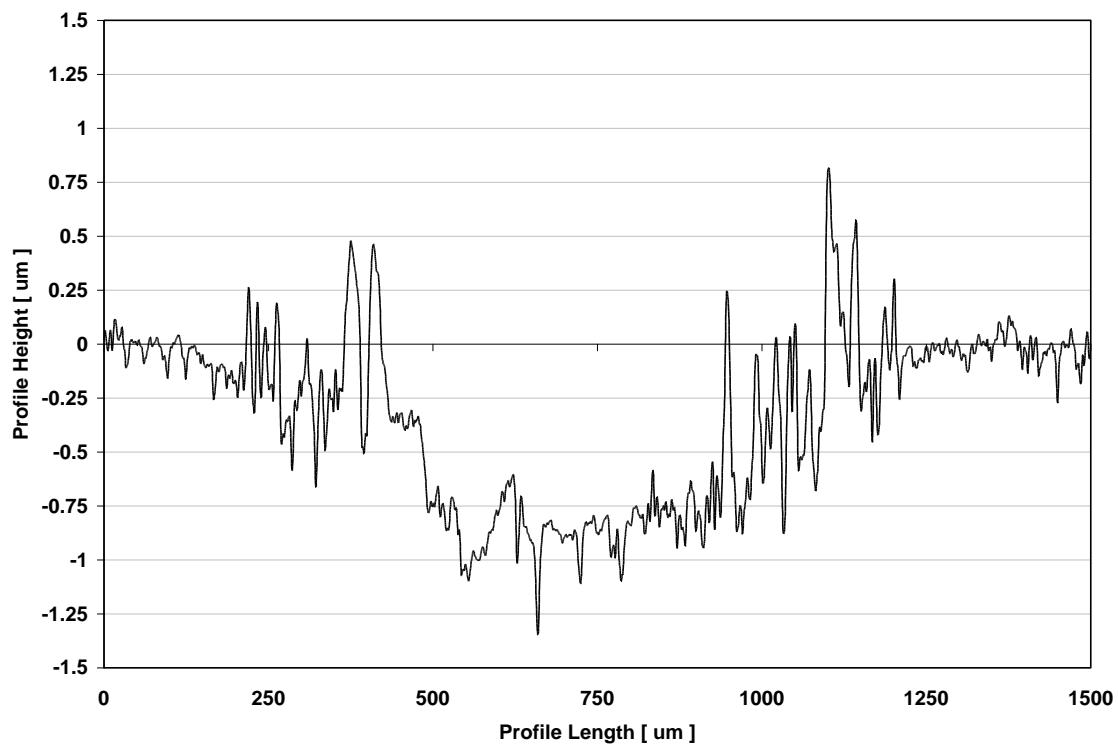
Appendix BoD – Ball-on-Disc Sliding Wear Data



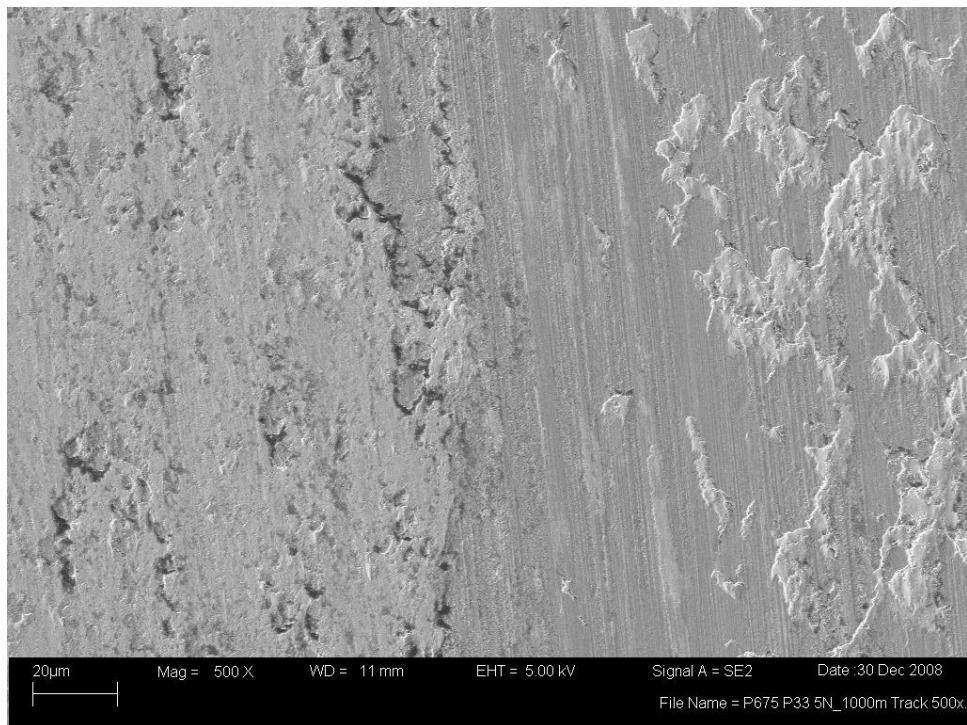
Ball Wear Scar Image and Profile

P675 (Disc) vs. M50 (Ball)

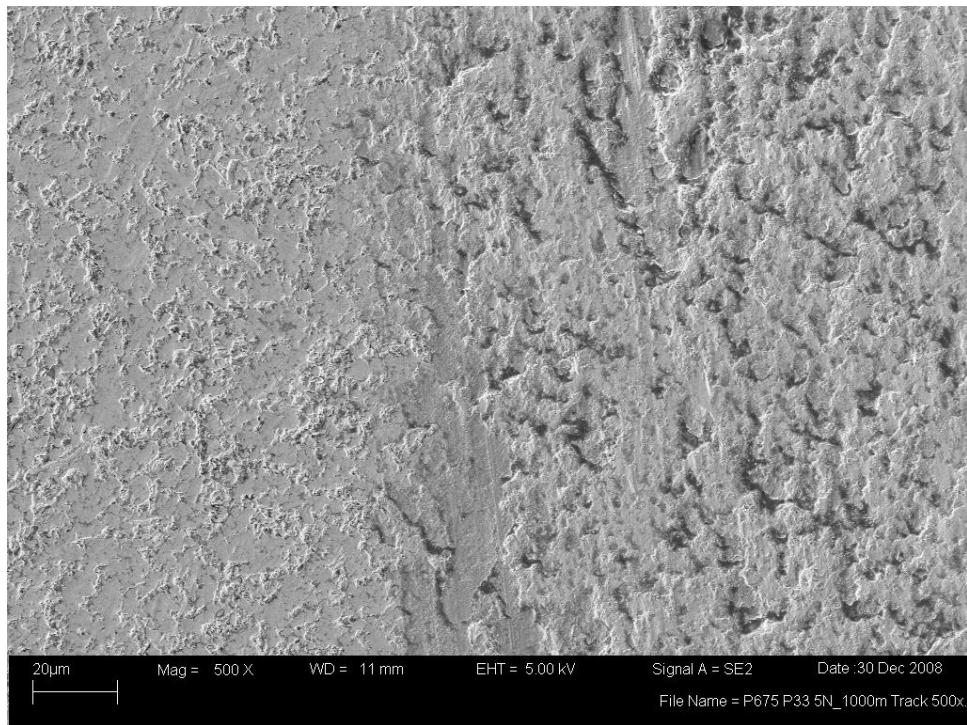
Load = 5N, Distance = 1000m, Speed = 300mm/sec, No Lubrication



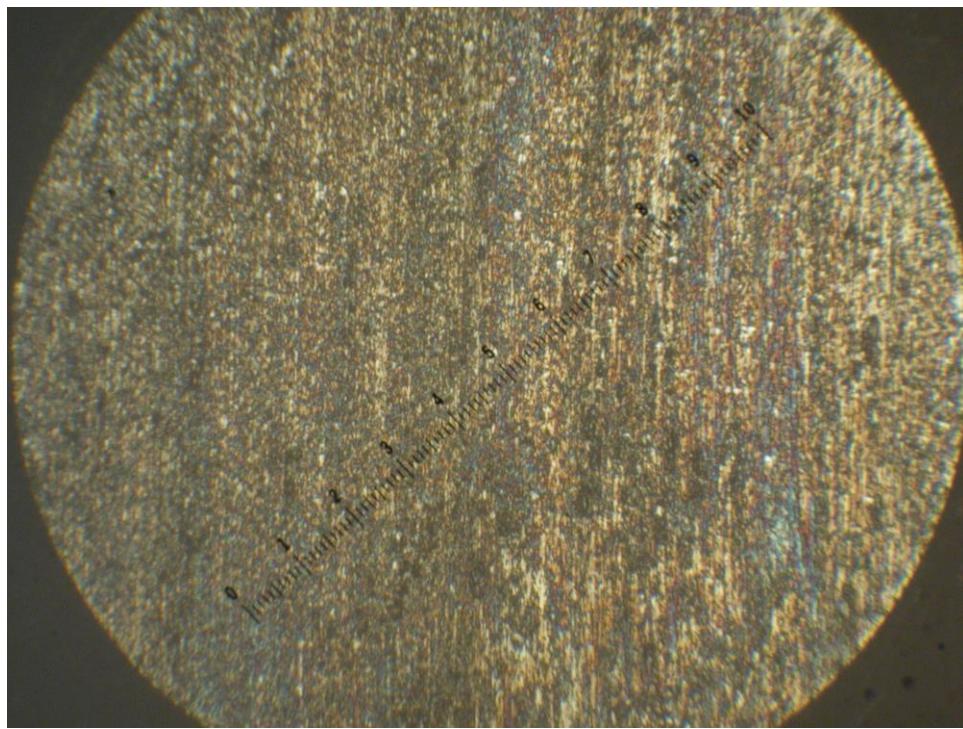
Appendix BoD – Ball-on-Disc Sliding Wear Data



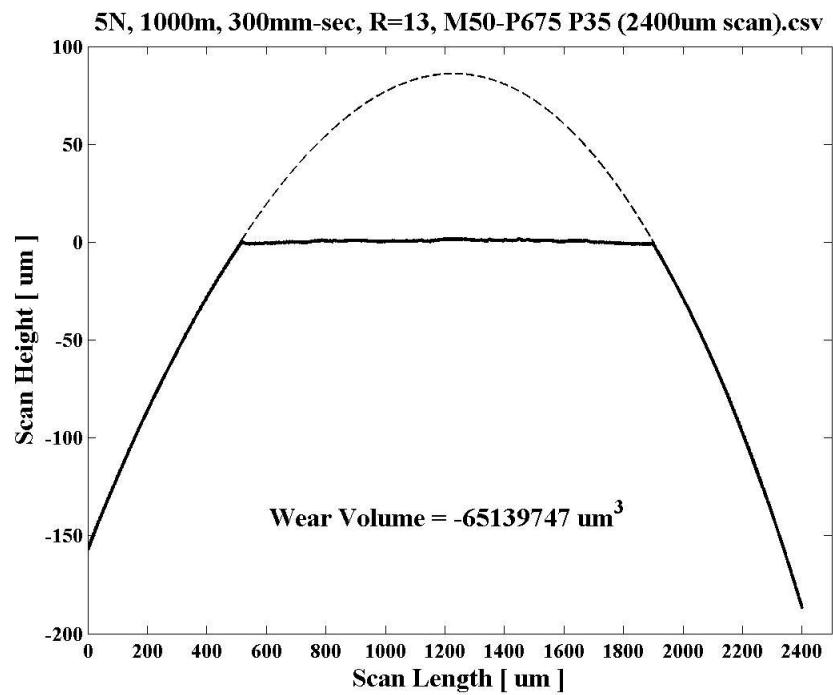
Disc Wear Track Center (above) SEM image @500x
Disc Wear Track Edge (below, non-contact area on left) SEM image @500x
P675 (Disc) vs. M50 (Ball)
Load = 5N, Distance = 1000m, Speed = 300mm/sec, No Lubrication



Appendix BoD – Ball-on-Disc Sliding Wear Data

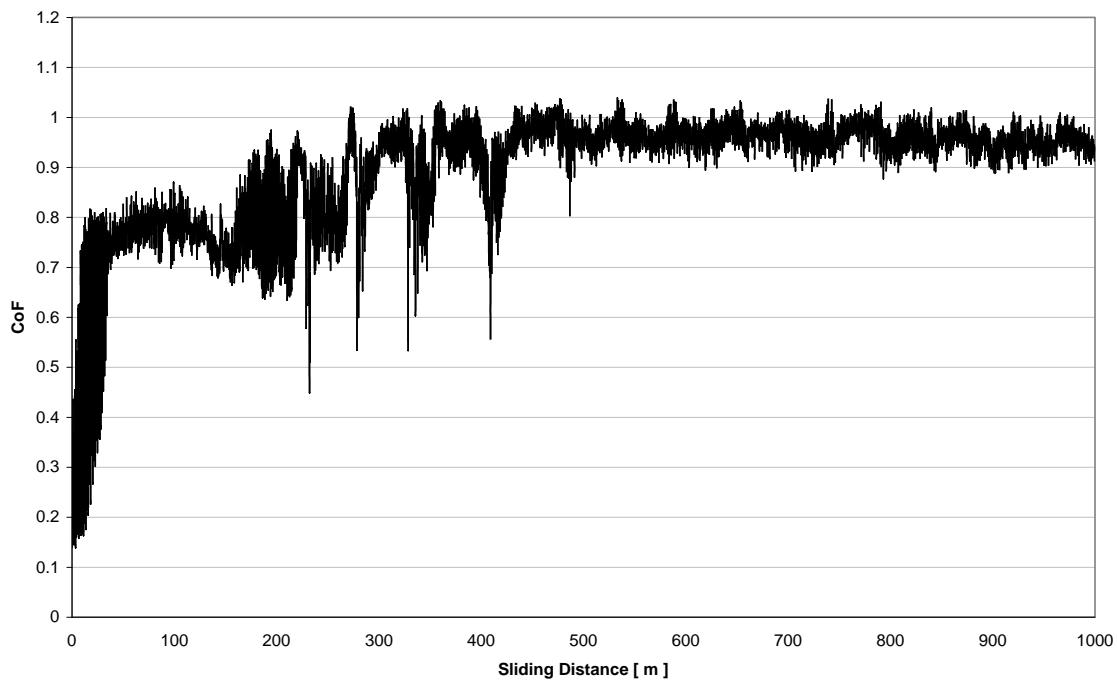


Ball Wear Scar Image and Profile
P675 (Disc) vs. M50 (Ball)
Load = 5N, Distance = 1000m, Speed = 300mm/sec, No Lubrication



Appendix BoD – Ball-on-Disc Sliding Wear Data

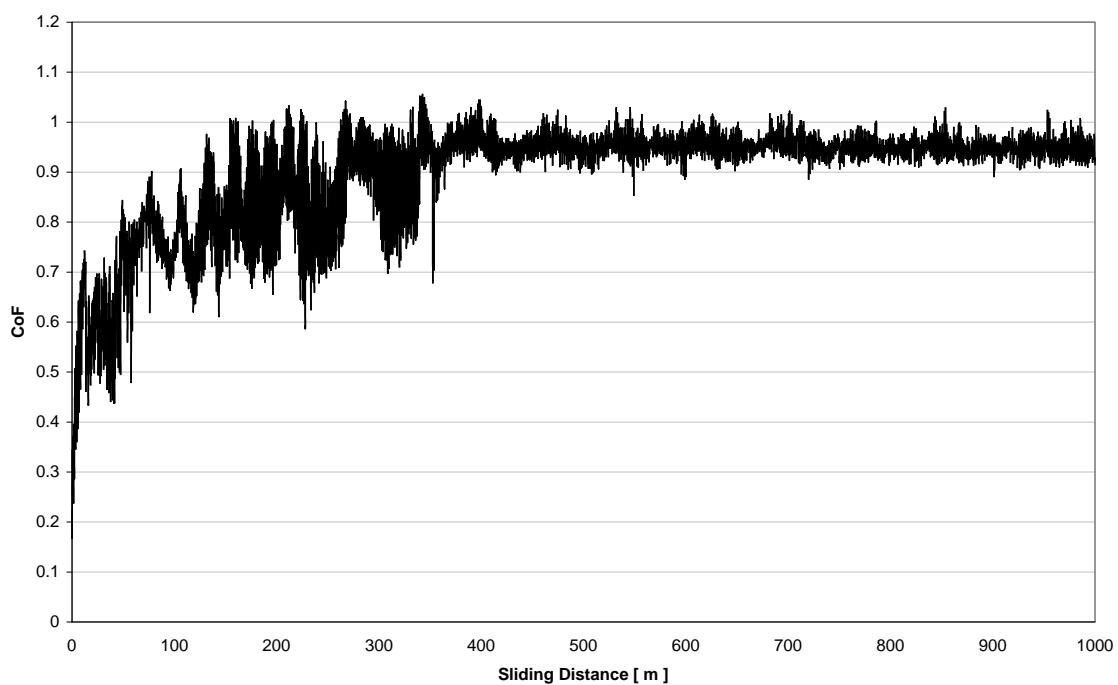
CoF vs. Distance for 5N, 1000m, 300mm-sec, R=13, P675 P35.txt



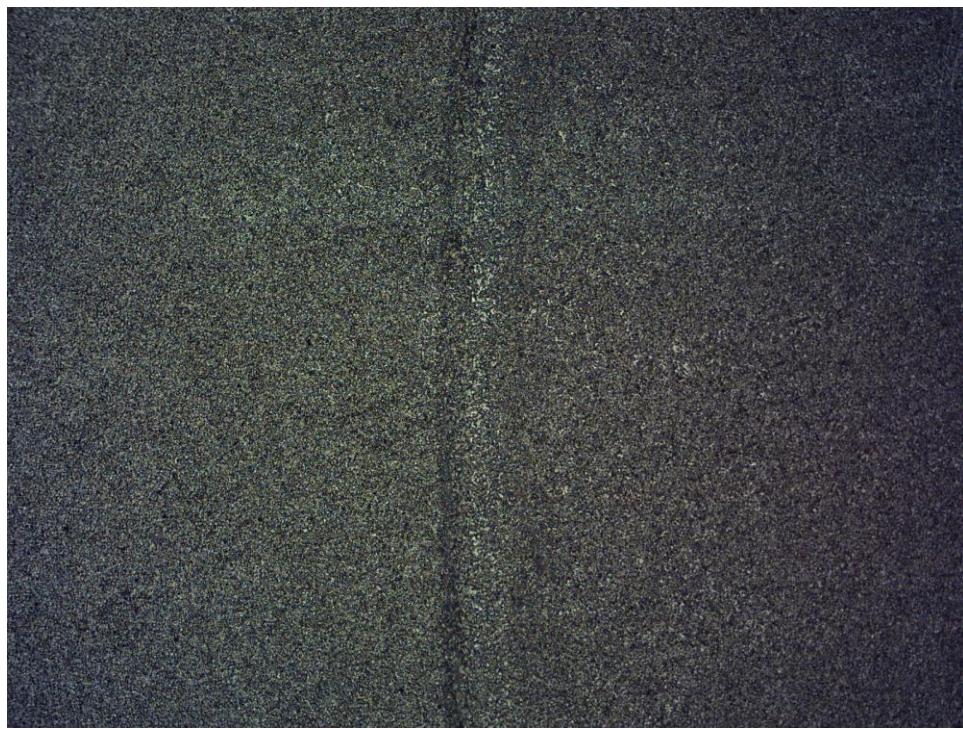
CoF vs. Sliding Distance
P675 (Disc) vs. M50 (Ball)

Load = 5N, Distance = 1000m, Speed = 300mm/sec, No Lubrication

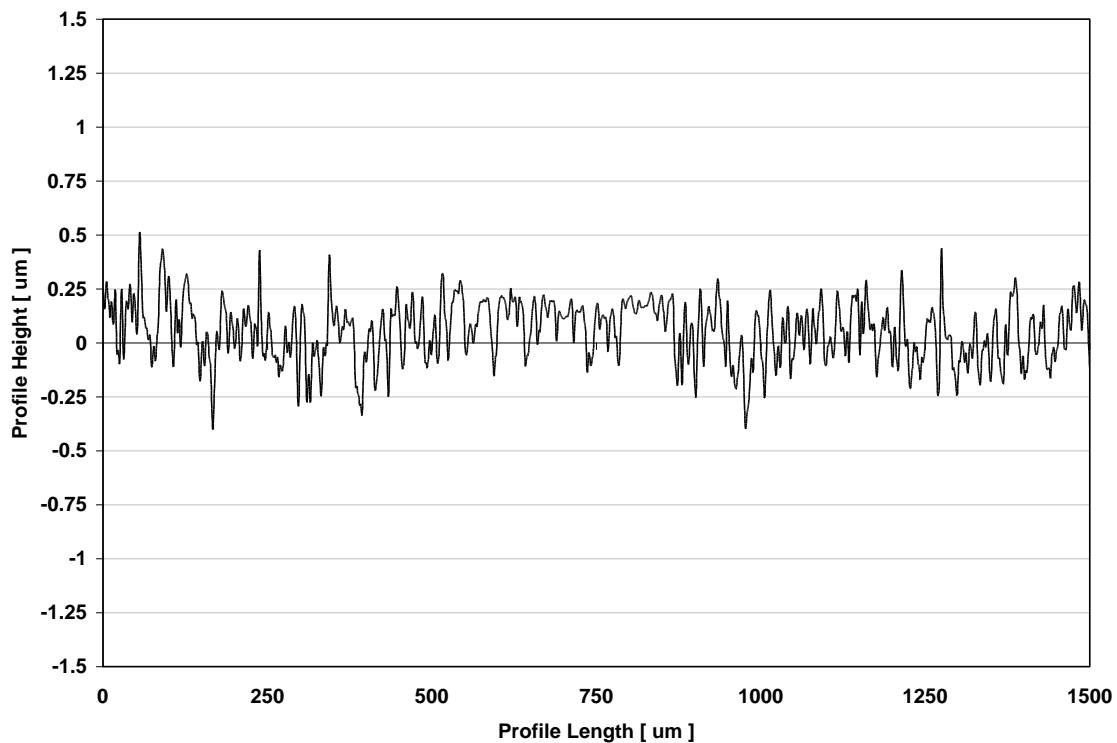
CoF vs. Distance for 5N, 1000m, 300mm-sec, R=13, P675 P33.txt



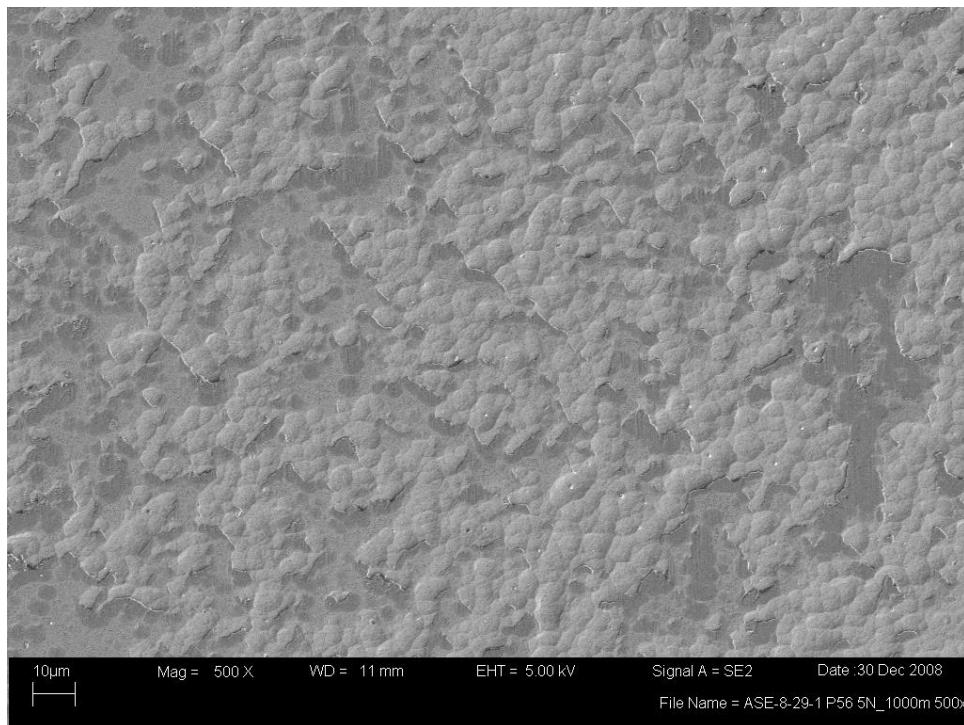
Appendix BoD – Ball-on-Disc Sliding Wear Data



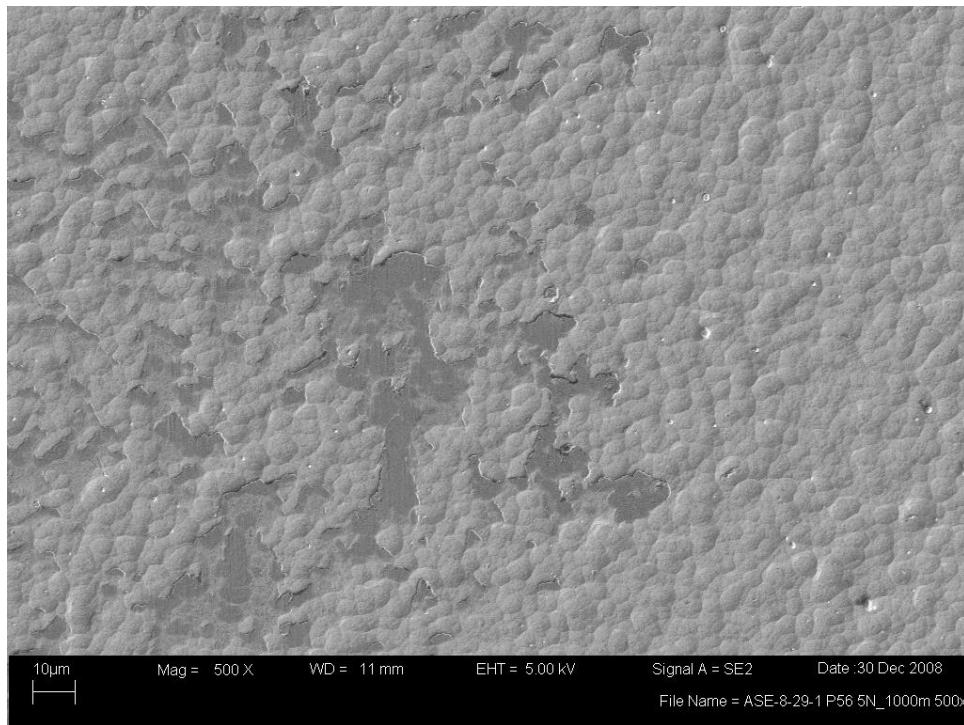
Ball Wear Scar Image and Profile
Cr-CrN (Disc) vs. TiCr-TiCrN (Ball)
Load = 5N, Distance = 1000m, Speed = 300mm/sec, No Lubrication



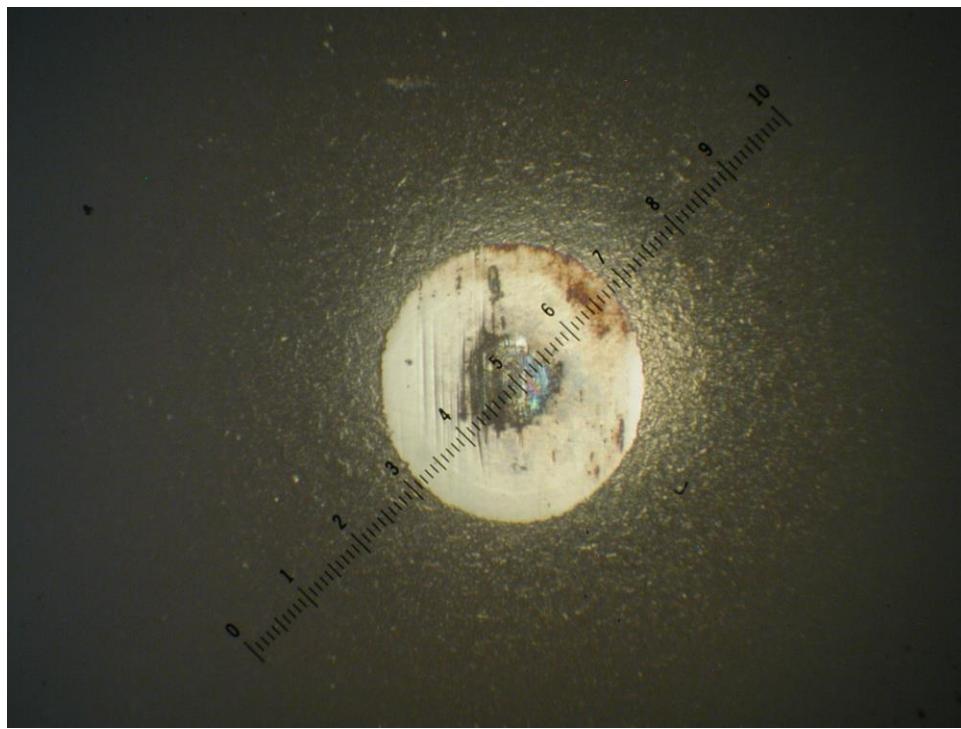
Appendix BoD – Ball-on-Disc Sliding Wear Data



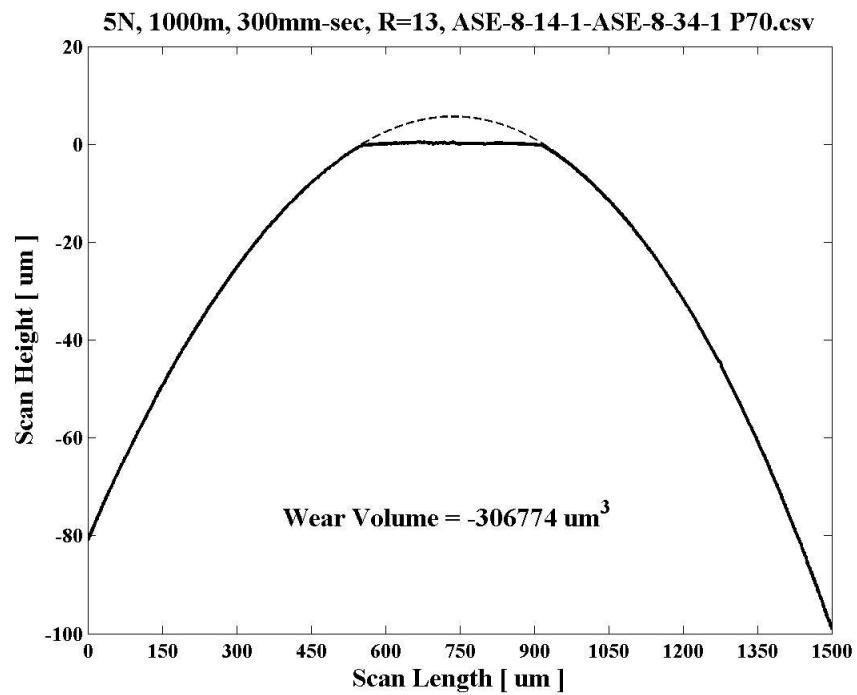
Disc Wear Track Center (above) SEM image @500x
Disc Wear Track Edge (below, non-contact area on left) SEM image @500x
Cr-CrN (Disc) vs. TiCr-TiCrN (Ball)
Load = 5N, Distance = 1000m, Speed = 300mm/sec, No Lubrication



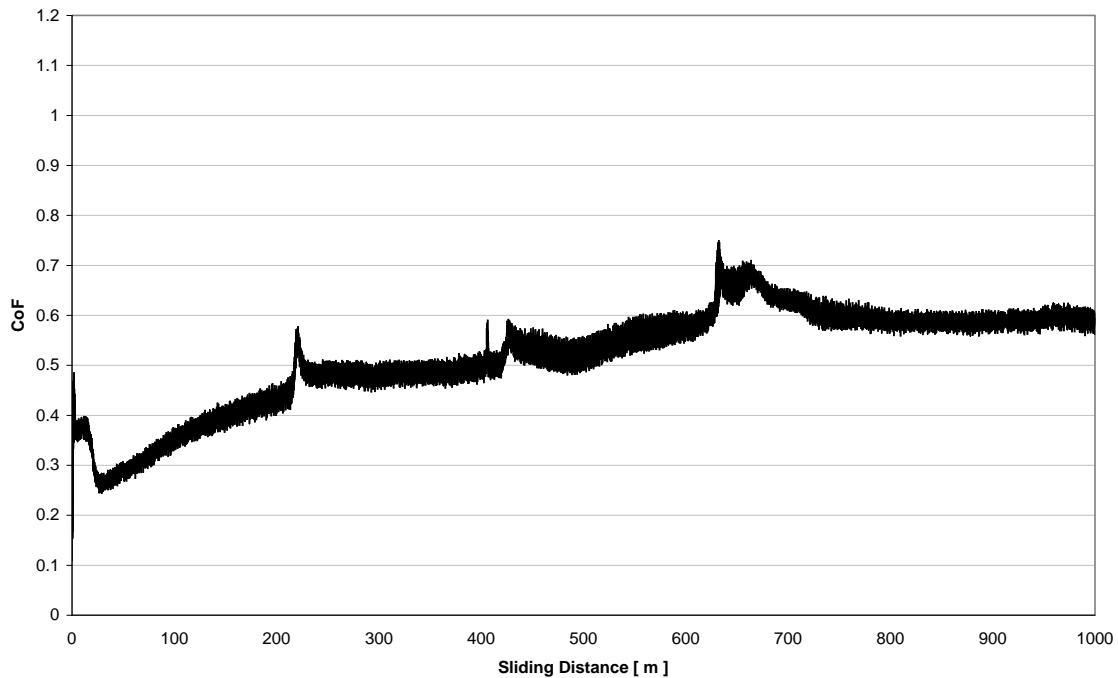
Appendix BoD – Ball-on-Disc Sliding Wear Data



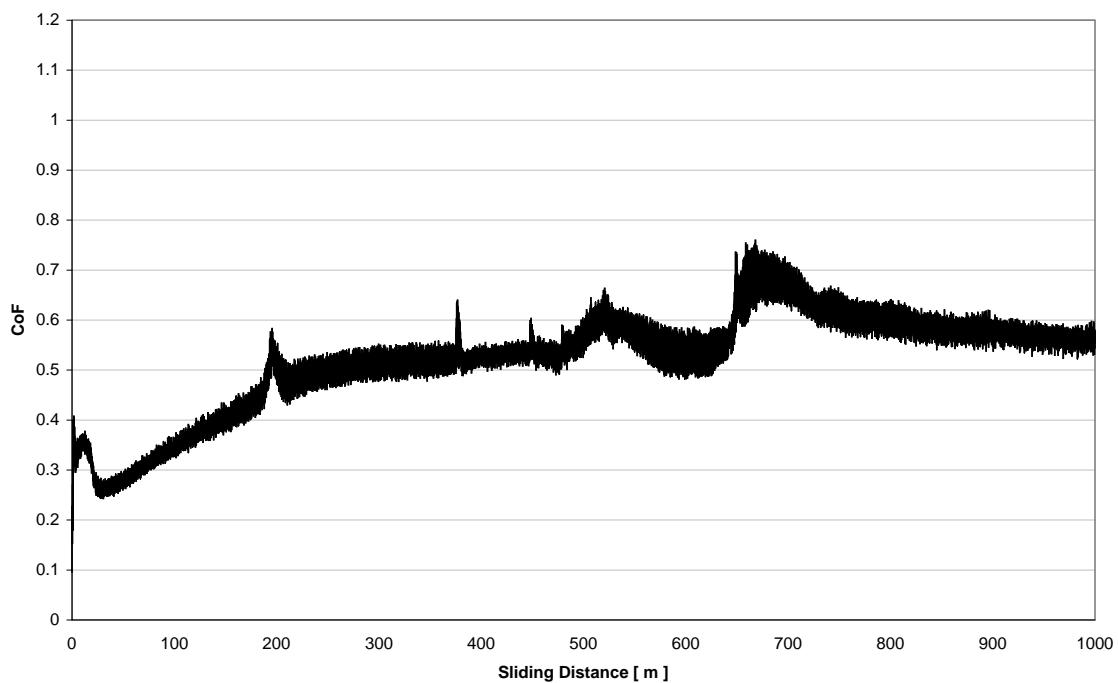
Ball Wear Scar Image and Profile
Cr-CrN (Disc) vs. TiCr-TiCrN (Ball)
Load = 5N, Distance = 1000m, Speed = 300mm/sec, No Lubrication



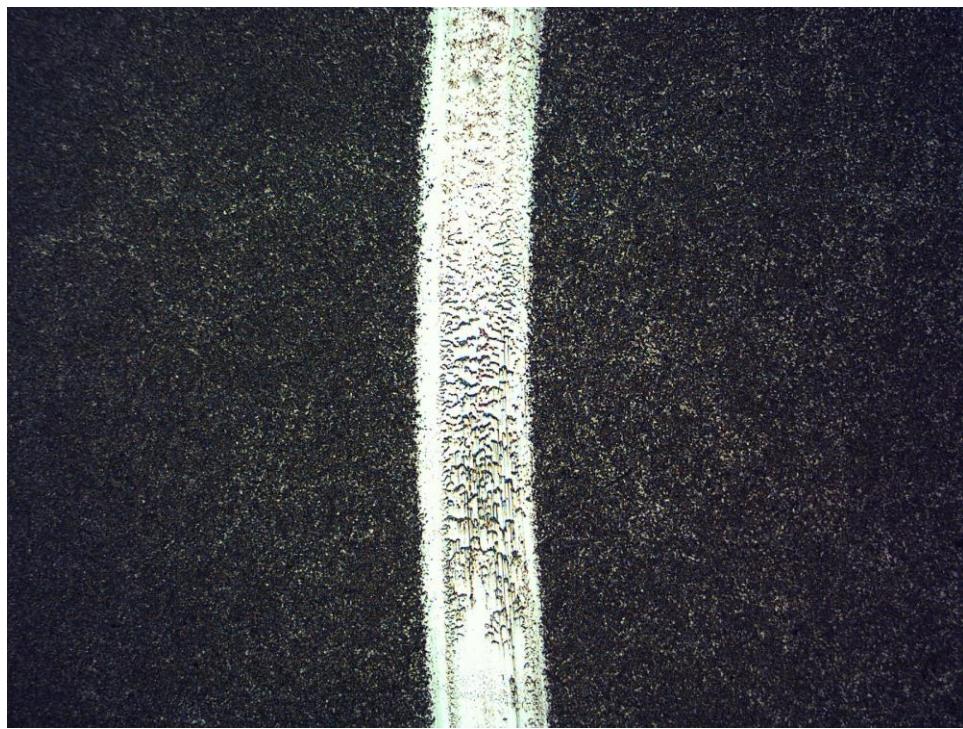
Appendix BoD – Ball-on-Disc Sliding Wear Data

CoF vs. Distance for 5N, 1000m, 300mm-sec, R=13, ASE-8-14-1-ASE-8-29-1 P56.txt

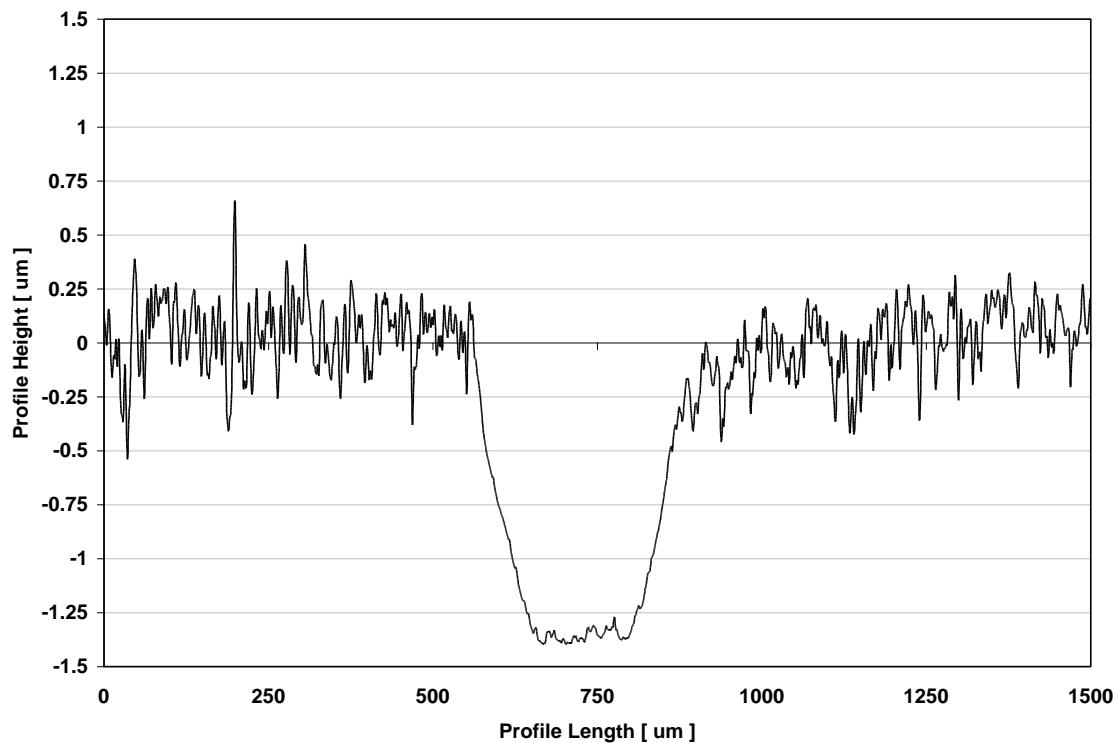
**CoF vs. Sliding Distance
Cr-CrN (Disc) vs. TiCr-TiCrN (Ball)
Load = 5N, Distance = 1000m, Speed = 300mm/sec, No Lubrication**

CoF vs. Distance for 5N, 1000m, 300mm-sec, R=13, ASE-8-14-1-ASE-8-34-1 P70.txt

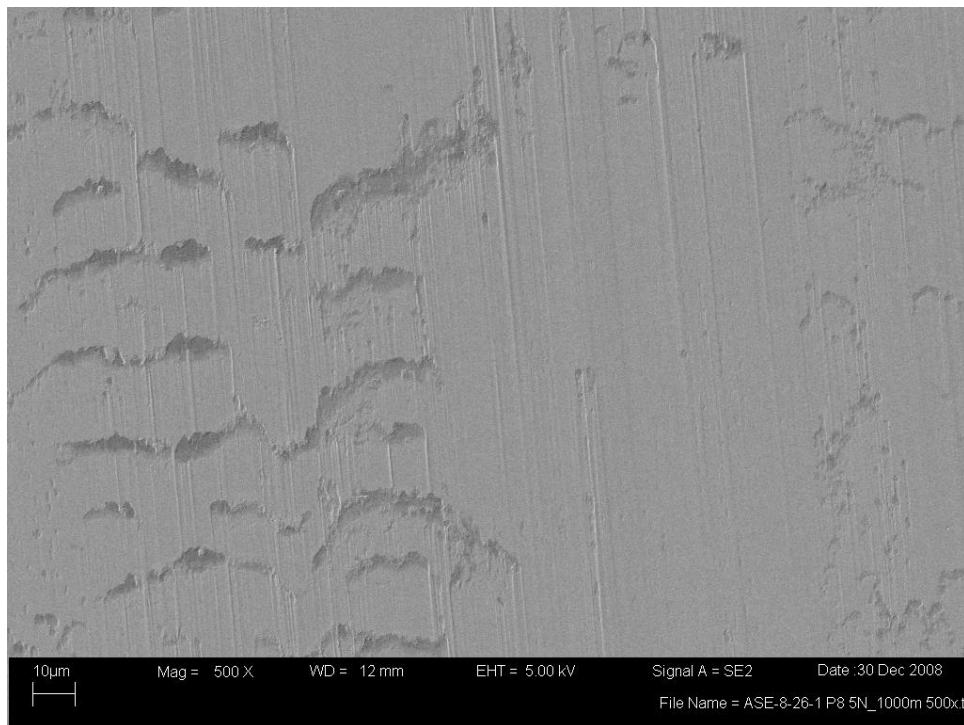
Appendix BoD – Ball-on-Disc Sliding Wear Data



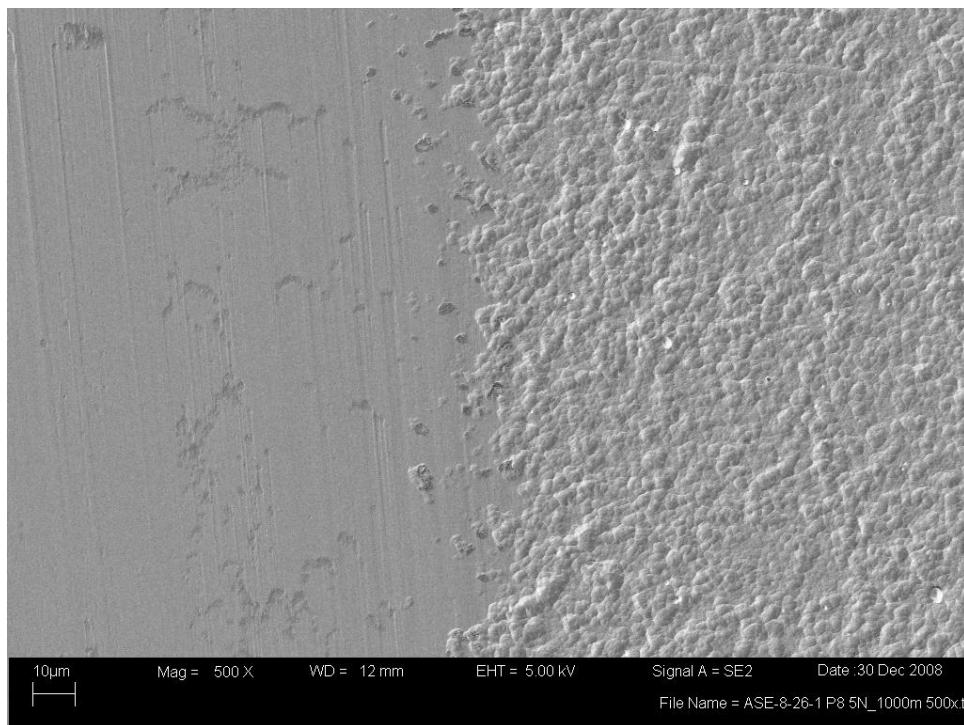
Ball Wear Scar Image and Profile
CrC (Disc) vs. TiCr-TiCrN (Ball)
Load = 5N, Distance = 1000m, Speed = 300mm/sec, No Lubrication



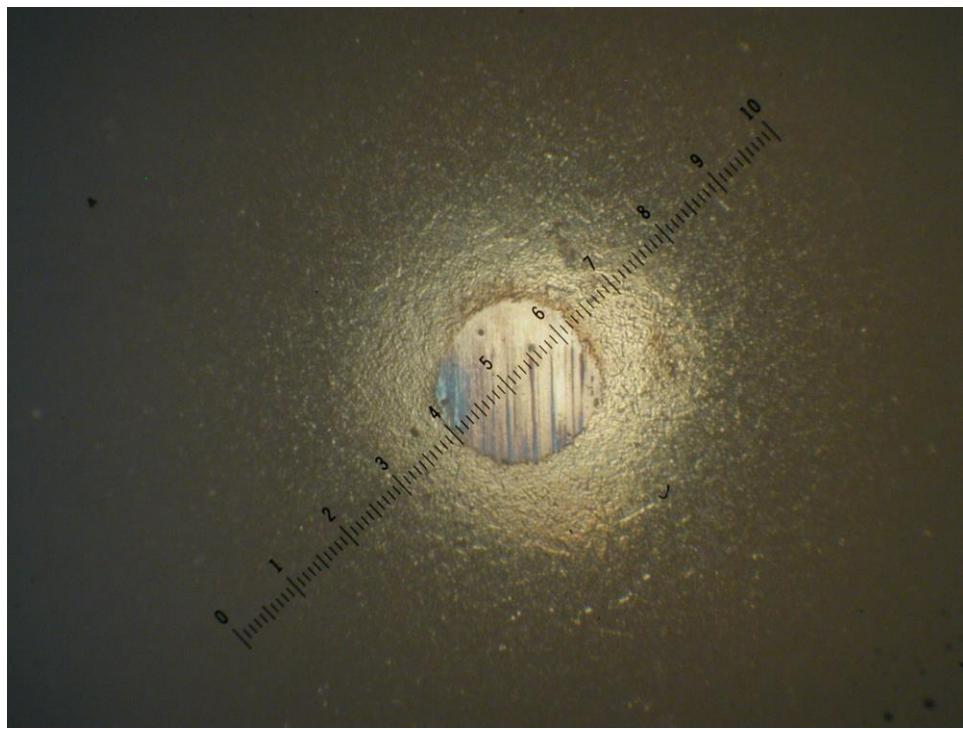
Appendix BoD – Ball-on-Disc Sliding Wear Data



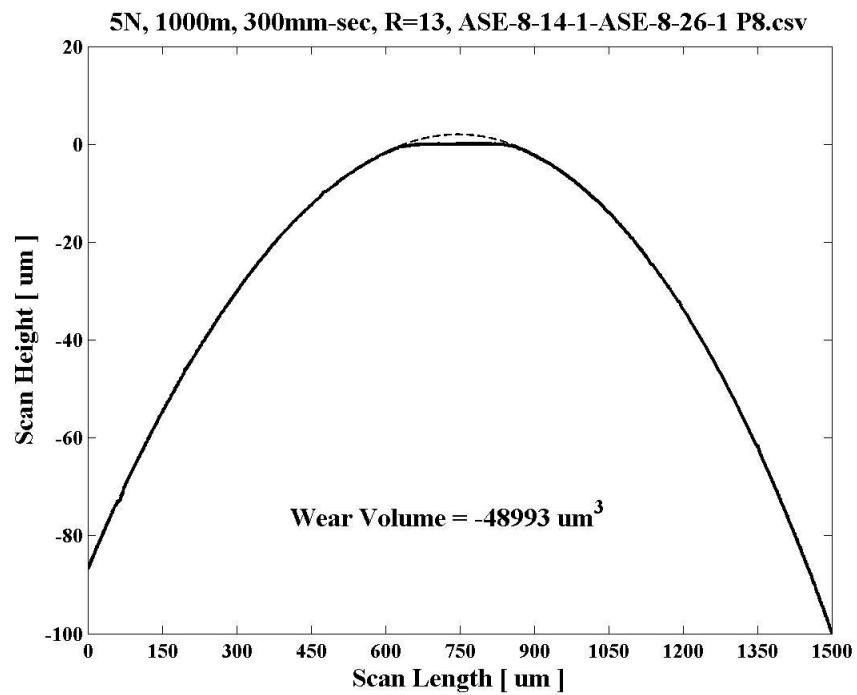
Disc Wear Track Center (above) SEM image @500x
Disc Wear Track Edge (below, non-contact area on left) SEM image @500x
CrC (Disc) vs. TiCr-TiCrN (Ball)
Load = 5N, Distance = 1000m, Speed = 300mm/sec, No Lubrication



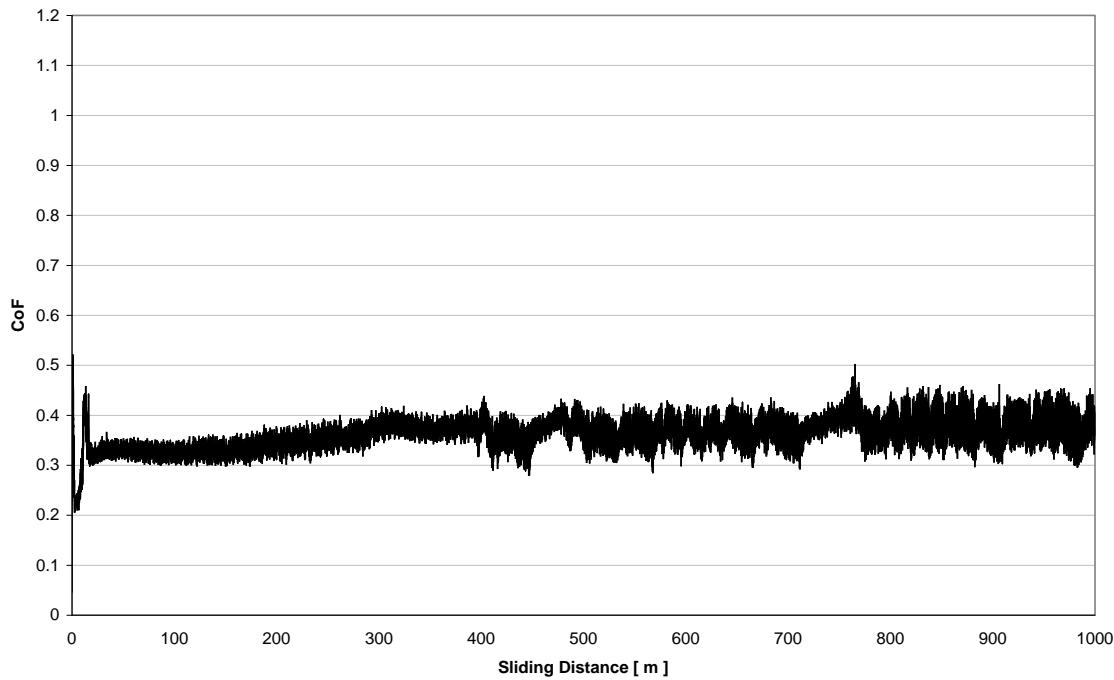
Appendix BoD – Ball-on-Disc Sliding Wear Data



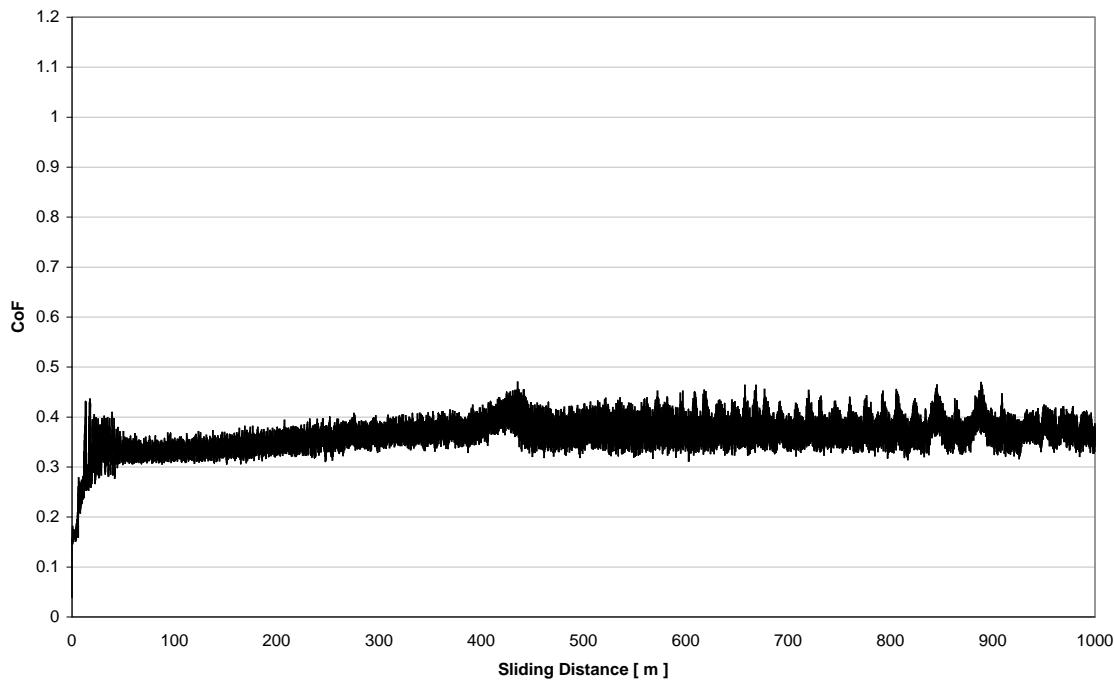
Ball Wear Scar Image and Profile
CrC (Disc) vs. TiCr-TiCrN (Ball)
Load = 5N, Distance = 1000m, Speed = 300mm/sec, No Lubrication



Appendix BoD – Ball-on-Disc Sliding Wear Data

CoF vs. Distance for 5N, 1000m, 300mm-sec, R=13, ASE-8-14-1-ASE-8-19-1 P13.txt

CoF vs. Sliding Distance
CrC (Disc) vs. TiCr-TiCrN (Ball)
Load = 5N, Distance = 1000m, Speed = 300mm/sec, No Lubrication

CoF vs. Distance for 5N, 1000m, 300mm-sec, R=13, ASE-8-14-1-ASE-8-26-1 P8.txt

Appendix CA – Coating Contact Angle (Oil Wet-ability) Data

Coating Hardness and Elastic Modulus Measurement Overview

1. Contact angle measurement is a convenient and useful parameter to determine the surface free energy and wet-ability of any given solid surface due to the non-deformability of the solid. According to the definition, the contact angle is read from the angle formed between substrate surface where a liquid droplet is placed and the tangent to the drop surface from the 3-phase point. The contact angle measurement is a useful and precise empirical technique to determine the interaction between a liquid and a substrate. It must be stated that contact angle is not a property of the liquid or the substrate but the interaction between the two.
2. Contact angle measurements were conducted for coatings in contact with Aeroshell 555 turbine oil (DOD-L-85734A) to determine any possible differences with the baseline uncoated Pyrowear 675 case. No specific performance inferences were made as to small differences in the absolute values of measured contact angles; the aim of the testing was to demonstrate that coatings exist which show similar oil wet-ability characteristics to uncoated Pyrowear 675.
3. A video-based optical contact angle measuring system OCA 20 with software SCA21 manufactured by DataPhysics GmbH was used for contact angle measurement. Future Digital Scientific Corporation (www.FDSC.com) was subcontracted to perform the testing.
4. Coated specimens were placed into a temperature controlled environment chamber at 80 ± 0.5 degree C. The chamber was placed on a sample stage of the OCA 20 device, a 500 μ l micro syringe filled with Aeroshell 555 turbine oil and 0.18 mm diameter dosing needle was used. A Droplet of 3 μ l volume of oil was dispensed at the dosing rate 0.2 μ l per second and deposited on the sample surface. The entire placement procedure of the drop onto the sample surface was recorded using an automated video recording function. A total of 30 seconds of images were captured using a recording rate of 12.5 images/sec. The contact angles were automatically calculated for each image using the ellipse fitting. Average of at least two tests is reported for contact angle of oil on the samples versus drop age.
5. Contact angle testing was conducted as a screening test for aid in down selection of coatings under evaluation for the LiftFan gear application; TiCr-TiCrN, TiCrC, Ti(Si)Cr-Ti(Si)CrN, Ti(Si)CrC, Cr-CrN, and CrC coatings were tested and compared with a baseline uncoated P675 sample.

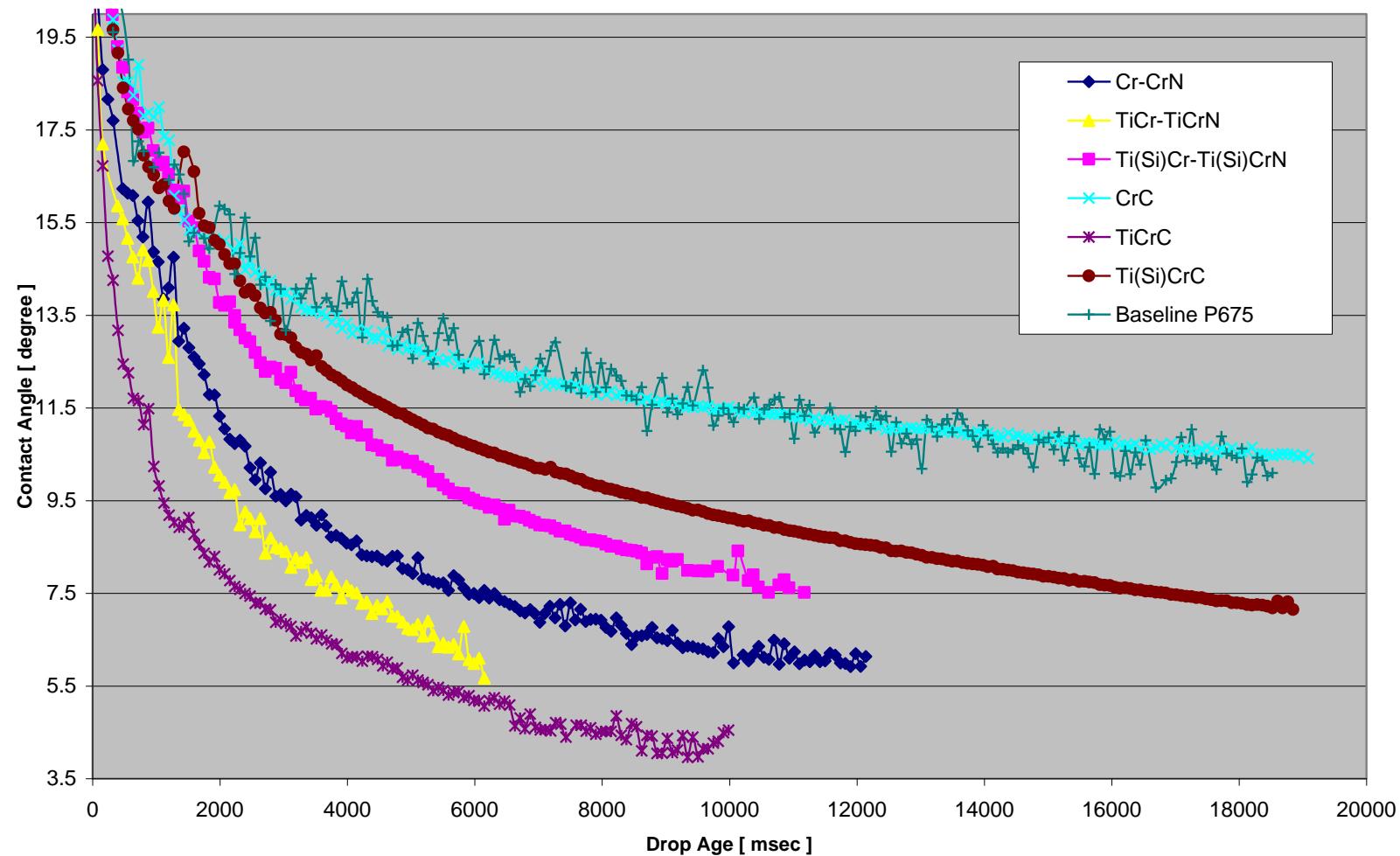
Appendix CA – Coating Contact Angle (Oil Wettability) Data

Contact Angle (Aeroshell 555 oil wet-ability) Results**Substrate - Pyrowear 675 (polished, RMS = 5nm [0.2 μ inch], HRC-64)**

Coating	Coating ID	Sample ID	RMS Roughness [μ m]	Average Contact Angle @ 4sec Drop Age [degree]
n/a	P675 Baseline	C133	0.005	13.8±0.2
CrC	ASE-7-92-1	C34	0.069	13.1±0.6
Ti(Si)CrC	ASE-7-142-1	C88	0.088	11.9±0.0
Ti(Si)Cr-Ti(Si)CrN	ASE-7-133-1	C36	0.102	11.0±0.5
Cr-CrN	ASE-8-5-1	C75	0.062	8.5±0.9
TiCr-TiCrN	ASE-7-136-1	C108	0.070	7.3±1.8
TiCrC	ASE-7-140-1	C40	0.114	6.1±0.7

Aeroshell 555 turbine oil spreads and can be considered to have excellent wet-ability on all samples tested at 80 degree C. Oil wet-ability increases as shown in the table from baseline P675 (highest contact angle, worst wet-ability in sample set) to a TiCrC coating (lowest contact angle, best wet-ability in sample set). The results show that there is not cause for concern for any of the coatings tested in regards to oil wet-ability when compared with the baseline uncoated Pyrowear 675 oil wet-ability.

Appendix CA – Coating Contact Angle (Oil Wettability) Data

Contact angle of Aeroshell 555 oil at 80 degree C

Appendix H-E – Coating Hardness and Elastic Modulus Data

Coating Hardness and Elastic Modulus Measurement Overview

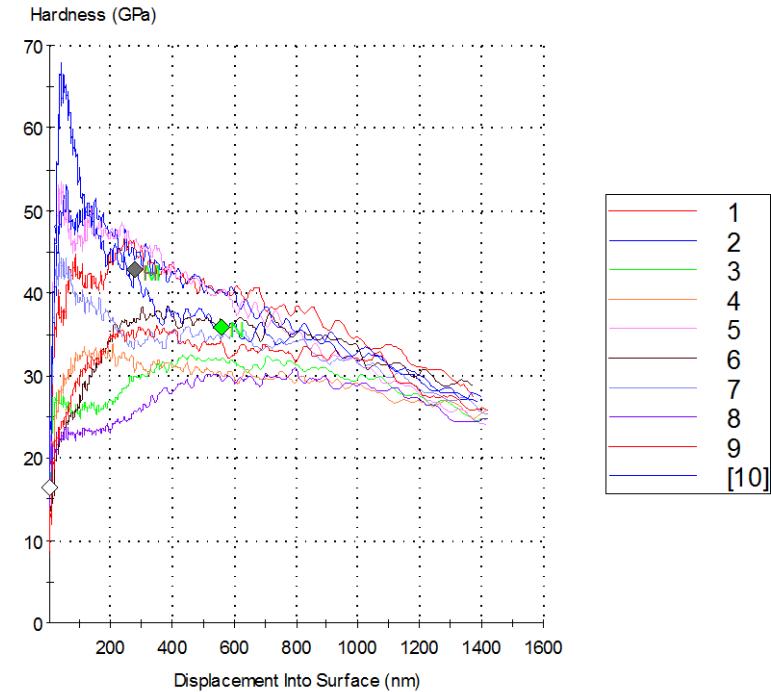
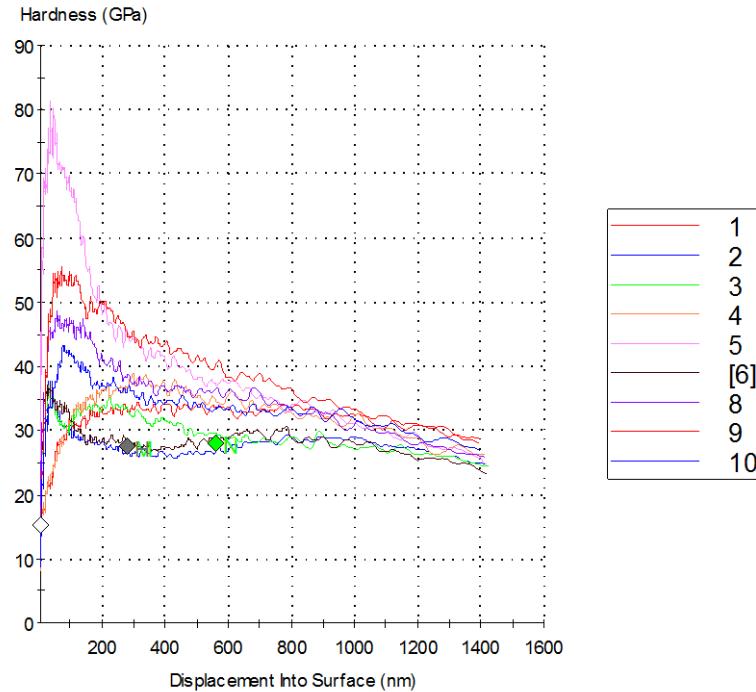
1. Instrumented Indentation Testing (IIT) is conducted per ISO/DIS 14577-4 for determination of coating hardness and elastic modulus. A MTS Nanoindenter XP is used with a Continuous Stiffness Measurement (CSM) module and a standard Berkovich tip. The CSM option allows for the continuous measurement of contact stiffness during loading, not just at the point of initial unload. This is accomplished by superimposing a small oscillation on the primary loading signal and analyzing the resulting response of the system by means of a frequency-specific amplifier. With a continuous measure of contact stiffness one obtains the hardness and elastic modulus as a continuous function of depth from a single indentation experiment.
2. Elastic modulus is calculated for all coatings with the assumption that Poisson's ratio $\nu=0.25$ since this value is unknown.
3. To improve the statistical viability of collected data for each coated sample measured, qty(10) indent locations are visually located using a 250x microscope to avoid coating defects and spaced at least 50 μm apart to avoid indent interaction. Hardness and modulus data are collected as a function of indenter penetration depth into the coating at a rate of 5datapoints/sec, on average about 1000 datapoints are collected for each measured parameter for a given indent. Coating thickness is directly measured on each sample using the CALOTest method. To minimize any substrate effects hardness and modulus data for each indent are reported as an average which is calculated over the range of %5-10% of the total coating thickness. The final coating hardness and modulus reported for a given sample represent the average of the qty(10) indents performed with percent covariance reported to indicate the statistical scatter in the data.
4. For each coating qty(2) P675 polished samples were measured. Super-finished P675 samples were not measured as the increased coating roughness results in greater data scatter.

Appendix H-E – Coating Hardness and Elastic Modulus Data

Hardness and Elastic Modulus Results**Substrate - Pyrowear 675 (polished, RMS = 5nm [0.2μinch], HRC-64)**

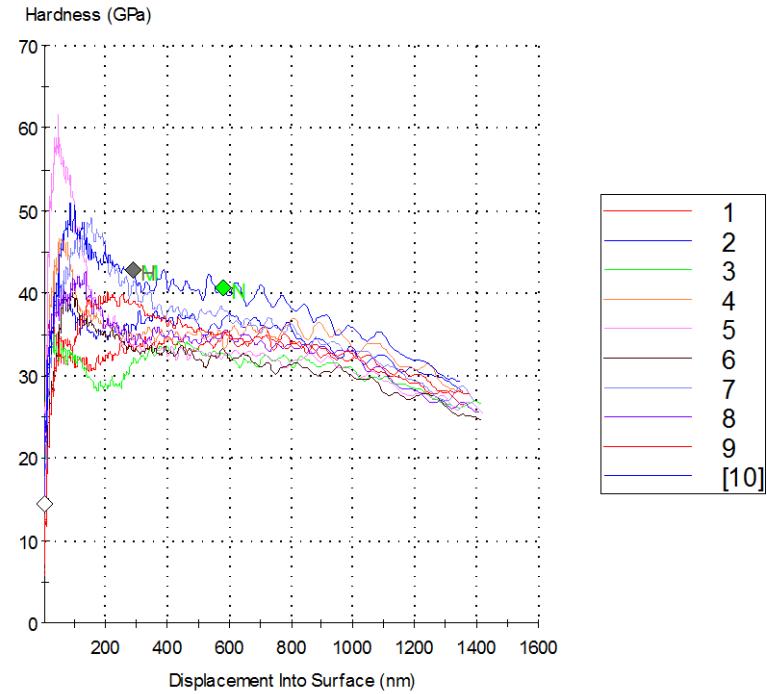
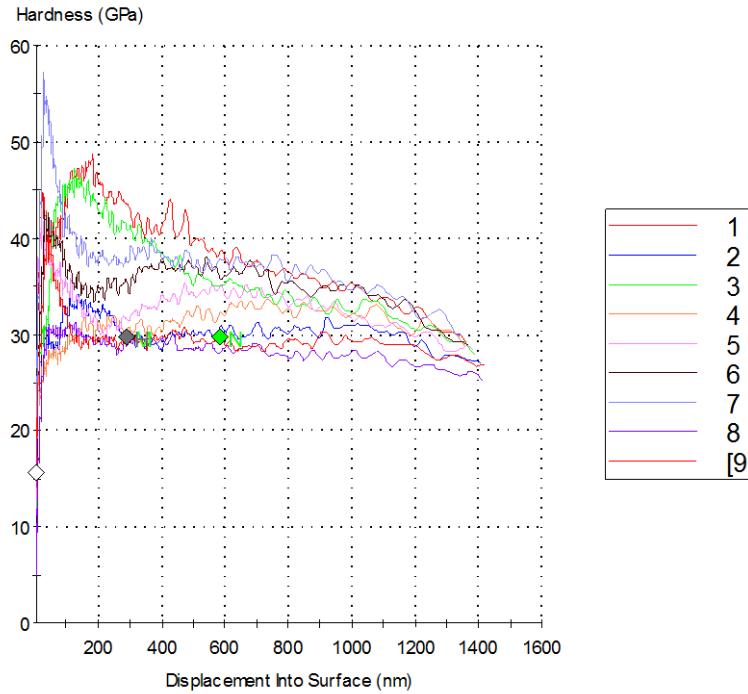
Coating	Coating ID	Sample ID	Thickness [μm]	RMS Roughness [μm]	Hardness [GPa]	Elastic Modulus [GPa]	H/E
TiCr-TiCrN	ASE-8-9-1 (Run1)	C144	5.6	0.097	34.5 +/- 5.6	401 +/- 44	0.086
TiCr-TiCrN	ASE-8-9-1 (Run1)	C148	5.6	0.112	36.3 +/- 5.3	430 +/- 42	0.084
TiCr-TiCrN	ASE-8-14-1 (Run2)	C93	5.8	0.124	34.1 +/- 4.5	404 +/- 36	0.084
TiCr-TiCrN	ASE-8-14-1 (Run2)	C78	5.8	0.086	35.5 +/- 2.7	429 +/- 31	0.083
TiCr-TiCrN	average		5.7	0.105	35.1 +/- 4.5	416 +/- 38	0.084
Cr-CrN	ASE-8-29-1 (Run1)	C138	6.3	0.084	27.3 +/- 2.7	329 +/- 25	0.083
Cr-CrN	ASE-8-29-1 (Run1)	C28	6.3	0.046	27.6 +/- 3.7	328 +/- 33	0.084
Cr-CrN	ASE-8-34-1 (Run2)	C152	6	0.076	26.2 +/- 2.4	321 +/- 24	0.082
Cr-CrN	ASE-8-34-1 (Run2)	C161	6	0.051	26.8 +/- 2.7	322 +/- 28	0.083
Cr-CrN	average		6.2	0.064	27.0 +/- 2.9	325 +/- 28	0.083
CrC	ASE-8-19-1 (Run1)	C81	6.3	0.164	33.5 +/- 5.3	446 +/- 57	0.075
CrC	ASE-8-19-1 (Run1)	C18	6.3	0.067	31.2 +/- 3.7	423 +/- 41	0.074
CrC	ASE-8-26-1 (Run2)	C63	5.4	0.102	32.8 +/- 3.7	434 +/- 43	0.076
CrC	ASE-8-26-1 (Run2)	C167	5.4	0.038	31.1 +/- 3.5	411 +/- 35	0.076
CrC	average		5.9	0.093	32.2 +/- 4.1	429 +/- 44	0.075

Appendix H-E – Coating Hardness and Elastic Modulus Data



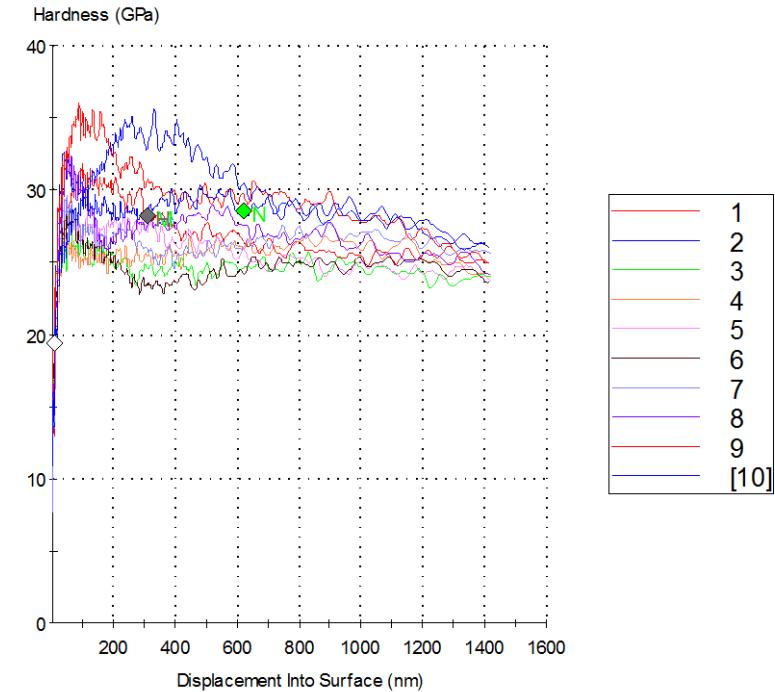
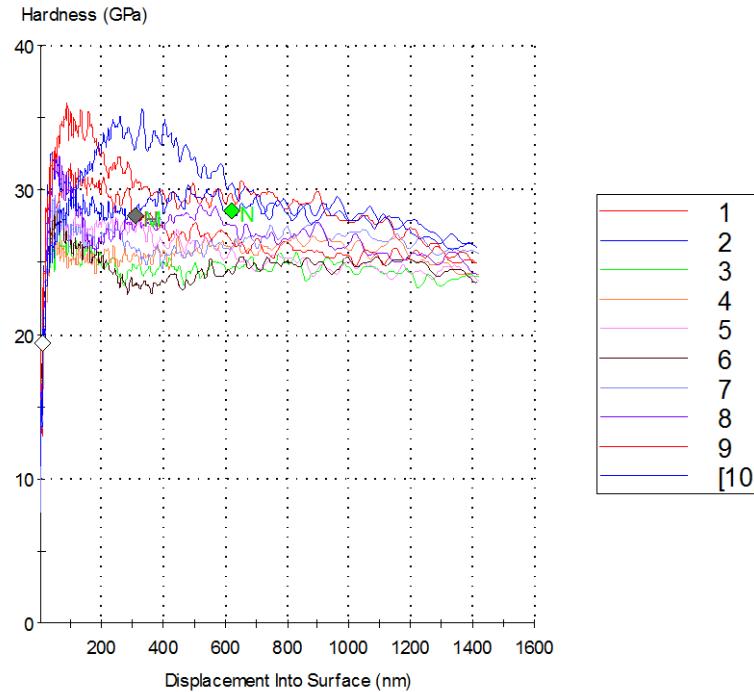
Hardness vs. Depth Plots for TiCr-TiCrN (Run1)
ASE-8-9-1 C144, C148

Appendix H-E – Coating Hardness and Elastic Modulus Data



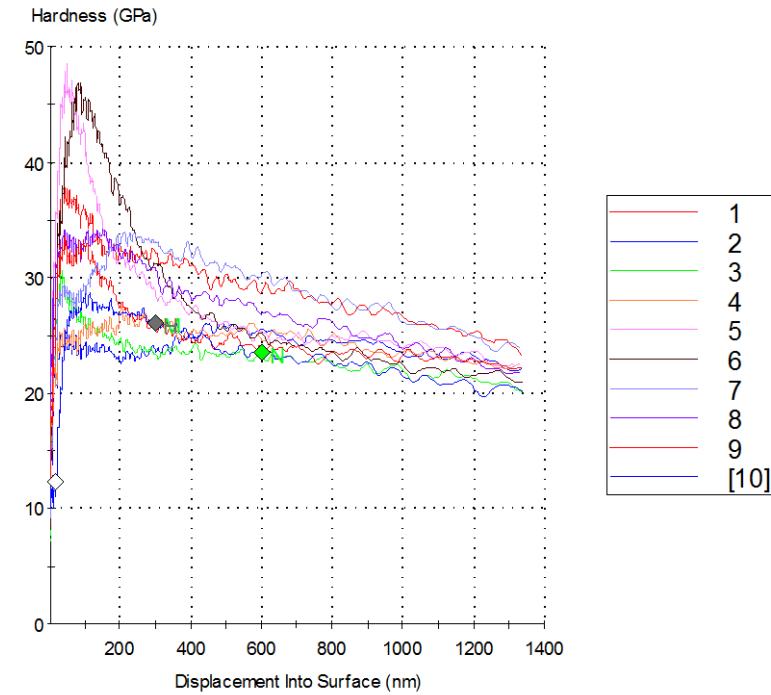
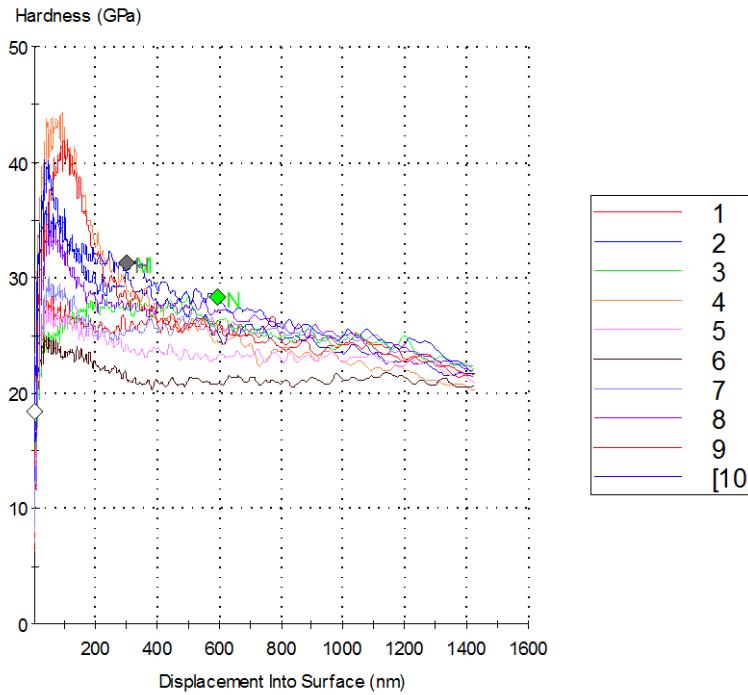
Hardness vs. Depth Plots for TiCr-TiCrN (Run2)
ASE-8-14-1 C93, C78

Appendix H-E – Coating Hardness and Elastic Modulus Data



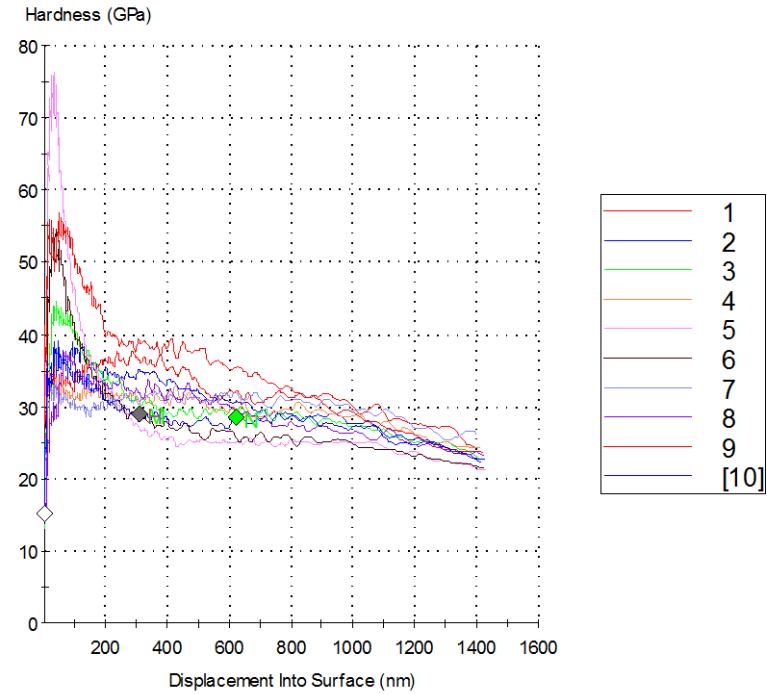
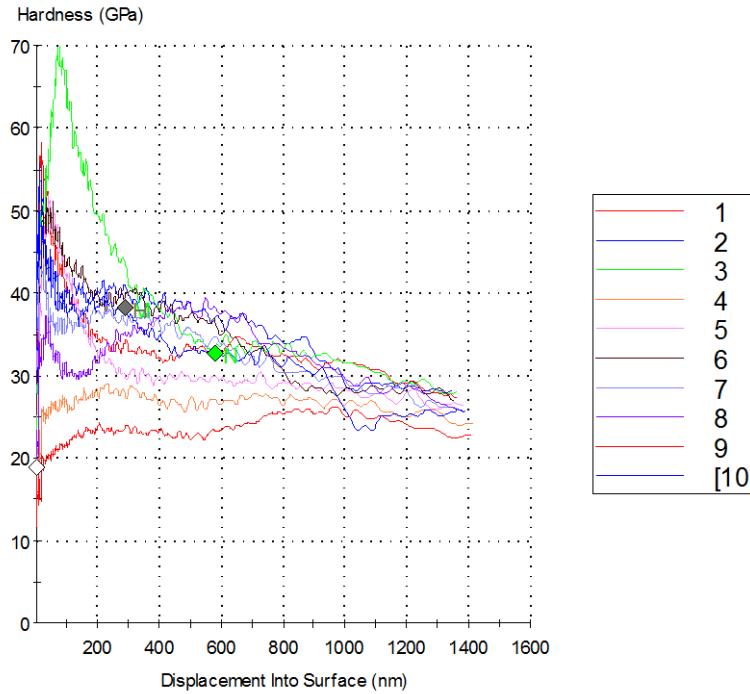
Hardness vs. Depth Plots for Cr-CrN (Run1)
ASE-8-29-1 C138, C28

Appendix H-E – Coating Hardness and Elastic Modulus Data



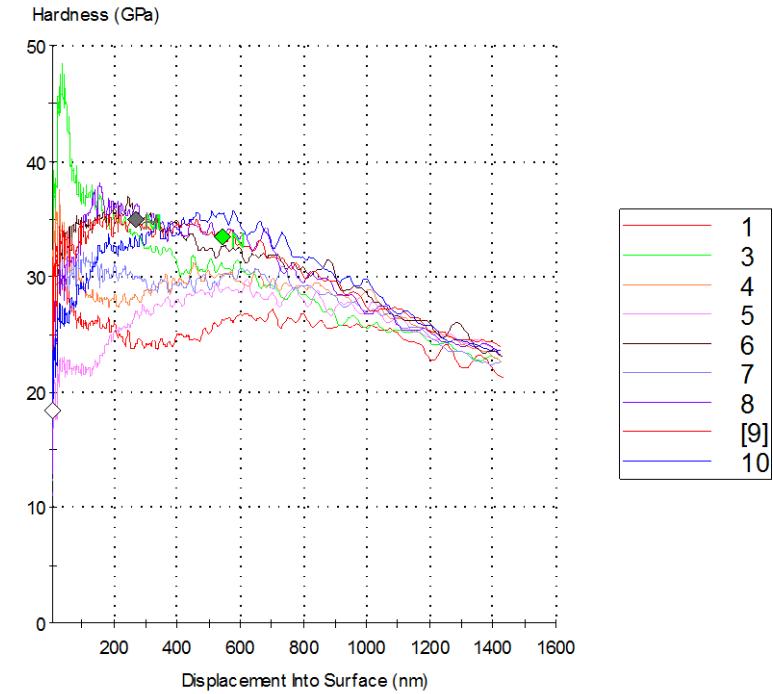
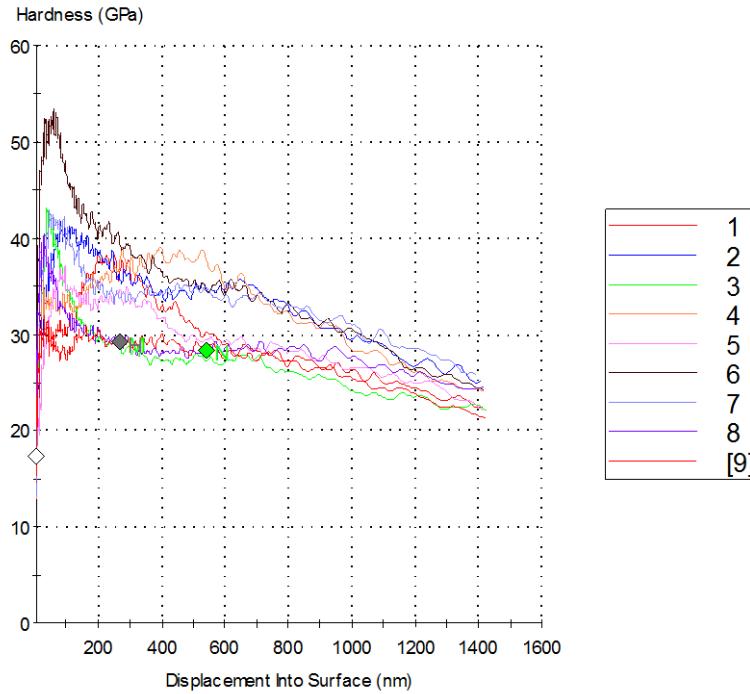
Hardness vs. Depth Plots for Cr-CrN (Run2)
ASE-8-34-1 C152, C161

Appendix H-E – Coating Hardness and Elastic Modulus Data



Hardness vs. Depth Plots for CrC (Run1)
ASE-8-19-1 C81, C18

Appendix H-E – Coating Hardness and Elastic Modulus Data



Hardness vs. Depth Plots for CrC (Run2)
ASE-8-26-1 C63, C167

Appendix HF – Rockwell Indent Adhesion Data

Rockwell Indent Adhesion Test Overview

1. This test consists of indenting a coated specimen under the standard Rockwell C testing protocol and qualitatively assessing and rating coating damage induced by plastic deformation of the substrate. A 120° angle diamond Rockwell C indenter with a 200 μm tip radius is indented with a force of 1470N per ASTM E18-08a standard which causes a repeatable deformation strain in the coating that can result in adhesive and/or cohesive coating failure modes. It should be noted that Rockwell indent adhesion results can only be correctly compared between coatings on substrates of equivalent hardness, comparison between substrates of different hardness is not advised as coating strain is inversely related to substrate hardness.
2. Rockwell indent adhesion is also referred to as HF adhesion and Mercedes Adhesion. The test was developed and documented by H. Jehn, et al, and has become a coating industry standard for simple qualitative assessment of coating adhesion/cohesion strength. The original reference in German which provides the guidelines for rating coating damage on a scale of HF1..HF6 is cited below.

H. Jehn, G. Reiners, N. Siegel, DIN-Fachbericht(Special Report) 39, Charakterisierung duenner Schichten
(Characterization of thin layers), Beuth-Verlag, Berlin, 1993.

3. Damage assessment is performed using an optical microscope at 75x and 150x magnifications, where the variable “a” is defined as the radius of the indent. For example, if coating cracking is reported to extend to a distance of “1.5a” this implies that the crack extends from the indent edge to a distance of 1.5a as measured from the center of the indent. Damage assessment is performed only for regions directly outside of the indent edge; damage inside the indent is usually severe, does not provide for repeatable comparisons, and cannot be imaged by optical microscopes due to a lack of reflected light.
 - a. **HF1** - No signs of delamination (cohesive or adhesive), radial or circumferential cracks to distances less than 1.5a
 - b. **HF2** - No signs of delamination (cohesive or adhesive), significant portion of radial or circumferential cracks extending past 1.5a
 - c. **HF3** - Cohesive delamination to distances less than 1.5a and covering less than 25% of the surface area within the 1.5a radius, no signs of adhesive delamination, radial or circumferential cracks to any distance and density
 - d. **HF4** - Significant cohesive delamination covering more than 25% of the area within the 1.5a radius and/or to distances greater than 1.5a, no signs of adhesive delamination, radial or circumferential cracks to any distance and density
 - e. **HF5** – Any evidence of adhesive delamination, any severity of cohesive failure, any severity of cracking
 - f. **HF6** - Instances where severe adhesive delamination occurs at the substrate interface and covers a significant area surrounding the indent

Appendix HF – Rockwell Indent Adhesion Data

HF Ratings**Substrate - Pyrowear 675 (polished, RMS = 5nm [0.2μinch], HRC-64)**

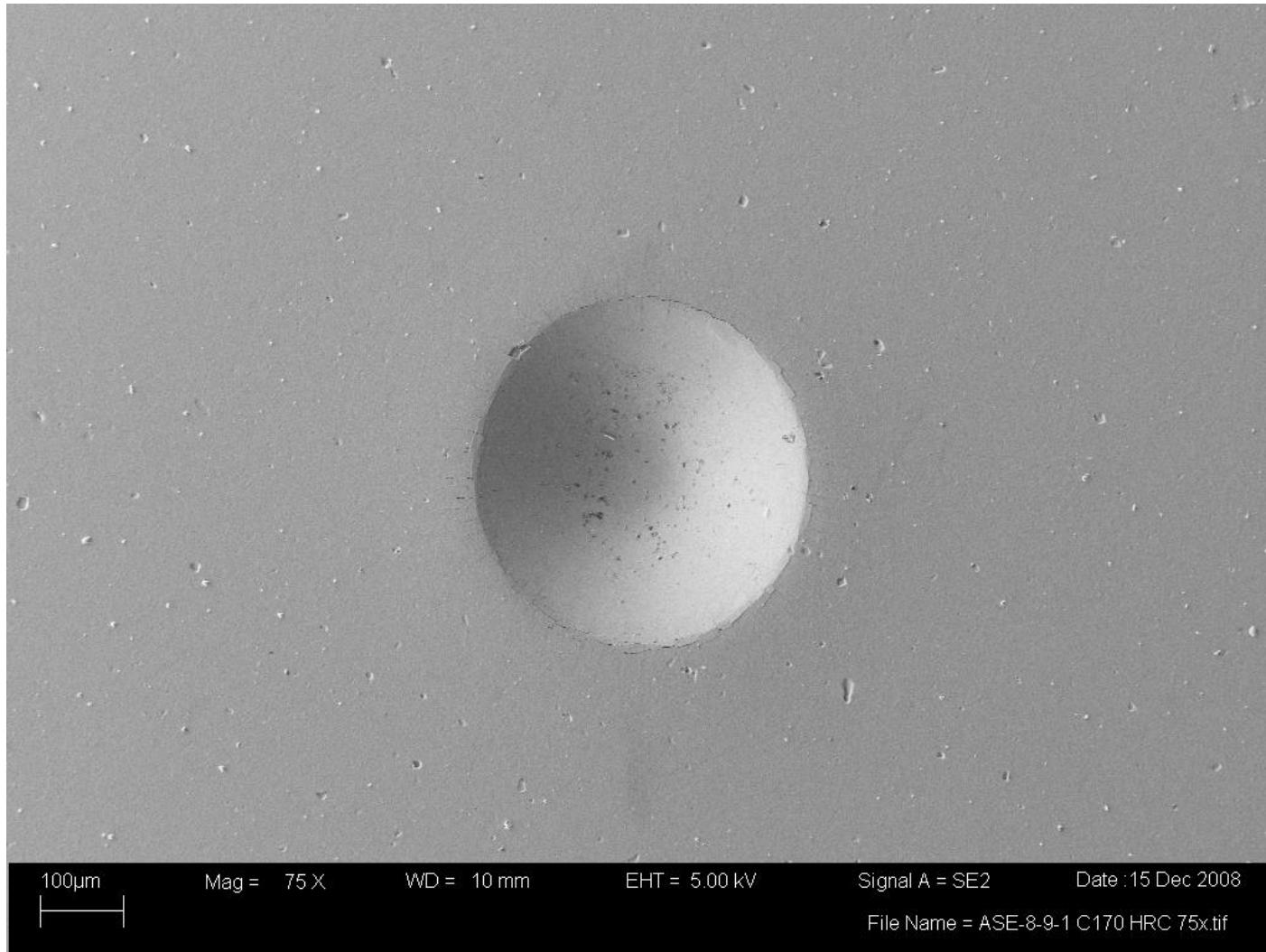
Coating	Coating ID	Sample ID	Thickness [μm]	HF1-HF6 Rating	Appendix Page SEM Image @75x	Appendix Page SEM Image @250x
TiCr-TiCrN	ASE-8-9-1 (Run1)	C170	5.6	HF1	HF_3	HF_4
TiCr-TiCrN	ASE-8-14-1 (Run2)	C78	5.8	HF1	HF_5	HF_6
Cr-CrN	ASE-8-29-1 (Run1)	C33	6.3	HF1	HF_9	HF_10
Cr-CrN	ASE-8-34-1 (Run2)	C79	6	HF3	HF_13	HF_14
CrC	ASE-8-19-1 (Run1)	C81	6.3	HF1	HF_17	HF_18
CrC	ASE-8-26-1 (Run2)	C60	5.4	HF1	HF_21	HF_22

HF Ratings**Substrate - Pyrowear 675 (REM super-finish, RMS = 50nm [2μinch], HRC-64)**

Coating	Coating ID	Sample ID	Thickness [μm]	HF1-HF6 Rating	Appendix Page SEM Image @75x	Appendix Page SEM Image @250x
TiCr-TiCrN	ASE-8-14-1 (Run2)	P20	5.8	HF3	n/a	n/a
TiCr-TiCrN	ASE-8-14-1 (Run2)	P76	5.8	HF3	HF_7	HF_8
Cr-CrN	ASE-8-29-1 (Run1)	P9	6.3	HF1	n/a	n/a
Cr-CrN	ASE-8-29-1 (Run1)	P56	6.3	HF1	HF_11	HF_12
Cr-CrN	ASE-8-34-1 (Run2)	P70	6	HF1	HF_15	HF_16
Cr-CrN	ASE-8-34-1 (Run2)	P41	6	HF1	n/a	n/a
CrC	ASE-8-19-1 (Run1)	P45	6.3	HF1	HF_19	HF_20
CrC	ASE-8-19-1 (Run1)	P13	6.3	HF1	n/a	n/a
CrC	ASE-8-26-1 (Run2)	P42	5.4	HF1	HF_23	HF_24
CrC	ASE-8-26-1 (Run2)	P8	5.4	HF1	n/a	n/a

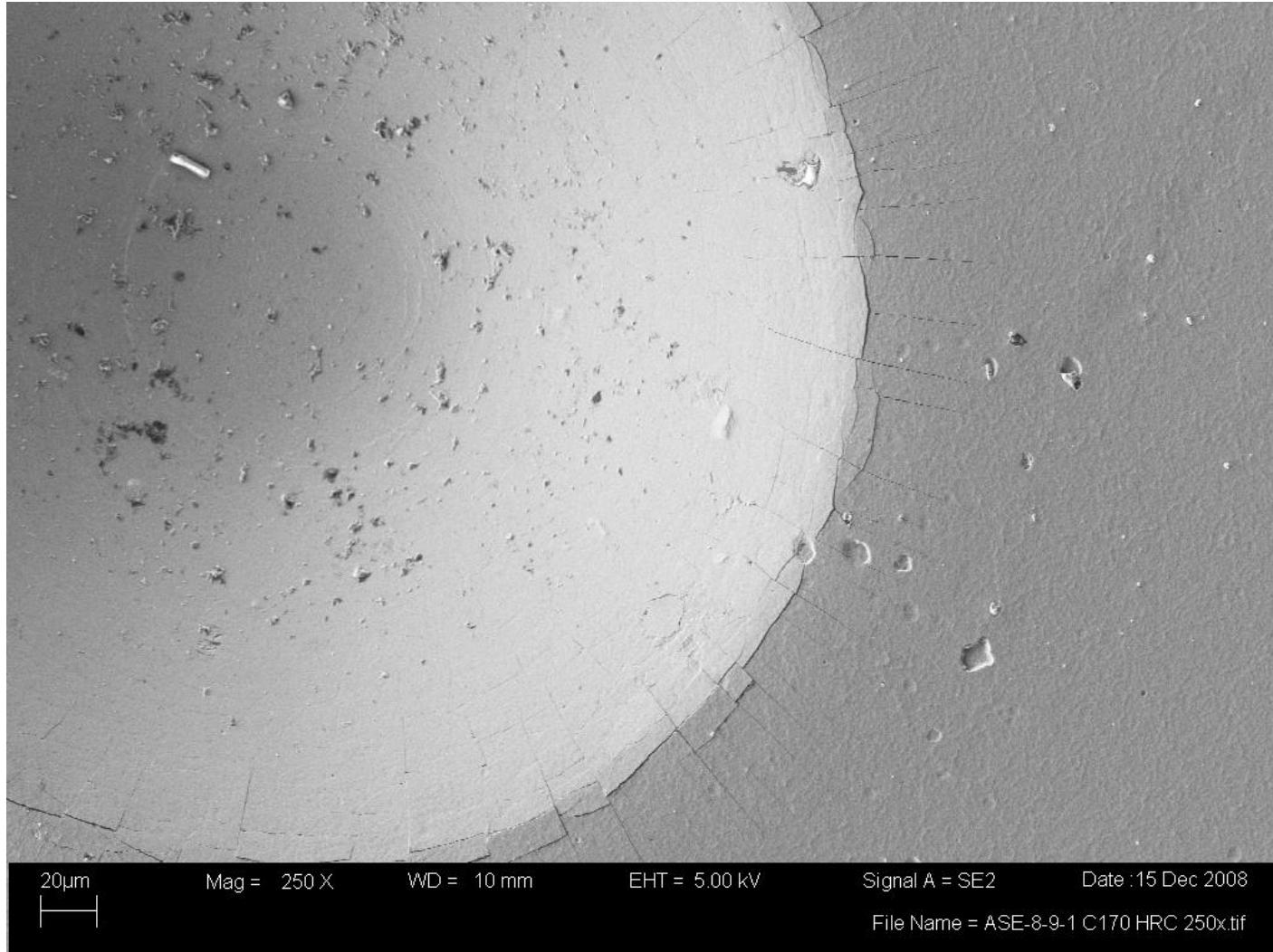
NOTE – HF ratings were assessed normally through observation by optical microscope, SEM images of indents are provided in order to show representative failure modes for each coating type in better quality and resolution than possible with an optical microscope.

Appendix HF – Rockwell Indent Adhesion Data



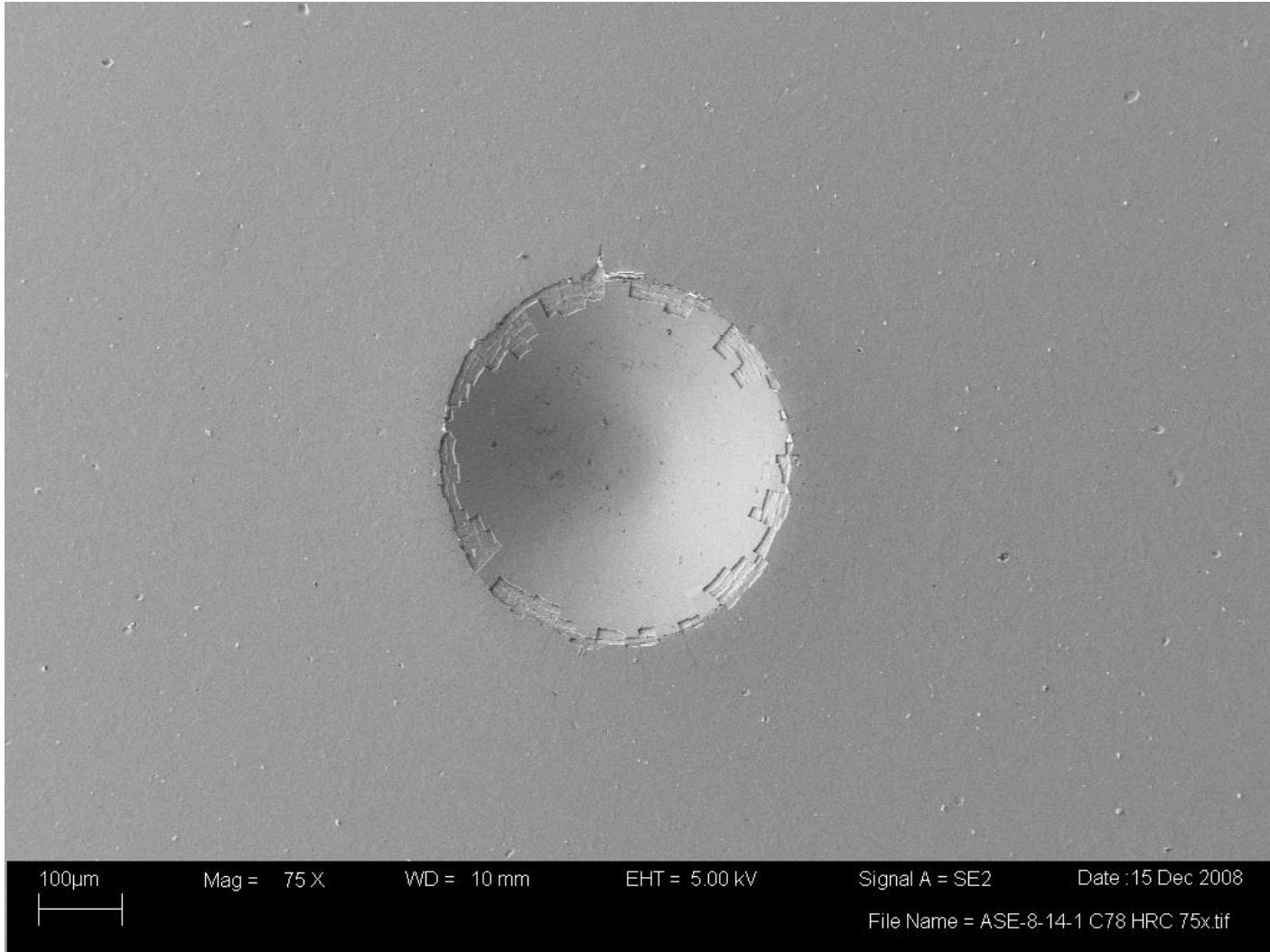
SEM image @ 75x: TiCr-TiCrN (Run1) on P675 (polished), HF1 (singular edge chip ignored)

Appendix HF – Rockwell Indent Adhesion Data



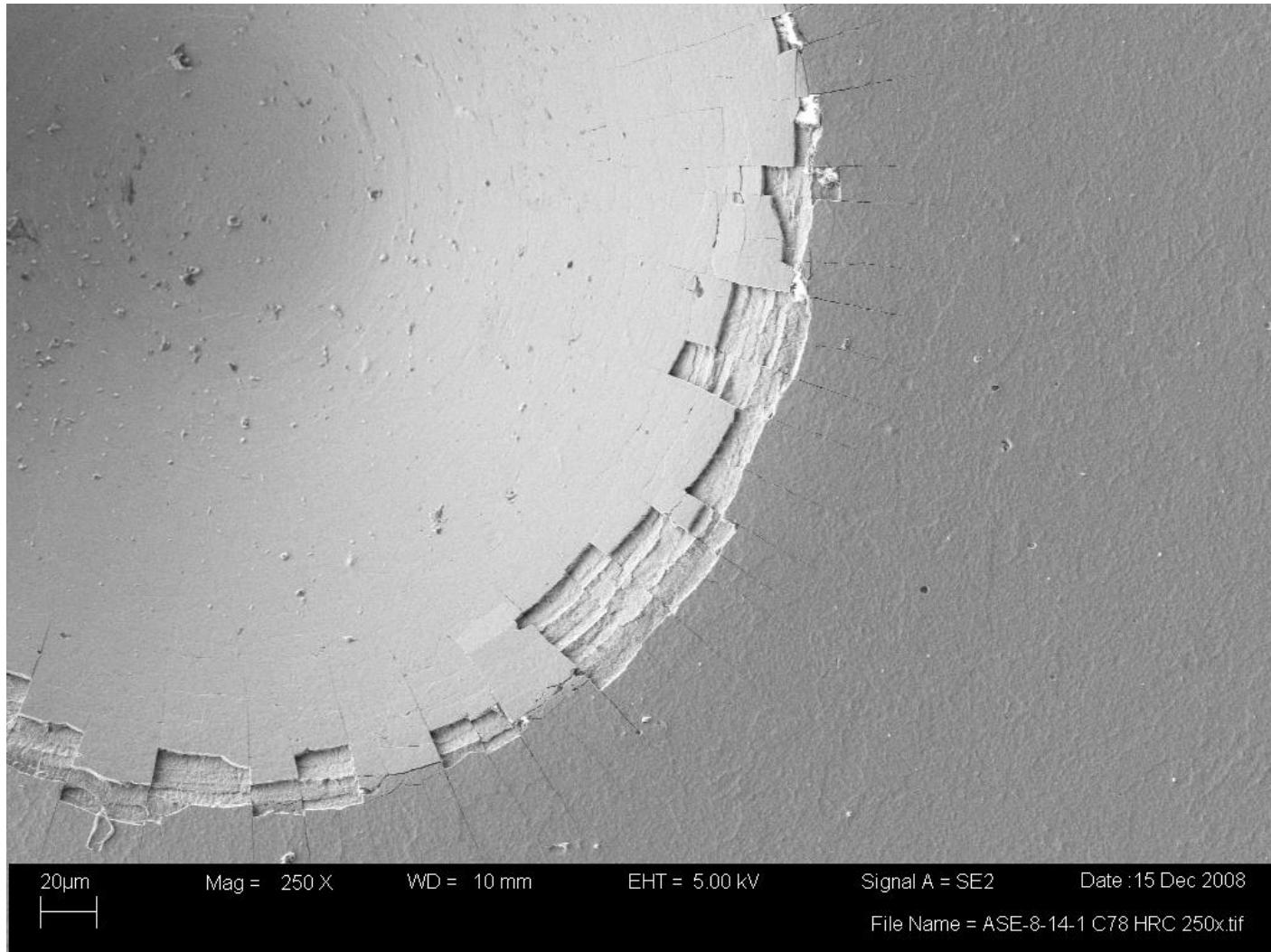
SEM image @ 250x: TiCr-TiCrN (Run1) on P675 (polished), HF1, minor radial cracking to distances <1.25a, minor chipping at indent edge.

Appendix HF – Rockwell Indent Adhesion Data



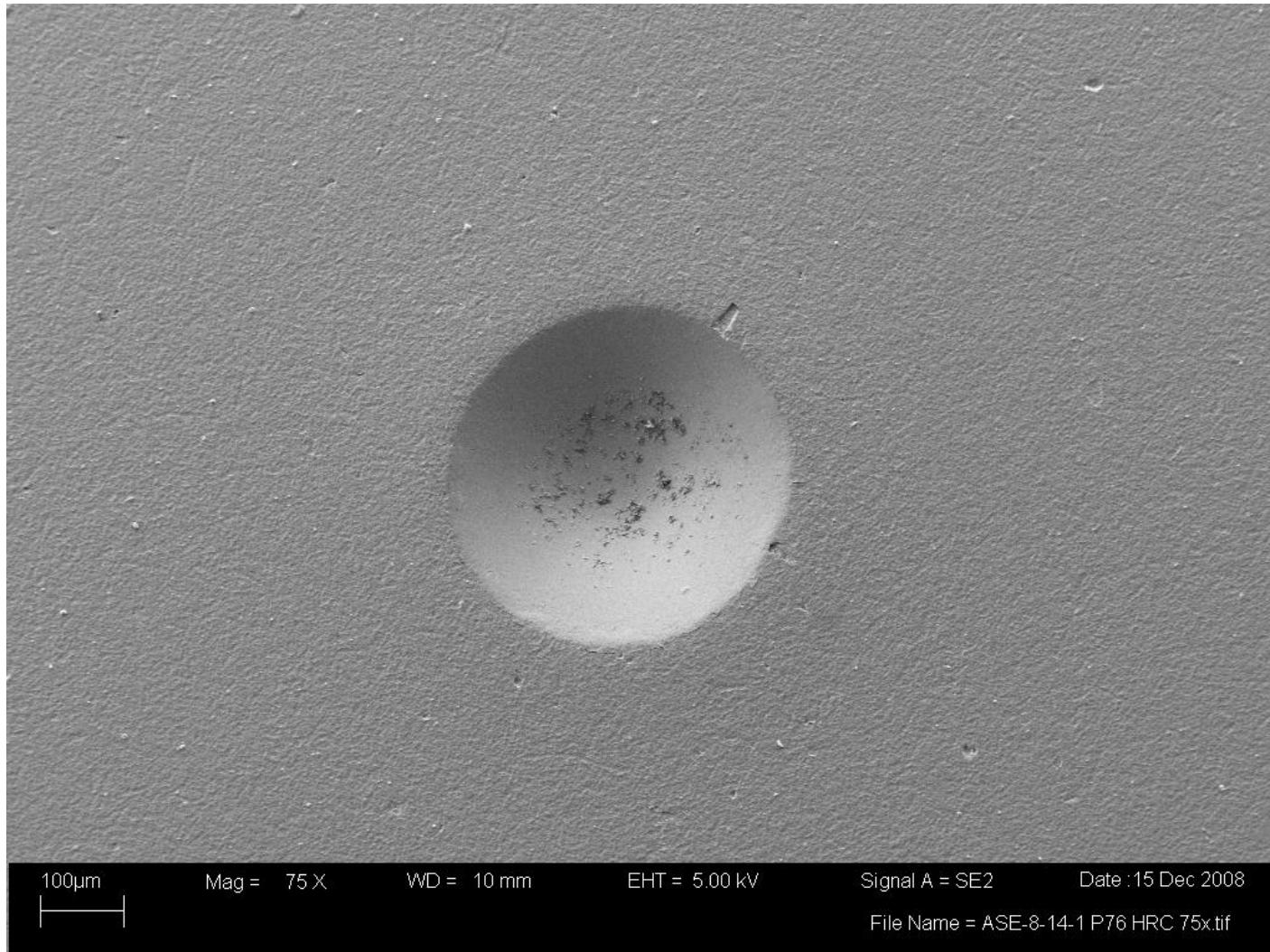
SEM image @ 75x: TiCr-TiCrN (Run2) on P675 (polished), HF1 (singular edge chip ignored)

Appendix HF – Rockwell Indent Adhesion Data



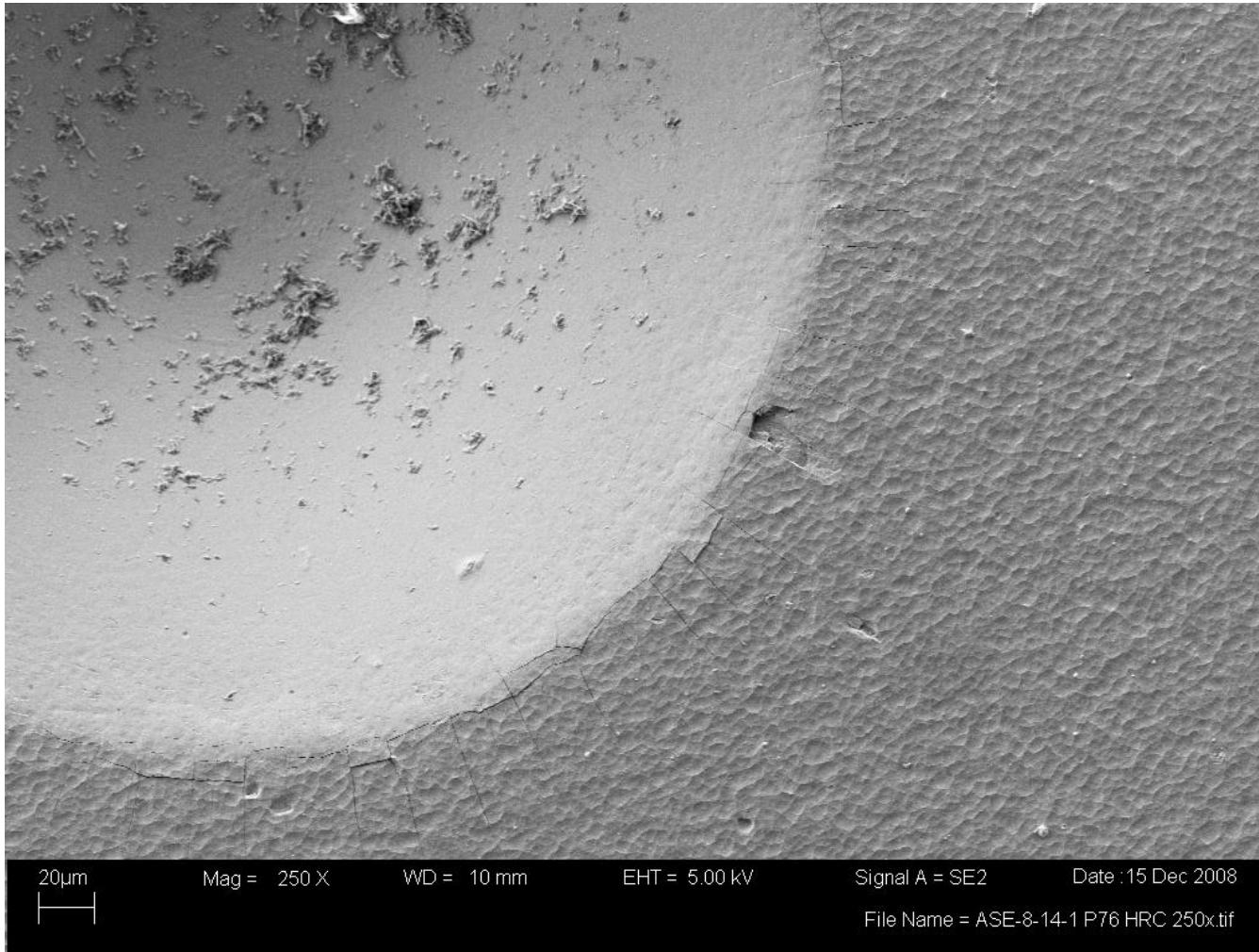
SEM image @ 250x: TiCr-TiCrN (Run2) on P675 (polished), HF1, minor radial cracking to distances <1.25a, minor chipping at indent edge, noted cohesive delamination inside the indent (features at indent edge or inside indent are not part of HF rating).

Appendix HF – Rockwell Indent Adhesion Data



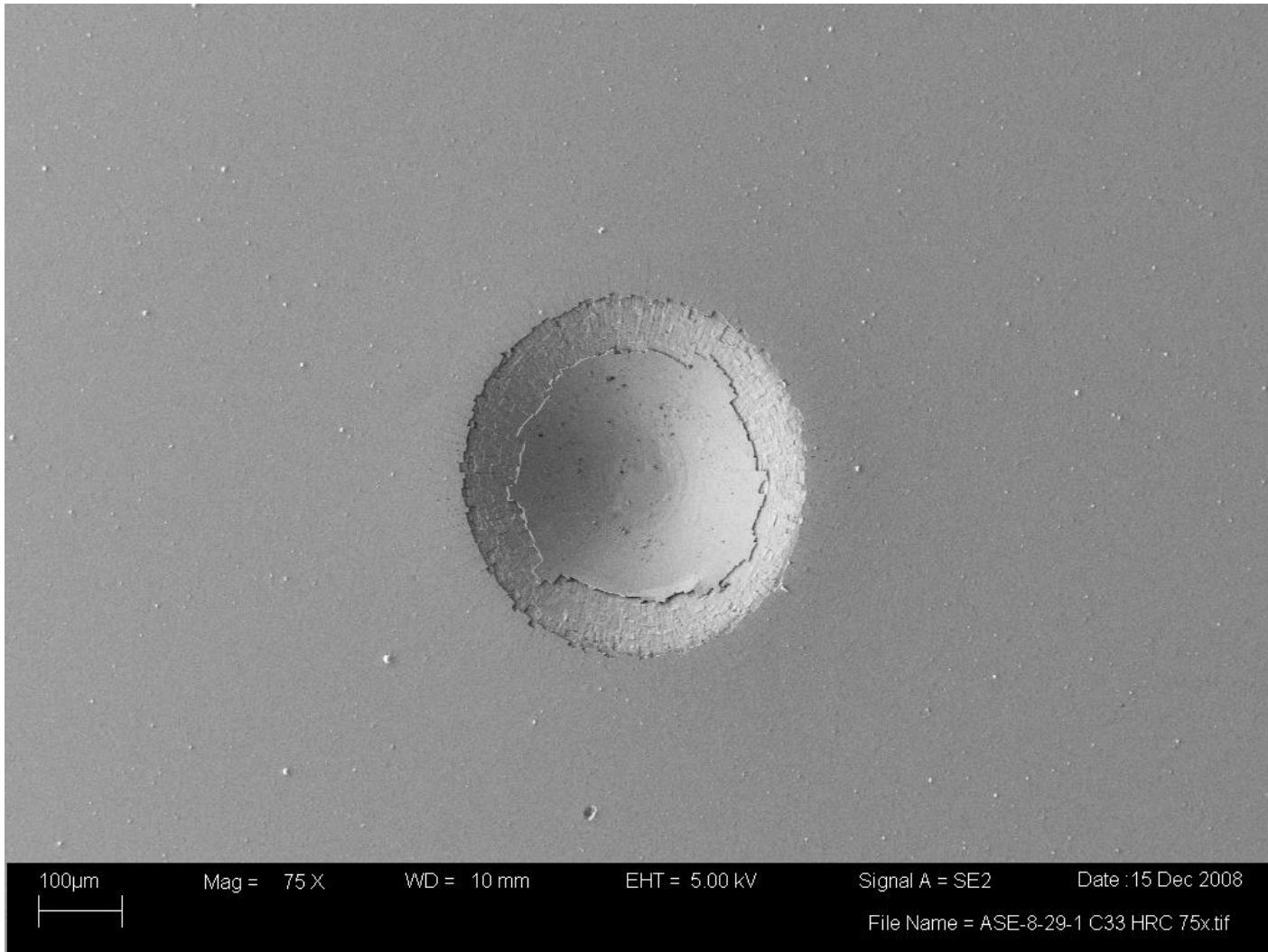
SEM image @ 75x: TiCr-TiCrN (Run2) on P675 (super-finished), HF3 (singular edge chip, otherwise HF1)

Appendix HF – Rockwell Indent Adhesion Data



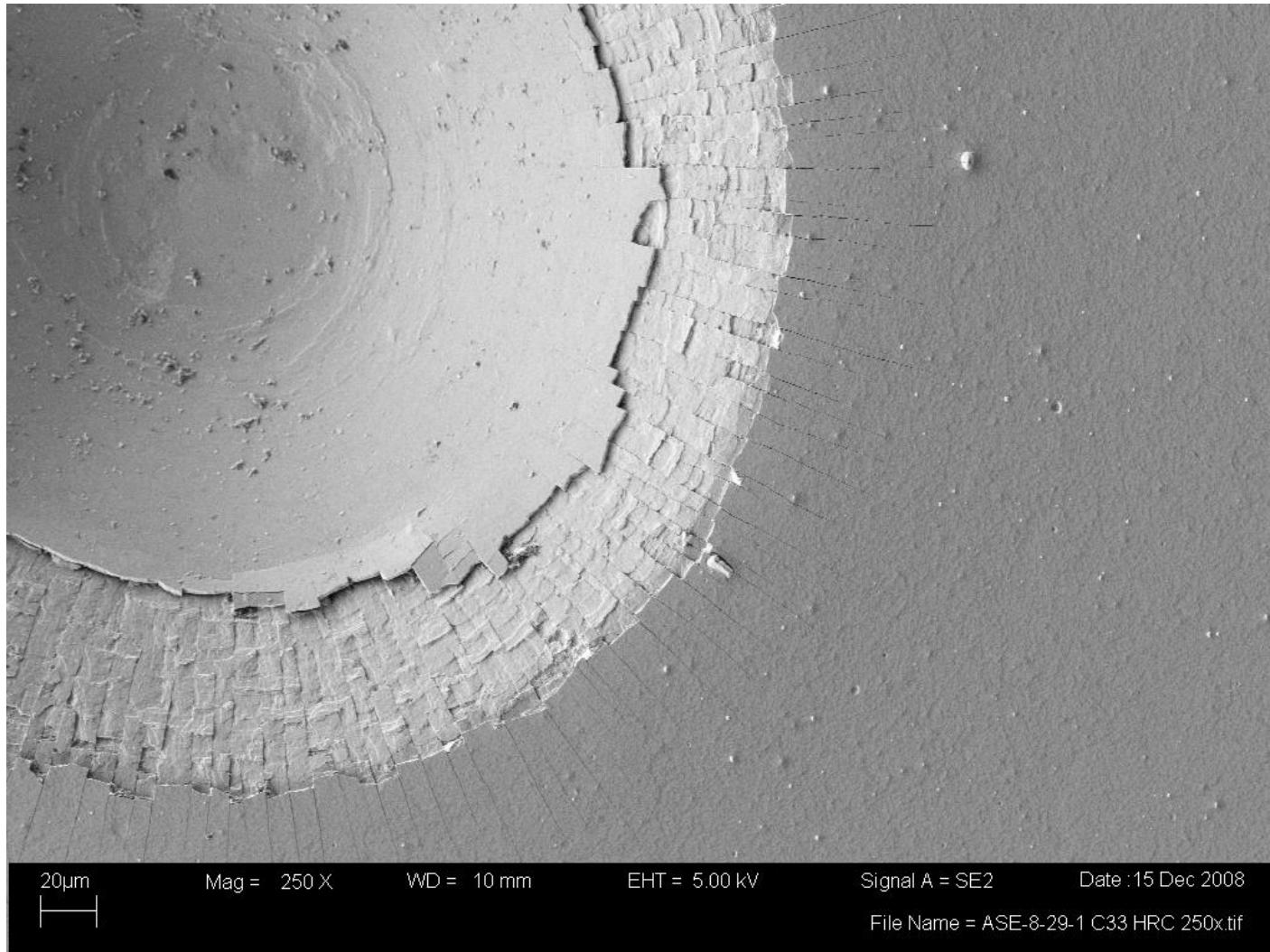
SEM image @ 250x: TiCr-TiCrN (Run2) on P675 (super-finished), HF3, minor radial cracking to distances <1.25a, minor chipping at indent edge, two small cohesive delaminations (1 shown) resulted in HF3 rating noted minimal cracking and no delamination inside indent.

Appendix HF – Rockwell Indent Adhesion Data



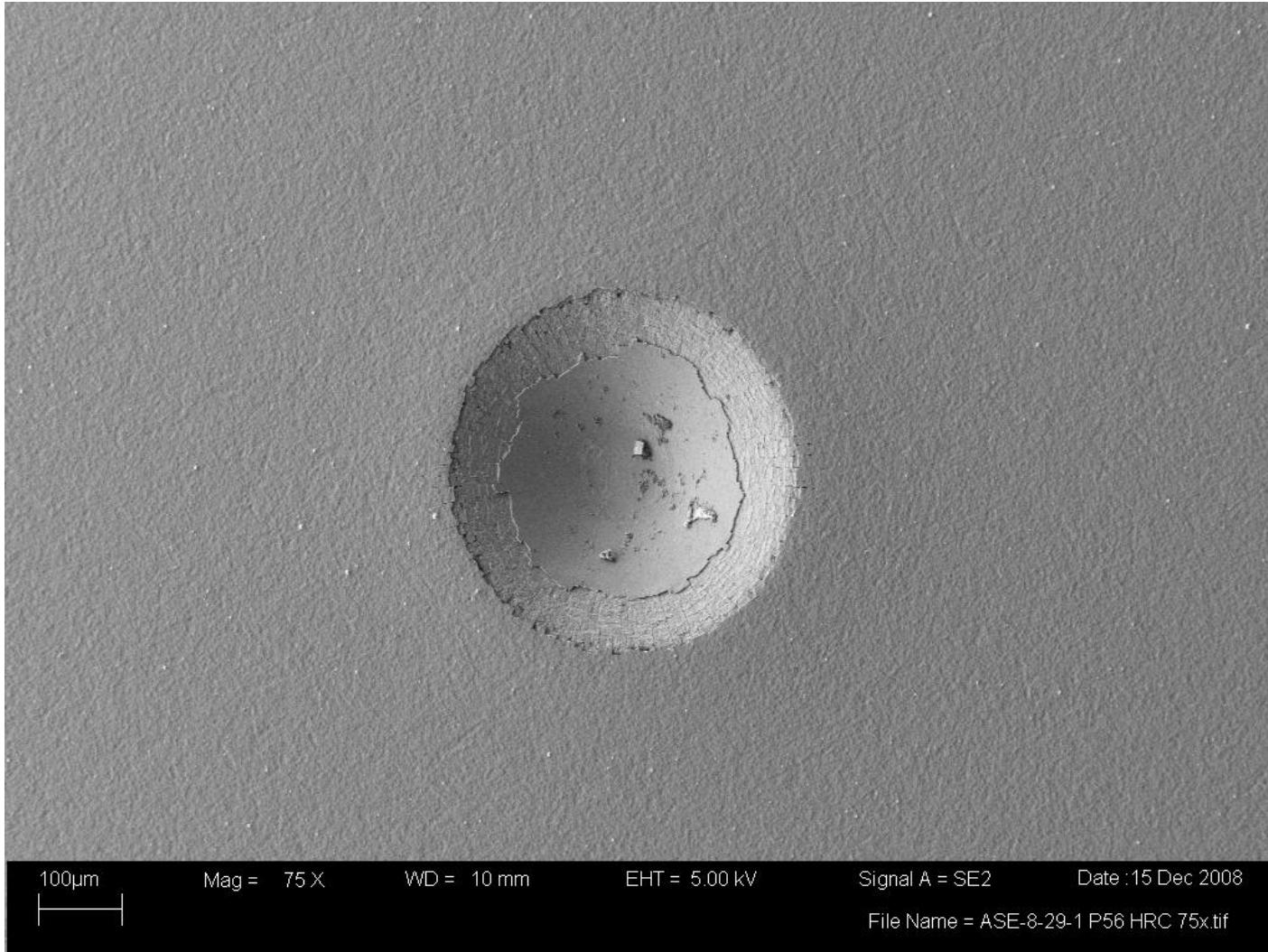
SEM image @ 75x: Cr-CrN (Run1) on P675 (polished), HF1 (damage features inside indent not part of HF rating)

Appendix HF – Rockwell Indent Adhesion Data



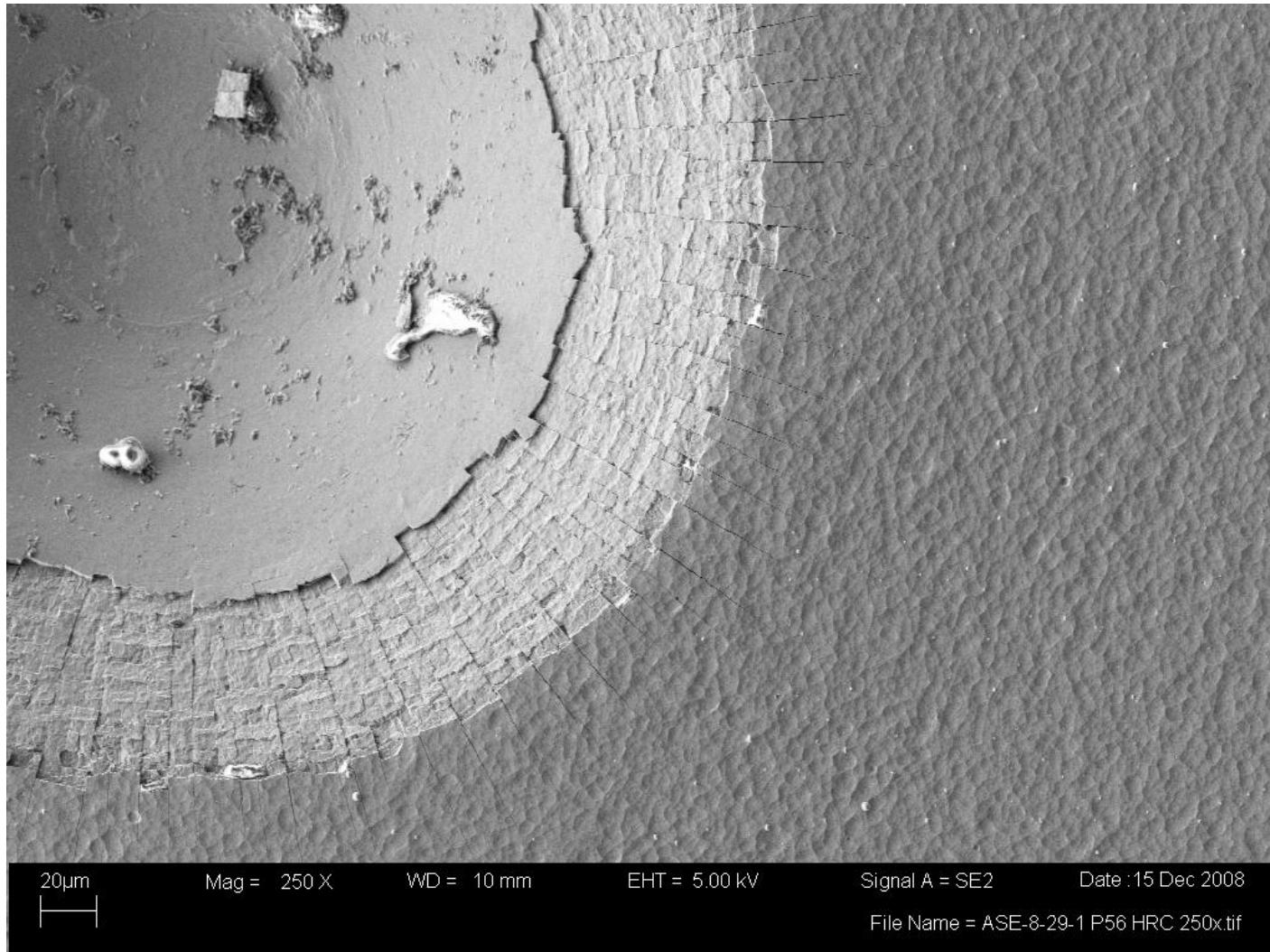
SEM image @ 250x: Cr-CrN (Run1) on P675 (polished), HF1, minor radial cracking to distances <1.25a, minor chipping at indent edge, noted cohesive delamination inside the indent (features at indent edge or inside indent are not part of HF rating).

Appendix HF – Rockwell Indent Adhesion Data



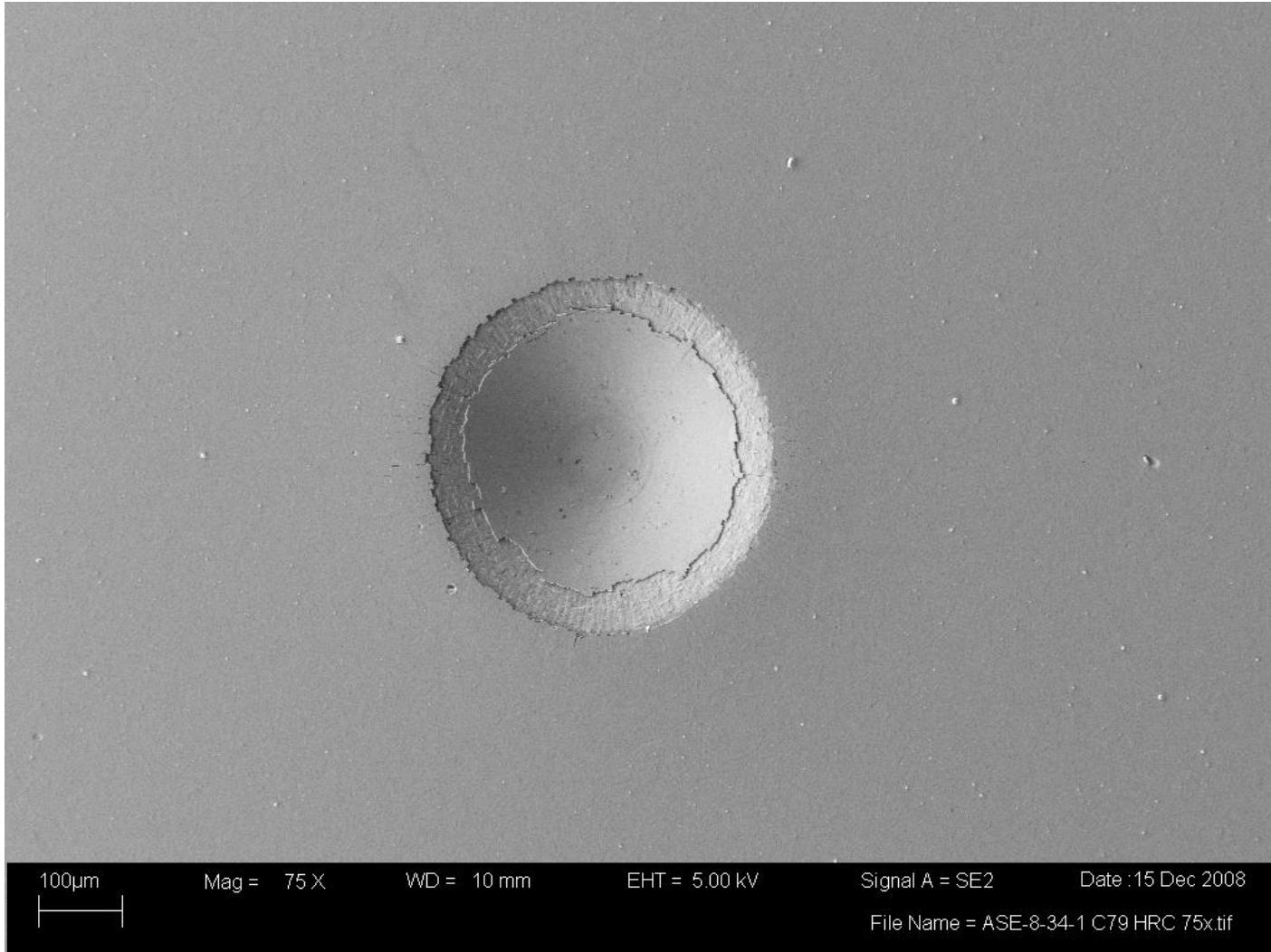
SEM image @ 75x: Cr-CrN (Run1) on P675 (super-finished), HF1 (damage features inside indent not part of HF rating)

Appendix HF – Rockwell Indent Adhesion Data



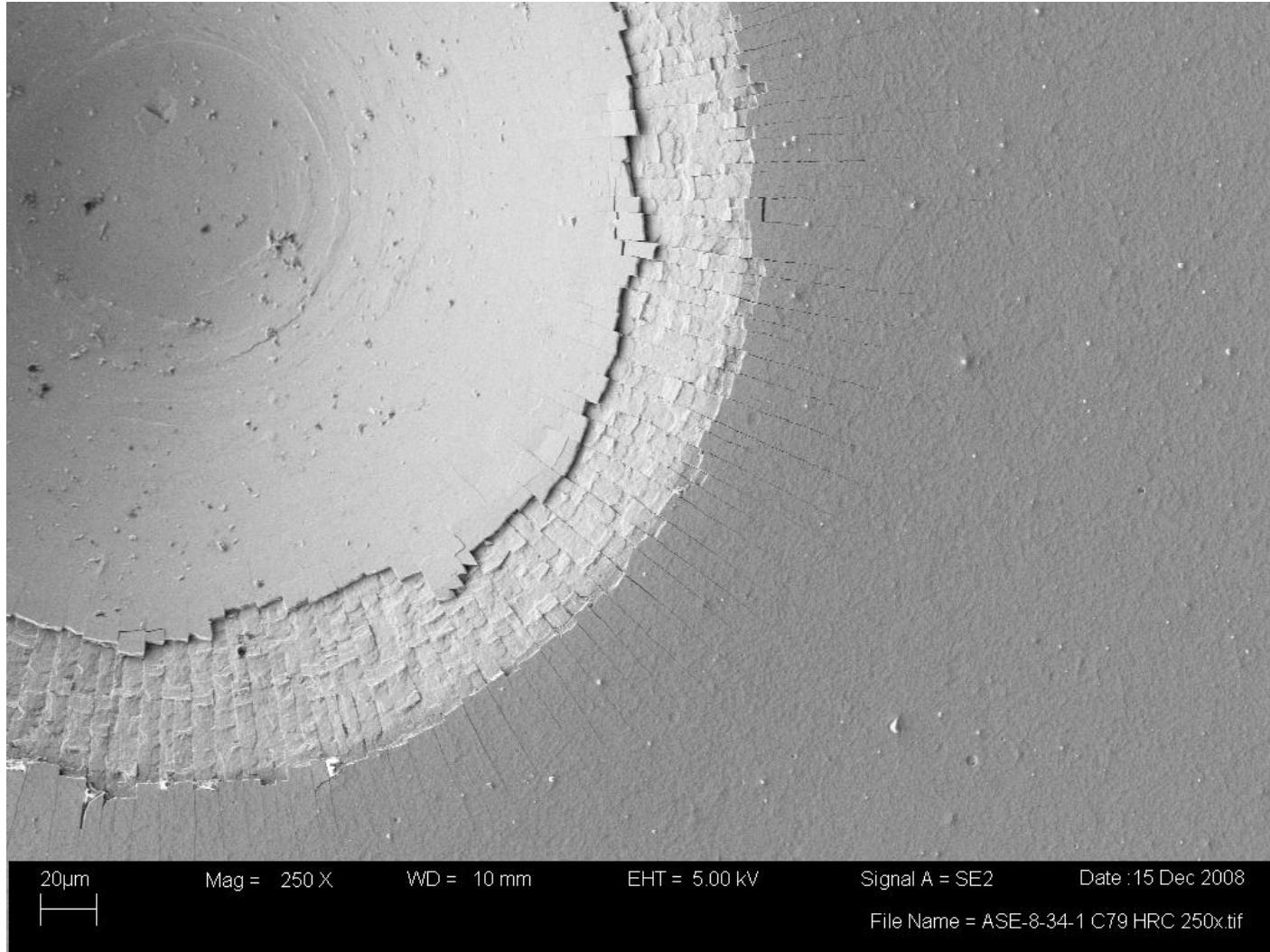
SEM image @ 250x: Cr-CrN (Run1) on P675 (super-finished), HF1, minor radial cracking to distances <1.25a, minor chipping at indent edge, cohesive delamination inside indent is assumed to not extend past the indent edge, hence no HF3 rating.

Appendix HF – Rockwell Indent Adhesion Data



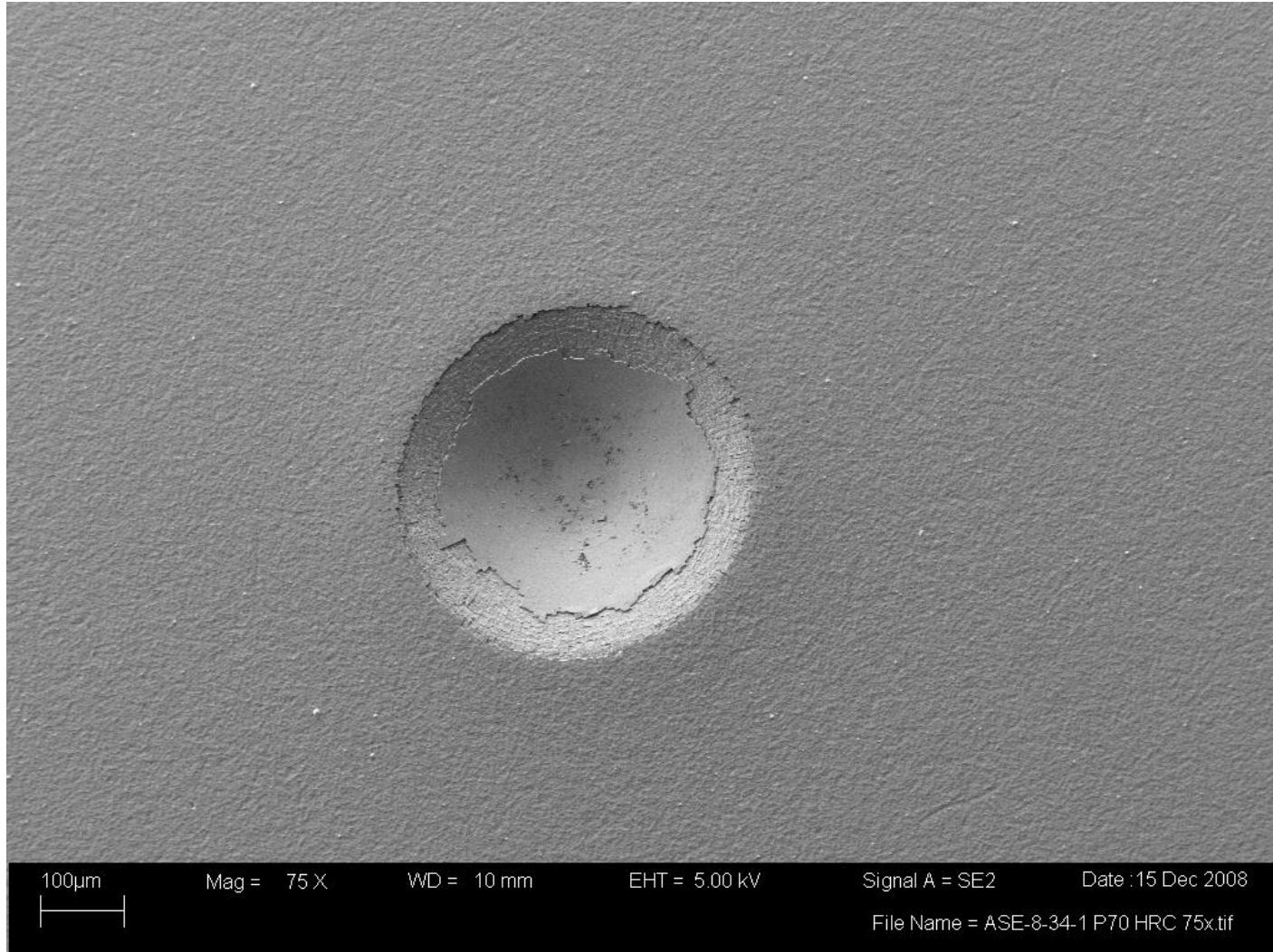
SEM image @ 75x: Cr-CrN (Run2) on P675 (polished), HF1 (damage features inside indent not part of HF rating)

Appendix HF – Rockwell Indent Adhesion Data



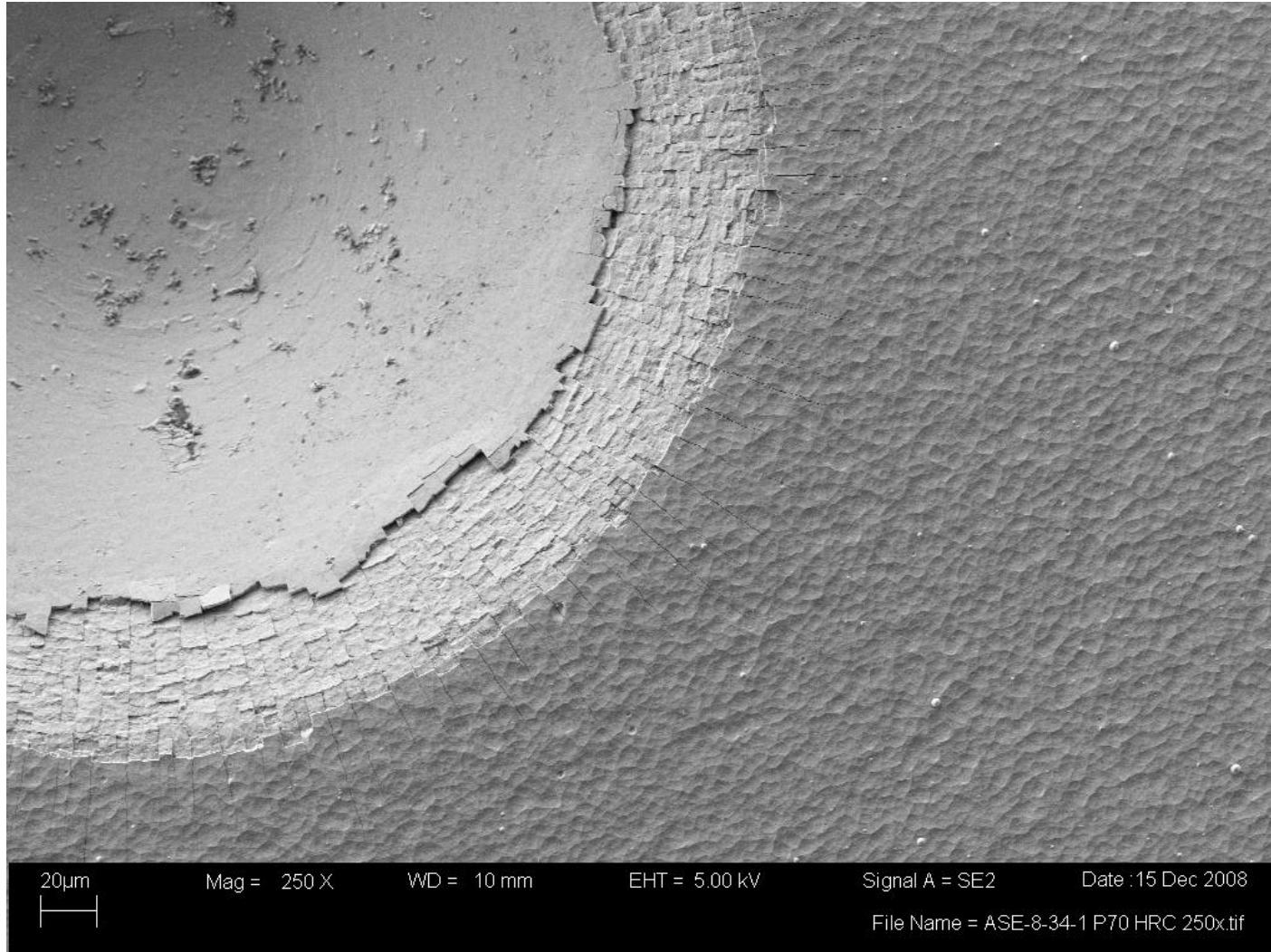
SEM image @ 250x: Cr-CrN (Run2) on P675 (polished), HF1, minor radial cracking to distances <1.25a, minor chipping at indent edge, cohesive delamination inside indent is assumed to not extend past the indent edge, hence no HF3 rating.

Appendix HF – Rockwell Indent Adhesion Data



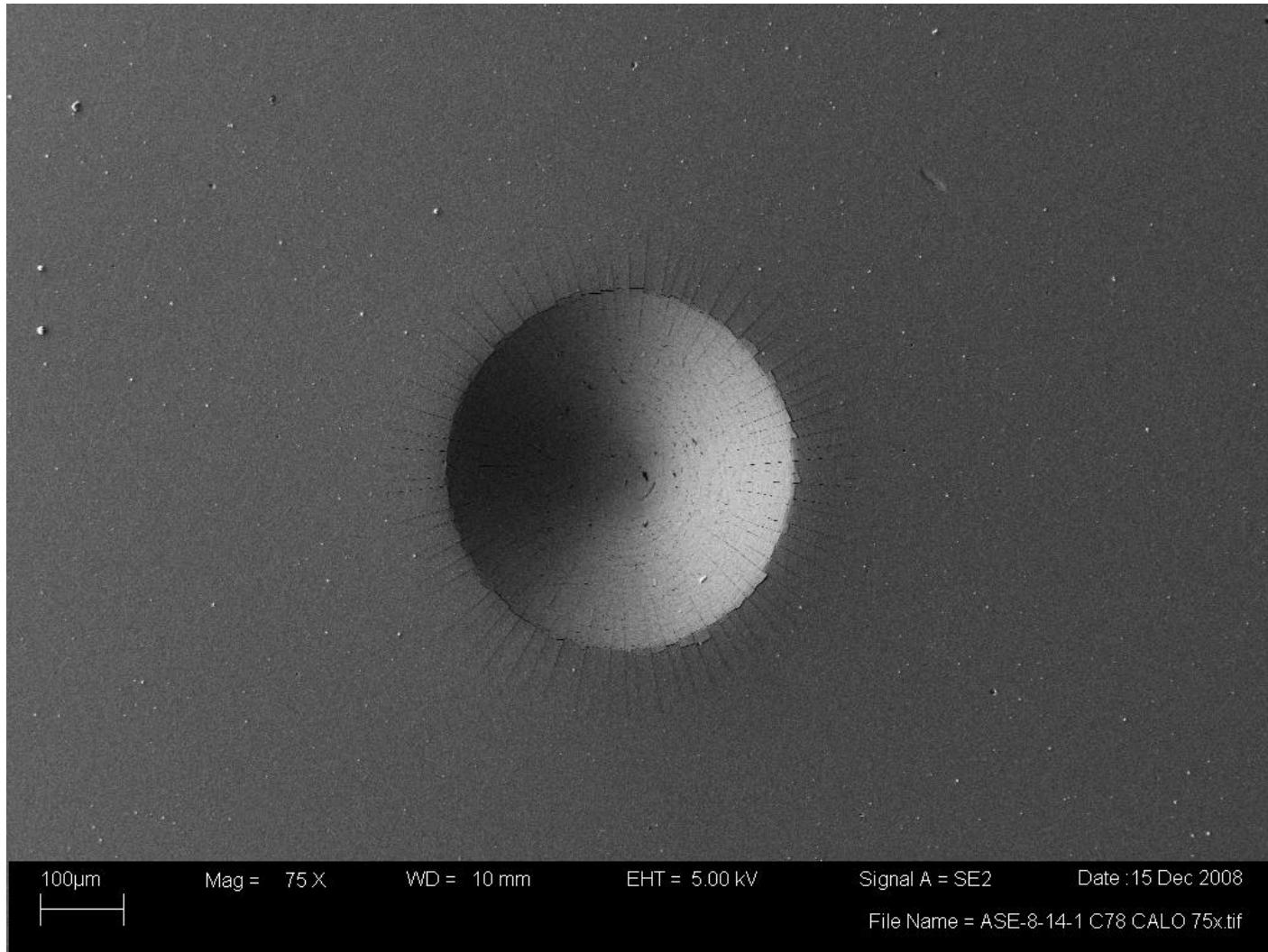
SEM image @ 75x: Cr-CrN (Run2) on P675 (super-finished), HF1 (damage features inside indent not part of HF rating)

Appendix HF – Rockwell Indent Adhesion Data



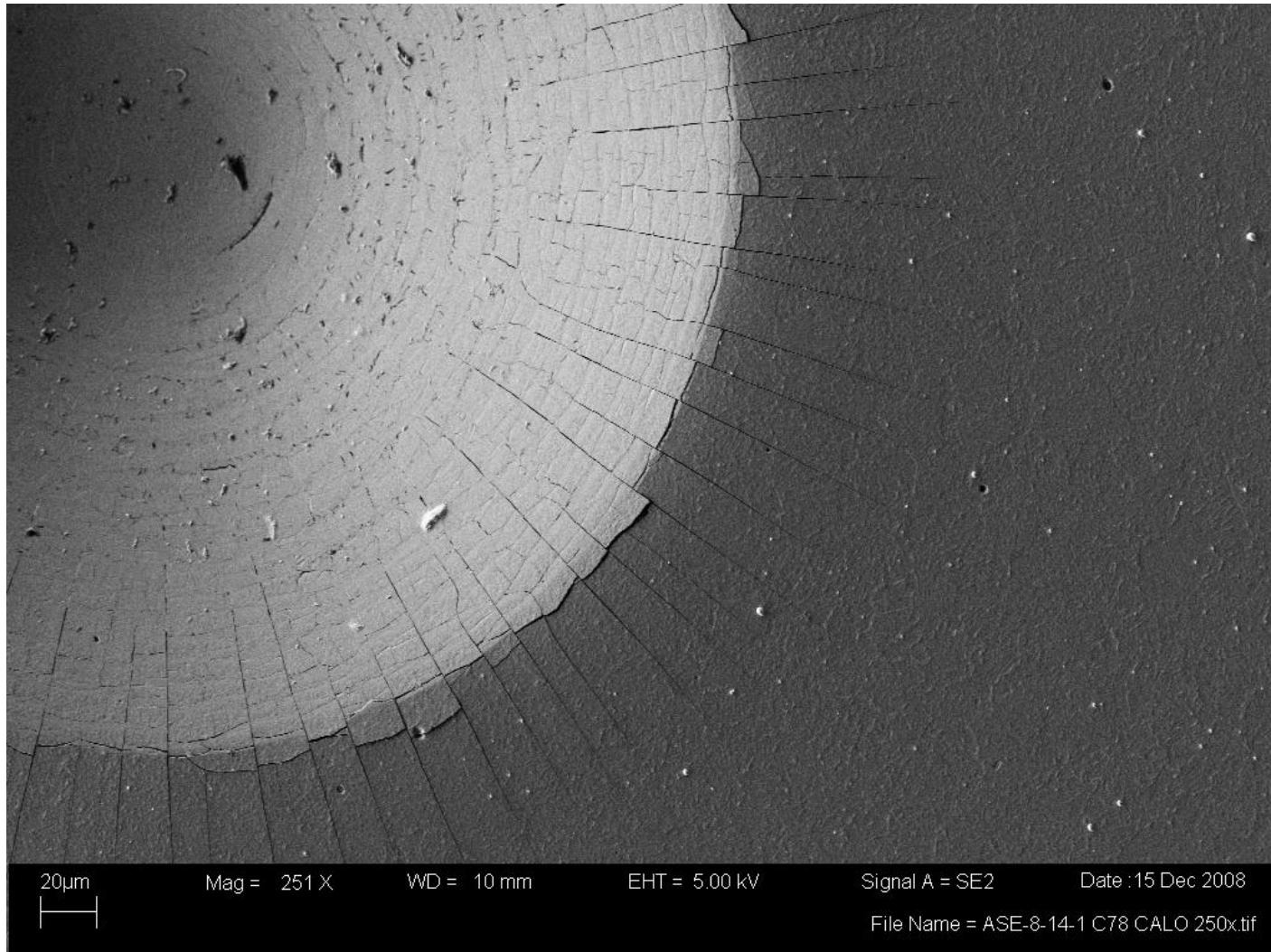
SEM image @ 250x: Cr-CrN (Run2) on P675 (super-finished), HF1, minor radial cracking to distances <1.25a, minor chipping at indent edge, cohesive delamination inside indent is assumed to not extend past the indent edge, hence no HF3 rating.

Appendix HF – Rockwell Indent Adhesion Data



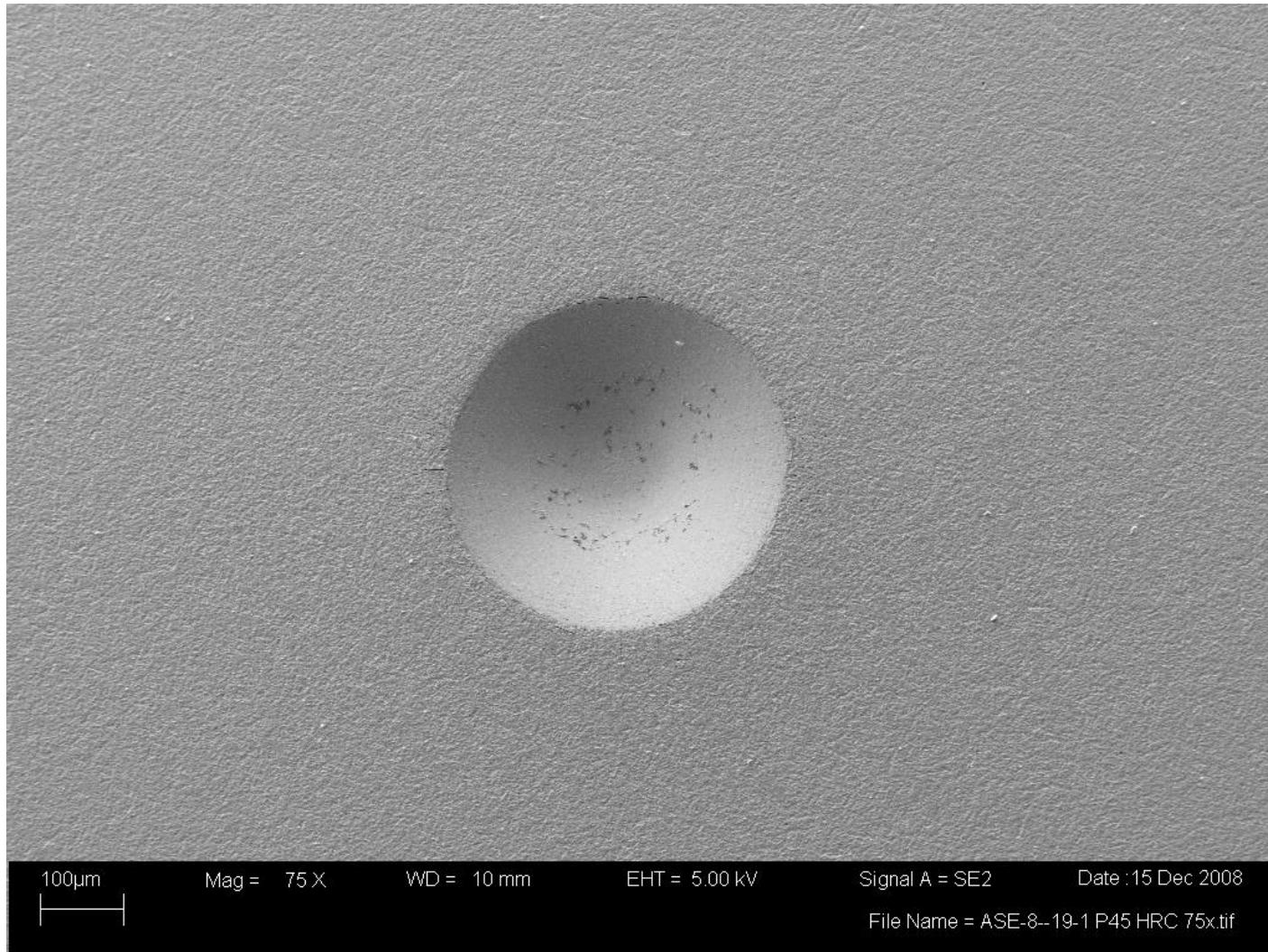
SEM image @ 75x: CrC (Run1) on P675 (polished), HF1 (damage features inside indent not part of HF rating)

Appendix HF – Rockwell Indent Adhesion Data



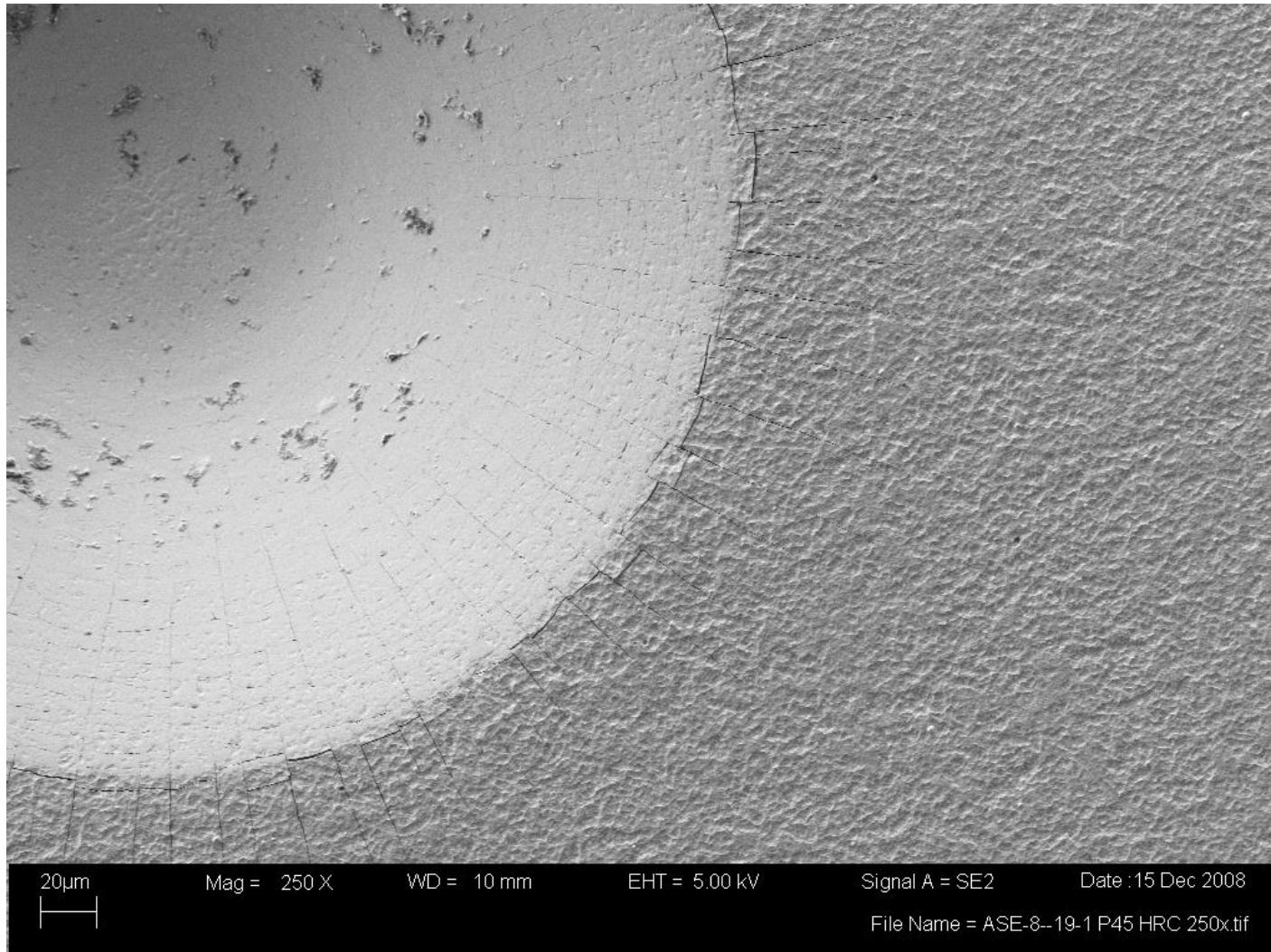
SEM image @ 250x: CrC (Run1) on P675 (polished), HF1, minor radial cracking to distances <1.25a, minor cohesive chipping at indent edge, noted extensive cracking inside indent but no cohesive delamination.

Appendix HF – Rockwell Indent Adhesion Data



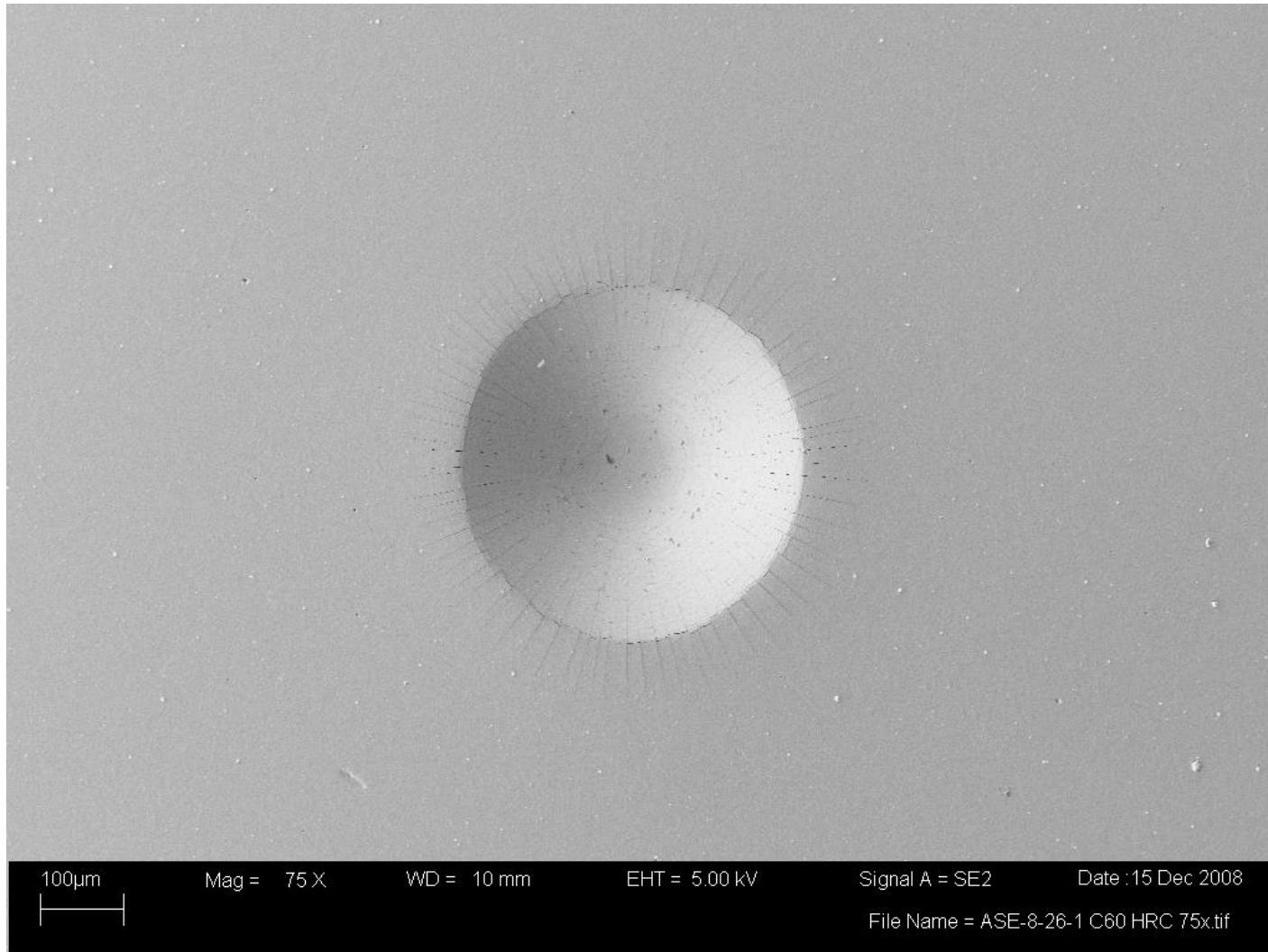
SEM image @ 75x: CrC (Run1) on P675 (super-finished), HF1

Appendix HF – Rockwell Indent Adhesion Data



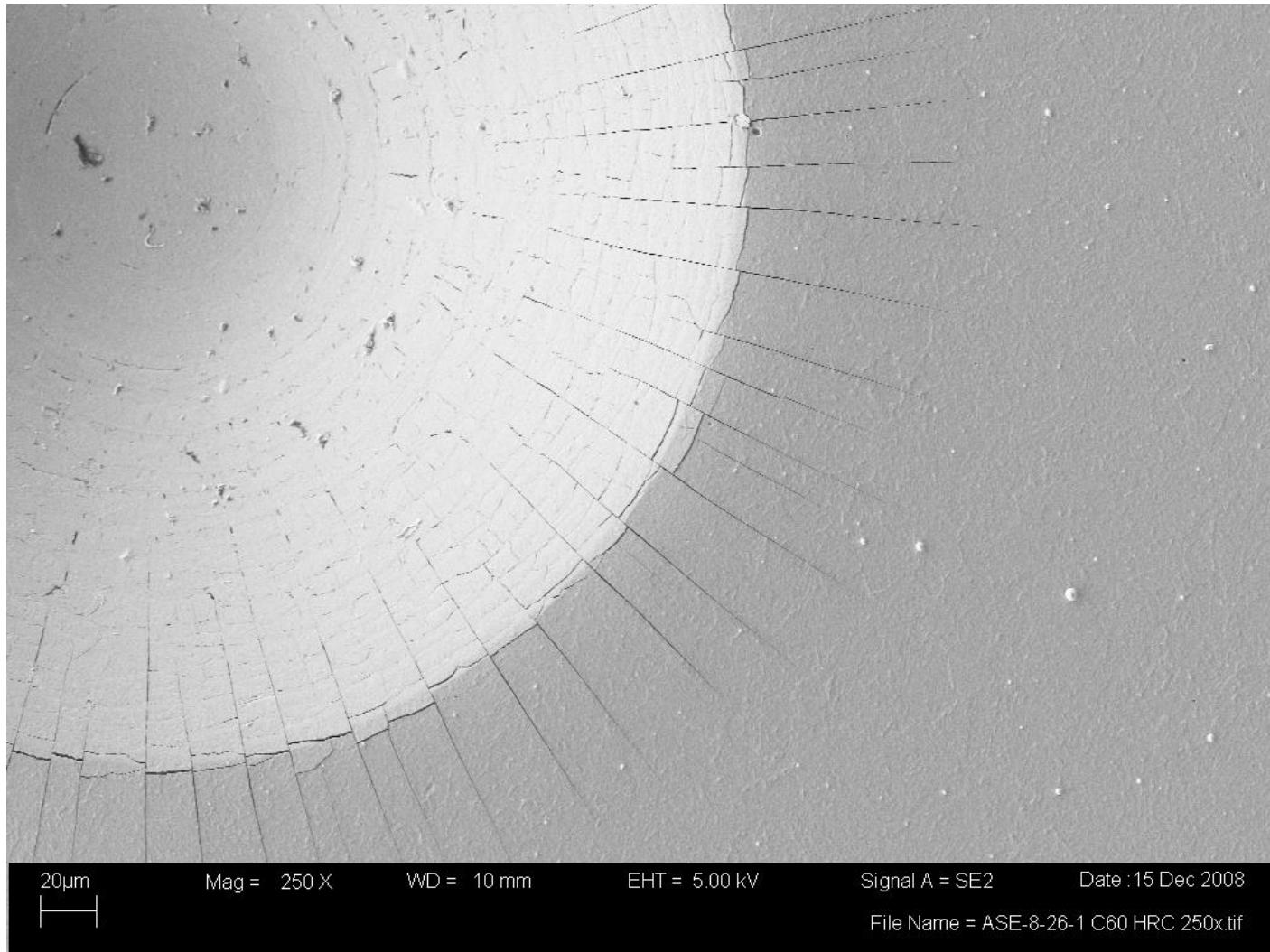
SEM image @ 250x: CrC (Run1) on P675 (super-finished), HF1, minor radial cracking to distances <1.25a, minor cohesive chipping at indent edge, noted extensive cracking inside indent but no cohesive delamination.

Appendix HF – Rockwell Indent Adhesion Data



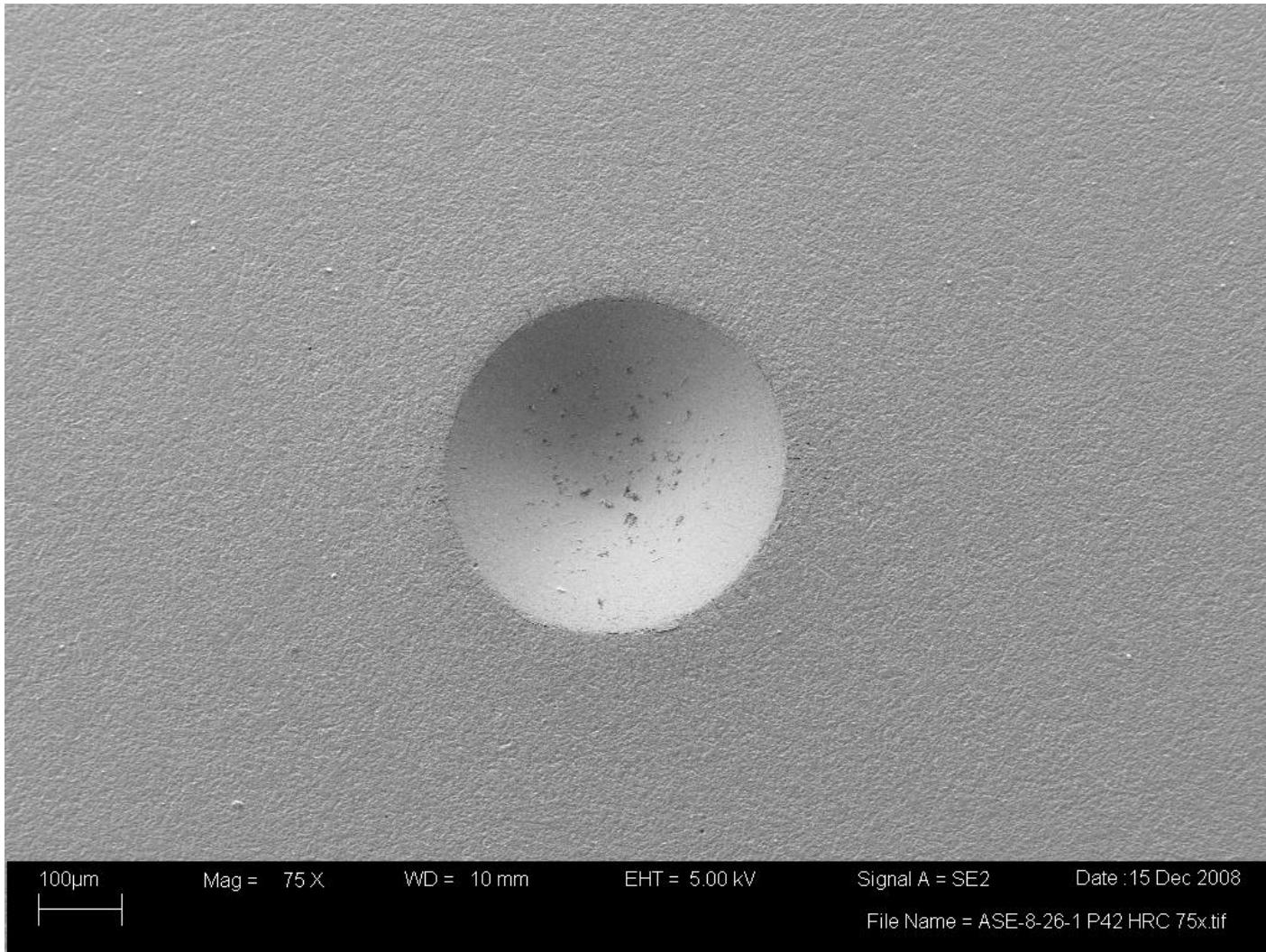
SEM image @ 75x: CrC (Run2) on P675 (polished), HF1

Appendix HF – Rockwell Indent Adhesion Data



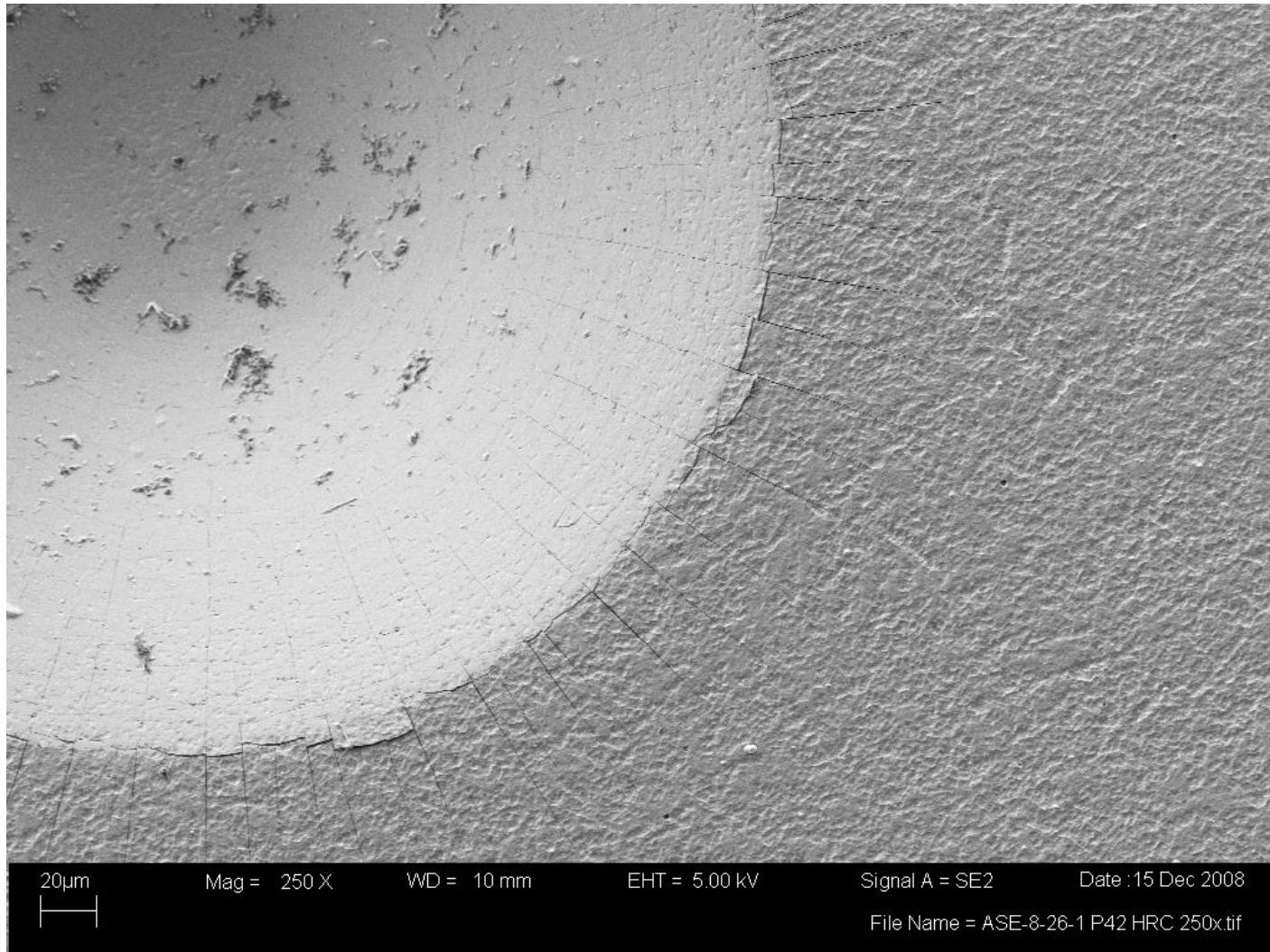
SEM image @ 250x: CrC (Run2) on P675 (polished), HF1, radial cracking to distances <1.5a, minor cohesive chipping at indent edge, noted extensive cracking but no delamination inside indent.

Appendix HF – Rockwell Indent Adhesion Data



SEM image @ 75x: CrC (Run2) on P675 (super-finished), HF1

Appendix HF – Rockwell Indent Adhesion Data



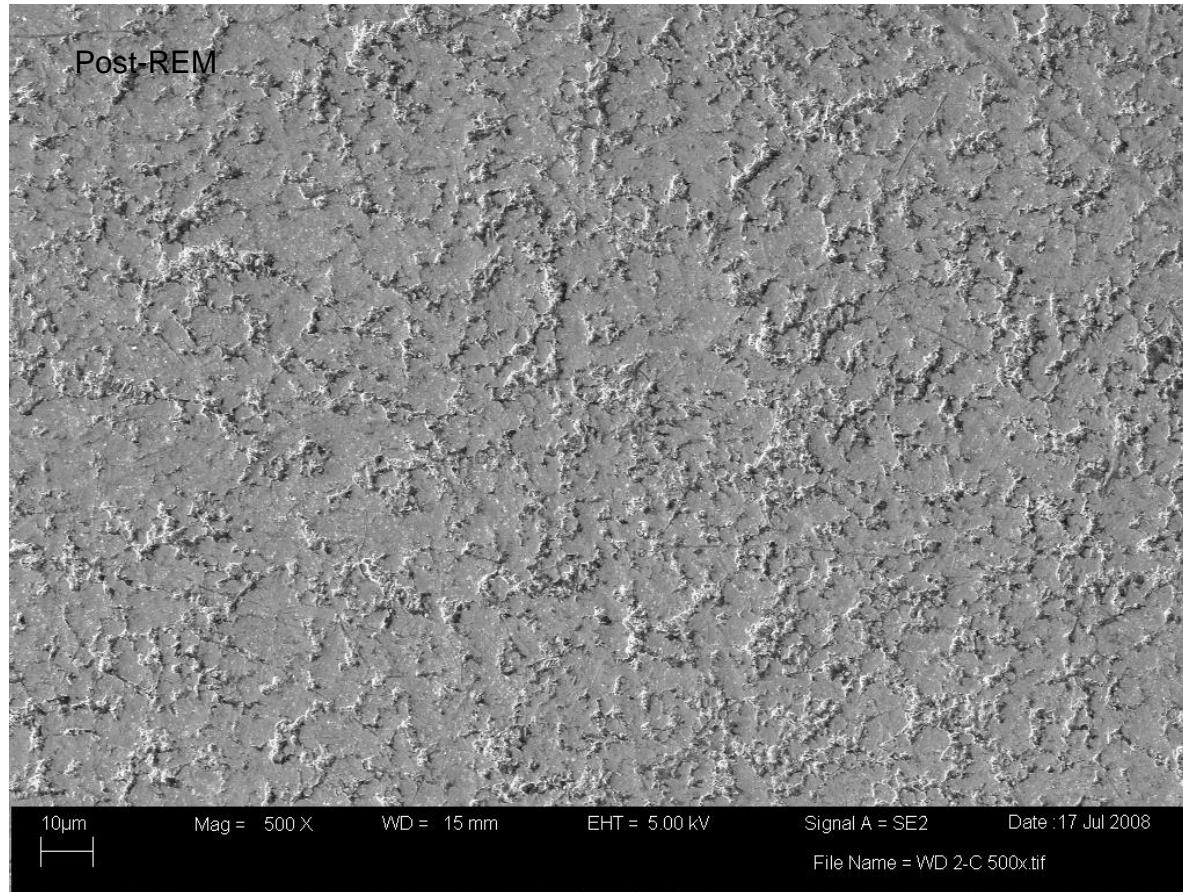
SEM image @ 250x: CrC (Run2) on P675 (super-finished), HF1, minor radial cracking to distances <1.25a, minor cohesive chipping at indent edge, noted extensive cracking inside indent but no cohesive delamination.

Appendix MOR – Coating Morphology Characterization

Coating Morphology Overview

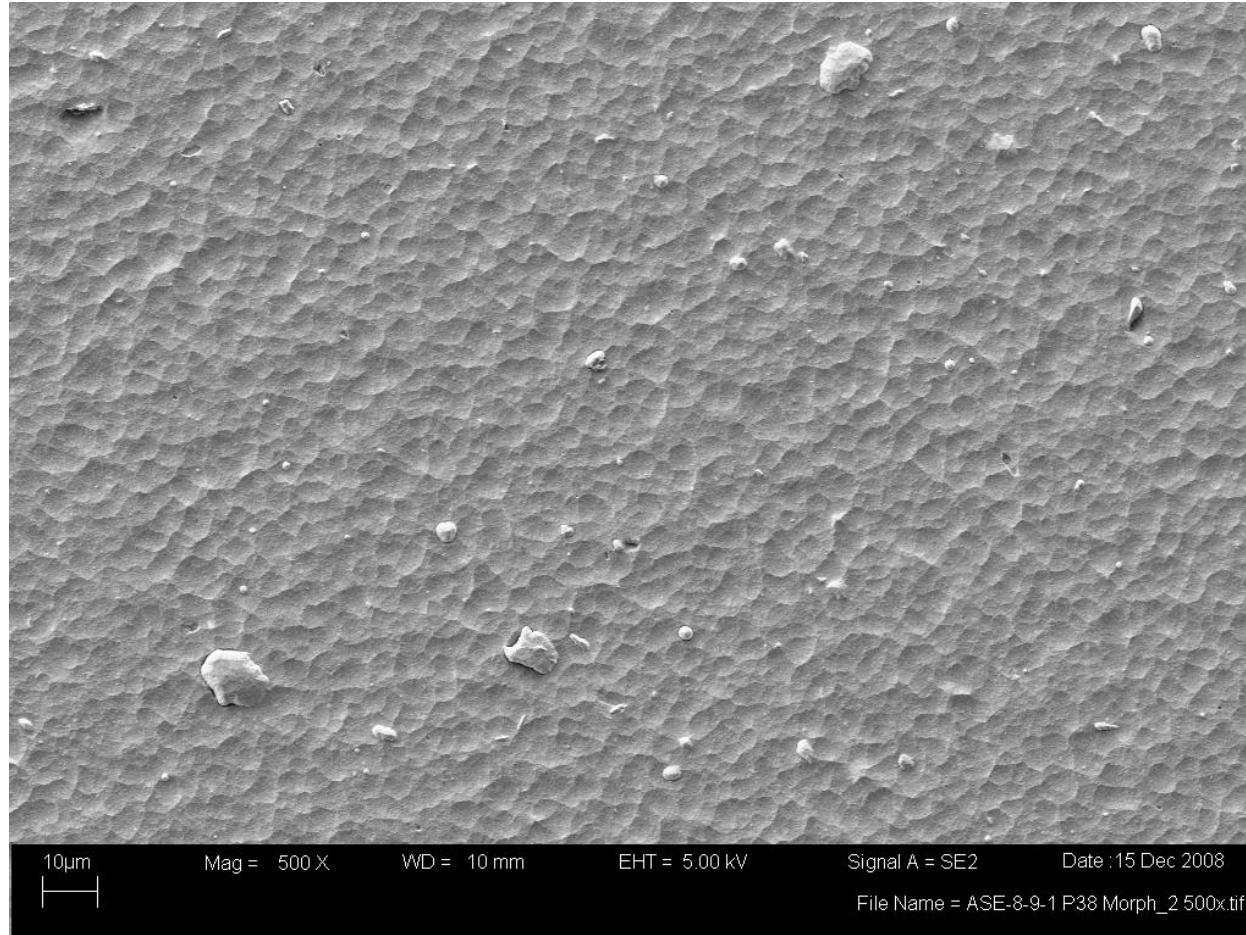
1. The purpose of this appendix is to illustrate the morphology characteristics of the Pyrowear 675 substrate and TiCr-TiCrN, Cr-CrN, and CrC coatings.
2. A Ziess Supra 55VP field emission scanning electron microscope (FE-SEM) was used characterize morphology. Standard settings are; secondary electron mode, 5keV accelerator voltage, 15mm working distance, and 30 μ m aperture.
3. Coating cross-sections (x-sec) for SEM imaging were prepared using precision sample cutting and metallographic polishing equipment from Allied High Tech Products Inc (TechCut5 and TechPrep products). Sample preparation involves applying a epoxy/glass slide stack to the coating which protects it from chipping during polishing. On the negative side the epoxy layer is often subjected to undercutting during the sequential polishing operations and tends to collect debris generated during polishing. This can be observed in some cases for x-sec images of coatings and it should be made clear that this is non-related to the coating itself.
4. SEM images at 500x magnification are presented for both depositions (Dep1 and Dep2) of each coating type to demonstrate basic repeatability. It is standard practice to collect three morphology images at 500x from random locations on each sample in order to asses particle defect density in the coating; the presented images are the most representative morphology for a given coating. A SEM image at 5000x is presented for each coating type; characteristic particle defects are intentionally included in each 5000x image as well.
5. Images of the most commonly observed particle defect types are included to compliment discussion on defect related failures in coating performance tests such as corrosion and rolling contact fatigue.

Appendix MOR – Coating Morphology Characterization



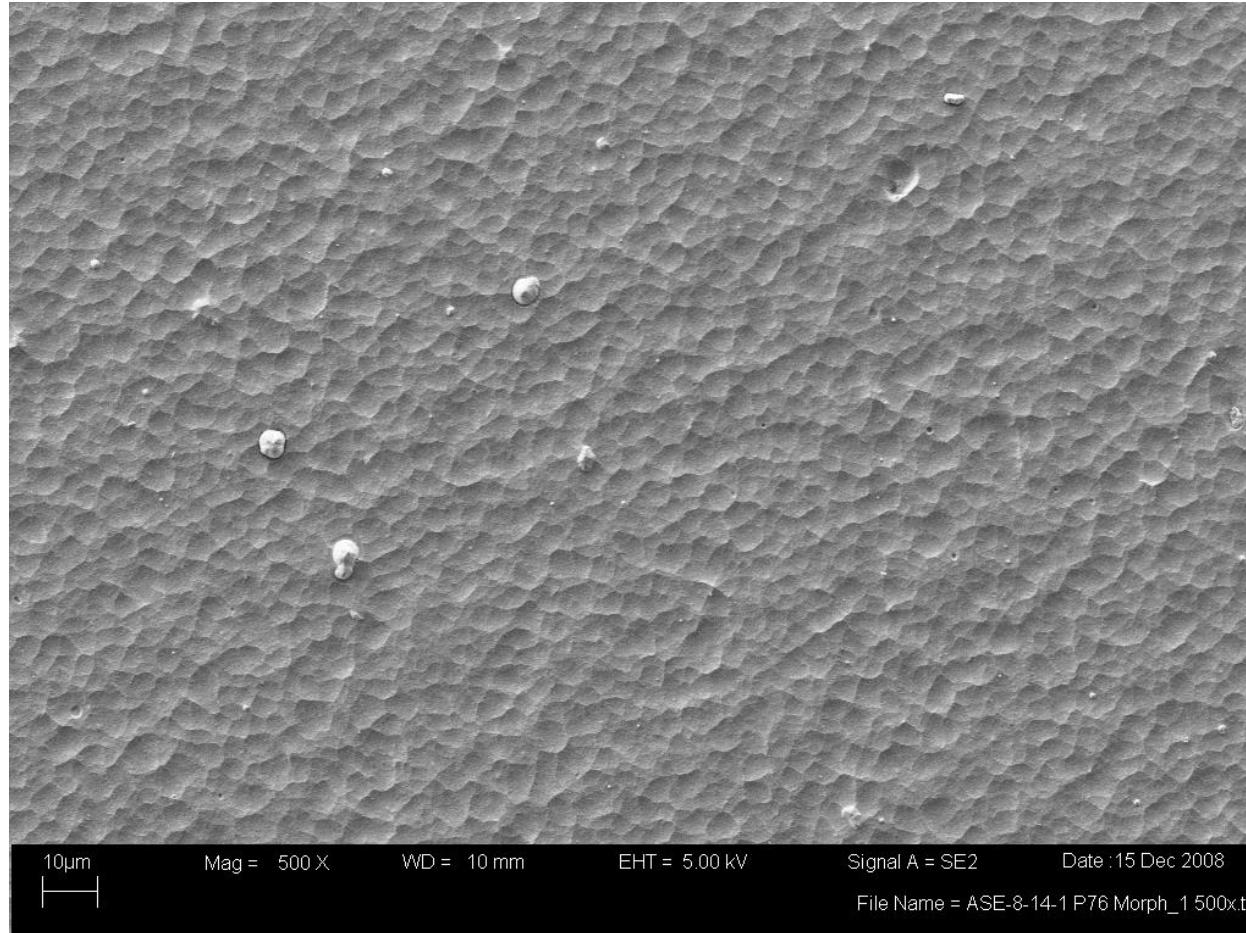
Pyrowear 675, super-finished: SEM image at 500x. All coatings presented in this appendix were deposited on super-finished P675 which has the initial morphology shown above.

Appendix MOR – Coating Morphology Characterization



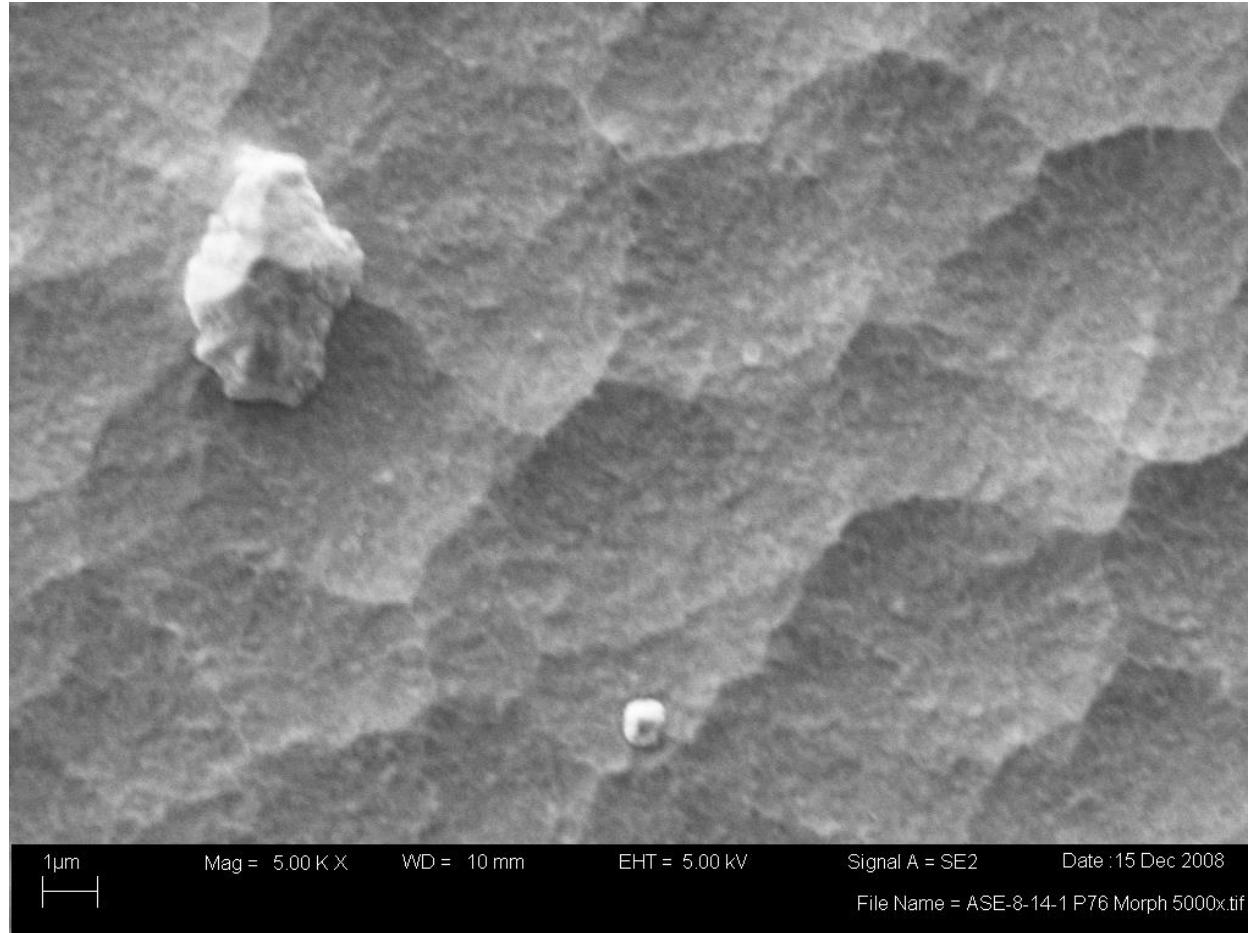
TiCr-TiCrN (Dep1), 500x: morphology characterized by interconnected concave features (not convex columnar protrusions), particle defects (spherical white objects) can be observed as well as a particle fall-out sites (upper left corner and right edge of image) where an embedded particle delaminated from the coating.

Appendix MOR – Coating Morphology Characterization



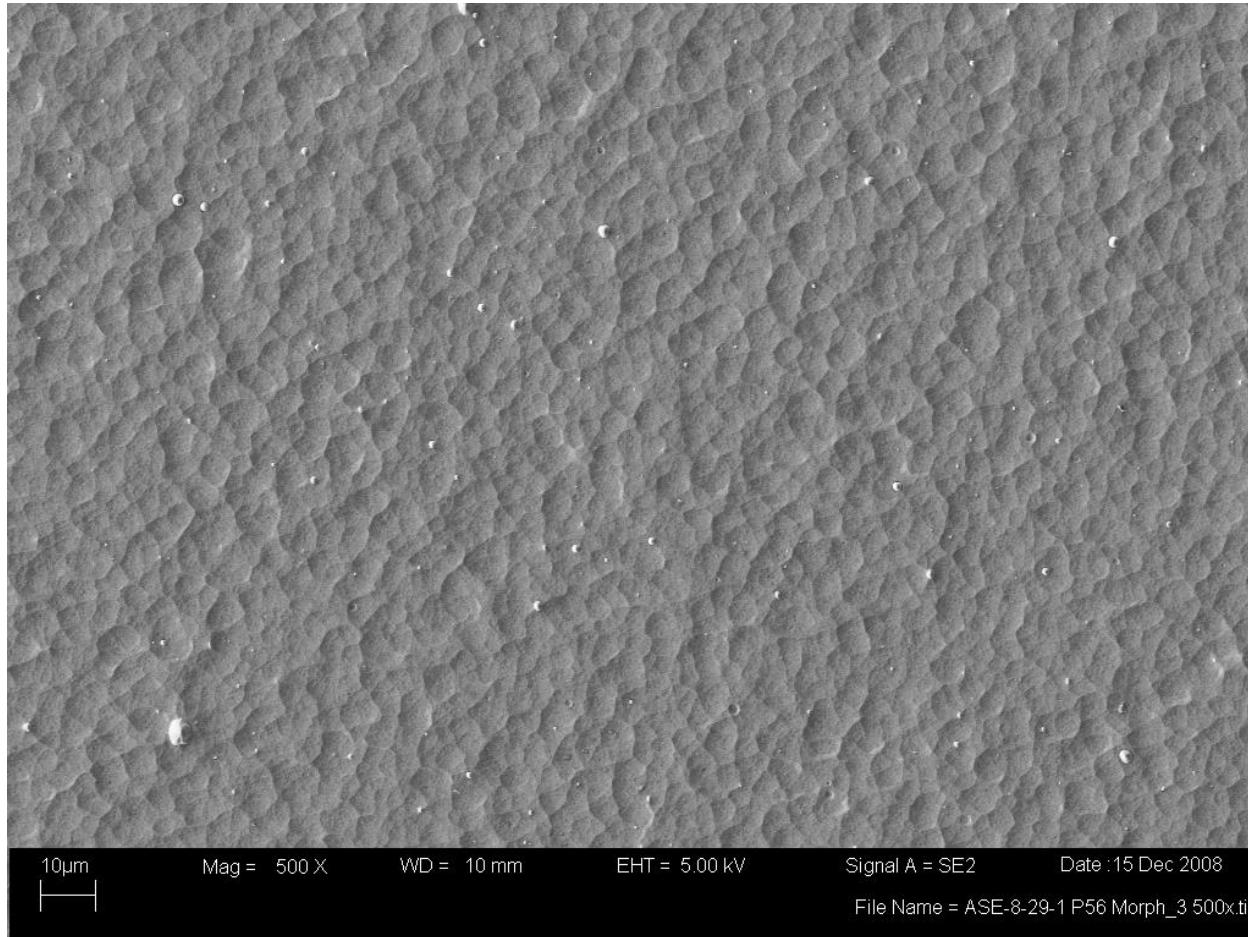
TiCr-TiCrN (Dep2), 500x: morphology characterized by interconnected concave features (not convex columnar protrusions), particle defects (spherical white objects) can be observed as well as a particle fall-out site (upper right quadrant) where an embedded particle delaminated from the coating.

Appendix MOR – Coating Morphology Characterization



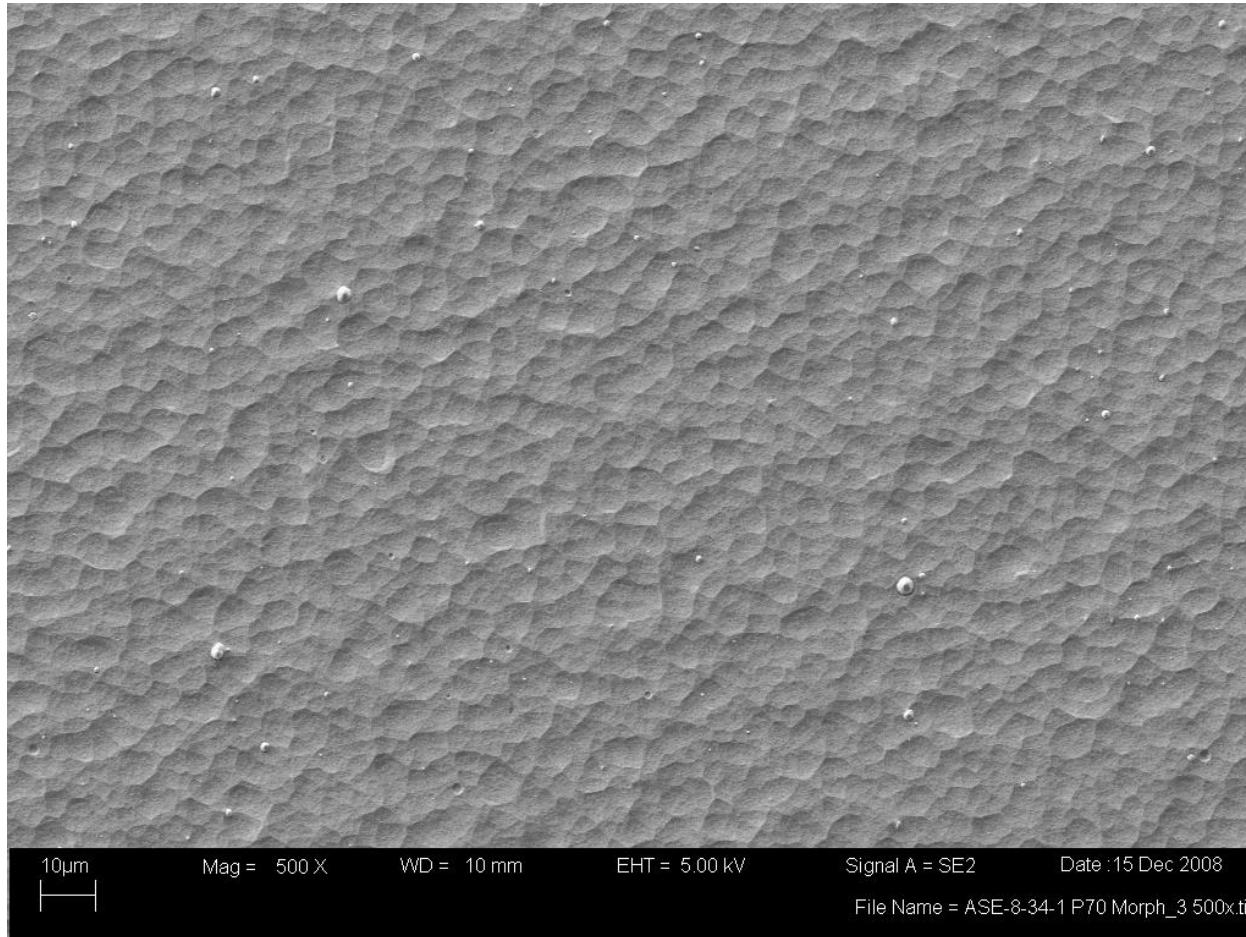
TiCr-TiCrN (Dep2), 5000x: The concave morphology of the coating surface is apparent when the highlight locations of the features are compared to a known positive height feature (particle), this “peened” surface morphology may be a result of self-sputtering of the coating during deposition. The dense fine-grain nature of the coating is apparent.

Appendix MOR – Coating Morphology Characterization



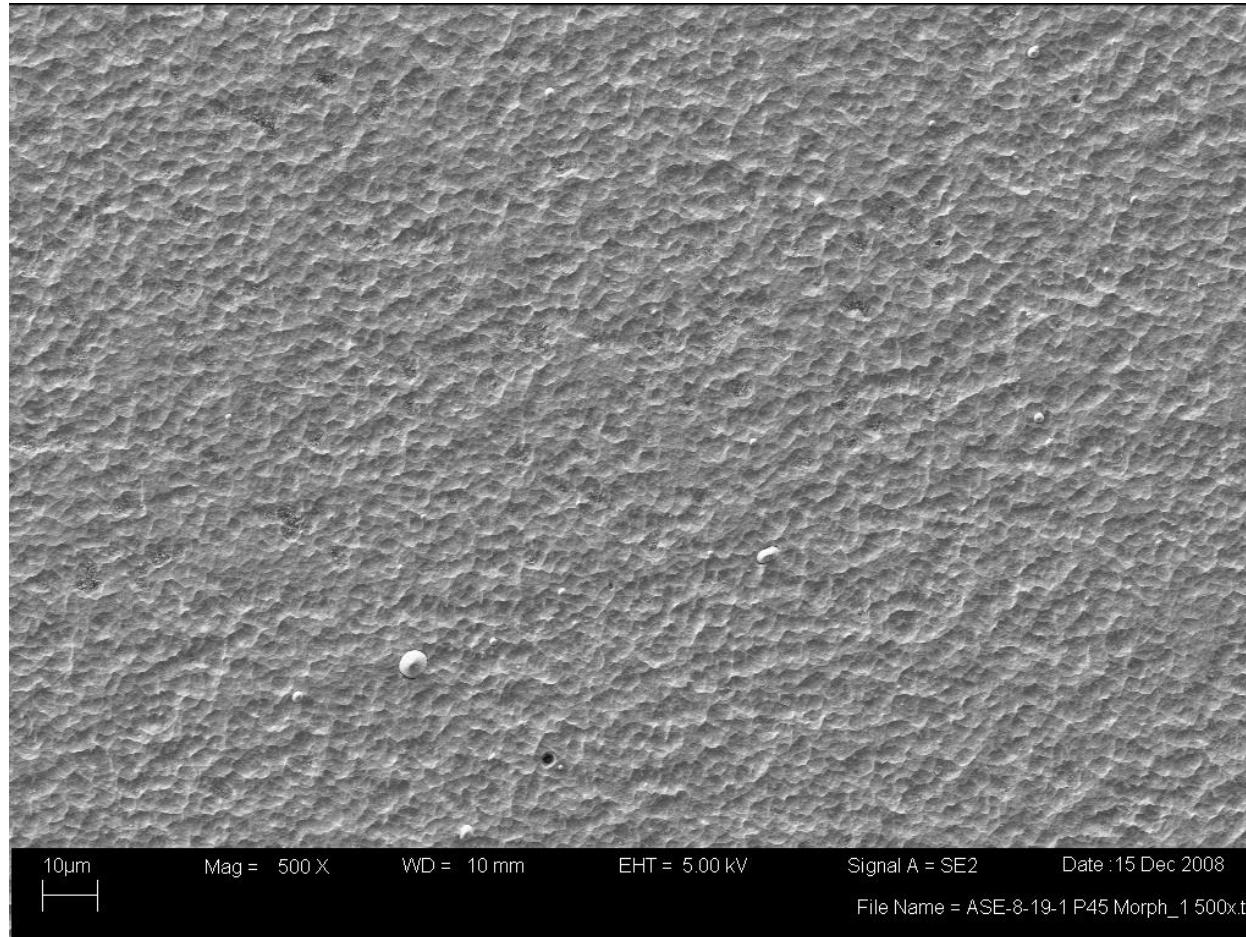
Cr-CrN (Dep1), 500x: Morphology characterized by interconnected concave features (not convex columnar protrusions), particle defects (spherical white objects) can be observed. Density of small particles, <1µm in diameter, was higher than the TiCr-TiCrN coatings.

Appendix MOR – Coating Morphology Characterization



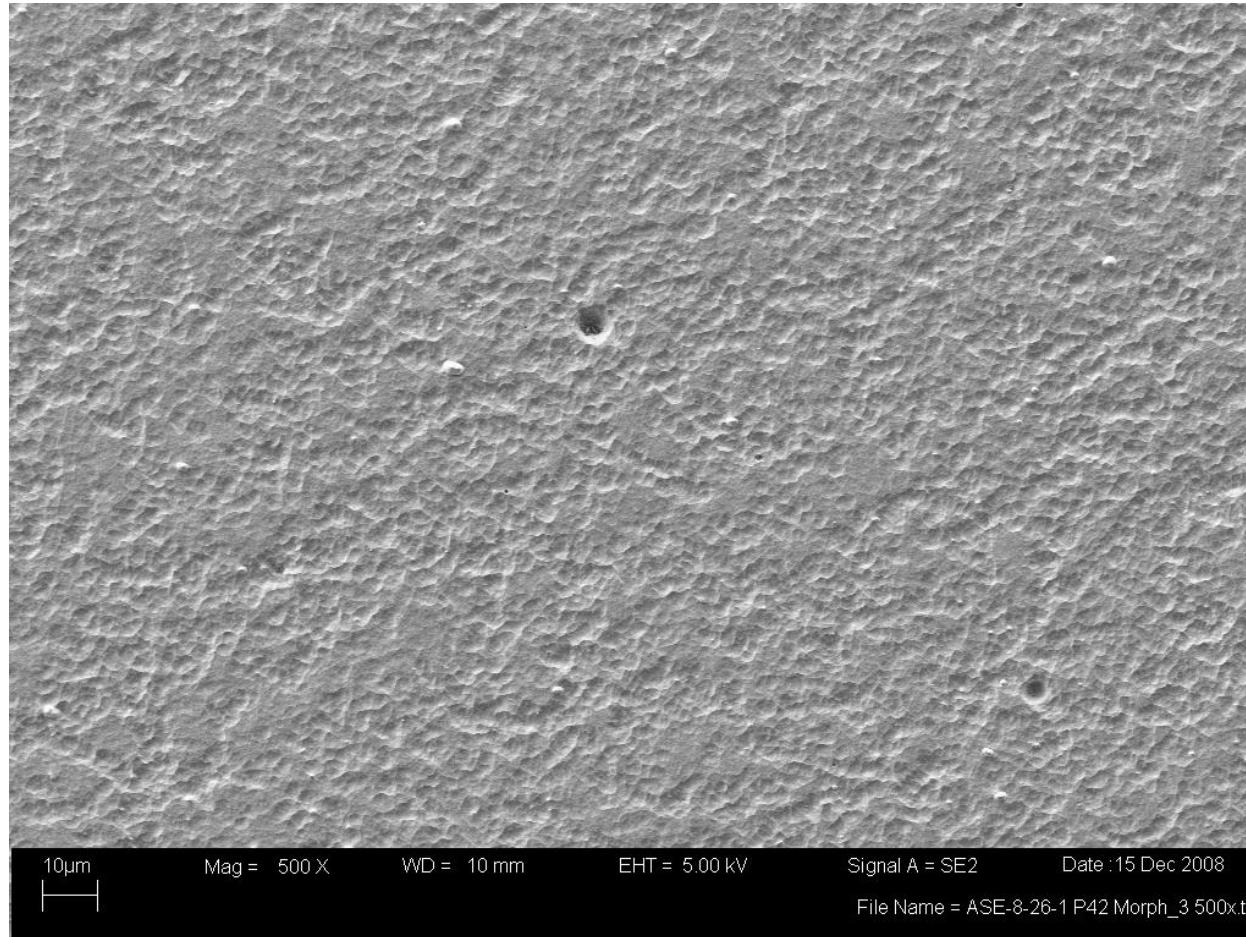
Cr-CrN (Dep2), 500x: Morphology characterized by interconnected concave features (not convex columnar protrusions), particle defects (spherical white objects) can be observed. Density of small particles, <1µm in diameter, was higher than the TiCr-TiCrN coatings.

Appendix MOR – Coating Morphology Characterization



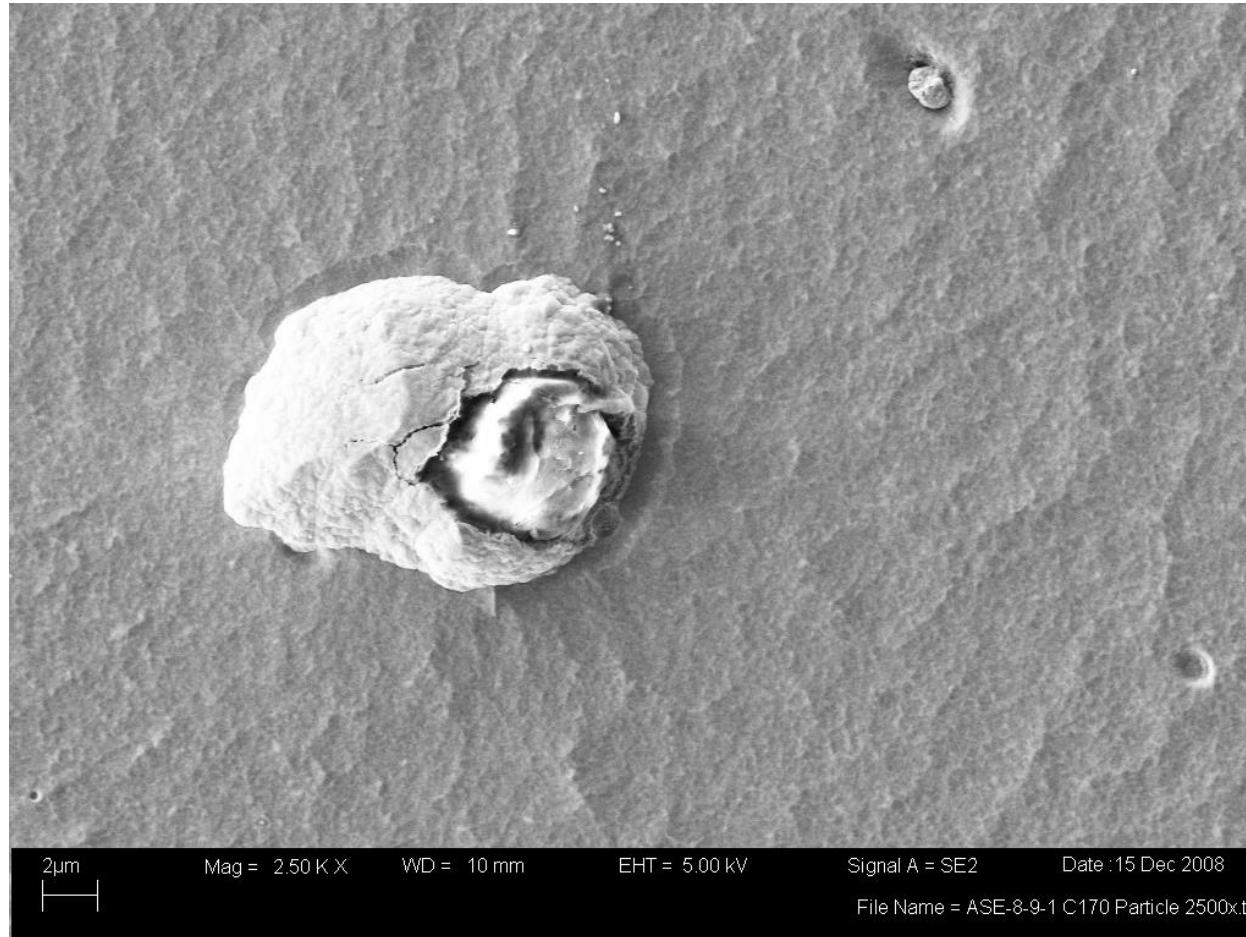
CrC (Dep1), 500x: Morphology appears random and is most likely related to propagation of the super-finished P675 substrate morphology. Particle defects (spherical white objects) can be observed. Density of particles on CrC coatings was the lowest as compared to Cr-CrN and TiCr-TiCrN coatings.

Appendix MOR – Coating Morphology Characterization



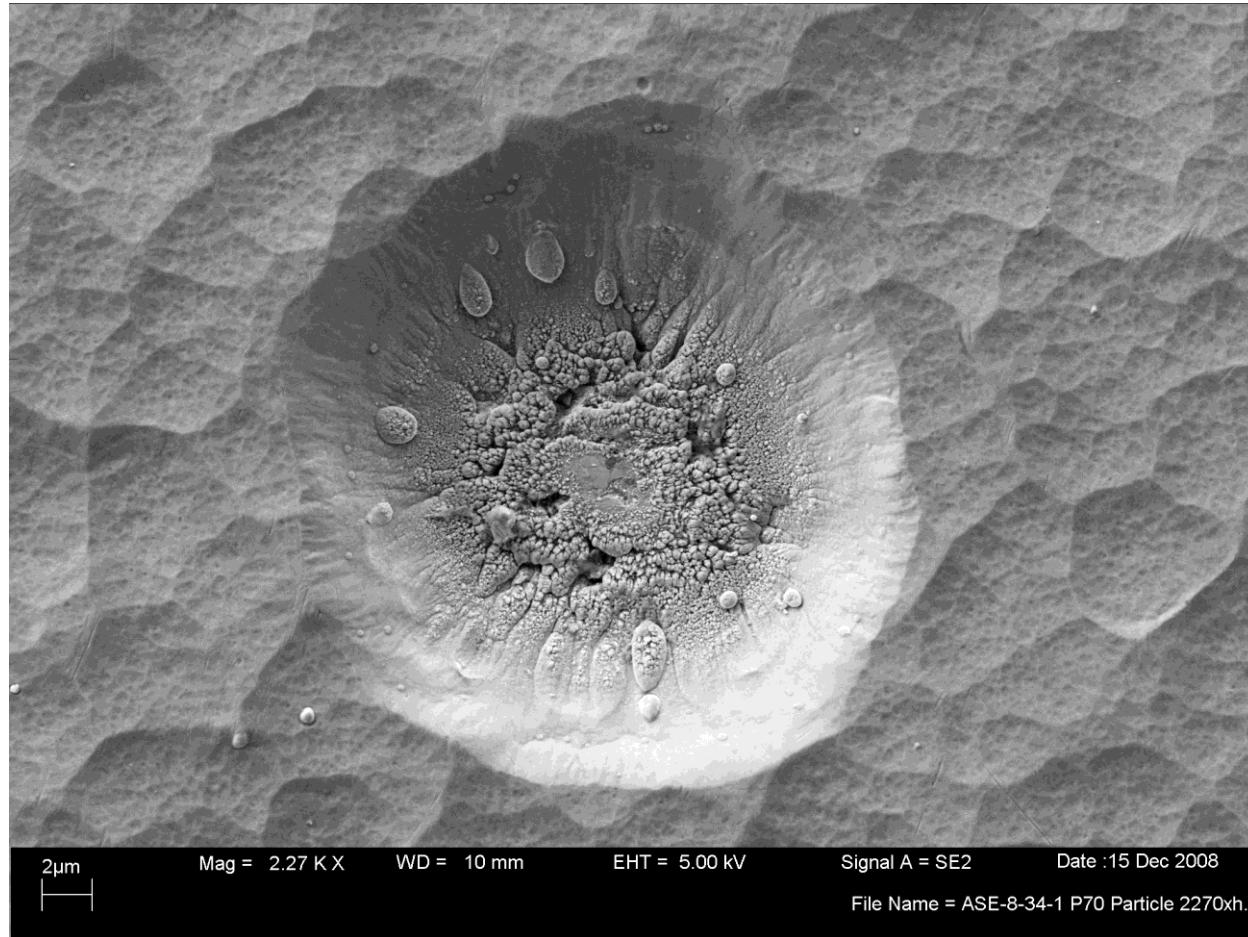
CrC (Dep2), 500x: Morphology appears random and is most likely related to propagation of the super-finished P675 substrate morphology. Particle defects (spherical white objects) can be observed. Two particle fall-out sites can be observed where an embedded particle delaminated from the coating, if the substrate is exposed corrosion is likely to initiate at these sites.

Appendix MOR – Coating Morphology Characterization



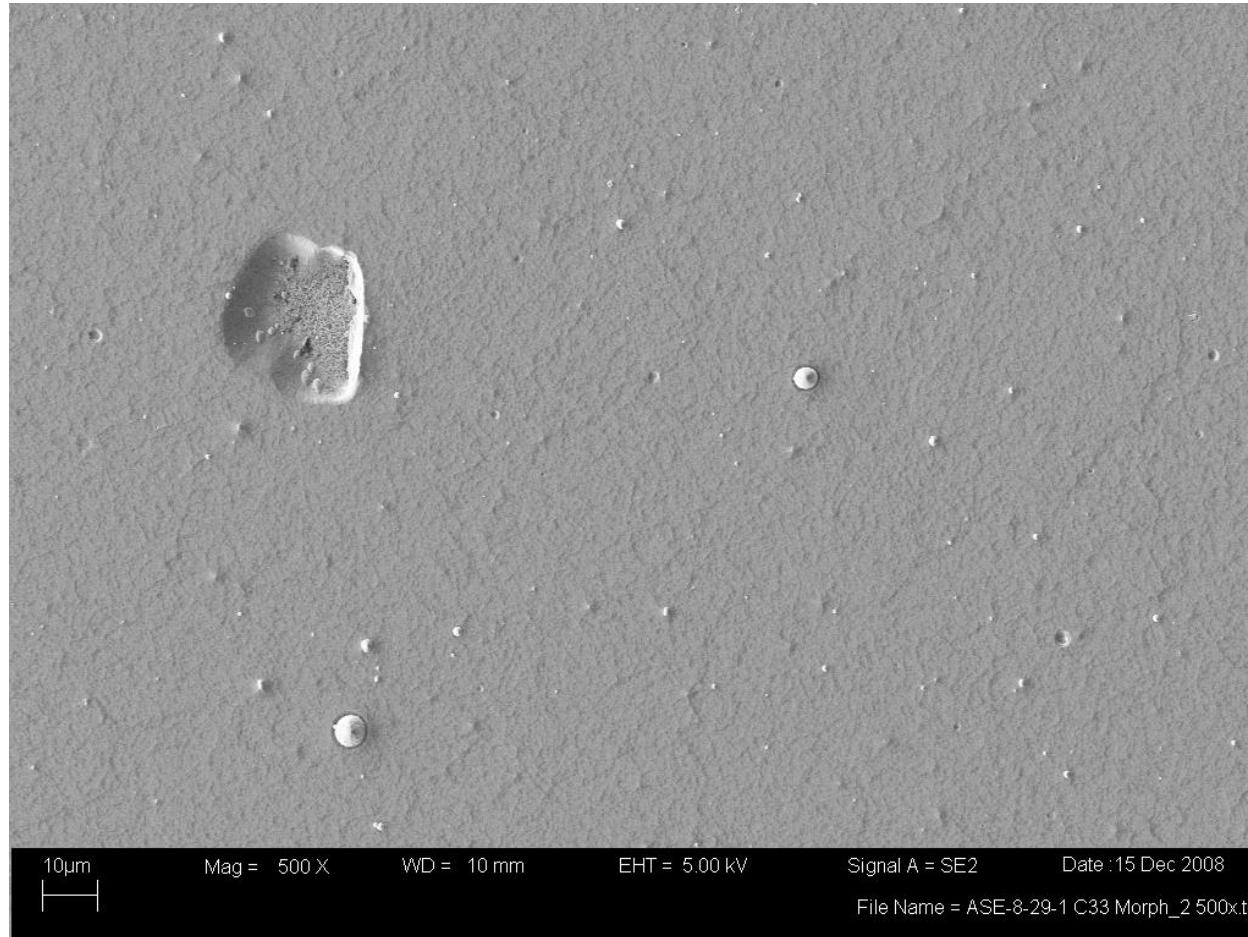
Particle Defect, 2500x: This image provides a good example of a particle which was embedded in the coating during deposition and then was progressively coated over. The coating “shell” has cracked exposing the particle inside. Particle defects such as this likely provide stress concentrations in the coating structure and provide locations for cracks to initiate and propagate under loading.

Appendix MOR – Coating Morphology Characterization



Particle Fall-out Defect, 2270x: This image provide a good example of the defect that results when an embedded particle delaminates from the coating structure and leaves a hole defect. Depending on the depth of the hole substrate exposure can occur, if that is the case then corrosion will favorably initiate at such a site due to the galvanic coupling between the noble coating and the less noble substrate.

Appendix MOR – Coating Morphology Characterization



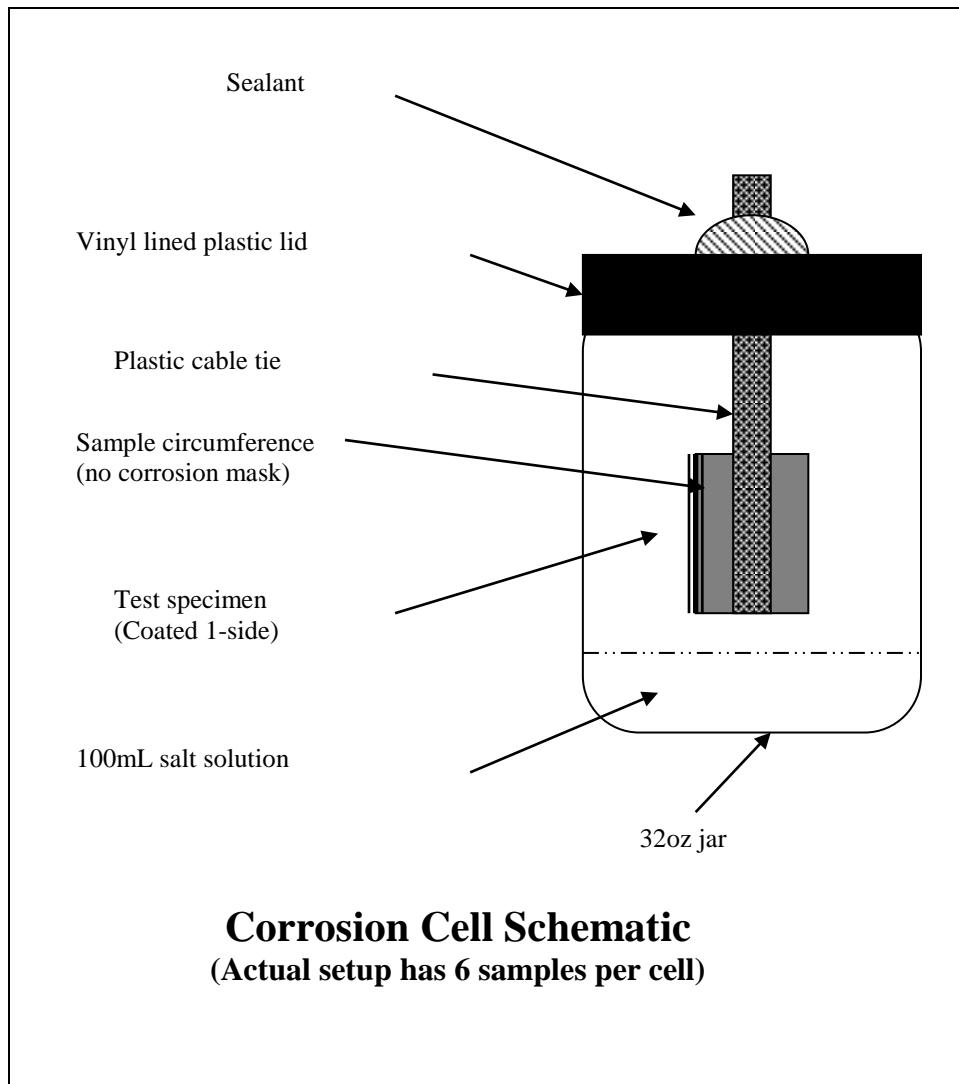
Particle Fall-out Defect, 500x: Another example of a particle fall-out defect which has exposed the P675 substrate.

Appendix NCT – Modified Navy Corrosion Test Results

Modified Navy Corrosion Test (NCT) Protocol Overview

1. The Modified Navy Corrosion Test (NCT) method sets forth the conditions for testing corrosion resistance of a material by exposing specimens to a humid, salt-water environment. Samples are suspended above salt-water in a sealed container and subjected to alternate temperature cycles which result in alternating condensing and drying cycles on the test samples. It is important to note that the samples are never actually submerged in the salt water solution so this test can also be thought of as a cyclic humidity test. The test protocol was obtained from Rolls Royce as a less aggressive corrosion test to supplement ASTM B117 salt-fog corrosion testing. In addition Rolls Royce has a historical database of NCT test results which allows good comparison with Arcomac coatings.
2. The testing procedure involves thermal cycling of the sealed corrosion cell which promotes alternating water condensation and drying cycles. A schematic of the test setup is provided (page # NCT_2) and the specific test protocol is outlined below.
 - Super-finished Pyrowear 675 (P675) samples 1.185"dia x 0.375" thick in uncoated and coated conditions were tested. No corrosion masking was applied to the samples.
 - Qty (6) samples are suspended and spaced so they do not contact each other by zip ties in a sealed plastic corrosion cell containing approximately 100ml of seawater (ASTM D1141). Note that the samples are suspended about the seawater and at no point make physical contact with the seawater during the test.
 - The sealed corrosion cells are temperature cycled; one cycle consists of 24 hours, beginning with 8 hours in an oven at 150°F (65°C), and ending with 16 hours in a refrigerator at 37°F (3°C). The corrosion test is conducted for 14 cycles (336 hours total) until completion.
 - Upon test completion the samples are air dried and photographed. Samples are then ultrasonically cleaned in acetone to remove loosely adhered corrosion products and then photographed. Additional analysis including optical microscopy, profilometry, and SEM imaging is conducted as necessary. Corrosion performance is gauged on the percent surface area of corrosion formation on the sample face.

Appendix NCT – Modified Navy Corrosion Test Results



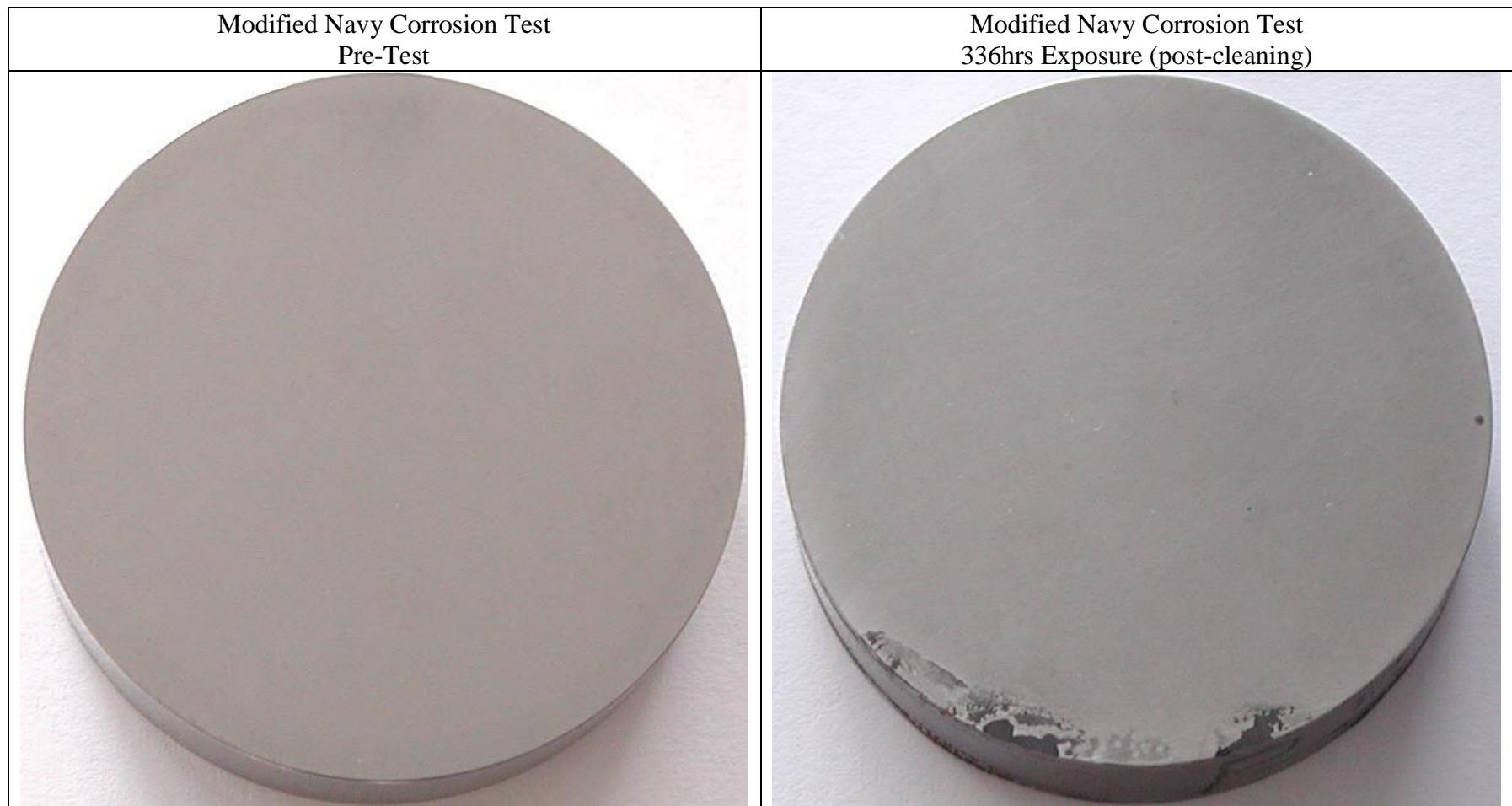
Appendix NCT – Modified Navy Corrosion Test Results

NCT Test Matrix

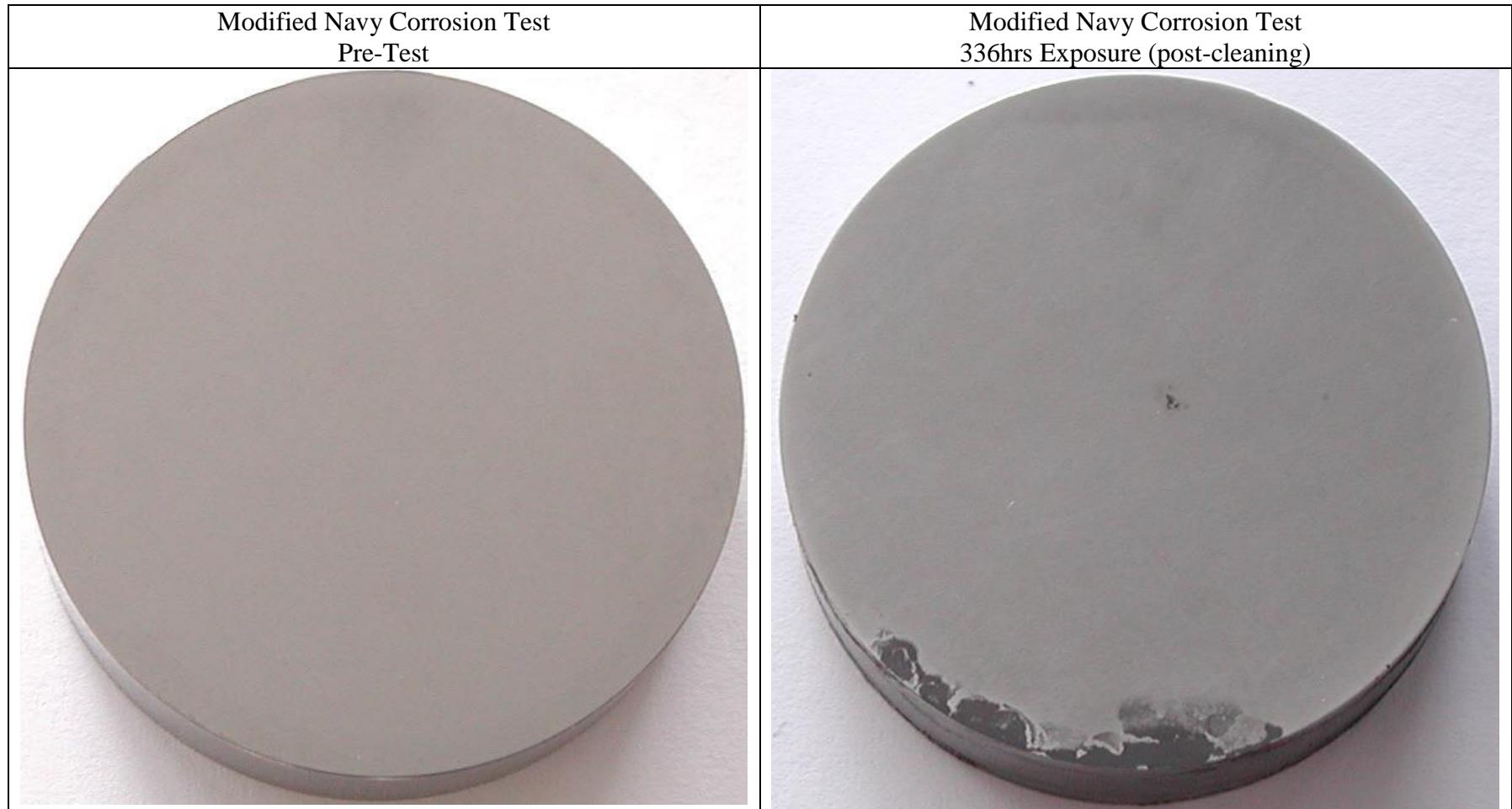
- Four samples are tested for each coating type (except TiCr-TiCrN, see below) with 2 samples coming from the 1st coating deposition batch (Dep1) and 2 samples coming from the second deposition batch (Dep2). The sample set allows for minimal statistical confidence for repeatability of corrosion performance among individual samples from a single coating deposition and also between identical coating formulations produced in separate deposition runs.
- Coating Substrate - Pyrowear 675 (REM super-finish, RMS = 50nm [2µinch], HRC-64)
- Cr-CrN and CrC samples were included in the test matrix which had been subjected to Rolling Contact Fatigue (RCF) and Ball-on-Disc (BoD) wear testing in order to demonstrate functional corrosion performance. TiCr-TiCrN samples were not included due to poor RCF performance which exposed the P675 substrate and limited sample availability.

Coating	Sample ID	Sample Type	Notes
n/a	P54	Masked Sharp Edge	Baseline super-finished P675
n/a	P14	Masked Sharp Edge	Baseline super-finished P675
TiCr-TiCrN (Dep1)	SF7	LiftFan Chamfered Edge	
TiCr-TiCrN (Dep2)	SF11	LiftFan Chamfered Edge	
Cr-CrN (Dep1)	P26	Masked Sharp Edge	RCF track, 4E+06 cycles
Cr-CrN (Dep1)	P74	Masked Sharp Edge	BoD @ 1N, 100m, 500m, and 1000m tracks
Cr-CrN (Dep2)	P49	Masked Sharp Edge	RCF track, 8E+06 cycles
Cr-CrN (Dep2)	P2	Masked Sharp Edge	BoD @ 1N, 100m, 500m, and 1000m tracks
CrC (Dep1)	P30	Masked Sharp Edge	RCF track, 10E+06 cycles
CrC (Dep1)	P37	Masked Sharp Edge	RCF track, 9.5E+06 cycles
CrC (Dep2)	P29	Masked Sharp Edge	
CrC (Dep2)	P46	Masked Sharp Edge	BoD @ 1N, 100m, 500m, and 1000m tracks

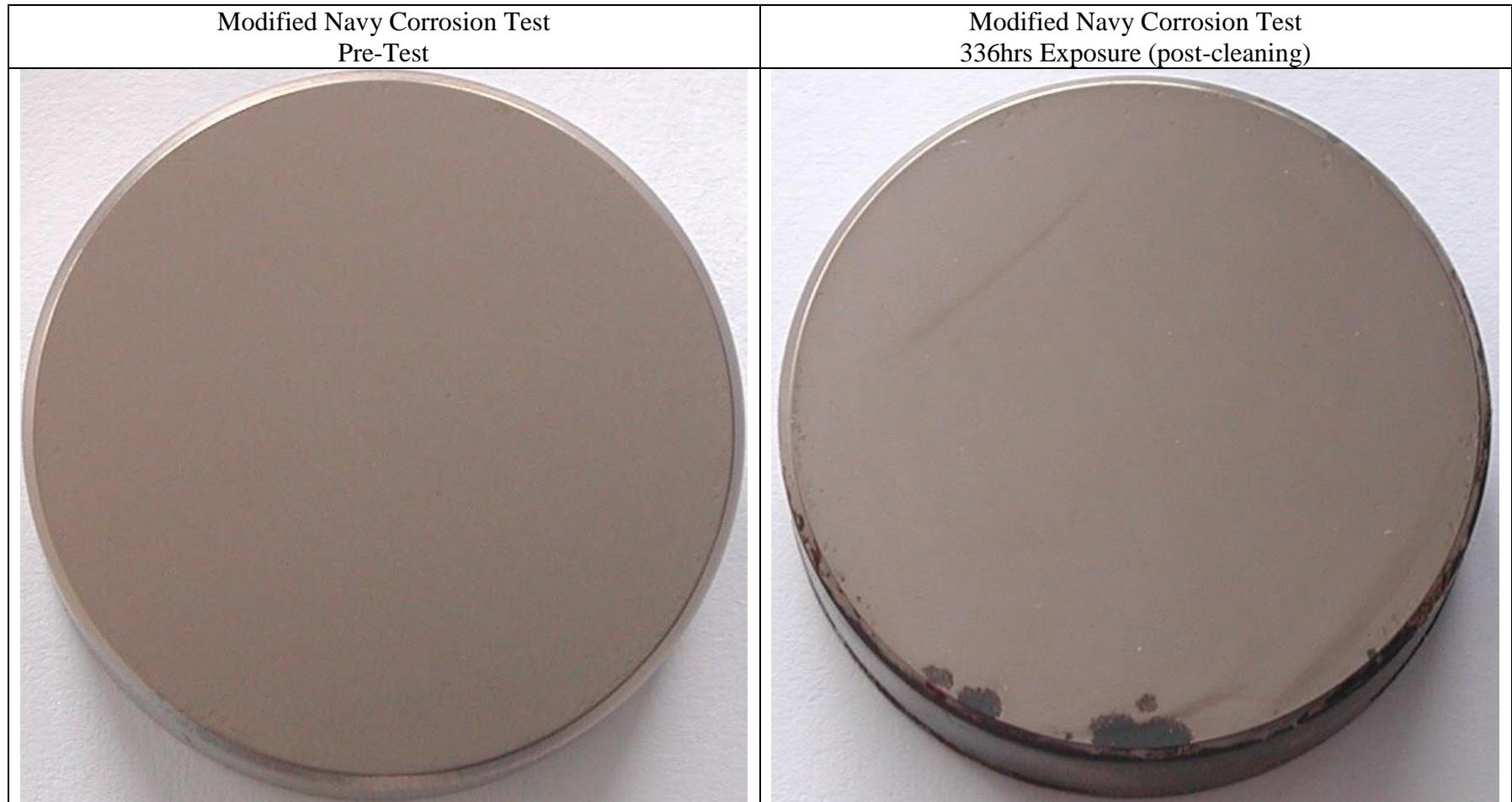
Appendix NCT – Modified Navy Corrosion Test Results

P675, Sample ID – P54, uncoated baseline

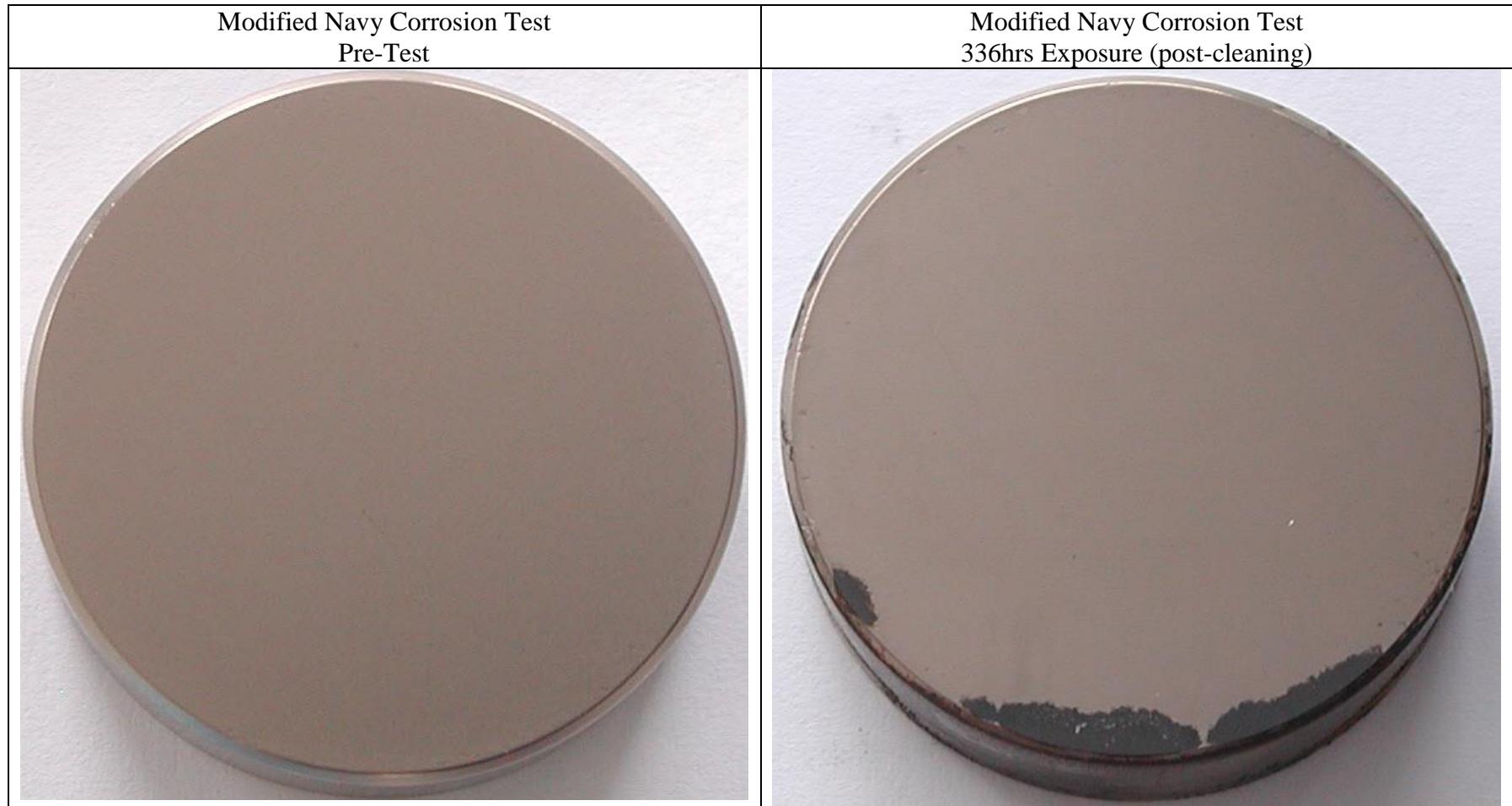
Appendix NCT – Modified Navy Corrosion Test Results

P675, Sample ID – P14, uncoated baseline

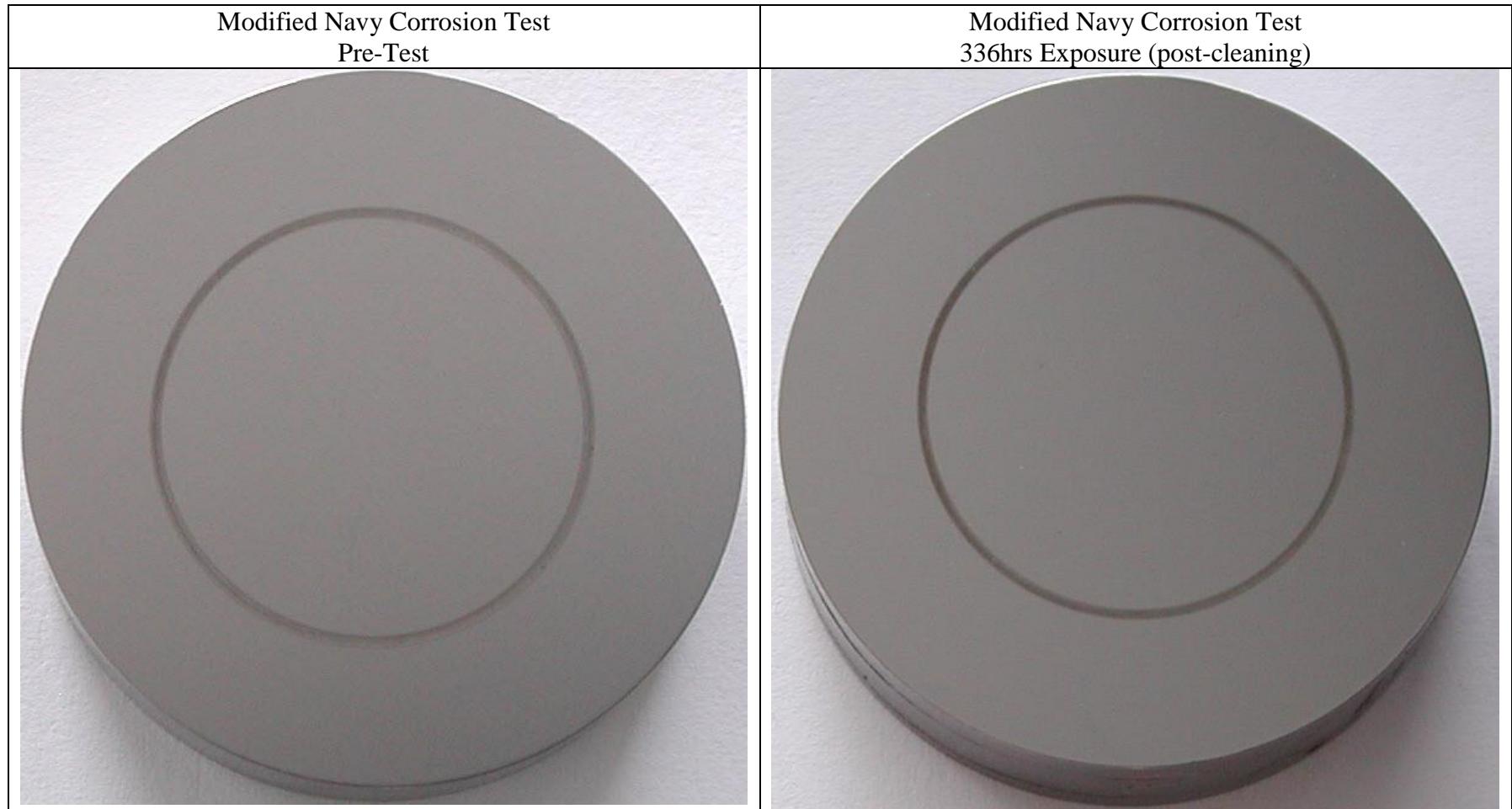
Appendix NCT – Modified Navy Corrosion Test Results

TiCr-TiCrN (Dep1), Sample ID – SF7

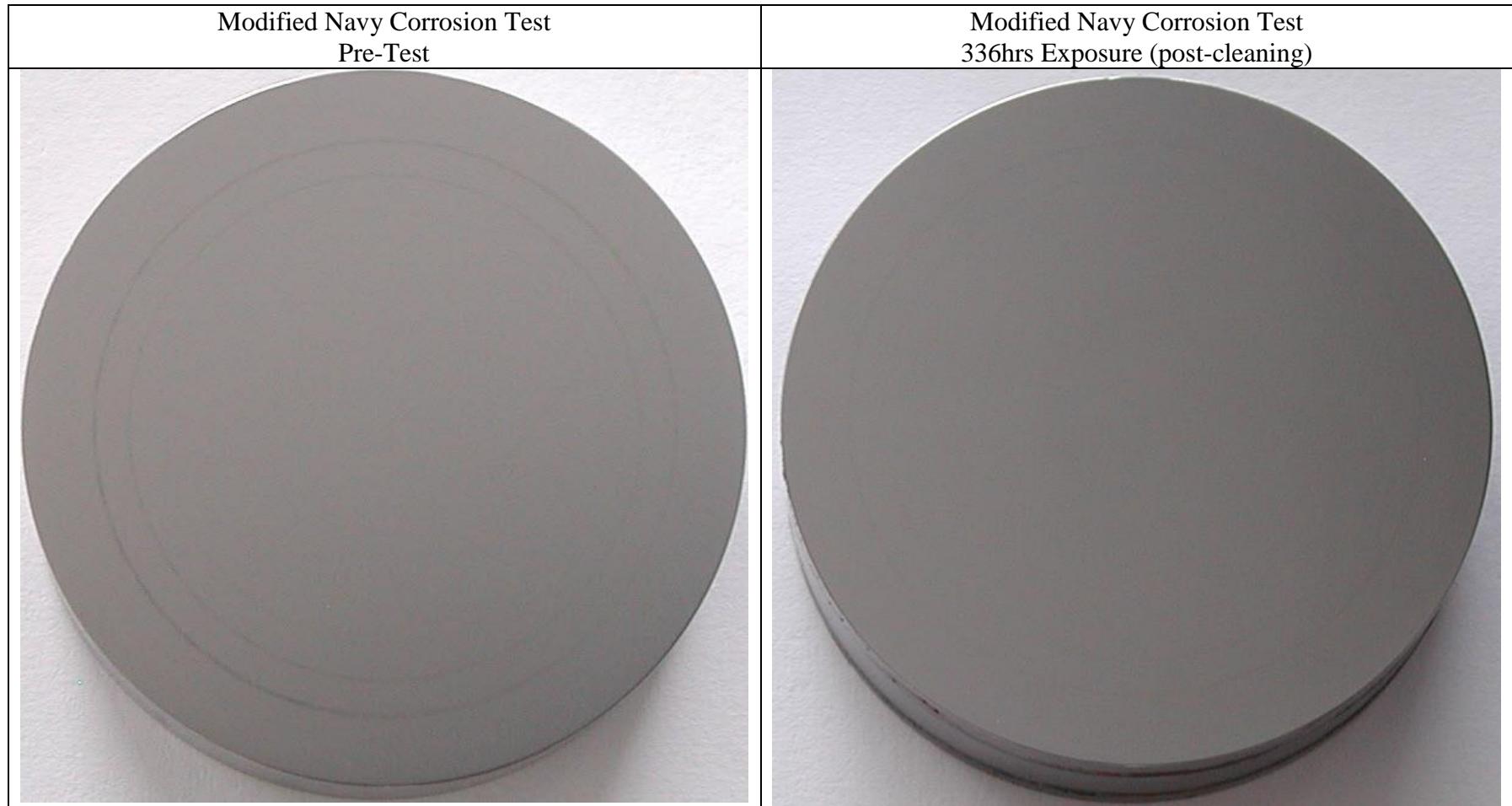
Appendix NCT – Modified Navy Corrosion Test Results

TiCr-TiCrN (Dep2), Sample ID – SF11

Appendix NCT – Modified Navy Corrosion Test Results

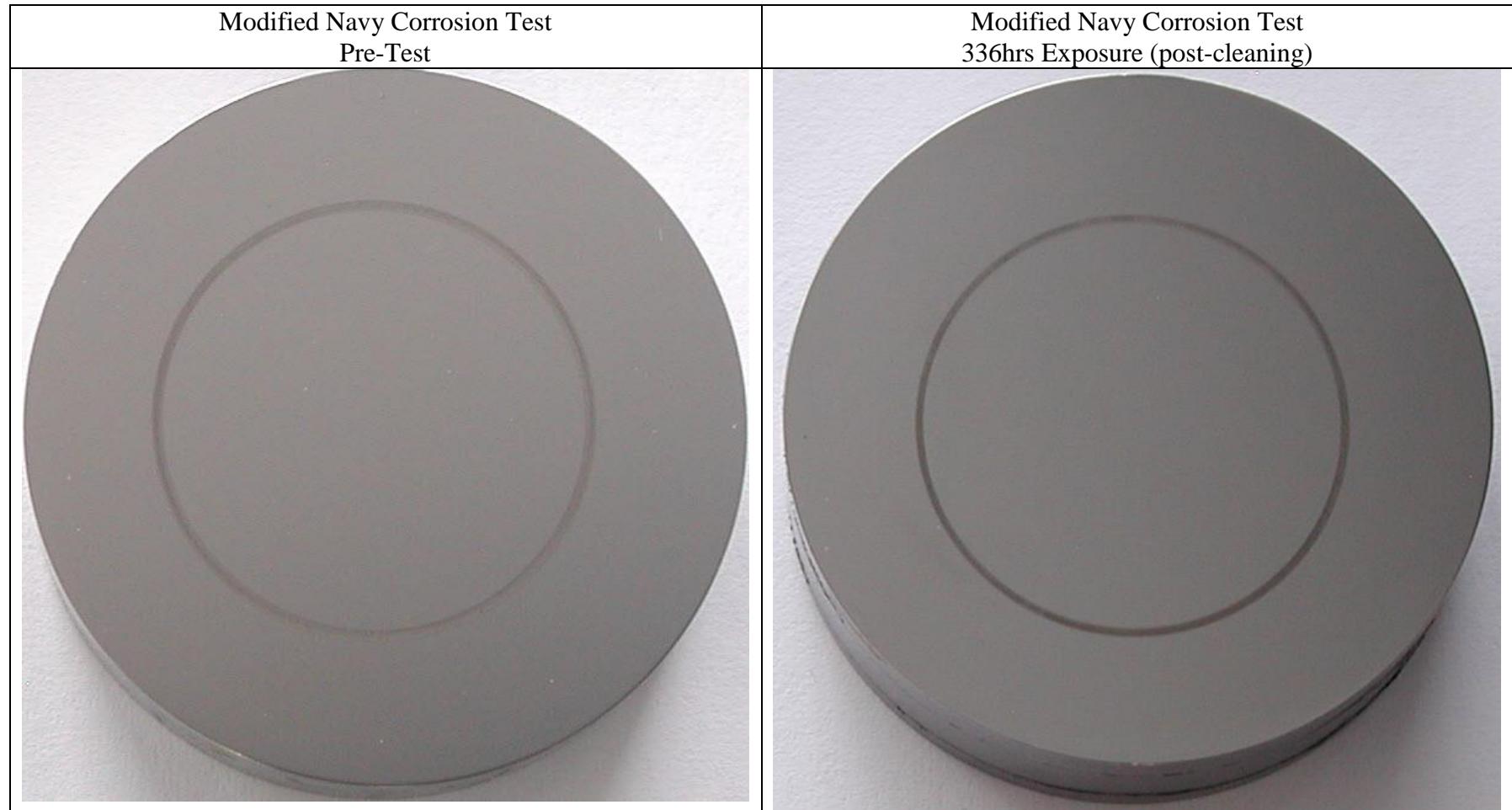
Cr-CrN (Dep1), Sample ID – P26, RCF track on sample

Appendix NCT – Modified Navy Corrosion Test Results

Cr-CrN (Dep1), Sample ID – P74, BoD tracks on sample

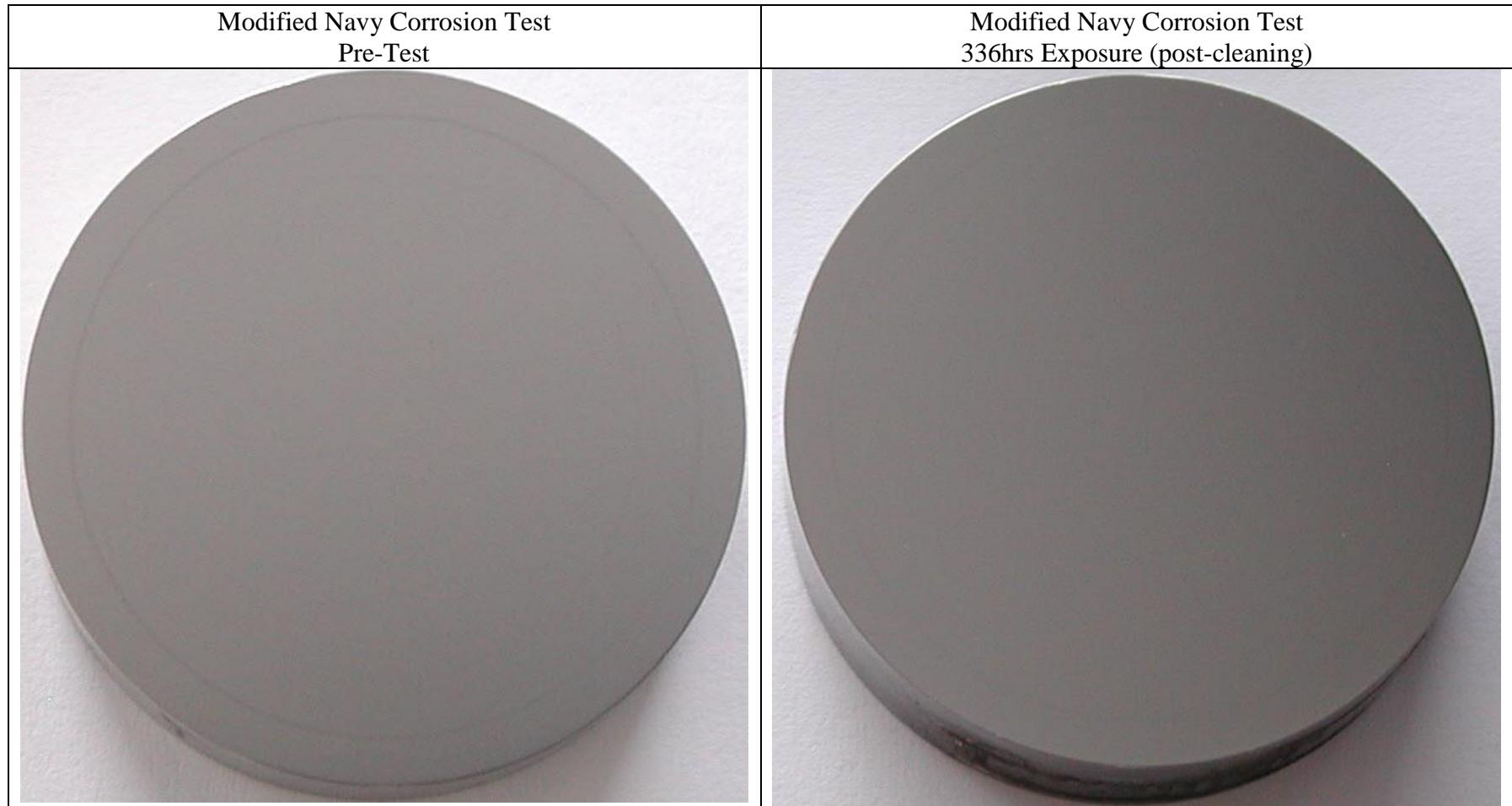
Appendix NCT – Modified Navy Corrosion Test Results

Cr-CrN (Dep2), Sample ID – P49, RCF track on sample



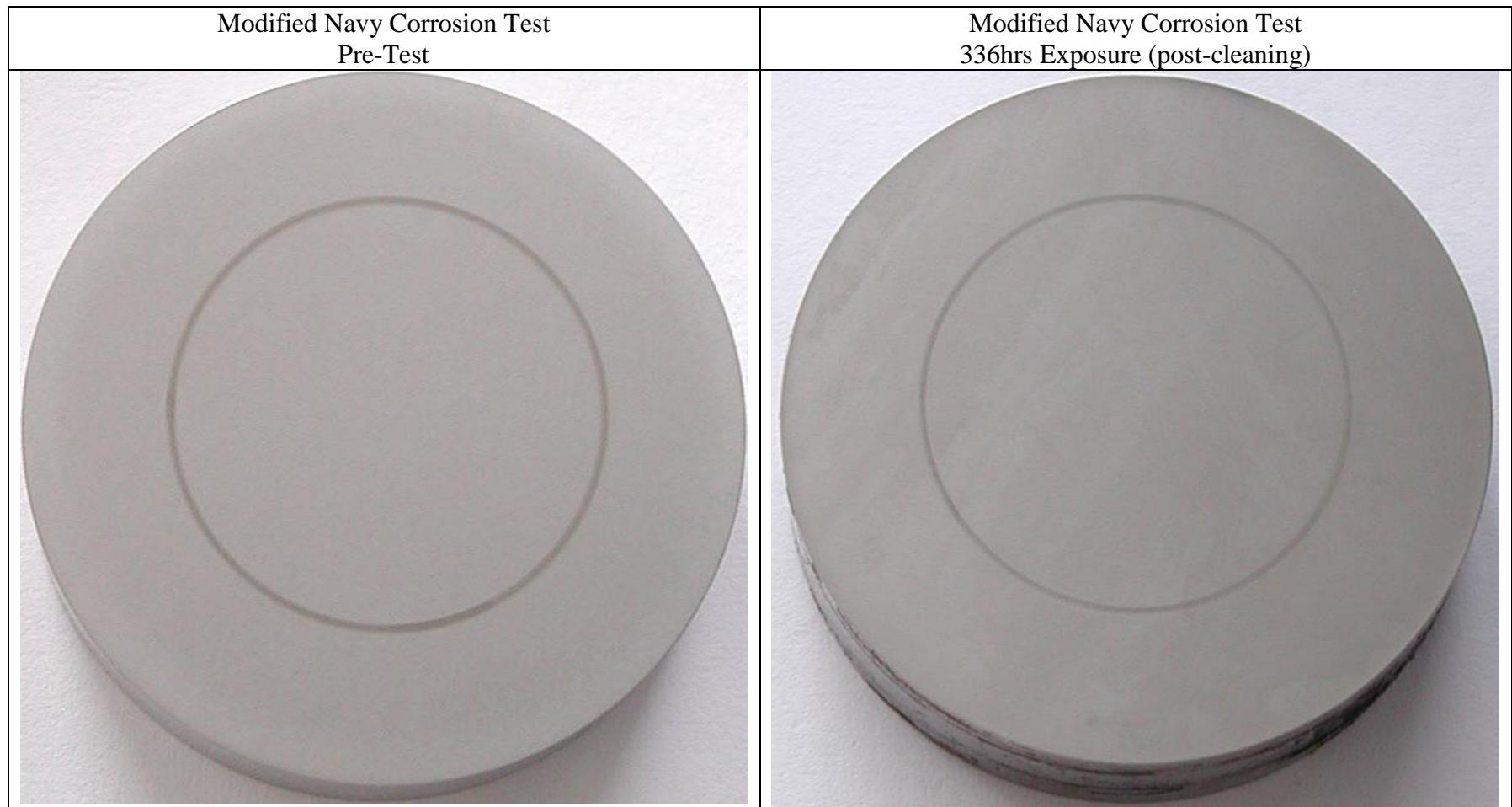
Appendix NCT – Modified Navy Corrosion Test Results

Cr-CrN (Dep2), Sample ID – P2, BoD tracks on sample



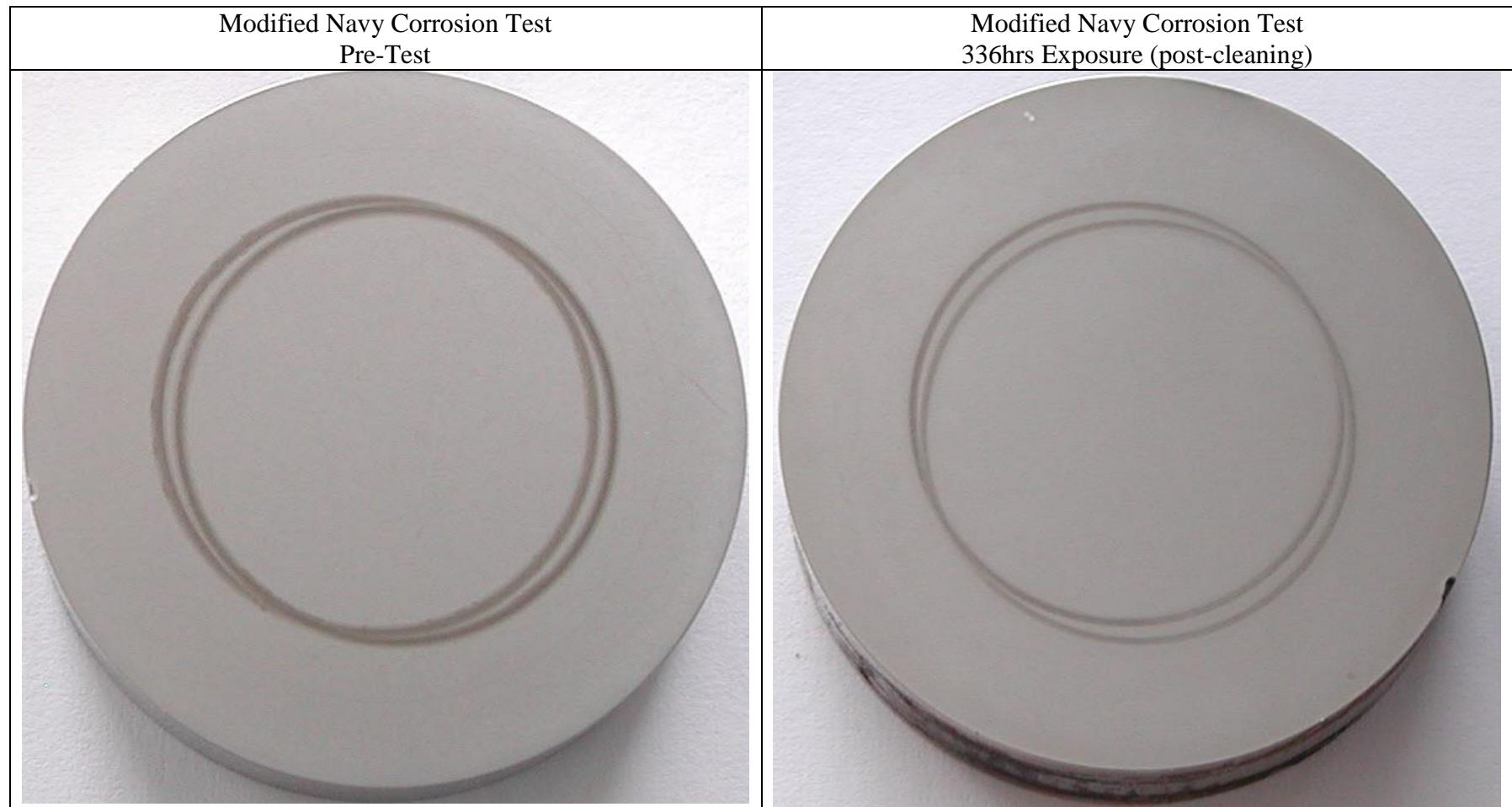
Appendix NCT – Modified Navy Corrosion Test Results

CrC (Dep1), Sample ID – P30, RCF track on sample



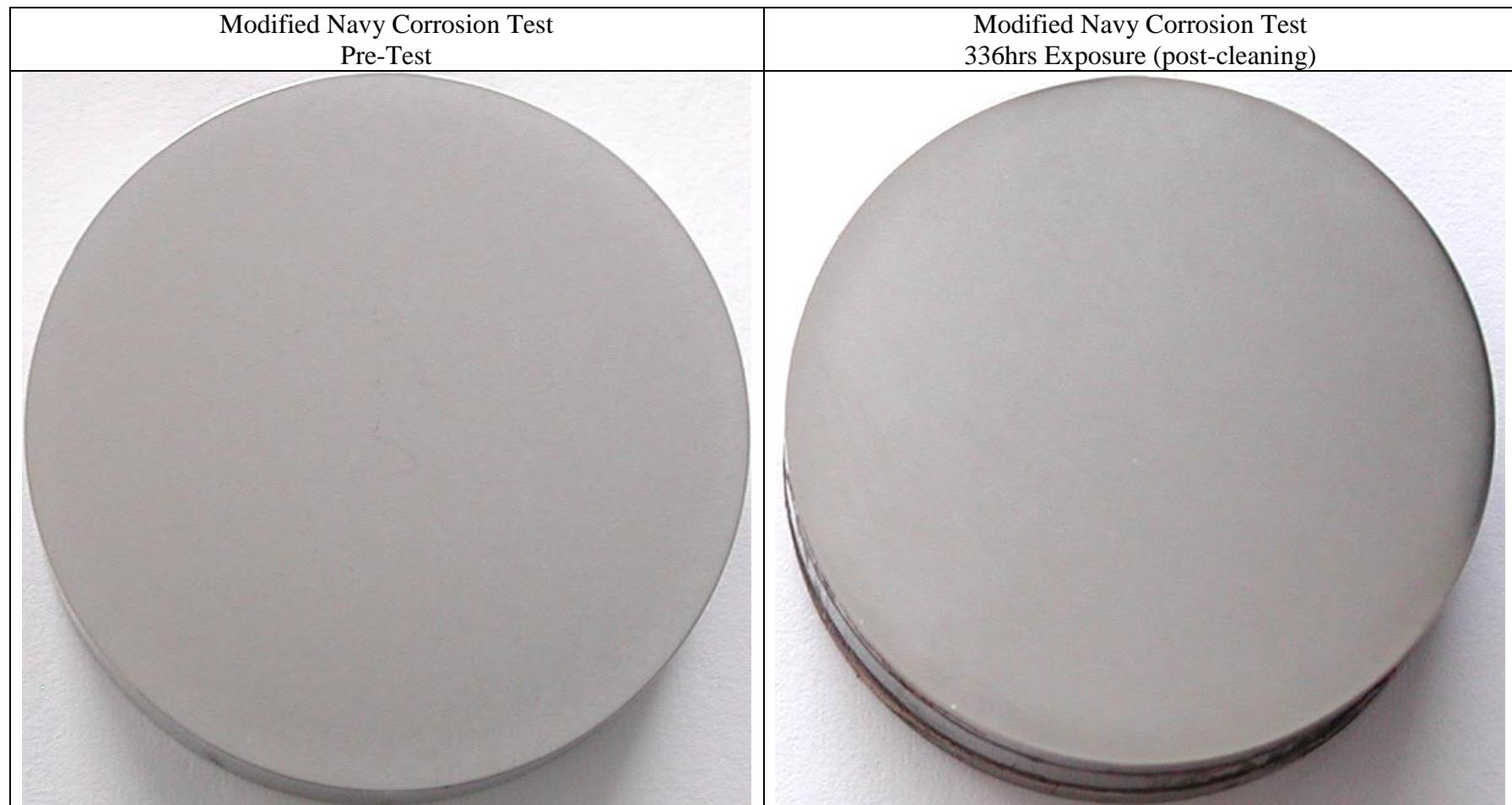
Appendix NCT – Modified Navy Corrosion Test Results

CrC (Dep1), Sample ID – P37, RCF track(s) on sample



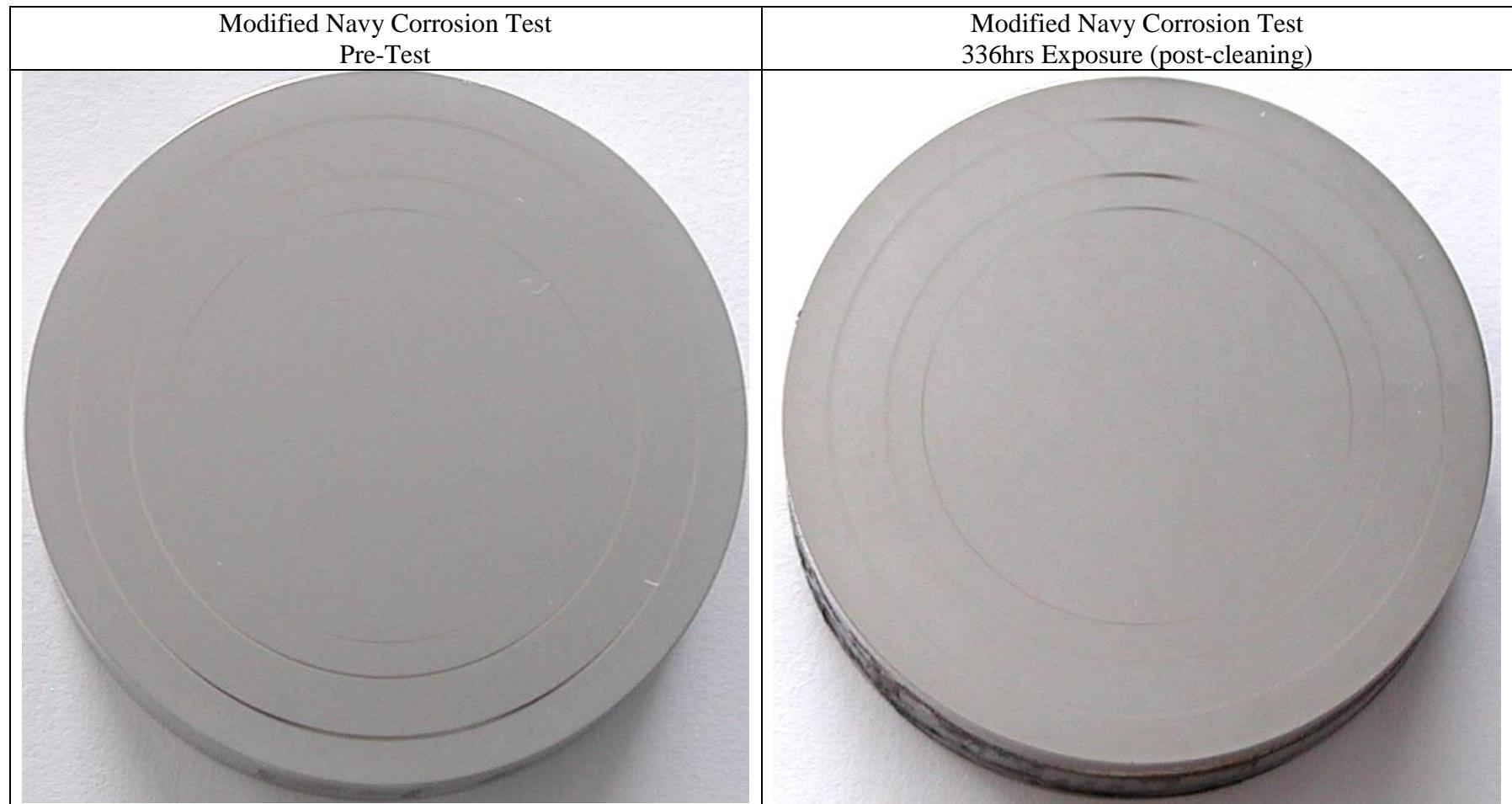
Appendix NCT – Modified Navy Corrosion Test Results

CrC (Dep2), Sample ID – P29



Appendix NCT – Modified Navy Corrosion Test Results

CrC (Dep2), Sample ID – P46, BoD tracks on sample

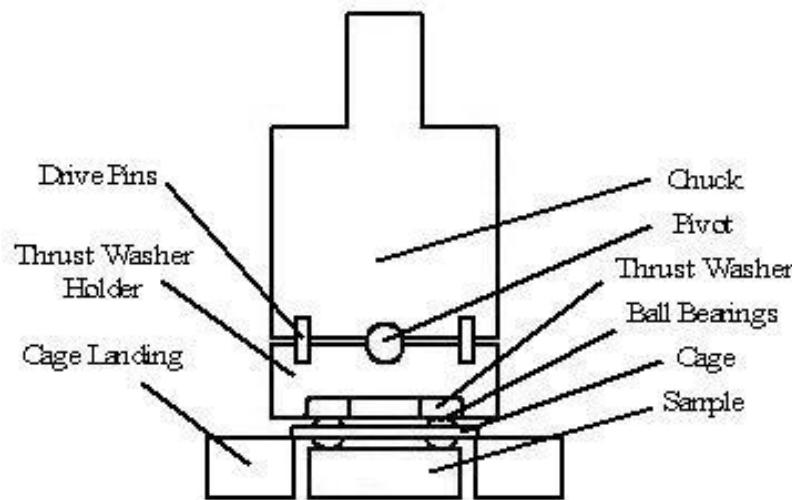


Appendix RCF – Rolling Contact Fatigue Testing Results

Rolling Contact Fatigue Testing Overview

1. The purpose of the rolling contact fatigue (RCF) test was to determine the high contact stress cyclic fatigue life of Pyrowear 675 and TiCr-TiCrN, Cr-CrN, and CrC coatings. The RCF test protocol was designed by Arcomac and is classified as a half-thrust bearing arrangement, very similar to rigs used by a number of researchers, Timken Bearing and also Rolls Royce in a large study of turbine bearing materials [Day, K. L., "Un-steel Testing of Aircraft Engine Bearing Steel," Rolling Contact Fatigue Testing of Bearing Steels. ASTM STP 771, J. J. C. Hoo, Ed., American Society for Testing and Materials, 1982, pp. 67-84]. The contact kinematics of the RCF test are point-on-flat with minimal sliding occurring, i.e. bearing conditions, this is in contrast to the line contact and slip conditions present in gear kinematics. The RCF test still serves to delineate fatigue performance between coatings and substrates and the data produced is more easily compared with the wealth of bearing fatigue data available in the literature.
2. The schematic and the detailed test parameters can be reviewed on page # RCF_2. The basic design of the test can be described as a half-thrust bearing arrangement where an upper grooved thrust washer (SKF part# 51200) is used to drive qty(8) 5.5mm diameter grade 5 chrome steel (AISI 52100) balls against a flat coated or uncoated 1.185"dia Pyrowear 675 (P675) test sample. The contact geometry is such that the contact stress generated on the flat test sample is much higher than the conformal contact stress developed on the grooved thrust washer ensuring that fatigue failure occurs on the test sample. Phenolic cages were specially made to radially locate 8 balls and the thrust washer holder was specially designed to allow for auto-leveling of the applied load ensuring even contact stresses all around the rolling track. The test load is applied via a loading arm and monitored with a load cell to create a contact stress of 4.5GPa. During testing the sample surface, balls and cage are submerged in ~20mL 555 jet oil (DOD-L-85734) and intake and outtake peristaltic pumps provide for a constant 1mL/sec circulation of Aeroshell 555 jet oil from a 1000mL reservoir. The test is run at 3450RPM which results in 1,656,000 contact fatigue cycles per hour. For RCF testing a contact cycle is defined as a pass of a loaded ball over a finite section of the sample, i.e. one revolution of the thrust bearing (with 8 balls) equals eight contact cycles. A computer with LabView software controls the RCF test apparatus and allows constant monitoring of revolutions of the AC motor, contact cycles, and oil flow. Acoustic signals were monitored using Physical Acoustic Corporation's PCI-2 DAQ Card and a R15-A sensor.
3. RCF failure was determined by a combination of acoustic emission (AE) monitoring and post-test analysis by optical microscope and surface profilometry. When fatigue damage initiates, energy is released in the form of elastic waves with high frequency. Acoustic emission sensors are piezoelectric transducers that convert these elastic waves into a voltage signal and allow for monitoring and determination of material failure in fatigue. Micro-pitting (coating cohesive or adhesive delamination) and/or macro-pitting (sub-surface crack formation and subsequent pull-out of material) are identified as the primary modes of fatigue failure. Material fatigue failure was determined by a rapid drop in AE signal counts at which point the RCF test was stopped. Post RCF test samples were examined using optical microscopy to confirm and characterize fatigue damage and profilometry was used to characterize fatigue damage depth. A precision mass scale was used to assess RCF test ball wear by assessing changes in pre/post test ball mass.

Appendix RCF – Rolling Contact Fatigue (RCF) Testing Results

**Cross-Section Schematic of RCF Test (oil cup and load arm assembly not shown)****RCF Test Parameters**

Failure Condition	Rapid drop in AE signal counts
Duration of Test	Failure or suspend test at 8-10E+06 contact cycles
Hertzian Contact Stress	4.5GPa
Speed	3450 RPM, 1,656,000 contact cycles per hour
Ball Track Diameter	17mm
Lubrication	Aersoshell 555 (DOD-L-85734), flowrate ~1ml/sec
Ball	Qty 8, 5.5mm, 52100 steel (SKF)
Thrust Washer	SKF 51200
Cage	Phenolic grade LE
Testing Temp	Ambient

Appendix RCF – Rolling Contact Fatigue (RCF) Testing Results

RCF Test Results

Coating	Coating ID	Sample ID	Contact Stress [GPa]	# of Cycles @ FAILURE	# of Cycles @ STOP	Notes
n/a	Baseline P675	P24	4.5	n/a	8.0E+06	No failure, test suspended
n/a	Baseline P675	P25	4.5	n/a	9.0E+06	No failure, test suspended
n/a	Baseline P675	P48	4.5	n/a	18.0E+06	No failure, test suspended
TiCr-TiCrN	ASE-8-14-1 (Dep2)	P76	4.5	0.09E+06	0.25E+06	Failure, coating delamination (100% of track)
TiCr-TiCrN	ASE-8-14-1 (Dep2)	P20	4.5	0.25E+06	1.0E+06	Failure, coating delamination (100% of track)
TiCr-TiCrN	ASE-8-14-1 (Dep2)	P32	4.5	0.33E+06	0.7E+06	Failure, coating delamination (100% of track)
Cr-CrN	ASE-8-29-1 (Dep1)	P9	4.5	3.0E+06	3.0E+06	Failure, coating delamination (~30% of track)
Cr-CrN	ASE-8-29-1 (Dep1)	P23	4.5	n/a	8.0E+06	No failure, test suspended
Cr-CrN	ASE-8-29-1 (Dep1)	P26	4.5	n/a	4.0E+06	No failure, test stopped due to EHD Breakdown
Cr-CrN	ASE-8-34-1 (Dep2)	P41	4.5	n/a	10.0E+06	No failure, test suspended
Cr-CrN	ASE-8-34-1 (Dep2)	P50	4.5	n/a	6.3E+06	No failure, test stopped due to mechanical problem
Cr-CrN	ASE-8-34-1 (Dep2)	P49	4.5	n/a	8.0E+06	No failure, test stopped due to EHD Breakdown
CrC	ASE-8-19-1 (Dep1)	P30	4.5	n/a	10.0E+06	No failure, test suspended
CrC	ASE-8-19-1 (Dep1)	P45	4.5	n/a	10.0E+06	No failure, test suspended
CrC	ASE-8-19-1 (Dep1)	P37	4.5	n/a	9.5E+06*	No failure, test stopped due to EHD Breakdown
CrC	ASE-8-26-1 (Dep2)	P39				test not completed by time of reporting
CrC	ASE-8-26-1 (Dep2)	P42				test not completed by time of reporting
CrC	ASE-8-26-1 (Dep2)	P29				test not completed by time of reporting

- No fatigue failures were observed for the baseline super-finished P675 or the CrC coated P675. The Cr-CrN coating passed 5 of 6 tests, with one test showing coating failure on ~30% of the track area after 3E+06 contact cycles. The TiCr-TiCrN coating failed by delamination over 100% of the track area in less than 500,000 contact cycles in 3 of 3 tests.
- As tests progressed a problem with the RCF test rig was discovered (breakdown of neoprene oil delivery tubing caused oil contamination) which caused a loss of full EHD film lubrication resulting in ball-disc sliding contact. The EHD breakdown caused steady sliding wear of the disc coating and balls and resulted in progressive vibration increases which required early suspension of the testing. See “notes” column for tests that were suspended.
- RCF testing conducted by other researchers under similar test conditions demonstrate fatigue lives of advanced bearing steels in the range of 60-90E+06 cycles; approximately 5-10 times the number of cycles tested presently. The current effort shows that the CrC and Cr-CrN coating have potential for good fatigue performance but an extended testing effort would need to be completed to confirm equal or better fatigue performance than the P675 substrate.

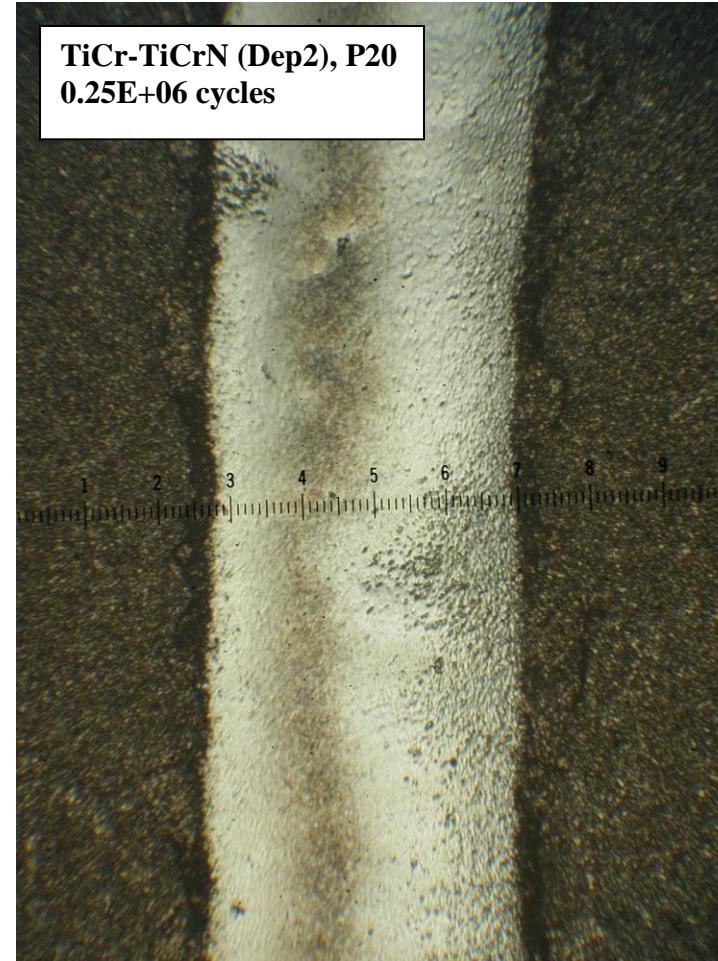
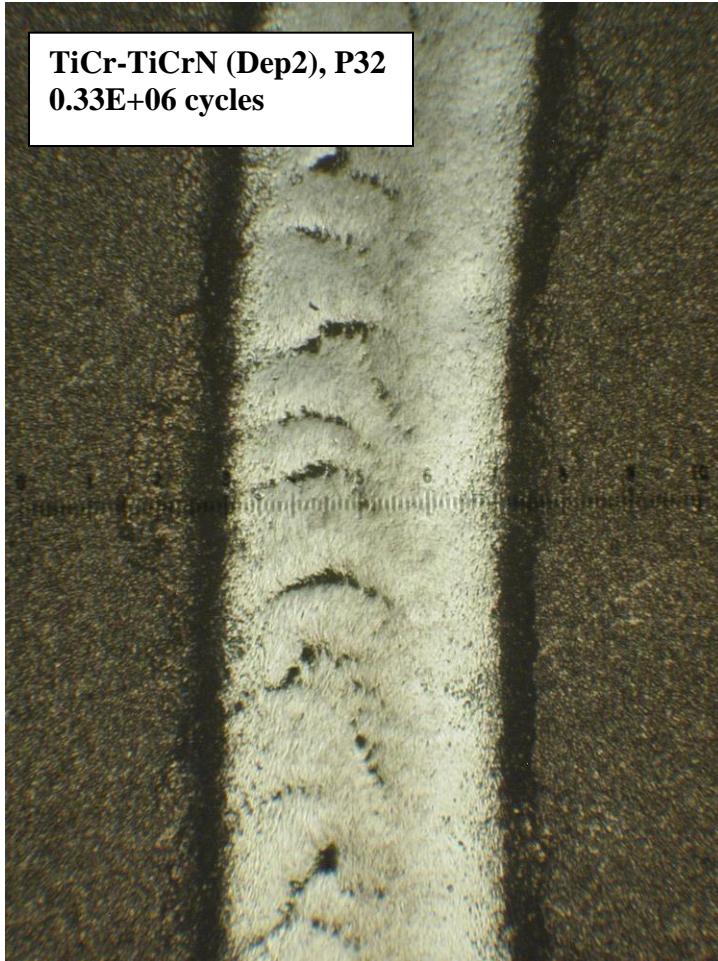
Appendix RCF – Rolling Contact Fatigue (RCF) Testing Results

RCF Test Results – Ball Wear

Test Sample Coating	RCF Cycles	8 Ball Mass [g]	8 Ball Mass Loss [g]	8 Ball % Mass Loss	Notes
TiCr-TiCrN (Dep2)	0.09E+06	5.41729	0.00839	-0.15%	
TiCr-TiCrN (Dep2)	0.33E+06	5.39865	0.02703	-0.50%	
CrC (Dep1)	10.0E+06	5.41649	0.00919	-0.17%	
CrC (Dep1)	10.0E+06	5.41626	0.00942	-0.17%	
CrC (Dep1)	5.75E+06	5.39287	0.03281	-0.60%	EHD oil film breakdown
CrC (Dep1)	3.75E+06	5.39847	0.02721	-0.50%	EHD oil film breakdown
Cr-CrN (Dep1)	8.00E+06	5.42288	0.00280	-0.05%	
Cr-CrN (Dep1)	3.00E+06	5.42175	0.00393	-0.07%	
Cr-CrN (Dep1)	4.00E+06	5.30234	0.12334	-2.27%	EHD oil film breakdown
Cr-CrN (Dep2)	8.00E+06	5.2806	0.14508	-2.67%	EHD oil film breakdown
Cr-CrN (Dep2)	6.30E+06	5.4198	0.00588	-0.11%	
Cr-CrN (Dep2)	10.0E+06	5.41651	0.00917	-0.17%	
P675 baseline	8.00E+06	5.42573	0.00000	0.00%	
P675 baseline	8.00E+06	5.42523	0.00045	-0.01%	
P675 baseline	9.00E+06	5.42537	0.00031	-0.01%	

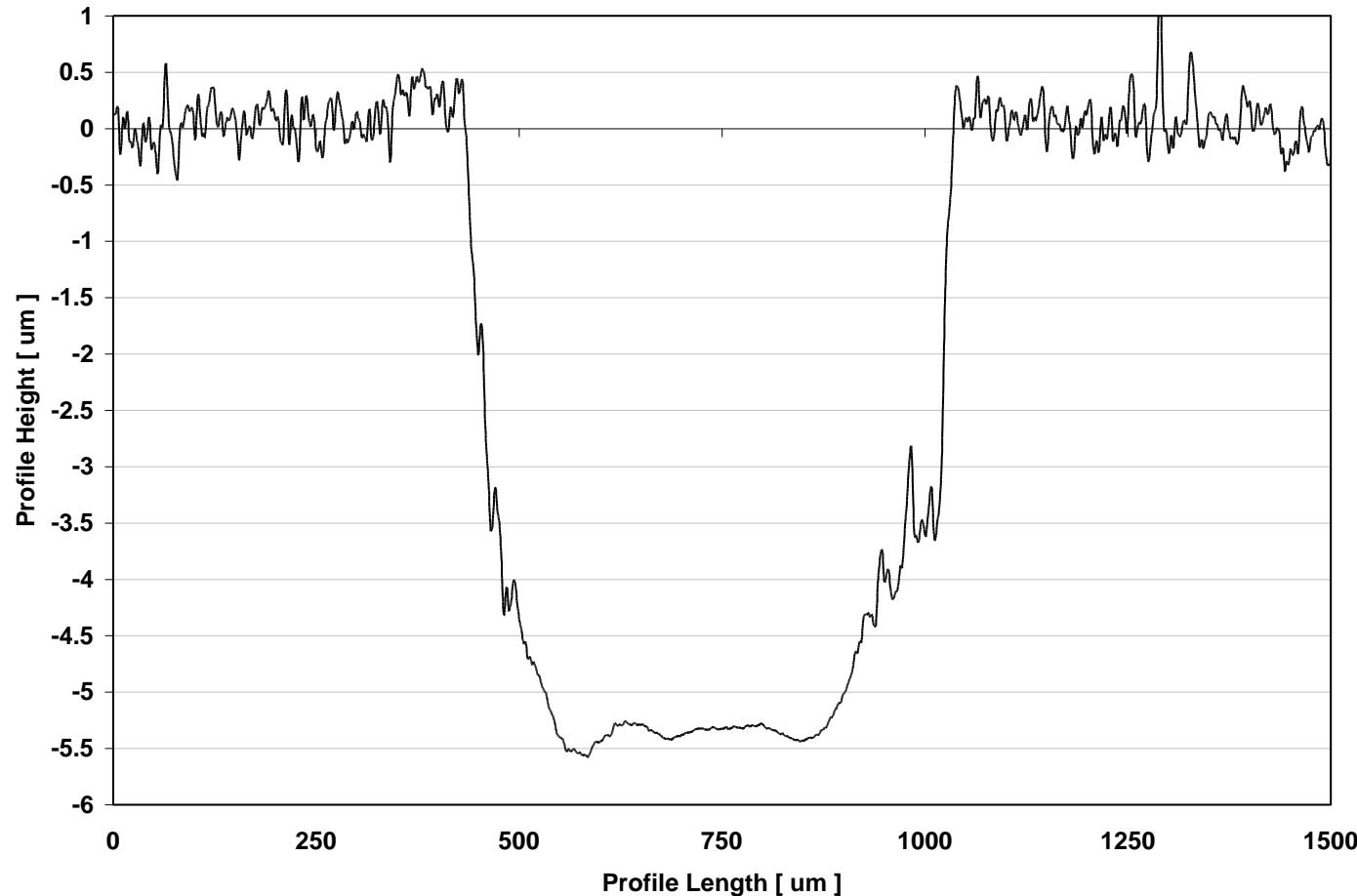
- Ball wear was determined by massing 5 randomly selected groups of 8 unworn AISI 52100 chrome steel balls to establish a pre-test ball mass and comparing this with the post-test mass. Repeatability of mass measurement for pre-test 8 ball groups was +/-0.002%, therefore for the data presented, confidence in accuracy of measurement is high.
- For RCF tests which ran to test suspension (no failure) the %mass loss was less than 0.2% for the CrC and Cr-CrN coatings and less than 0.01% for baseline P675. This indicates that essentially no wear occurred on the balls and that full EHD lubrication was maintained for the duration of the RCF test. The slight increase in wear of the balls for the CrC and Cr-CrN coatings is caused by to run-in asperity wear of the coating surface roughness (RMS 150nm, 6 μ inch) as compared to no run-in asperity contact for the super-finished P675 surface roughness (RMS 50nm, 2 μ inch). Although the post-test ball surface roughness was not measured the coatings may have a beneficial polishing effect (mild wear) on the 52100 balls as compared to the P675 baseline.
- RCF tests which were suspended due to EHD breakdown show increased ball wear as would be expected. The balls have a %mass loss of ~2.5% when running against the Cr-CrN coating which is more abrasive than the CrC coating for which the balls have a %mass loss of ~0.55%.

Appendix RCF – Rolling Contact Fatigue (RCF) Testing Results



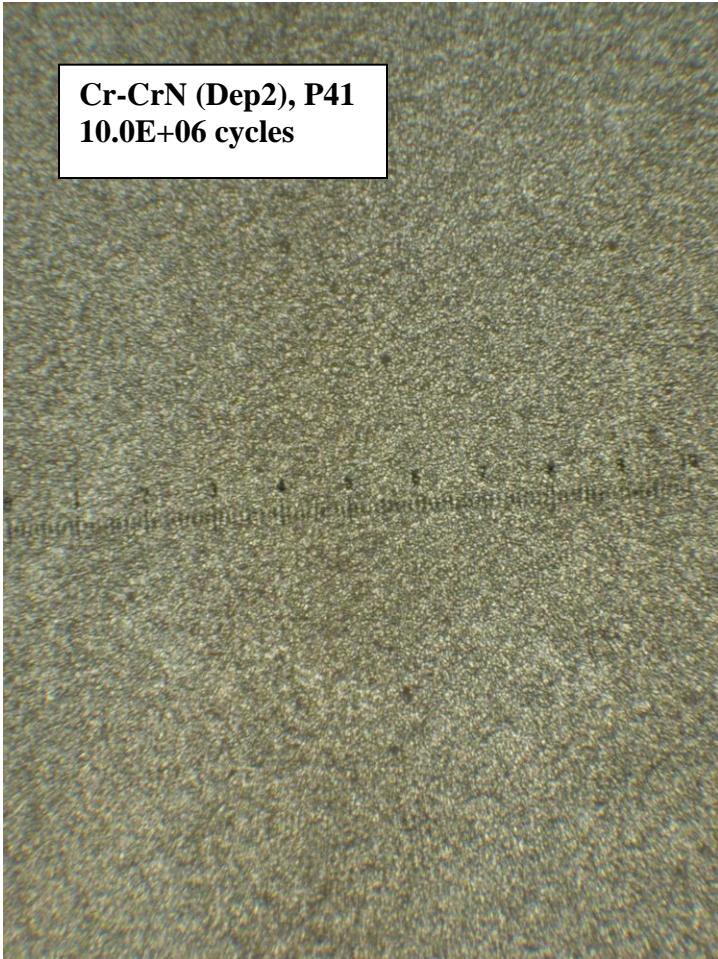
Optical microscope images of RCF track on TiCr-TiCrN coated P675 (scale 1div = 105 μ m). The TiCr-TiCrN fails by adhesive delamination from the P675 substrate and cohesive interlayer delamination can be observed along the edges of the rolling track. For all TiCr-TiCrN coatings tested, 100% of the track area failed as shown. The ~400 μ m track width correlates well with the theoretical Hertz elastic contact width of 350 μ m at 4.5GPa contact stress.

Appendix RCF – Rolling Contact Fatigue (RCF) Testing Results



Typical profile scan of a TiCr-TiCrN coating RCF track. The depth of the profile indicates complete adhesive delamination of the TiCr-TiCrN coating in the center of the track (profile length range ~500 μm to 900 μm). Outside of the track center the profile steps show evidence of cohesive interlayer delaminations in the TiCr-TiCrN at the multi-layer coating interfaces.

Appendix RCF – Rolling Contact Fatigue (RCF) Testing Results



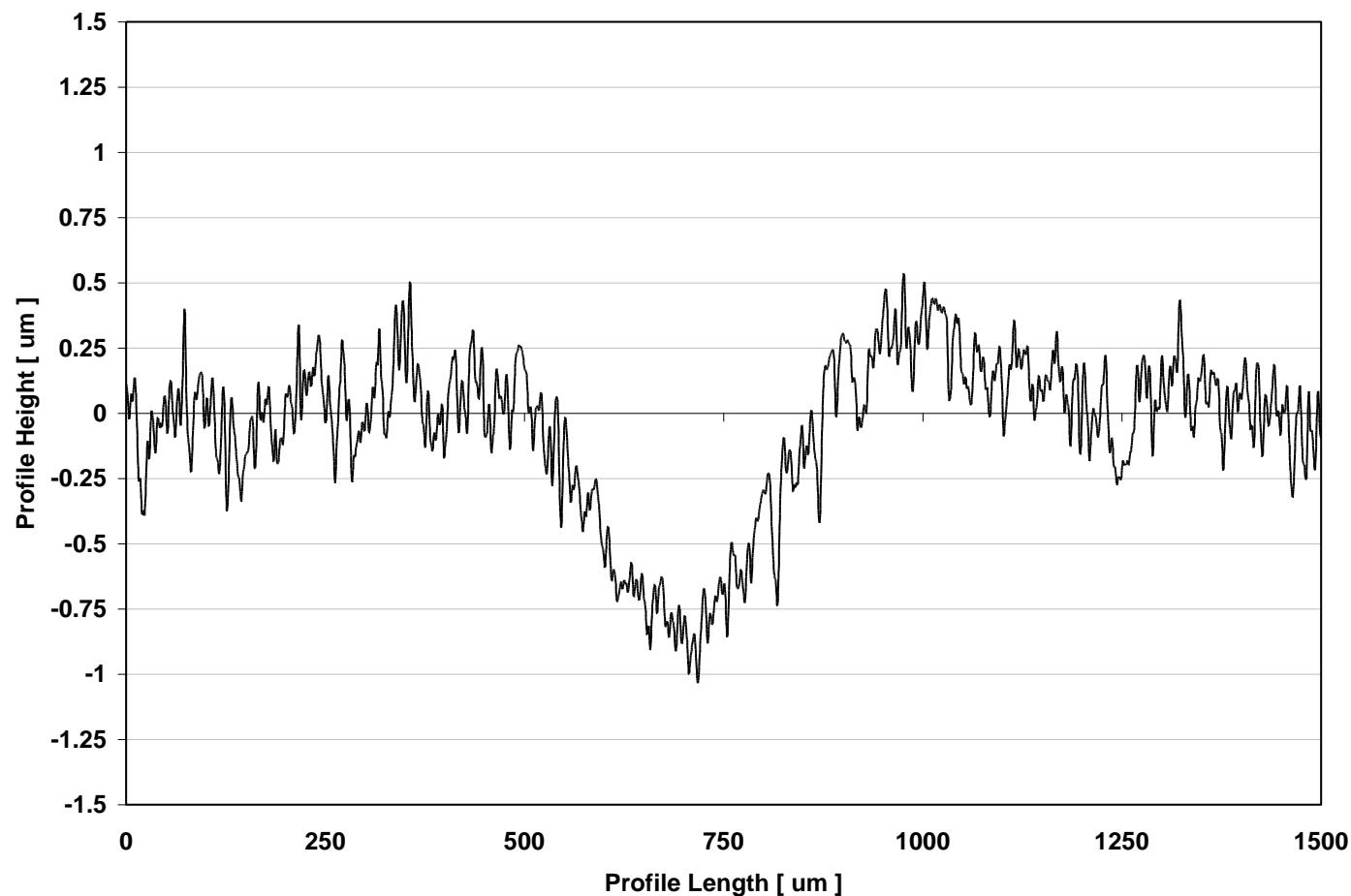
Cr-CrN (Dep2), P41
10.0E+06 cycles



Cr-CrN (Dep1), P9
3.0E+06 cycles

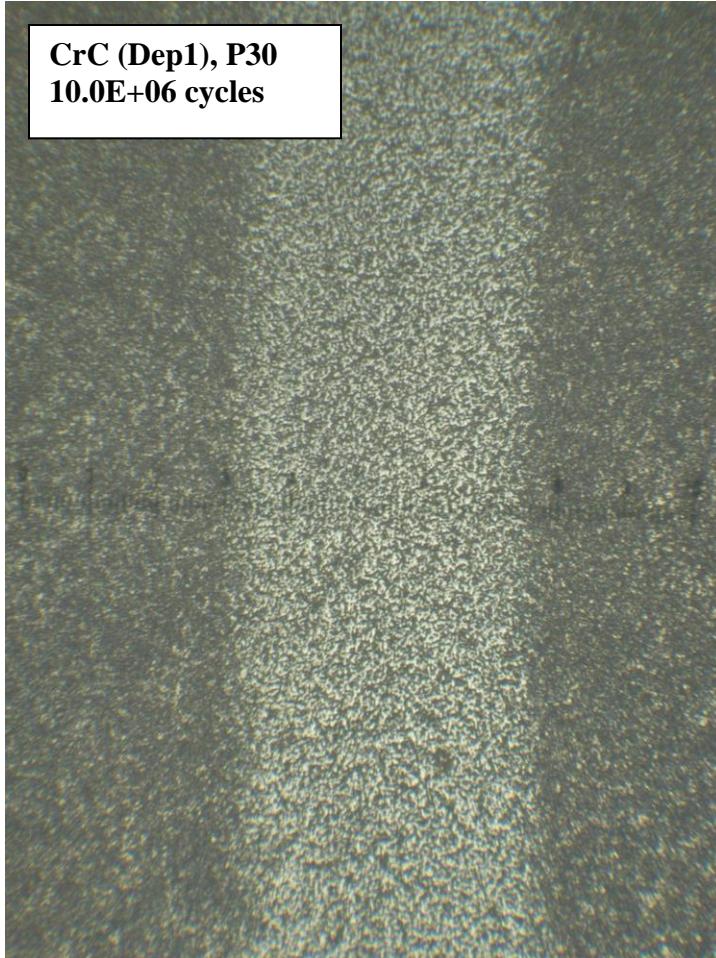
Optical microscope images of RCF track on Cr-CrN coated P675 (scale 1div = 105 μ m). The RCF track in the left image is representative of the 5 out of 6 Cr-CrN coating tests that were run until test suspension and showed no fatigue failures. In general Cr-CrN coating RCF tracks showed only light discoloration and no wear or change in surface morphology was visually apparent. The right image shows the Cr-CrN test which failed at 3.0E+06 contact cycles by adhesive delamination from the P675 substrate over ~30% of the track area. The image shows a section of track which illustrates the boundary between delaminated track and undamaged track.

Appendix RCF – Rolling Contact Fatigue (RCF) Testing Results

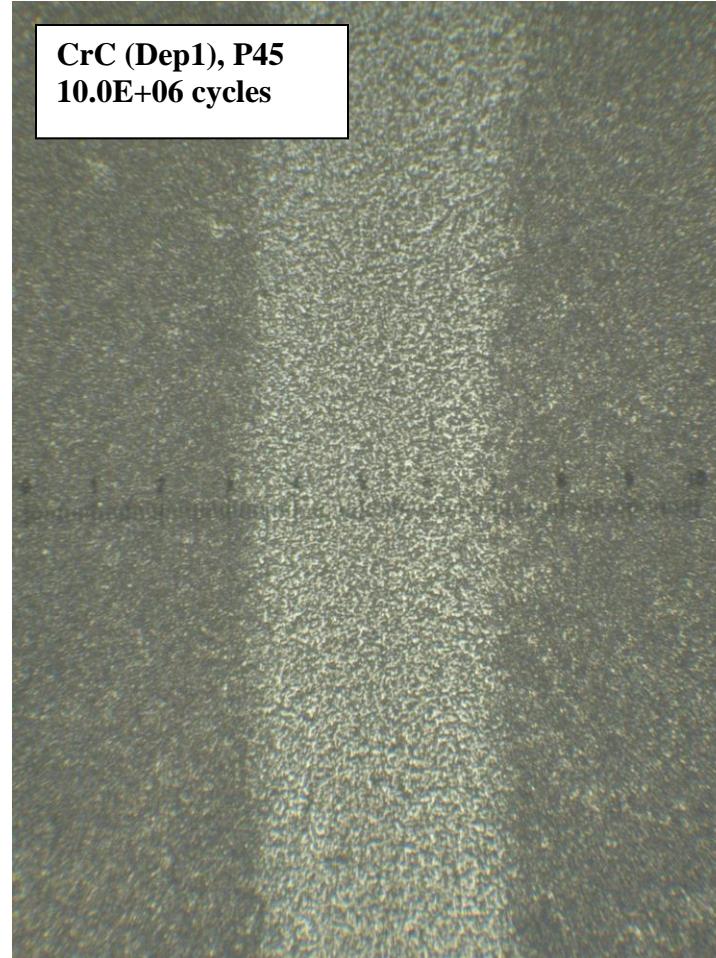


Typical profile scan of a Cr-CrN coating RCF track. A conformal profile can be observed with a depth of ~0.5-0.75 μ m. The profile is hypothesized to be primarily the result of plastic deformation of the P675 substrate and secondarily the result of polishing run-in wear of the coating.

Appendix RCF – Rolling Contact Fatigue (RCF) Testing Results



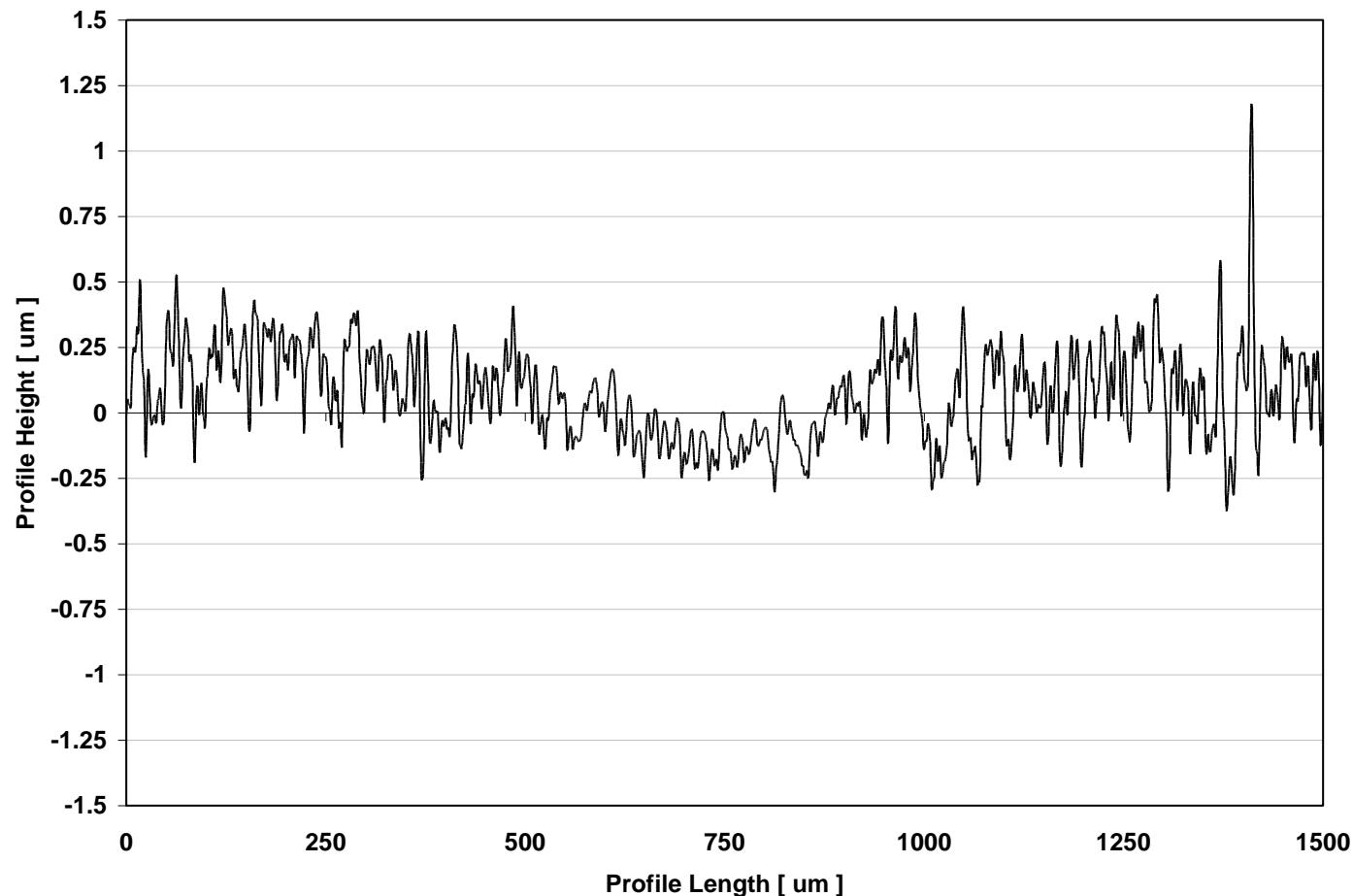
CrC (Dep1), P30
10.0E+06 cycles



CrC (Dep1), P45
10.0E+06 cycles

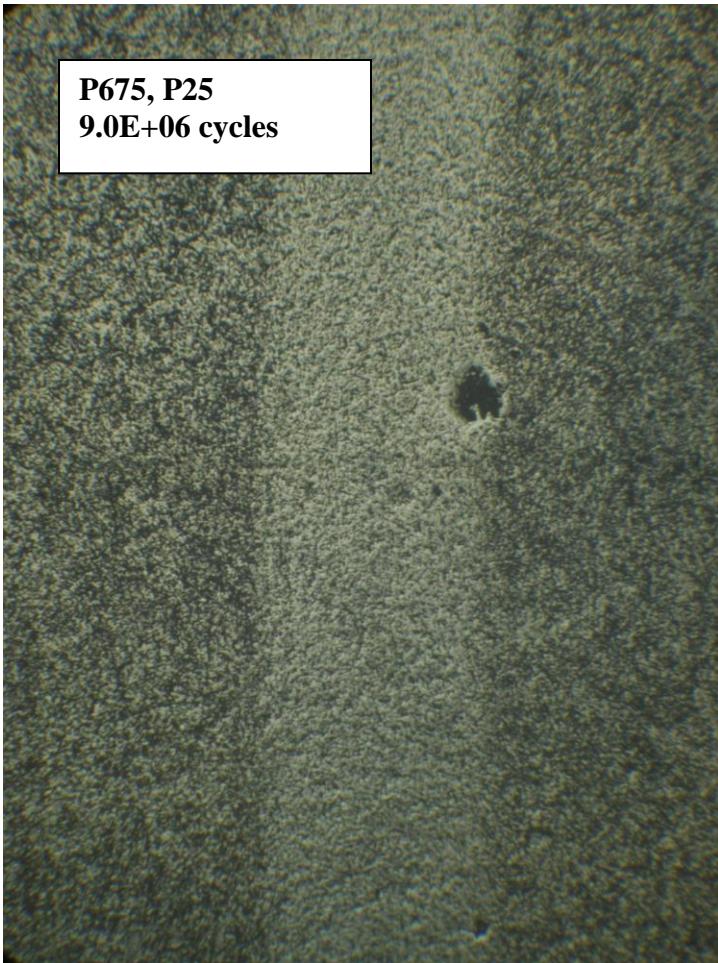
Optical microscope images of RCF track on CrC coated P675 (scale 1div = 105 μ m). The images of two separate tests are representative of the RCF track on all CrC coatings tested. Slight polishing wear of the CrC coatings was observed which reduced the surface roughness in the rolling track. The ~400 μ m track width correlates well with the theoretical Hertz elastic contact width of 350 μ m at 4.5GPa contact stress.

Appendix RCF – Rolling Contact Fatigue (RCF) Testing Results



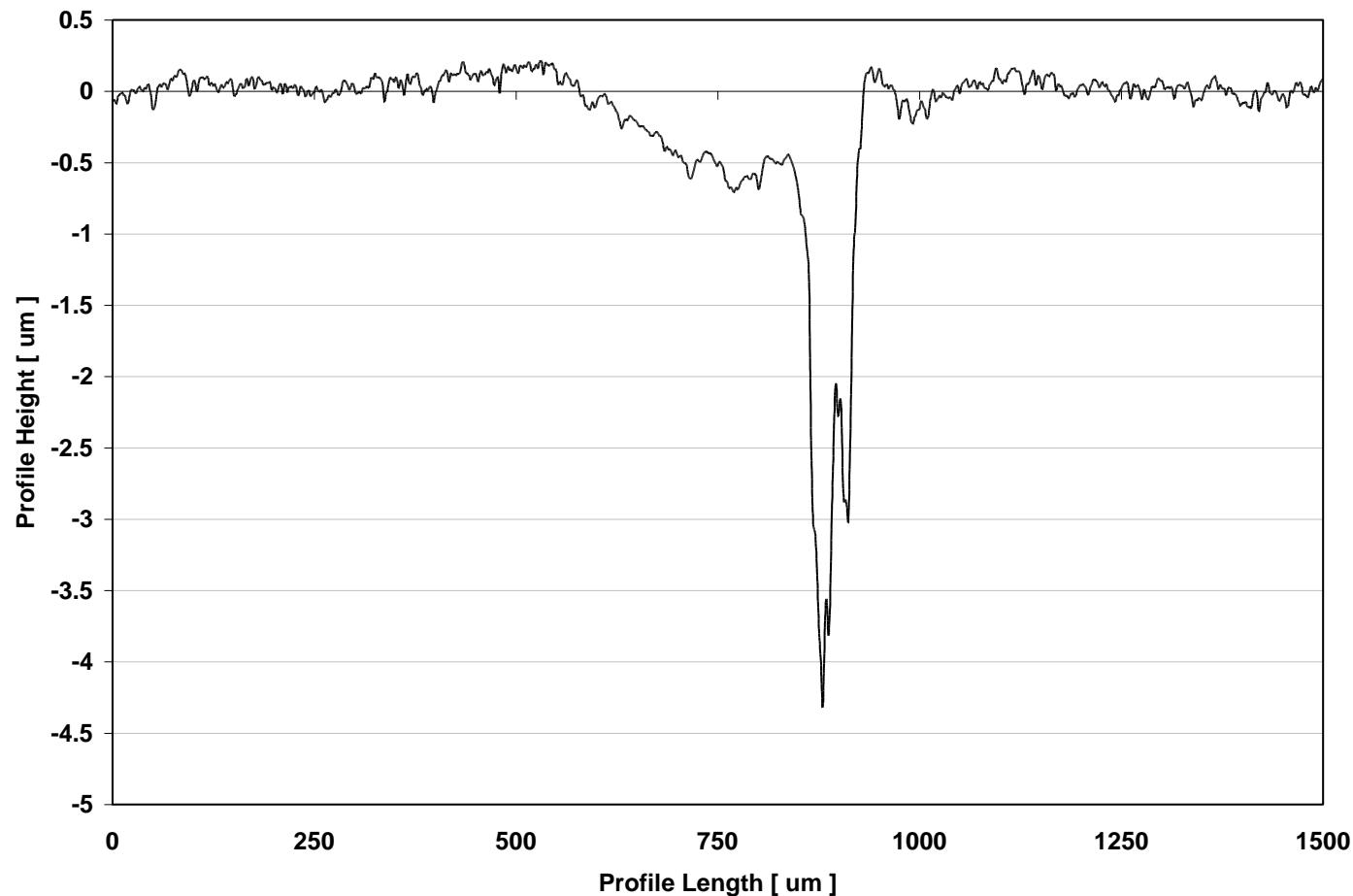
Typical profile scan of a CrC coating RCF track. A conformal profile can be observed with a depth of ~0.2 μ m. The profile is hypothesized to be primarily the result of plastic deformation of the P675 substrate and secondarily the result of polishing run-in wear of the coating.

Appendix RCF – Rolling Contact Fatigue (RCF) Testing Results



Optical microscope images of RCF track on baseline P675 (scale 1div = 105 μ m). The images of two separate tests are representative of the RCF track on all P675 samples tested. Plastic deformation, not polishing run-in wear, is the hypothesized mechanism for morphology differences between the track and surrounding non-contact areas. The left image illustrates small micro-pits ~3-5 μ m deep and ~25-100 μ m in diameter which were observed (~5-10 per sample). The origin of the micro-pits seems track related but it could not be ruled out that the defects were inherent prior to testing. The ~350 μ m track width correlates well with the theoretical Hertz elastic contact width of 350 μ m at 4.5GPa contact stress.

Appendix RCF – Rolling Contact Fatigue (RCF) Testing Results



Profile scan across RCF track and micro-pit on P675 sample P25 (left image on page # RCF_9). The conformal track profile of ~0.5 μ m depth is thought to be the result of plastic deformation. The micro-pit depth is ~4 μ m and may be a result of surface initiated fatigue or may have been an inherent substrate defect that was present prior to testing.

Appendix RCF – Rolling Contact Fatigue (RCF) Testing Results



Typical profile scan of baseline P675 RCF track. The conformal profile was ~0.3-0.5 μ m deep on all P675 samples tested. Given the high 4.5GPa contact stress the conformal profile is most likely the result of plastic deformation. The lack of ball wear measured in P675 RCF tests further supports a plastic deformation mechanism since the AISI 51200 balls are not likely to preferentially wear P675.

Appendix RMS – Pyrowear 675 and Coating Roughness Data

Surface Roughness Measurement Overview

1. Surface roughness is measured per ASME standard B46.1-2002. This standard is concerned with the geometric irregularities of surfaces. It defines surface texture and its constituents: roughness, waviness, and lay. It also defines parameters for specifying surface texture. Roughness is defined as the finer irregularities of the surface texture that usually result from the inherent action of the production process or material condition. Lay is the predominant direction of the surface pattern ordinarily determined by the production method used. Waviness is the more widely spaced component of the surface texture. Roughness may be considered as superimposed on a wavy surface.
2. Root Mean Square (RMS, also referred to as R_q) roughness is reported as the roughness parameter. RMS roughness is the root mean square average of the profile height deviations taken within the evaluation length and measured from the mean line. This is in contrast to Average Roughness (R_a) which is also commonly reported and is calculated as the arithmetic average of the absolute values of the profile height deviations.
3. Accurate RMS measurements are made per B46.1 guidelines for selection of profile length and cutoff filter length. In the practical range of surface RMS values profile length is $1250\mu\text{m}$ for surfaces in the RMS range of 20-100nm and profile length is set to $4000\mu\text{m}$ for surface in the RMS range of 100nm-2000nm. The profile cutoff filter is the filter which separates the roughness from waviness and form error components of the primary profile. This filter consists of a digital implementation of a 2RC filter. The filter cutoff length is set to 1/5 of the profile length for a given scan.
4. Measurements are made using a Veeco Dektak8 advanced skidless contact profilometer. A $5\mu\text{m}$ radius tip diamond stylus tip is used. Scan resolution is normally set to $0.5\mu\text{m}/\text{scan}$.
5. A statistical dataset is generated in the following way: RMS data from 5 profiles is averaged on each sample, in all cases 3-6 samples are measured per substrate type resulting in a final reported RMS value. One sigma covariance (CoV) is calculated for each RMS profile measured then averaged over the total number of profiles collected and reported to allow indication of the deviation of the RMS dataset for a given substrate type.

Appendix RMS – Pyrowear 675 and Coating Roughness Data

Pyrowear 675 and Coating RMS Data

Substrate Type	Coating	Coating ID	Coating Thickness [μm]	RMS [nm] / [μinch]		CoV [%]
P675, disc, super-finished	n/a	n/a	n/a	56 / 1.4	+/-	5.5%
P675, ball, super-finished	n/a	n/a	n/a	113 / 4.4	+/-	16.0%
P675, disc, ground ¹	n/a	n/a	n/a	190 / 7.5	+/-	
P675, ball, ground ²	n/a	n/a	n/a	279 / 11	+/-	
P675, disc, super-finished	TiCr-TiCrN (Dep1)	ASE-8-9-1	5.6	247 / 9.7	+/-	26.4%
P675, disc, super-finished	TiCr-TiCrN (Dep2)	ASE-8-14-1	5.8	223 / 8.7	+/-	21.4%
P675, ball, super-finished ³	TiCr-TiCrN		~4	166 / 6.5	+/-	6.4%
P675, disc, super-finished	Cr-CrN (Dep1)	ASE-8-29-1	6.3	153 / 6.0	+/-	10.0%
P675, disc, super-finished	Cr-CrN (Dep2)	ASE-8-34-1	6.0	160 / 6.3	+/-	16.2%
P675, disc, super-finished	CrC (Dep1)	ASE-8-19-1	6.3	153 / 6.0	+/-	12.0%
P675, disc, super-finished	CrC (Dep2)	ASE-8-26-1	5.4	132 / 5.2	+/-	12.2%

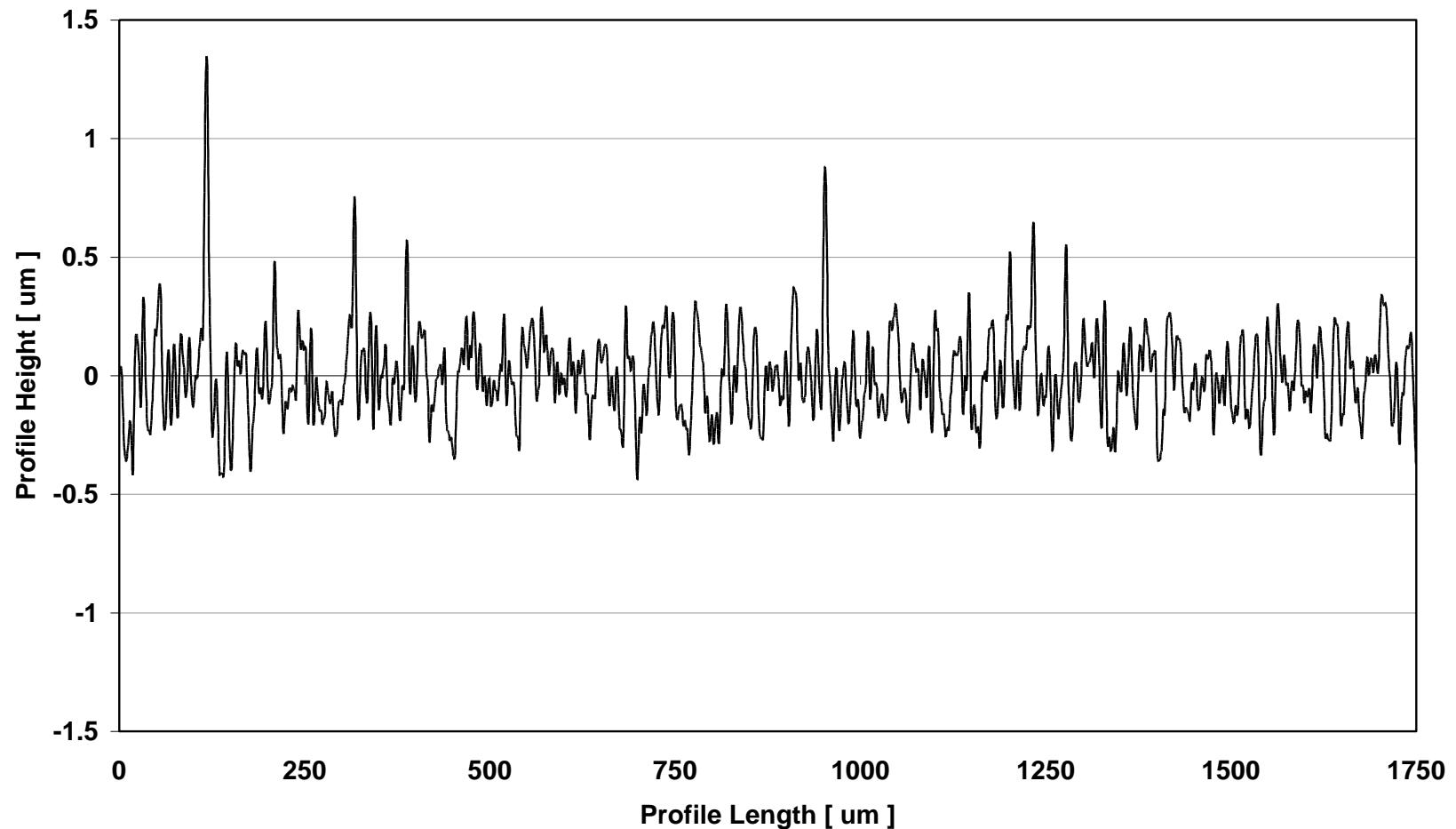
¹ P675 ground disc RMS measured by Wedeven Associates, statistical data not available

² P675 ground ball RMS measured by Wedeven Associates, statistical data not available

³ All coated P675 super-finished balls are the balls used in Wedeven Load Capacity and Performance Mapping tests, coated M50 balls used in ball-on-disc unidirectional sliding tests are assumed to have the same roughness as discs.

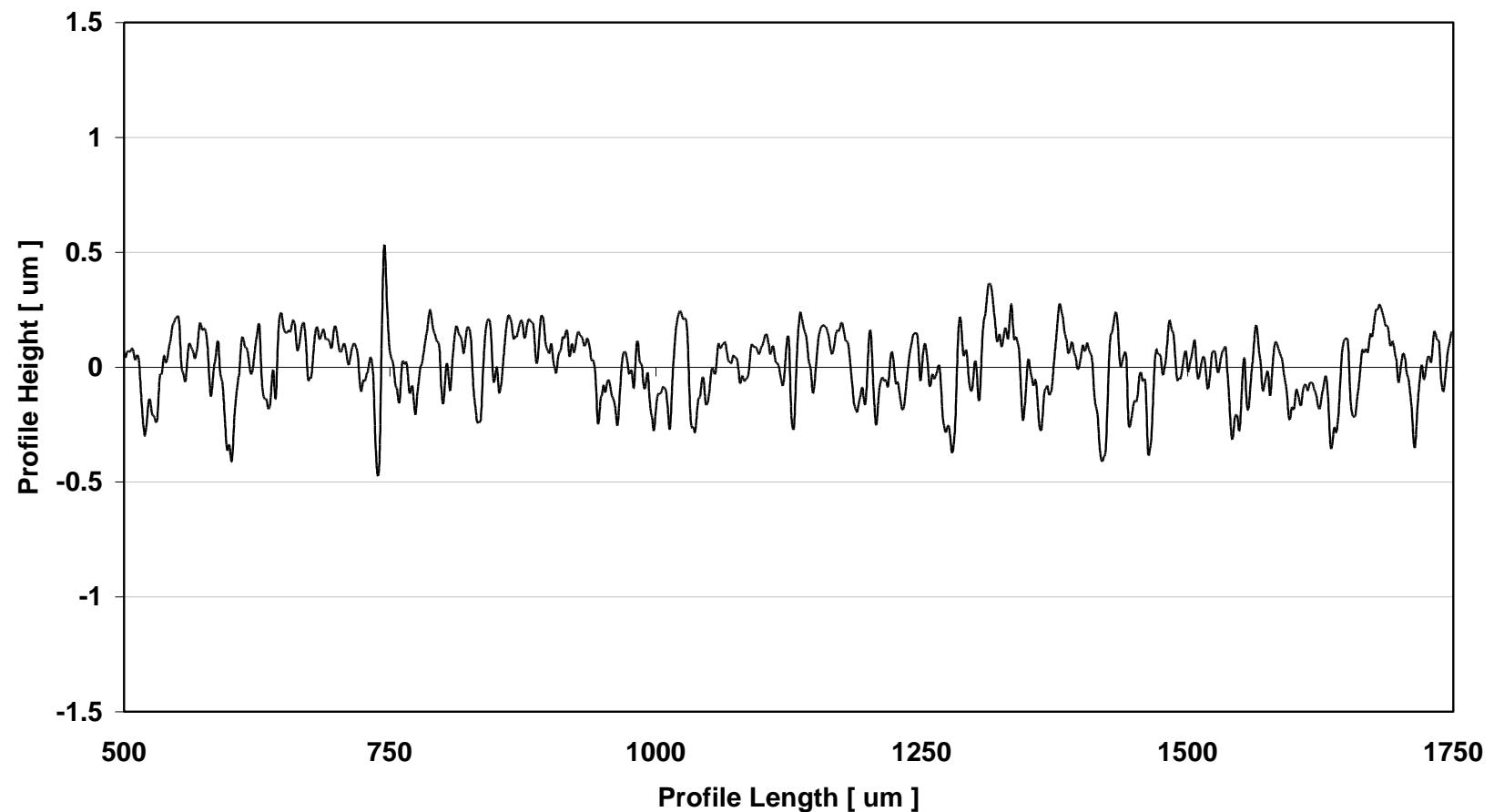
Appendix RMS – Pyrowear 675 and Coating Roughness Data

TiCr-TiCrN (disc)
Typical Surface Roughness Profile



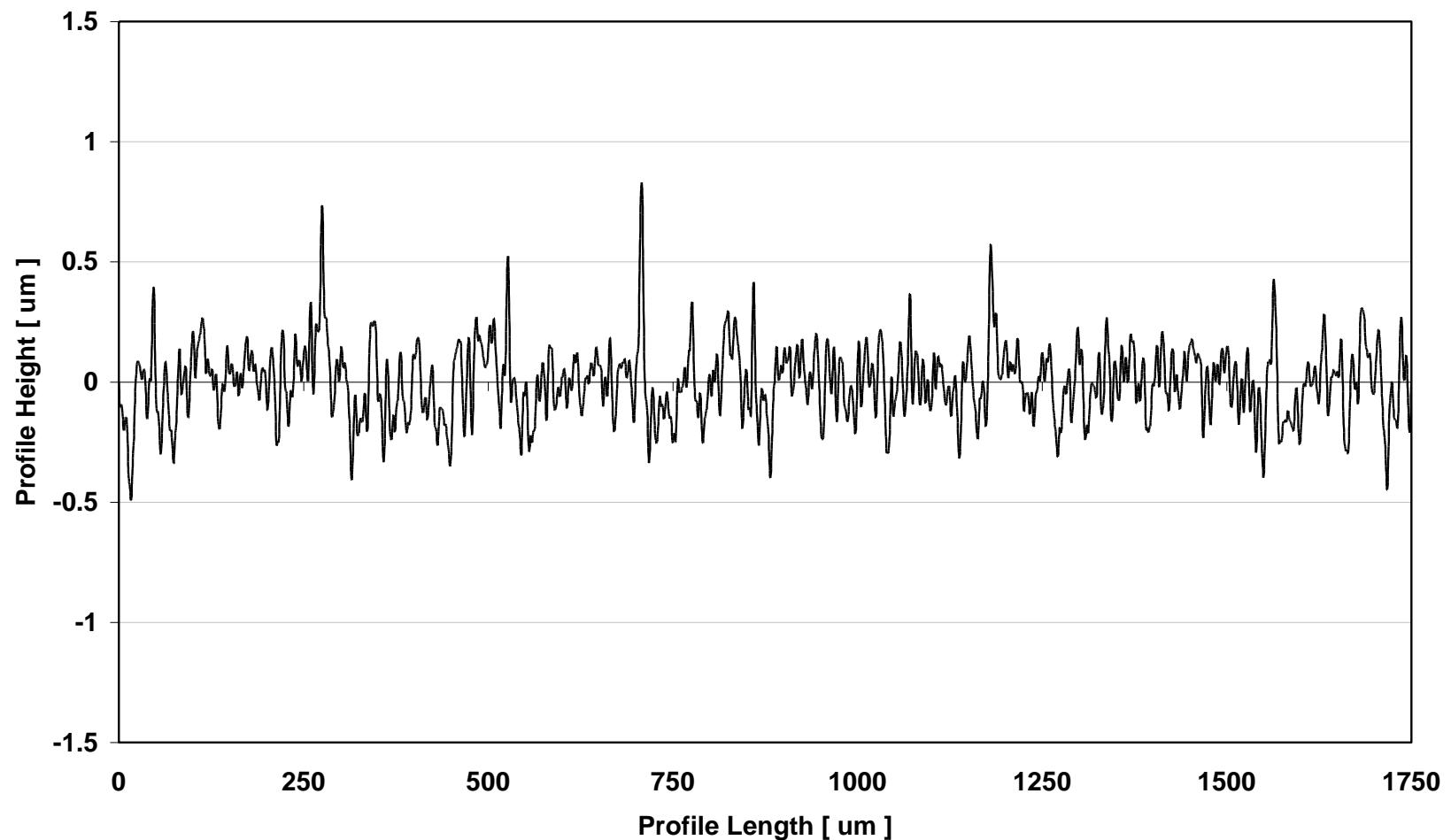
Appendix RMS – Pyrowear 675 and Coating Roughness Data

TiCr-TiCrN (ball)
Typical Surface Roughness Profile
(note ball curvature has been filtered)



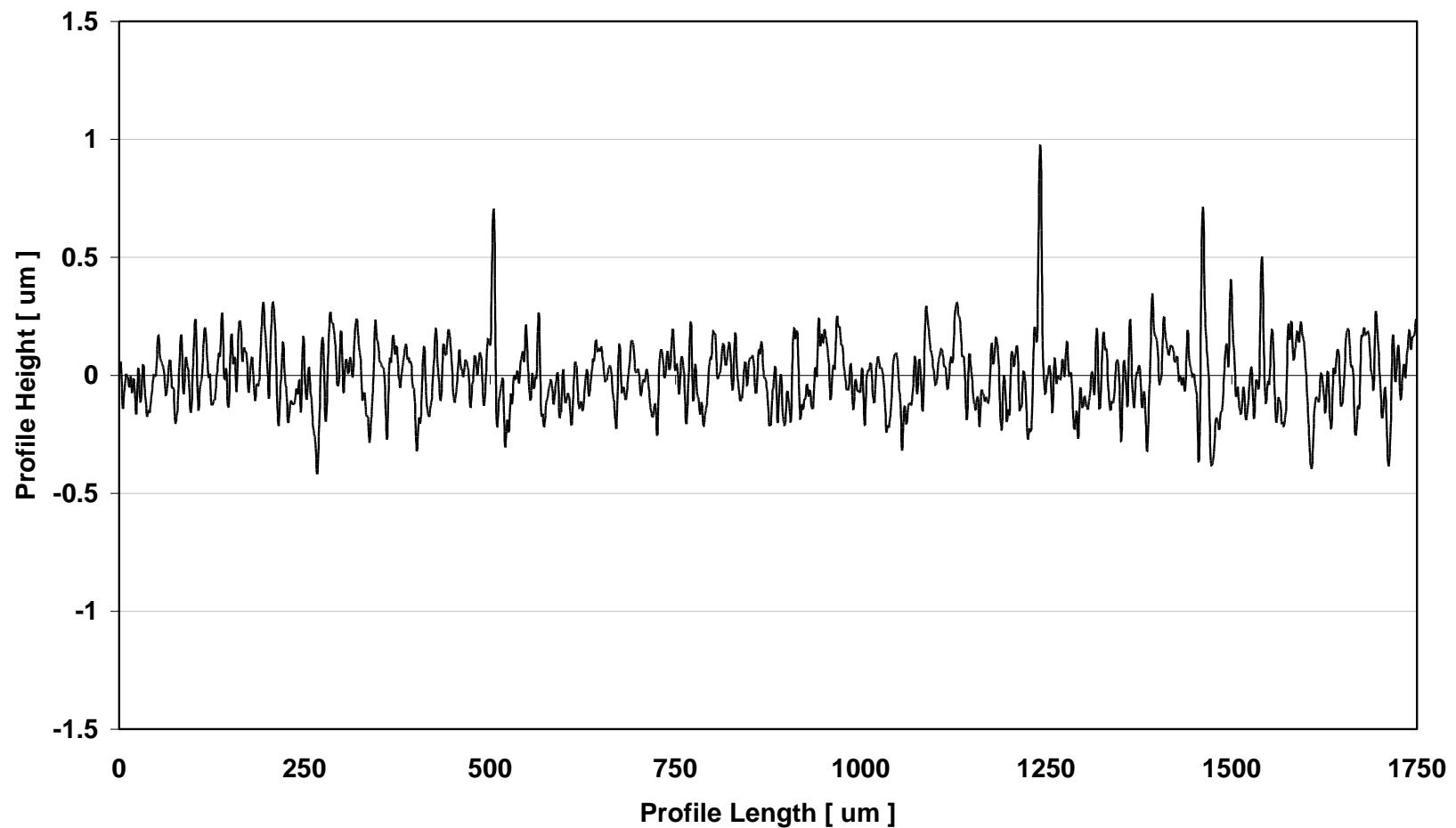
Appendix RMS – Pyrowear 675 and Coating Roughness Data

Cr-CrN (disc)
Typical Surface Roughness Profile



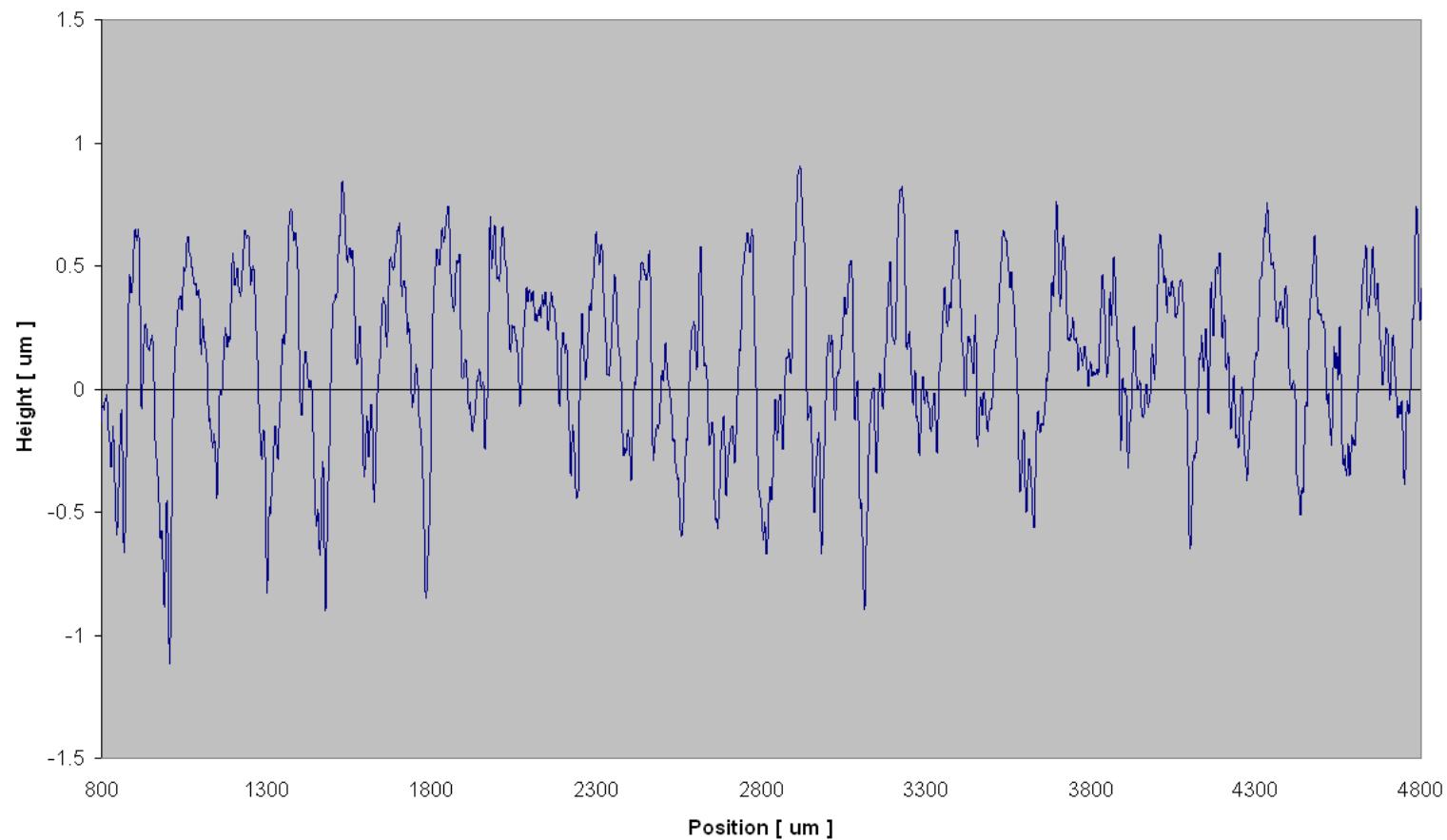
Appendix RMS – Pyrowear 675 and Coating Roughness Data

CrC (disc)
Typical Surface Roughness Profile



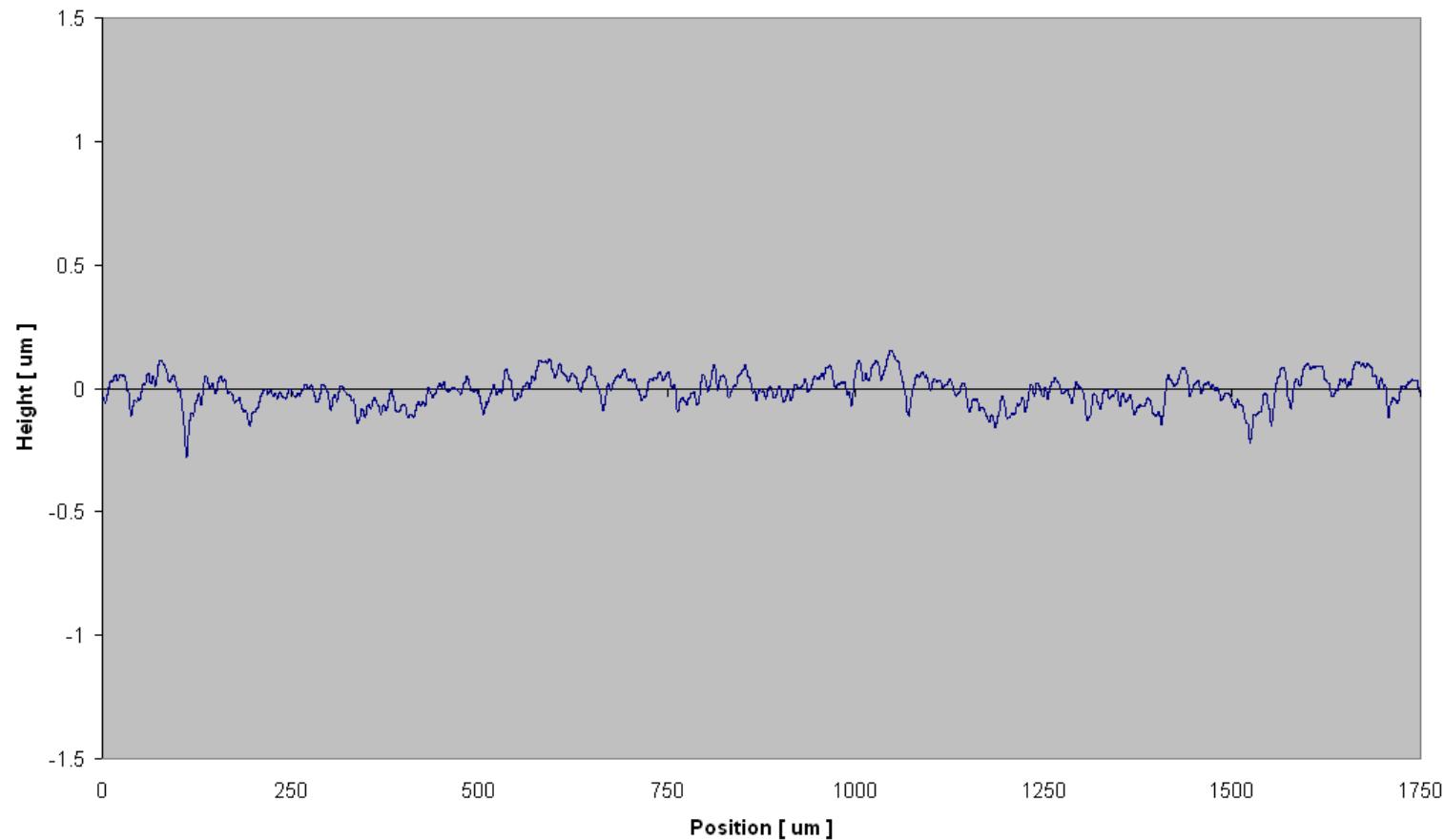
Appendix RMS – Pyrowear 675 and Coating Roughness Data

P675 Ground (Disc)
Typical Surface Roughness Profile
(note x scale is larger than other plots)



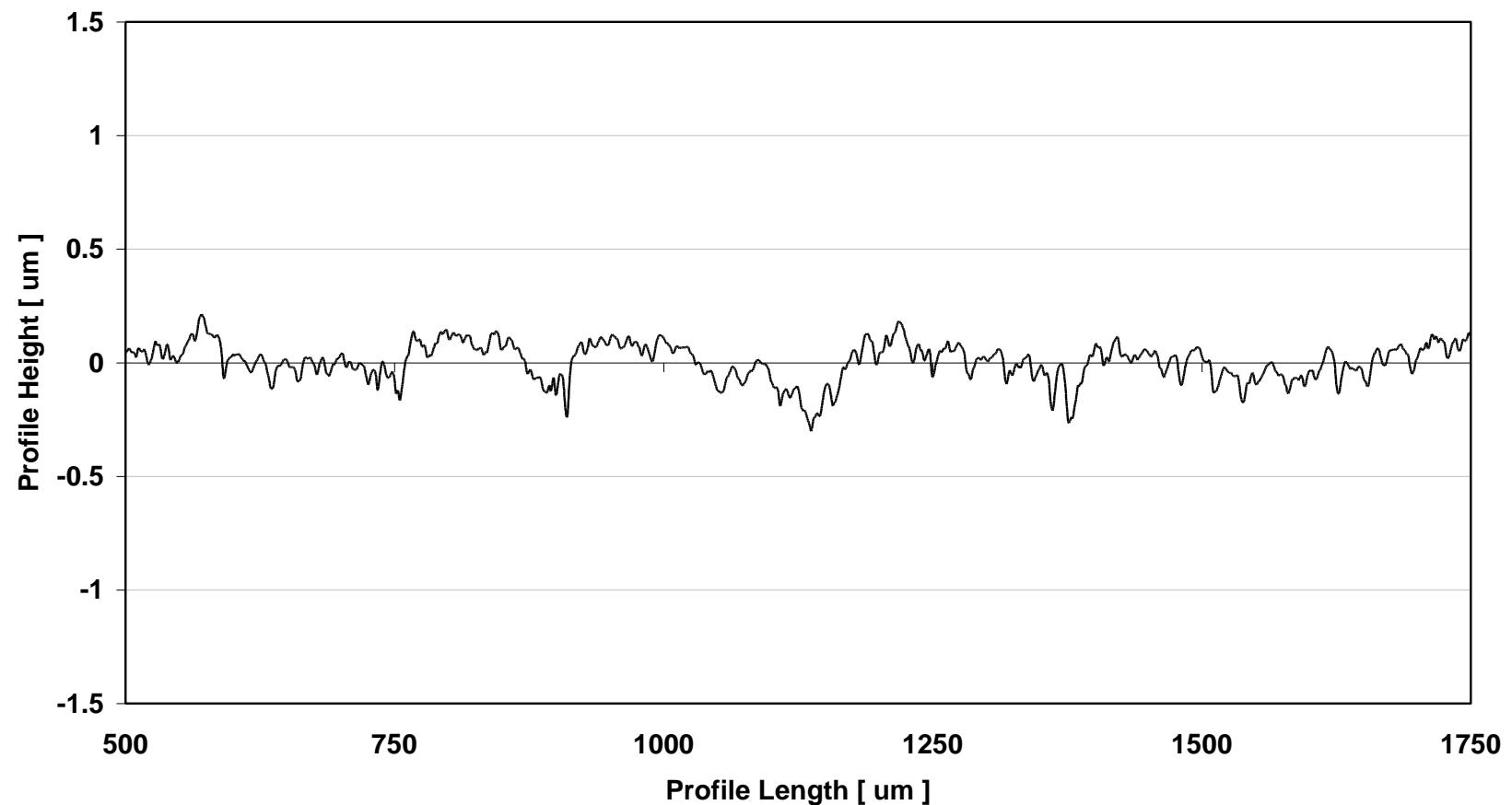
Appendix RMS – Pyrowear 675 and Coating Roughness Data

P675 Super-finished (Disc)
Typical Surface Roughness Profile



Appendix RMS – Pyrowear 675 and Coating Roughness Data

P675 super-finished (ball)
Typical Surface Roughness Profile
(note ball curvature filtered from profile)



Appendix RS – Coating Residual Stress Data

Coating Residual Stress Measurement Overview

1. Coating residual stress is calculated by measuring the coating stress induced curvature on coated silicon beams. Si <111> beams of dimensions 5mm x 50mm x 0.300mm are laser cut from 100mm diameter wafers. Curvature of each beam is individually “pre” measured using a Dektak8 contact profilometer and then “post” measured after a coating has been applied. A 5th order polynomial is used to fit the pre and post beam profiles $y(x)$ and the curvature is calculated as a function of position per the below equation [Stony, 1909]

$$R(x) = \frac{(1+y'^2)^{\frac{3}{2}}}{y''}$$

where $y' = dy/dx$, and $y'' = d^2y/dx^2$

2. Coating residual stress as a function of beam position is then directly calculated using the modified Stony equation [Jaccodine, Schlegel, 1965] where R_{pre} and R_{post} are the pre and post curvature functions, E and ν are the elastic modulus and Poisson ratio of Si <111>, and t_s and t_f are the thickness of the silicon beam and the thickness of the coating. The effective modulus $E' = E/(1-\nu)$ for Si <111> of 229GPa is taken from [W.A. Brantley, J. Appl. Phys., Vol. 44 (1973) p.534-535].

$$\sigma = \frac{1}{6} \left(\frac{1}{R_{\text{post}}} - \frac{1}{R_{\text{pre}}} \right) \frac{E}{(1-\nu)} \frac{t_s^2}{t_f}$$

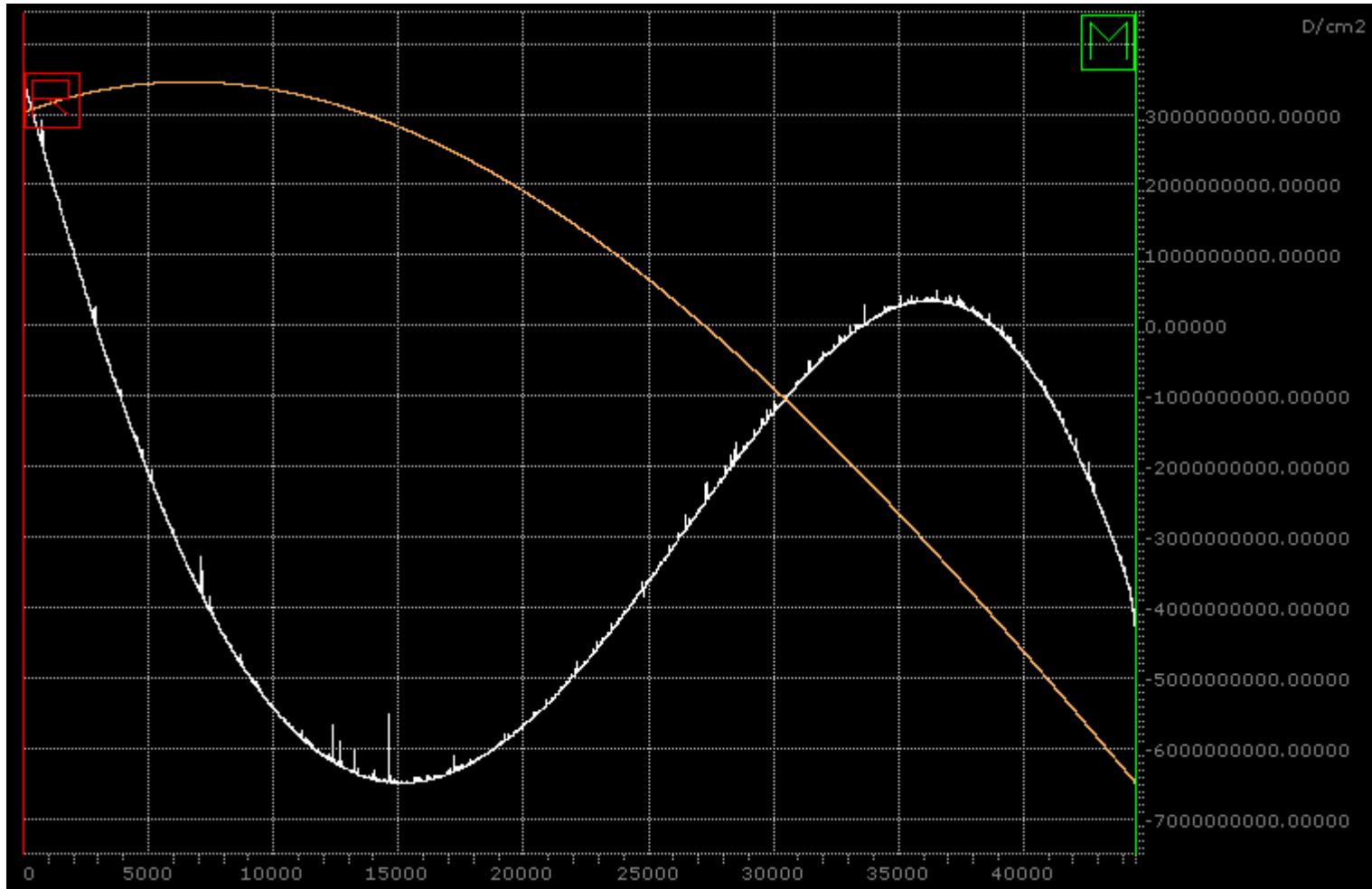
3. One Si beam was coated and used as a residual stress reference for each of the TiCr-TiCrN, Cr-CrN, and CrC coating depositions. Curvature of beams was only measured if the coating was intact, i.e. without any signs of delamination or cracking. Coating thickness was directly measured on the Si beam by CALOTest after curvature measurements were made. It is important to note that residual stress calculations on Si are best compared relatively to other coatings deposited on Si and are considered a general reference to the stress state for identical coatings deposited on metallic substrates.

Appendix RS – Coating Residual Stress Data

Coating Residual Stress Results**Substrate: Si <111> beams 5mm x 50mm x 0.300mm**

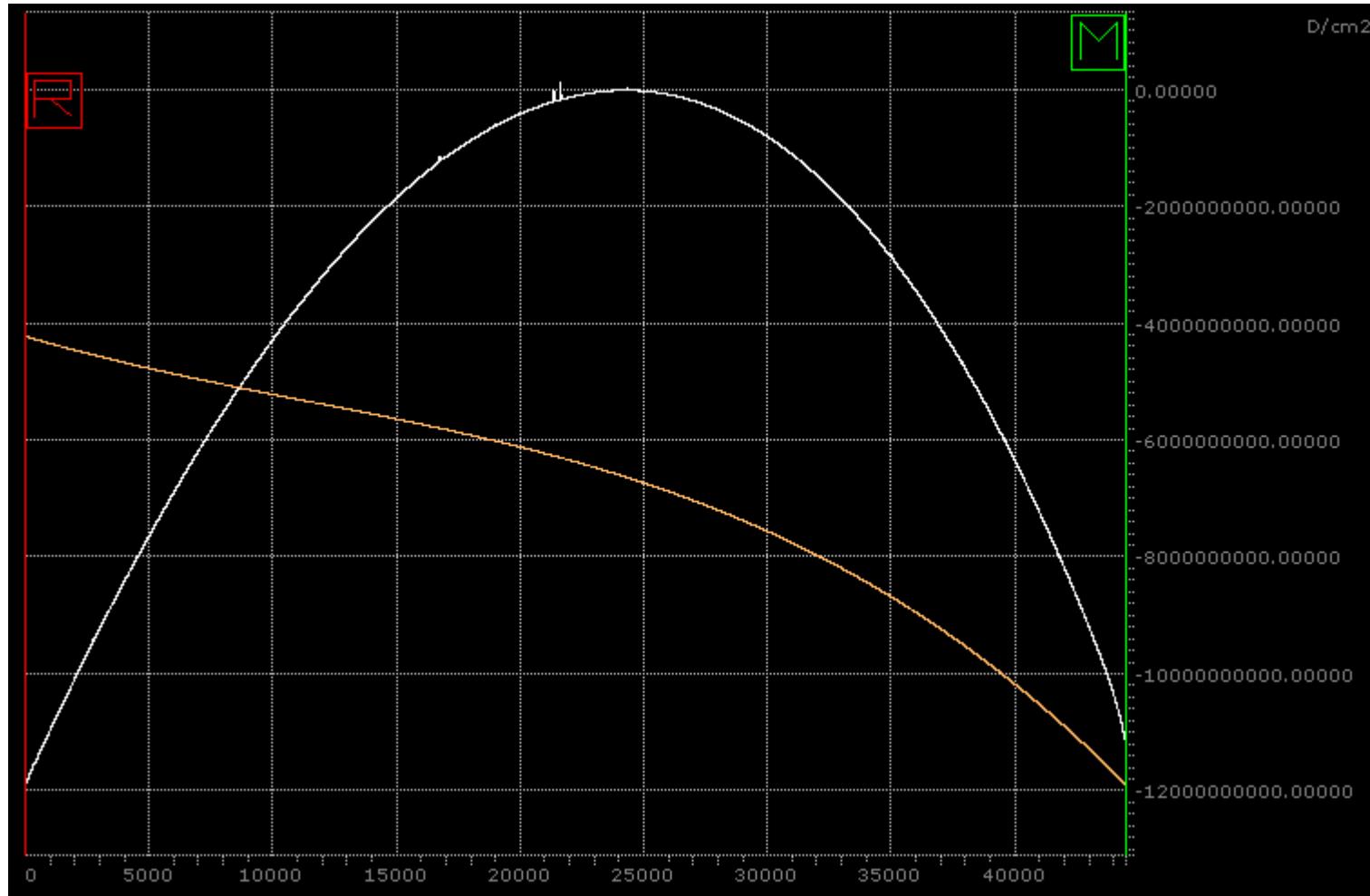
Coating	Coating ID	Coating Thickness on Si [μm]	Coating Residual Stress (average) [GPa]	Notes
TiCr-TiCrN	ASE-8-9-1 (Run1)	n/a	See notes	Assume residual stress greater than -6GPa, beam broken in-situ
TiCr-TiCrN	ASE-8-14-1 (Run2)	n/a	See notes	Assume residual stress greater than -6GPa, beam broken in-situ
Cr-CrN	ASE-8-29-1 (Run1)	5.7	-0.12, 0.15	Beam stress changes from compressive to tensile (see stress plot on page RS_3)
Cr-CrN	ASE-8-34-1 (Run2)	n/a	n/a	Si beam not measured due to delaminations near beam tip
CrC	ASE-8-19-1 (Run1)	6.0	-0.7	Previous data suggests that the compressive residual stress measured may be a result of Cr-CrN bond layer, CrC layer may be slightly tensile or close to zero stress
CrC	ASE-8-26-1 (Run2)	5.4	-0.66	Previous data suggests that the compressive residual stress measured may be a result of Cr-CrN bond layer, CrC layer may be slightly tensile or close to zero stress

Appendix RS – Coating Residual Stress Data



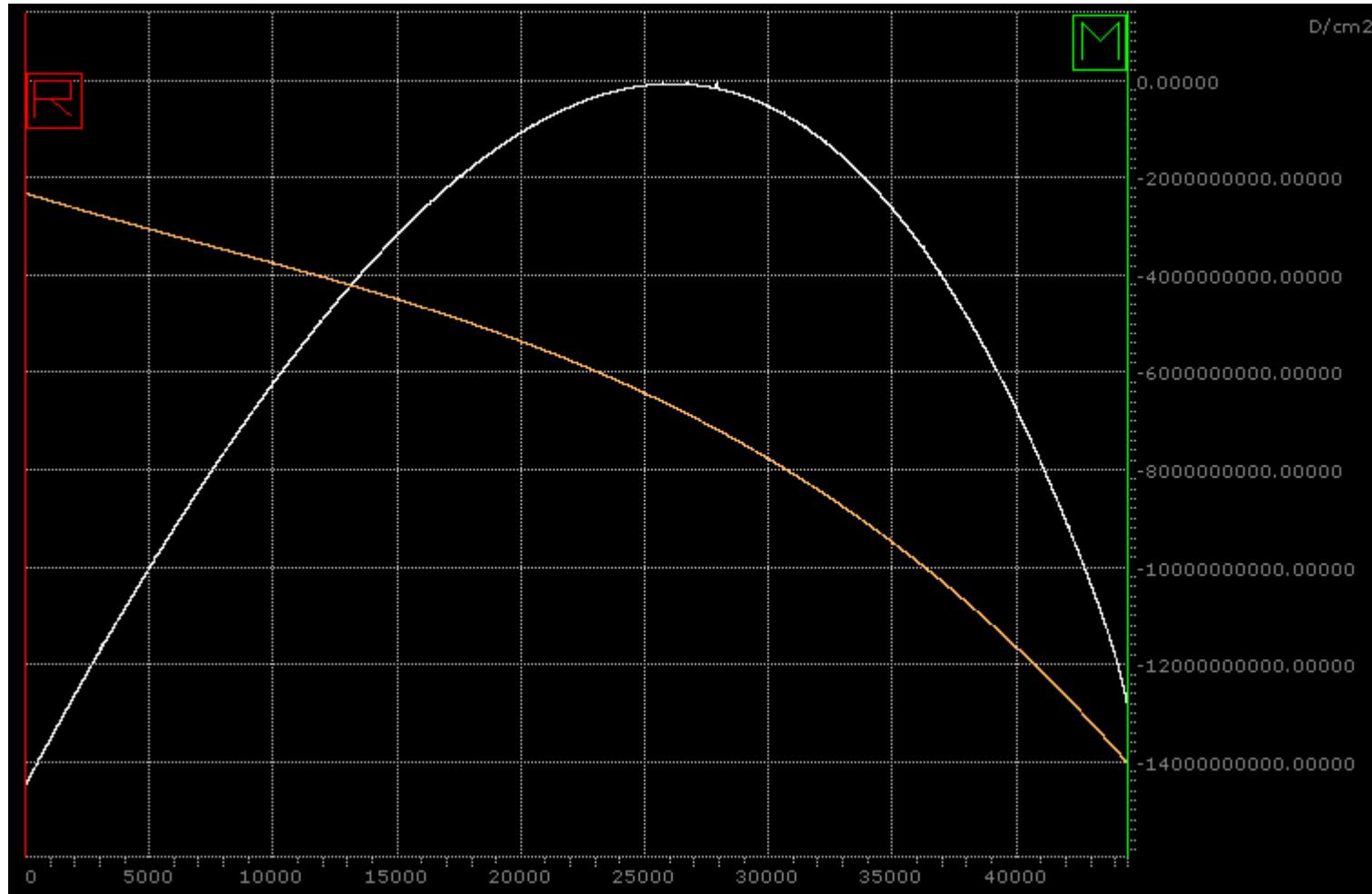
Residual Stress plot for Cr-CrN (Run1) (yellow line, white line is beam profile, profile height scale not shown)
x-axis: position along Si beam in μm
y-axis: residual stress in dyne/cm^2 ($1\text{GPa} = 1\text{E}+10\text{dyne}/\text{cm}^2$)

Appendix RS – Coating Residual Stress Data



Residual Stress plot for CrC (Run1) (yellow line, white line is beam profile, profile height scale not shown)
x-axis: position along Si beam in μm
y-axis: residual stress in dyne/cm² (1GPa = 1E+10dyne/cm²)

Appendix RS – Coating Residual Stress Data



Residual Stress plot for CrC (Run2) (yellow line, white line is beam profile, profile height scale not shown)
x-axis: position along Si beam in μm
y-axis: residual stress in dyne/cm² (1GPa = 1E+10dyne/cm²)

Appendix SA - Scratch Adhesion Data

Load: 0-100N, Distance: 10mm, Load Rate: 10N/mm, Indenter 200 μ m radius diamond

Appendix SA – Scratch Adhesion Data

ASTM C 1624 -05 (active standard): *Standard Test Method for Adhesion Strength and Mechanical Failure Modes of Ceramic Coatings by Quantitative Single Point Scratch Testing*

Scratch Test Overview

1. This test consists of producing and assessing controlled damage in a hard ceramic coating by single point scratch action (see schematic on page SA_2). The scratch is developed on a coated test specimen by drawing a diamond stylus of defined geometry and tip size (Rockwell C, 200 μ m radius) across the flat surface of the specimen for a distance of 10mm at a constant speed of 10mm/min and a controlled and measured normal force of 0-100N (progressively increasing at a rate of 10N/mm). With increasing applied normal force, the stylus produces progressive mechanical damage in the coating and the substrate through the complex combination of elastic/plastic indentation stresses, frictional forces, and residual internal stresses in the coating/substrate system.
2. The specific levels and types of progressive damage in the scratch track were assessed and associated with the applied normal stylus forces. The normal force which produced a specific, defined, reproducible type/level of damage was defined as a critical scratch load (Lc). Five unique critical scratch loads (Lc1, Lc2...Lc5) were used to identify various modes of cohesive and adhesive failures in the coatings (as defined on page SA_2).
3. Coating damage was assessed by optical microscopy or scanning electron microscopy, or both, after the scratch test was completed. Tangential force (CoF) and acoustic emission (AE) signals were measured and recorded during the scratch test process and used as supplementary test data to identify different coating damage levels. To provide statistical relevance to the identified critical loads two unique scratch tests were performed on each sample and a minimum of one polished P675 sample and a minimum of two super-finished P675 samples were tested for each coating deposition.
4. Lc data is presented in table form, representative CoF and AE plots are included for each coating type as deposited on P675 polished and super-finished substrates. Representative microscope images of Lc2, Lc3 and Lc5 failure modes are included for each coating type as deposited on P675 polished and super-finished substrates. Failure mode identification follows the criteria set forth in ASTM C 1624 Appendix X1 primarily established by Bull, Blau, et al.

Appendix SA - Scratch Adhesion Data

Load: 0-100N, Distance: 10mm, Load Rate: 10N/mm, Indenter 200 μ m radius diamond**Definition of Critical Scratch Loads (Lc)**

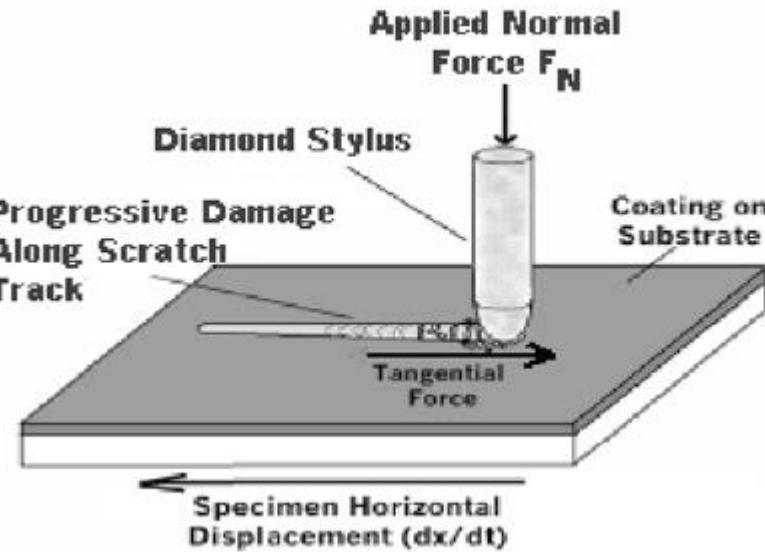
Lc1 = Cohesive micro-cracking failure mode. Identified when a consistent AE signal $> \sim 0.01\text{-}0.02\text{V}$ is measured. Visual identification of isolated micro-cracks can be by optical microscope although the micro-cracks for this failure mode are usually only visible by SEM observation.

Lc2 = Cohesive cracking failure mode. Identified when the first AE hit $> 0.1\text{V}$ occurs. Visually identified by optical microscope and/or SEM at the load where consistent cohesive cracking is evident in the scratch track.

Lc3 = Consistent micro cohesive/adhesive delamination mode (within or just outside of the track). Identified when a consistent AE signal occurs $> 1.0\text{V}$. Visually identified using an optical microscope.

Lc4 = Consistent macro cohesive delamination mode. Visually identified using an optical microscope.

Lc5 = Consistent adhesive delamination mode (coating completely removed from scratch track). Identified when CoF data jumps from coating value to substrate value. Visually identified using an optical microscope.



Appendix SA - Scratch Adhesion Data

Load: 0-100N, Distance: 10mm, Load Rate: 10N/mm, Indenter 200μm radius diamond

Coating – TiCr-TiCrN

Substrate – Pyrowear 675 (polished, RMS = 5nm [0.2μinch], HRC-64)

Coating	Coating ID	Sample ID	Thickness [μm]	Lc1 (AE) [N]	Lc1 (visual) [N]	Lc2 (AE) [N]	Lc2 (visual) [N]	Lc3 (AE) [N]	Lc3 (visual) [N]	Lc4 (visual) [N]	Lc5 (CoF) [N]	Lc5 (visual) [N]		
TiCr-TiCrN	ASE-8-9-1 (Run1)	C148	5.6	29.3		51.7	38	51.7	52.4	n/a	63.6	67.2		
TiCr-TiCrN	ASE-8-9-1 (Run1)	C148	5.6	30		43.4	40	57	63.4	n/a	74.5	74.7		
TiCr-TiCrN	ASE-8-9-1 (Run1)	C170	5.6	28.6		50	37.3	55.7	54.6	n/a	81.4	82.8		
TiCr-TiCrN	ASE-8-9-1 (Run1)	C170	5.6	28.9		51.5	36.8	53.5	54.3	n/a	75	76.6		
TiCr-TiCrN	ASE-8-9-1 (Run1)	average		29.2		49.2	38.0	54.5	56.2	n/a	73.6	75.3		
TiCr-TiCrN	ASE-8-14-1 (Run2)	C43	5.8	30		57.4	34.5	57.4	56.5	n/a	79.6	79.1		
TiCr-TiCrN	ASE-8-14-1 (Run2)	C43	5.8	32.1		51.3	36.8	51.3	50.3	n/a	74.5	76.2		
TiCr-TiCrN	ASE-8-14-1 (Run2)	average		31.1		54.4	35.7	54.4	53.4	n/a	77.1	77.7		
TiCr-TiCrN	average			29.8		50.9	37.2	54.4	55.3	n/a	74.8	76.1		
TiCr-TiCrN	% coefficient of variation (CoV)			4%		9%	5%	5%	8%	n/a	8%	7%		

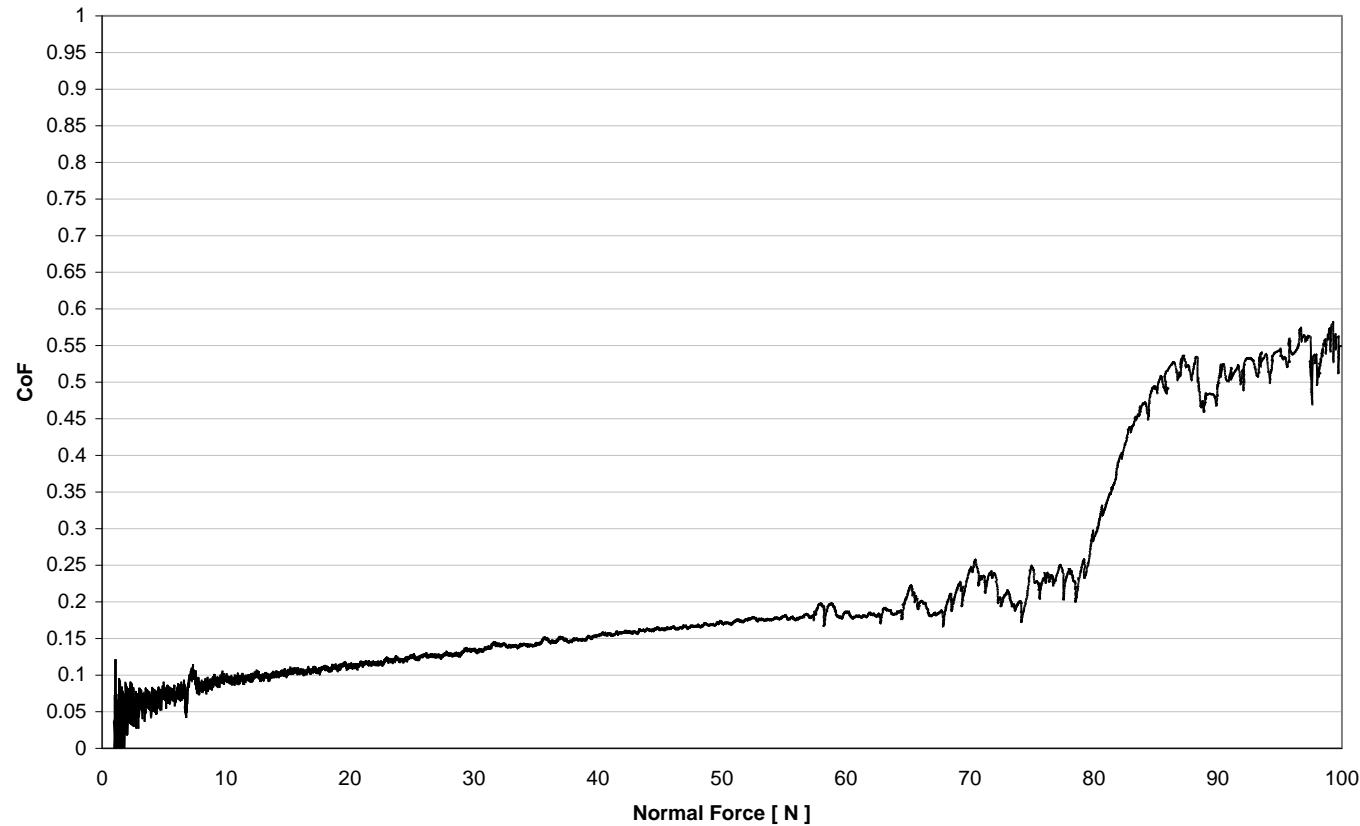
Appendix SA - Scratch Adhesion Data

Load: 0-100N, Distance: 10mm, Load Rate: 10N/mm, Load Rate: 100N/min, Indenter 200 μ m radius diamond**Representative CoF Plot**

Coating – TiCr-TiCrN

Substrate – Pyrowear 675 (polished, RMS = 5nm [0.2 μ inch], HRC-64)

CoF vs. Fz for ASE-8-14-1 C43 -3.txt



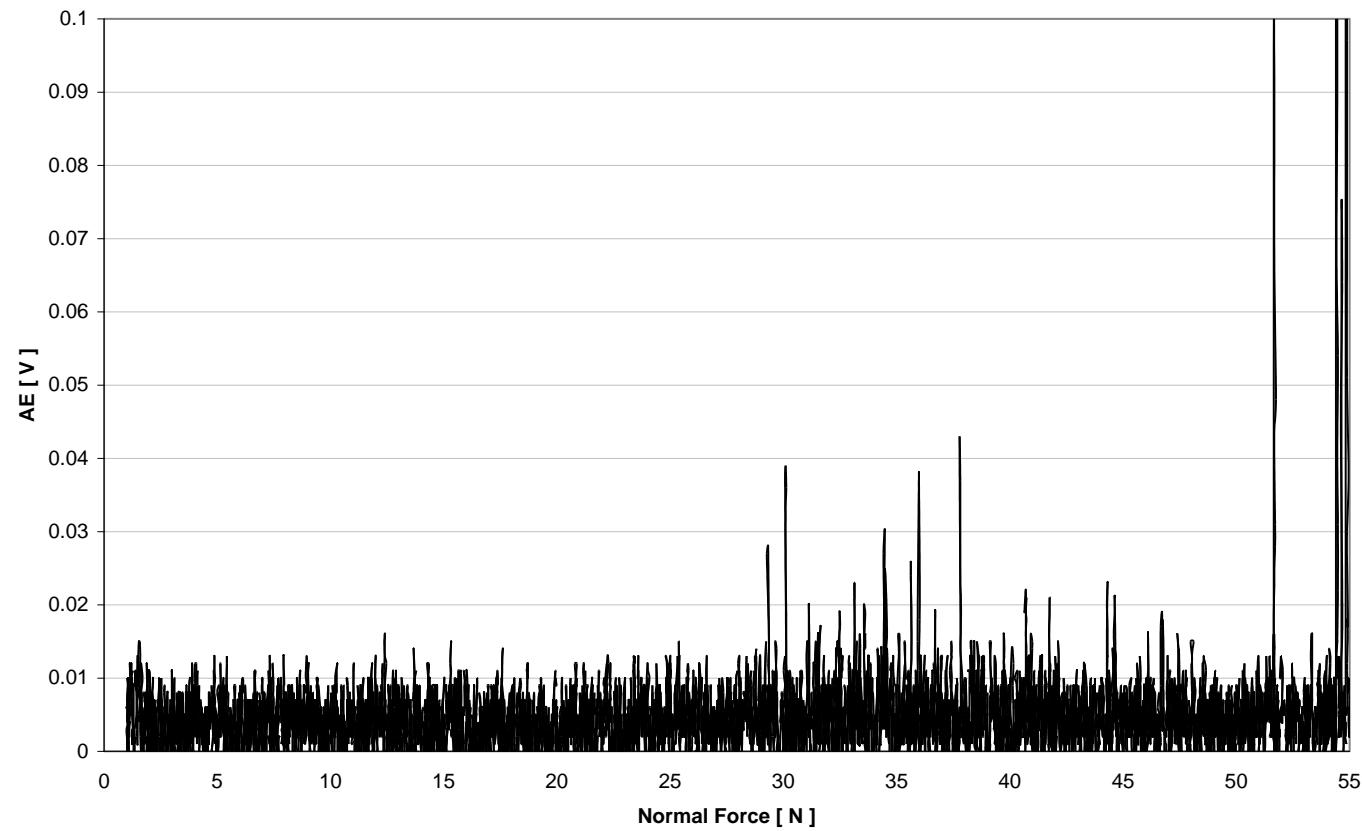
Appendix SA - Scratch Adhesion Data

Load: 0-100N, Distance: 10mm, Load Rate: 10N/mm, Indenter 200 μ m radius diamond**Representative AE Plot (low energy signal, 0-0.1V range)**

Coating – TiCr-TiCrN

Substrate – Pyrowear 675 (polished, RMS = 5nm [0.2 μ inch], HRC-64)

AE vs. Fz for ASE-8-9-1 C148 -3.txt



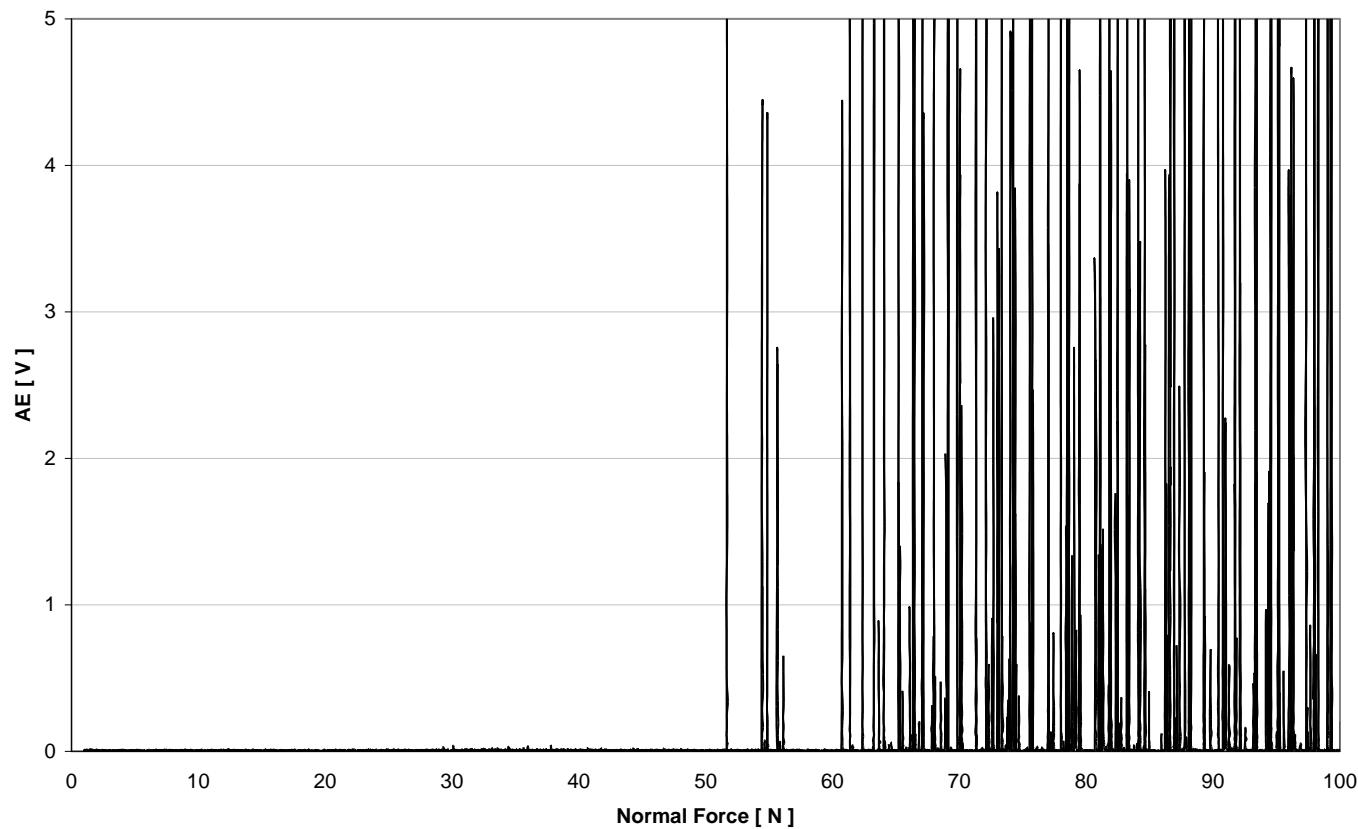
Appendix SA - Scratch Adhesion Data

Load: 0-100N, Distance: 10mm, Load Rate: 10N/mm, Indenter 200 μ m radius diamond**Representative AE Plot (high energy signal, 0-5V range)**

Coating – TiCr-TiCrN

Substrate – Pyrowear 675 (polished, RMS = 5nm [0.2 μ inch], HRC-64)

AE vs. Fz for ASE-8-9-1 C148 -3.txt



Appendix SA - Scratch Adhesion Data

Load: 0-100N, Distance: 10mm, Load Rate: 10N/mm, Load Rate: 100N/min, Indenter 200 μ m radius diamond

Representative Image of Lc2 Failure Mode

Coating – TiCr-TiCrN

Substrate – Pyrowear 675 (polished, RMS = 5nm [0.2 μ inch], HRC-64)



TiCr-TiCrN Lc2 failure mode(s) – arc tensile cracks and lateral edge cracks

Appendix SA - Scratch Adhesion Data

Load: 0-100N, Distance: 10mm, Load Rate: 10N/mm, Load Rate: 100N/min, Indenter 200 μ m radius diamond

Representative Image of Lc3 Failure Mode

Coating – TiCr-TiCrN

Substrate – Pyrowear 675 (polished, RMS = 5nm [0.2 μ inch], HRC-64)



TiCr-TiCrN Lc3 failure mode(s) – buckling and wedging delamination (cohesive and adhesive)

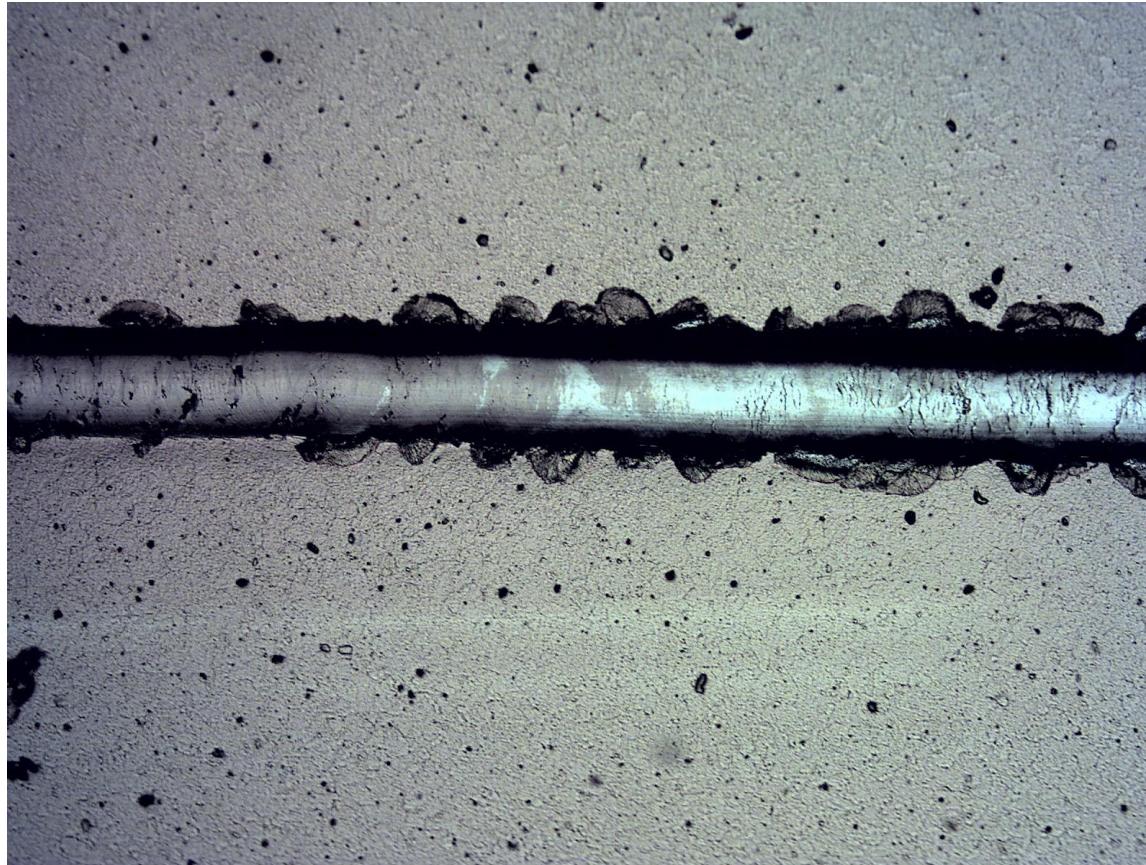
Appendix SA - Scratch Adhesion Data

Load: 0-100N, Distance: 10mm, Load Rate: 10N/mm, Load Rate: 100N/min, Indenter 200 μ m radius diamond

Representative Image of Lc5 Failure Mode

Coating – TiCr-TiCrN

Substrate – Pyrowear 675 (polished, RMS = 5nm [0.2 μ inch], HRC-64)



TiCr-TiCrN Lc5 failure mode(s) – adhesive failure in track, wedging delamination at track edges

Appendix SA - Scratch Adhesion Data

Load: 0-100N, Distance: 10mm, Load Rate: 10N/mm, Indenter 200µm radius diamond

Coating – Cr-CrN

Substrate – Pyrowear 675 (polished, RMS = 5nm [0.2µinch], HRC-64)

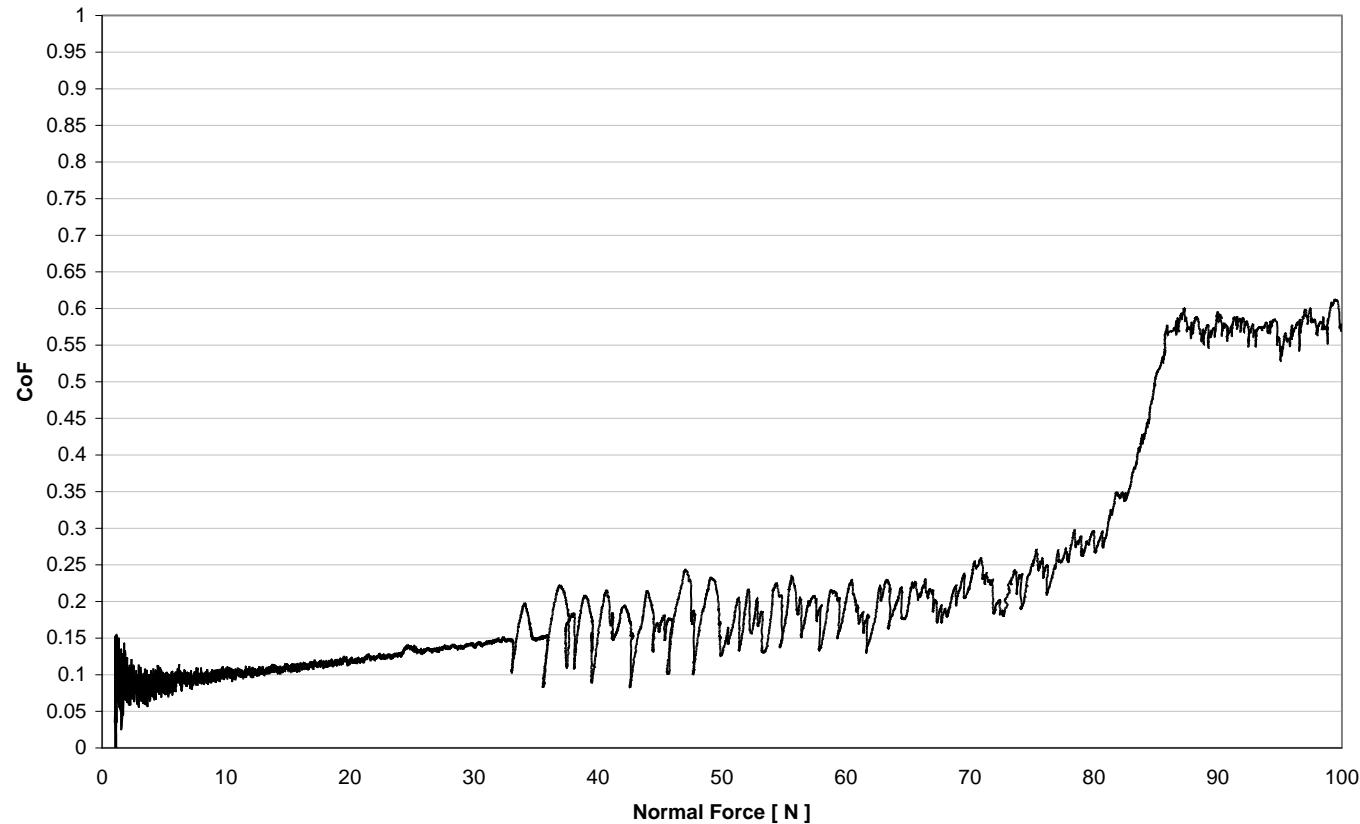
Coating	Coating ID	Sample ID	Thickness [µm]	Lc1 (AE) [N]	Lc1 (visual) [N]	Lc2 (AE) [N]	Lc2 (visual) [N]	Lc3 (AE) [N]	Lc3 (visual) [N]	Lc4 (visual) [N]	Lc5 (CoF) [N]	Lc5 (visual) [N]
Cr-CrN	ASE-8-29-1 (Run1)	C33	6.3	13	12.8	33.1	23.3	33.1	31.9	n/a	76.4	77.6
Cr-CrN	ASE-8-29-1 (Run1)	C33	6.3	11.5	12.6	17.9		33.1	31.3	n/a	81	82.2
Cr-CrN	ASE-8-29-1 (Run1)		average	12.3	12.7	25.5	23.3	33.1	31.6	n/a	78.7	79.9
Cr-CrN	ASE-8-34-1 (Run2)	C79	6.0	10.9	9.8	15.8	31	41.1	39.8	n/a	78	77.5
Cr-CrN	ASE-8-34-1 (Run2)	C79	6.0	10.8		15.2	28.4	40.3	37.7	n/a	76.4	77.3
Cr-CrN	ASE-8-34-1 (Run2)		average	10.9	9.8	15.5	29.7	40.7	38.8	n/a	77.2	77.4
Cr-CrN			average	11.6	11.7	20.5	27.6	36.9	35.2	n/a	78.0	78.7
Cr-CrN			Std dev +/- % (1 sigma)	9%	14%	41%	14%	12%	12%	n/a	3%	3%

Appendix SA - Scratch Adhesion Data

Load: 0-100N, Distance: 10mm, Load Rate: 10N/mm, Load Rate: 100N/min, Indenter 200 μ m radius diamond

Representative CoF Plot**Coating – Cr-CrN****Substrate – Pyrowear 675 (polished, RMS = 5nm [0.2 μ inch], HRC-64)**

CoF vs. Fz for ASE-8-29-1 C33 +3.txt



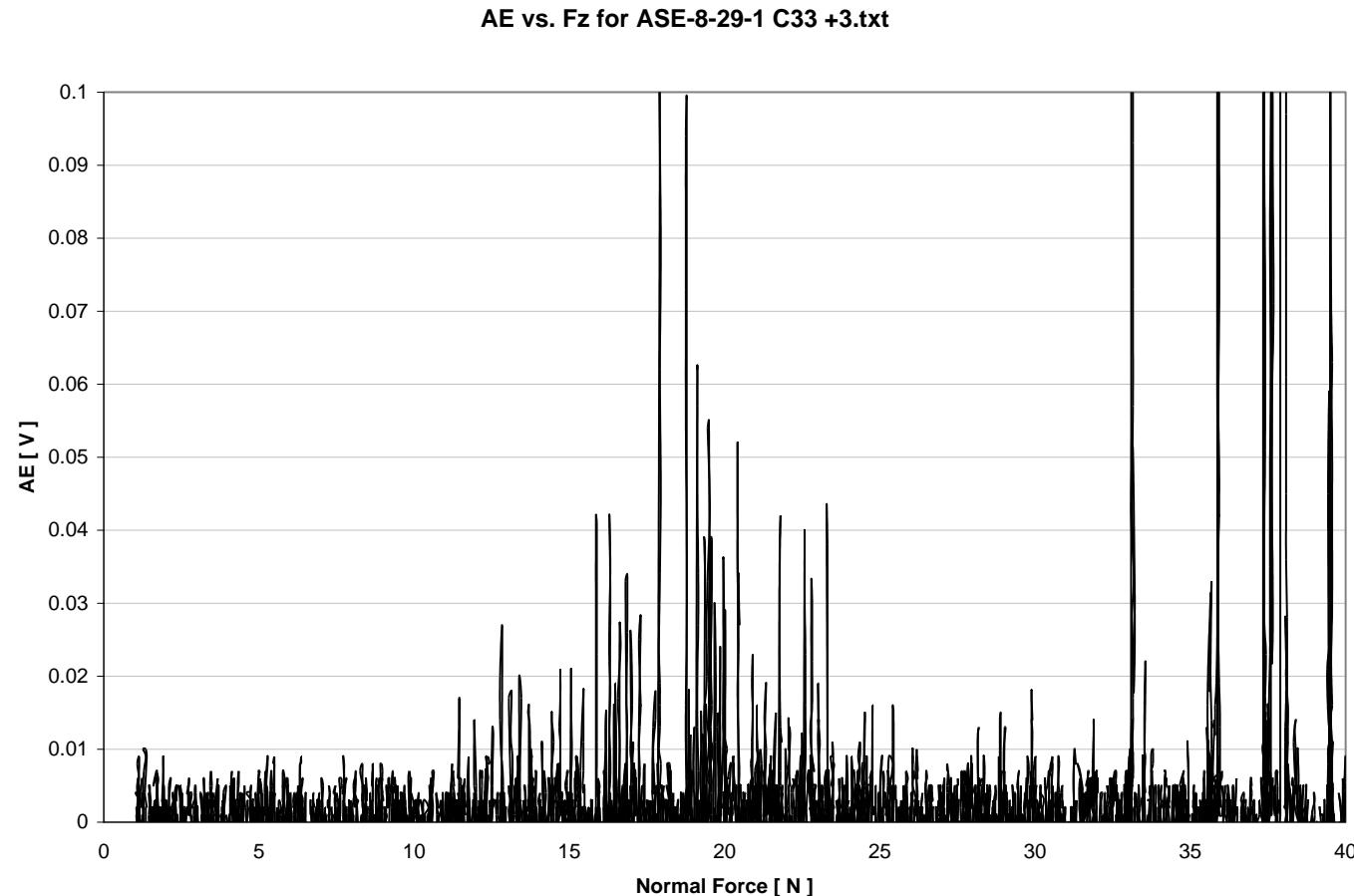
Appendix SA - Scratch Adhesion Data

Load: 0-100N, Distance: 10mm, Load Rate: 10N/mm, Load Rate: 100N/min, Indenter 200 μ m radius diamond

Representative AE Plot (low energy signal, 0-0.1V range)

Coating – Cr-CrN

Substrate – Pyrowear 675 (polished, RMS = 5nm [0.2 μ inch], HRC-64)



Appendix SA - Scratch Adhesion Data

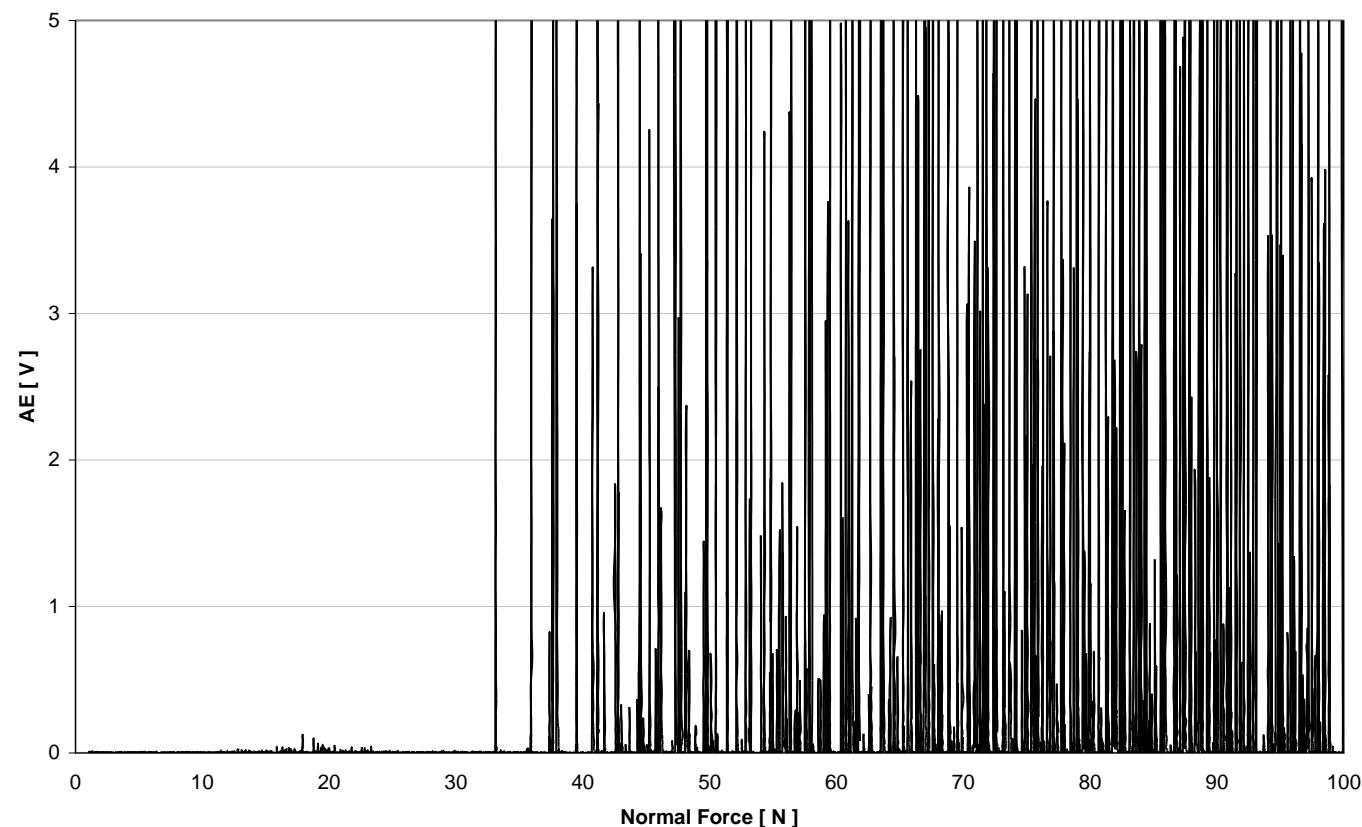
Load: 0-100N, Distance: 10mm, Load Rate: 10N/mm, Load Rate: 100N/min, Indenter 200 μ m radius diamond

Representative AE Plot (high energy signal, 0-5V range)

Coating – Cr-CrN

Substrate – Pyrowear 675 (polished, RMS = 5nm [0.2 μ inch], HRC-64)

AE vs. Fz for ASE-8-29-1 C33 +3.txt



Appendix SA - Scratch Adhesion Data

Load: 0-100N, Distance: 10mm, Load Rate: 10N/mm, Load Rate: 100N/min, Indenter 200 μ m radius diamond

Representative Image of Lc2 Failure Mode

Coating – Cr-CrN

Substrate – Pyrowear 675 (polished, RMS = 5nm [0.2 μ inch], HRC-64)



Cr-CrN Lc2 failure mode(s) – arc tensile cracks and lateral edge cracks

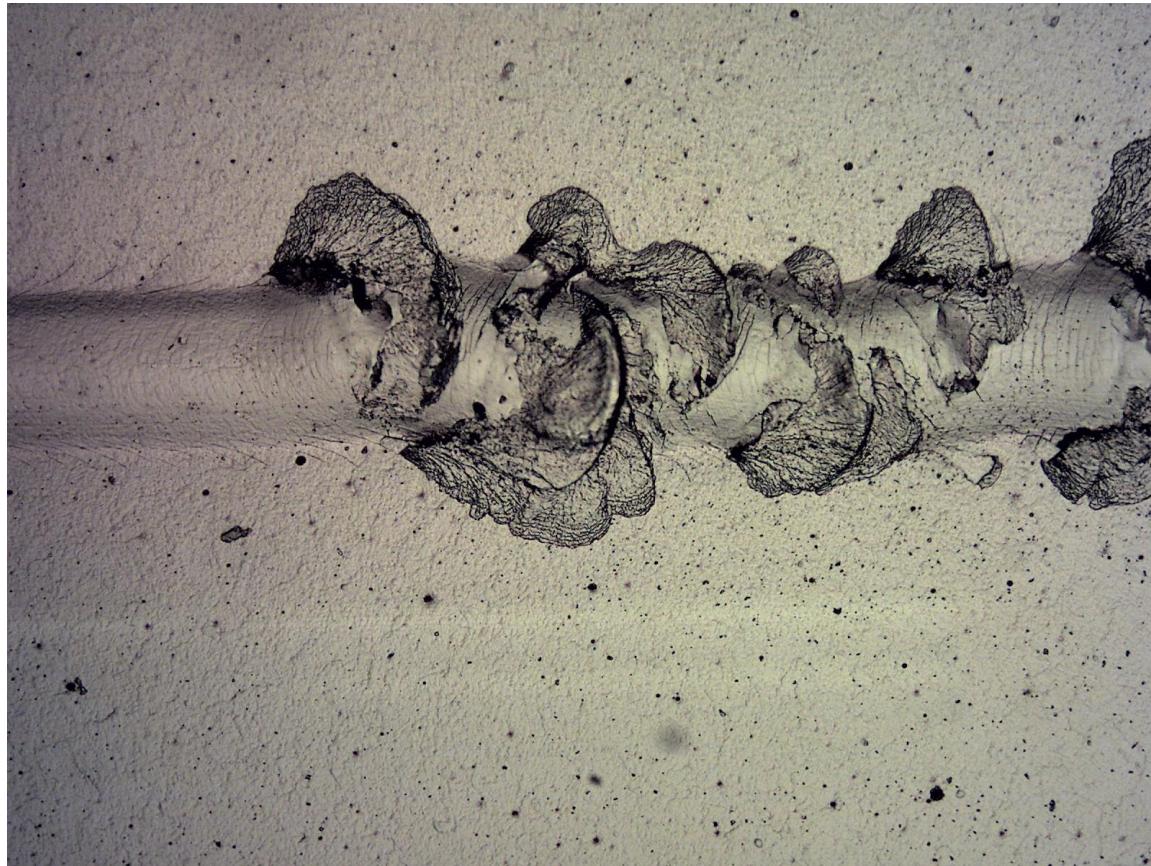
Appendix SA - Scratch Adhesion Data

Load: 0-100N, Distance: 10mm, Load Rate: 10N/mm, Load Rate: 100N/min, Indenter 200 μ m radius diamond

Representative Image of Lc3 Failure Mode

Coating – Cr-CrN

Substrate – Pyrowear 675 (polished, RMS = 5nm [0.2 μ inch], HRC-64)



Cr-CrN Lc3 failure mode(s) – relatively severe wedging delamination (primarily cohesive)

Appendix SA - Scratch Adhesion Data

Load: 0-100N, Distance: 10mm, Load Rate: 10N/mm, Load Rate: 100N/min, Indenter 200 μ m radius diamond

Representative Image of Lc5 Failure Mode

Coating – Cr-CrN

Substrate – Pyrowear 675 (polished, RMS = 5nm [0.2 μ inch], HRC-64)



Cr-CrN Lc5 failure mode(s) – adhesive failure in track, wedging delamination at track edges

Appendix SA - Scratch Adhesion Data

Load: 0-100N, Distance: 10mm, Load Rate: 10N/mm, Indenter 200µm radius diamond

Coating – CrC**Substrate – Pyrowear 675 (polished, RMS = 5nm [0.2µinch], HRC-64)**

Coating	Coating ID	Sample ID	Thickness [µm]	Lc1 (AE) [N]	Lc1 (visual) [N]	Lc2 (AE) [N]	Lc2 (visual) [N]	Lc3 (AE) [N]	Lc3 (visual) [N]	Lc4 (visual) [N]	Lc5 (CoF) [N]	Lc5 (visual) [N]
CrC	ASE-8-19-1 (Run1)	C18	6.3	13.4		14.6	24.3	29	30	n/a	See notes	
CrC	ASE-8-19-1 (Run1)	C18	6.3	13.7		14	22.1	25.5	27.4	n/a	See notes	
CrC	ASE-8-19-1 (Run1)		average	13.6		14.3	23.2	27.3	28.7	n/a		
CrC	ASE-8-26-1 (Run2)	C167	5.4	12.7		13		25.3	26.6	n/a	See notes	
CrC	ASE-8-26-1 (Run2)	C167	5.4	11.9	11.1	12.8		30.4	30	n/a	See notes	
CrC	ASE-8-26-1 (Run2)		average	12.3	11.1	12.9		27.9	28.3	n/a		
CrC			average	12.9	11.1	13.6	23.2	27.6	28.5	n/a		
CrC			Std dev +/- % (1 sigma)	6%	n/a	6%	7%	9%	6%	n/a		

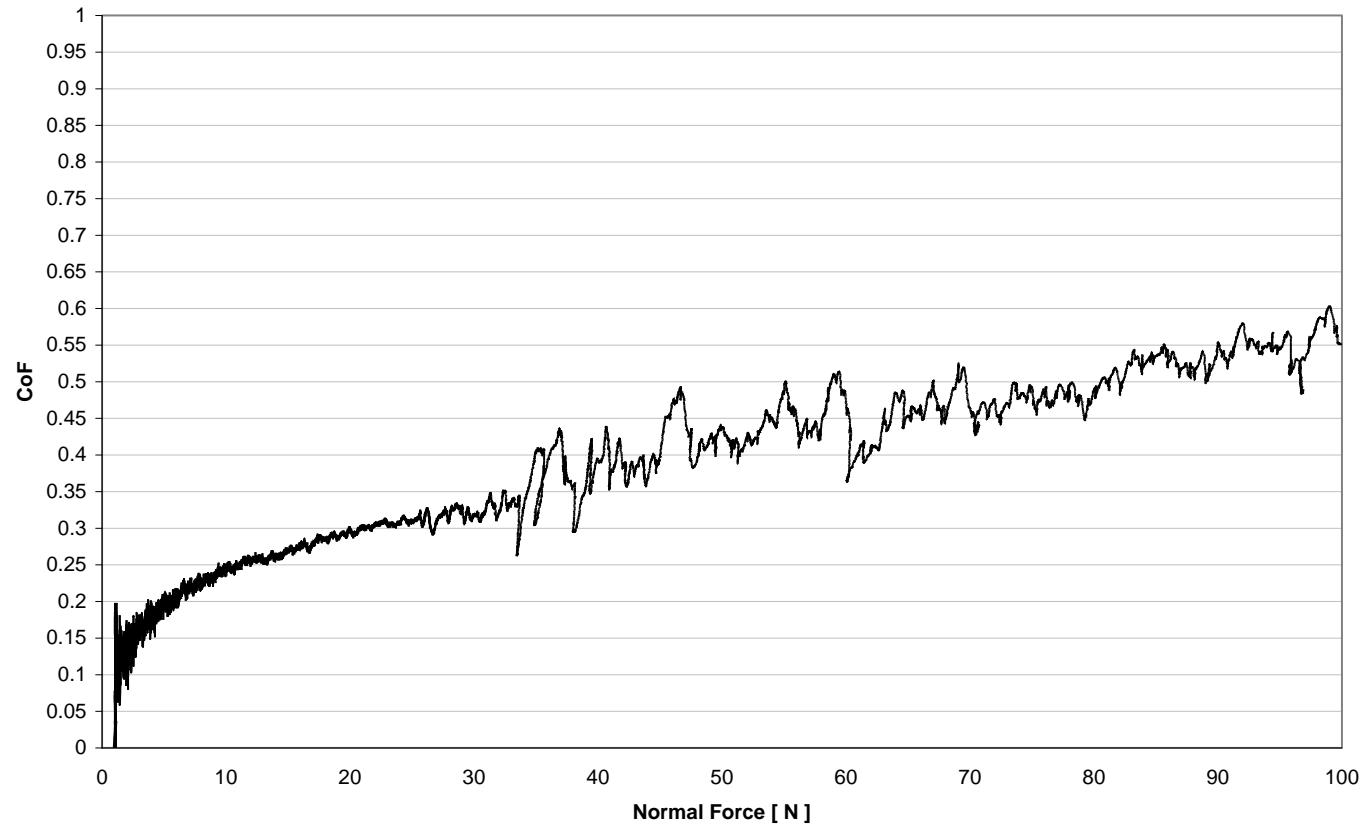
Notes – Lc5 failure load indeterminate by CoF data or by visual methods, coating appears to fail shortly after Lc3 but patches of coating remain up to 100N. Lc2 was also difficult to determine visually on sample C167, hence it was left blank.

Appendix SA - Scratch Adhesion Data

Load: 0-100N, Distance: 10mm, Load Rate: 10N/mm, Load Rate: 100N/min, Indenter 200 μ m radius diamond

Representative CoF Plot**Coating – CrC****Substrate – Pyrowear 675 (polished, RMS = 5nm [0.2 μ inch], HRC-64)**

CoF vs. Fz for ASE-8-19-1 C18 +3.txt



Appendix SA - Scratch Adhesion Data

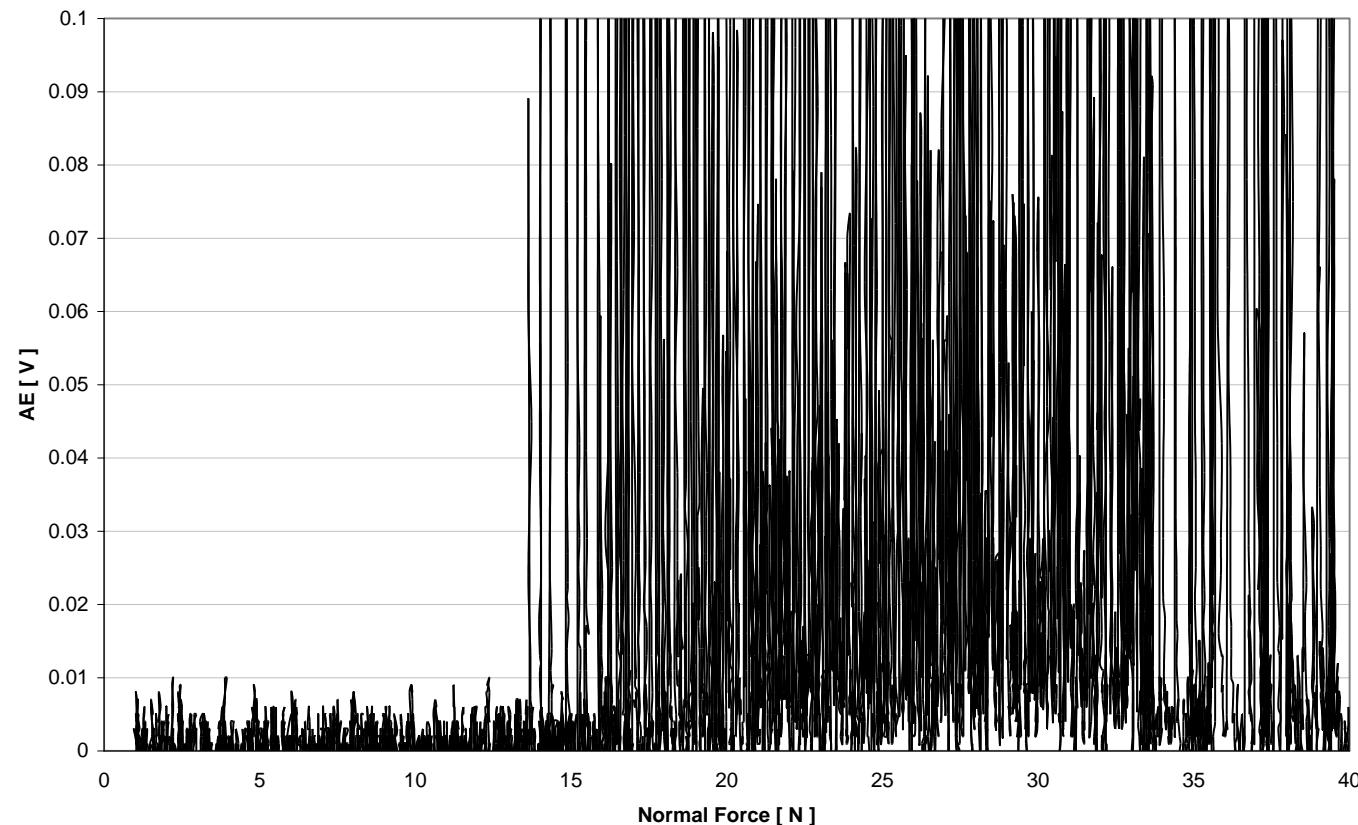
Load: 0-100N, Distance: 10mm, Load Rate: 10N/mm, Load Rate: 100N/min, Indenter 200 μ m radius diamond

Representative AE Plot (low energy signal, 0-0.1V range)

Coating – CrC

Substrate – Pyrowear 675 (polished, RMS = 5nm [0.2 μ inch], HRC-64)

AE vs. Fz for ASE-8-19-1 C18 +3.txt



Appendix SA - Scratch Adhesion Data

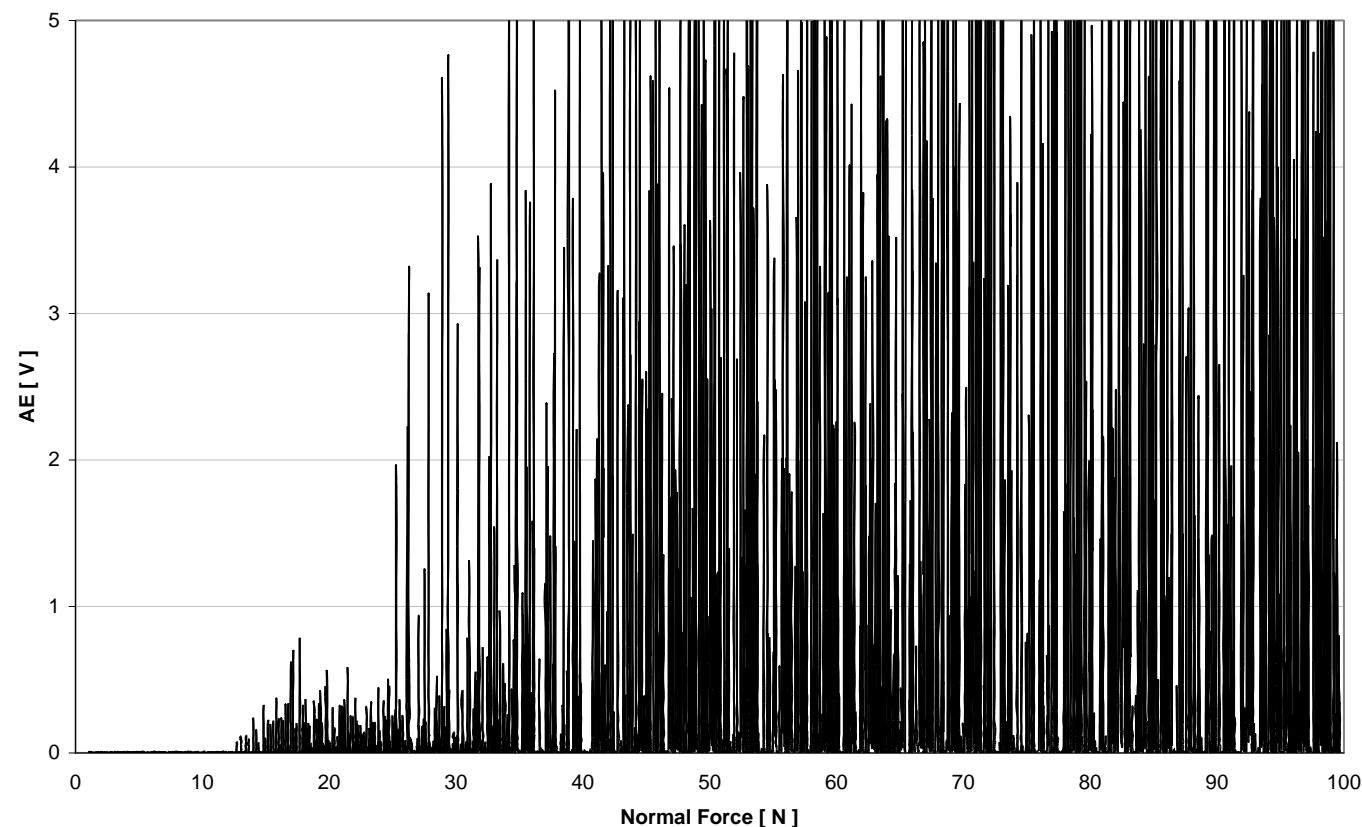
Load: 0-100N, Distance: 10mm, Load Rate: 10N/mm, Load Rate: 100N/min, Indenter 200 μ m radius diamond

Representative AE Plot (high energy signal, 0-5V range)

Coating – CrC

Substrate – Pyrowear 675 (polished, RMS = 5nm [0.2 μ inch], HRC-64)

AE vs. Fz for ASE-8-26-1 C167 -3.txt



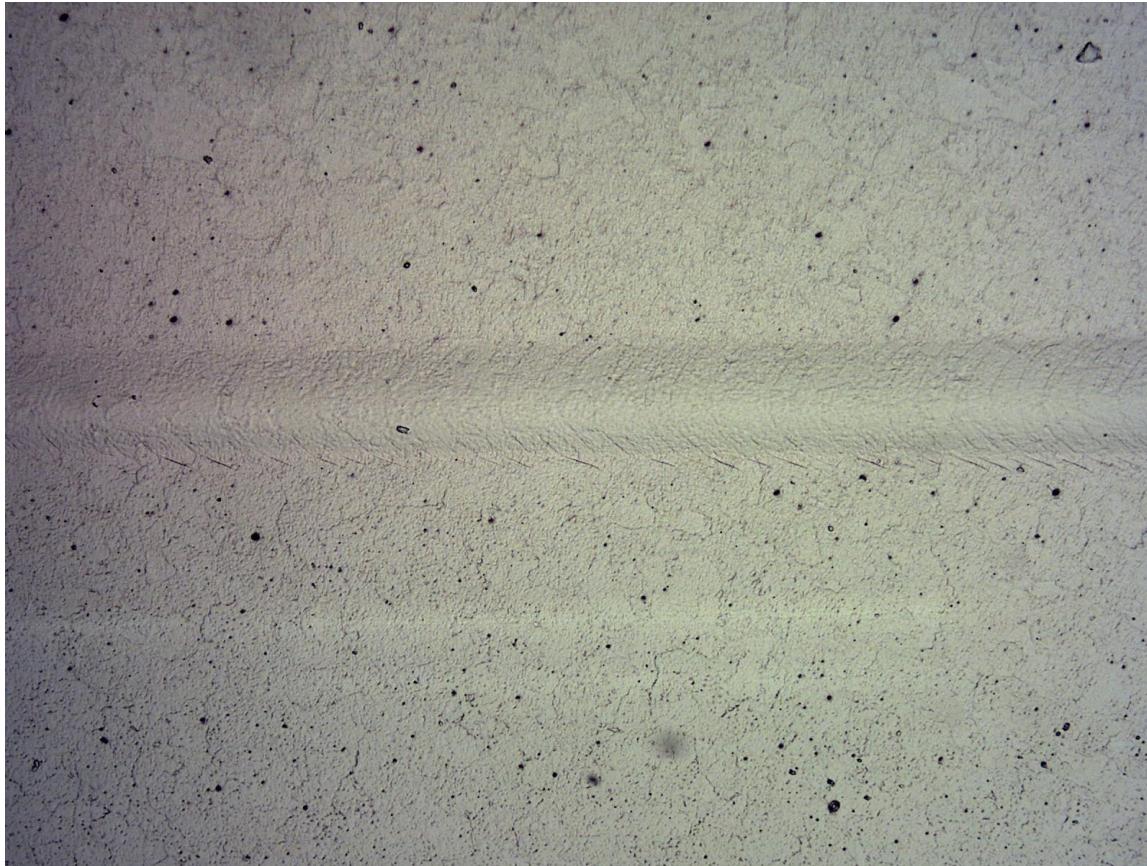
Appendix SA - Scratch Adhesion Data

Load: 0-100N, Distance: 10mm, Load Rate: 10N/mm, Load Rate: 100N/min, Indenter 200 μ m radius diamond

Representative Image of Lc2 Failure Mode

Coating – CrC

Substrate – Pyrowear 675 (polished, RMS = 5nm [0.2 μ inch], HRC-64)



CrC Lc2 failure mode(s) – arc tensile cracks which extend past the indent edge

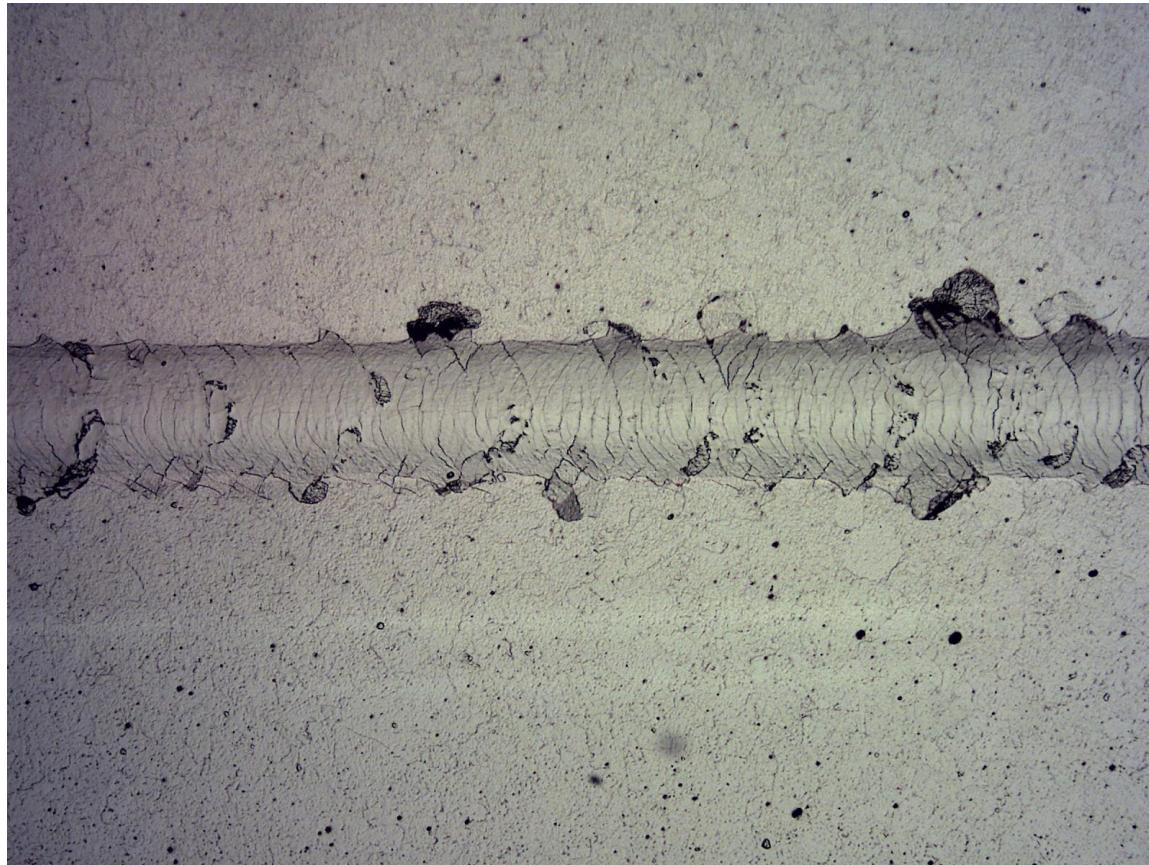
Appendix SA - Scratch Adhesion Data

Load: 0-100N, Distance: 10mm, Load Rate: 10N/mm, Load Rate: 100N/min, Indenter 200 μ m radius diamond

Representative Image of Lc3 Failure Mode

Coating – CrC

Substrate – Pyrowear 675 (polished, RMS = 5nm [0.2 μ inch], HRC-64)



CrC Lc3 failure mode(s) – cohesive delamination between nested buckling and arc tensile cracks, spare wedging delamination

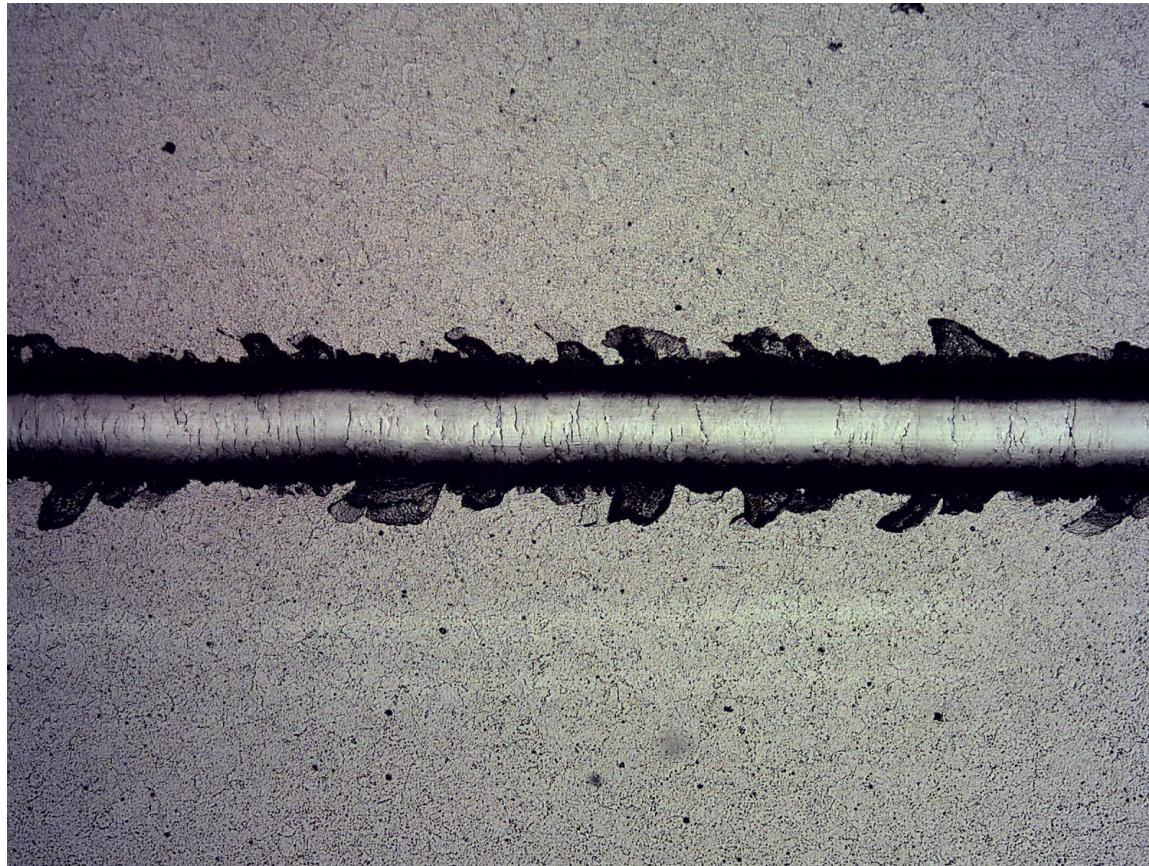
Appendix SA - Scratch Adhesion Data

Load: 0-100N, Distance: 10mm, Load Rate: 10N/mm, Load Rate: 100N/min, Indenter 200 μ m radius diamond

Representative Image of Lc5 Failure Mode

Coating – CrC

Substrate – Pyrowear 675 (polished, RMS = 5nm [0.2 μ inch], HRC-64)



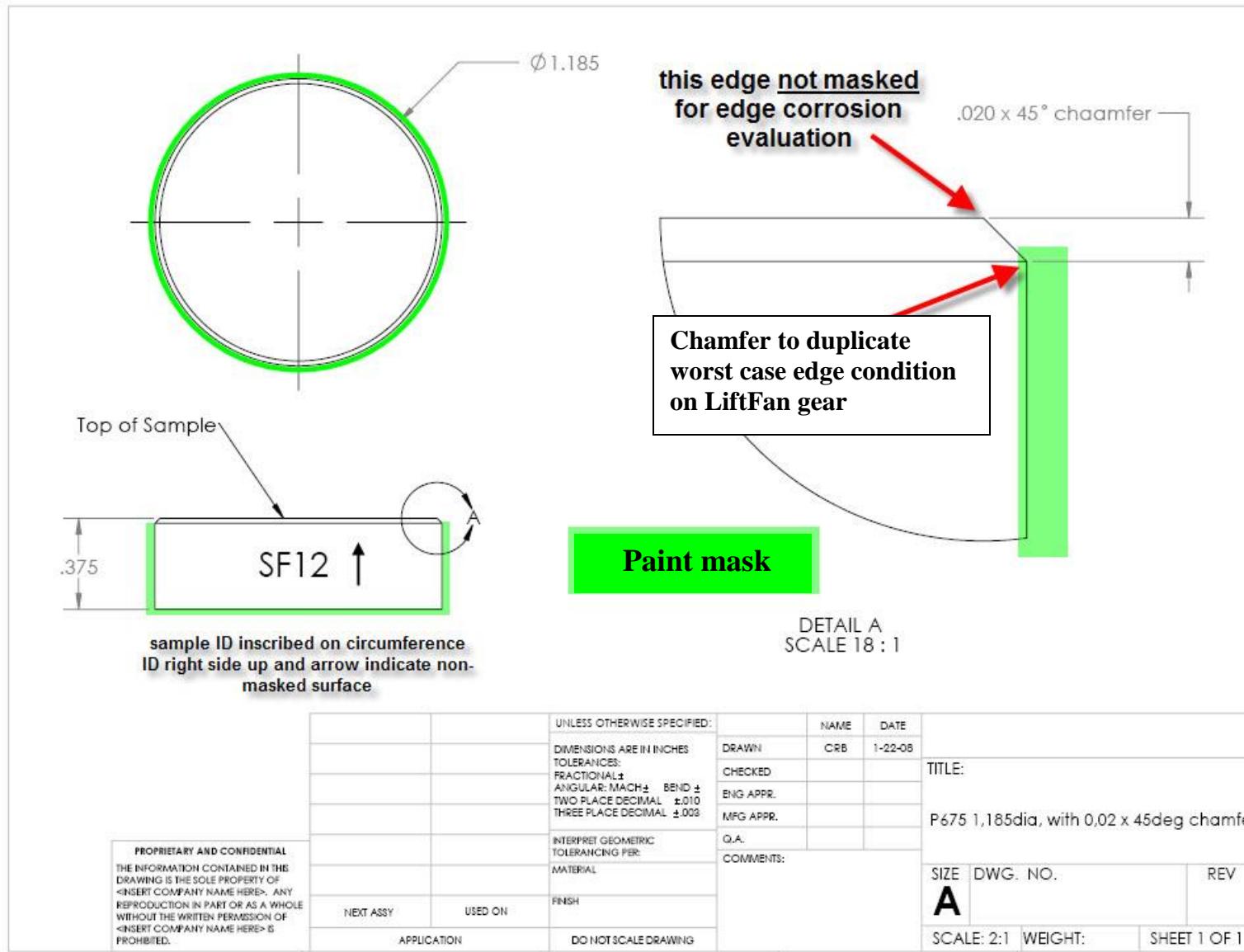
CrC Lc5 failure mode(s) – adhesive failure in track occurs in patches, wedging/buckling delamination at track edges

Appendix SF – ASTM B117 Salt Fog Corrosion Results

ASTM B117 corrosion test protocol

1. The B117 protocol can be used to test the relative resistance to corrosion of coated and uncoated metallic specimens, when exposed to a salt spray climate at an elevated temperature. The terms salt spray, salt fog and salt mist are all in widespread use for this type of testing and are generally interchangeable terms, as is the term cabinet or chamber, which is used to describe the equipment in which the test is conducted. Testing was subcontracted to Assured Testing Services (www.assuredtestingservices.com) and results were analyzed by Arcomac.
2. A 5% salt solution, prepared by dissolving sodium chloride into water that meets the requirements of ASTM D1193 Specification for Reagent Water, Type IV is supplied to the chamber. At the time the samples are placed into test, the cabinet should be pre-conditioned to the operating temperature of 35°C and fogging a 5% salt solution at a rate of 1-2ml/hr over 80cm² surface area. The fog collection rate is determined by placing a minimum of two 80 sq. cm. funnels inserted into measuring cylinders graduated in ml. inside the chamber. One collection device is located nearest the nozzle and one in the farthest corner. The sample face of interest is oriented at a 15° angle to allow condensation to run down the sample. Test duration was set to 336hrs with interruption at 96hrs to allow for digital photographs of the sample condition. Percent red corrosion surface area coverage was calculated and reported at the end of testing.
3. Super-finished Pyrowear 675 (P675) 1.185"dia x 0.375" thick samples were tested uncoated and with TiCr-TiCrN, Cr-CrN and CrC coatings. All samples were masked with epoxy paint (see schematic page SF#2) on the circumference and bottom face to ensure that all corrosion would occur on the sample face of interest.
4. Experience has shown that the sharp circumferential edges that result from grinding disc samples to a low RMS surface roughness are very often sites of corrosion initiation for coated samples. This is due to the increased chance that the coating will delaminate at sharp edges and/or that the 5% salt mixture has an increased opportunity to work under the edges of the coating. For this reason samples with sharp edges have masking which was applied to mask the sharp edge (in addition to the circumference and bottom face) while leaving 95% of the sample face surface area unmasked. Since the sharp edges do not represent actual conditions existing in gears Arcomac worked with Rolls Royce to determine the worst case edge condition in the LiftFan gear design and then replicated this condition as a chamfer on the coated samples (see schematic page SF#2). This approach allows for determination of the corrosion performance of the coatings on actual edge conditions that exist in the LiftFan gear design.

Appendix SF – ASTM B117 Salt Fog Corrosion Results



5

4

3

2

1

Appendix SF – ASTM B117 Salt Fog Corrosion Results

ASTM B117 Test Matrix

- Four samples are tested for each coating type with 2 samples coming from the 1st coating deposition batch (Dep1) and 2 samples coming from the second deposition batch (Dep2). The sample set allows for minimal statistical confidence for repeatability of corrosion performance among individual samples from a single coating deposition and also between identical coating formulations produced in separate deposition runs.
- Coating Substrate - Pyrowear 675 (REM super-finish, RMS = 50nm [2μinch], HRC-64)
- Cr-CrN samples were included in the test matrix which had been subjected to Rolling Contact Fatigue (RCF) testing in order to demonstrate functional corrosion performance. TiCr-TiCrN samples were not included due to poor RCF performance which exposed the P675 substrate. CrC samples were not included due to logistical issues with not being able to complete RCF testing prior to the start of B117 corrosion testing.

Coating	Sample ID	Sample Type	Notes
n/a	P61	Masked Sharp Edge	Baseline super-finished P675
n/a	P62	Masked Sharp Edge	Baseline super-finished P675
TiCr-TiCrN (Dep1)	SF9	LiftFan Chamfered Edge	
TiCr-TiCrN (Dep1)	SF12	LiftFan Chamfered Edge	
TiCr-TiCrN (Dep2)	SF4	LiftFan Chamfered Edge	
TiCr-TiCrN (Dep2)	SF6	LiftFan Chamfered Edge	
Cr-CrN (Dep1)	SF2	LiftFan Chamfered Edge	
Cr-CrN (Dep1)	P23	Masked Sharp Edge	RCF track on sample, 8E+06 contact cycles
Cr-CrN (Dep2)	P60	Masked Sharp Edge	
Cr-CrN (Dep2)	P50	Masked Sharp Edge	RCF track on sample, 6.3E+06 contact cycles
CrC (Dep1)	SF10	LiftFan Chamfered Edge	
CrC (Dep1)	SF1	LiftFan Chamfered Edge	
CrC (Dep2)	SF8	LiftFan Chamfered Edge	
CrC (Dep2)	P39	Masked Sharp Edge	

Appendix SF – ASTM B117 Salt Fog Corrosion Results

ASTM B117 Test Results - % Area Coverage of Red Corrosion

Coating	Sample ID	%Area Coverage Red Corrosion	Notes
n/a	P61	100%	
n/a	P62	100%	
TiCr-TiCrN (Dep1)	SF9	80%	
TiCr-TiCrN (Dep1)	SF12	99%	
TiCr-TiCrN (Dep2)	SF4	70%	
TiCr-TiCrN (Dep2)	SF6	60%	
Cr-CrN (Dep1)	SF2	0%	
Cr-CrN (Dep1)	P23	4%	Corrosion originates from RCF track
Cr-CrN (Dep2)	P60	2%	
Cr-CrN (Dep2)	P50	7%	Corrosion originates from RCF track
CrC (Dep1)	SF10	~50%	Oxide did not adhere, see discussion
CrC (Dep1)	SF1	~50%	Oxide did not adhere, see discussion
CrC (Dep2)	SF8	5%	
CrC (Dep2)	P39	~40%	Oxide did not adhere, see discussion

Appendix SF – ASTM B117 Salt Fog Corrosion Results

P675, Sample ID – P61, uncoated baseline

ASTM B117 Corrosion Test Pre-Test	ASTM B117 Corrosion Test 96hrs Exposure	ASTM B117 Corrosion Test 336hrs Exposure
		
	<p>ASTM B117 Corrosion Test 336hrs Exposure Sample Lapped to remove red oxide</p> 	

Appendix SF – ASTM B117 Salt Fog Corrosion Results

P675, Sample ID – P62, uncoated baseline

ASTM B117 Corrosion Test Pre-Test	ASTM B117 Corrosion Test 96hrs Exposure	ASTM B117 Corrosion Test 336hrs Exposure
		
	<p>ASTM B117 Corrosion Test 336hrs Exposure Sample Lapped to remove red oxide</p>	

Appendix SF – ASTM B117 Salt Fog Corrosion Results

TiCr-TiCrN (Dep1), Sample ID – SF9

ASTM B117 Corrosion Test Pre-Test	ASTM B117 Corrosion Test 96hrs Exposure	ASTM B117 Corrosion Test 336hrs Exposure
		
	ASTM B117 Corrosion Test 336hrs Exposure Sample Lapped to remove red oxide	

Appendix SF – ASTM B117 Salt Fog Corrosion Results

TiCr-TiCrN (Dep1), Sample ID - SF12

ASTM B117 Corrosion Test Pre-Test	ASTM B117 Corrosion Test 96hrs Exposure	ASTM B117 Corrosion Test 336hrs Exposure
		
	<p>ASTM B117 Corrosion Test 336hrs Exposure Sample Lapped to remove red oxide</p> 	

Appendix SF – ASTM B117 Salt Fog Corrosion Results

TiCr-TiCrN (Dep2), Sample ID – SF4

ASTM B117 Corrosion Test Pre-Test	ASTM B117 Corrosion Test 96hrs Exposure	ASTM B117 Corrosion Test 336hrs Exposure
		
	<p>ASTM B117 Corrosion Test 336hrs Exposure Sample Lapped to remove red oxide</p> 	

Appendix SF – ASTM B117 Salt Fog Corrosion Results

TiCr-TiCrN (Dep2), Sample ID – SF6

ASTM B117 Corrosion Test Pre-Test	ASTM B117 Corrosion Test 96hrs Exposure	ASTM B117 Corrosion Test 336hrs Exposure
		
	<p>ASTM B117 Corrosion Test 336hrs Exposure Sample Lapped to remove red oxide</p> 	

Appendix SF – ASTM B117 Salt Fog Corrosion Results

Cr-CrN (Dep1), Sample ID – SF2

ASTM B117 Corrosion Test Pre-Test	ASTM B117 Corrosion Test 96hrs Exposure	ASTM B117 Corrosion Test 336hrs Exposure
		
	<p>ASTM B117 Corrosion Test 336hrs Exposure Sample Lapped to remove red oxide</p> 	

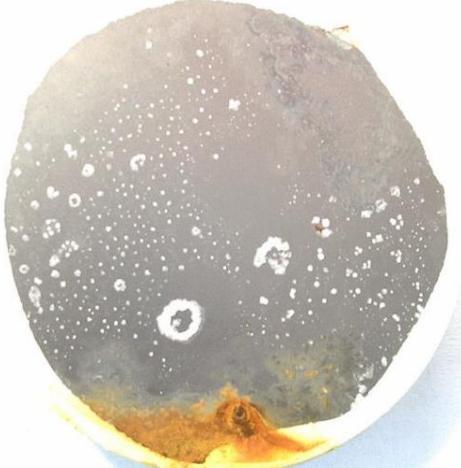
Appendix SF – ASTM B117 Salt Fog Corrosion Results

Cr-CrN (Dep1), Sample ID – P23, RCF track on sample

ASTM B117 Corrosion Test Pre-Test	ASTM B117 Corrosion Test 96hrs Exposure	ASTM B117 Corrosion Test 336hrs Exposure
		
	<p>ASTM B117 Corrosion Test 336hrs Exposure Sample Lapped to remove red oxide</p> 	

Appendix SF – ASTM B117 Salt Fog Corrosion Results

Cr-CrN (Dep2), Sample ID – P60

ASTM B117 Corrosion Test Pre-Test	ASTM B117 Corrosion Test 96hrs Exposure	ASTM B117 Corrosion Test 336hrs Exposure
		
	<p>ASTM B117 Corrosion Test 336hrs Exposure Sample Lapped to remove red oxide</p> 	

Appendix SF – ASTM B117 Salt Fog Corrosion Results

Cr-CrN (Dep2), Sample ID – P50, RCF track on sample

ASTM B117 Corrosion Test Pre-Test	ASTM B117 Corrosion Test 96hrs Exposure	ASTM B117 Corrosion Test 336hrs Exposure
		
	<p>ASTM B117 Corrosion Test 336hrs Exposure Sample Lapped to remove red oxide</p> 	

Appendix SF – ASTM B117 Salt Fog Corrosion Results

CrC (Dep1), Sample ID – SF10

ASTM B117 Corrosion Test Pre-Test	ASTM B117 Corrosion Test 96hrs Exposure	ASTM B117 Corrosion Test 336hrs Exposure
		
	<p>ASTM B117 Corrosion Test 336hrs Exposure Sample Lapped to remove red oxide</p> 	

Appendix SF – ASTM B117 Salt Fog Corrosion Results

CrC (Dep1), Sample ID – SF1

ASTM B117 Corrosion Test Pre-Test	ASTM B117 Corrosion Test 96hrs Exposure	ASTM B117 Corrosion Test 336hrs Exposure
		
	<p>ASTM B117 Corrosion Test 336hrs Exposure Sample Lapped to remove red oxide</p>	

Appendix SF – ASTM B117 Salt Fog Corrosion Results

CrC (Dep2), Sample ID – SF8

ASTM B117 Corrosion Test Pre-Test	ASTM B117 Corrosion Test 96hrs Exposure	ASTM B117 Corrosion Test 336hrs Exposure
		
	<p>ASTM B117 Corrosion Test 336hrs Exposure Sample Lapped to remove red oxide</p> 	

Appendix SF – ASTM B117 Salt Fog Corrosion Results

CrC (Dep2), Sample ID – P39

ASTM B117 Corrosion Test Pre-Test	ASTM B117 Corrosion Test 96hrs Exposure	ASTM B117 Corrosion Test 336hrs Exposure
		
	<p>ASTM B117 Corrosion Test 336hrs Exposure Sample Lapped to remove red oxide</p>	

Appendix SF – ASTM B117 Salt Fog Corrosion Results

Appendix Th – Coating Thickness Data

Coating Thickness Measurement Overview

1. Coating thickness is measured using the CALOtest™ method. This test is also referred to more generally as a spherical abrasion technique. A grade 5 0.3750" radius (R) chrome steel ball is rotated at 2000rpm against a coated specimen with ~0.5µm diamond slurry used as the abrasive medium (see Figure 1). The abrasion scar is circular when viewed from above and results in two diameters; D and d, which represent the coating surface (D) and coating/substrate interface (d) (see Figure 1). Accurate measurement of D and d is achieved by use of an optical microscope fitted with a linear scale.
2. Coating thickness can be calculated by

$$s = \frac{1}{2} \left(\sqrt{4R^2 - d^2} - \sqrt{4R^2 - D^2} \right)$$

Where s is the coating thickness

3. Accuracy of thickness measurement is +/-0.1µm when the substrate has a low roughness, i.e. RMS <25nm. Greater substrate roughness introduces measurement inaccuracies in "d" due to roughness at the coating/substrate interface.

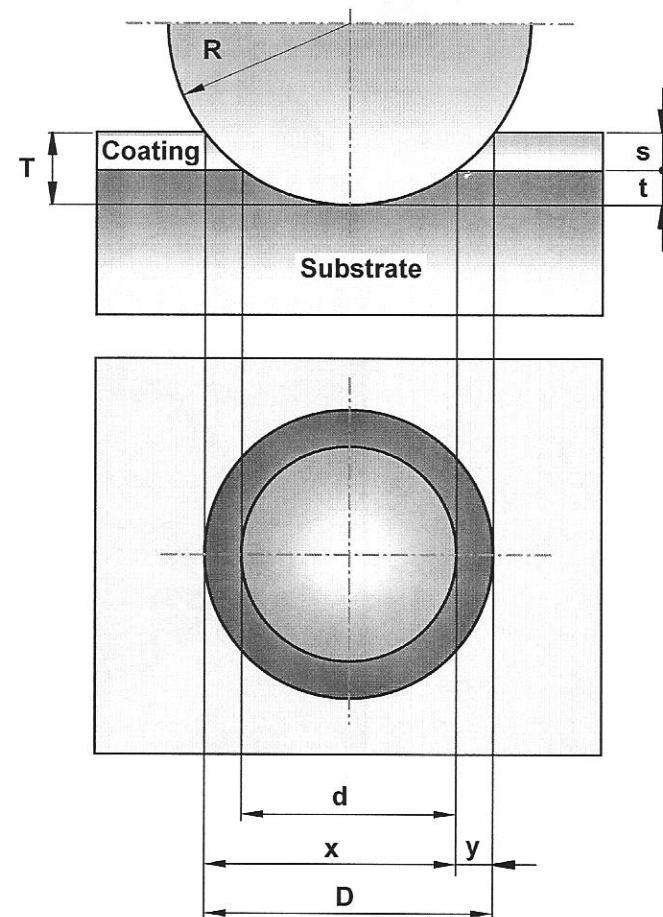


Figure 1: CALOtest schematic

Appendix Th – Coating Thickness Data

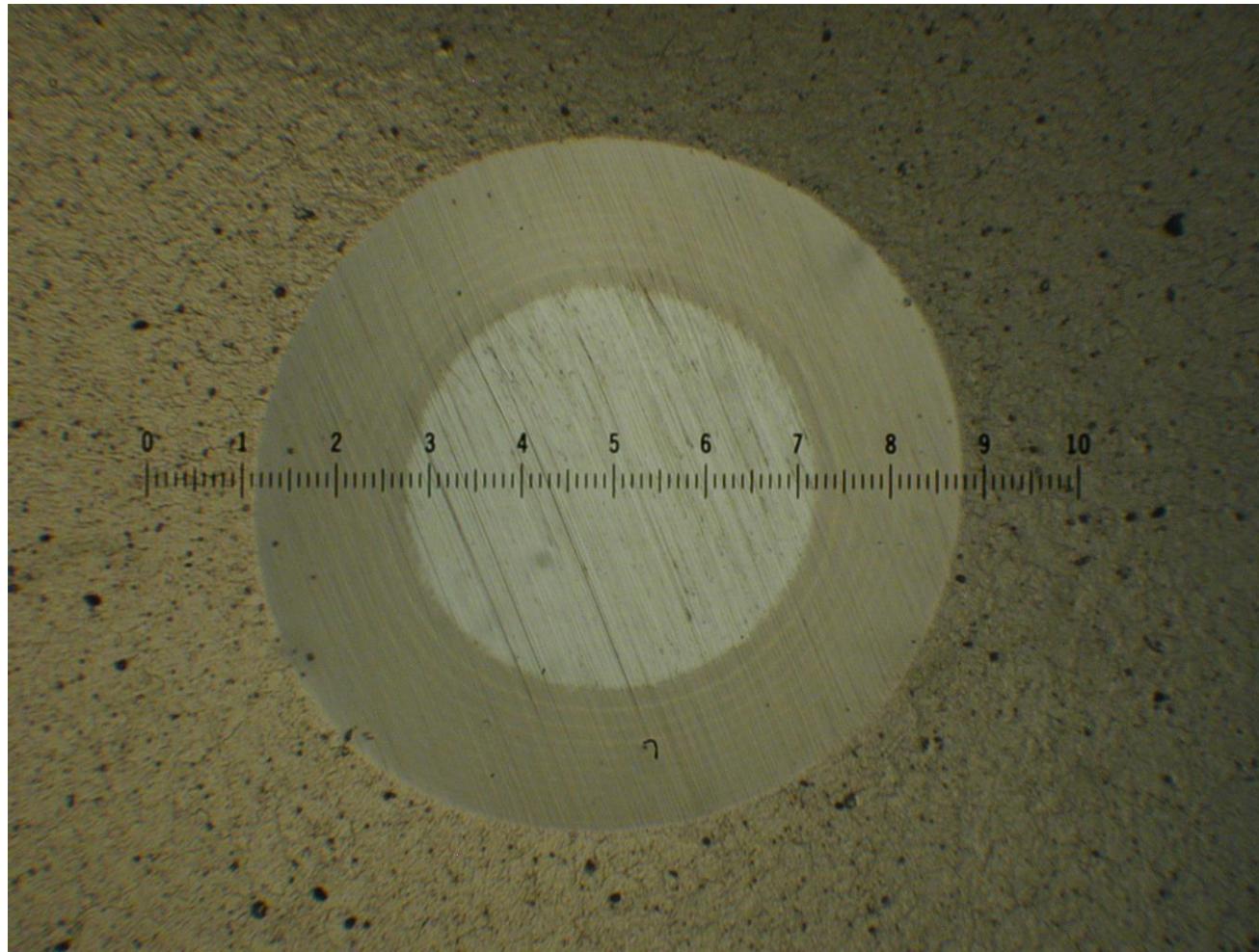
Coating Thickness Measurement Approach

1. Coating thickness was measured on qty(1) polished P675 sample per coating type and coating run. This value is reported as the official coating thickness
2. Coating thickness was measured on qty(2) super-finished P675 samples per coating type and coating run. The value was used to confirm coating thickness on the super-finished P675 samples within +/-0.5µm, but was not reported as measurement accuracy is compromised by roughness at the coating/substrate interface.
3. Optical microscope images are included for CALOtests performed on polished P675 substrates.
4. SEM images are included for reference for CALOtests performed on super-finished P675 substrates.

Coating Thickness**Substrate - Pyrowear 675 (polished, RMS = 5nm [0.2µinch], HRC-64)**

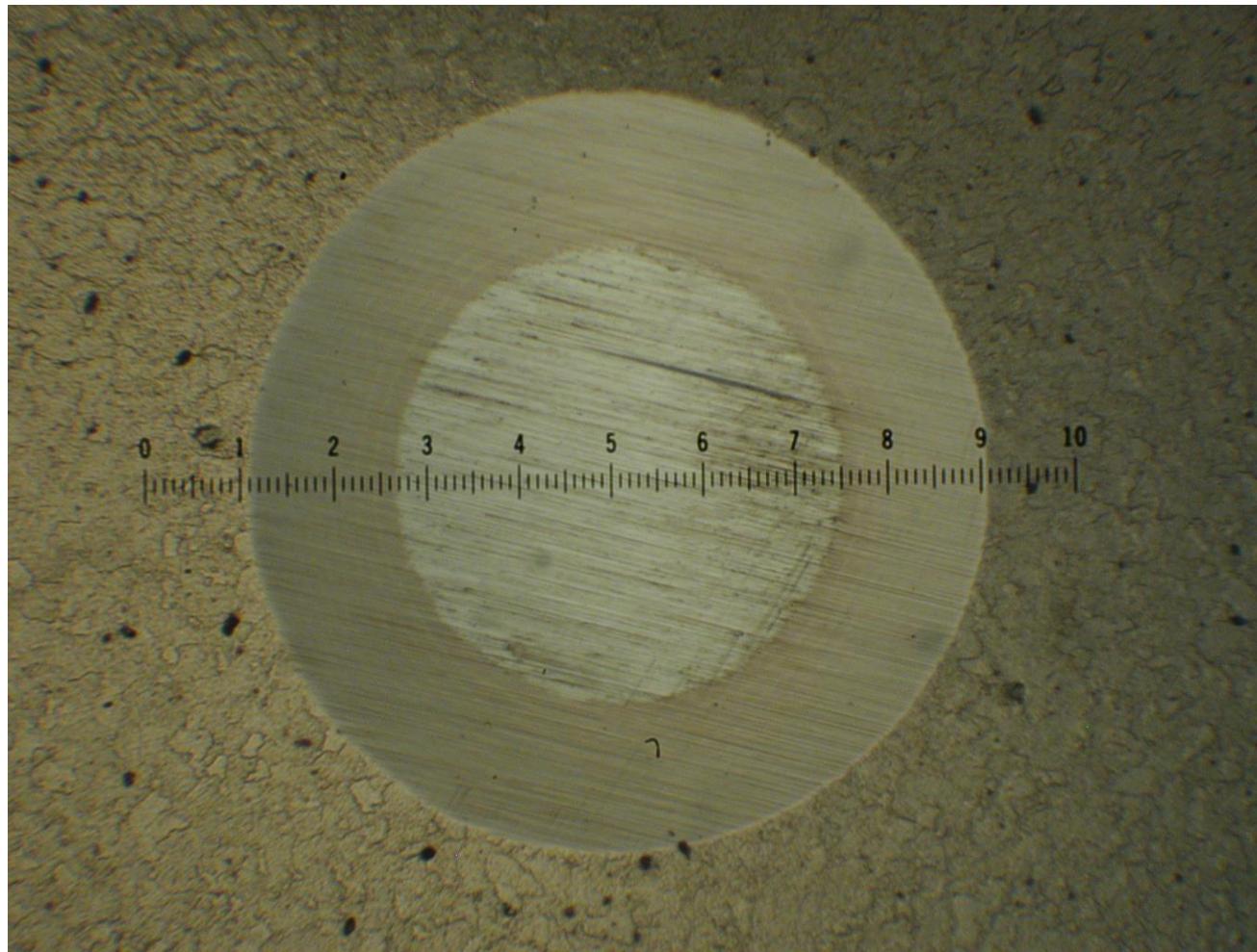
Coating	Coating ID	Sample ID	Thickness [µm]	Appendix Page CALO Image @75x
TiCr-TiCrN	ASE-8-9-1 (Run1)	C170	5.6	Th_3
TiCr-TiCrN	ASE-8-14-1 (Run2)	C78	5.8	Th_4
Cr-CrN	ASE-8-29-1 (Run1)	C33	6.3	Th_5
Cr-CrN	ASE-8-34-1 (Run2)	C79	6	Th_6
CrC	ASE-8-19-1 (Run1)	C81	6.3	Th_7
CrC	ASE-8-26-1 (Run2)	C60	5.4	Th_8

Appendix Th – Coating Thickness Data



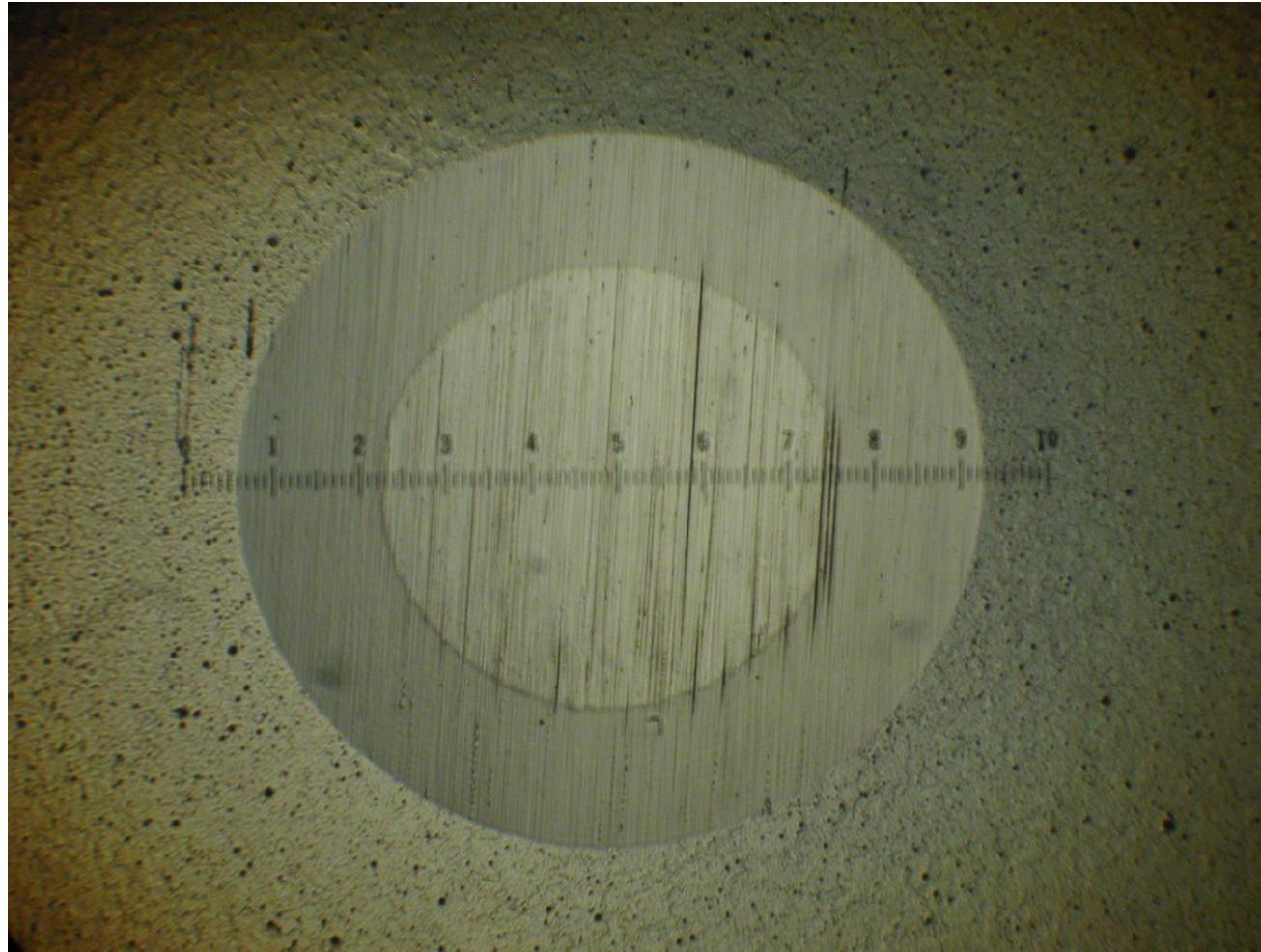
TiCr-TiCrN (Run1): note multilayer structure is visible
Substrate - Pyrowear 675 (polished, RMS = 5nm [0.2 μ inch], HRC-64)
Optical Microscope Image @ 75x (linear scale 1div = 105 μ m)

Appendix Th – Coating Thickness Data



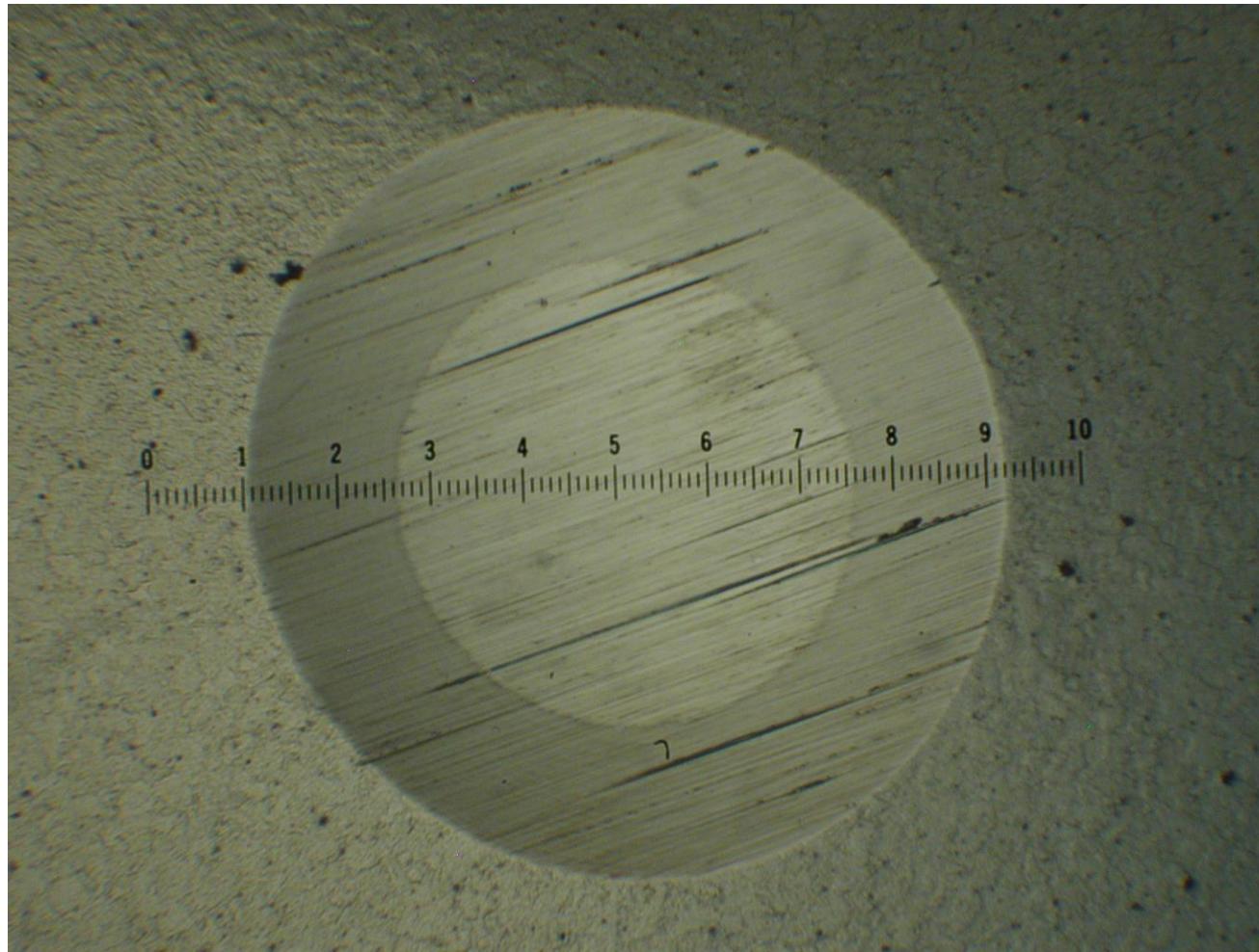
TiCr-TiCrN (Run2): note multilayer structure is visible
Substrate - Pyrowear 675 (polished, RMS = 5nm [0.2 μ inch], HRC-64)
Optical Microscope Image @ 75x (linear scale 1div = 105 μ m)

Appendix Th – Coating Thickness Data



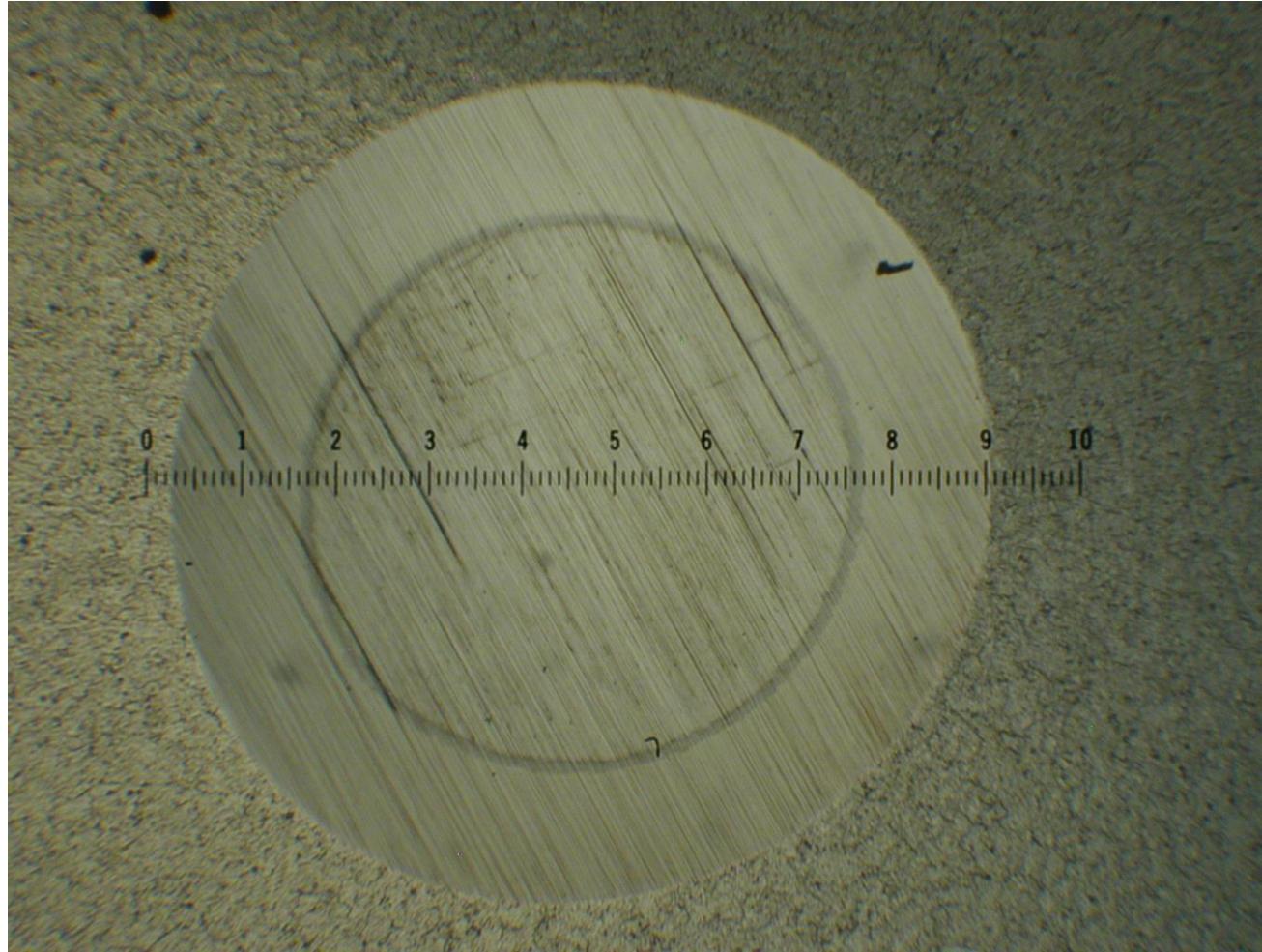
Cr-CrN (Run1): note multilayer structure is visible (bottom quadrant of scar)
Substrate - Pyrowear 675 (polished, RMS = 5nm [0.2 μ inch], HRC-64)
Optical Microscope Image @ 75x (linear scale 1div = 105 μ m)

Appendix Th – Coating Thickness Data



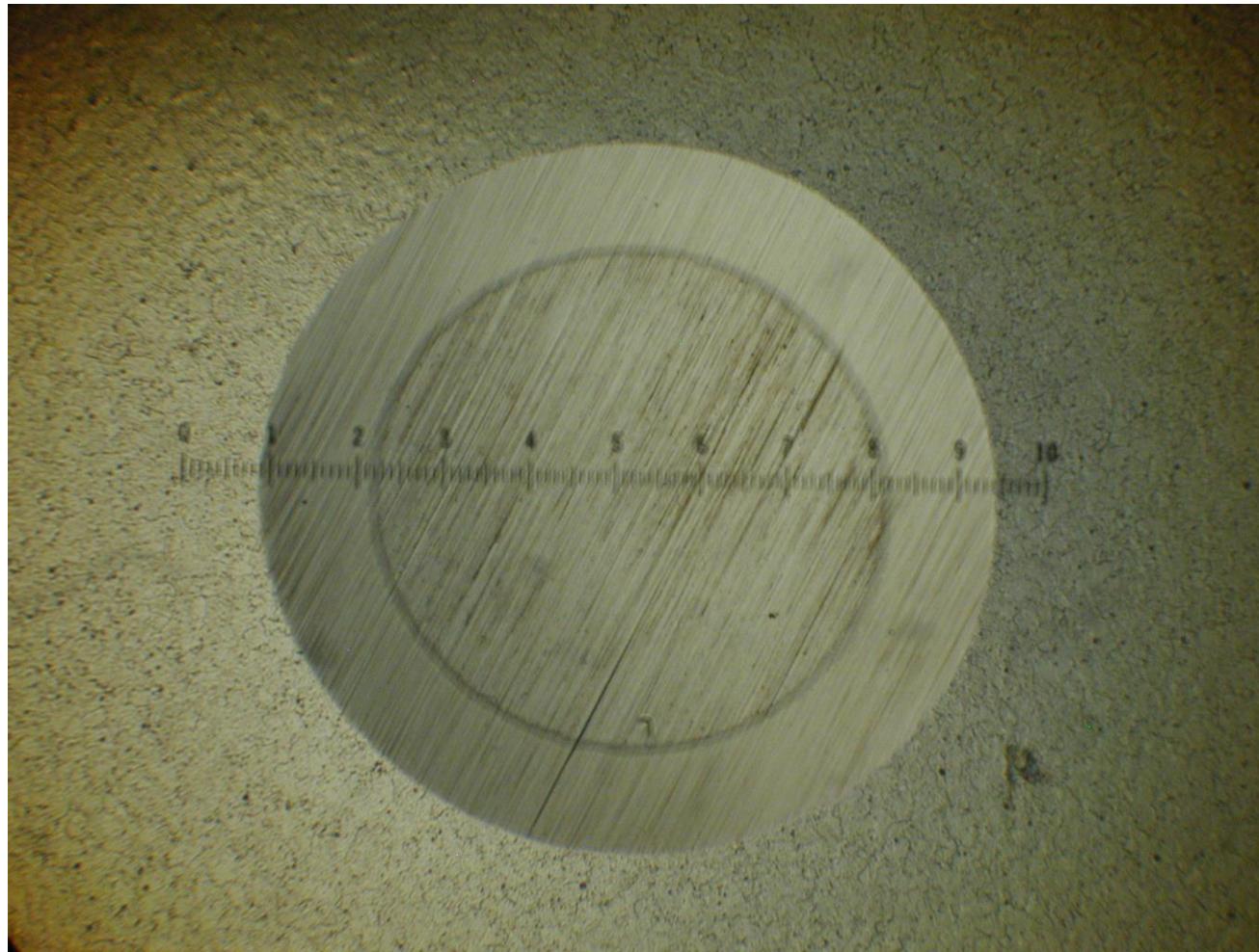
Cr-CrN (Run2): note multilayer structure is visible (bottom quadrant of scar)
Substrate - Pyrowear 675 (polished, RMS = 5nm [0.2 μ inch], HRC-64)
Optical Microscope Image @ 75x (linear scale 1div = 105 μ m)

Appendix Th – Coating Thickness Data



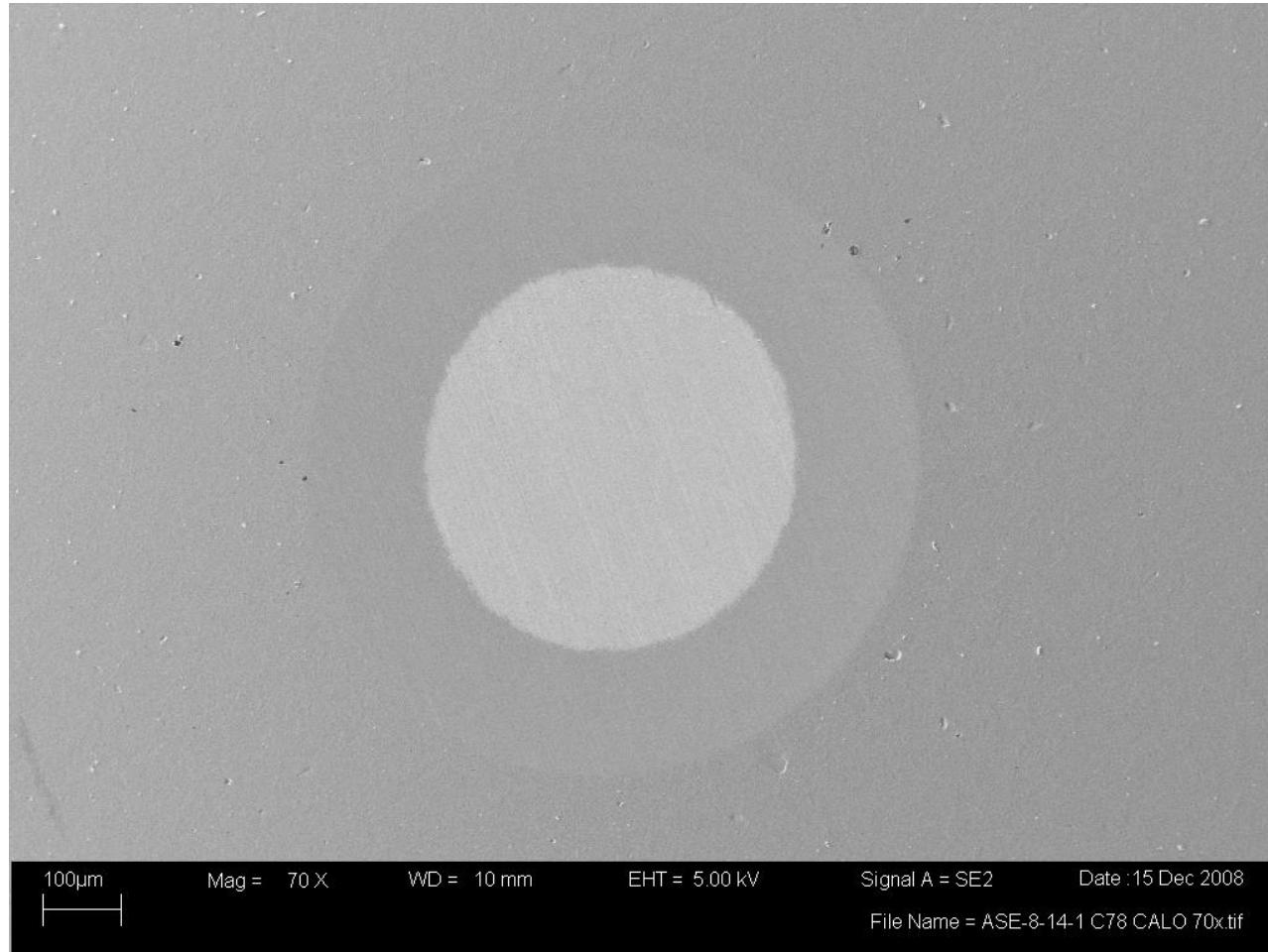
CrC (Run1): note inner gray ring is the Cr-CrN bond layer
Substrate - Pyrowear 675 (polished, RMS = 5nm [0.2 μ inch], HRC-64)
Optical Microscope Image @ 75x (linear scale 1div = 105 μ m)

Appendix Th – Coating Thickness Data



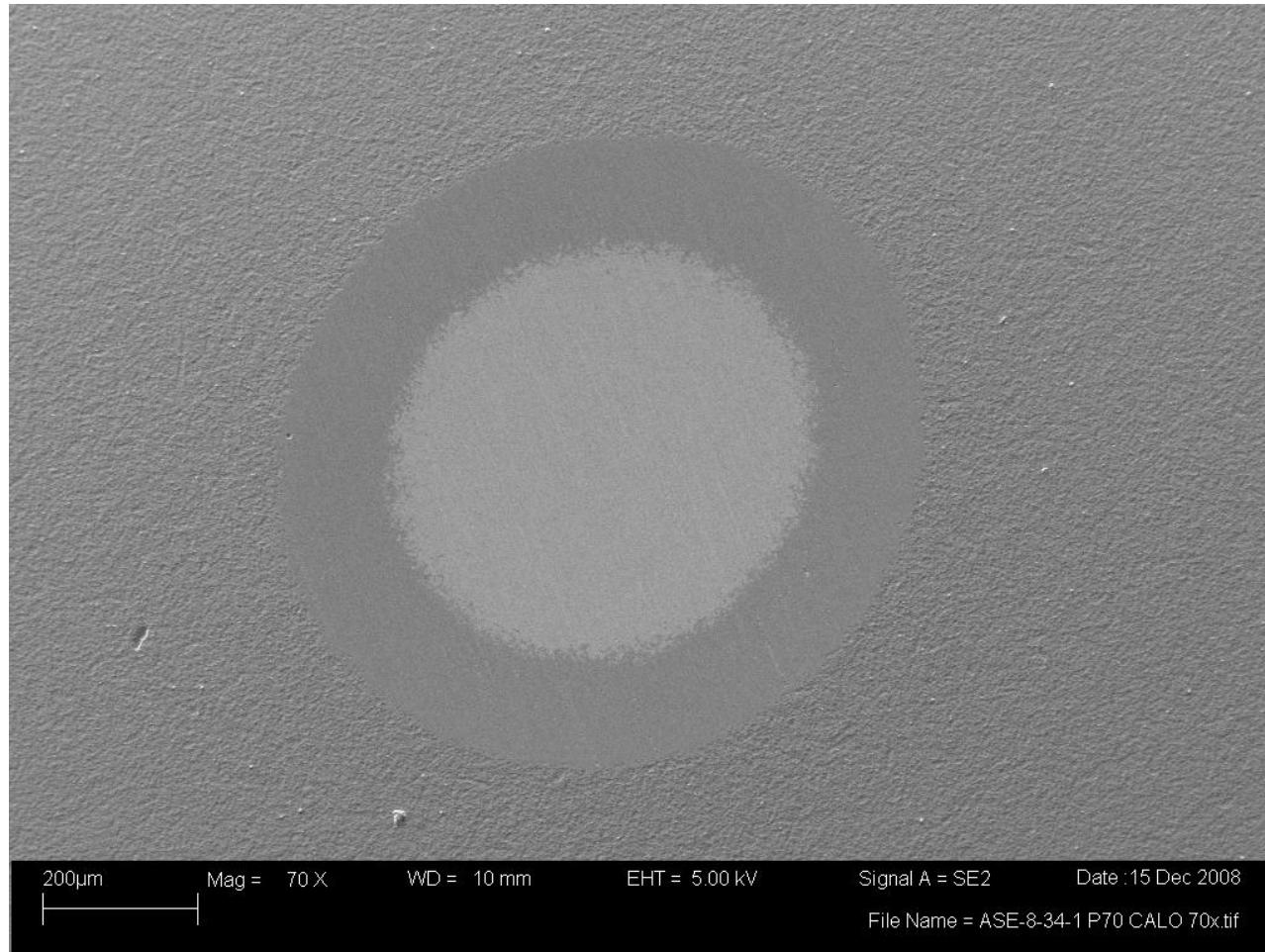
CrC (Run2): note inner gray ring is the Cr-CrN bond layer
Substrate - Pyrowear 675 (polished, RMS = 5nm [0.2 μ inch], HRC-64)
Optical Microscope Image @ 75x (linear scale 1div = 105 μ m)

Appendix Th – Coating Thickness Data



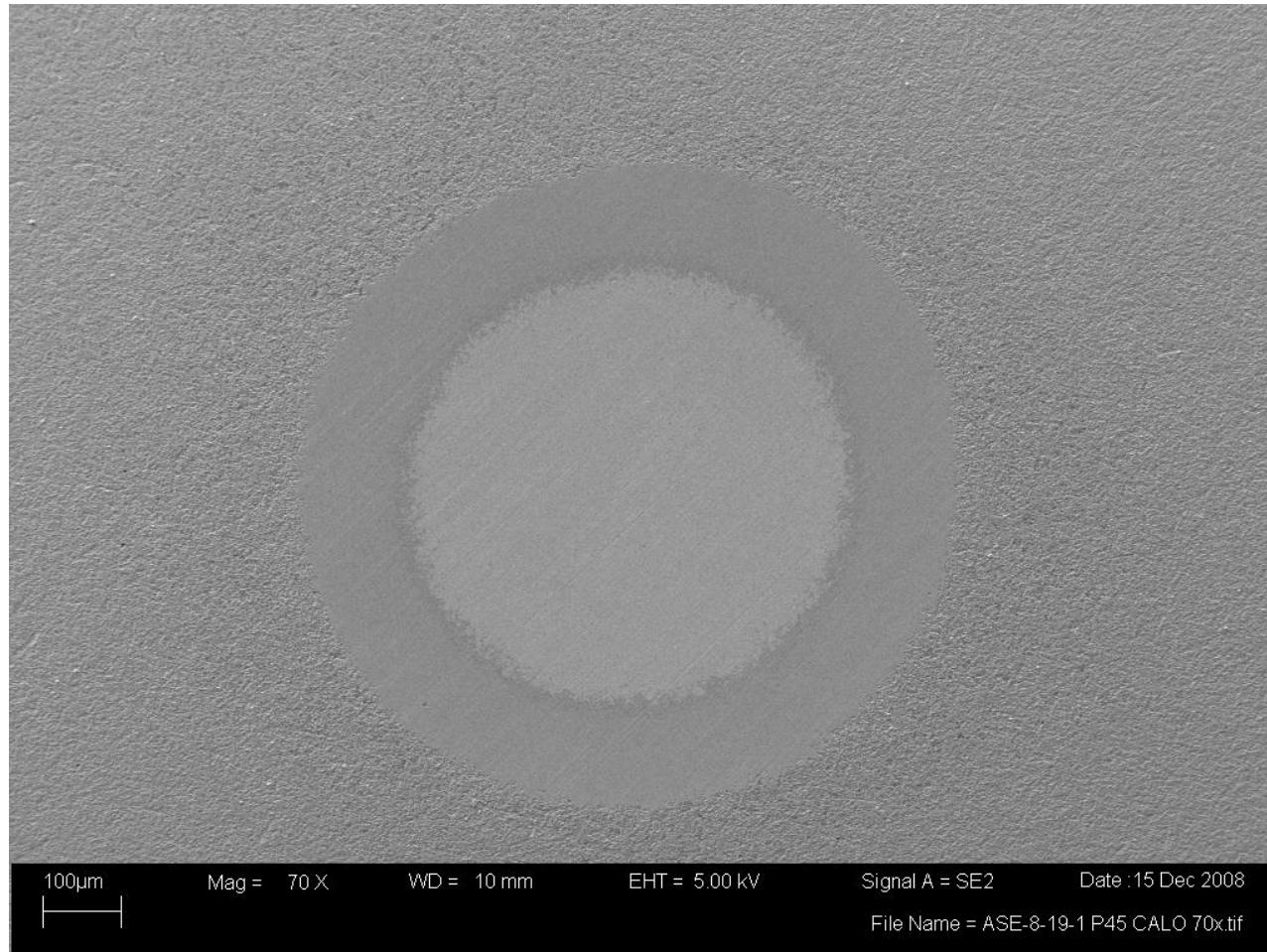
TiCr-TiCrN (Run2)
Substrate - Pyrowear 675 (super-finished, RMS = 50nm [2µinch], HRC-64)
SEM Image @ 70x

Appendix Th – Coating Thickness Data



Cr-CrN (Run2)
Substrate - Pyrowear 675 (super-finished, RMS = 50nm [2µinch], HRC-64)
SEM Image @ 70x

Appendix Th – Coating Thickness Data



100µm

Mag = 70 X

WD = 10 mm

EHT = 5.00 kV

Signal A = SE2

Date : 15 Dec 2008

File Name = ASE-8-19-1 P45 CALO 70x.tif

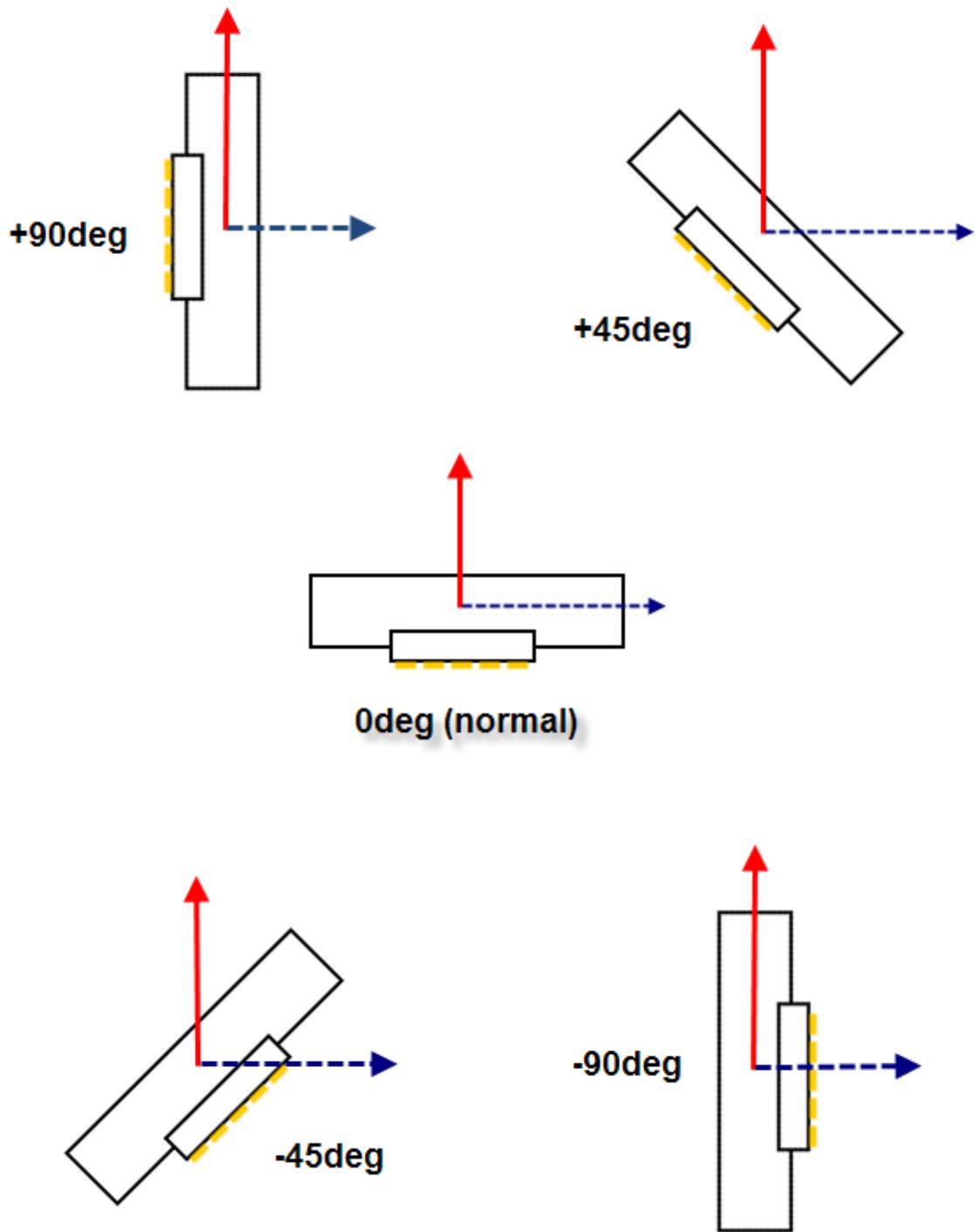
CrC (Run1)
Substrate - Pyrowear 675 (super-finished, RMS = 50nm [2µinch], HRC-64)
SEM Image @ 70x

Appendix UNI – Coating Uniformity Study Results

Coating Uniformity Measurement Overview

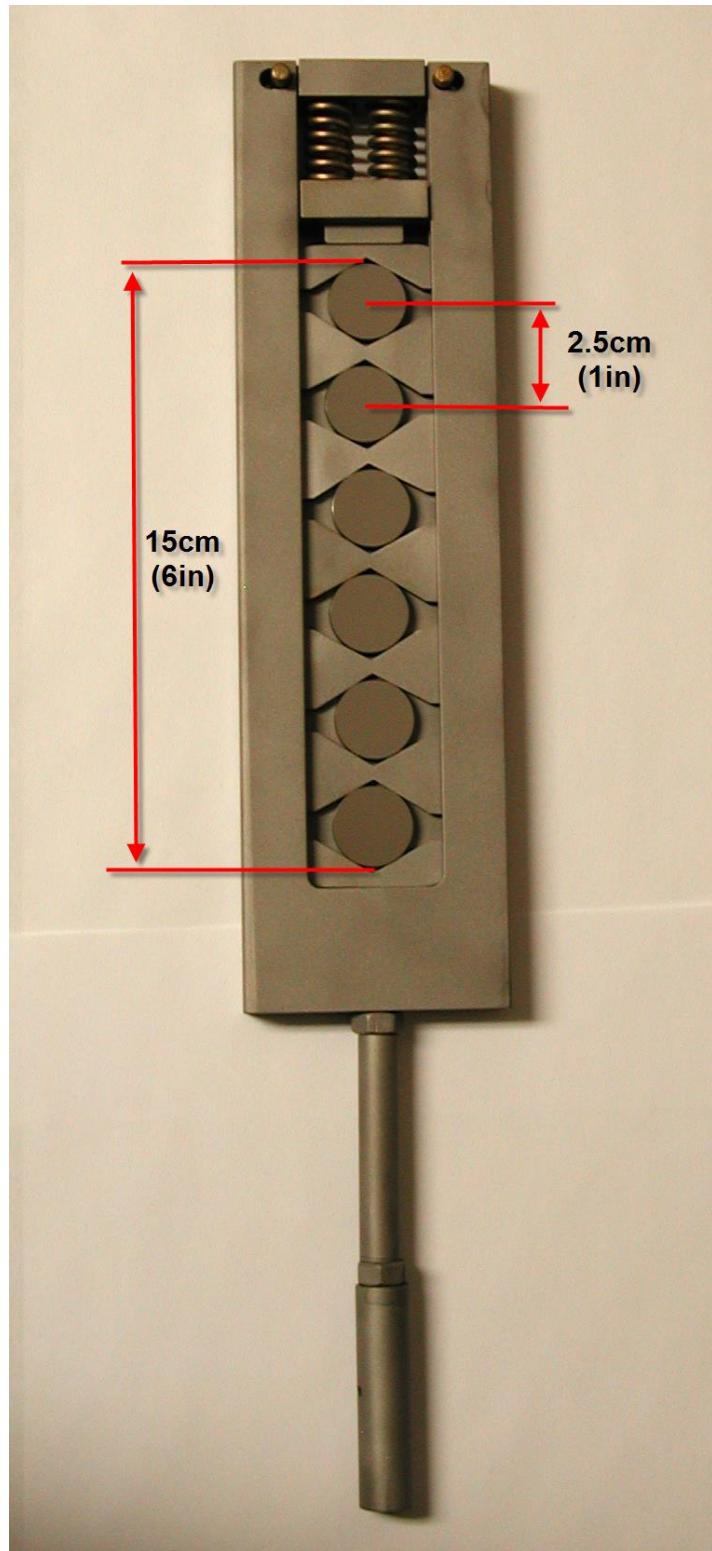
1. For any coating solution to be ultimately successful it must be transferred from flat substrate geometries commonly used for coating development to the complex geometry of the LiftFan helical bevel gears. Early in the Phase II SBIR effort acquisition of a LiftFan gear section was planned to demonstrate coating uniformity, although the gear acquisition ended up not being possible. Instead two methods were used to characterize coating uniformity; placement of witness samples at different positions and angles to the plasma flow to replicate the angles of LiftFan gear teeth and coating of 2"dia spur gears with tooth-to-root aspect ratios matching the LiftFan gear to demonstrate coating thickness uniformity on complex shapes.
2. A vertical distribution sample fixture was used to assess the dependence of coating thickness and mechanical properties on position and angle in the plasma flow. Qty(6) 19mm diameter 440A samples (RMS ~25nm, HRC ~58) were loaded into a fixture which distributes the samples vertically over a 15cm (6in) coating zone with 2.5cm spacing between the centers of the samples. The samples were coated in fixed single rotation mode and were set at specific angles to the plasma flow to encompass the range of plasma exposure angles for LiftFan gear teeth. Variations due to position or facing angle in coating thickness, coating adhesion, coating composition, coating hardness were assessed. The schematic on page #UNI_2 further illustrates the sample orientation matrix.
3. Spur gears were coated in double rotation (DR) to provide demonstration of coating thickness uniformity on complex shapes. 5cm (2in) diameter spur gears were used to replicate the ~1.37 tooth height to root width ratio on the LiftFan helical bevel gears. Standard spur gears are commercially available normally only with very rough (RMS >300nm) grind surface finishes for basic industrial use; coating of such rough surfaces does not lend itself to visualization of uniformity and also does not represent the super-finished LiftFan gear. Arcomac worked with Alion Science and Technology to obtain super-finished spur gears; the work was developmental research for Alion. Super-finishing on spur gears improved the surface finish but non-uniform results were problematic in the tooth root areas due to poor polishing media mobility and overall just due to poor manufacturing quality (surface gouges, tool marks, etc) common to bulk production gear. Coated spur gears were precision cross-sectioned and polished to demonstrate the coating thickness uniformity over the profile of the spur gear tooth.

Appendix UNI – Coating Uniformity Study Results



Schematic (top down view of fixture) of sample angular position as the sample passes by the center of the plasma filter duct in single rotation. Plasma flow direction (red solid arrow) and substrate table rotation direction (blue dashed arrow) are shown. The sample face being coated is indicated by the dashed yellow line.

Appendix UNI – Coating Uniformity Study Results



Schematic of vertical fixture with qty(6) 440A samples loaded, position 1 (lowest) through position 6 (highest)

Appendix UNI – Coating Uniformity Study Results

Vertical Thickness Distribution Results

Angular Position →	-90deg (normal)	0deg (normal)	+45deg*	-45deg**	0deg*** (normal)	+90deg	0deg (normal)
Coating →	Cr-CrN (Dep1)	Cr-CrN (Dep2)	TiCr-TiCrN (Dep1)	TiCr-TiCrN (Dep2)	TiCr-TiCrN (Dep2)	CrC (Dep1)	CrC (Dep2)
Thickness [µm] Position 1	2.93	4.45	3.57	4.02	n/a	2.13	4.22
Thickness [µm] Position 2	3.38	5.84	4.23	5.13	n/a	2.84	5.47
Thickness [µm] Position 3	3.62	6.65	5.07	5.97	5.65	3.51	5.70
Thickness [µm] Position 4	3.28	6.67	5.44	6.01	5.82	2.54	5.56
Thickness [µm] Position 5	2.68	5.70	4.97	6.07	n/a	2.42	5.33
Thickness [µm] Position 6	2.26	4.14	3.67	4.74	n/a	1.91	4.03
% Change in Thickness Versus 0deg (normal) Orientation (average of position #3 and #4)	48% decrease	-	8% decrease	4.5% increase	-	46% decrease	-
Nominal Thickness [µm]	2.94	5.4	4.51	5.05	n/a	2.71	4.87
Uniformity Over ~13mm Deposition Zone	+/-23%	+/-23%	+/-21%	+/-20%	n/a	+/-30%	+/-17%

* +45deg orientation results in samples facing towards Cr target and away from Ti target

** -45deg orientation results in samples facing towards Ti target and away from Cr target

*** 0deg data for TiCr-TiCrN coating taking from thickness measurements on P675 samples located in positions 3 and 4.

- Results indicate that no decrease in coating thickness occurs for sample orientations up to 45° to the plasma duct. Samples oriented at 90° to the plasma duct show ~50% decrease in coating thickness as compared with normally oriented samples.
- The results indicate that sample angular orientation has no effect on vertical uniformity (thickness distribution); all orientations show approximately +/-20% uniformity over a 13mm (5in) vertical coating zone (maximum thickness being in the center of this zone with the distribution being roughly Gaussian)(+90deg CrC uniformity is likely high due to an error in thickness measurement for position 3)

Appendix UNI – Coating Uniformity Study Results

Rockwell Adhesion (HF rating) Results

- Rockwell 1470N adhesion assessment on 440A samples, HF1 (best) to HF6 (worst) scale
- Comparison can only be made between like coatings deposited at different angular orientations

Angular Position →	-90deg (normal)	0deg (normal)	+45deg*	-45deg**	0deg (normal)	+90deg	0deg (normal)
Coating →	Cr-CrN (Dep1)	Cr-CrN (Dep2)	TiCr-TiCrN (Dep1)	TiCr-TiCrN (Dep2)	TiCr-TiCrN (Dep2)	CrC (Dep1)	CrC (Dep2)
Position 1	HF1	HF1	HF1	HF1	HF1	HF3	HF3
Position 2	HF1	HF1	HF1	HF1	HF1	HF3	HF3
Position 3	HF1	HF1	HF1	HF3	HF1	HF3	HF3
Position 4	HF1	HF1	HF1	HF3	HF1	HF3	HF3
Position 5	HF1	HF1	HF1	HF3	HF1	HF3	HF3
Position 6	HF1	HF1	HF1	HF1	HF1	HF3	HF3

* +45deg orientation results in samples facing towards Cr target and away from Ti target

** -45deg orientation results in samples facing towards Ti target and away from Cr target

- Overall the results indicate that sample orientation angles over the range of -90deg to +90deg have no detrimental effect on coating adhesion.
- Cr-CrN coatings deposited at -90deg orientation show the same adhesion as Cr-CrN coatings deposited on samples with normal orientation.
- CrC coatings deposited at +90deg orientation show the same adhesion as CrC deposited on samples with normal orientation.
- TiCr-TiCrN coatings deposited at +45deg orientation show the same adhesion as TiCr-TiCrN coatings deposited on samples with normal orientation.
- TiCr-TiCrN coatings deposited at -45deg orientation show a small decrease in adhesion in positions 3, 4, and 5. This is thought to be the result of a preferential exposure to the Ti target plasma flow (i.e. higher Ti/Cr ratio). This is a combined effect resulting from sample angular orientation and the use of opposing targets of different composition (Ti and Cr) in the LAFAD source. Deposition from two composite Ti/Cr targets rather than a Ti and Cr target would be expected to remedy any dependence of coating properties on angular orientation.

Appendix UNI – Coating Uniformity Study Results

Coating Hardness and Elastic Modulus Results

- Hardness and Modulus measurements made on 440A samples in positions 3 and 4 (test protocol can be reviewed in Appendix H-E)
- Comparison can only be made between like coatings deposited at different angular orientations

Angular Position →	-90deg (normal)	0deg (normal)	+45deg*	-45deg**	0deg*** (normal)	+90deg	0deg (normal)
Coating →	Cr-CrN (Dep1)	Cr-CrN (Dep2)	TiCr-TiCrN (Dep1)	TiCr-TiCrN (Dep2)	TiCr-TiCrN (Dep2)	CrC (Dep1)	CrC (Dep2)
Hardness, Modulus [GPa]							
Position 3	H = 28.5 E = 354	H = 25.5 E = 315	H = 36.3 E = 432	H = 34.3 E = 416	H = 35.4 E = 415	H = 29.6 E = 400	H = 30.0 E = 422
Hardness, Modulus [GPa]	H = 27.3 E = 334	H = 25.7 E = 325	H = 34.3 E = 410	H = 36.3 E = 436	H = 34.8 E = 417	H = 30.1 E = 404	H = 31.8 E = 435

* +45deg orientation results in samples facing towards Cr target and away from Ti target

** -45deg orientation results in samples facing towards Ti target and away from Cr target

*** 0deg data for TiCr-TiCrN coating taking from thickness measurements on P675 samples located in positions 3 and 4.

- Hardness and modulus for TiCr-TiCrN coatings deposited at -45deg, +45deg, and 0deg(normal) orientation angles all show effectively the same hardness (when measurement error and deviation are taken into account)
- Hardness and modulus for Cr-CrN coatings deposited at -90deg and 0deg(normal) orientation angles show a small increase in hardness and modulus for the -90deg facing angle. The increase in hardness is likely due to a decrease in bi-layer thickness by ~50% (although bilayer thickness ratio and number of bi-layers remains the same, the decrease in deposition rate proportionally decreases the bilayer thickness)
- Hardness and modulus for CrC coatings deposited at +90deg and 0deg(normal) orientation angles all show effectively the same hardness (when measurement error and deviation are taken into account)

Appendix UNI – Coating Uniformity Study Results

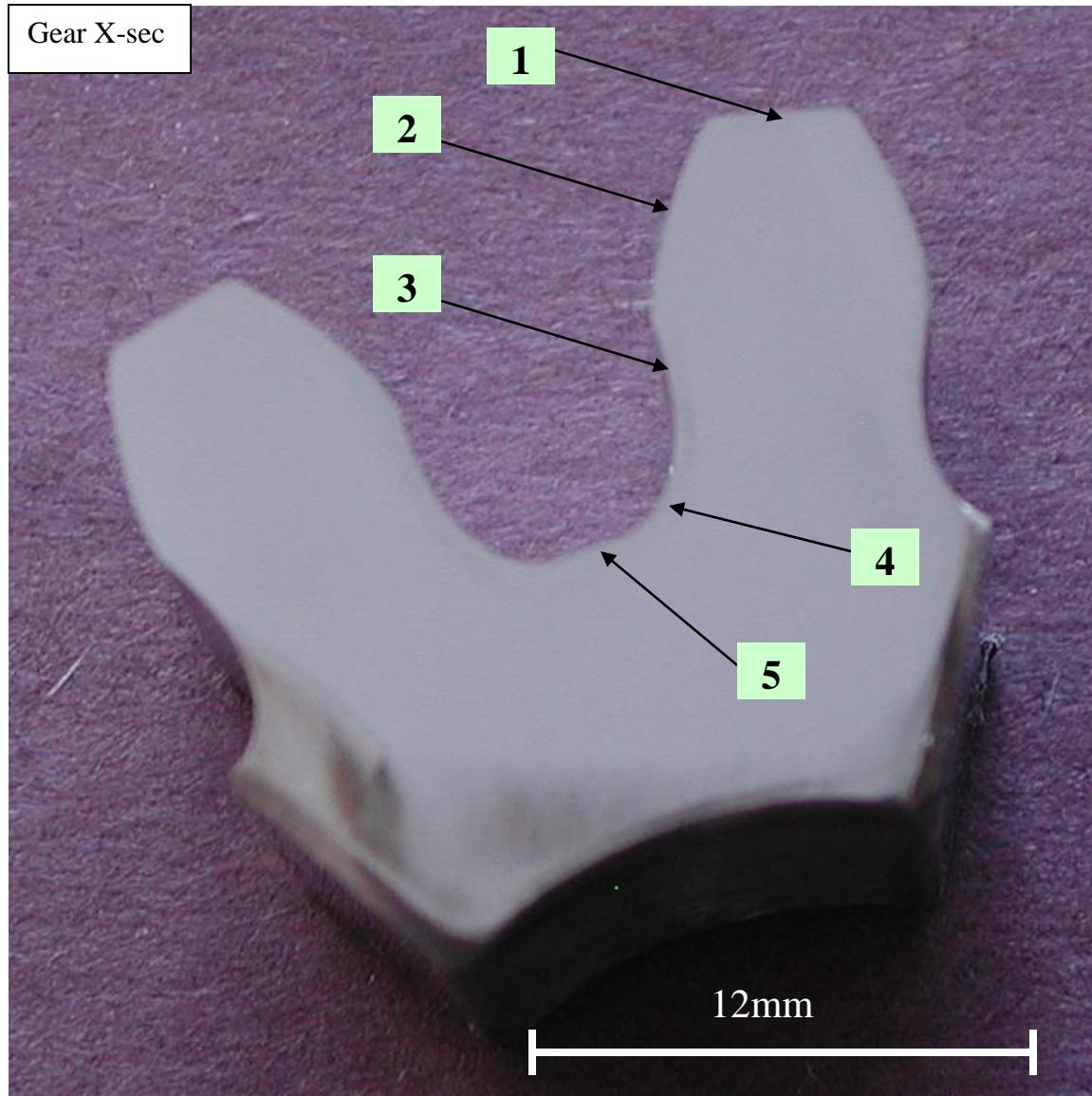
Coating Composition Uniformity Results

- Coating composition (atomic %) was measured by energy dispersive x-ray spectroscopy (EDS or EDX). Accurate quantification with this technique is difficult with light elements such as N, C, and O. For this reason XPS techniques were used for actual coating composition calculation and these results are reported in appendix XPS. Even though the absolute quantification of coating composition is not accurate for EDX measurements, relative comparisons can still be confidently made to assess uniformity of composition between samples with different orientation angles. Relative comparisons can also be made to assess the repeatability of identical coating formulations produced in different deposition runs.
- Coating composition (atomic %) is reported as an average of 2 EDX measurements per samples over ~3-5samples measured per coating deposition. A (-) entry in the table denotes that the element was not part of the quantification. It is likely ~2-4% of C and O exist in all coatings due to imperfect vacuum conditions; Ti and N are not present if not measured.

Coating	Orientation	Atomic % Concentration				
		Ti	Cr	N	C	O
TiCr-TiCrN (Dep1)	+0deg (normal)	51.0	21.6	27.4	-	-
TiCr-TiCrN (Dep2)	+0deg (normal)	50.7	24.8	24.5	-	-
TiCr-TiCrN (Dep1)	+45deg (towards Cr target)	47.6	29.6	22.8	-	-
TiCr-TiCrN (Dep2)	-45deg (towards Ti target)	56.8	20.0	23.2	-	-
Cr-CrN (Dep1)	+0deg (normal)	-	82.5	17.5	-	-
Cr-CrN (Dep2)	+0deg (normal)	-	82.4	17.6	-	-
CrC (Dep1)	+0deg (normal)	-	70.2	-	23.7	6.0
CrC (Dep2)	+0deg (normal)	-	71.9	-	21.5	6.6
CrC (Dep1)	+90deg		68.9		26.0	5.1

- The results show that coating composition repeatability is excellent between separate deposition runs (Dep1 and Dep2) for all coating types; TiCr-TiCrN, Cr-CrN, and CrC.
- Coating composition is consistent for CrC coatings deposited at +90deg and +0deg (normal) orientations, indicating that coating composition is not dependent on sample orientation as long as identical target materials are used in the LAFAD source.
- For the TiCr-TiCrN coating sample orientation angle shows the expected Ti or Cr concentration increase depending on the facing angle of the samples. This data supports the increase in coating thickness observed for the -45deg orientation since the Ti erosion rate is higher than Cr, and also supports the reduction in adhesion for the -45deg orientation since it is known that a higher Ti/Cr ratio results in reduction in adhesion. Since the non-uniformity in TiCr-TiCrN coating composition is based on the use of a Ti and a Cr target in the LAFAD source it can be anticipated that uniformity would be achieved independent of sample orientation angle if two composite Ti/Cr targets were used instead.

Appendix UNI – Coating Uniformity Study Results



Coating Thickness Uniformity Assessment

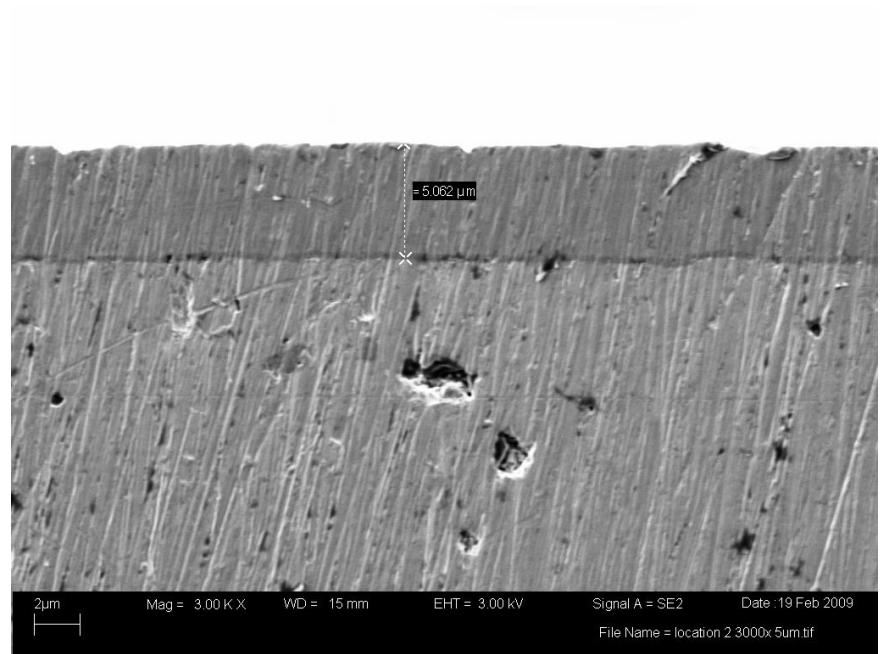
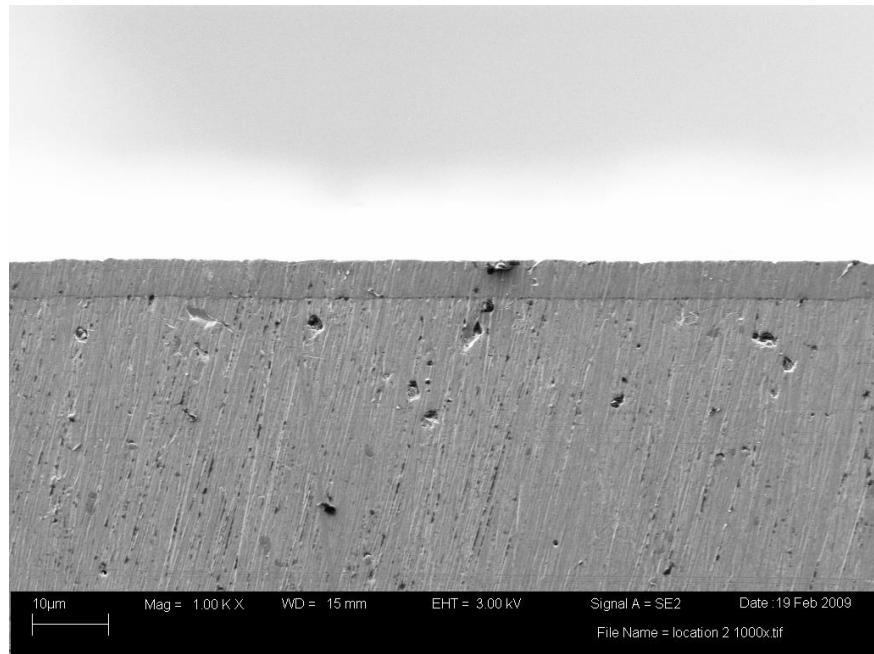
- Gear cross-section
- CrC coating used in this example
- Thickness measurement locations indicated on figure
- Gear surface facing angles are measured in the same manner as $\frac{3}{4}$ "dia 440A samples
- Coating thickness measured by SEM
- Normalized thickness referenced from Location 1

Location	Facing Angle	Coating Thickness	Normalized Thickness
1	0°	$5.0\mu\text{m}$	1
2	$+62^\circ$	$4.1\mu\text{m}$	0.82
3	$+100^\circ$	$2.5\mu\text{m}$	0.5
4	$+25^\circ$	$3.8\mu\text{m}$	0.76
5	0°	$3.7\mu\text{m}$	0.74

Discussion:

The results on the gear x-sec for locations 1, 2, and 3 correlate with the results from the $\frac{3}{4}$ "dia samples; i.e. both datasets show similar decrease in thickness for facing angles up to $\sim\pm 90^\circ$. A 25% decrease in thickness was measured for Locations 4 and 5 even though the facing angles are less than 45° . While the projected area of the trench is the same as a 0° flat facing surface the total surface area to be covered is $\sim 3x$ the projected area, therefore a 25% decrease is a good result.

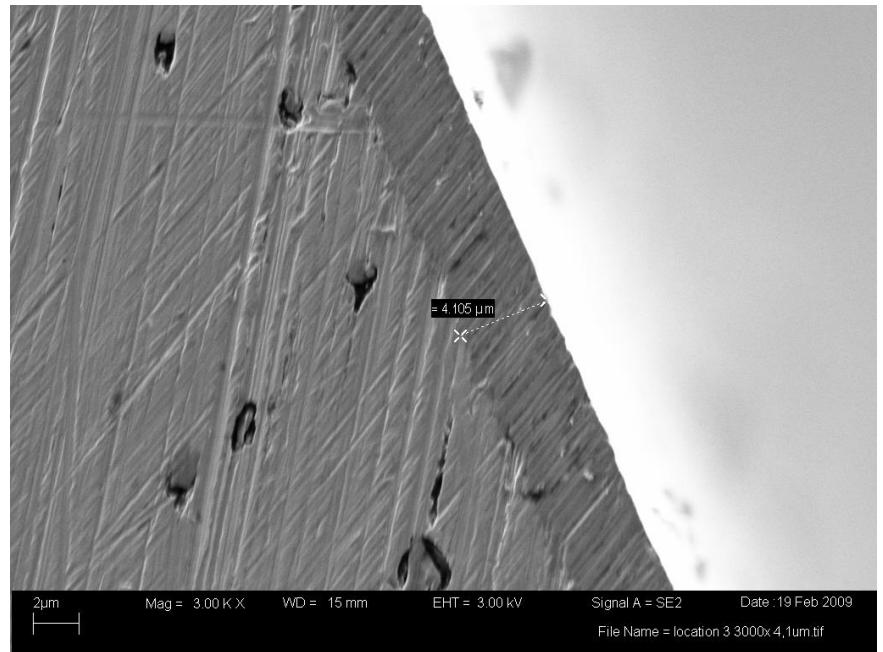
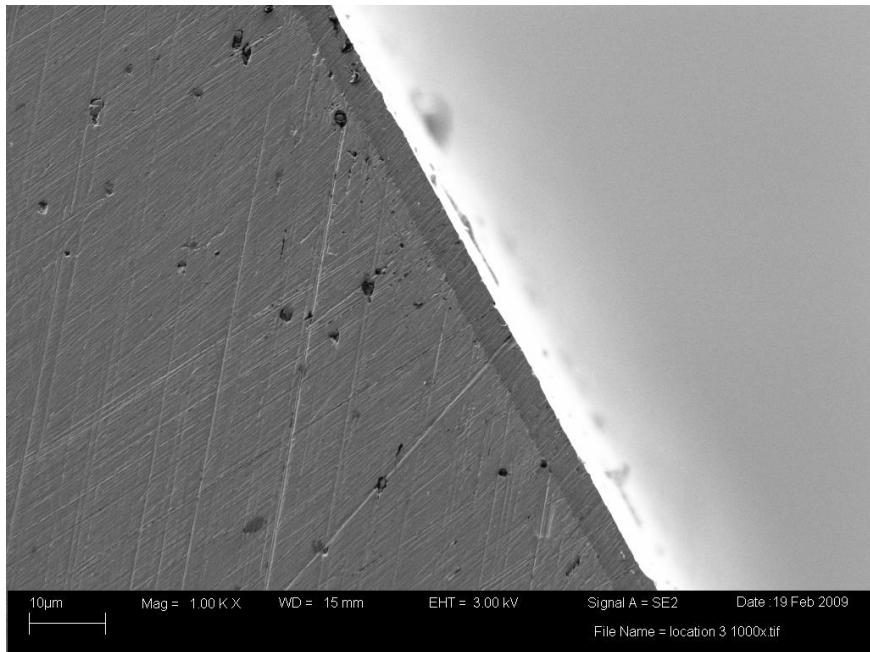
Appendix UNI – Coating Uniformity Study Results



Gear X-sec Location 1 (left image at 100x, right image at 3000x)

0° facing angle, CrC = 5.0µm

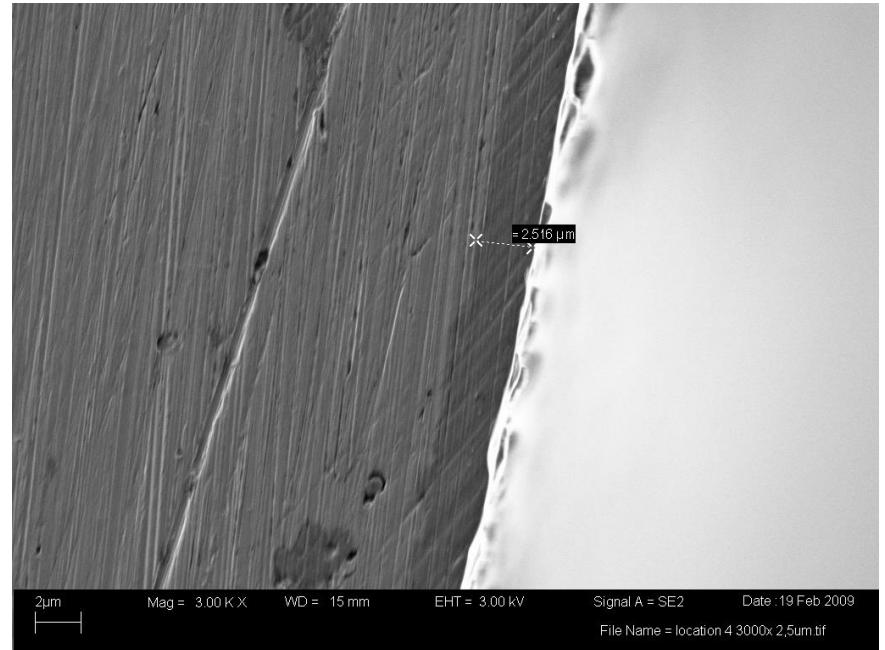
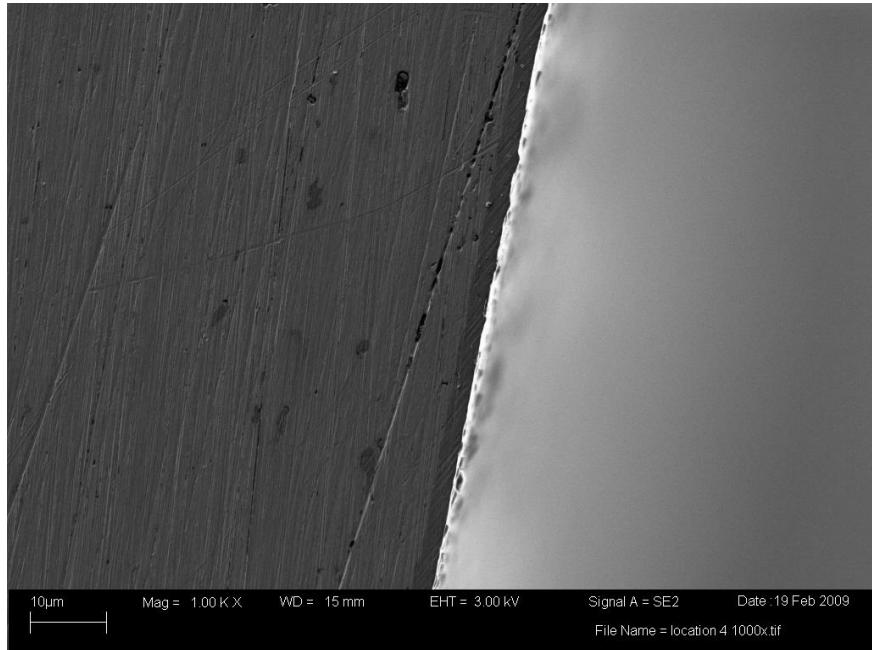
Appendix UNI – Coating Uniformity Study Results



Gear X-sec Location 2 (left image at 1000x, right image at 3000x)

+62° facing angle, CrC = 4.1µm

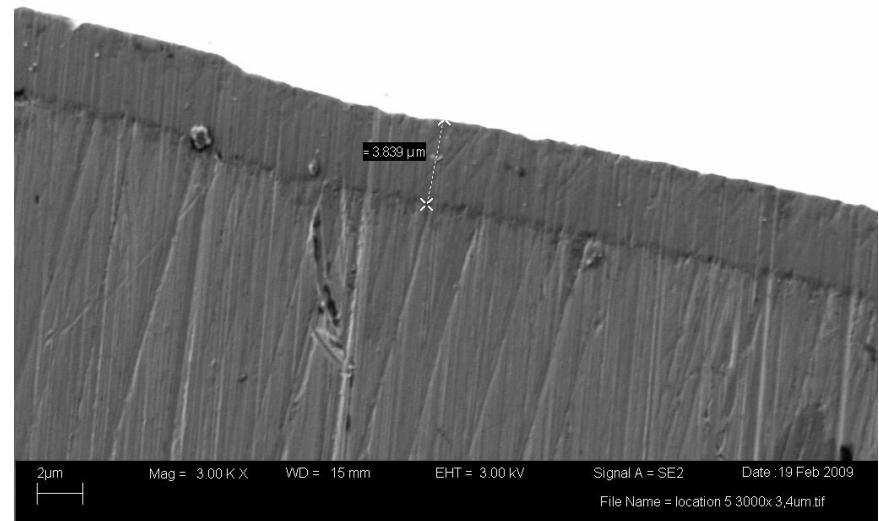
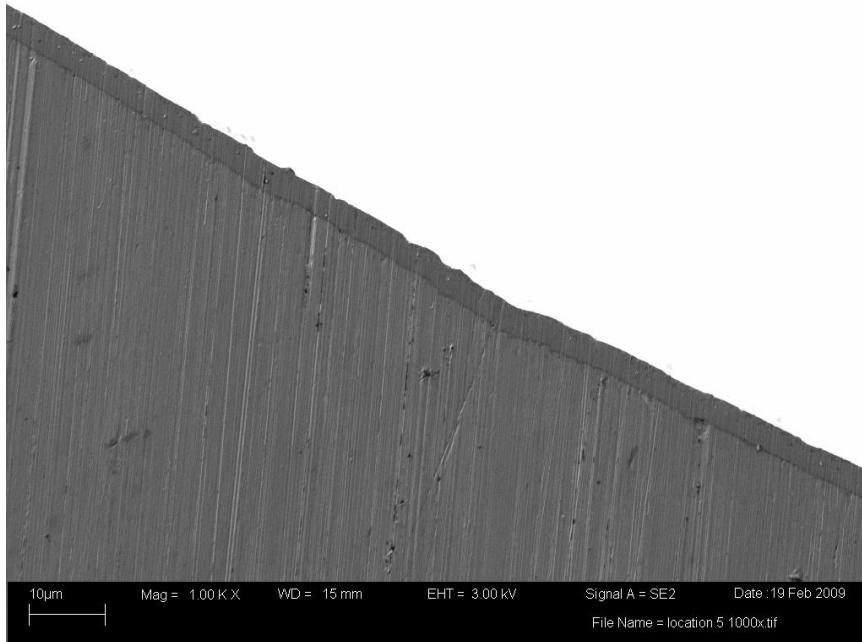
Appendix UNI – Coating Uniformity Study Results



Gear X-sec Location 3 (left image at 1000x, right image at 3000x)

 $+100^\circ$ facing angle, CrC = 2.5µm

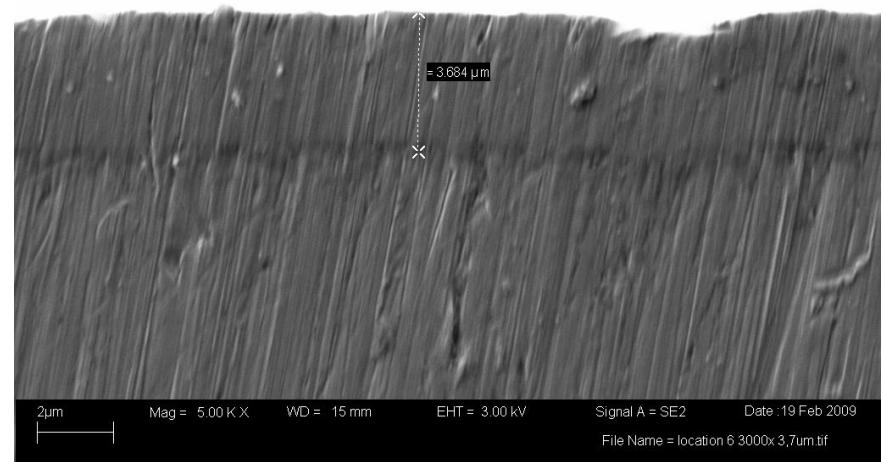
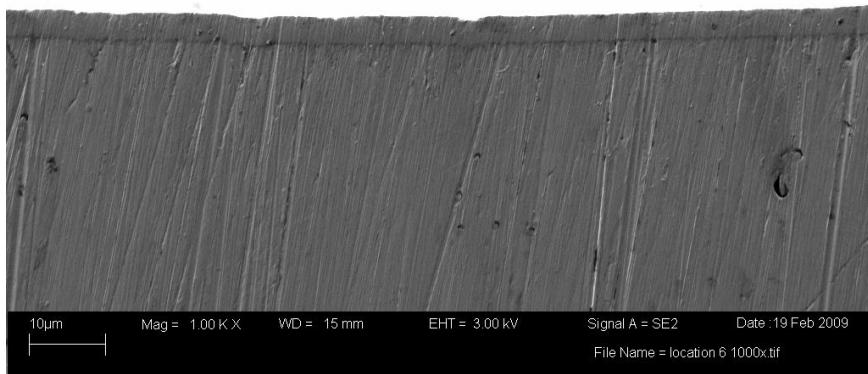
Appendix UNI – Coating Uniformity Study Results



Gear X-sec Location 4 (left image at 1000x, right image at 3000x)

+25° facing angle, CrC = 3.8µm

Appendix UNI – Coating Uniformity Study Results



Gear X-sec Location 5 (left image at 1000x, right image at 3000x)

0° facing angle, CrC = 3.7µm

Appendix WLC – Gear Simulation Testing: Wedeven Load Capacity (LC) Results

Load Capacity Testing Method and Analysis Overview

- 1) The Load Capacity (LC) testing method was designed and conducted by Wedeven Associates (www.wedeven.com). Wedeven Associates was subcontracted for this effort to perform all testing and data collection. Analysis was conducted by Wedeven Associates and Arcomac Surface Engineering. Some of the included text for testing description has been provided courtesy of Wedeven Associates.
- 2) The original purpose of this test method is to evaluate oils according to the Ryder Gear Test Method, with enhanced sensitivity for lower than average lubricating performance. Additionally the method has been used to evaluate material/oil compatibility and as a means to evaluate performance improvements based on surface morphology (roughness) for specific material/oil combinations. In the present evaluation Royco 555 oil is used exclusively and the scuffing performance of Pyrowear 675 and TiCr-TiCrN, Cr-CrN, and CrC coatings are evaluated with contact pair material and surface finish as the primary variables.
- 3) Micro-scuffing is generally associated with surface damage at low load stages where contact stresses are too low to cause “macro” scuffing. Scuffing, or “macro-scuffing”, is associated with the complete loss of surface integrity. Scuffing involves gross failure of near-surface material, in addition to surface roughness features. When traction (friction) is measured, micro-scuffing is generally detected by a rapid decline in traction coefficient. The decline in traction coefficient is associated with the removal of surface roughness features. While this action actually restores some of the EHD fluid film separation between the surfaces, the rapid removal of surface features by plastic flow and rapid polishing wear reflects a failure of the oil to provide adequate surface films for boundary lubrication. In contrast, macro-scuffing is associated with a sudden increase in traction coefficient resulting from massive adhesion and plastic flow of near surface material. A sudden and massive scuffing failure requires high contact stresses in the presence of high sliding velocities.
- 4) The load capacity test protocol is conducted with a WAM test facility. The test machine controls specimen position, contact load and motions of a single contact in space. A computerized run file controls load and contact kinematics between the specimens. Specimen temperatures are recorded with trailing thermocouples. Load exponentially increases from 1.8 kg (4 lbs) to 63.6 kg (140 lbs) in 30 stages (0.7GPa to 2.4GPa). Test duration is until a macro-scuff event occurs, or test suspension (30 stages = 30 minutes). Failure criteria; macro-scuff (test stop) defined by loss of surface integrity and sudden increase in traction, micro-scuff defined by rapid decline in traction coefficient. Performance is judged by the load at which failure occurs. Specimen temperature is dictated by frictional heating and surface temperatures increase with load stage from ambient to ~200 °C. Oil supply

Appendix WLC – Gear Simulation Testing: Wedeven Load Capacity (LC) Results

is computer controlled by a peristaltic pump at approximately 1 drop/sec and oil flow rate is selected for adequate lubrication without significant cooling.

The entraining velocity (U_e) and sliding velocity (U_s) are defined below:

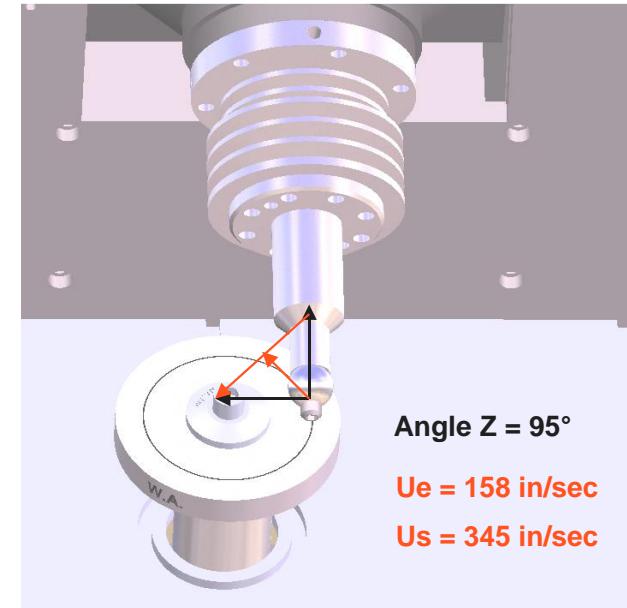
$$U_e = \frac{1}{2}(U_b + U_d)$$

$$U_s = (U_b - U_d)$$

U_b = surface velocity vector of the ball at the contact point

U_d = surface velocity vector of the disc at the contact point

The entraining velocity (U_e) and sliding velocity (U_s) are key parameters that control the degree of surface separation and the rate of surface tangential shear that the oil must accommodate. With the parameters selected, the initiation of a load capacity test is similar to the Ryder Gear Test in that there is generally little or no evidence of surface damage during the first load stage.



A test plot includes the contact load, ball and disc temperatures and traction coefficient. Typical traction coefficients during the first few load stages are on the order of 0.03. The test conditions during the first few load stages provide nearly full-film EHD lubrication. Ball and disc temperatures increase with load stage due to frictional heating. As load and temperature increase, the ratio of EHD film thickness to surface roughness decreases. An increasing traction coefficient reflects a greater degree of asperity interaction within the contact. The rate of rise in traction coefficient reflects the ability of the oil to form surface films at asperity sites for wear resistance. A decreasing traction coefficient reflects polishing wear. A sudden drop in traction is associated with a rapid loss of surface topographical features (micro-scuffing). Micro-scuffing events, represented by momentary reductions in traction coefficient, reflect marginal oil chemistry to sustain surface films for protection against local adhesion and wear of surface features. A macro-scuffing event is easily detected by a sudden increase in traction coefficient.

Appendix WLC – Gear Simulation Testing: Wedeven Load Capacity (LC) Results

LC Test Parameters and Matrix

- Load Capacity test parameters set to exceed the worst case gear sliding velocity mesh condition for F-35B LiftFan gears which is 304in/sec. The LC test parameters match historical testing conducted by Rolls Royce on gear materials, including parallel testing conducted on uncoated ground finish and super-finished P675 samples (see matrix below).
 - Ball Velocity = 234in/sec
 - Disc Velocity = 234in/sec
 - Skew Angle = 95°
 - Entrainig Velocity = 158in/sec
 - Sliding Velocity = 345in/sec

Arcomac LC Test Matrix – Fall 2008

Test #	Ball ID	Ball Coating	Ball RMS [uinch]	Disc ID	Disc Coating	Disc RMS [uinch]	Oil Type
Test #4a	WB-4	TiCr-TiCrN (Run 1)	~14	WD 2-C	Cr-CrN (Run 1)	6	Royco 555 Grade 5
Test #4b	WB-4	TiCr-TiCrN (Run 1)	~14	WD 2-C	Cr-CrN (Run 1)	6	Royco 555 Grade 5
Test #5a	WB-24	TiCr-TiCrN (Run 2)	~14	WD 5-C	CrC (Run 2)	6	Royco 555 Grade 5
Test #5b	WB-24	TiCr-TiCrN (Run 2)	~14	WD 5-C	CrC (Run 2)	6	Royco 555 Grade 5
Test #6a	WB-10	TiCr-TiCrN (Run 1)	~14	WD 8-C	Cr-CrN (Run 2)	6	Royco 555 Grade 5
Test #6b	WB-10	TiCr-TiCrN (Run 1)	~14	WD 8-C	Cr-CrN (Run 2)	6	Royco 555 Grade 5
Test #7a	WB-1	TiCr-TiCrN (Run 2)	~14	WD 6-C	CrC (Run 1)	6	Royco 555 Grade 5
Test #7b	WB-1	TiCr-TiCrN (Run 2)	~14	WD 6-C	CrC (Run 1)	6	Royco 555 Grade 5

Rolls Royce LC Test Matrix – Fall 2008 (baseline P675 characterization)

Test #	Ball ID	Ball Coating	Ball RMS [uinch]	Disc ID	Disc Coating	Disc RMS [uinch]	Oil Type
Test #2a	Ground finish	n/a	~10	Ground finish	n/a	~6	Royco 555 Grade 5
Test #2b	Ground finish	n/a	~10	Ground finish	n/a	~6	Royco 555 Grade 5
Test #3a	Super-finished	n/a	~10	Super-finished	n/a	~4	Royco 555 Grade 5
Test #3b	Super-finished	n/a	~10	Super-finished	n/a	~4	Royco 555 Grade 5

Appendix WLC – Gear Simulation Testing: Wedeven Load Capacity (LC) Results

LC Test Method - Results Summary

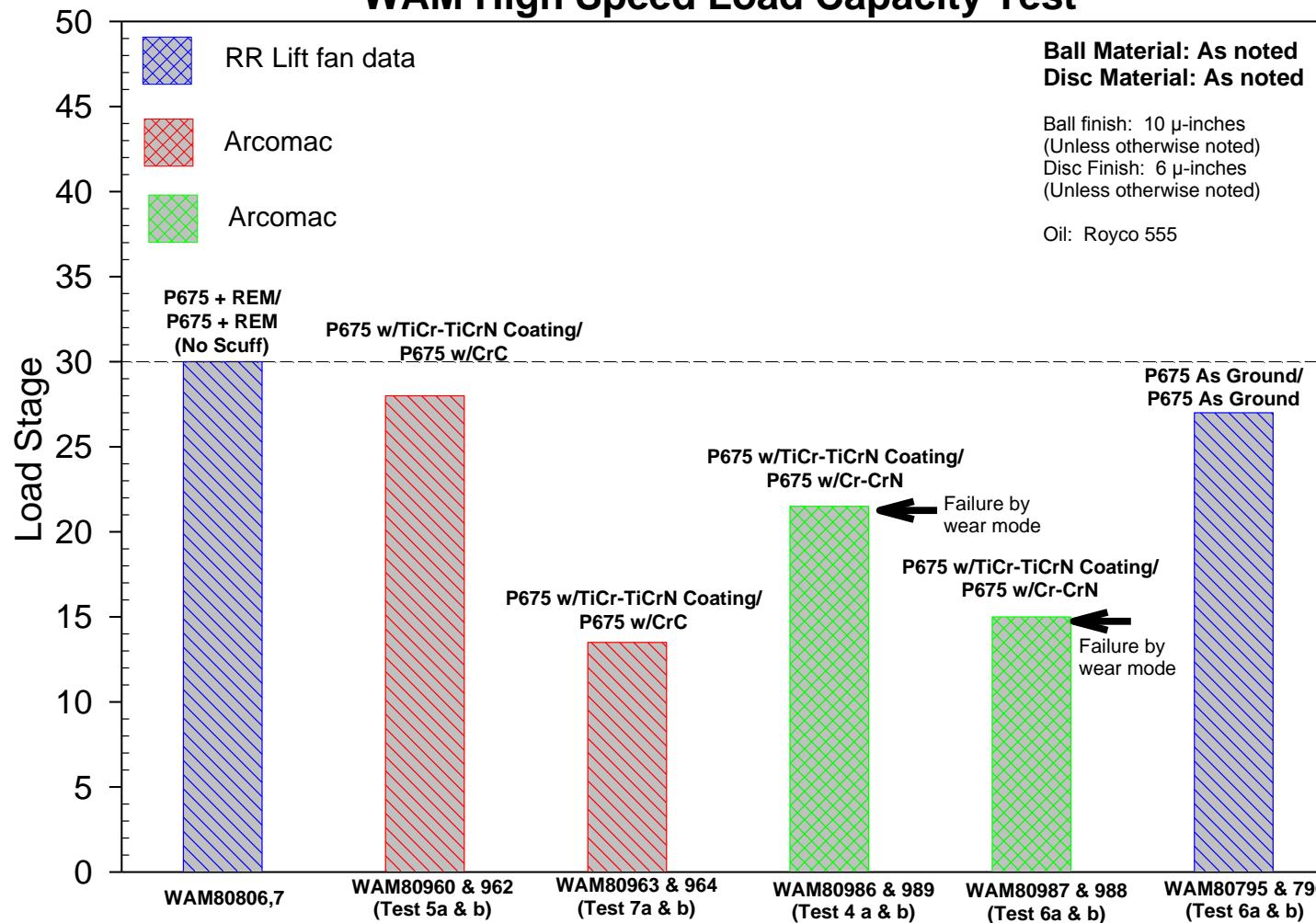
Ball	Disc	Macro-Scuffing Failure @ Load [N]	Macro-Scuffing Failure @ Stress [GPa]
TiCr-TiCrN (Dep1)	Cr-CrN (Dep1)	277	1.84
TiCr-TiCrN (Dep1)	Cr-CrN (Dep2)	168	1.54
TiCr-TiCrN (Dep1)	Cr-CrN (average)	223	1.69
TiCr-TiCrN (Dep2)	CrC (Dep1)	145	1.43
TiCr-TiCrN (Dep2)	CrC (Dep2)	517	2.26
TiCr-TiCrN (Dep2)	CrC (average)	331	1.95
P675 (ground finish)	P675 (ground finish)	468	2.18
P675 (super-finish)	P675 (super-finish)	No failure	No Failure
M50 (ground finish)	M50 (ground finish)	517	2.26
9310 (ground finish)	9310 (ground finish)	315	1.91

Notes

1. These initial results indicate poor repeatability of coating performance. The test matrix size does not allow for determination of the origin of the variance in results; it is hypothesized that the variation is coming from the TiCr-TiCrN ball coating. This hypothesis is predicated on the early 145N load failure of the TiCr-TiCrN ball in contact with the CrC (Dep1) coating which was characterized by isolated cohesive delaminations of the TiCr-TiCrN and no damage to the CrC coating. Given that the data set is very small, more testing would need to be conducted to confirm a problem with coating performance repeatability.
2. The industry performance criterion for 5cst oil is a macro-scuffing failure load greater than 288N (1.86GPa contact stress). Using Royco 555 oil the average macro-scuff load for the Cr-CrN coating falls just under this criteria at 233N, and the CrC exceeds this criteria at 331N. CrC (Dep2) performed very well with a failure load of 517N (2.26GPa) while CrC (Dep1) posted the lowest macro-scuffing failure load in the test group at 145N (1.43GPa) performance repeatability concerns.
3. P675/P675 contact using the standard ground finish produced good results with a macro-scuffing failure load of 468N (2.18GPa). Super-finished P675/P675 contact produced excellent results and did not fail over the load range of the test protocol, the results can be attributed to the reduction in surface asperity sliding contact due to improved surface roughness.

Appendix WLC – Gear Simulation Testing: Wedeven Load Capacity (LC) Results

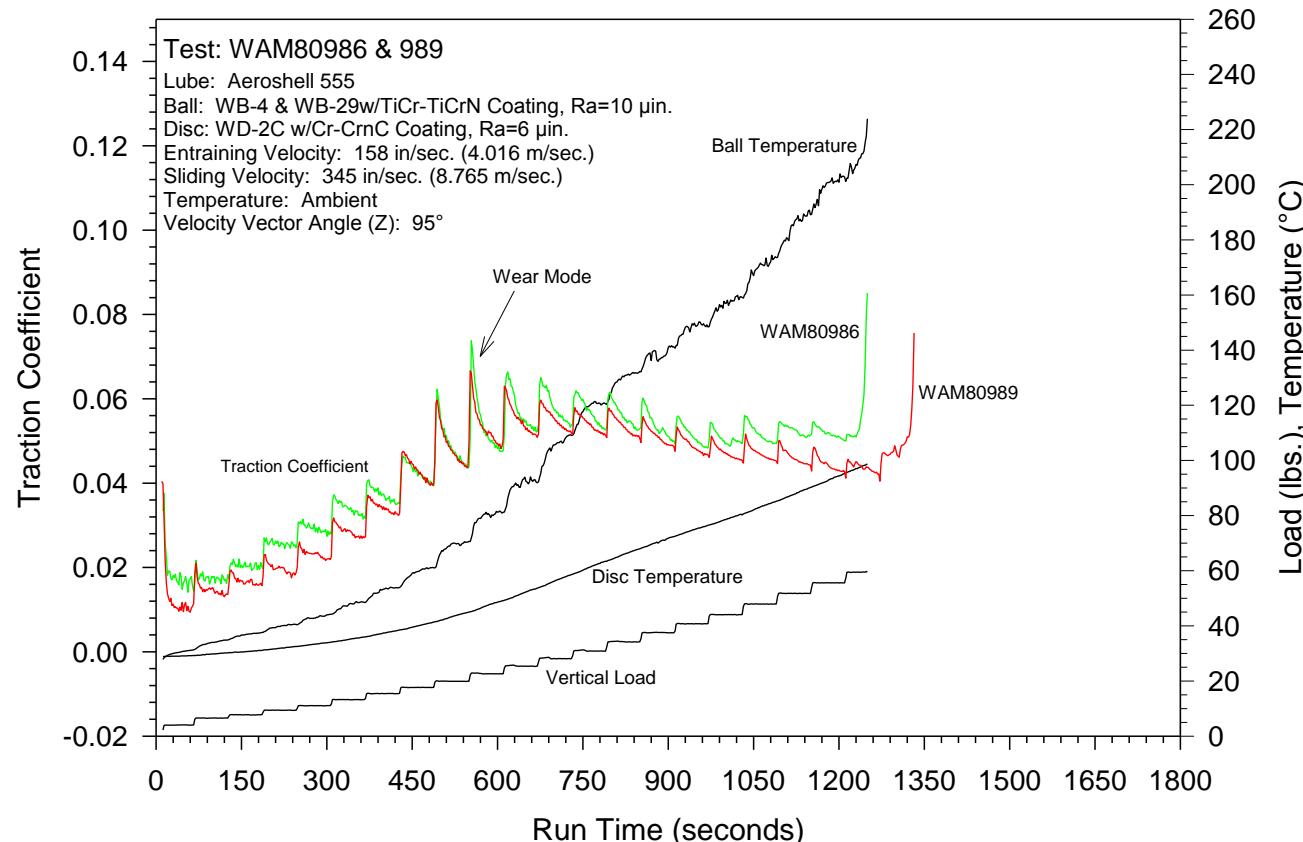
Average Scuffing Load Stage WAM High Speed Load Capacity Test



W/Testing/Arcomac/ARC-02606/LoadCapacity.jnb

Appendix WLC – Gear Simulation Testing: Wedeven Load Capacity (LC) Results

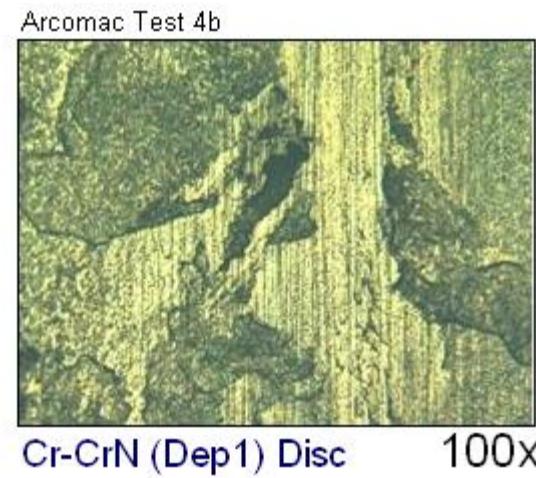
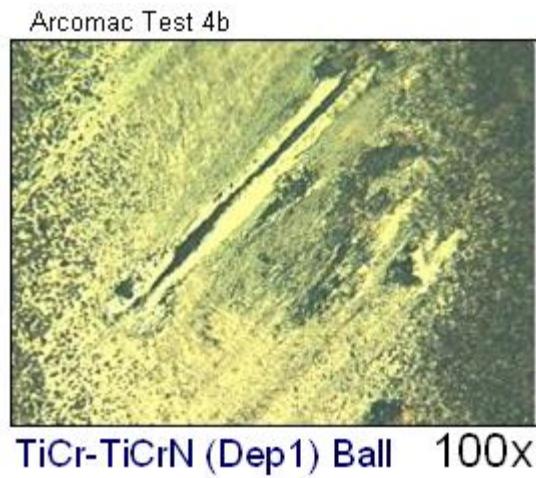
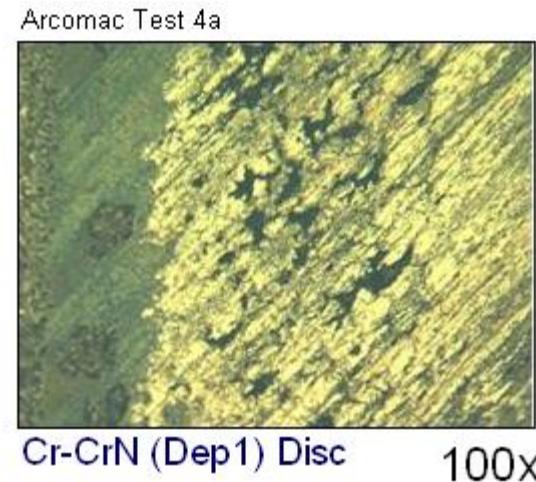
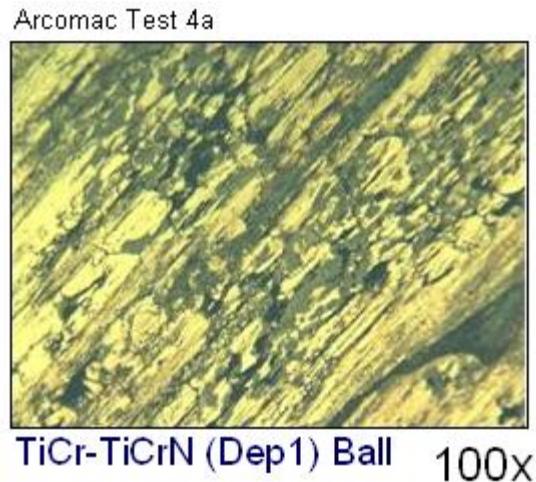
Ball – TiCr-TiCrN (Dep1)
Disc – Cr-CrN (Dep1)



NOTES:

- 1) Test 4a and Test 4b fail at 266N and 288N respectively. The traction on average is higher than uncoated specimens and similar to as-ground specimens. Higher traction for the coated specimens is most likely due to higher roughness compared to uncoated specimens. The “steps” in traction as load changes are attributed to coating run-in wear. Traction step size becomes pronounced and the traction coefficient begins to decrease at 79N, indicating run-in wear is occurring between the coatings which reduces the coating roughness and improves the EHD response.

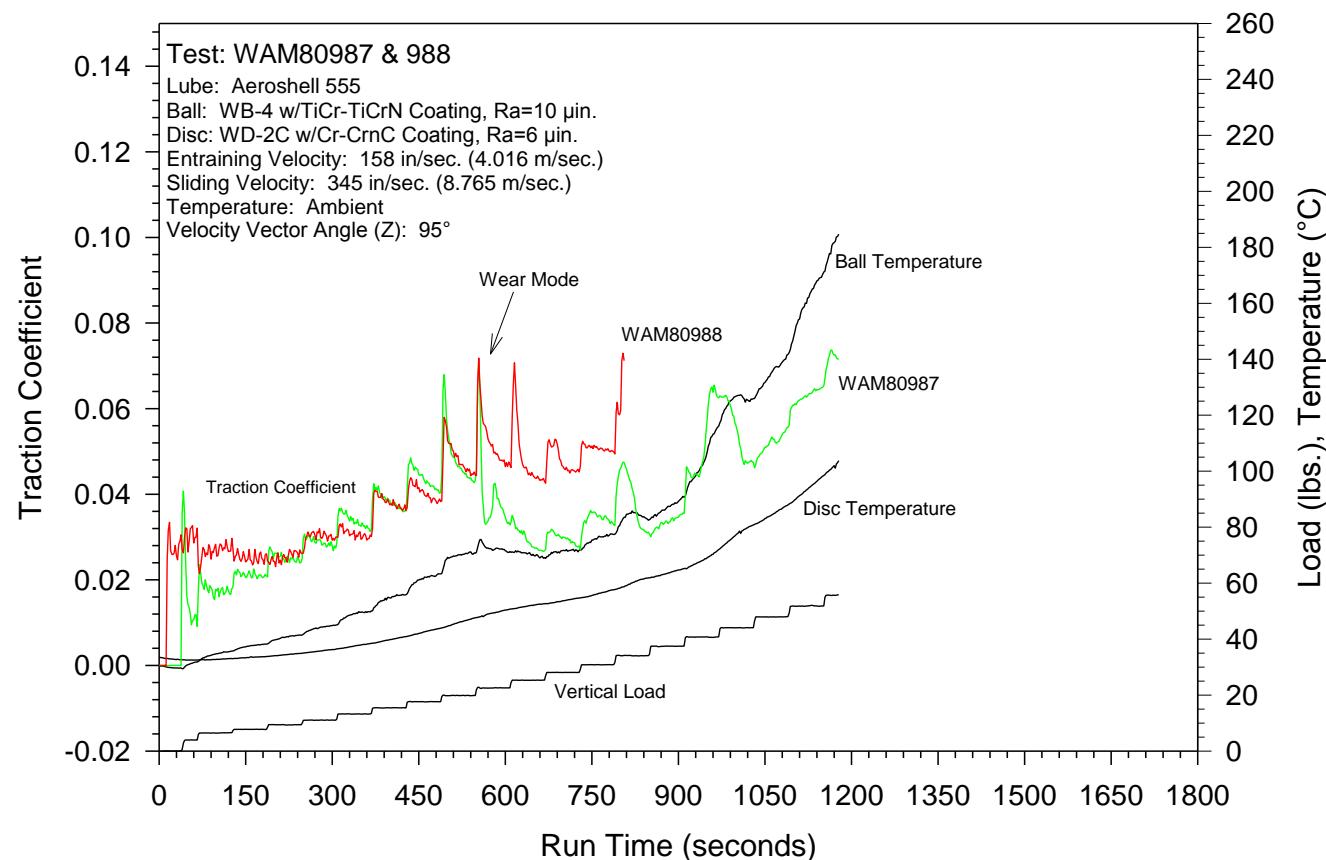
Appendix WLC – Gear Simulation Testing: Wedeven Load Capacity (LC) Results



Macro-scuff failure of the TiCr-TiCrN vs Cr-CrN contact pair for test 4a results in severe damage, the wear profile depth on the Cr-CrN disk is $\sim 9.0\mu\text{m}$ (coating worn through). The track on sample 4b was generally $\sim 0.3\mu\text{m}$ in depth, with isolated cohesive delamination areas around the track, perhaps $\sim 15\%$ of the track area. Both 4a and 4b tests fail at approximately the same load.

Appendix WLC – Gear Simulation Testing: Wedeven Load Capacity (LC) Results

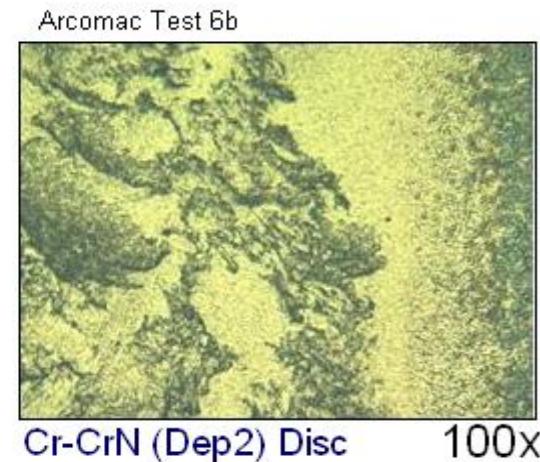
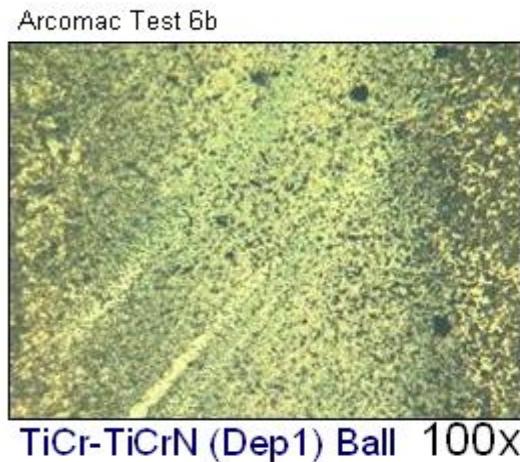
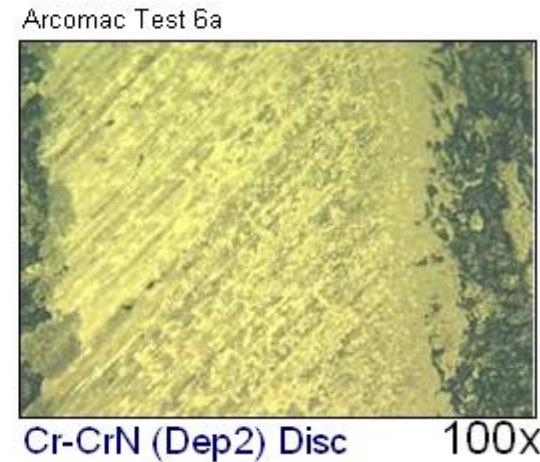
Ball – TiCr-TiCrN (Dep1)
Disc – Cr-CrN (Dep2)



NOTES:

- 1) Test 6a and Test 6b fail at 152N and 182N respectively. The traction on average is higher than uncoated specimens and similar to as-ground specimens. Higher traction for the coated specimens is most likely due to higher roughness compared to uncoated specimens. The “steps” in traction as load changes are attributed to coating run-in wear. Traction step size becomes pronounced and the traction coefficient begins to decrease at 79N, indicating run-in wear is occurring between the coatings which reduces the coating roughness and improves the EHD response.

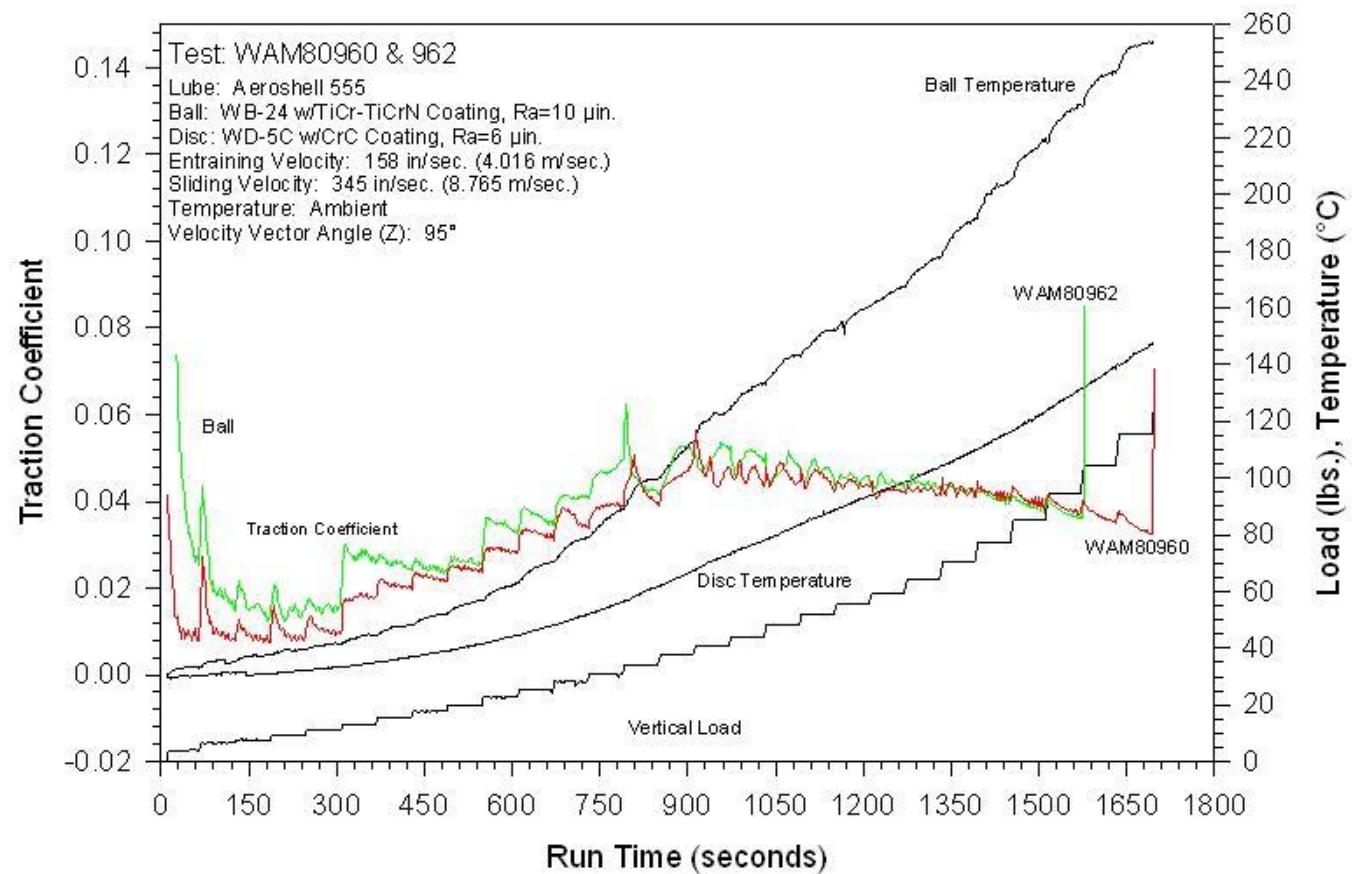
Appendix WLC – Gear Simulation Testing: Wedeven Load Capacity (LC) Results



Macro-scuff failure for test 6a at 184N load results in severe damage to both coatings, wear track depth on the Cr-CrN disc was ~6.0 μ m which equals the coating thickness; it appears that polishing wear may be predominant up to a point where cohesive delamination occurs on the TiCr-TiCrN ball. Test 6b failed at 152N and showed minor wear to the disc (depth ~0.5 μ m) over most of the track with isolated cohesive delamination areas to depths of 3-4 μ m (very similar to test 4b).

Appendix WLC – Gear Simulation Testing: Wedeven Load Capacity (LC) Results

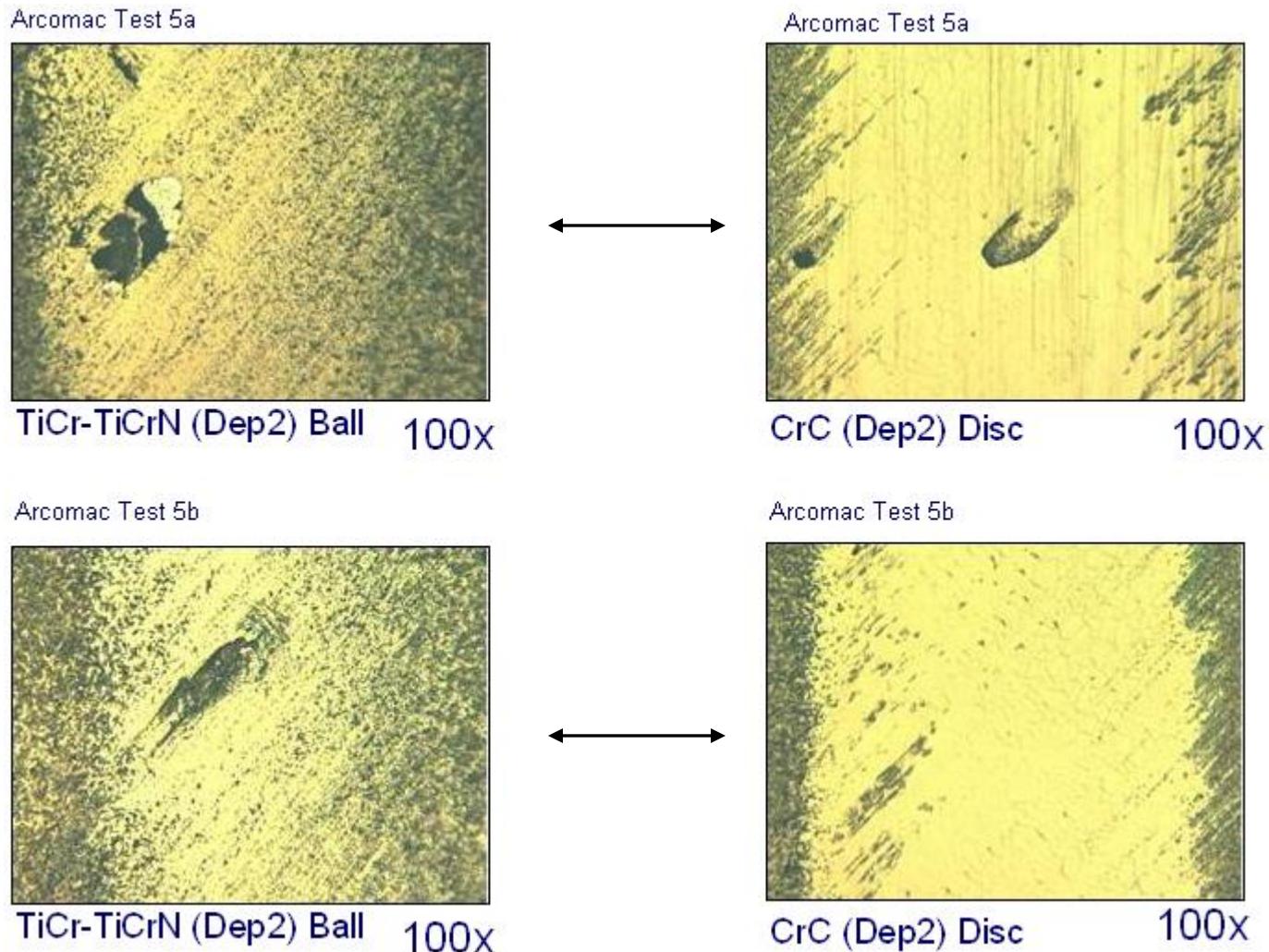
Ball – TiCr-TiCrN (Dep2)
Disc – CrC (Dep2)



NOTES:

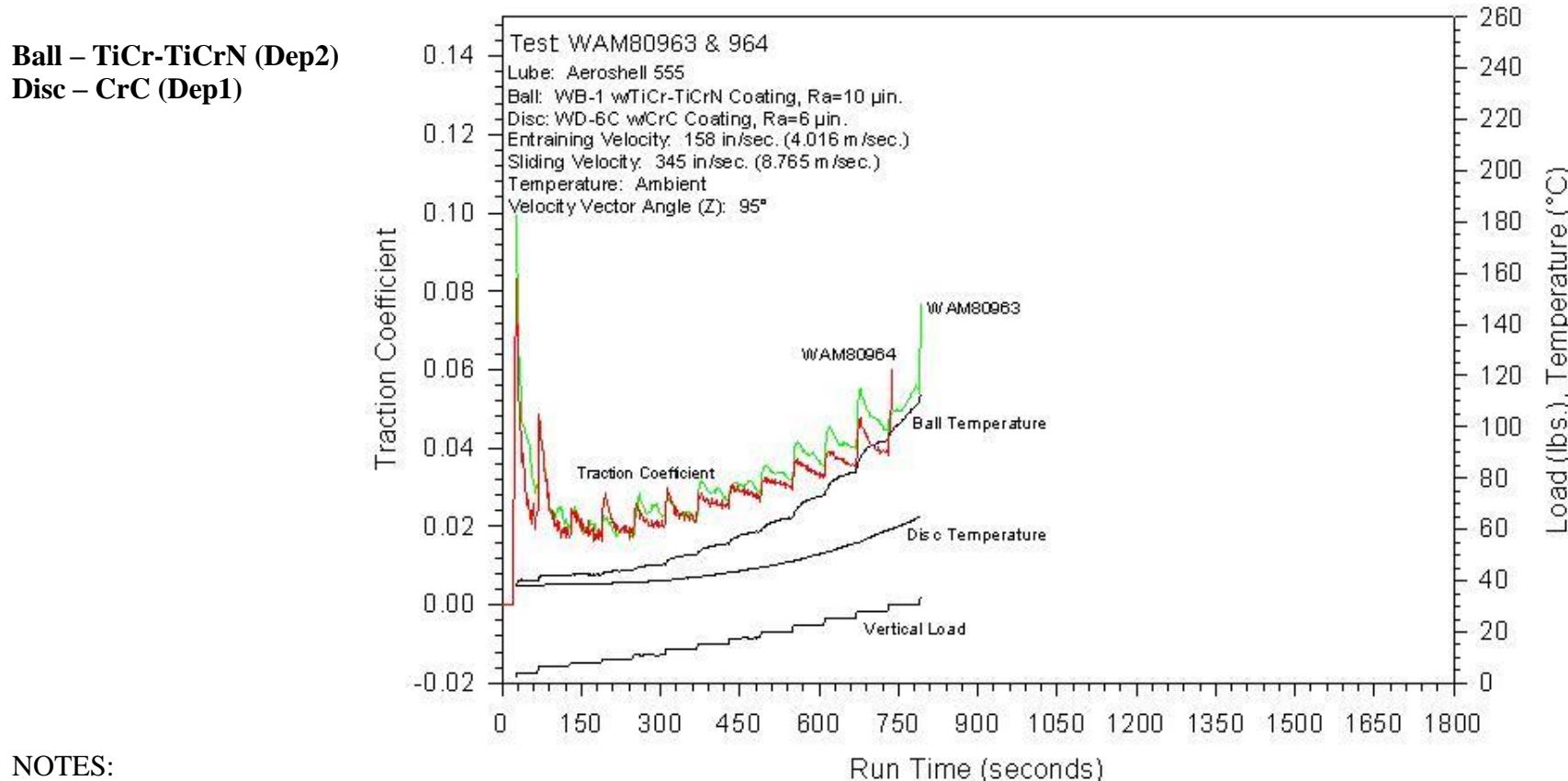
- 2) Test 5a and Test 5b fail at 468N and 571N respectively. The traction on average is higher than uncoated specimens and similar to as-ground specimens. Higher traction for the coated specimens is most likely due to higher roughness compared to uncoated specimens. The “steps” in traction as load changes are attributed to coating run-in wear.
- 3) The coating appears to remain intact; it shows only polishing wear up to the scuffing failure point.
- 4) See optical microscope images of wear tracks on next page.

Appendix WLC – Gear Simulation Testing: Wedeven Load Capacity (LC) Results



CrC and TiCr-TiCrN coatings demonstrate mild polishing wear at the macro-scuff failure point, isolated micro-delaminations on the TiCr-TiCrN ball coating are sufficient to increase traction and result in test termination. CrC disc wear track depth was $\sim 1.2\mu\text{m}$ for tests 5a and 5b (coating thickness $\sim 6\mu\text{m}$).

Appendix WLC – Gear Simulation Testing: Wedeven Load Capacity (LC) Results



NOTES:

- 1) Test 7a and Test 7b fail at 138N and 153N respectively. The traction on average is higher than uncoated specimens and similar to as-ground specimens. Higher traction for the coated specimens is most likely due to higher roughness compared to uncoated specimens. The “steps” in traction as load changes are attributed to coating run-in wear.
- 2) Wear of the CrC and TiCr-TiCrN coatings upon test termination is minor, showing only polishing wear. Isolated micro-cohesive delaminations on the TiCr-TiCrN ball coating resulted in traction increases and early test termination.
- 3) See optical microscope images of wear tracks on next page.

Appendix WLC – Gear Simulation Testing: Wedeven Load Capacity (LC) Results

Arcomac Test 7a



TiCr-TiCrN (Dep2) Ball 100x

Arcomac Test 7a



CrC (Dep1) Disc 100x

Arcomac Test 7b



TiCr-TiCrN (Dep2) Ball 100x

Arcomac Test 7b

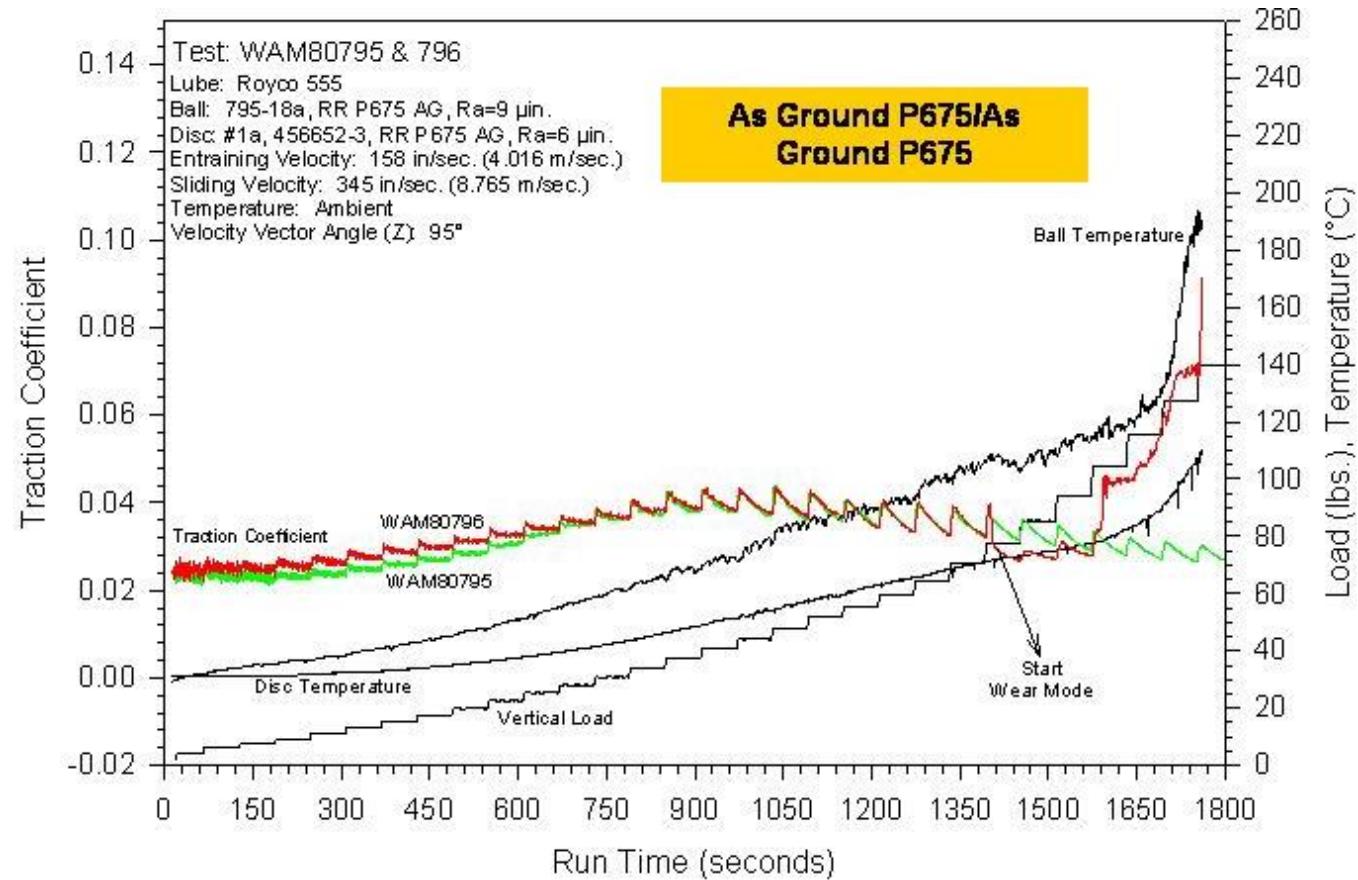


CrC (Dep1) Disc 100x

Wear of the CrC and TiCr-TiCrN coatings upon test termination is generally minor, showing only polishing wear. Isolated micro-cohesive delaminations on the TiCr-TiCrN ball coating resulted in traction increases and early test termination. For both tests the wear track profile depth averaged $\sim 0.3\mu\text{m}$, essentially a minor reduction in the coating surface roughness.

Appendix WLC – Gear Simulation Testing: Wedeven Load Capacity (LC) Results

**Ball – P675 (ground)
Disc – P675 (ground)**

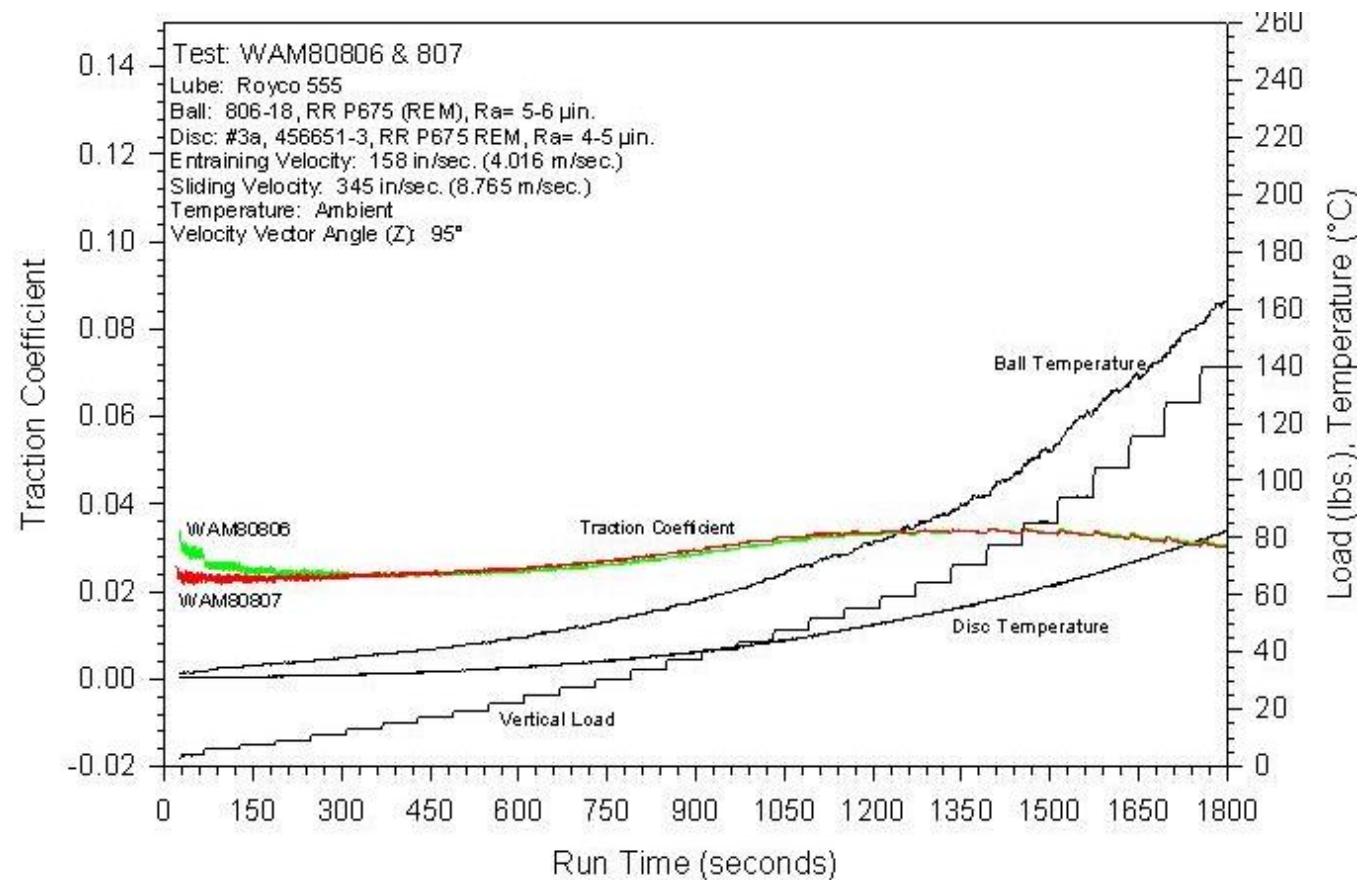


Notes:

- 1) For ground finish P675/P675 contact stage oil film recovery ratcheting is more pronounced than with super-finished P675 indicating more run-in wear due to increased surface roughness of the ground finish. One of two tests has a micro-scuff event at load stage 24 and macro scuff at load stage 29. The second test was run to suspension without failure.

Appendix WLC – Gear Simulation Testing: Wedeven Load Capacity (LC) Results

Ball – P675 (super-finished)
Disc – P675 (super-finished)



Notes:

- 1) The low average surface roughness between the super-finished P675 ball and super-finished P675 disc result in EHD oil conditions until ~load stage 24. This implies no material contact or run-in wear occurs until stage 24. Both test ran to test suspension without failure.

Appendix WLC – Gear Simulation Testing: Wedeven Load Capacity (LC) Results

Wedeven Performance Mapping Method and Analysis Overview

- 1) The Performance Mapping (PM) testing method was designed and conducted by Wedeven Associates (www.wedeven.com). Wedeven Associates was subcontracted for this effort to perform all testing and data collection. Analysis was conducted by Wedeven Associates and Arcomac Surface Engineering. Some of the included text for testing description has been provided courtesy of Wedeven Associates.
- 2) The PM test method is primarily used to evaluate oils over a range of lubrication regimes; full EHD lubrication (no asperity contact), boundary lubrication (asperity contact), and oil film breakdown (significant contact between pairs). Additionally the method has been used to evaluate material/oil compatibility and as a means to evaluate performance improvements based on surface morphology (roughness) for specific material/oil combinations. In the present evaluation Royco 555 oil is used exclusively and the scuffing performance of Pyrowear 675 and TiCr-TiCrN, Cr-CrN, and CrC coatings are evaluated with contact pair material and surface finish as the primary variables.
- 3) The PM test method involves multiple stages where the skew angle is systematically increased from $\sim 30^\circ$ to $\sim 180^\circ$ which causes the sliding velocity to increase and oil entraining velocity to decrease; this results in increased contact between the test pairs and transition from EHD lubrication to boundary lubrication to lubrication break-down. Failure is denoted by a macro-scuff event at a given sliding/entraining velocity stage. Scuffing, or “macro-scuffing”, is associated with the complete loss of surface integrity. Scuffing involves gross failure of near-surface material, in addition to surface roughness features. A sudden and massive scuffing failure requires high contact stresses in the presence of high sliding velocities.
- 4) The PM test protocol is conducted with a WAM test facility. The test machine controls specimen position, contact load and motions of a single contact in space. A computerized run file controls load and contact kinematics between the specimens. Specimen temperatures are recorded with trailing thermocouples. Two test series are run; a “cold scuffing” series in which the sliding/entraining velocities range from $\sim 0.5\text{m/sec}$ to $\sim 9\text{m/sec}$ and $\sim 1.3\text{m/sec}$ to 0m/sec respectively and a “hot scuffing” series in which the sliding/entraining velocities range from $\sim 2.5\text{m/sec}$ to $\sim 25\text{m/sec}$ and $\sim 5\text{m/sec}$ to 0m/sec respectively. A test stage is defined as a sliding/entraining velocity combination which falls within a specific lubrication regime; 14 test stages are performed for the cold-scuffing series and 13 test stages for the hot-scuffing series. Each test stage runs for 10min and test duration is until a macro-scuff event occurs, or test suspension. Successive test stages are conducted at the same track location of the previous stage, in other words wear and damage accumulate until failure. Load is held constant at 344N which imparts a 1.95GPa max contact stress. Failure criteria; macro-scuff (test stop) defined by loss of surface integrity and sudden increase in

Appendix WPM – Gear Simulation Testing: Wedeven Performance Mapping (PM) Results

traction, micro-scuff defined by rapid decline in traction coefficient. Performance is judged by sliding/entraining velocity stage at which failure occurs. Specimen temperature is dictated by frictional heating. Oil supply is computer controlled by a peristaltic pump at approximately 1 drop/sec and oil flow rate is selected for adequate lubrication without significant cooling.

The entraining velocity (U_e) and sliding velocity (U_s) are defined below:

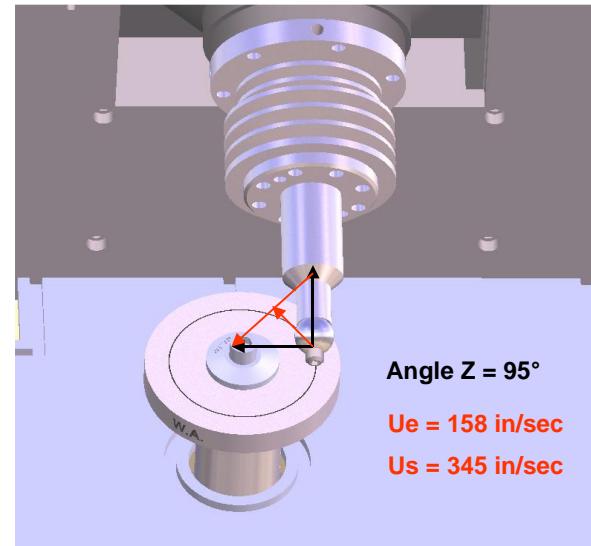
$$U_e = \frac{1}{2}(U_b + U_d)$$

$$U_s = (U_b - U_d)$$

U_b = surface velocity vector of the ball at the contact point

U_d = surface velocity vector of the disc at the contact point

The entraining velocity (U_e) and sliding velocity (U_s) are key parameters that control the degree of surface separation and the rate of surface tangential shear that the oil must accommodate.



A test plot includes the contact load, ball and disc temperatures and traction coefficient. Typical traction coefficients during the first few load stages are on the order of 0.03. The test conditions during the first few load stages provide nearly full-film EHD lubrication. Ball and disc temperatures increase with each stage due to frictional heating. As load and temperature increase, the ratio of EHD film thickness to surface roughness decreases. An increasing traction coefficient reflects a greater degree of asperity interaction within the contact. The rate of rise in traction coefficient reflects the ability of the oil to form surface films at asperity sites for wear resistance. A decreasing traction coefficient reflects polishing wear. A sudden drop in traction is associated with a rapid loss of surface topographical features (micro-scuffing). Micro-scuffing events, represented by momentary reductions in traction coefficient, reflect marginal oil chemistry to sustain surface films for protection against local adhesion and wear of surface features. A macro-scuffing event is easily detected by a sudden increase in traction coefficient.

Appendix WPM – Gear Simulation Testing: Wedeven Performance Mapping (PM) Results

PM Test Parameters and Matrix (Cold Scuffing Series)

14 Stages, Load 344N (1.95 GPa contact stress), Royco 555 oil

Stage	Skew (°)	Ball spd	Disc Spd	Sliding Spd	Ue
		(m/sec)	(m/sec)	(m/sec)	m/sec
1	31	1.21	1.21	0.64	1.17
2	60	1.27	1.27	1.27	1.09
3	87.6	1.38	1.38	1.91	0.99
4	107.95	1.57	1.57	2.54	0.91
5	125.9	1.78	1.78	3.18	0.81
6	138	2.04	2.04	3.81	0.74
7	148	2.31	2.31	4.45	0.64
8	156	2.59	2.59	5.08	0.53
9	161.5	2.90	2.90	5.72	0.46
10	167.5	3.2	3.2	6.35	0.36
11	170.5	3.51	3.51	6.99	0.28
12	174.6	3.81	3.81	7.62	0.12
13	177.5	4.17	4.17	8.26	0.10
14	180	4.45	4.45	8.89	0.00

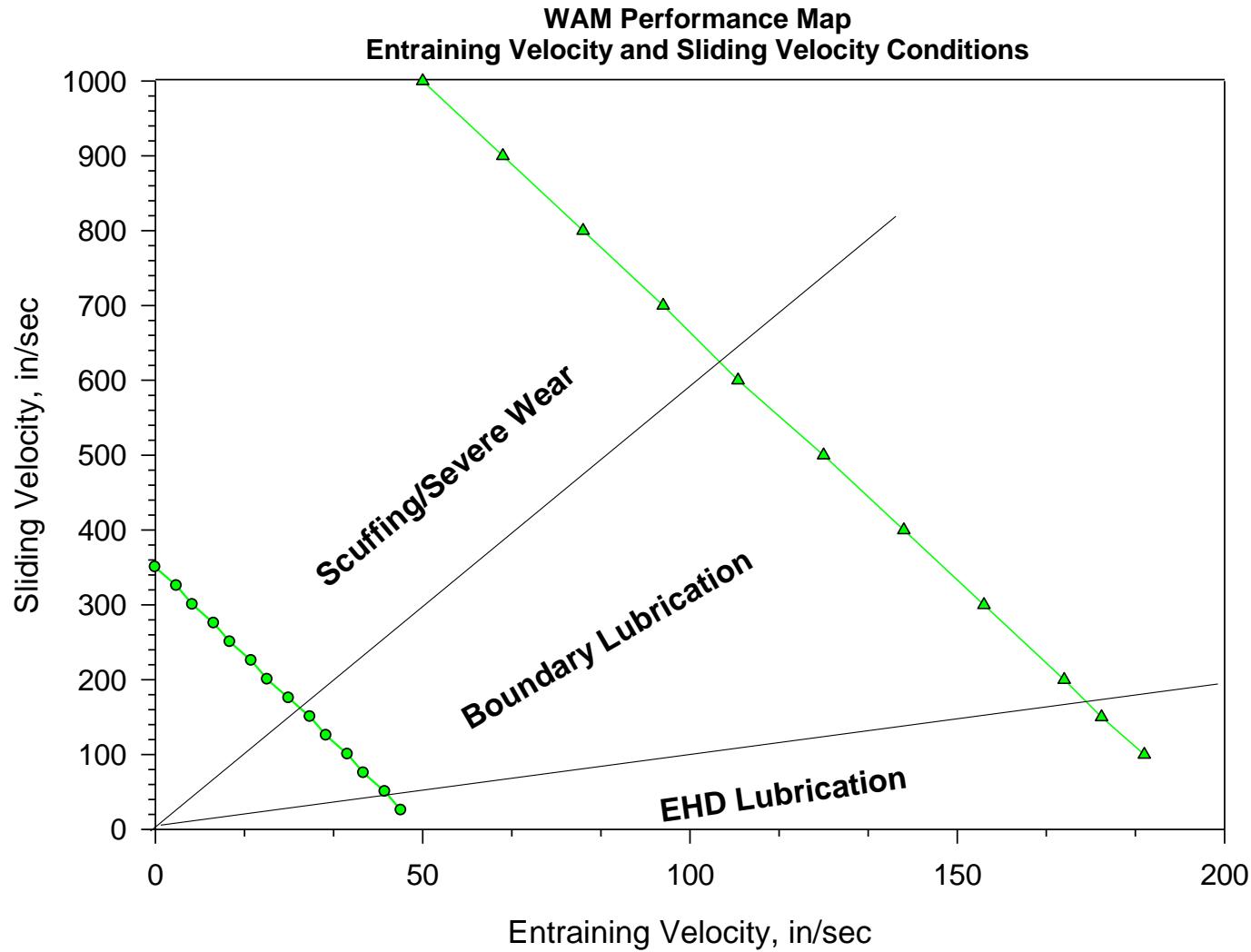
Appendix WPM – Gear Simulation Testing: Wedeven Performance Mapping (PM) Results

PM Test Parameters and Matrix (Hot Scuffing Series)

13 Stages, Load 344N (1.95 GPa contact stress), Royco 555 oil

Stage	Skew	Ball spd <u>(m/sec)</u>	Disc Spd <u>(m/sec)</u>	Sliding Spd <u>(m/sec)</u>	Ue <u>m/sec</u>
1	30.3	4.88	4.88	2.54	4.70
2	45.8	4.89	4.89	3.81	4.50
3	61	5.00	5.00	5.08	4.32
4	88	5.49	5.49	7.62	3.94
5	110	6.20	6.20	10.16	3.56
6	126.7	7.10	7.10	12.70	3.18
7	140	8.10	8.10	15.24	2.77
8	149.5	9.21	9.21	17.78	2.41
9	157.3	10.36	10.36	20.32	2.03
10	163.6	11.55	11.55	22.86	1.65
11	168.5	12.77	12.77	2.54	1.27
12	172.7	14.00	14.00	27.90	0.89
13	176.2	15.24	15.24	30.50	0.51

Appendix WPM – Gear Simulation Testing: Wedeven Performance Mapping (PM) Results

PM Test Parameters and Matrix (Lubrication Regimes for Cold and Hot Scuffing Series)

Appendix WPM – Gear Simulation Testing: Wedeven Performance Mapping (PM) Results

Arcomac PM Test Matrix – Fall 2008

Test	Test ID #'s	Ball ID	Ball Coating	Ball RMS [uinch]	Disc ID	Disc Coating	Disc RMS [uinch]	Oil Type
Cold Scuffing	WAM80965-974	WB-13a	TiCr-TiCrN (Dep1)	~14	WD 4-C	CrC (Dep2)	6	Royco 555 Grade 5
Hot Scuffing	WAM80975-985	WB-13b	TiCr-TiCrN (Dep1)	~14	WD 4-C	CrC (Dep2)	6	Royco 555 Grade 5
Cold Scuffing	WAM80990 -993	WB-8a	TiCr-TiCrN (Dep2)	~14	WD 1-C	Cr-CrN (Dep1)	6	Royco 555 Grade 5
Hot Scuffing	WAM80994 -998	WB-8b	TiCr-TiCrN (Dep2)	~14	WD 1-C	Cr-CrN (Dep1)	6	Royco 555 Grade 5

Rolls Royce PM Test Matrix – Fall 2008 (baseline P675 characterization)

Test	Test ID #'s	Ball ID	Ball Coating	Ball RMS [uinch]	Disc ID	Disc Coating	Disc RMS [uinch]	Oil Type
Cold Scuffing	RR proprietary	P675 ground	n/a	~11	P675 ground	n/a	8	Royco 555 Grade 5
Hot Scuffing	RR proprietary	P675 ground	n/a	~11	P675 ground	n/a	8	Royco 555 Grade 5
Cold Scuffing	RR proprietary	P675 super-finished	n/a	~4	P675 super-finished	n/a	2	Royco 555 Grade 5
Hot Scuffing	RR proprietary	P675 super-finished	n/a	~4	P675 super-finished	n/a	2	Royco 555 Grade 5

Appendix WPM – Gear Simulation Testing: Wedeven Performance Mapping (PM) Results

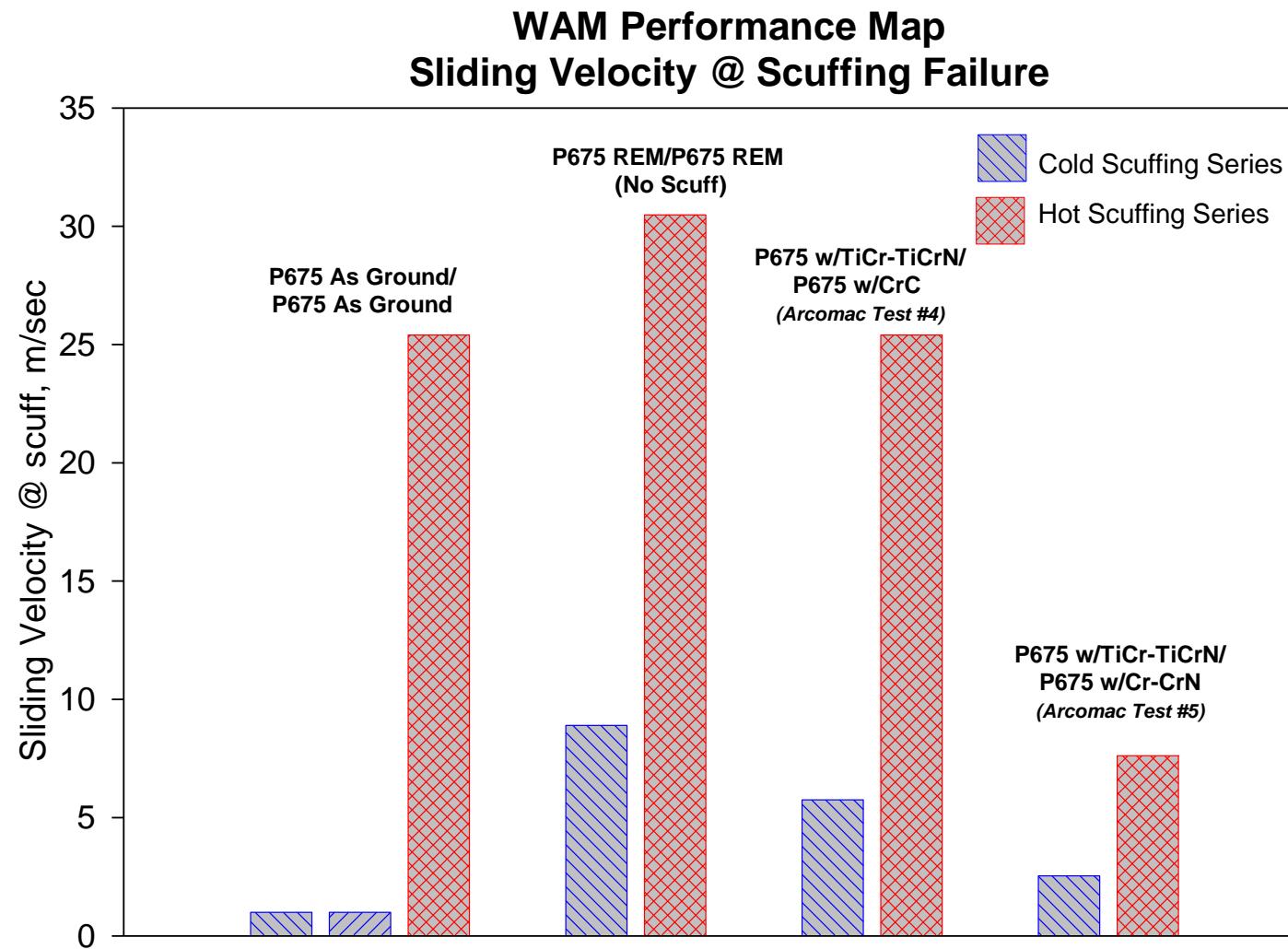
PM Test Method - Results Summary

Test Series	Ball	Disc	Sliding Velocity [m/sec]	Entrainig Velocity [m/sec]	Lubrication Regime	Stage @ Failure
Cold-Scuffing	TiCr-TiCrN (Dep1)	CrC (Dep2)	5.71	0.46	Boundary	4
Hot-Scuffing	TiCr-TiCrN (Dep1)	CrC (Dep2)	25.4	1.27	Wear	11
Cold-Scuffing	TiCr-TiCrN (Dep2)	Cr-CrN (Dep1)	2.5	0.91	Boundary	4
Hot-Scuffing	TiCr-TiCrN (Dep2)	Cr-CrN (Dep1)	7.6	3.9	Boundary	4
Cold-Scuffing	P675 (ground finish)	P675 (ground finish)	1.3	1.1	EHD/Boundary	2
Hot-Scuffing	P675 (ground finish)	P675 (ground finish)	25.4	1.27	Wear	11
Cold-Scuffing	P675 (super-finish)	P675 (super-finish)	8.3	0.1	Wear	13
Hot-Scuffing	P675 (super-finish)	P675 (super-finish)	n/a	n/a	Wear	>13, No Failure

Notes

1. The CrC coating in contact with the TiCr-TiCrN coating posts better results over the P675 ground-finish contact pair and does not perform as well as super-finished P675. In particular the ground-finish P675 performed very poorly in the cold scuffing series, failing just as the transition to boundary wear is made (a duplicate test was run to confirm this result). The Cr-CrN coating in contact with the TiCr-TiCrN coating performs marginally; both the hot and cold scuffing series see failures relatively early into the boundary lubrication regime. The CrC coating performs well and fails at stages well into the severe wear lubrication regime. The super-finished P675 contact pair performed exceptionally; failure occurred at stage 13 of 14 for the cold scuffing series and no failure (test suspension) occurred for the hot scuffing series.
2. Surface roughness plays an important role in PM testing but it is difficult to determine the weighted affect of surface roughness on the PM test results as compared to material composition. The super-finished P675 contact pairs have a lower starting roughness than any of the other sample pairs which shifts the transition to boundary and wear lubrication regimes to higher test stages which could in part or in whole explain the good results. Conversely it can also be assumed that continual asperity wear that occurs during boundary lubrication regime stages of PM testing likely improves surface finish (polishing wear) making failure hypothesis based on initial surface roughness in part or in whole irrelevant. A failure hypothesis based on material combination must take into account oil chemistry and considering that Royco 555 oil is designed to react with Fe based alloys it is not difficult to assume that beneficial oil chemistry may not occur with the Ti, Cr, N, and C based coatings. The lower performance of the coatings in the PM testing versus the super-finished P675, which are known to greatly out-perform super-finished P675 in dry sliding wear tests, is likely due to a combination if increased surface roughness and non-existent or limited beneficial oil chemistry.

Appendix WPM – Gear Simulation Testing: Wedeven Performance Mapping (PM) Results



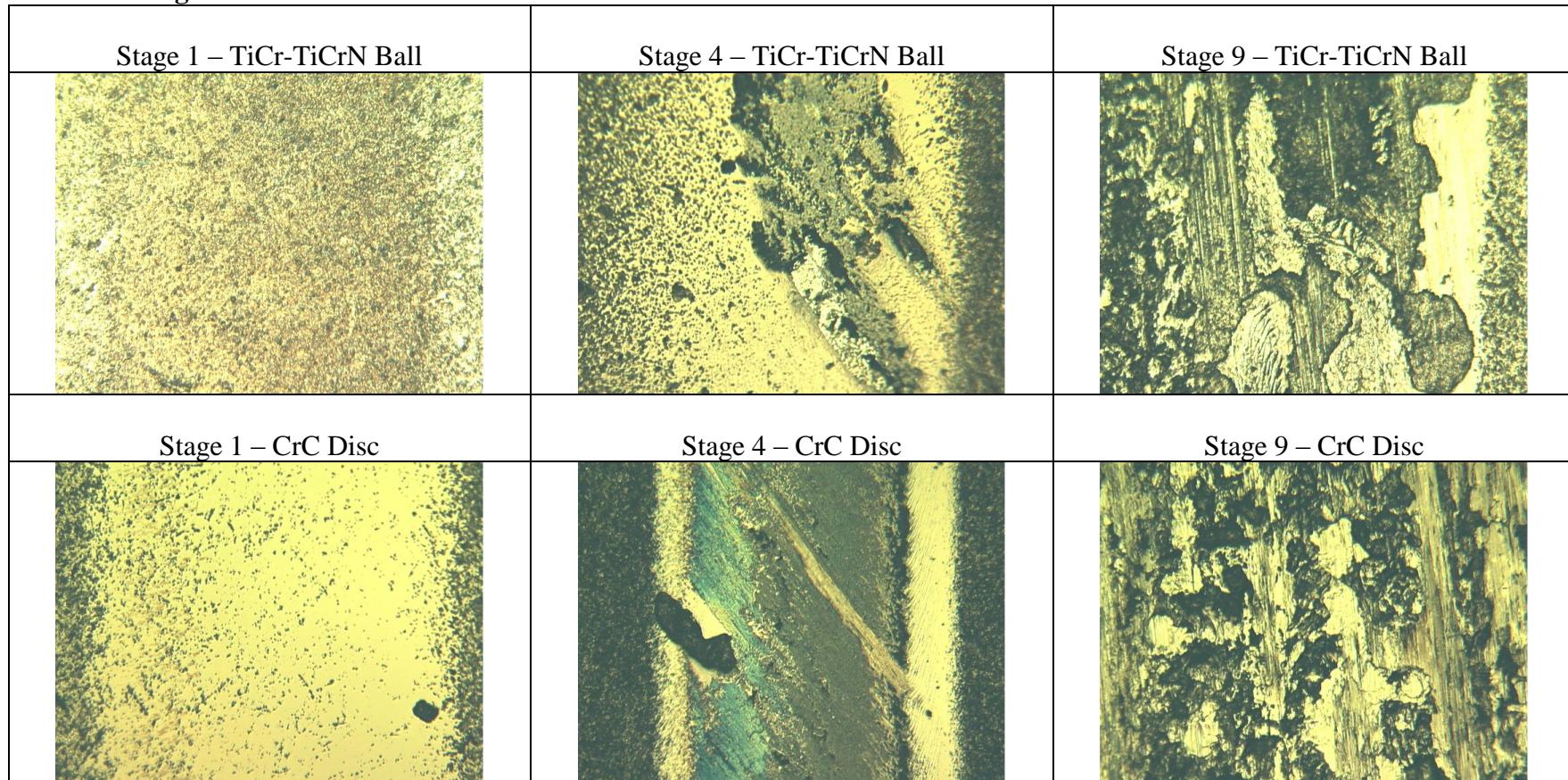
Appendix WPM – Gear Simulation Testing: Wedeven Performance Mapping (PM) Results

PM Test Method – Detailed Results: TiCr-TiCrN (ball) vs. CrC (disc)**Cold Scuffing Series**

Stage	Ball	Disc	Sliding Velocity [m/sec]	Entraining Velocity [m/sec]	Average Traction Coefficient	Comments
1	TiCr-TiCrN (Dep1)	CrC (Dep2)	0.635	1.1684	0.0613	
2	TiCr-TiCrN (Dep1)	CrC (Dep2)	1.27	1.0922	0.0473	
3	TiCr-TiCrN (Dep1)	CrC (Dep2)	1.905	0.9906	0.0408	
4	TiCr-TiCrN (Dep1)	CrC (Dep2)	2.54	0.9144	0.0771	Significant Wear Begins*
5	TiCr-TiCrN (Dep1)	CrC (Dep2)	3.175	0.8128	0.0665	
6	TiCr-TiCrN (Dep1)	CrC (Dep2)	3.81	0.7366	0.0512	
7	TiCr-TiCrN (Dep1)	CrC (Dep2)	4.445	0.635	0.0705	
8	TiCr-TiCrN (Dep1)	CrC (Dep2)	5.08	0.5334	0.0804	
9	TiCr-TiCrN (Dep1)	CrC (Dep2)	5.715	0.4572	0.0896	Macro-scuff Failure (friction spike)

*Microscope images of ball and disc wear tracks are made after each test. After Stage 4 isolated cohesive delaminations on the TiCr-TiCrN ball can be observed. After stage 6 cracks in the TiCr-TiCrN ball coating can be observed along with isolated delaminations in the CrC coating. By stage 8 the damage to both coatings appears severe but the testing protocol is to denote failure by a macro-scuff event which occurred in stage 9. In terms of surface integrity this test could be stated to have failed at stage 4.

Appendix WPM – Gear Simulation Testing: Wedeven Performance Mapping (PM) Results

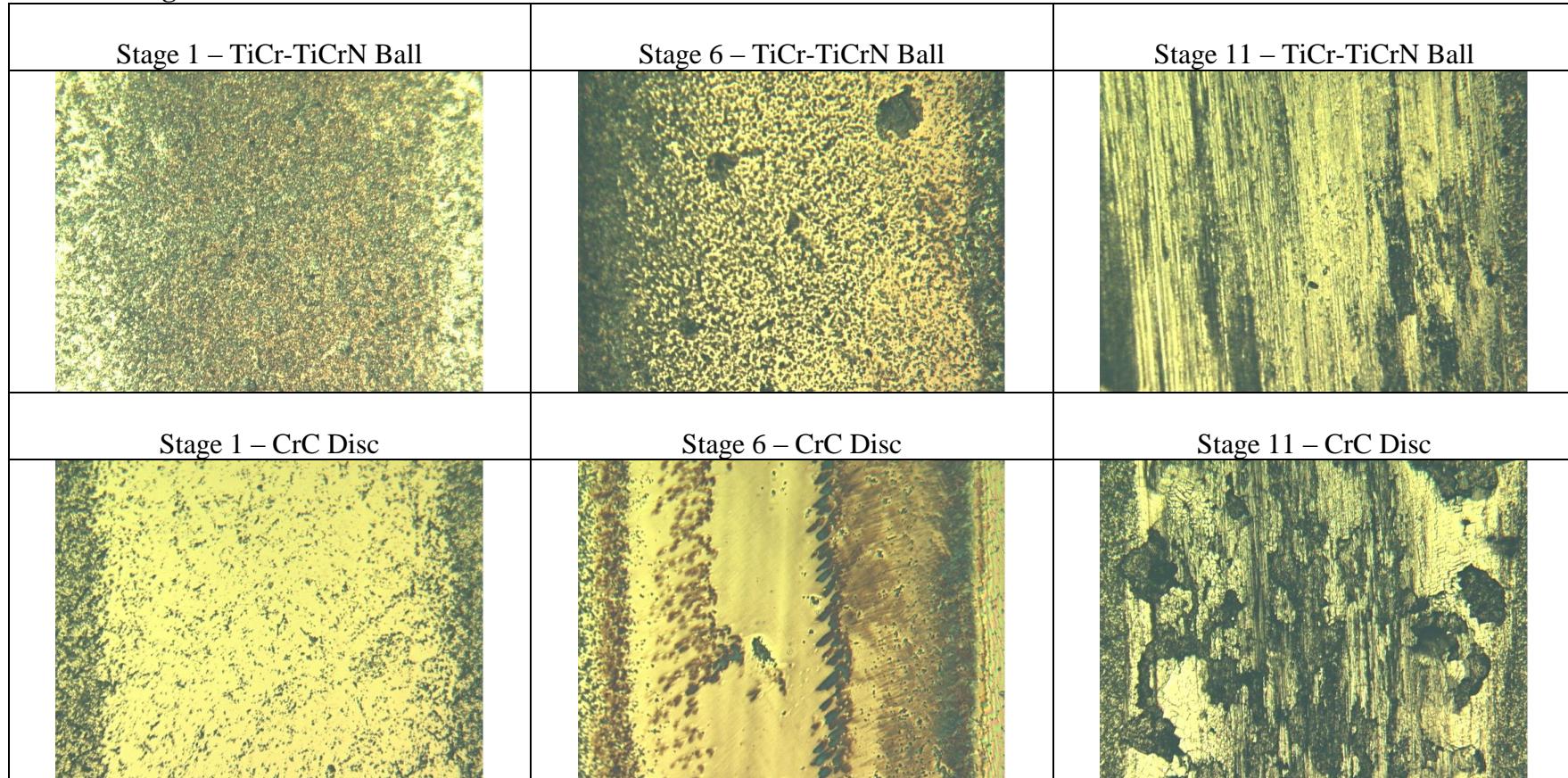
PM Test Method – Detailed Results: TiCr-TiCrN (ball) vs. CrC (disc)**Cold Scuffing Series**

Appendix WPM – Gear Simulation Testing: Wedeven Performance Mapping (PM) Results

PM Test Method – Detailed Results: TiCr-TiCrN (ball) vs. CrC (disc)**Hot Scuffing Series**

Stage	Ball	Disc	Sliding Velocity [m/sec]	Entraining Velocity [m/sec]	Average Traction Coefficient	Comments
1	TiCr-TiCrN (Dep1)	CrC (Dep2)	2.54	4.70	0.040	
2	TiCr-TiCrN (Dep1)	CrC (Dep2)	3.81	4.50	0.033	
3	TiCr-TiCrN (Dep1)	CrC (Dep2)	5.08	4.32	0.032	
4	TiCr-TiCrN (Dep1)	CrC (Dep2)	7.62	3.94	0.029	
5	TiCr-TiCrN (Dep1)	CrC (Dep2)	10.16	3.56	0.033	
6	TiCr-TiCrN (Dep1)	CrC (Dep2)	12.70	3.18	0.032	
7	TiCr-TiCrN (Dep1)	CrC (Dep2)	15.24	2.77	0.029	
8	TiCr-TiCrN (Dep1)	CrC (Dep2)	17.78	2.41	0.023	
9	TiCr-TiCrN (Dep1)	CrC (Dep2)	20.32	2.03	0.030	
10	TiCr-TiCrN (Dep1)	CrC (Dep2)	22.86	1.65	0.024	
11	TiCr-TiCrN (Dep1)	CrC (Dep2)	25.40	1.27	0.023	Macro-scuff Failure (friction spike)

Appendix WPM – Gear Simulation Testing: Wedeven Performance Mapping (PM) Results

PM Test Method – Detailed Results: TiCr-TiCrN (ball) vs. CrC (disc)**Hot Scuffing Series**

Appendix WPM – Gear Simulation Testing: Wedeven Performance Mapping (PM) Results

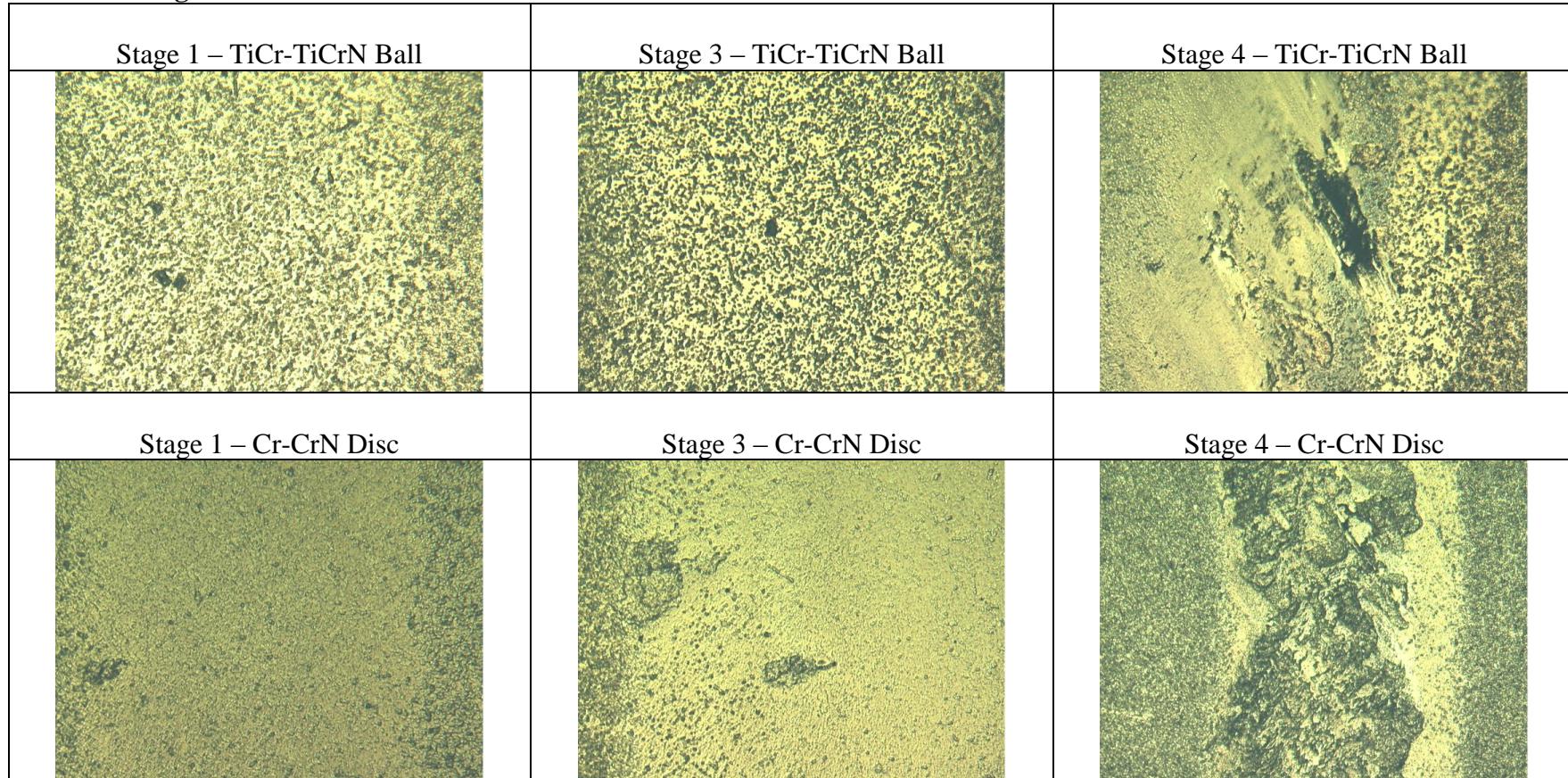
PM Test Method – Detailed Results: TiCr-TiCrN (ball) vs. Cr-CrN (disc)**Cold Scuffing Series**

Stage	Ball	Disc	Sliding Velocity [m/sec]	Entrainig Velocity [m/sec]	Average Traction Coefficient	Comments
1	TiCr-TiCrN (Dep2)	Cr-CrN (Dep1)	0.635	1.1684	0.060	
2	TiCr-TiCrN (Dep2)	Cr-CrN (Dep1)	1.27	1.0922	0.052	
3	TiCr-TiCrN (Dep2)	Cr-CrN (Dep1)	1.905	0.9906	0.041	
4	TiCr-TiCrN (Dep2)	Cr-CrN (Dep1)	2.54	0.9144	0.030	Macro-scuff Failure (friction spike)

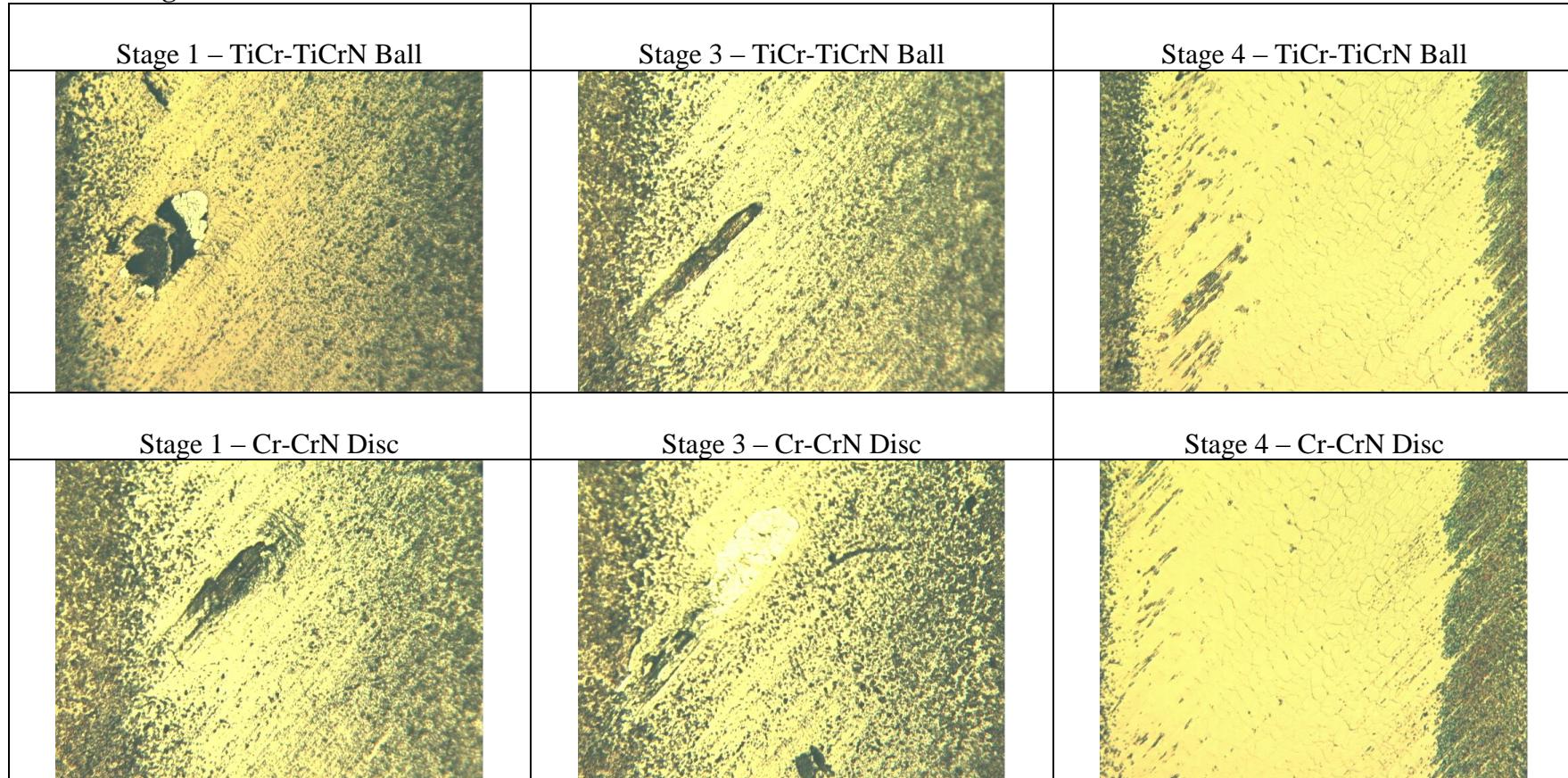
Hot Scuffing Series

Stage	Ball	Disc	Sliding Velocity [m/sec]	Entrainig Velocity [m/sec]	Average Traction Coefficient	Comments
1	TiCr-TiCrN (Dep2)	Cr-CrN (Dep1)	2.54	4.70	0.030	
2	TiCr-TiCrN (Dep2)	Cr-CrN (Dep1)	3.81	4.50	0.029	
3	TiCr-TiCrN (Dep2)	Cr-CrN (Dep1)	5.08	4.32	0.030	
4	TiCr-TiCrN (Dep2)	Cr-CrN (Dep1)	7.62	3.94	0.028	Macro-scuff Failure (friction spike)

Appendix WPM – Gear Simulation Testing: Wedeven Performance Mapping (PM) Results

PM Test Method – Detailed Results: TiCr-TiCrN (ball) vs. Cr-CrN (disc)**Cold Scuffing Series**

Appendix WPM – Gear Simulation Testing: Wedeven Performance Mapping (PM) Results

PM Test Method – Detailed Results: TiCr-TiCrN (ball) vs. Cr-CrN (disc)**Hot Scuffing Series**

Appendix XPS – Coating Structure, Phase and Grain Size Data

XPS analysis overview

1. The composition and bonding structure of the coatings were investigated using an X-ray photoelectron spectroscopy (XPS) instrument (PHI Model 5600ci, Casa XPS Analytical Software). A monochromatic Al K α x-ray source was used for all samples. The conditions used for the survey scans were as follows: energy range, 1100-0 eV; pass energy, 160 eV; step size, 0.7 eV; sweep time, 180 s; and x-ray spot size, 700 \times 400 μ m. For the high-resolution spectra, an energy range of 40-20 eV was used, depending on the peak being examined, with a pass energy of 10 eV and a step size of 0.05 eV.
2. All samples were sputter cleaned in Ar for 5min prior to data collection to remove near surface impurities such as oxides. Data presented for multilayered TiCr-TiCrN and Cr-CrN coatings represents the composition of the topmost TiCrN and CrN layers only. The analysis volume (i.e. depth) for XPS does not encompass the metallic TiCr or Cr layers. The ~6 μ m thick CrC coating is monolithic (with the exception of the bond Cr-CrN single bi-layer) and hence the analysis interaction volume concerns mentioned for multilayer coatings do not apply; the data presented represents the composition of the CrC coating only.
3. In order to characterize the composition and bonding structure of the TiCr-TiCrN, Cr-CrN, and CrC coatings, high-resolution spectra of Ti 2p, N 1s, Cr 2p, and C 1s, were collected and fitted using the Gaussian function. All spectra were calibrated using the adventitious C 1s peak with a fixed value of 284.6 eV. The background from each spectrum was subtracted and the area of under each peak was used to calculate the coating composition using relative sensitivity factors from the manufacturer's handbook: Ti (1.798), N (0.477), Cr (2.201), and C (0.296).
4. One sample for each coating type, i.e. TiCr-TiCrN, Cr-CrN, and CrC as deposited on super-finished P675 was analyzed. After the first analysis where oxygen was found to be present in the coating a second set of data was collected on different Cr-CrN and CrC samples. Sputter time was increased to 20min (~30nm of coating removed) and atomic percent quantification was re-calculated with oxygen included.

Appendix XPS – Coating XPS Data

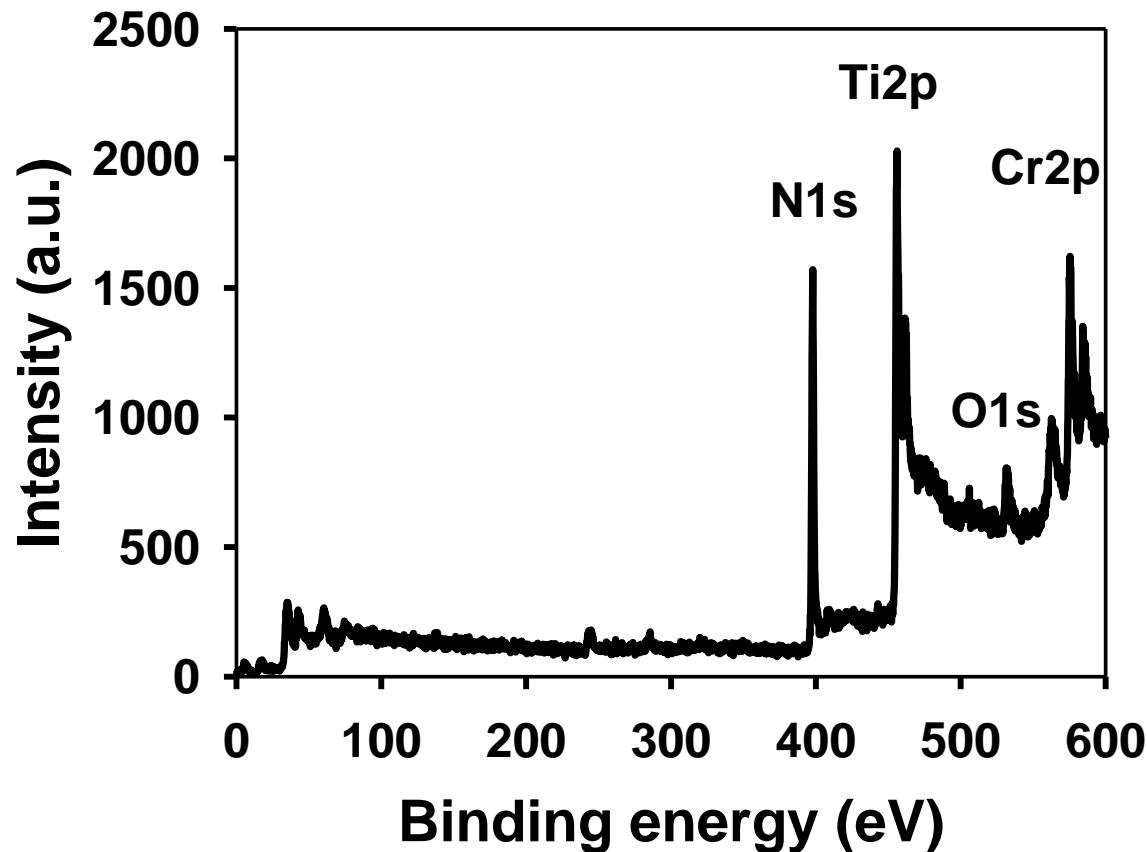
XPS Results Summary**Substrate - Pyrowear 675 (REM super-finish, RMS = 50nm [2 μ inch], HRC-64)**

Coating	Coating ID	Sample ID	Atomic % Concentration				
			Ti	Cr	N	C	O
TiCr-TiCrN*	ASE-8-14-1 (Dep2)		37.8	19.8	42.4	n/a**	n/a**
Cr-CrN	ASE-8-29-1 (Dep1)	SF2	-	64.5	35.5	n/a**	n/a**
Cr-CrN	ASE-8-34-1 (Dep2)	P3	-	55.8	34.1	4.1	6.0
CrC	ASE-8-19-1 (Dep1)	P74	-	63.3	-	36.7	n/a**
CrC	ASE-8-26-1 (Dep2)	P57	-	62.8	-	34.9	2.3

*Ratio of Ti/Cr in TiCr-TiCrN Coating = 1.91, Ratio of Ti/Cr volumetric target erosion rate = 2.16

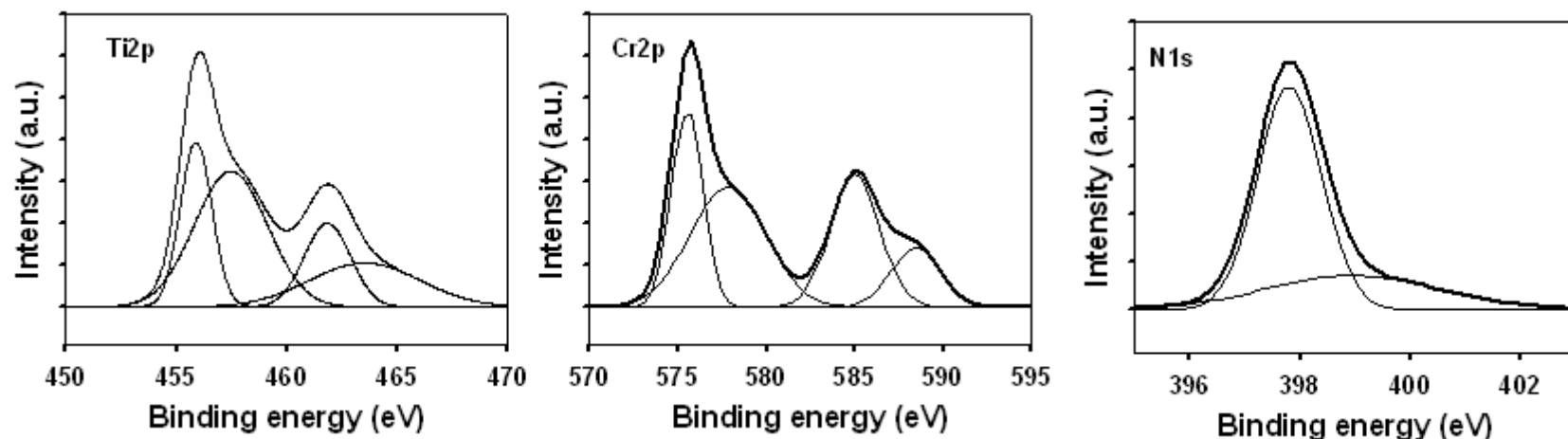
** For the first XPS analysis it was assumed oxygen content was coming from surface oxides and oxygen was not included in the quantification. A second analysis conducted at increased sputter depth confirmed low concentrations of oxygen and carbon contamination in the Cr-CrN and CrC coatings (TiCr-TiCrN not measured, assumed to have similar oxygen and carbon content).

Appendix XPS – Coating XPS Data



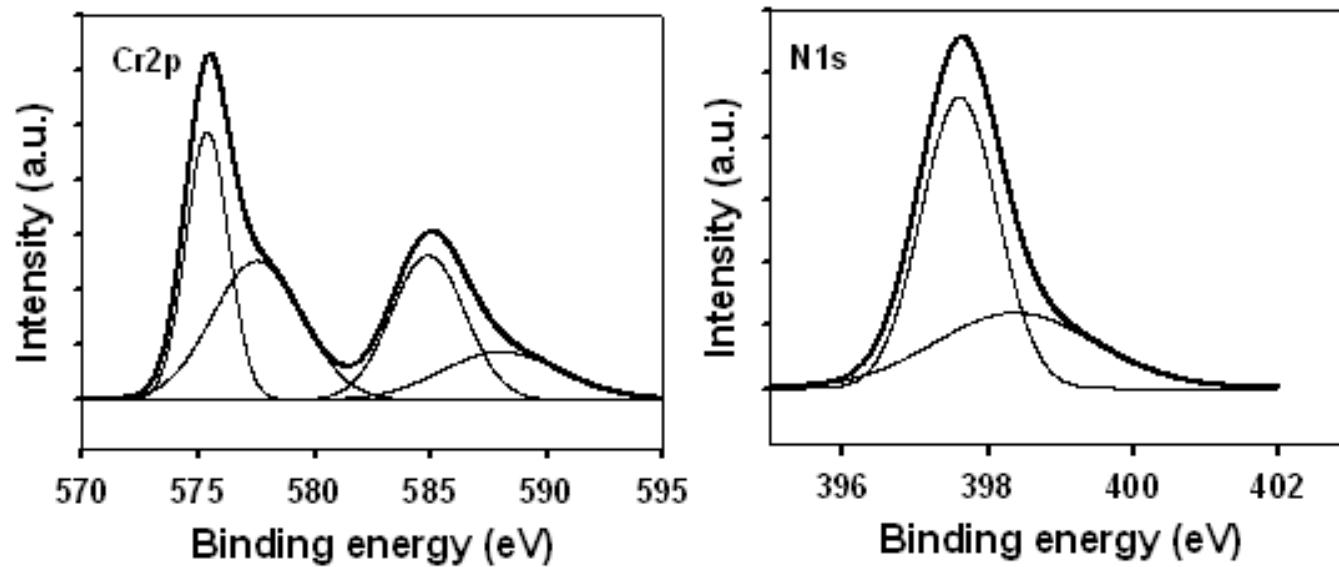
XPS survey spectrum of a TiCrN coating layer. The spectrum consists of three strong peaks corresponding to N 1s, Ti 2p, and Cr 2p, and a weak O1s peak. The area under Ti 2p, Cr 2p, and N 1s peaks were used to calculate the coating composition.

Appendix XPS – Coating XPS Data



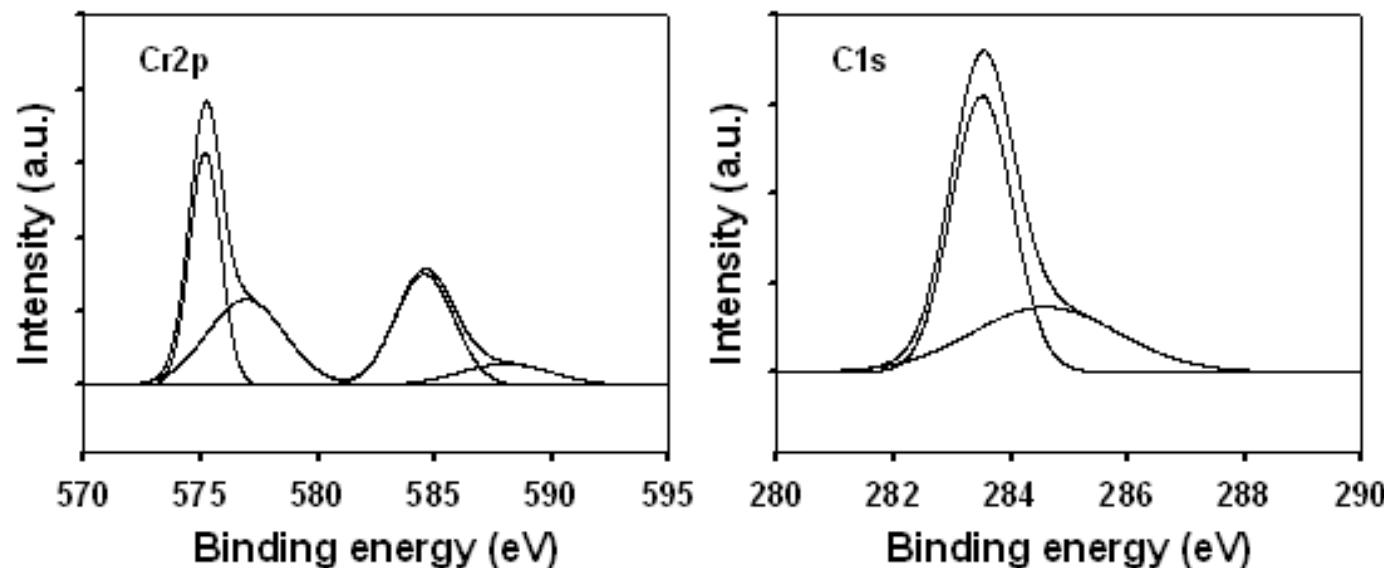
The above plots are high-resolution Ti 2p, Cr 2p, and N 1s XPS spectra of the TiCrN coating. The Ti 2p spectra could be fitted with four Gaussian functions as shown in the figure. The binding energy of the four peaks is centered at 455.9, 457.5, 461.8, and 463.5 eV, respectively. The first and third main peaks correspond to the Ti $2p_{3/2}$ splitting and their respective $2p_{1/2}$ splitting, respectively, of the TiN phase. The second and forth shoulder peaks are inherent characteristic features of TiN phase, but it can't rule out the contribution of the Ti-O bonds in the intermediate phases. The Cr 2p spectrum was also fitted well with 4 peaks centered at 575.2, 577.8, 585.0, and 588.4 eV, respectively, of the CrN phase. According to reference [P.L. Tam, Z.F. Zhou, P.W. Shum, K.Y. Li, Thin Solid Films 516(2008)5725], the first and third peaks are attributed to the Cr $2p_{3/2}$ splitting and their respective $2p_{1/2}$ splitting, respectively. The second and forth peaks results from the Cr_2O_3 . No peaks from Cr or Cr_2N can be observed. The N 1s XPS spectrum can be fitted with 2 peaks at 397.8 and 398.9 eV. The first peak can be attributed to the nitrides (Ti-Cr-N, TiN, or CrN), and the second peak was attributed to the synergistic effect of the oxygen, titanium, and the nitrogen atoms in the coatings.

Appendix XPS – Coating XPS Data



The above plots are high resolution Cr 2p and N 1s XPS spectra of the CrN coating. The Cr 2p spectrum can be fitted well with 4 peaks centered at 575.4, 577.5, 584.9, and 588.0 eV. The first and third peaks correspond to the Cr 2p_{3/2} and Cr 2p_{1/2} splitting, respectively, of the CrN phase, and the second and forth peaks result from the Cr₂O₃. No peaks from Cr or Cr₂N can be observed. The N 1s spectrum was fitted using 2 peaks centered at 397.6 and 398.4 eV, which were attributed to the CrN and CrNO, respectively.

Appendix XPS – Coating XPS Data



The above plots show the high resolution Cr 2p and C 1s XPS spectra of the CrC coating. The Cr 2p spectrum can be fitted well with 4 peaks centered at 575.2, 576.9, 584.5, and 588.0 eV. The first and third peaks correspond to the Cr 2p_{3/2} and Cr 2p_{1/2} splitting, respectively, of the CrC phase, and the second and forth peaks arise from the Cr₂O₃. The C 1s spectrum was fitted using 2 peaks centered at 283.5 and 284.6 eV. The first peak is attributed to carbide peak, while the peak at 284.6 eV corresponds to the amorphous carbon peak. The high intensity of the first peak indicates that most of the carbon in the coating exists as C-Cr bond.

Appendix XRD – Coating Structure, Phase and Grain Size Data

XRD analysis overview

1. Coating structure, phase and grain size identification analysis was subcontracted to Evans Analytical Group Labs (EAG). Job Number: T08V9336, work performed by Delrose Winter Senior Scientist, XRD.
2. Data was collected on the Rigaku Ultima III in standard θ : 2θ coupled focusing mode, with CuKa radiation with a standard wavelength of 1.54051nm, with variable slits and no diffracted beam monochromator. Data was also collected on the Panalytical X'pert system in GI (Grazing Incidence) mode with parallel beam, with a GI incident angle of 0.9°. The most representative data is included in the report.
3. Phase identification is accomplished by searching the ICDD/ICSD data base to obtain the best matches on the standard materials from the ICDD/ICSD data base. All compounds (phases) are not present in the data base, so in some cases a good match can not be obtained. Since XRD is not used to determine the chemistry, it is likely that the exact formulas of the phase(s) present are somewhat different, this is particularly true for the Cr/N or Cr/Ti ratios of the tested coatings.
4. The broadening of an observed diffraction peak can be characterized in a simplistic way by its FWHM (Full Width at Half Maximum) value at a particular 2θ angle. Because the apparent FWHM of a peak is a mathematical combination (convolution) of the specimen broadening FW(S) and the instrumental broadening FW(I), instrumental broadening is subtracted from that of the observed diffraction peak. If the crystallites (i.e., crystalline domains) in the specimen are free of lattice strain, their average size can be estimated from the specimen broadening FW(S) of any single peak in the observed pattern according to the Scherrer formula:
$$\text{Crystallite Size} = K \cdot 1 / (FW(S) \cdot \cos(\theta))$$
where θ is the peak position, and K is the shape factor of the average crystallite.
5. One sample for each coating type, i.e. TiCr-TiCrN, Cr-CrN, and CrC as deposited in super-finished P675 was analyzed.

Appendix XRD – Coating XRD Data

Results Summary**Substrate - Pyrowear 675 (REM super-finish, RMS = 50nm [2μinch], HRC-64)**

Coating	Coating ID	Sample ID	Crystalline Structure	Best Match ICDD/ICSD Phase ID	Second Best Match ICDD/ICSD Phase ID	Crystal Size <111> [nm]	Crystal Size <200> [nm]
TiCr-TiCrN	ASE-8-14-1 (Run2)	P47	FCC	Ti _{0.5} Cr _{0.5} N	TiN _{0.9}	23.5	14.0
Cr-CrN	ASE-8-29-1 (Run1)	P74	FCC	CrN	n/a	11.7	16.7
CrC	ASE-8-19-1 (Run1)	P43	amorphous	n/a	n/a	n/a	n/a

TiCr-TiCrN Coating

The TiCr-TiCrN coating is Face Centered Cubic, with a formula similar to (although not exactly) Ti_{0.5}Cr_{0.5}N, as shown in the table above. The TiCr-TiCrN coating shows no preferred orientation. A significant line shift from the standard ICDD/ICSD card for Cr_{0.5}Ti_{0.5}N suggests a slightly different Cr/Ti ratio (page #XRD_4). FCC TiNx match is almost as good (almost equal Figure of Merit) to that of the Cr_{0.5}Ti_{0.5}N phase. Therefore, TiNx Osbornite is listed under the “Second best match” column above. Phase identification for hexagonal and/or BCC pure Ti or Cr were negative, indicating no crystalline metallic phases are present in the coating (page #XRD_4).

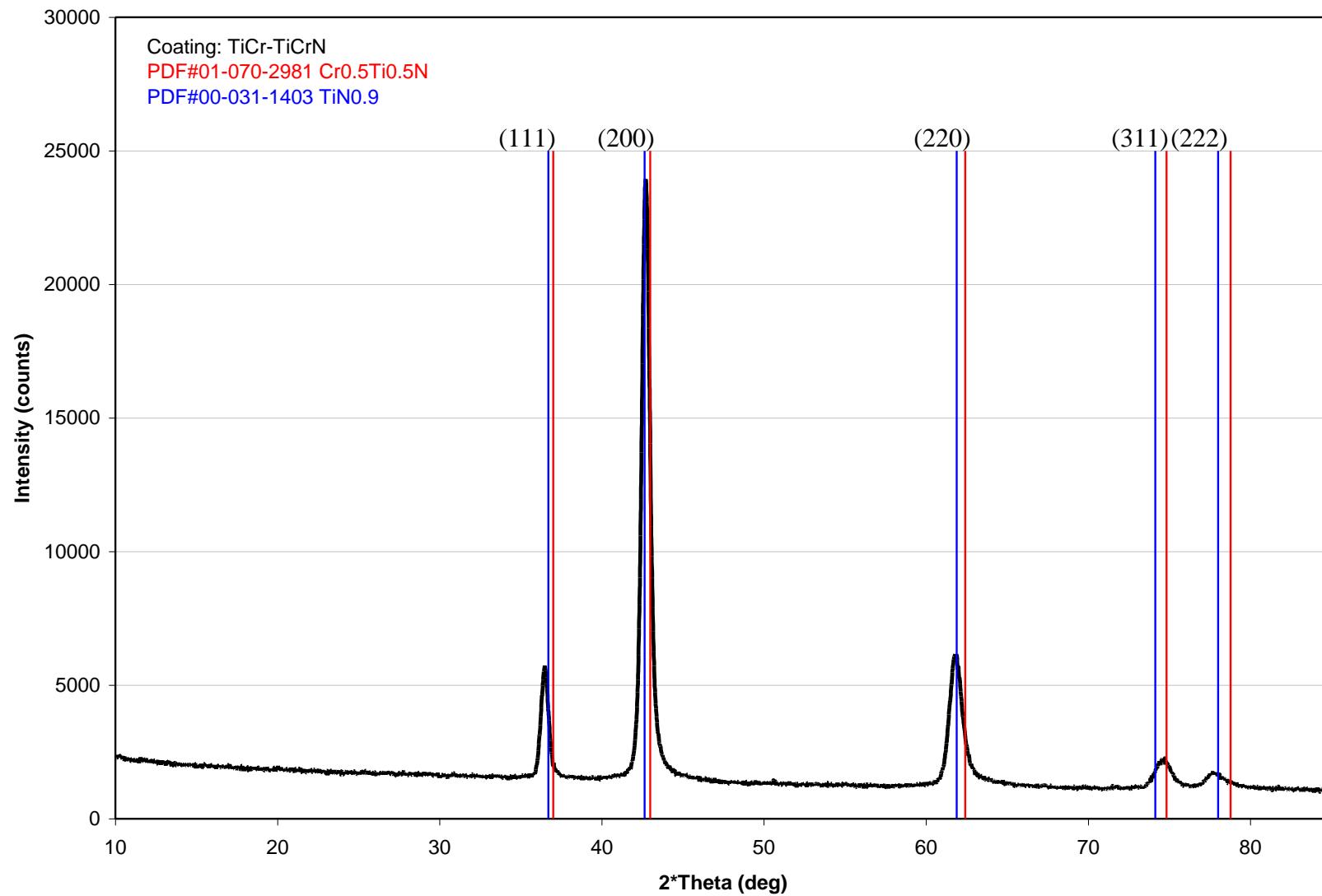
Cr-CrN Coating

The Cr-CrN coating is also Face Centered Cubic, with the best ICDD/ICSD phase match being on CrN, although this match shows significant line shift from the card. The next closest phase match is actually Ti_{0.5}Cr_{0.5}N, but given that there is no Ti in this coating the phase shift is most likely indicative of a different chemical Cr/N ratio. Using standard grazing incidence data collection methods the Cr-CrN coatings shows a strong preferred orientation on the (200) plane (page #XRD_5). A 2D detector and x-ray point source was also used to generate a higher resolution scan which allowed for better certainty with CrN phase identification (page #XRD_6). Phase identification for BCC pure Cr was negative, indicating no crystalline metallic phases are present in the coating (page #XRD_6).

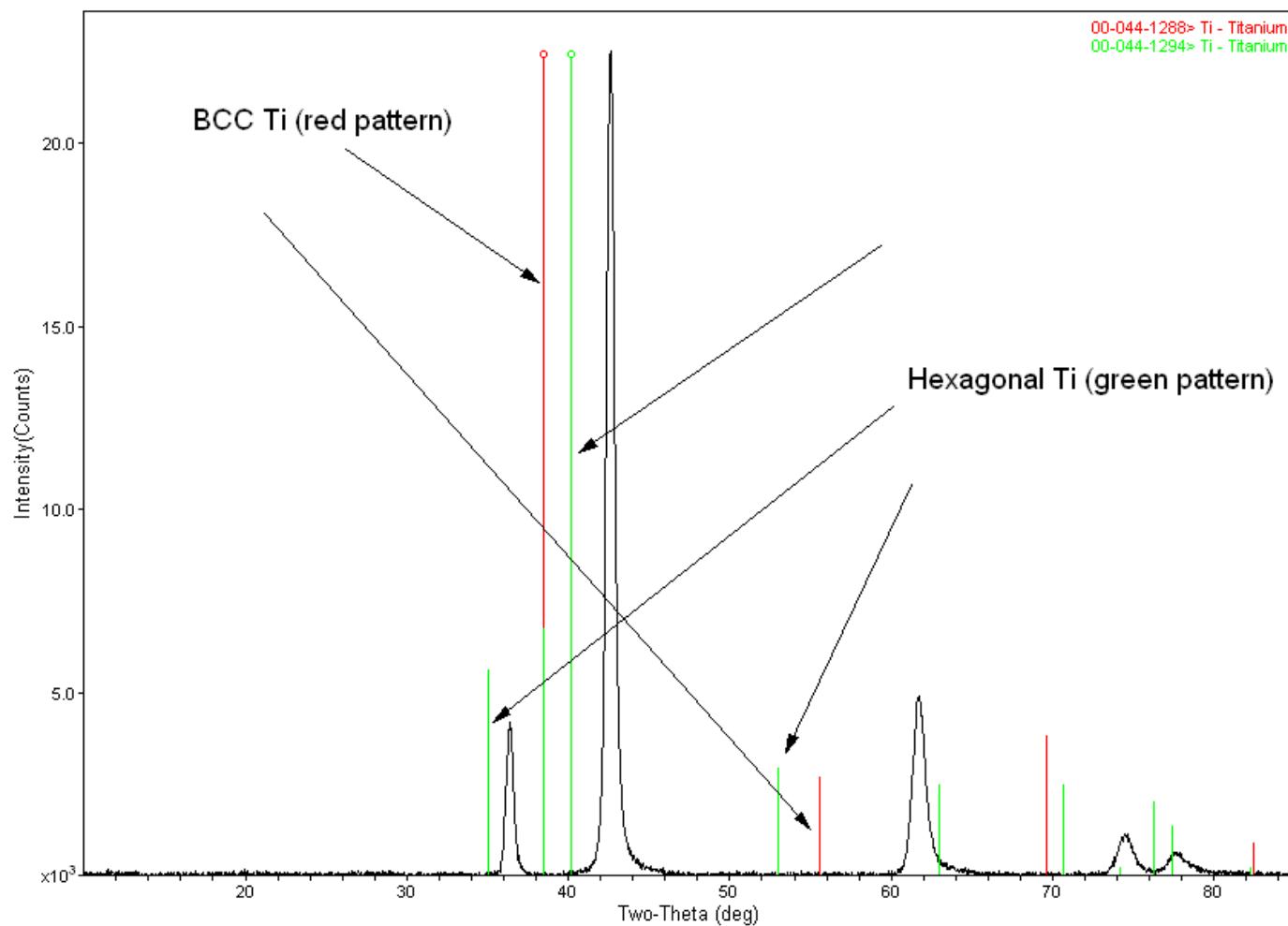
CrC Coating

The CrC coating is primarily amorphous. No clear crystalline peaks are observed (page #XRD_7), and the one broad peak that is shown in the plot below is too broad to be considered crystalline. It may be that the coating has too small a crystallite size to observe distinct lattice spacing. It is possible that crystallites are beginning to form, but have not formed three dimensional crystallites with reasonable unit cell stacking order in three dimensions. Percent crystallinity measurements were not performed.

Appendix XRD – Coating XRD Data

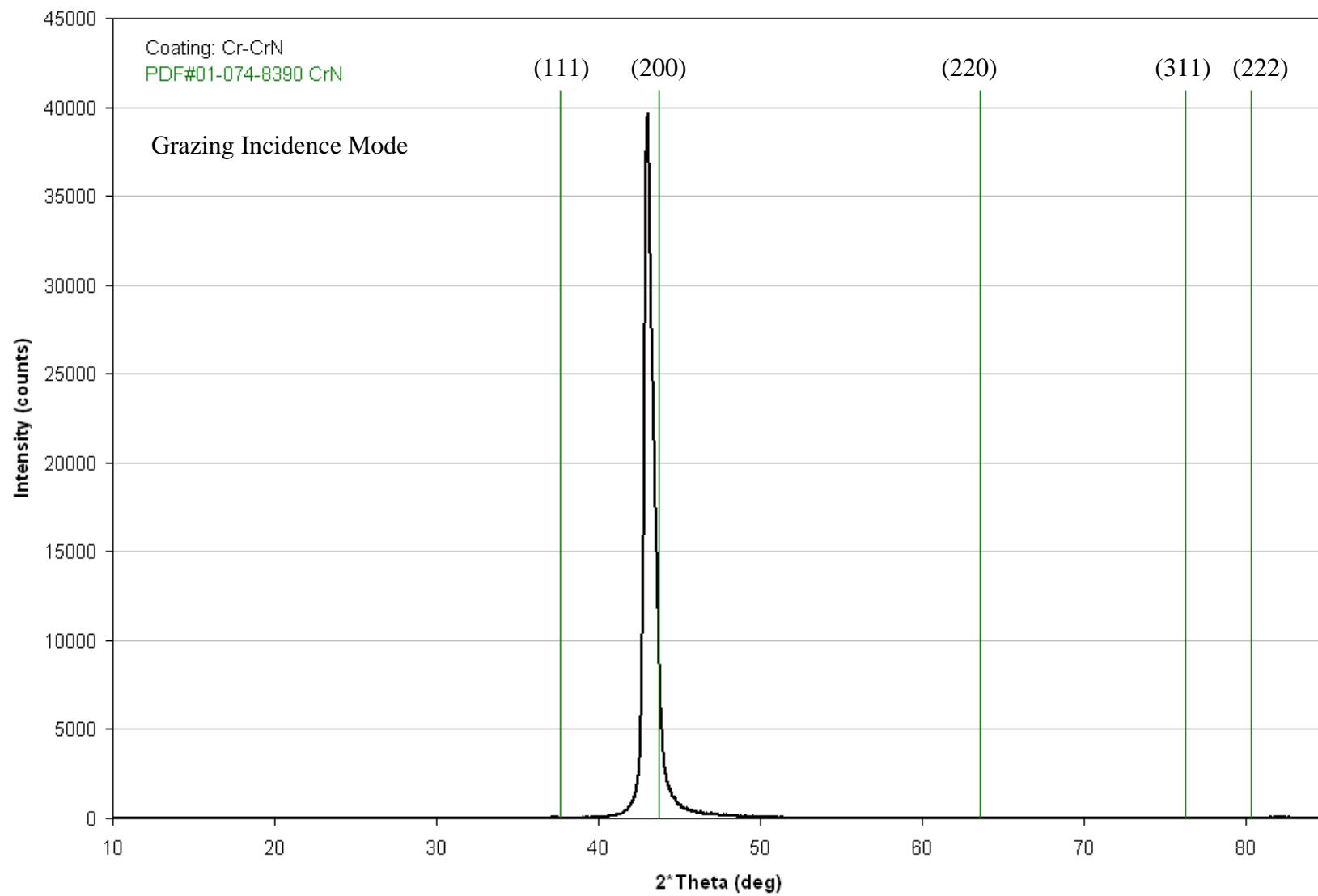


Appendix XRD – Coating XRD Data

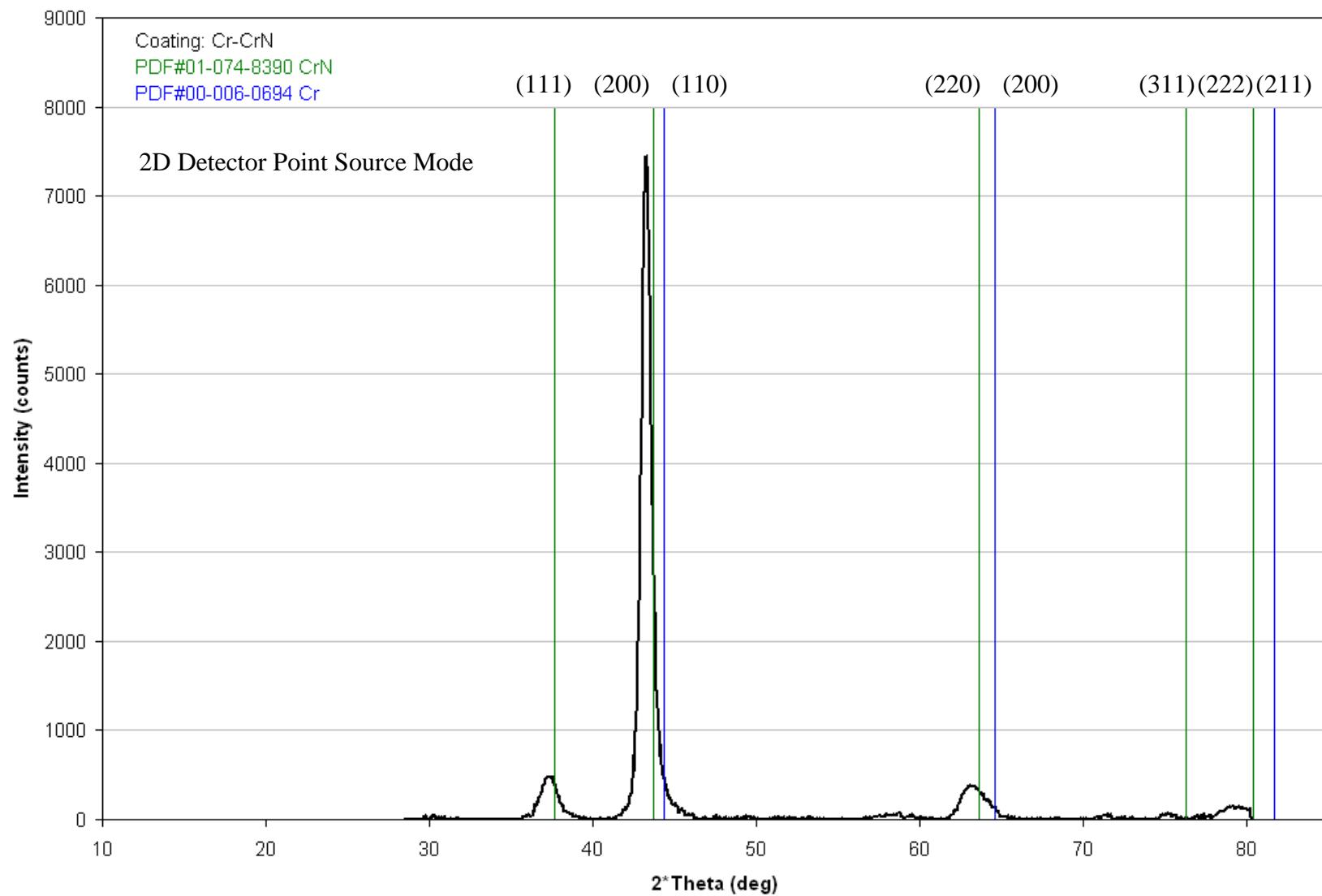


TiCr-TiCrN coating with phase patterns for BCC Ti and HCP Ti
No evidence of metallic phases in the coating

Appendix XRD – Coating XRD Data



Appendix XRD – Coating XRD Data



Appendix XRD – Coating XRD Data

